Olena Fesenko
Leonid Yatsenko
Mikhaylo Brodin   *Editors*

Nanomaterials Imaging Techniques, Surface Studies, and Applications

Selected Proceedings of the FP7 International Summer School Nanotechnology: From Fundamental Research to Innovations, August 26–September 2, 2012, Bukovel, Ukraine

Springer

Springer Proceedings in Physics

Volume 146

Olena Fesenko · Leonid Yatsenko
Mikhaylo Brodin
Editors

Nanomaterials Imaging Techniques, Surface Studies, and Applications

Selected Proceedings of the FP7 International
Summer School Nanotechnology: From
Fundamental Research to Innovations,
August 26–September 2, 2012,
Bukovel, Ukraine

Springer

Editors
Olena Fesenko
Leonid Yatsenko
Mikhaylo Brodin
Institute of Physics
National Academy of Sciences of Ukraine
Kiev
Ukraine

Preface

This book presents a selection of the latest developments in nanotechnology and nanomaterials. It features articles written by lecturers and young scientists from Europe, in particular from Ukraine, and the US who participated in the International Summer School "Nanotechnology: From Fundamental Research to Innovations," held in Bukovel, Ukraine from August 26 to September 2, 2012 within the framework of the FP7 project Nanotwinning. This International Summer School provided early-career scientists the opportunity to participate in a series of lectures on the emerging fields of nanoscience and nanotechnology. The International Summer School was hosted by the Institute of Physics of NAS of Ukraine in conjunction with its Nanotwinning project partners: University of Tartu (Estonia), European Profiles A.E. (Greece), University of Turin (Italy), and Pierre and Marie Curie University (France).

The beginning of the twenty first century witnessed tremendous breakthroughs in nanoscience and nanotechnology. Today, nanotechnology is used in computer technology and electronics; the aerospace, chemical, and construction industries; medicine and pharmacology; and in the manufacture of new unprecedented materials. The present volume surveys some of the latest advances in the field and points the way to exciting future investigations and applications. The book chapters cover such currently important topics as microscopy of nanostructures; nanocomposites; nanostructured interfaces and surfaces; nanooptics; nanoplasmonics; and enhanced vibrational spectroscopy. The book demonstrates that researching nanocarbons, nanosilicon, biomolecular nanostructures, and their applications is a very interesting and exciting area of modern science, which will certainly attract the attention of scientists and engineers for many years to come.

The book is divided into three parts: Part 1: *Imaging Techniques:Microscopy, Spectroscopy, and Lasers*; Part 2: *Interface Studies and Techniques*; and Part 3: *Nanocomposites and Applications of Nanotechnologies*.

An overview of the chapters is provided below. The reader is recommended to read the following descriptions first, as they provide insights into the book's contents and the results presented.

Part I: Imaging Techniques: Microscopy, Spectroscopy and Lasers

Chapter 1 (Rao), *Nano-Bio Architectures: Combining Chemistry and Biology in Nanotechnology* provides a summary of nanobiocomposites and an overview of the technical challenges in the development, purification, and characterization of biopolymers, and in their integration with other inert organic and inorganic chemical components in the fabrication of bionanocomposites. The chapter discusses the importance of the interactions between the functional components of active bionano structures with the inert layers in the development of biologically effective functional bionanocomposite architectures. A brief summary of current US and European regulations on the release of nanoparticles in the environment and current risk assessment approaches to measure potential adverse effects on public health and the ecosystem is also provided. Chapter 2 (Dovbeshko) presents a comparative analysis of the IR signal enhancement of biomolecules adsorbed on graphene and graphene oxide nanosheets. Chapter 3 (Kamnev) provides an overview of some representative examples related to the applications of modern Fourier transform infrared spectroscopy in nanobiotechnology-oriented fields, including spectroscopic aspects of the biofunctionalisation processes of gold nanoparticles and possibilities for the detection and study of various biospecific interactions ("recognising molecule–target molecule") involving colloidal gold bioconjugates. Chapter 4 (Lacaze) analyzes the formation of nanoparticle chains within liquid crystal defect arrays. Chapter 5 (Kovalska) presents a novel method for the deagglomeration of carbon nanotubes (CNTs) in aqueous solutions, opening a new path in CNT/polymer composites preparation. The results help, firstly, to explain the behaviour of carbon nanotube agglomerates during the homogenizing procedure, and, secondly, to underline the factors which help to homogenize CNTs in aqueous solutions. Using a CNT/water-soluble polymer/ionic surfactant mixture coupled with homogenizer machine exhibited the best results in terms of the solution stability, particles size and their distribution.

Chapter 6 (Chepyga) reports on graphene-like autointercalated Niobium Diselenide nanoparticles, a new route for 2D nanomaterials design. In Chap. 7 (Leonenko), the development of a simple sol-gel based method for producing high quality mesostructured hybrid films within different concentration Rhodamine 6 G is reported. Chapter 8 (Lyashchova) investigates the nonlinear optical properties of cadmium alkanoate composites with CdSe nanoparticles. Nonlinear refraction and absorption in pure matrix were not observed at the excitation conditions used in the study, whereas the nonlinear response of the samples is caused exclusively by the presence of CdSe nanoparticles. Fast self-defocusing, together with nonlinear absorption makes these nanocomposites attractive media for optical limiters. The nonlinear response of nanocomposites can be extremely fast and will be investigated in the near future. A general method for obtaining dispersion equations for surface plasmons in the n-layer graphene system was developed in Chap. 9 (Saroka).

This method, along with long wave and tight-binding approximations, was applied to derive dispersion equations for single layer and bilayer graphene.

Part II: Interface Studies and Techniques

Chapter 10 (Dolgov) describes a new goniometric setup and demonstrates that it operates successfully not only with reflected but also with plasmon-coupled fluorescent light. The setup enables transformation of the isotropic rare earth fluorescence into a strongly polarized and directional one suitable for use in sensing applications and induction of low loss coherent surface plasmon-polaritons. The mesoscopic approach to the processes of nanoparticle formation proposed in Chap. 11 (Konstantinova) enables deeper understanding and a theoretical description of a significant amount of experimental data as well as opening the way for purposeful governing by oxide powder system in the stages of obtaining, compaction, and sintering. Chapter 12 (Martra) reviews techniques to highlight atomic/molecular details of the surface of nanomaterials by IR spectroscopy of their interaction with molecules in controlled conditions. Details of experimental setups and procedures are provided, with particular attention devoted to the use of different probe molecules (CO, CH_3CN, H_2O). Such molecules, when adsorbed in controlled conditions, become useful "molecular tools", because of the sensitivity of their vibrational features to the physical–chemical properties of surface sites. The results of the investigations discussed in Chap. 13 (Liapina) show the possibility of preparing stable suspensions of metal particles on the nanoscale by dissolution of salt shells of nanopowders, using both water-soluble organic complexes based on amine derivatives, and a glycerin-water system solution. An advantage of this method is the achievement of a high degree of uniformity of metal nanoparticles by dimensions. The possibility of adding biogenic or bioactive components to the suspension means that such a material can be made to be biocompatible or bioactive. Chapter 14 (Klar) focuses on metal nanostructures and active materials. The chapter discusses the fundamental physical concepts governing the effects of active materials in close proximity as well as applications for biosensing and for lasers on the nanometre scale.

Part III: Nanocomposites and Applications of Nanotechnologies

Chapter 15 (Kadashchuk) presents an overview of current achievements in the theoretical description of the charge transport in disordered organic semiconductors, with emphasis on charge transport behaviours at large carrier concentrations as realized in organic field-effect transistors (OFETs). Particular attention is given to the Effective Medium Approximation (EMA) analytical method, which was applied

to describe the carrier concentration-, electric field-, and temperature-dependent charge transport in organic materials used as active layers in OFET devices.

The microstructural evolution and grain-growth kinetics of nanocrystalline titanium nitride powders under isothermal annealing using microwave and conventional sintering are investigated in Chap. 16 (Ragulya). The results show that microwave sintering of nanocrystalline TiN results in fine microstructure ~220 nm, as compared to the conventional sintering 335 nm. Imaging of unmarked DNA infiltrated into a silica photonic crystal at room temperature is achieved by authors of Chap. 17 (Boiko). The improved imaging of the DNA could be related to its fluorescence enhancement mediated by the photonic crystal in the range 470–520 nm. Localization of light in the photonic crystal can decrease fluorescence lifetimes in the case of undoped opal in comparison with bulk amorphous silica and assist improved imaging of DNA. The authors of Chap. 18 (Tomylko) showed that adding a small amount (0.1 wt. %) of organomodified laponite (LapO) nanoplatelets results in drastic changes of dielectric and electro-optical characteristics of carbon nanotube suspensions in nematic liquid crystal E7. Chapter 19 (Karachevtsev) reviews and compares poly(rI) and poly(rA) adsorption on carbon nanotubes. Chapter 20 (Apartsin) investigates non-covalent immobilization of oligonucleotides on single-walled carbon nanotubes. Chapter 21 (Smola) presents the synthesis and spectral-luminescent properties of sol-gel organic-inorganic hybrid materials containing lanthanide complexes with polydentate acyclic and cyclic ligands. Chapter 22 (Zobnina) presents a combined approach for the investigation of the structure of amino acid and organic polyether nanocomposites involving experimental electrospray mass spectrometry and computer modelling by molecular dynamics simulation. It is shown that oligomers of polyethers form stable complexes with amino acids valine, proline, hisidine, glutamic and aspartic acids. The results of molecular dynamics simulation show that stabilization of amino acid-polyether complexes is achieved due to winding of the polymeric chain around charged groups of amino acids. In Chap. 23 (Kopanchuk), the authors propose an approach to systematically monitor three separate stages of cellular signaling: ligand binding to the receptor, G protein activation, and second messenger production. Chapter 24 (Kopylovsky) describes the interplay of quadratic and cubic nonlinear optical responses in KDP single crystals with incorporated TiO_2 nanoparticles.

Acknowledgments

Contents

Contributors

Valentina Aina Dipartimento di Chimica and Interdipartimental Centre of Excellence "Nanostructured Interfaces and Surfaces-NIS", University of Torino, Via P. Giuria 7, 10125 Torino, Italy

Lev G. Akselrud Franko Lviv National University, 6, Cyril and Mefody Str., Lviv 79005, Ukraine

Gabriele Alberto Dipartimento di Chimica and Interdipartimental Centre of Excellence "Nanostructured Interfaces and Surfaces-NIS", University of Torino, Via P. Giuria 7, 10125 Torino, Italy

Evgeny K. Apartsin Institute of Chemical Biology and Fundamental Medicine SB RAS, 8, Lavrentiev ave, 630090 Novosibirsk, Russia

V. N. Asaula V. Vernadsky Institute of General and Inorganic Chemistry, National Academy of Sciences of Ukraine, Acad. Palladina Ave. 32-34, Kiev 03142, Ukraine

Konstantin Batrakov Institute for Nuclear Problems, Belarusian State University, Bobruyskaya 11, Minsk 220030, Belarus

V. V. Boiko Department of Physics of Biological Systems, Institute of Physics, National Academy of Sciences of Ukraine, Prospect Nauki, 46, Kyiv 03680, Ukraine

O. A. Boryak B. Verkin Institute for Low Temperature Physics and Engineering of the National Academy of Sciences of Ukraine, 47, Lenin Avenue, Kharkov 61103, Ukraine

M. S. Brodyn Institute of Physics, NAS of Ukraine, Pr. Nauki, 46, Kiev 03680, Ukraine

Marina Yu Buyanova Institute of Chemical Biology and Fundamental Medicine SB RAS, 8, Lavrentiev ave., Novosibirsk 630090, Russia

V. V. Chagovets B. Verkin Institute for Low Temperature Physics and Engineering of the National Academy of Sciences of Ukraine, 47, Lenin Avenue, Kharkov 61103, Ukraine

Liudmyla Mykolaivna Chepyga Frantsevich Institute of Problems of Materials Science of NASU, 3, Krzhyzhanovsky Str., Kiev-142 03680, Ukraine

D. Coursault UMR 7588, INSP, UPMC Univ Paris 06, 75005 Paris, France

Alessandro Damin Dipartimento di Chimica and Interdipartimental Centre of Excellence "Nanostructured Interfaces and Surfaces-NIS", University of Torino, Via P. Giuria 7, Torino 10125, Italy

I. Danilenko Donetsk Institute for Physics and Engineering, NASU, R.Luxembourg 72, Donetsk 83114, Ukraine

Chiara Deiana Dipartimento di Chimica and Interdipartimental Centre of Excellence "Nanostructured Interfaces and Surfaces-NIS", University of Torino, Via P. Giuria 7, Torino 10125, Italy

Dmytro Demirskyi Frantsevich Institute for Problems in Material Science, 3 Krzhizhanovsky str., Kyiv 03680, Ukraine

L. Dolgov Institute of Physics, University of Tartu, Riia 142, Tartu 51014, Estonia

G. I. Dovbeshko Department of Physics of Biological Systems, Institute of Physics, National Academy of Sciences of Ukraine, Prospect Nauki, 46, Kyiv 03680, Ukraine

Galyna Dovbeshko Institute of Physics of the National Academy of Sciences of Ukraine, 46 Nauki Ave., Kyiv 03028, Ukraine

P. G. Dulnev Institute of Bioorganic Chemistry and Petrochemistry, Kyiv, Ukraine

E. N. Fadeyev Department of Chemistry of Lanthanides, A.V. Bogatsky Physico-Chemical Institute, National Academy of Sciences of Ukraine, Lustdorfskaya doroga, 86, Odessa 65080, Ukraine

D. V. Fedorenko Institute of Physics, National Academy of Sciences of Ukraine, Prospect Nauki, 46, Kiev 03680, Ukraine

O. M. Fesenko Department of Physics of Biological Systems, Institute of Physics, National Academy of Sciences of Ukraine, Prospect Nauki, 46, Kyiv 03680, Ukraine

Olena Fesenko Institute of Physics of the National Academy of Sciences of Ukraine, 46 Nauki Ave., Kyiv 03028, Ukraine

I. I. Fishchuk Institute for Nuclear Research, NAS of Ukraine, Prospekt Nauky 47, Kyiv 03680, Ukraine

V. Ya. Gayvoronsky Institute of Physics, NAS of Ukraine, Pr. Nauki, 46, Kiev 03680, Ukraine

J. Genoe IMEC, Kapeldreef 75, Leuven 3001, Belgium

G. O. Gladchenko B.I. Verkin Institute for Low Temperature Physics and Engineering, Kharkov 61103, Ukraine

Olena Gnatyuk Institute of Physics of the National Academy of Sciences of Ukraine, 46 Nauki Ave., Kyiv 03028, Ukraine

Dezhiv Goer Institute of Electron Physics, National Academy of Sciences of Ukraine, 21 Universitetska St., Uzhgorod 88017, Ukraine

V. F. Gorchev O.V. Palladin Institute of Biochemistry, National Academy of Sciences of Ukraine, Leontovicha str., 9, Kyiv 01601, Ukraine

V. S. Gorelik P.N. Lebedev Physical Institute of the Russian Academy of Sciences, Leninsky Prospect, 53, Moscow 117924, Russia

A. Kadashchuk IMEC, Kapeldreef 75, Leuven 3001, Belgium

Alexander A. Kamnev Laboratory of Biochemistry, Institute of Biochemistry and Physiology of Plants and Microorganisms, Russian Academy of Sciences, Prosp. Entuziastov 13, Saratov 410049, Russia

M. V. Karachevtsev B.I. Verkin Institute for Low Temperature Physics and Engineering, Kharkov 61103, Ukraine

V. A. Karachevtsev B.I. Verkin Institute for Low Temperature Physics and Engineering, Kharkov 61103, Ukraine

S. O. Karakhim O.V. Palladin Institute of Biochemistry, National Academy of Sciences of Ukraine, Leontovicha str., 9, Kyiv 01601, Ukraine

V. Kiisk Institute of Physics, University of Tartu, Riia 142, Tartu 51014, Estonia

Thomas A. Klar Johannes Kepler University Linz, Institute of Applied Physics, Altenberger Straße 69, Linz 4040, Austria

I. I. Fishchuk Institute for Nuclear Research, NAS of Ukraine, Prospekt Nauky 47, Kyiv 03680, Ukraine

G. V. Klimusheva Institute of Physics, National Academy of Sciences of Ukraine, Prospect Nauki, 46, Kiev 03680, Ukraine

T. Konstantinova Donetsk Institute for Physics and Engineering, NASU, R.Luxembourg 72, Donetsk 83114, Ukraine

Sergei Kopanchuk Institute of Chemistry, University of Tartu, Tartu, Estonia; Competence Centre on Reproductive Medicine and Biology, Tartu, Estonia

M. A. Kopylovsky Institute of Physics, NAS of Ukraine, Pr. Nauki, 46, Kiev 03680, Ukraine

M. V. Kosevich B. Verkin Institute for Low Temperature Physics and Engineering of the National Academy of Sciences of Ukraine, 47, Lenin Avenue, Kharkov 61103, Ukraine

O. Kovalchuk Institute of Physics, NASU, Prospekt Nauky 46, Kyiv 03028, Ukraine

E. O. Kovalska O.O. Chuiko Institute of Surface Chemistry, NASU, 17, General Naumov str., Kiev 03164, Ukraine

Leonid M. Kulikov Frantsevich Institute of Problems of Materials Science of NASU, 3, Krzhyzhanovsky Str., Kiev-142 03680, Ukraine

E. Lacaze UMR 7588, INSP, UPMC Univ Paris 06, 75005 Paris, France

N. Lebovka Institute of Biocolloidal Chemistry, NASU, Vernads'koho Boulevard 42, Kyiv 03142, Ukraine

Evgen Leonenko L.V. Pisarzhevsky Institute of Physical Chemistry National Academy of Sciences of Ukraine, 31 Nauki pr., Kiev 03128, Ukraine

X. Li Department of Chemical Engineering and Chemistry, Eindhoven University of Technology, Eindhoven, MB 5600, The Netherlands

K. V. Liapina E.O. Paton Electric Welding Institute, Kyiv, Ukraine

R. Lõhmus Institute of Physics, University of Tartu, Riia 142, Tartu 51014, Estonia

A. Loot Institute of Physics, University of Tartu, Riia 142, Tartu 51014, Estonia

A. G. Lyashchova Institute of Physics, National Academy of Sciences of Ukraine, Prospect Nauki, 46, Kiev 03680, Ukraine

Petro Manoryk L.V. Pisarzhevsky Institute of Physical Chemistry, National Academy of Sciences of Ukraine, 31 Nauki pr., Kiev 03128, Ukraine

A. I. Marinin National Institute of Food Technologies, Kyiv, Ukraine

Gianmario Martra Dipartimento di Chimica and Interdipartimental Centre of Excellence "Nanostructured Interfaces and Surfaces-NIS", University of Torino, Via P. Giuria 7, Torino 10125, Italy

Olga Mazina Institute of Chemistry, University of Tartu, Tartu, Estonia; Competence Centre on Reproductive Medicine and Biology, Tartu, Estonia

T. V. Melnichenko E.O. Paton Electric Welding Institute, Kyiv, Ukraine

T. A. Mirnaya V. Vernadsky Institute of General and Inorganic Chemistry, National Academy of Sciences of Ukraine, Acad. Palladina Ave. 32-34, Kiev 03142, Ukraine

Darya S. Novopashina Institute of Chemical Biology and Fundamental Medicine SB RAS, 8, Lavrentiev ave., Novosibirsk 630090, Russia

L. Pelliser UMR 7588, INSP, UPMC Univ Paris 06, 75005 Paris, France

S. Pikker Institute of Physics, University of Tartu, Riia 142, Tartu 51014, Estonia

A. S. Popov Institute of Physics, NAS of Ukraine, Pr. Nauki, 46, Kiev 03680, Ukraine

Oleg Posudievsky L.V. Pisarzhevsky Institute of Physical Chemistry National Academy of Sciences of Ukraine, 31 Nauki pr., Kiev 03128, Ukraine

I. M. Pritula Institute for Single Crystals NAS of Ukraine, Pr. Lenin, 60, Kharkov 61001, Ukraine

Andrey Ragulya Frantsevich Institute for Problems in Material Science, 3 Krzhizhanovsky str., Kyiv 03680, Ukraine

Venkat Rao National and Defense Programs, CSC Defense Group, Alexandria, Virginia

Ago Rinken Institute of Chemistry, Universiy of Tartu, Tartu, Estonia; Competence Centre on Reproductive Medicine and Biology, Tartu, Estonia

N. V. Rusakova Department of Chemistry of Lanthanides, A.V. Bogatsky Physico-Chemical Institute, National Academy of Sciences of Ukraine, Lustdorfskaya doroga, 86, Odessa 65080, Ukraine

Elena I. Ryabchikova Institute of Chemical Biology and Fundamental Medicine SB RAS, 8, Lavrentiev ave., Novosibirsk 630090, Russia

Anna Rynder Institute of Physics of the National Academy of Sciences of Ukraine, 46 Nauki Ave., Kyiv 03028, Ukraine; National University of "Kyiv-Mohyla academy", 2 Skovorody St., Kyiv 04070, Ukraine

Yuriy Sakhno Dipartimento di Chimica and Interdipartimental Centre of Excellence "Nanostructured Interfaces and Surfaces-NIS", University of Torino, Via P. Giuria 7, 10125 Torino, Italy

Vasil Saroka Institute for Nuclear Problems, Belarusian State University, Bobruyskaya 11, Minsk 220030, Belarus

YuI Sementsov O.O. Chuiko Institute of Surface Chemistry, NASU, 17, General Naumov str., Kiev 03164, Ukraine

I. Sildos Institute of Physics, University of Tartu, Riia 142, Tartu 51014, Estonia

S. S. Smola Department of Chemistry of Lanthanides, A.V. Bogatsky Physico-Chemical Institute, National Academy of Sciences of Ukraine, Lustdorfskaya doroga, 86, Odessa 65080, Ukraine

O. V. Snurnikova Department of Chemistry of Lanthanides, A.V. Bogatsky Physico-Chemical Institute, National Academy of Sciences of Ukraine, Lustdorfskaya doroga, 86, Odessa 65080, Ukraine

Viktor M. Talash Frantsevich Institute of Problems of Materials Science of NASU, 3, Krzhyzhanovsky Str., Kiev-142 03680, Ukraine

German Telbiz L.V. Pisarzhevsky Institute of Physical Chemistry, National Academy of Sciences of Ukraine, 31 Nauki pr., Kiev 03128, Ukraine

S. Tomylko Institute of Physics, NASU, Prospekt Nauky 46, Kyiv 03028, Ukraine

Lauri Tõntson Institute of Chemistry, University of Tartu, Tartu, Estonia

A. I. Ustinov E.O. Paton Electric Welding Institute, Kyiv, Ukraine

V. Varyukhin Donetsk Institute for Physics and Engineering, NASU, R.Luxembourg 72, Donetsk 83114, Ukraine

Santa Veiksina Institute of Chemistry, University of Tartu, Tartu, Estonia; Competence Centre on Reproductive Medicine and Biology, Tartu, Estonia

Alya G. Venyaminova Institute of Chemical Biology and Fundamental Medicine SB RAS, 8, Lavrentiev ave., Novosibirsk 630090, Russia

O. Yaroshchuk Institute of Physics, NASU, Prospekt Nauky 46, Kyiv 03028, Ukraine

V. O. Yatsyna Institute of Physics, NAS of Ukraine, Pr. Nauki, 46, Kiev 03680, Ukraine

V. G. Zobnina B. Verkin Institute for Low Temperature Physics and Engineering of the National Academy of Sciences of Ukraine, 47, Lenin Avenue, Kharkov 61103, Ukraine

Part I
Imaging Techniques: Microscopy, Spectroscopy and Lasers

Chapter 1
Nano-Bio Architectures: Combining Chemistry and Biology in Nanotechnology

Venkat Rao

1.1 Introduction

Nanobiocomposites represent a revolutionary breakthrough in materials design and development by uniquely combining biologically inspired structures and design elements with nanotechnology manufacturing processes. Essentially, nanobiocomposites are reinforced nanofabrics with a second phase, involving an organic or inorganic material to produce a polymer composite with unique physicochemical and mechanical properties. For example, production of modern plastics using biocomposites represents an entirely alternative route to conventional polymer composite manufacturing, where the inclusion of as little as 2 % volume of inorganic materials in nanomaterial-based products results in doubling of tensile modulus and strength without concomitant loss in impact resistance. Besides superior physical and mechanical properties, nanocomposites are less heavy and leave a relatively small environmental footprint. A recent study indicated that US vehicle manufacturers deploying polymer nanocomposite tires in automobile manufacture would result in reduced fuel consumption by more than 8 billion gallons of fuel and $24 billion savings in fuel costs annually, and at the same time reduce carbon dioxide emission by more than 22 million tons on an annual basis Chu [1]. Despite these obvious benefits, design and development of nanobiocomposites remain in the realm of arts rather than science and technology, meaning that the process fundamentals are yet in the developmental stages and incorporation of advanced biology-based nanocomposite design has remained largely empirical. Similarly, using current technologies it is a challenge to predict the ultimate material limit or maximum performance for various categories of nanocomposites comprising inorganic and bioorganic impregnated nanofabrics.

V. Rao (✉)

Chem-Bio Programs, Parsons Corporation, 100 M Street SE, Washington, DC 20003, USA
e-mail: venkat.rao@parsons.com

Description of challenges related to design and development of Nanobiocomposites should not be confused with the nanoscale manufacturing technologies which are more recently employed on a large scale in the semiconductor industry. The chemical industry, however, without naming the process as nanotechnology, has been working with nanoscale particles at the molecular level as in the chemical design and synthesis of organic chemicals and nanoparticles substances such as dyes and pigments.

A basic challenge in the design and synthesis of nanobiocomposites is the ability of the process to control the nanoassembly of inorganic or bioorganic materials with nanofabrics. It is well known to technologists that nanobiocomposite design and assembly is a complicated process that requires a lot of skill and technical expertise on the part of scientists, as well as process methodology and control elements that are scaled down to manipulate at nanoscale levels and a flexibility to scale-up the fabric morphology and assembly processes at meso and macro levels. Established process methodologies currently employed in nanomaterial production such as sonochemical processes, cavitation, microemulsion, and high-energy ball milling are being explored for design and assembly with layered complexity in structure without concomitant loss of functional properties.

Researchers working on the nanobioarchitecture and development of biomimetic components follow either a top-down or bottom-up method. Whereas the top-down process in essence involves a process such as sonochemical processing, or cavitation processing to reduce block of material to a desired size and shape, bottom-up methods are technically more elegant bioarchitecture involving a self-assembly design feature based on carefully designed chemical processes of combining bioorganic and inorganic moieties to form higher level structures. The physicochemical properties of chemical moieties such as ionic charge, polarizability, magnetic dipole, and reactive chemical groups are the key to self-assembly in a control and directed fabrication process. However, this process is better described as controlled chemical synthesis rather than self-assembly. A key limitation to chemical synthesis-based self-assembly is that the process works well when the bioarchitecture involves less than 1000 atoms and processes involving electrochemical interactions such as electrovalent and covalent bonds resulting in stable structures. Consequently, the self-assembly concept is gaining considerable attention from scientific researchers on nanobioarchitecture of large molecules or molecular aggregates where physical forces play a predominant role in the formation and stabilization of higher level fabric structures.

It is noteworthy that creating a uniform dispersion of nanoparticles in the polymer matrix continues to be a major challenge in the design and fabrication of nanocomposites in general and Nanobiocomposites in particular. Formation of aggregates during the dispersion process, a key reason for lack of homogeneity, is mitigated by employing techniques such as mechanical agitation, ultrasonic vibration, shear mixing, non-contact mixing, and use of dispersing agent during fabrication stage. This would be a crucial phase when the fabrication process involves dispersion of pharmacologically active organic compounds or complex macromolecular materials during formulation of an advanced pharmaceutical

product. The product development scientists in this arena expend considerable efforts to standardize the dispersion and curing steps as part of process standardization during the fabrication, synthesis, and functional characterization stages in the production process.

Most often, advanced nanocomposite architectures involve a combination of conventional chemical synthesis and computationally driven self-assembly processes in a bottom-up design and fabrication plan. It is relevant to note that a supervised self-assembly process in nanofabrication attempts to mimic natural processes in biology and biochemistry. For instance, the semiconductor industry reported a biologically inspired self-assembly process to design and build the next generation Airgap microprocessor chips IBM [2]. The natural pattern in the creation of snowflakes, enamel on the teeth, and patterns on seashells was harnessed to create nanostructures inside the microprocessor chips. Self-assembly processes are the reason that nanotechnology has such a profound impact on chemical products development, especially nanocomposite-based structures in industrial products. From a scientific research standpoint self-assembly processes—once standardized for design and fabrication of complex structures with desired properties—pave the way for molecular assembly, propelling nanotechnology to even more sophisticated levels in the creation of productive nanosystems such as from "molecules-to-super products" type of product design, development, and manufacturing models.

Molecular self-assembly is a biologically inspired concept aimed at transitioning the nanocomposite design and fabrication process to a new framework. Notably, current deliberations on this topic remain mostly at the conceptual, proof-of-concept level and prototypes of elementary system in synthetic biology attempting to simulate biological molecular assembly process. The notion of self-assembly in this context refers to an engineered ecosystem of self-replicating nanomachines, where machines self-assemble themselves and replicate repeatable functional characteristics within the engineered ecosystem. Several recent publications in synthetic biology point to engineered ecosystems, attempting to replicate the biological process through a self-directed molecular assembly process [3–5].

Although DNA-based nanotechnology systems are persuasive examples for molecular self-assembly methods to design and construct functionally relevant nanostructures, much of the current evidence remain at a proof-of-concept level. There are no manufacturing level demonstrations of nanotechnology systems based on molecular self-assembly involving a combination of chemical synthesis and self-assembly. The design concept in ongoing investigations involve DNA molecules serving as precisely controllable and programmable building blocks for layered nanostructures with demonstrable properties such as sensors, biological actuators, biosimulants, and pharmacological agents.

1.2 Component Elements of Nanobioarchitecture

In order to better understand the design and fabrication challenges and potential application areas of nanobiocomposites, it is essential to first define the term bioarchitecture. Published studies have defined the term bioarchitecture variously as the art and science governing the design and fabrication of building spaces aimed to create, support, and enhance life and living systems. At the conceptual level, this definition captures the integrated nature of all aspects related to design and fabrication processes from the macro to micro levels. However, nanobio-composite components defining a bioarchitecture would have to emulate the built-in biological functional property at the lowest micro level and scale-up to a macro level retaining interface integrity in structural and functional property. Formula-tions for nanobiocomposite usually comprise chemical components such as (a) polymeric matrix, (b) embedded bio-organic filler, and (c) stabilizers. Note that at least one of the component materials would have to be at least one dimension of the order of nanometers (less than 100 nm) to achieve the desirable nanoscale properties.

In the broadest sense, the bioorganic nanomaterial in the formulation could be porous solid, colloids, hydrogels, or copolymers formulated in a bulk continuous phase. A notable feature is that the mechanical, electrochemical, or catalytic properties of a nanobiocomposite material are significantly different from the component materials. Scientific investigations in new nanobioarchitecture design attempts to replicate the microstructures of biological nanocomposites as a way to incorporate exceptional mechanical or physiological functional property in man-made designs.

Figure 1.1 illustrates the greater mechanical properties of bone and seashell, two well-studied multiscale, multi-component nanobiocomposite materials from nature. As illustrated in the figure, biological nanocomposites such as bone and seashell demonstrate exceptionally superior mechanical properties compared to their component elements. The microstructures building the higher order complex structural features are governed by the physical and chemical properties of various bioorganic and inorganic elements forming the material composition in bone and seashell. As a result, much of the current scientific research is directed at (a) understanding the key structural factors contributing to the biological functional characteristics, whether it is strength, toughness, catalytic property, or tissue regenerative stimulus and (b) design and formulate new nano-bioarchitecture that meet and even surpass their biological counterparts using a combination of novel inorganic and synthetic organic compounds.

The published literature illustrates through experimental systems the criticality of structure–function integrity of biologically active components in nanocom-posites. Investigations have a variety of nanoscale techniques such as layer-by-layer deposition, scaffold engineering, hydrogel crosslinking, modified peptide synthesis, and substrate deposition techniques to create biologically active protein/polymeric fabric. Takahasni et al. [6] reported a layer-by-layer construction of
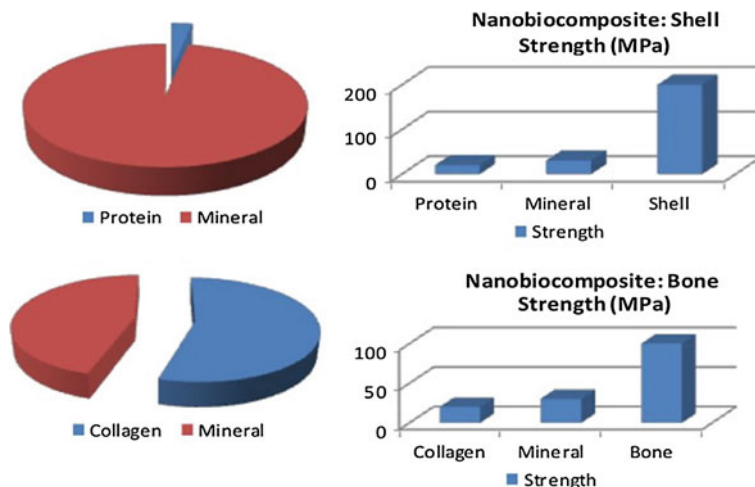
Fig. 1.1 Biological nanocomposites demonstrate greater mechanical properties compared to their component materials

protein architectures based on the biochemical interactions of avidin–biotin and concanavalin A-sugar moiety for biosensor applications. A key challenge in the layer-by-layer bioarchitecture design involved a controlled deposition of the avidin and biotin-labeled enzymes on the surface of optical and electrochemical biosensors, such that the nanobiocomposites retain enzymatic activity. Authors demonstrated that the layer-by-layer deposition with avidin–biotin did not result in loss of binding interactions of Concanavalin A with monosaccharides such as glucose and galactose. Retaining the sugar binding property was essential to the design and use as an optical and electrochemical detection system for sugars in biological samples. In a related study, Kim et al. [7], report fabrication of a three-dimensional architecture using a layer-by-layer deposition of two active enzymes on a pre-patterned matrix comprising avidin/biotin. The design methodology involved layered deposition via coupling of two layers of lactate oxidase and horseradish peroxidase to create functionally active building blocs in the fabrication of three-dimensional nanostructures for biosensing applications.

Use of biologically active materials such as heparin to improve performance of nanobiocomposites in biomedical applications has recently been investigated. These studies attempt to enhance the biological activity of heparin when composited with nanoparticles such as magnetic and metallic nanoparticles, or biodegradable polymeric materials have introduced numerous possibilities in design and delivery of heparin and other biologically active macromolecules for use in anticancer therapy, tissue engineers, and use as biosensors in disease diagnostics. Tan et al. [8] reported assembly of a nanofibrous hyaluronic acid hydrogel network produced through interaction of a low molecular weight heparin and heparin interacting protein with a modified hyaluronic acid derivative to support adipose tissue-derived stem cell proliferation and differentiation. Apart from the key

requirement of physiologically relevant composition and properties of polymeric materials, the investigation demonstrated use of nanobiocomposite formulations as therapeutically effective delivery mechanism for generation of adipose tissue-derived stem cells.

Application of nanobiocomposite materials through scaffold-based engineering is another emerging area where design and fabrication approaches are targeted for anticancer drug delivery to specific targeted cell masses, or provide biodegradable matrix with or without biomolecules such as growth factors, cytokines, and peptides to promote tissue repair and regeneration. In this case nanobiocomposite fabrications should ultimately meet the unique requirements of scaffold properties in tissue injury and repair process such as cell adhesion, support proliferation, and promote tissue regeneration.

Table 1.1 summarizes published studies where NBC material was used to design and fabricate scaffolding architecture that meets complex anatomical features and physiological requirements of neural tissues. The selection of just one category of tissue engineering points to the level of detail and sophistication required in modifying conventional surgical processes through use of more advanced nanobiocomposite scaffolds. Specifically, success in tissue engineering depends to a large measure on the physicochemical properties of the scaffolding material support to cellular regulation and tissue proliferation.

Investigators have reported promising results when the bioarchitecture of biodegradable polymer matrix and organic nano-sized fillers follow a hierarchical order characteristic of biological material. For instance, bone is a multifunctional nanocomposite material with a hierarchical structure, where the external bone exterior is made up of concentric rings of mineral and collagen forming larger fibrils that act as protein matrix, and the spongy interior, the bone marrow, allows for compression and withstands crack-like flaw at different levels of hierarchy. Using a combination of biodegradable polymer matrix and nano-sized fillers such as bio-ceramic, bio-glass, and carbon nanotube, new designs mimicking the hierarchical structure of bone have been reported [9, 10]. A key design consideration was to enhance tissue compatibility and osteoconductivity together with improved mechanical and surface properties. A recent study reported a scaffolding design and fabrication using calcium phosphate/poly(hydroxybutyrateco-hydroxyvalerate) nanobiocomposite microsphere for growth factor delivery in bone tissue engineering. Microspheres were embedded with recombinant human bone morphogenetic protein-2 (rBMP-2) using a heparin-based delivery mechanism to promote osteogenesis differentiation of mesenchymal stem cells [10].

Another line of investigation involves employment of peptides and peptide derivates to create biocompatible architectures for a variety of biomedical applications. Biologically active peptides and peptide fragments demonstrate self-assembling property in biological systems, which is a key component criteria in the design of biocompatible, synthetic extracellular matrices with novel biochemical or pharmacological properties for applications in tissue engineering and regenerative medicine. Investigators have modified functional moieties of bioactive peptides to introduce or modify properties such as binding affinity to

Table 1.1 Nanobiocomposite materials and fabrication techniques used to design and fabricate scaffolding architecture for neuronal injury and tissue regeneration systems

Composite matrix	Bioorganic compound/substance	Fabrication technique	Desired property	Reference
Chitosan	Y-Glycidoxypropyltrimethoxy- silane	Surface modification	Mechanical strength	[31]
Poly(sialic acid)	Polylysine;poly-L-ornithine; Laminin; or Collagen	Hydrogel/adsorption	Cell adhesive property	[32]
Chitosan	*Polylysine-functionalized chitosan -poly (N-isopropyl acrylamide)*	Hydrogel crosslinking	Mechano compatibility; surface property	[33]
Collagen	Tyr-Ile-Gly-Ser-Arg (YIGSR) peptide dendrimers	Hydrogel crosslinking	Promote growthof corneal epithelial cells and neurite outgrowth	[34]
Poly(ε-aprolactone)	Polymer blending with collagen	Electrospinning	Cell adhesion, migration and differentiation	[35]
Star-poly(ethylene glycol)	Heparin	Hydrogel	Mechanical properties to adopt specific tissue requirements	[31]
Poly(D, L-lactide-co-ε-caprolactone	Polypyrrole nanoparticle/poly (D, L-lactide) (PDLLA)/caprolactone composite	Substrate deposition	Biosensor for multiple cell functions	[36]
Sucrose-coating microfabricated silicon	Poly(glycerol-sebacate)	Replica coating	Flexibility; surface degradability	[37]
Montmorillonite (MMT)	Soy protein isolate (SPI)	Melt extrusion	Mechanical and dynamic properties	[38]

receptors, trigger cellular signaling mechanisms, promote tissue repair, and regeneration [11]. Synthetic peptides crosslinking to form secondary structures such as α-helices and β-sheet have been variously employed to create peptide-embedded hydrogels. Investigators have reported better results with β-sheet fibriling peptides such as glutamine rich sequences in DN1 protein [12], or peptide from amyloidogenic protein such as Transthyretin [13] for embedding multi-functional features. These studies best illustrate current trends in the incorporation of synthetic peptides and peptide derivatives to architect highly specialized nanobiocomposite materials for biomedical applications.

The first generation polymer nanocomposites for biomedical applications were designed to merely serve as an inert material scaffold to promote wound healing and tissue regeneration. The underlying material and engineering specifications on functional properties were elementary such as strength, biocompatibility, non-corrosivity, non-toxicity, and biodegradability. More recently, investigations are focused biomimetic approaches using organic polymeric compounds such as hydroxyapatite-based nanobiocomposites. Although hydroxyapatite has a long history of use as a prosthetic surgical implant in orthopedic surgery, its incorporation in polymeric nanocomposites has dramatically improved its functional properties. As a result, a number of organic compounds and polymeric materials are attractive candidates for design and synthesis of nanobiocomposites.

Figure 1.2 summarizes the naturally occurring polymeric materials such as polysaccharides and polypeptides more commonly used in nanocomposites design and formulation. Investigators have used a variety of polysaccharides to bring different properties and functionalities to the nanocomposites. One of the more typical biopolymers for biomedical applications is chitosan, a cationic, biodegradable polysaccharide, which demonstrates excellent physicochemical properties such as molecular flexibility high resistance upon heating for nanomaterial processes. Investigators have reported highly flexible chitosan-hydroxyapatite polymer nanobiocomposites for novel prosthetics in orthopedic surgery [14].

Researchers have exploited the electrostatic attractive forces between the positively charged amino groups of chitosan and negatively charged inorganic ions to create nanocomposites for a multitude of applications. For instance, gold nanoparticles embedded in chitosan resulted in the formation of stable metal-chitosan conjugates with high catalytic activity for industrial applications [15].

Polypeptides and proteins from natural sources have proven to be flexible and polymeric matrix for embedding a variety of physical and physiologically relevant properties for biomedical applications. Gelatin, a protein derived from collagen, has a high number of functional groups amenable to conjugation with other organic compounds such as hydroxyapatite to promote tissue proliferation of human osteoblast cells. The functional groups on gelatin could be chemically modified to prepare a variety of engineering biomaterials such as pharmaceutical adhesives, wound dressing, scaffolds to promote cellular attachment, and group promoting wound repair and tissue regeneration. Polypeptides are structurally more versatile, which creates opportunities to incorporate a variety of functional groups on the primary structure of peptide backbone. The secondary structure of polypeptide
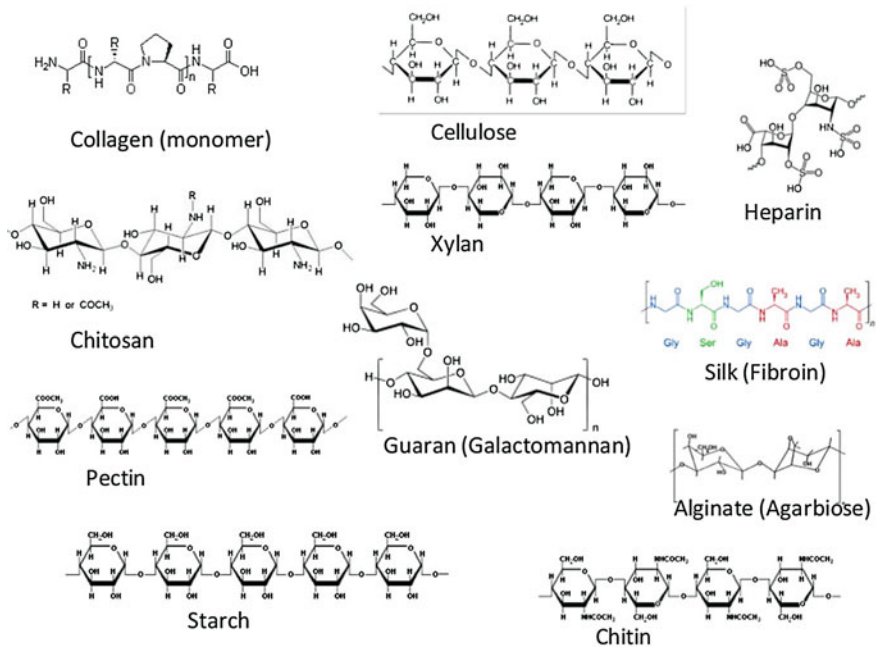
Fig. 1.2 Naturally occurring biopolymers frequently used in the nanobiocomposite design and formulation for biomedical applications

enables condensation to form a layered structure of random coil, α-helix, or β-sheet in aqueous solution. With slight modification in the reaction conditions such as, pH, salt concentration, or temperature, transition between structural conformation results in a multidimensional polymeric fabric for chemical modification or insertion of other materials. Polypeptides that provide extracellular matrix support in biological systems are modified to provide biological ligands for cell-scaffolding interactions to promote cellular attachment, cell proliferation, tissue engineering, neural tissue repair, and regeneration [16, 17]. Polypeptide-based nanobiocomposites are amenable to biodegradation, and form strong gel matrix to retain a multitude of morphology and functionality of the fibrillar fillers. Polypeptide-based nanocomposites are ideal platforms for designing drug delivery systems, scaffolding material for tissue engineering, and biosensor materials.

Figure 1.3 summarizes synthetic polymeric materials such as aliphatic polyesters, homopolymers derived from glycolic acid, urethane, ethylene oxide, and lysine, which are more commonly used in nanocomposite formulations for biomedical applications.

Aliphatic polyesters are one of the more frequent categories of organic compounds used in biodegradable drug delivery systems. This class of compounds includes polymeric derivatives of glycolic acid, lactic acid, and ε-caprolactone. These polyesters providing the matrix support for pharmaceutical or biologics
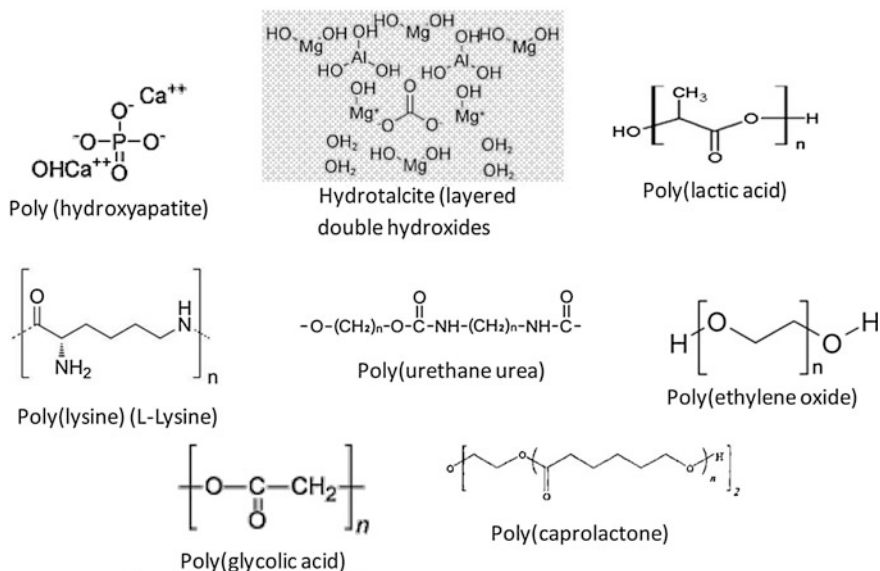
Fig. 1.3 Synthetic polymeric materials frequently used as matrix material in nanobiocomposite design and formulation for biomedical applications

hydrolyze both under acidic and basic conditions releasing the active drug as formulated. Among aliphatic polyesters (shown in Fig. 1.3), poly(L-Lactic acid) has widespread applications in biomedical devices due to its non-toxicity, excellent mechanical properties, and ability to copolymerize with other products; three main reasons for its use in sutures, drug delivery devices, prosthetics, scaffolds, vascular grafts, bone screws, pins, and plates for temporary retention and fixation of tissue in surgery and regenerative medicine.

Polyurethanes are another category of polymeric biomaterials with desirable biocompatibility and mechanical properties, although a number of recent investigators have attempted to modify the problem of permeability to water and air damaging the microelectronics. New nanocomposite structures are reported by chemically modifying the polymeric backbone with other chemical moieties such as polyisobutylene and nanoparticles such as modified silicate, Montmorillonite clay, to achieve superior barrier properties for medical/surgical devices [18, 19].

Nanocomposites matrix based on poly(glycolic acid) and ε-caprolactone are other synthetic aliphatic polyesters that have reported uses in drug delivery systems and biomedical devices. High water permeability is a limiting factor for homoesters of glycolic acid, but caprolactone has better physiochemical properties allowing diffusion of low molecular weight chemicals such as drugs, making it a better candidate for nanocomposites matrix for drug delivery and tissue engineering applications.

1.3 Systems Approaches to Synthesis
of Nanobiocomposites

A key challenge in nanobiocomposite development is the ability to precisely manipulate polymeric material morphologies at the molecular levels without compromising the biological functional characteristics during the scaling process. This is essentially a bottom-up approach mimicking, in principle, natural biological processes of constructing complex nanocomposites such as silk, bone, tooth, and wood, where the basic principle is to produce materials with exceptional mechanical properties such as stiffness, strength, toughness, elastic stability, and interface properties. Laboratory techniques aimed at standardizing design and fabrication and scale to manufacturing levels would have to consider reliability of the scale-up process, reproducibility, life-cycle consistency, and systems compatibility.

After the components of a nanobioarchitecture are identified and characterized toward a biomedical applications domain, the next step involves a rational nanoengineering approach to systematically assemble the core components at the lowest level and scale to higher levels of complexity. This is a highly interdisciplinary area with much of the work in the research and development levels and where a complex interplay of the domains related to mathematics, biomedical sciences, biotechnology, systems biology, systems engineering, and computational sciences govern the design and build process.

Investigators are exploring a systems-centric approach to nanobiocomposite design and fabrication with concepts mostly derived from nature. Multiscale systems (MSS) are considered by nanotechnologists as one of the more attractive systems-centric models toward a design, fabricate, and optimization framework to account for the hierarchical morphology of the nanocomposites. The structures at length scale in the nano- and micrometer ranges with a high aspect ratio of particle size within the polymer matrix.

According to published studies, there are several motivations for multiscale modeling of physiological systems toward product design and fabrication: First, there exists a need for modeling temporal and spatial scales to take into account material behavior and interactions at the lowest molecular to the highest organism levels. Biological systems best demonstrate the complex interrelationship of structure and functional processes between all levels, which pretty much guide conceptual framework for a multiscale system in nanobiocomposite design and fabrication.

Second, computational tools, models, data standards, and testing methods are available for the multiscale modeling community to better understand the behavior of physical systems at atomic, molecular, microscopic, and macroscopic levels, and then build experimental systems and interpret experimental results that are cross-scale in space, time, and state. Finally, in-depth application of mathematical and physical principles in modern biological research has paved the way for application multiscale modeling in biomimetic engineering systems for biological

applications, where conventional modeling and simulation and design engineering are not suitable for nanocomposite product design and development.

Unlike conventional engineering processes, the multiscale systems are fundamentally different in that materials in various scales interface and interact toward a product development whereby the fundamental properties governed by scale are compatible at every level and complexity in the product structure and function.

Multiscale modeling methodologies for nanobiocomposites generally comprise a combination of computational and experimental techniques to model structure–function composition of multiscale systems, characterize structural morphology and functional aspects, and finally optimize the scale-up parameters for component assembly at lowest nanoscale to the macroscopic fabric morphologies. Multiscale modeling methodologies would have to accurately represent through simulation the molecular dynamics for physical and mechanical properties of the polymer starting at the lowest scale. Most often a combination of experiment-driven approaches and computational modeling is used to assess structure–function relationships for multiscale composites. Computational techniques provide added flexibility to multiscale modelers to modify key parameters in the model to better predict the final functional outcomes such as mechanical properties or kinetics in biological systems for bioactive nanocomposites. These model-derived predictive values are then compared with results obtained from experimental studies to validate and further refine the computational techniques.

Existing predictive models for multiscale nanocomposite systems are inadequate, as they fail to accurately represent the underlying physicochemical mechanisms of nanoscale reinforcement in the micro- and nanomechanics of multiscale composites. In particular, model systems are less able to predict the chemomechanics of the organic–inorganic bonding mechanisms and interfacial binding and interactions that result in significant improvements in mechanical properties. These limitations create impediments to optimize design and fabrication of biologically active nanocomposites.

Although all materials are hierarchically structured, it is only in biological materials that this hierarchical organization is part of the inherent design. A prominent feature of the hierarchical organization in biological nanocomposites is the organic–inorganic interfacial interactions that form the basis for the structure and functional properties.

Figure 1.4 illustrates the hierarchical features from an atomic to macroscopic scale of the assembly of the primary protein, fibroin, from the basic backbone chemical structure at the atomic level, to higher level microfiber assembly at the micro level, to finally form silk fabric at the macroscopic level.

Molecular self-assembly of silk protein components is essentially a multiscale design. Silk is a complex assortment of multiple variants of the core protein polymer, fibroin, where the repeating units of amino acids differ in combinatorial sequence resulting in 20 different structural variants with differing physiochemical and mechanical properties. The 20 different variants assemble as a multiscale system in a specific sequence creating higher order polymer morphologies and biological functionality. As shown in Fig. 1.4, at the fundamental atomic scale,
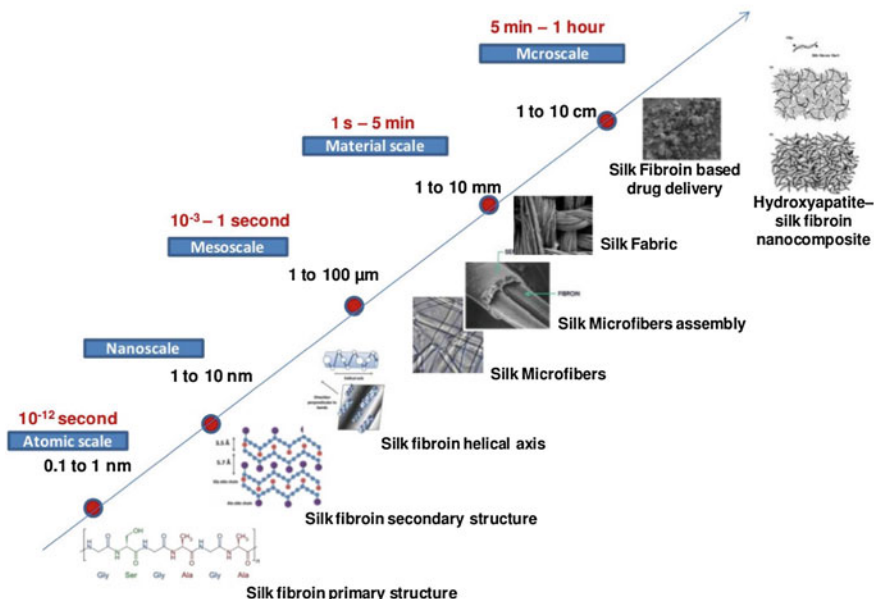
Fig. 1.4 Multiscale systems explore design space and timescales involving multiple scale and feedback to achieve desired morphologies and performance specification

amino acids glycine, alanine and serine residues form the core repeatable peptide units forming the core backbone structure of the crystalline region in the 6–15 Å scale. The secondary structure level is established by alteration of glycine with either alanine or serine that results in the spontaneous formation of β-pleated sheet crystals. These crystalline sheets account for up to 40–50 % of the total volume of the silk fiber as the β-pleated sheets fold into tertiary helical structures. Study of fibroin microfibers have revealed the non-crystalline fraction as having a much less ordered, possibly amorphous structure representing nearly half of the total volume of silk fiber. Only recent studies have revealed the nanocomposite structural motif for the hierarchical molecular origin for structure and mechanical properties. At a micro-scale level, however, fibroin exists in two distinct structures in the solid state, a predominant β-sheet (silk fiber I and II) and a α-helical crystal structure (silk fiber III). Investigations have revealed that the unique strength and flexibility of silk fiber is due to the uniaxial orientation of the crystalline structure with helical axis oriented perpendicular to the plane of the film [20]. The self-assembly process of fibroin component peptides and inorganic elements from the atomic level to the macroscopic level faithfully replicate a multiscale design outlined here to achieve desired morphologies and biologically specified physical properties.

Key temporal and physical scales to the behavior of a polymeric protein components of silk, an all organic polymeric matrix that makes it an ideal matrix for nanobiocomposites. A major ongoing effort in the development of biomimetic nanocomposites is finding a multiscale pathway for artificial analogs which can

emulate physical and mechanical properties of biological materials such as fibroin and other all organic biopolymers.

Among several biological source materials, fibroin as the fabric to design and build nanoscale drug delivery system has received considerable attention. Compared to synthetic non-degradable nanoparticles such as silicone, or polyethylene glycol, silk fibroin is biodegradable and biocompatible, and can be fabricated at less than 100 nm in diameter to enable therapeutic encapsulation of drugs to increase entrapment efficiency and increased bioavailability.

Figure 1.5 is a schematic illustration of design options for multiscale nanoengineering a fibroin-embedded nanocomposite drug delivery system. As a biopolymer with a molecular weight of 370 kDa, silk protein when dissolved in concentrated salts, results in a liquid form, which can be molded in various forms as film, gel, power, and fiber. As shown in Fig. 1.5, biologically active substances such as insulin or drugs are conjugated in the presence of catalysts and additives to prepare a Fibroin-Insulin conjugate. After the chemical reaction phase, the multistage process involves a process to stabilize the physical form of the bioconjugate and retain physiochemical properties relevant to bioavailability. Yan et al. (2009) prepared fibroin nanoparticles by first dissolving the fibroin fabric in a water–acetone mixture and subsequently precipitating fibroin crystals in an aqueous solution [21]. The secondary structure of silk nanoparticles is controlled during this process using a combination of pH and salt concentrations, where at acidic pH of 6 crystalline fibroin appears to be the dominating structure, whereas at basic pH of 9 and above the fibroin is less crystalline. These forms of fibroin are unique
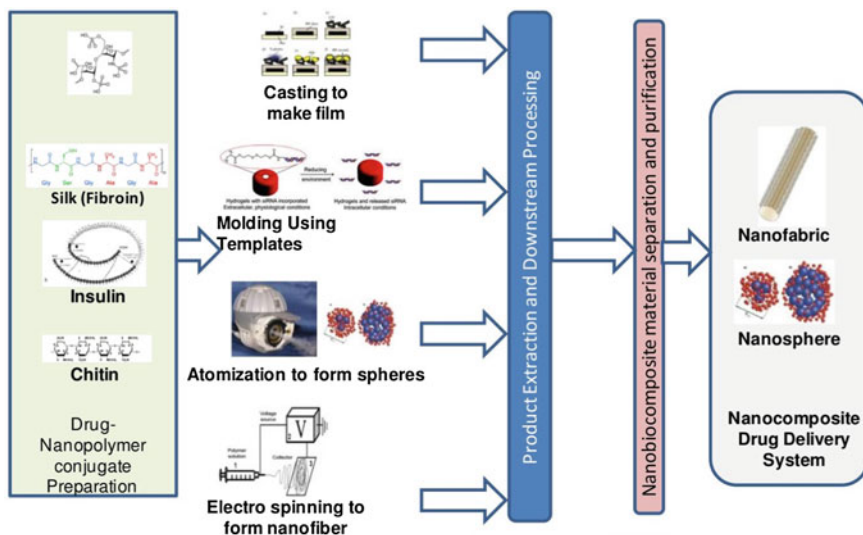

Fig. 1.5 A schematic representation of biosynthesis and options for multiscale nanoengineering of nanobiocomposite drug delivery systems

matrix to load both small drug molecules and large molecules such as insulin based on electrostatic interactions.

The selection of the scale-up process for encapsulation depends on the final product specifications, according to which the fibroin–insulin complex could be cast into a film, molded using template blocks, atomized to form spheres, or spun into a nanofiber. The scale-up process for the next step involves purification of the fibroin–insulin conjugated product using standard biologics purification process. Release of insulin or other pharmacological agents from the fibroin nanofabrics depends on the electrostatic interactions where fibroin secondary structure was considered crucial to drug release kinetics in experimental systems. This brief narrative attempts to highlight the biomimetic multiscale design in nanobiocomposite product development, where a combination of nanoengineering and traditional biologics product development process are interlinked to attain the desired product physical features and biological/pharmacological outcomes.

1.4 Nanomaterial Risk Assessment

Research, development on nanocomposites, and commercialization of nanotechnology-derived products has far outpaced regulatory agencies responsible for the protection of occupational health and environmental protection. Nanocomposites with embedded toxic heavy metals such as titanium oxide (TiO_2), Zinc oxide (ZnO), and silver (Ag) are present in a wide range products such as sunscreens, cosmetics, wound dressings, surgical tools, detergents, automotive paints, and tires [22]. Rapid entry of nonmaterial-based products into the marketplace, introduced considerable uncertainties on the potential adverse impact on human health and environment, and particularly long-term effects involving chronic exposures.

Scientific studies on the safety of heavy metal-embedded nanocomposites and risks associated with nanomaterial-derived products require additional nanotoxicological research, risk assessment protocol development, biosafety guidelines catering to occupational safety, and workers' health. Regulatory agencies have begun international and national reviews of safety regulations to ensure the unique physicochemical properties are nanomaterials sufficiently addressed in the existing methodologies for hazard and toxicity assessments used in risk analysis of hazardous chemical and biological substances [23].

Two interrelated aspects of nanomaterials and products require careful scrutiny. First, a growing body of the published literature indicates certain categories of nanomaterials-based products that have the potential to cause significant adverse impact on exposed environmental receptors due to the unique properties of material composition, shape and size, photoactivity, and redox potentials. The particle size range is such that particles below 5 nm could cross cell membrane and have dual capability of inducing response due to physical structure and chemical properties. Second, nanoparticles demonstrate environmental transport and fate and agglomeration with high aspect ratios due to a very large surface area.

Much of the environmental transport and fate studies have focused largely on nanomaterial-derived products that are already in production and/or in commercial use. The environmental impact of the processes surrounding nanocomposite fabrication have received relatively less attention, and safe handling and facility biosafety measures at production facilities generally follow established standard procedures, which are less suitable to addressing the unique and inherent hazard posed by nanomaterials.

1.4.1 Guiding Principles for Hazard Assessment

Toxicity assessment is based primarily on the physicochemical composition and structural complexity of the nanomaterial. For instance, published studies reporting dose–response relationship for induction of toxic effects have concluded that conventional description of dose as a "dose by mass" does not apply to nanomaterials, and that biological activity may depend on physical and chemical properties that are generally not captured in traditional toxicity assessments [24]. For instance, investigations have indicated surface area of nanomaterials [25], and particle number (Wittmaack [26]), and number of functional groups on the particle surface (Warheit et al. [27]) as better indicators of dose–response relationships, particularly for less soluble and low toxicity particles. Nevertheless, these studies are inconclusive on the physicochemical properties that critically determine the toxicity of nanomaterials.

Hazard assessment of nanomaterials attempts to classify the physical attribute and chemical composition of the nanomaterial under study as:

1. Nanomaterials as structures: Defined here are nanomaterials with complex structures, where toxicity is directed by unique physical structural features and very limited contribution from the chemical composition. Some evidence exist that carbon nanotubes demonstrate toxicity like asbestos fibers. Nanomaterials belonging to this category are grouped under the foundational concepts guiding toxicology of fibers and fibrous materials.
2. Nanomaterials as particles: Defined here are nanomaterials exhibiting physicochemical properties of particulates in terms of size, shape, and surface area in determining toxicity. Some evidence exist that automobile nanoparticles emissions demonstrate particle-oriented toxicity. The chemical composition of particulates has a limited role on the dose–response dependency on toxic effects.
3. Nanomaterials as depot: Defined here are nanomaterials with hazardous chemical composition. Nanomaterials acting as a depot release highly toxic chemicals which in turn induce toxic effects through conventional toxicodynamics. Nanomaterials as depot under this analysis merely serve as a novel toxicokinetics releasing hazardous chemicals in exposed receptors. Metallic

nanomaterials are reported to induce dose-dependent effects along this pathway.

Nanoparticles can have various shapes and forms and range from nanocrystals, quantum dots, fullerenes, nanowires, nanotubes which investigators have classified under four subcategories of systems depending on the physical structural attributes and binding characteristics. Thus, nanoparticles may remain bound, suspended in other solids or liquids that are not in the nanoparticulates range, or they may remain airborne [28].

Recognizing the importance of the structure of nanomaterials in safety and hazard assessments, many international standards setting institutions have begun classifying nanotechnology based on the different kinds of nanoparticles. These definitions include nanotubes, nanorods, quantum dots and for nanocrystalline materials based on the size, shape, and nanostructural properties. As a result, industries are increasingly adopting nanostructure-based hazard and toxicity assessment in product development, safe handling, and disposal for nanomaterials and nanomaterial-based products.

1.4.2 Toxicity and Safety Assessment Framework

Studies on toxicity and/or safety assessments fundamentally rely on data gathered from experimental studies and extrapolation models to assess their relevance to human exposures and risks. Based on these broad criteria, data on toxicity and safety of specific engineered nanomaterials and their component systems are not amenable to inter-species extrapolation [29, 30]. Studies have revealed that nanomaterial-induced adverse effects are fundamentally different from their bulk counterparts and there are no methodologies available to perform a systematic analysis to extrapolate existing data to nanostructural materials.

Figure 1.6 illustrates the proposed framework for toxicity assessment of nanomaterials based on the established tenets of fiber and particulate matter toxicity assessments. Since published studies have consistently indicated that fibers and particulate matter produce toxic effects through unique mechanisms, a similar trend is expected even in finely divided particulates and fibers in the nanometer ranges.

Figure 1.7 illustrates the dose–response range comparing cytotoxicity (IC_{50}) and lethal dose (LD_{50}) for nanomaterials comprising metallic compounds and toxic heavy metal mixtures.

Hence, severity of toxicity when mapped by kinetic considerations and molecular mechanism of action indicate that nanomaterial fiber-induced toxic effects are driven by toxicodynamics factors, and elucidated through biological pathways uniquely similar to fiber-induced toxicity. The toxicity of nanomaterials comprises metals and metalloid complex are driven by kinetics of absorption, uptake, and distribution comparable to their bulk counterparts. Published data on a

Fig. 1.6 Nanoparticulate and nanofiber toxicity sorted by behavior and capacity induce harmful effects that guide hazard assessment and risk assessment methods
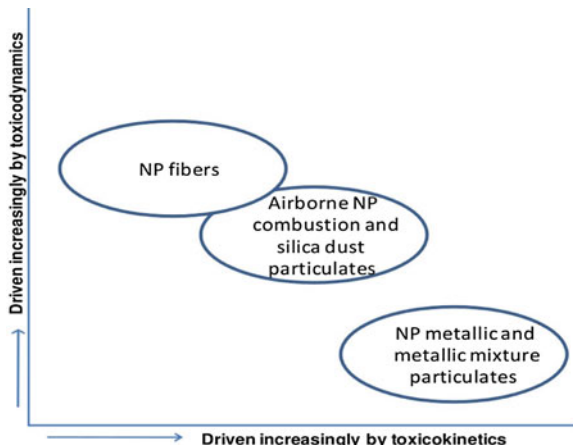
variety of nanomaterials comprise mixtures of toxic heavy metal and metallic compounds indicating a close correlation between lethal and cytotoxic doses and more easily soluble metallic mixtures such as copper, cobalt, nickel, and silver which consistently demonstrate a higher toxic response both for the induction of cytotoxic and lethal effects.

Fig. 1.7 Nanocomposites embedded with toxic heavy metals demonstrate a wide spread in dose–response for toxicity such as lethality, measured as LD_{50}, and cytotoxicity, measured as IC_{50}, in experimental systems

A considerable body of published literature describes toxicity of nanomaterials from inhalation exposures. Most studies have concluded that:
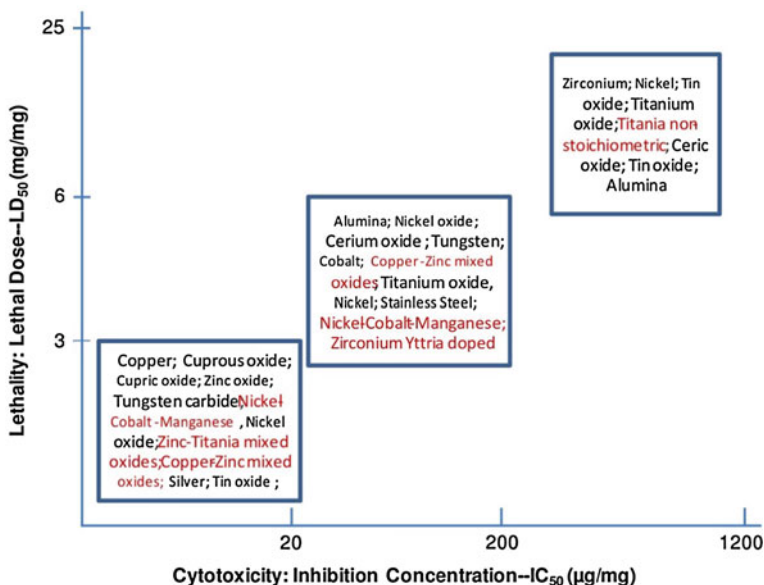
(a) Small particle size is a critical determinant in bioavailability, normally not the case with larger particle size. Nanomaterials are capable of easily translocating cellular barriers and transfer from lungs to circulating blood.
(b) Small particle size create enormously large surface area, which is directly linked to the increased lethal and cytotoxic effects of nanoscale metallic compounds.
(c) Large surface area of nanomaterials increases solubility and thereby increases bioavailability, having a direct bearing on the induction of toxic effects.
(d) Nanoscale particles have high aspect ratio similar to hazardous fibers such as asbestos. The physical shape, size, and dimension results in these materials remain embedded in various body compartments for extended periods, causing injury and long-term adverse effects, such as induction of carcinogenesis.

In conclusion, bionanocomposites represent a unique category of nanocomposites where the inspiration for design and fabrication is derived from naturally occurring materials. The current research work in this area will revolutionalize medical technology used to diagnose, treat, and cure diseases through product developments such as medical devices, surgical implants, drug delivery systems, and tissue engineering and regeneration. Research and design teams working on this integrate knowledge, data, and tool from vast interdisciplinary domains covering biotechnology, nanotechnology, information technology, and biomedical technologies. Much of the current work remains in the research and design concepts mostly derived from natural materials and attempts to better understand the unique physical and chemical properties of multi-component nanomaterials that are sensitive to change in nanoscale structures and morphologies. Multiscale system models are more actively investigated to design well-organized hierarchical patterns, where the key challenge is to precisely and carefully design organic–inorganic interfaces as systems scale from atomic to higher order structures while retaining the synergy of mechanisms acting over multiple scales across the fabric interface and to ensure optimal functional behavior of the fabricated product.

Health hazards and environmental impact of nanotechnology-based products have received considerable attention from government regulators all over the industrialized world. The hazard and risk assessment framework used for hazardous chemical and biological materials does not apply to nanocomposites. In the coming decades it is safe to conclude that scientists will devote considerable attention to study and better understand nanobiocomposites and their end-use applications, whereas regulators will carefully assess the potentials for long-term impact of nanocomposites on the environment.

References

1. Chu C (2010) Development of polymer nanocomposites for automotive applications. Thesis presented to Georgia Institute of Technology. December http://smartech.gatech.edu/jspui/bitstream/1853/37128/1/chu_chun_201012_mast.pdf
2. IBM (2007) IBM Brings Nature to computer chip manufacturing: First-ever manufacturing application of "self assembly" used to create a vacuum—the ultimate insulator—around nanowires for next-generation microprocessors. http://www-03.ibm.com/press/us/en/press release/21473.wss
3. Napp N, Klavins E (2011) A compositional framework for programming stochastically interacting robots. Int J Robot Res 30(6):713–729
4. US National Academy of Sciences (NAS) (2008) Inspired by biology: from molecules to materials to machines. ISBN-10:0-309-11704-6. National Academy Press, Washington DC
5. Bromley EH, Channon K, Moutevelis E, Woolfson DN (2008) Peptide and protein building blocks for synthetic biology: from programming biomolecules to self-organized biomolecular systems. ACS Chem Biol 3(1):38–50
6. Takahashi S, Sato M, Anzai J (2012) Layer-by-layer construction of protein architectures through avidin-biotin and lectin-sugar interactions for biosensor applications. Anal Bioanal Chem 402(5):1749–1758
7. Kim DC, Sohn JI, Zhou D, Duke TA, Kang DJ (2010) Controlled assembly for well-defined 3D bioarchitecture using two active enzymes. ACS Nano 4(3):1580–1586
8. Tan H, Zhou Q, Qi H, Zhu D, Ma X, Xiong D (2012) Heparin interacting protein mediated assembly of nano-fibrous hydrogel scaffolds for guided stem cell differentiation. Macromol Biosci 12(5):621–627
9. Li X, Koller G, Huang J, Di Silvio L, Renton T, Esat M, Bonfield W, Edirisinghe M (2010) A novel jetbased nano-hydroxyapatite patterning technique for osteoblast guidance. J R Soc Interface 7:189–197
10. Duan B, Wang M (2010) Customized Ca–P/PHBV nanocomposite scaffolds for bone tissue engineering: design, fabrication, surface modification and sustained release of growth factor. J R Soc Interface 7:S615–S629
11. Jung JP, Gasiorowski JZ, Collier JH (2010) Fibrillar peptide gels in biotechnology and biomedicine. Biopolymers. 94(1):49–59
12. Riley JM, Aggeli A, Koopmans RJ, McPherson MJ (2009) Bioproduction and characterization of a pH responsive self-assembling peptide. Biotechnol Bioeng 103:241–251
13. Gras SL, Tickler AK, Squires AM, Devlin GL, Horton MA, Dobson CM, MacPhee CE (2008) Functionalised amyloid fibrils for roles in cell adhesion. Biomaterials 29:1553–1562
14. Yamaguchi I, Tokuchi K, Fukuzaki H, Koyama Y, Takakuda K, Monma H, Tanaka J (2001) Preparation and microstructure analysis of chitosan/hydroxyapatite nanocomposites. J Biomed Materi Res 55(1):20–27
15. Wei D, Sun W, Qian W, Ye Y, Ma X (2009) The synthesis of chitosanbased silver nanoparticles and their antibacterial activity'. Carbohydr Res 344(17):2375–2382
16. Lee JY, Choi YS, Lee SJ, Chung CP, Park YJ (2011) Bioactive peptide-modified biomaterials for bone regeneration. Curr Pharm Des 17(25):2663–2676
17. Subramanian A, Krishnan UM, Sethuraman S (2009) Development of biomaterial scaffold for nerve tissue engineering: biomaterial mediated neural regeneration. J Biomed Sci 16:108
18. Xu RJ, Manias E, Snyder AJ, Runt J (2003) Low permeability biomedical polyurethane nanocomposites. J Biomed Mater Res Part 64A:114–119
19. Xu R, Manias E, Snyder AJ, Runt J (2001) New biomedical poly(urethane urea)-layered silicate Nanocomposites. Macromolecules 34:337–339
20. Valluzzi R, Gido SP, Muller W, Kaplan DL (1999) Bombyx mori silk fibroin liquid crystallinity and crystallization at aqueous fibroin-organic solvent interfaces. Int J Biol Macromol 24:227–236

21. Yan HB, Zang YQ, Ma YL, Zhou LX (2009) Biosynthesis of insulin-silk fibroin nanoparticles conjugates and *in vitro* evaluation of a drug delivery system. J Nanopart Res 11:1937–1946
22. Teow Y, Asharani PV, Prakash M, Valiyaveettil S (2011) Health impact and safety of engineered nanomaterials. Chem Commun 47:7025–7038
23. Novikova LN, Pettersson J, Brohlin M, Wiberg M, Novikov LN (2008) Biodegradable poly-b-hydroxybutyrate scaffold seeded with Schwann cells to promote spinal cord repair. Biomaterials 29:1198–1206
24. Oberdorster G, Maynard A, Donaldson K, Castranova V, Fitzpatrick J, Ausman K, Carter J, Karn B, Kreyling W, Lai D, Olin S, Monteiro-Riviere N, Warheit D, Yang H (2005) Principles for characterizing the potential human health effects from exposure to nanomaterials: elements of a screening strategy. Part Fibre Toxicol 2(8):1–35
25. Stoeger T, Takenaka S, Frankenberger B, Ritter B, Karg E, Maier K, Schulz H, Schmid O (2009) Deducing in vivo toxicity of combustion-derived nanoparticles from a cell-free oxidative potency assay and metabolic activation of organic compounds. Environ Health Perspect 117:54–60
26. Wittmaack K (2007) In search of the most relevant parameter for quantifying lung inflammatory response to nanoparticle exposure: particle number, surface area, or what? Environ Health Perspect 115:187–194
27. Warheit DB, Sayes CM, Reed K. Swai KA (2008) Health effects related to nanoparticle exposures: Environmental, health and safety considerations for assessing hazards and risks. Pharmacology Therapeutics, 120:35–42
28. Maynard AD, Aitken RJ (2007) Assessing exposure to airborne nanomaterials: current abilities and future requirements. Nanotoxicology 1(1):26–41
29. Thomas T, Thomas K, Sadrieh N, Savage N, Adair P, Bronaugh R (2006) Research strategies for safety evaluation of nanomaterials, Part VII: evaluating consumer exposure to nanoscale materials. Toxicol Sci 91(1):14–19
30. Lam CW, James JT, McCluskey R, Hunter RL (2004) Pulmonary toxicity of single-wall carbon nanotubes in mice 7 and 90 days after intratracheal instillation. Toxicol Sci 77:126–134
31. Uwe F, Andreas H, Petra BW, Katja S, Sigrid CS, Milauscha G, Andrea Z, Woranan P, Stefan Z, Dorit M, Alexander S, Carsten W (2009) A star-PEG-heparin hydrogel platform to aid cell replacement therapies for neurodegenerative diseases. Biomaterials 30:5049–5060
32. Haile Y, Berski S, Drager G, Nobre A, Stummeyer K, Gerardy-Schahn R, Grothe C (2008) The effect of modified polysialic acid based hydrogels on the adhesion and viability of primary neurons and glial cells. Biomaterials 29:1880–1891
33. Crompton KE, Goud JD, Bellamkonda RV, Gengenbach TR, Finkelstein DI, Hornet MK, Forsythe JS (2007) Polylysine-functionalised thermo responsive chitosan hydrogel for neural tissue engineering. Biomaterials 28:441–449
34. Duan X, McLaughlin C, Griffith M, Sheardown H (2007) Biofunctionalization of collagen for improved biological response: Scaffolds for corneal tissue engineering. Biomaterials 28:78–88
35. Schnell E, Klinkhammer K, Balzer S, Brook G, Klee D, Dalton P, Mey J (2007) Guidance of glial cell migration and axonal growth on electrospun nanofibers of poly-e-caprolactone and a collagen/poly-e-caprolactone blend. Biomaterials 28:3012–3025
36. Zhang Z, Rouabhia M, Wang Z, Roberge C, Shi G, Roche P, Li J, Dao LH (2007) Electrically conductive biodegradable polymer composite for nerve regeneration: electricity-stimulated neurite outgrowth and axon regeneration. Artif Organs 31:13–22
37. Bettinger CJ, Orrick B, Misra A, Langer R, Borenstein JT (2006) Microfabrication of poly (glycerol-sebacate) for contact guidance applications. Biomaterials 27:2558–2565
38. Kumar P, Sandeep KP, Alavi S, Truong VD, Gorga RE (2010) Preparation and characterization of bio-nanocomposite films based on soy protein isolate and montmorillonite using melt extrusion. J Food Eng 100:480–489

Chapter 2
Comparative Analysis of the IR Signal Enhancement of Biomolecules Adsorbed on Graphene and Graphene Oxide Nanosheets

Galyna Dovbeshko, Olena Fesenko, Olena Gnatyuk, Anna Rynder and Oleg Posudievsky

2.1 Introduction

Carbon nanostructures, namely, single-wall carbon nanotubes (SWCNT) and graphenes, are of great interest due to their unique electronic, thermal, optical, mechanical, and transport properties. Here we study a possibility of using these materials as enhancers of optical signals of adsorbed biomolecules similar to the effect earlier known for metallic and semiconducting surfaces in surface enhanced spectroscopy [1, 2]. Surface enhanced infrared absorption (SEIRA) and surface enhanced Raman scattering (SERS) effects have been known for the past 40 years. They consist in enhancement of optical process cross section for molecules located near curved metal surface. The enhancement for IR signal could be up to $(2–5) \times 10^2$ and up to 10^6 for RS. The explanation of the effect is complex and usually includes electromagnetic (the increase of the electromagnetic field near rough metal surface or island metal film) and chemical (the increase of the dipole transition moment of the adsorbed molecules) mechanisms. Earlier, we studied the SEIRA effect for DNA molecules absorbed on carbon nanotubes [3] and graphene [4] and found it to be up to 10 and 4, correspondingly. We also considered the

G. Dovbeshko (✉) · O. Fesenko · O. Gnatyuk · A. Rynder
Institute of Physics of the National Academy of Sciences, 46 Nauki Ave,
Kyiv 03028, Ukraine
e-mail: gd@iop.kiev.ua

A. Rynder
National University of Kyiv-Mohyla Academy, 2 Skovorody St, Kyiv 04070, Ukraine
e-mail: rynder@ukr.net

O. Posudievsky
L.V. Pisarzhevsky Institute of Physical Chemistry of the National Academy of Sciences,
31 Nauki Ave, Kyiv 03028, Ukraine
e-mail: posol@inphyschem-nas.kiev.ua

SERS effect for poly(A) molecules adsorbed on carbon nanotubes, the enhancement factor of which reached 10^5 [5]. In this work we compare different graphene-based nanostructured supports and reply to the question of what type of support, graphene or its oxide form, is more efficient. This study was done using thymine (Thy) molecule, one of the bases of DNA that could be useful for further sensor application of the nanocarbons.

2.2 Materials and Methods

Preparation of graphene and graphene oxide was based on primary mechano-chemical delamination of graphite microflakes (Alfa Aesar) [6]. Briefly, a dry mixture of the graphite microflakes and sodium chloride was mechanochemically treated in an agate grinding bowl using planetary ball mill. The product, a mixture of the nanostructured graphite and crystals of NaCl, was thoroughly washed with water to remove the salt and dried in vacuum at room temperature. To prepare a graphene dispersion, a definite amount of the prepared nanostructured graphite was ultrasonically disintegrated in dimethylformamide. The dispersion was purified by centrifugation, and the upper half of its volume was selected for further studies. The concentration of the graphene dispersion was about 0.13 mg/mL. The typical longitudinal size of the graphene sheets was in the range of 20–50 nm.

To prepare the graphene oxide, sodium chloride was replaced by potassium permanganate and a definite quantity of sulfuric acid. The mechanochemical treatment of the reaction mixture was carried out in the same conditions. A definite amount of the prepared nanostructured graphite oxide was dispersed in water. Dispersion was purified by centrifugation, and the upper half of its volume was selected for further studies. The concentration of the aqueous graphene oxide dispersion was about 1.0 mg/mL. The typical longitudinal size of the graphene sheets was in the range of 30–50 nm [6].

SWCNTs (A.M. Prokhorov General Physics Institute of Russian Academy of Sciences) were synthesized in arc discharge in the atmosphere of He, and then purified and characterized by high resolution transmission electron microscopy and Raman scattering [7]. The length of SWCNTs was from 1 to 2 μ, and the diameter from 0.9 to 1.6 nm with preferential fraction of 1.4–1.5 nm. The concentration of the stock aqueous dispersion of SWCNT prepared according to [5] was 0.1 mg/ml.

Thy was used as received from Sigma-Aldrich. We first prepared the stock solution of Thy (1 mg/mL) and divided it onto 4 aliquots. The probe with 1 weight part of the stock solution was mixed with SWCNTs (0.1–1 weight part of nanotubes) by ultrasonic disintegrator UZDN-A (Sumy-Pribor) and subsequent centrifugation (9,000 rpm) during 40 min. A probe of graphene and graphene oxide (0.03–0.1 weight part) was also ultrasonically mixed with 1 weight part of the stock solution of Thy for 15 min. Then, the samples for further studies were prepared by depositing a drop of the solution of Thy and that of Thy with graphene, graphene oxide, or carbon nanotubes on the gold support. The procedure

used for preparation of the samples ensured the same Thy/SWCNT, Thy/graphene, and Thy/graphene oxide weight ratios.

Home-made gold support for IR spectroscopy (Fig. 2.1) was produced in the Institute of Physics of NASU (Kiev, Ukraine) [8]. A thin layer of gold was prepared by vacuum deposition of the metal (99.999 pure) on the glass supports (TF-1 glass, 20 × 20 mm) via an intermediate adhesive Cr layer. Before the deposition, glass surface was cleaned by $NH_4OH:H_2O_2:H_2O$ and $HCl:H_2O_2:H_2O$ solution subsequently, both 1:2:2 by volume concentration for 5 min at boiling temperature. Then it was rinsed in distilled water and dried in a flow of pure nitrogen. The gold was evaporated from molybdenum heater and deposited at a rate of 1.0–1.5 nm s^{-1} on room temperature substrate. The thickness of gold surface was within 300–350 Å in the different experiments, the Cr interlayer being not thicker than 20 Å. The gold surface just after deposition looks like hydrophobic surface with wetting angle close to 80° and random roughness about 10–20 Å.

Confocal microscope LCM-510 (Germany) with laser excitation of 405, 543, and 488 nm was used to characterize the samples prepared for IR spectroscopy studies. The images were registered by a digital camera AxioCam [9].

Bruker IFS-66 instrument with a reflection attachment (the incidence angle of 16°30′) was used to register Fourier transform infrared (FTIR) spectra of Thy and its complexes with graphene, graphene oxide, and SWCNT in the reflectance mode (Fig. 2.2) in the 400–4,000 cm^{-1} range. Evaluation of the spectra was done with Opus 5.5 software. The position of the bands was estimated using the method of second derivative and/or standard method. Reproducibility of the frequency in the IR spectra was equaled to ±0.5 cm^{-1} and for absorption ±0.0005 a.u. The experimental enhancement factor was determined as the ratio of the integral intensity of the absorbance bands of Thy registered for Thy-graphene oxide/Au, Thy-graphene/Au, and Thy-SWCNT/Au systems to that for Thy/Au for the same

Fig. 2.1 AFM image of the *gold* support used in SEIRA studies
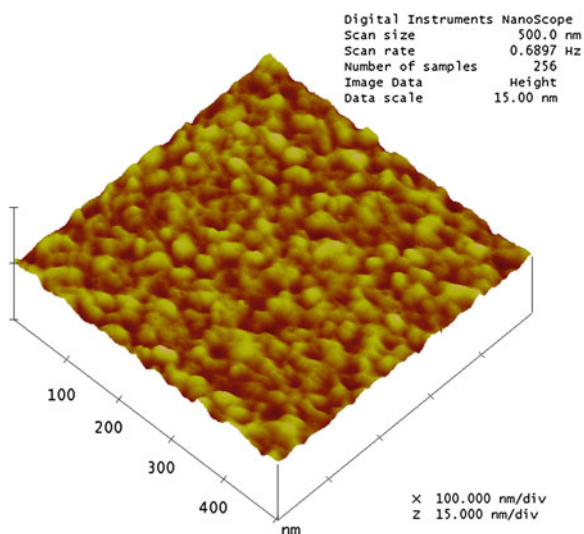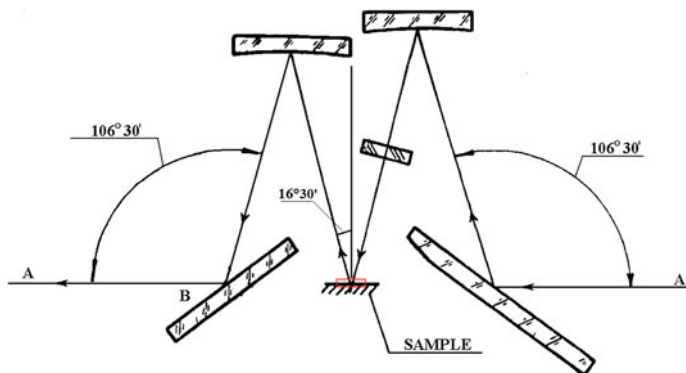
Fig. 2.2 Transmittance geometry of IR studies

amount of Thy. We used gold as IR substrate [9] for Thy due to the fact that CaF_2 or any other IR substrate will restrict the registration region (900–400 cm^{-1}) of IR spectra, especially the region of the most enhanced bands of Thy on graphene or SWCNT.

The total enhancement factor in the 500–1,800 cm^{-1} range for Thy adsorbed on graphene-based substrates was calculated as the ratio of the integral intensity of all bands of Thy adsorbed on graphene, graphene oxide, or nanotubes to that of Thy adsorbed on the gold support.

2.3 Results and Discussion

It is well known that all carbon materials can be effectively characterized by Raman spectroscopy. The main feature of the Raman spectra of graphite structure is the so called G-mode ($\sim$1,600 cm^{-1}) with lines of E_{2g}, E_{1g}, and A_{1g} symmetry in the Γ point of Brillouin zone that correlates with the ordering of crystal lattice of graphite structure. The second characteristic mode of the graphite-like materials is the so called D-mode ($\sim$1300cm^{-1}), with A_{1g} symmetry that characterizes the disorder of graphene layer lattice [10]. It refers to breathing vibrations of rings in graphene layer in the K point of Brillouin zone [10]. The second order mode of this vibration (so-called 2D or G$^{'}$ band) is registered at 2,600–2,700 cm^{-1}, and has the intensity that usually exceeds the intensity of second-order vibrations and even first order tones [11].

By analogy with SWCNT, Raman spectrum of graphene also contains G, D, and 2D bands. Position, line shape, and intensity of 2D (or G$'$) band could be used as a characteristic of the number of layers in the graphene sheets [11, 12]. The Raman spectra of the graphene and graphene oxide films are shown in Fig. 2.3. From the analysis of the graphene spectrum we could suppose that the sample has

Fig. 2.3 Raman spectra of graphene ($\lambda_{ex} = 532$ nm) and graphene oxide films ($\lambda_{ex} = 633$ nm)
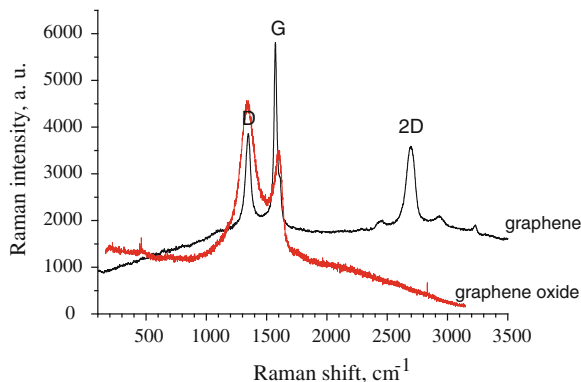
more than three layers. In the spectrum of graphene oxide we do not obtain the 2D mode.

Confocal microscopy data showed that graphene and graphene oxide films on the gold support have flake-like forms of different size: large fragments (more than 1 μ) and small ones (less than 1 μ) which consist of subclusters; graphene oxide has round-like homogeneous fragments, and their size is usually more than 2 μ (Fig. 2.4). The images in Fig. 2.4 were received by superimposition of three images obtained using lasers with the wavelengths of 405, 543, and 488 nm.

It is well known from the data of the numerical calculations [13] that adsorption of nucleobases on carbon nanotubes occurs by π–π stacking resulting in nearly flat geometry of Thy (or adenine). Here, we compare the experimental data obtained with vibration spectroscopy for Thy adsorbed on SWCNT, graphene and graphene oxide. The obtained Thy-graphene and Thy-graphene oxide complexes were characterized by IR spectroscopy (Fig. 2.5) and compared with Thy-SWCNT system. The enhancement factor in the case of SWCNT was generally greater in comparison with that obtained for graphene sheets. Its value for SWCNT was up to 5.3 and the largest enhancement factors were found for vibrations of C–H, C–OH, and C–N bonds. The maximum enhancement factor in the case of graphene equal to 3.7 was found for ring and deformational vibrations of N–H bonds. In our previous work [5] the obtained experimental data allowed us to suppose that H-bonds influence the interaction between SWCNT and Thy in Thy-SWCNT system, while the chemically induced charge transfer is likely dominant in the case of Thy-graphene/Au.

Complexes of Thy with graphene, graphene oxide, and SWCNT are assigned according to [14–17] and characterized by the following spectroscopic features:

1. In all complexes of Thy-graphene (Fig. 2.5), Thy-graphene oxide (Fig. 2.5) and Thy-SWCNT (Table 2.1), the $C_2=O$ vibration shows the enhancement of the intensity and a shift in the low-frequency region from 1,774 to 1,761 cm^{-1} (both for Thy-graphene and for Thy-SWCNT) and to 1,759 cm^{-1} (for Thy-graphene oxide) that indicates the formation of new intermolecular H-bonds with $C_2=O$ participation for these complexes.
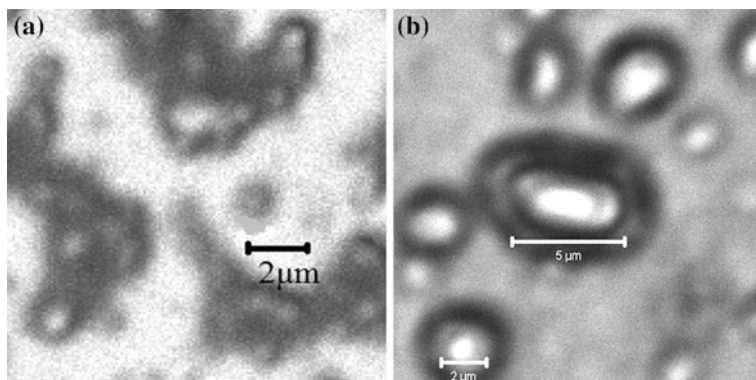
Fig. 2.4 Confocal images of graphene (**a**) and graphene oxide (**b**) (excitation wavelength: 405 nm—39 %, 543 nm—71 %, 488 nm—31 %; Filters: Ch2: LP 420, Ch3: LP 560, Ch2: LP 505; Pinhole Ch2: 150 μm, Ch3: 200 μm, Ch2: 180 μm)
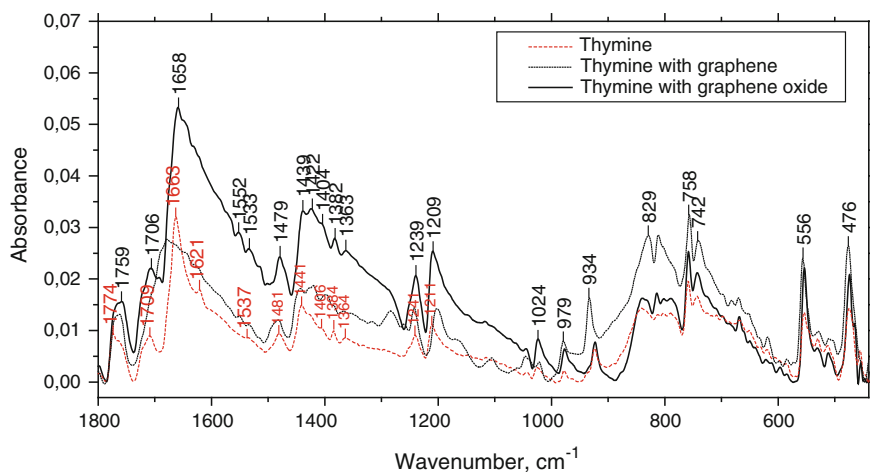
Fig. 2.5 SEIRA spectra of Thy and Thy adsorbed on graphene and graphene oxide

2. Thy-graphene (Fig. 2.5) and Thy-SWCNT (Table 2.1) shows decrease in the intensity of C_4=O vibration and a shift from 1,663 to 1,678 cm^{-1} in the case of graphene and to 1,679 cm^{-1} in the case of SWCNT [14], indicating the breaking of some of the inter- or intramolecular H-bonds with participation of C_4=O. In the case of graphene oxide, we observe an increase in the intensity of C_4=O vibration and a shift from 1,663 to 1,658 cm^{-1}.

3. The spectral range from 978 to 474 cm^{-1} assigned to deformation N–C_2, ring-bending, γ-CH, CO, N–H, and ring-bending vibrations for both Thy-graphene and Thy-SWCNT complexes show 4–5-fold increase in intensity of the major bands (Fig. 2.5). It should be noted that we observed 3–4 enhancement factor

Table 2.1 Enhancement factors and assignments of IR bands of Thy/Au; Thy-graphene/Au; Thy-graphene oxide/Au and Thy-SWCNT/Au systems [14–17]

Thy	Thy-Graphene		Assignment	Thy-Graphene oxide		Assignment	Thy + SWCNT		Assignment
	Wavenumber, cm^{-1}	g^{2}*		Wavenumber, cm^{-1}	g^{2}*		Wavenumber, cm^{-1}	g^{2}*	
1,774	1,761	1.5	C2=O	1,759	1.8	C2=O	1,761	2.1	C2=O
1,709	1,706	1.9	C$_2$=O	1,706	2.5	C$_2$=O	1,709	1.8	C$_2$=O
1,663	1,678	0.9	C$_4$=O	1,658	3.3	C$_4$=O	1,679	1.4	C$_4$=O
1,550	1,550	1.4	C=C	1,552	3.2	C=C	1,550	2.3	C=C
1,481	1,482	1.3	N$_1$-H def	1,479	2.6	N$_1$-H def	1,481	2.7	C-H$_3$ def
1,440	1,443	1.2	N$_1$-H def, C$_3$-H	1,439	2.8	N$_1$-H def, C$_3$-H	1,441	4.0	N$_1$-H def
1,427	1,420	1.4	C$_3$H def	1,422	2.9	C$_3$ H def	1,421	5.3	N$_1$-H def, C$_3$-H
1,364	1,366	3.0	N$_3$-H def	1,363	3.9	N$_3$-H def	1,364	4.0	N$_3$-H def.
1,241	1,241	1.7	C-C, C$_6$-H$_{def}$	1,239	2.7	C-C, C$_6$-H$_{def}$	1,241	1.7	C-C
1,211	1,202	1.3	C$_6$-H def, C$_2$-N$_3$ str.	1,209	2.3	C$_6$-H def, C$_2$-N$_3$ str.	1,201	2.3	C$_6$-H def, C$_2$-N$_3$ str.
1,025	1,022	1.5	CH, C-OH	1,024	3.0	CH, C-OH	1,024	4.2	C-H, C-OH
978	979	3.7	N-C$_2$, ring-bending	977	3.0	N-C$_2$, ring-bending	980	4.1	N-C$_2$, ring-bending
920	934	2.6	γ-CH	923	1.2	γ-CH	933	5.0	γ-CH
842	829	2.0	N$_3$-H, γ-C$_2$=O	832	1.2	N$_3$-H, γ-C$_2$=O	831	2.6	N$_3$-H, γ-C$_2$ = O
812	811	2.2	N$_1$-H, γ-C$_2$=O, γ-C$_4$=O	812	1.3	N$_1$-H, γ-C$_2$=O, γ-C$_4$=O	810	2.7	N$_1$-H, γ-C$_2$=O, γ-C$_4$=O
758	757	1.7	Skeletal ring mode	758	1.2	Skeletal ring mode	757	2.5	Skeletal ring mode
743	741	1.7	C$_4$=O	742	1.3	C$_4$=O			
619	617	2.2	γ- C$_4$=O	621	1.2	γ- C$_4$=O	617	2.3	γ-C$_4$=O
554	556	2.0	N-H	554	1.2	N-H	557	4.2	β-C$_4$=O
474	476	1.9	N-H	474	1.3	N-H	475	2.8	α-ring-bending

*g^{2} —enhancement factor

for N_3–H deformation vibrations (1,364 cm^{-1} for Thy on gold), N-C_2 ring-bending vibrations (978 cm^{-1} for Thy on gold) for all studied complexes Thy-graphene, Thy-graphene oxide (Fig. 2.5) and Thy-SWCNT (Table 2.1). However, the enhancement factor of the band of about 923 cm^{-1} for Thy-graphene oxide system is rather low as it is equal to 1.2 (Fig. 2.5). For Thy-graphene system, similar to that of Thy-SWCNT, we observed the increase in the intensity of γ-CH vibration and a shift from 920 to 934 cm^{-1} (933 cm^{-1} in the case of SWCNT).

Also, we have calculated the total enhancement factors for Thy-graphene and Thy-graphene oxide and found that they are equal to 1.6 and 2.0, correspondingly (Fig. 2.5). The dependence of the enhancement factor on the wavenumber for Thy-graphene (2), Thy-SWCNT (2), and Thy-graphene oxide is presented in Fig. 2.6.

As one can see from Fig. 2.6, the frequency dependence of the enhancement factor in the region of 1,800–400 cm^{-1} for Thy-SWCNT is similar to that for Thy-graphene. Such dependence for Thy-graphene oxide system has another tendency. Namely, in the case of Thy-graphene oxide we observed the enhancement in the region of 1,600–1,800 cm^{-1} in contrast to Thy-graphene and Thy/SWCNT, but did not observe it in the region of 400–900 cm^{-1}. However, both Thy-graphene and Thy-SWCNT show large enhancement in the region of 600–400 cm^{-1} for the majority of the bands. It could be assumed that in the case of Thy-graphene oxide the chemical mechanism is more preferential than in the case of Thy-graphene or Thy-SWCNT. The oxidation of graphene influences the enhancement factor of the infrared absorption.
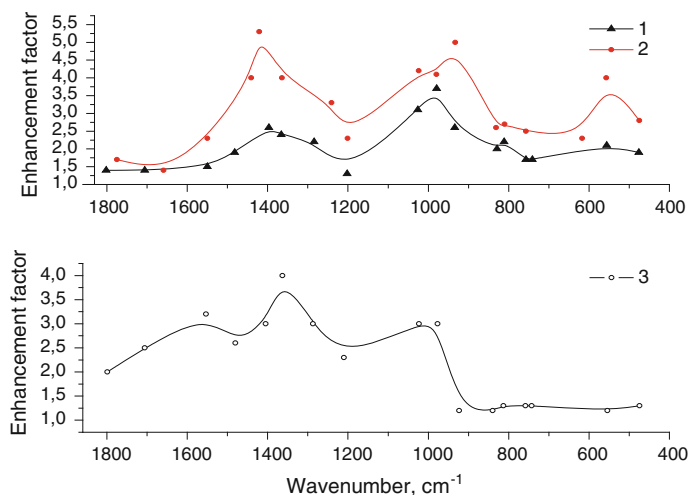

Fig. 2.6 The dependence of enhancement factor on the wavenumber for Thy-graphene (*1*), Thy-SWCNT (*2*), and Thy-graphene oxide (*3*)

We suppose that the local field enhancement mechanism weakly influences the enhancement of the vibrations of Thy adsorbed on graphene and does not influence the vibrations of Thy adsorbed on graphene oxide in contrast to those on SWCNT. In case of Thy adsorbed on SWCNT we registered an enhancement factor of up to 4.2 for all vibrations in the 400–900 cm^{-1} region. Local field enhancement on the edges of the carbon nanotubes is reported in [18]. They calculated and measured the peak in terahertz region which was connected with plasmon oscillations.

According to earlier publications, the plasmon frequency of carbon nanotubes is located in the far IR region [19, 20]. Plasmons in graphene seem to be located in the same region as well [20, 21]. Changing the length of nanotubes could influence the position of plasmon resonance [19] and shift it to far IR (FIR). Therefore, the presence of carbon nanotubes of different lengths in the Thy-SWCNT system could be a reason for the large enhancement factor for the bands in the spectrum region close to FIR. In general, one more reason for the SEIRA effect for Thy adsorbed on graphene and SWCNT in low frequency region is connected with crystalline packing of Thy molecules. We believe that in contrast to Thy-SWCNT with the total enhancement factor of 2.8, the lower total enhancement factor for Thy-graphene system (1.6) is due to decreased number of contact sites owing to the flake-type structure of graphene. For Thy-graphene oxide system the total enhancement factor is equal to 2.0 and the effect is characterized by selectively enhanced bands connected with C–O sites in graphene oxide.

2.4 Conclusion

It was first shown that graphene and graphene oxide can be used as a substrate for surface enhanced infrared spectroscopy. The enhancement factor for Thy molecules adsorbed on SWCNT is greater than that on graphene or graphene oxide nanosheets. The obtained experimental data allowed us to suppose that H-bonds influence the interaction between SWCNT and Thy in Thy-SWCNT, while the chemically induced charge transfer is likely dominant in the case of Thy-graphene and Thy-graphene oxide complexes. It was shown that the type of the frequency dependence of the enhancement factor in the region of 1,800–400 cm^{-1} is the same for Thy-SWCNT/Au and Thy-graphene/Au systems, but is different for Thy-graphene oxide/Au. That fact indicates that the oxidation degree of graphene has influence on the enhancement factor of the infrared absorption.

References

1. Domingo C (2004) Infrared spectroscopy on nanosurfaces. Opt Pur Apl 16:567–571
2. Kosobukin V (1983) The effect of enhancement the external field near the surface of metal and its manifestation in spectroscopy. Surface: Phys Chem Mech 12:5–20
3. Dovbeshko G, Gnatyuk O, Yakovkin K, Shuba MV, Maksimenko SA (2011) Chap. 2 in Physics, chemistry and application of nanostructure, Borisenko VE et al World Scientific London, Singapore, 291–294
4. Dovbeshko G, Fesenko O, Rynder A, Posudievsky O et al (2012) Enhancement of infrared absorption of biomolecules absorbed on single-wall carbon nanotubes and graphene nanosheets. J Nanophoton 6:061711
5. Dovbeshko G, Woods L, Damin A et al. (2010) Carbon nanotubes. In: Marulanda JM, In-Tech, pp 697–719
6. Posudievsky O, Khazieieva O, Koshechko V et al (2012) Preparation of graphene oxide by solvent-free mechanochemical oxidation of graphite. J Mater Chem 22:12465–12467
7. Obraztsova E, Bonard JM, Kuznetsov V et al (1999) Structural measurements for single-wall carbon nanotubes by Raman scattering technique. Nanostruct Mater 12:567–572
8. Panek J, Jezierska A, Dovbeshko G et al (2011) p-Nitrobenzoic acid adsorption on nanostructured Au surface investigated by combined experimental and computational approaches. Chem Phys Chem 12:1–12
9. Paddock S (ed) (1998) Confocal microscopy methods and protocols. Humana Press, Newcastle
10. Malard L, Pimenta M, Dresselhaus G et al (2009) Raman spectroscopy in graphene. Phys Reports 473:51–87
11. Saito R, Hofmann M, Dresselhaus G et al (2011) Raman spectroscopy in graphene and carbon nanotubes. Adv Phys 60:413–550
12. Thomsen C, Reich S et al (2000) Double resonant Raman scattering in graphite. Phys Rev Lett 85:5214–5217
13. Meng S, Maragakis P, Papaloukas C, Kaxiras E (2007) DNA nucleosides interaction and identification with carbon nanotubes. Nano Lett 7:45–50
14. Dovbeshko G, Woods L, Shtogun YA, Fesenko O (2009) Modeling of DNA base interactions with carbon nanotubes: ab initio calculations and SEIRA data. AIP C 1148:416–420
15. Colarusso P et al (1997) The infrared spectra of uracil, thymine, and adenine in the gas phase. Chem Phys Lett 269:39–48
16. Haiss W, Roelfs B, Port SN et al (1998) In-situ infrared spectroscopic studies of thymine adsorption on a Au(111) electrode. J Electroanal Chem 454:107–113
17. Nowak M, Lapinski L, Kwiatkowski J et al (1995) Molecular Structure and Infrared Spectra of Adenine. Experimental Matrix Isolation and Density Functional Theory Study of Adenine ^{15}N Isotopomers. J Phys Chem 100:3527–3534
18. Slepyan GY, Shuba MV, Maksimenko SA, Thomsen C, Lakhtakia A et al (2012) Experimental evidence of localized plasmon resonance in composite materials containing single-wall carbon nanotubes. Phys Rev B 85:165435
19. Slepyan GY, Shuba MV, Maksimenko SA, Thomsen C, Lakhtakia A (2010) Terahertz conductivity peak in composite materials containing carbon nanotubes: Theory and interpretation of experiment. Phys Rev B 81:205423
20. Crassee I, Orlita M, Potemski M, Walter A, Ostler M, Seyllller Th, Gaponenko I et al (2012) Intrinsic terahertz plasmons and magnetoplasmons in large scale monolayer graphene. Nano Lett 12:2470–2474
21. Yan H, Li X, Chandra B, Tulevski G et al (2012) Tunable infrared plasmonic devices using graphene/insulator stacks. Nat Nanotechnol 7:330–334

Chapter 3
Infrared Spectroscopy in Studying Biofunctionalised Gold Nanoparticles

Alexander A. Kamnev

Abbreviations

ATR	Attenuated total reflectance
DRIFT	Diffuse reflectance infrared fourier transform
FGNP	Functionalised gold nanoparticles
FTIR	Fourier transform infrared
GlcNAc	N-acetyl-D-glucosamine
(GlcNAc)$_3$	N', N'', N'''-triacetylchitotriose
GOX	Glucose oxidase
hIgG	Human immunoglobulin
IR	Infrared
SEIRA	Surface-enhanced infrared absorption
TEM	Transmission electron microscopy
WGA	Wheat germ agglutinin

3.1 Introduction

Over the last decade, nano-sized particles of noble metals with surface plasmon-resonance properties have found numerous applications in nanotechnology and scientific research, including diverse biological and biomedical fields (for recent reviews see, e.g. [1–9]. This also refers to (bio) functionalised metal nanoparticles, where the term "functionalisation" (or "biofunctionalisation") means conjugation of metal nanoparticles via either covalent bonds (e.g. involving thiol groups easily forming –S–metal bonds) or non-covalent binding forces (adsorption via charge attraction and/or hydrophobic interactions) with specific types of molecules [5, 10–12].

A. A. Kamnev (✉)
Laboratory of Biochemistry, Institute of Biochemistry and Physiology of Plants and Microorganisms, Russian Academy of Sciences, Prospekt Entuziastov 13, Saratov, Russia, 410049
e-mail: aakamnev@ibppm.sgu.ru; a.a.kamnev@mail.ru

The latter include, in particular, recognising bio(macro)molecules, such as antibodies, lectins, enzymes, peptide aptamers or nucleic acid aptamers, etc. [3], which are capable of participating in various biospecific interactions of the type "recognising molecule—target molecule". These types of biofunctionalised noble-metal nanoparticles can be useful in revealing such biospecific interactions with the relevant target molecules with a high sensitivity. In such cases either the noble-metal nanoparticles *per se* play the role of a direct "visualising agent" (in microscopic methods) or their surface plasmon-resonance properties are made use of (in optical and spectroscopic techniques).

To understand in detail the properties, stability and behaviour of these sophisticated metal nanoparticle–biomacromolecule conjugate systems [5, 13–15] and, also very importantly, to control their synthesis as well as to explore and develop proper useful applications [3, 16–18], various experimental methods and modern instrumental techniques are absolutely necessary [6, 19]. Among the latter, a range of molecular spectroscopy techniques has been successfully used [20], including UV–Vis spectrophotometry and vibrational [mainly Raman scattering and Fourier transform infrared (FTIR)] spectroscopy.

Spectrophotometry, largely in the visible region and, occasionally, in the near-IR, is useful for controlling the shape, size and aggregation of metal nanoparticles [21–25]. This is due to their typical extinction bands in the characteristic regions of plasmon resonance, both the position (wavelength in the maximum) and intensity of which are sensitive to the aforementioned characteristics of metal nanostructures. Thus, UV–Vis spectrophotometry is often used as a supplementary technique for the characterisation and/or monitoring of nanoparticle-based systems in suspensions and some of the processes occurring therein.

Vibrational spectroscopic techniques are of great importance both in the characterisation of functionalised metal nanoparticles (this refers primarily to their 'outer functional shells' of biomolecules which give specific vibrational patterns, depending on the state of their functional groups as well as on selective 'surface enhancement' effects) and in their diverse bioanalytical applications (for general reviews see, e.g. [26–28]). In particular, for functionalised metal nanoparticles the 'surface enhancement' effects and surface selection rules play a significant role in increasing the spectral sensitivity.

It is well known that in surface-enhanced Raman scattering (SERS) spectroscopy (for reviews on SERS see, e.g. [27, 29–31]), the enhancement factors reaching 10^{10}–10^{12} (up to 10^{15} for a combination of electromagnetic, resonance and chemical enhancements at 'hot spots') are much greater than those in surface-enhanced IR absorption (SEIRA) spectroscopy (for reviews on SEIRA see, e.g. [27, 32–34]). In SEIRA, the enhancement factors can reach values of the orders of 10^2–10^3 at best, while more usually they are of the order of units or tens [28, 35]. Owing to that, SEIRA spectroscopy is far less developed, studied and, consequently, less frequently used, being virtually "the neglected child of surface enhanced spectroscopies" [28]. Nevertheless, the cross-section values in infrared absorption are significantly higher than those in Raman scattering, so that the overall average sensitivities in SEIRA and SERS may be well comparable [33].
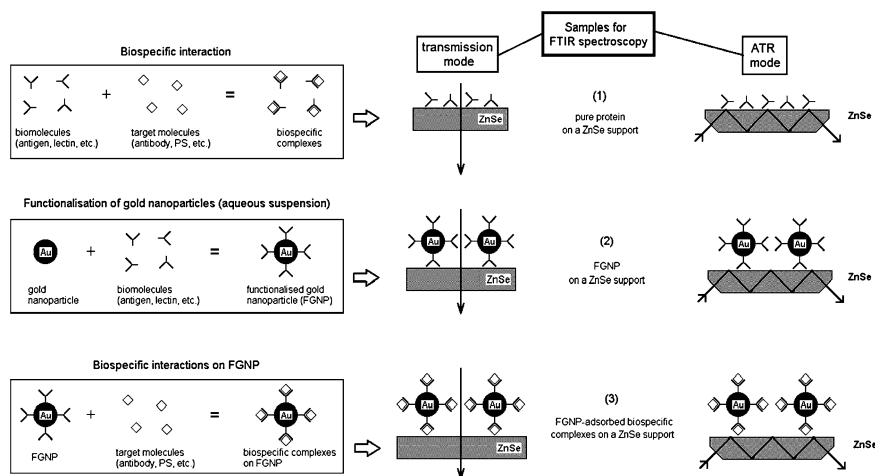
Fig. 3.1 Schematic presentation of the processes of biospecific interactions between pure biomolecules in solution (*upper left-hand panel*), functionalisation of gold nanoparticles by biomacromolecules (*middle left-hand panel*) and biospecific interactions on functionalised gold nanoparticles (FGNP; *lower left-hand panel*), as well as of the corresponding samples for FTIR spectroscopic measurements in the transmission or ATR modes on ZnSe supports (*right-hand panels* 1–3, respectively)

In addition, as a 'useful' supplement (partly compensating for the drawback of the strong water absorption in the infrared), FTIR/SEIRA spectra may give a wealth of complementary information as compared with Raman/SERS spectra.

In this chapter, some representative examples are reviewed and discussed in which Fourier transform infrared (FTIR) spectroscopy in various modes (transmission, diffuse reflectance (DRIFT), attenuated total reflectance (ATR) [36]) was applied for studying biofunctionalised gold nanoparticles, as well as for the detection and analysis of relevant biospecific interactions of the type "recognising molecule—target molecule" (e.g., using antigen–antibody or lectin–carbohydrate biospecifically interacting pairs) at the molecular level, where one type of the molecules from a pair was conjugated with gold nanoparticles (Fig. 3.1). The experimental results considered herein illustrate some possibilities of FTIR/SEIRA spectroscopy complementary to those discussed in previous reviews on its applications in biological or biomedical fields [28, 33–35, 37].

3.2 FTIR Spectroscopy in Studying Gold Nanoparticles Functionalised by Biomacromolecules

Virtually, the only significant intrinsic drawback of IR spectroscopy, as compared with Raman scattering, consists in a very strong IR absorption of water in several regions related to its O–H stretching and different bending vibrations. This fact is

of utmost importance, especially in biological and biomedical studies. Thus, if a biological sample contains a substantial amount of water (or is studied wet, which is sometimes practised for tissues and cells or even for biomacromolecules), in order to obtain reliable spectroscopic data, the spectral contribution of water must be carefully and fully compensated by its removal from the resulting IR spectrum (e.g. by quantitatively subtracting the spectrum of water obtained from a similar adequate "blank reference" sample). This is often a very challenging task, and it may also be additionally complicated by multiple hydrogen bonding in which water is readily involved. What is even more important, different types of such hydrogen bonding can significantly (and, quantitatively, almost always unpredictably) alter not only the intrinsic vibration frequencies of water contained in the sample in an appreciable proportion, but also those of the functional groups of the sample which are involved in the H-bonding. An alternative way of avoiding water-induced 'spectroscopic artefacts' while using 'wet' samples in FTIR spectroscopic studies implies the analysis of FTIR absorption regions or selected bands not overlapping with the typical water absorption regions.

In an earlier paper devoted to the development of SEIRA-based immunoassays [38], silicon plates were used sputter-coated with a very thin ($\sim$10 nm) gold film. Onto the film, either of the two proteins, glucose oxidase (GOX) or antibodies to glucose oxidase (anti-GOX), was immobilised, and FTIR/SEIRA spectra were compared for the immobilised protein and after its biospecific interaction with the other one. Whatever the results, it has to be noted that damp samples (immediately after their removal from the aqueous solutions) were used for measuring FTIR spectra. Thus, it could be seen that the strong and broad water absorption, particularly in the region at $\sim$1,650 cm^{-1}, completely masked the typical amide I ($\sim$1,650 cm^{-1}) and amide II ($\sim$1,540 cm^{-1}) bands of the proteins, so that other regions, with a few weak bands, were analysed [38].

In the next report from virtually the same group [39], goat anti-GOX immunoglobulin (IgG) and a few other immunoglobulins were conjugated with gold nanoparticles (10 nm average diameter), the conjugates were collected by vacuum filtering through porous Qualitative Polyethylene Infrared Cards (3M), and each of their FTIR/SEIRA spectra was measured also on such a wet porous polyethylene 3M IR card. The amide I band of any of the IgG proteins used (at $\sim$1,650 cm^{-1}) could also not be observed in that case owing to the presence of liquid water on the surface. However, it was specially mentioned [39] that the amide II region at $\sim$1,540 cm^{-1}, which was outside the water band absorption, was still not observed in the spectrum of the antibodies. (We would like to note here that a well-resolved amide II band at 1,540 cm^{-1} yet appeared in the SEIRA spectrum of the colloidal gold/anti-GOX/GOX complex on a similar wet 3M IR card [39], i.e. after the biospecific interaction of nanoparticle-conjugated GOX with anti-GOX; see our discussion below in Sect. 3.3).

The absence of the typical amide II band in FTIR/SEIRA spectra of a protein (IgG conjugated with gold nanoparticles), despite its being outside the water band absorption, was intriguing. In order to check whether it was still the effect of water or of the gold nanoparticle surface, a study was undertaken using ATR-FTIR

(SEIRA) spectroscopy of dried films of 30 nm-diameter gold nanosphere–protein conjugates [40].

The ATR-FTIR spectrum of pure staphylococcal protein A (shown in Fig. 3.2a), widely used in immunoassays [41], represented characteristic IR absorption regions of proteins, including the stretching modes of amide N–H at 3,290 and 3,077 cm^{-1} (on the background of a very broad absorption of carboxylic and alcoholic O–H groups in side chains centred at about 3,400 cm^{-1}); symmetric and antisymmetric vibration bands of CH_2 and CH_3 groups of amino acid side chains (within 3,000–2,800 cm^{-1}); strong typical amide I and amide II bands (representing mainly the stretching C=O and bending N–H modes of peptide moieties, respectively, at 1,652 and 1,540 cm^{-1}); bending CH_2 modes at 1,453 cm^{-1}; stretching $C–NH_2$ of side-chain primary amines near 1,400 cm^{-1}, as well as various weaker bands related to C–N, C–O and C–C–O vibrations of the protein backbone and amino acid residues under 1,350 cm^{-1} [36, 38–40, 42].

Interestingly, the spectrum of protein A conjugated with CG (shown in Fig. 3.2b) was found to be essentially different from that of pure protein A (cf. Fig. 3.2a). First of all, it should be noted that the amount of protein A in the sample of its CG conjugate taken for ATR-FTIR measurement (see Fig. 3.2b) was approximately fivefold less than that of pure protein A (see Fig. 3.2a). Nevertheless, the two to threefold higher absorbance values in maxima in Fig. 3.2b as compared to those in Fig. 3.2a indicate that a SEIRA effect was observed with enhancement factors of the order of 10–15. These values correspond largely to the electrostatic and hydrophobic nature of the gold nanoparticle surface conjugation with a biospecific probe due to the net effect of relatively weak non-covalent interactions, which allows the nativity of biomacromolecules and their functional

Fig. 3.2 ATR-FTIR spectra of dry films of staphylococcal protein A: (a) pure (100 μg of protein), (b) conjugated with colloidal gold (20 μg of protein; schemes of the samples are shown above each spectrum). All spectra were measured on a standard ZnSe 45° flat-plate ATR contact sampler (12 reflections). Redrawn using some data from [40] to illustrate information presented therein
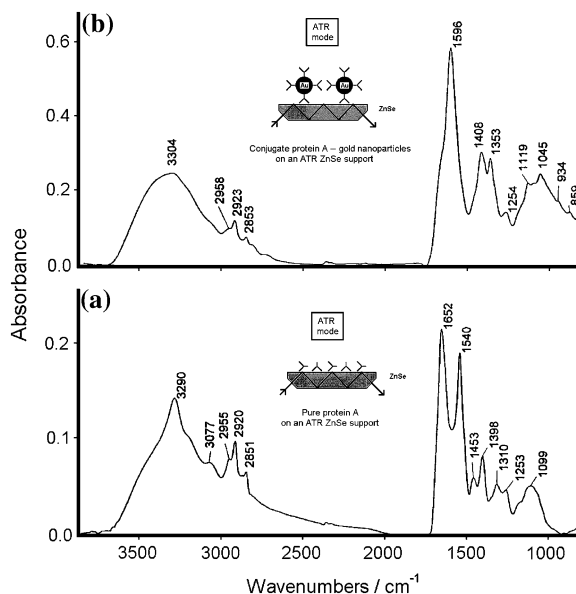
activity to be conserved (see [40] and references reported therein). It is known that stronger chemical (covalent) interactions of adsorbed molecules with the metal surface can result in enhancement factors increased by over one order of magnitude [32].

Second, the SEIRA spectrum (see Fig. 3.2b) showed that the amide N–H band at 3,290 cm^{-1} (see Fig. 3.2a) virtually disappeared. Moreover, instead of the amide I (1,652 cm^{-1}) and amide II (1,540 cm^{-1}) bands, in the SEIRA spectrum of the dry film of the gold nanoparticle–protein A conjugate there appeared a single intermediate strong peak centred at 1,596 cm^{-1} (with a shoulder at about 1,650 cm^{-1}). These changes may indicate that N–H moieties of the protein are directly involved in its interaction with the metal surface. Also enhanced are the regions of C–NH$_2$ vibrations near 1,400 cm^{-1} (see Fig. 3.2b), suggesting the involvement of side chain amino groups, and of C–C/C–O vibrations (1,150–1,000 cm^{-1}). Note that according to the SEIRA theory [32], only those molecular vibrations which appear perpendicular to the metal surface are enhanced, accounting for the selectivity of enhancement.

Thus, the ATR-FTIR/SEIRA result obtained using the dried film of the gold nanoparticle–protein A conjugate (see Fig. 3.2b; [40]) accounts for the absence of amide II band in the SEIRA spectra of wet colloidal gold conjugates with immunoglobulins discussed above [39]. In addition, the drastic changes in the spectrum of protein A induced by gold nanoparticles upon conjugation can provide evidence that protein molecules are attached directly to the gold nanoparticle surface, which is of primary importance for the synthesis of haptens with colloidal gold for subsequent immunisation of animals [43]. Thus, the FTIR-SEIRA methodology may be used for controlling the bioconjugation process [40].

It may be reasoned that, upon protein conjugation with the surface of a nanoparticle, the protein conformation may undergo some changes. It is important to emphasise that, if so, this could only partly, but certainly not fully, account for the observed FTIR (SEIRA) spectroscopic changes, since the latter are expected to be induced largely by the specific and selective surface enhancement of certain functional groups most close to the gold surface, considering also the surface selection rules for their vibrations [32]. For instance, conformational changes in bovine serum albumin (BSA) upon its conjugation with gold nanospheres (18 ± 2 nm in diameter) were also suggested [44] on the basis of comparative Raman scattering and SERS spectroscopic data. Note that the S–S stretching vibration of disulphide bridges observed in Raman spectra of BSA at 515 cm^{-1} was also observed in the SERS spectrum of BSA conjugate (with a slight shift to 520 cm^{-1}) with a comparable intensity [44]. This result showed that the disulphide bonds in BSA molecules remained largely unbroken upon BSA adsorption onto the 18 nm gold nanospheres.

On the other hand, there is a noteworthy report [45] where BSA was used for functionalisation of very small gold nanoparticles (less than 2 nm in diameter). For the resulting conjugate, the involvement of –S–Au protein–nanoparticle covalent bonds was proven by Raman spectroscopy (the S–S stretching mode of disulphide bonds in BSA reported to be at 508 cm^{-1} was found to completely disappear upon

BSA conjugation with the nanoparticles) and confirmed by calculations from energy-dispersive X-ray spectra (EDS). As a result, the FTIR spectra of pristine BSA and of the BSA–nanoparticle conjugate (both measured in dry powder pellets pressed with KBr) were found to be essentially similar, including the typical amide I (at 1,653 cm^{-1}) and amide II ($\sim$1,550 cm^{-1}) bands. This may be attributed to the absence of noticeable conformational changes of the protein backbone upon conjugation with such small nanoparticles. Last but not least, such small gold nanoparticles (<2 nm) are characterised by the absence of surface plasmon resonance owing to quantum size effects [45, 46] and, hence, lack of any selective surface enhancement (SEIRA) effects which could affect the FTIR spectrum of the conjugated protein.

A similar virtually undisturbed FTIR spectrum of pepsin (with the typical amide I band at 1,648 cm^{-1} and amide II at 1,536 cm^{-1}) was observed for a drop-dried pepsin conjugate with small gold nanoparticles (3.5 nm in diameter) on a Si(111) substrate measured in the diffuse reflectance (DRIFT) mode [47]. In that case, however, a weak broad feature at 2,520 cm^{-1} (typical of the –S–H stretching vibrations of cysteine residues in pepsin) was observed also in the conjugate, showing that not all of the cysteine residues were bound to the gold surface. Nevertheless, in that case 3.5 nm Au nanoparticles still exhibited a plasmon resonance band, which was reported to be initially at 512 nm and, for the conjugate in aqueous suspension (at pH $\sim$3 common for pepsin), was observed in UV–Vis spectra as a broadened peak at higher wavelengths (between 500 and 600 nm) together with the absorbance at 280 nm (π–π* transitions of the tryptophan and tyrosine residues in conjugated pepsin).

The FTIR spectroscopic data discussed above imply that in certain cases, e.g. when the size of the gold nanoparticles used for conjugation with a protein is relatively small (a few nm), the FTIR spectra of the pristine protein and of the protein attached to the gold nanoparticles may well show similar patterns (with much smaller differences than those seen in Fig. 3.2a, b, particularly in the amide I and amide II regions within $\sim$1,700–1,500 cm^{-1}). Of course, this spectroscopic similarity would be additionally facilitated when the small Au nanoparticles lack surface plasmon resonance owing to quantum size effects, so that no bands of the gold-conjugated protein could be selectively surface-enhanced.

It may also be suggested that, when a protein is bound to the gold nanoparticle surface largely by a number of covalent –S–Au bonds (rather than by non-covalent bonds via adsorption), its FTIR spectrum may well be generally similar to that of the pristine protein, showing only slight changes (e.g. in the secondary and/or tertiary structure). For example, in a recent paper [48], transforming growth factor-beta 1 (TGF-β1) was shown to conjugate to gold nanospheres ($\sim$13 nm in average diameter) via S–Au bonds. High-resolution X-ray photoelectron spectroscopy data for the TGF-β1–Au conjugate showed that 70.2 % of the three-component sulphur signal (S 2p) were due to S–Au bonds (the component at 162.1 eV), with the remaining 17.3 % of free thiol groups (S–H, 163.2 eV) and 12.5 % of disulphide (S–S, 163.8 eV), while pristine TGF-β1 contains only disulphide bonds in its dimeric molecule [48]. In the FTIR spectra (measured in the reflection mode from

Fig. 3.3 FTIR spectra of free A3 dodecapeptide (*1*) and A3 conjugated with gold nanoparticles (*2*). Redrawn using some data from [49] (Supporting Information) to illustrate information presented therein
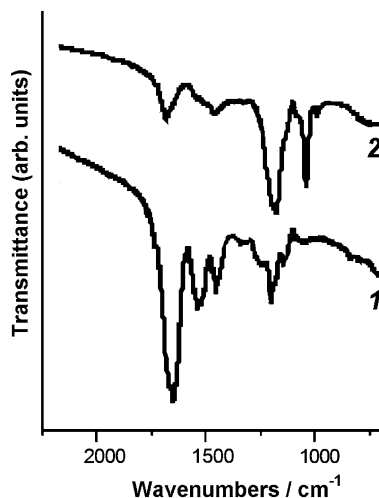
dry films on an Al plate), both the amide I and amide II bands were well resolved, while the comparative analysis of the amide I band profiles showed substantial conformational changes of TGF-β1 upon conjugation (note that the quantitative data for the secondary structure components in pristine TGF-β1 were found to be close to those for the NMR structure of solution-form TGF-β1 in the Protein Data Bank).

Yet, in many cases, FTIR data reported in the literature provide evidence for noticeable changes, involving both the band positions and redistribution of intensities, observed in FTIR spectra of proteins upon their adsorption onto gold nanoparticles or gold films. This may be illustrated by marked spectroscopic changes exhibited by an oligopeptide upon adsorption on gold nanoparticles. The A3 dodecapeptide (AYSSGAPPMPPF, where A = alanine, Y = tyrosine, S = serine, G = glycine, P = proline, M = methionine, F = phenylalanine) contains amino acids capable of interacting with the Au surface via non-covalent bonds. Its conjugate with gold nanospheres ($\sim 13 \pm 3$ nm in diameter determined by TEM) showed a FTIR spectrum (measured from a film on a Si wafer) which significantly differed from that of pure A3 [49] both in band positions and in redistribution of intensities (Fig. 3.3).

3.3 FTIR Spectroscopy in Studying Biospecific Interactions Involving Biofunctionalised Gold Nanoparticles

3.3.1 Immunochemical Interactions

It is well known that biomacromolecules which can be involved in biospecific interactions of the type "recognising molecule—target molecule", when conjugated with gold nanoparticles, particularly via non-covalent bonding, most often

Fig. 3.4 ATR-FTIR spectra (in the region under 2,000 cm^{-1}) of dried films of (**a**) pure protein A (100 μg of protein), (**b**) protein A conjugated with 30 nm gold nanospheres (20 μg of protein), (**c**) the same as (**b**) after interaction with hIgG in aqueous solution (schemes of the samples are shown on the right-hand panels). All spectra were measured on a standard ZnSe 45° flat-plate ATR contact sampler (12 reflections). Redrawn using some data from [51] to illustrate information presented therein
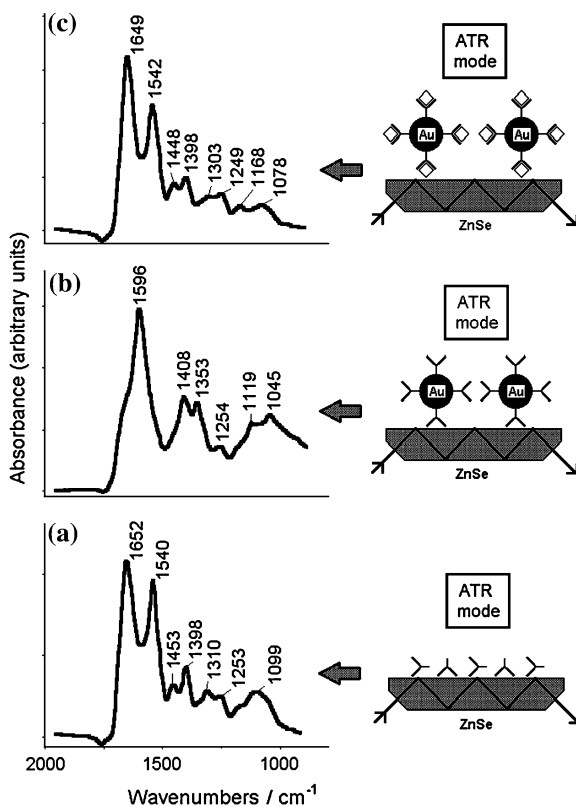
retain their binding capability, which is used in various assays involving colloidal gold bioconjugates [3]. In view of that, considering also the FTIR/SEIRA spectroscopic changes observed upon functionalisation of gold nanoparticles by biomacromolecules (see Sect. 3.2 and Fig. 3.2), it was of interest to study the FTIR spectroscopic behaviour of the biospecifically interacting pair.

With regard to the biospecifically interacting pair protein A—immunoglobulin, an important effect was observed after the immunochemical interaction of the gold nanospheres/protein A complex with human immunoglobulin (hIgG) in solution [40]. When the gold nanoparticles functionalised by protein A (antigen) were mixed in aqueous suspension with traces of hIgG (antibody) dissolved in water (see Fig. 3.1, lower left-hand panel), the resulting biospecific complex on gold nanoparticles (see Fig. 3.1, lower right-hand panel, sample 3) exhibited further FTIR spectroscopic alterations, in particular, in the amide I–amide II regions (~1,700–1,500 cm^{-1}).

In Fig. 3.4, FTIR-ATR spectra (in the most informative region under 2,000 cm^{-1}) of dried films on a ZnSe support are shown for pure protein A (spectrum *a*) as well as its conjugate with 30 nm gold nanospheres before (spectrum *b*) and after biospecific interaction with hIgG (spectrum *c*). The spectroscopic

changes observed in going from spectrum *b* to spectrum *c* consist in the 'resto-ration' of the main shape of the initial spectrum of protein A (see spectrum *a*), in particular, the well-resolved amide I and amide II bands, with a ca. 15-fold enhancement; the latter is somewhat smaller only in the C–C–O spectral region $(1{,}150–1{,}000 \text{ cm}^{-1})$. This finding accounts for the appearance of the amide II band observed after immunochemical interaction of gold nanoparticle-conjugated GOX with anti-GOX on wet 3M IR cards, while the amide I band was still 'obscured' by water absorption near $1{,}650 \text{ cm}^{-1}$ [39], as discussed above in Sect. 3.2.

This result makes it possible to detect such immunochemical interactions using the SEIRA effect with an enhancement factor found to be 10–15 [40], typical for SEIRA of adsorbed biomolecules. Importantly, the addition of BSA, which does not react with protein A, as a control to the colloidal gold/protein A complex had no effect on its spectrum.

In is important to emphasise that the spectrum of pure hIgG (reported also for comparison by [40], although generally resembling that of protein A (see Fig. 3.2a), was shown to have some essential differences. The fact that spectrum c in Fig. 3.4 (for the gold nanoparticle/protein A/hIgG complex) largely coincides in shape with that of pure protein A (see spectrum *a*) and differs from that of the gold nanoparticle/protein A complex (see spectrum *b*, Fig. 3.4) suggests that upon the reaction of hIgG with protein A on the surface of gold nanoparticles, the config-uration of protein A is modified. This is in line with the observations obtained earlier using SERS spectroscopy for another immune reaction on colloidal gold [50]. Moreover, it is unlikely that hIgG bound to protein A on gold nanoparticles as an 'outer shell' (i.e. additionally separated from the CG surface; see Fig. 3.1, lower right panel, sample 3) would exhibit any comparable SEIRA effect.

Note also that smaller gold nanoparticles (e.g., 15 nm in diameter) are more stable in solution and, although giving a somewhat less clear-cut FTIR-SEIRA spectroscopic changes than those observed on 30 nm particles (see [51] and ref-erences reported therein), can also be used for the SEIRA spectroscopic detection of biospecific interactions.

3.3.2 Lectin–Carbohydrate Interactions

A similar approach was attempted for FTIR spectroscopic investigation of lectin–carbohydrate interactions [51, 52]. It should be mentioned that there are relatively few reports related to lectin–carbohydrate specific biosensors (see, e.g. [53–56], and references therein).

A plant lectin, wheat germ agglutinin (WGA), was used for functionalising gold nanoparticles [52]. Wheat lectin (WGA) has been reported to induce multiple metabolic effects in wheat-associated rhizobacteria under appropriate conditions (see [51, 57], and references reported therein). The development of such effects is commonly initiated by biospecific interactions in a pair "receptor molecule—target molecule". In particular, WGA is well known to specifically bind *N*-acetyl-

Fig. 3.5 FTIR spectra of dried films of (**a**) pure wheat germ agglutinin (WGA; ca. 20 μg), (**b**) its conjugate with 15 nm gold nanoparticles (ca. 10 μg of WGA), as well as (**c**) the same as (**b**) after interaction with 5 μg (GlcNAc)$_3$ in aqueous solution. All spectra were measured in the transmission geometry on standard ZnSe crystal discs (Ø 13 mm, 2 mm thick). Redrawn using some data from [51, 52] to illustrate information presented therein
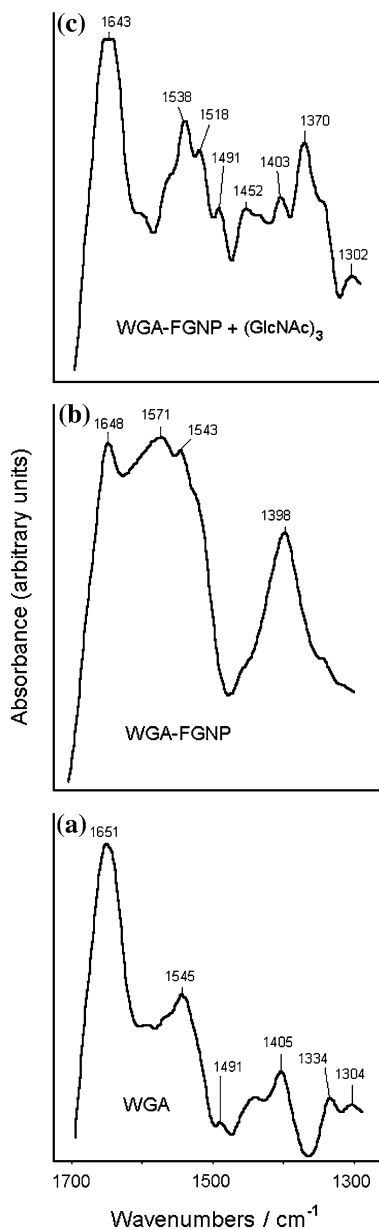
D-glucosamine (GlcNAc) residues (see, e.g. [58], which are present in some bacterial cell-surface biomacromolecules, thus bringing about the aforementioned multiple metabolic effects in bacterial cells under appropriate conditions.

Gold nanospheres (mean diameter 15 nm) functionalised by WGA were found to give SEIRA spectroscopic changes, as compared to pure WGA (cf. Fig. 3.5a, b),

similar to those for the protein A–gold nanoparticle system (see Fig. 3.4a, b). For WGA, the region of amide I and amide II bands is represented by maxima at 1,651 and 1,545 cm^{-1}, respectively, in agreement with the FTIR data reported earlier [58].

In the FTIR absorption spectrum of the dried film of the WGA-gold nanoparticle conjugate (Fig. 3.5b), instead of typical well-resolved amide I and amide II bands, there is an intermediate strong band centred at 1,571 cm^{-1} superimposed on the amide I and II band residues. In addition, there appears a strong band at 1,398 cm^{-1}. These changes, although less clear-cut than in FTIR-ATR spectra of 30 nm gold nanoparticles (see Fig. 3.4), are analogous to those observed in the FTIR spectrum of protein A conjugate with gold nanospheres measured in the transmission geometry [59]. These changes reflect the interactions of amide moieties and amino groups with the gold nanoparticle surface, in agreement with the conclusions drawn by other authors (see above; [51] and references therein). Note that proteins adsorbing onto the gold nanoparticle surface have been shown [60] to displace citrate ions weakly bound at colloidal gold particles formed upon reduction of [AuCl$_4$]$^-$ ions by citrate. The SEIRA enhancement factors for the WGA-gold nanoparticle system (Fig. 3.5b) were estimated to be also around 10–20 for different bands [52], depending on the orientations of transition dipole moment (TDM) components relative to the metal surface.

After biospecific interactions of the WGA-gold nanoparticle system in aqueous suspension with the GlcNAc trimer, (GlcNAc)$_3$ (N′, N″, N‴-triacetylchitotriose), further IR spectroscopic changes are observed (Fig. 3.5c). In particular, separate amide I and amide II bands have restored, in line with the spectroscopic changes observed for the protein A–hIgG system (cf. Fig. 3.4b, c). As mentioned above, such changes imply that upon biospecific interactions of the proteins with their target molecules, the configuration of the protein attached to the gold surface is modified. This conclusion is in agreement with the observations reported earlier for an immune reaction on colloidal gold using SERS spectroscopy [50]. It was also shown using FTIR spectroscopy [58] that WGA interaction with GlcNAc oligomers as well as with GlcNAc-bearing liposomes is accompanied by conformational changes in the lectin molecules reflected, in particular, in the amide I band profile.

Thus, the FTIR-SEIRA spectroscopic methodology has been shown to be applicable to the detection of lectin–carbohydrate biospecific interactions, using the example of WGA-gold nanospheres interacting with GlcNAc-containing haptens [52] and also with GlcNAc-containing bacterial cell-surface macromolecules [61], in line with their involvement in plant-bacterial interactions via WGA-mediated signalling.

3.4 Conclusions and Outlook

Applications of modern FTIR spectroscopy (in different modes) in biological fields continue to grow, and this is a logical consequence of its versatility, sensitivity, informativity and non-destructive nature. Nevertheless, as has been shown by

several examples in this chapter, further development of FTIR methodology in nanobiotechnology and nanobiosensing is very promising. This concerns not only structural studies of nanomaterials, but also sensitive monitoring of the bioconjugation processes involving metal nanostructures, resulting in their biofunctionalisation. A separate important field relates to further exploiting the surface plasmon resonance properties of biofunctionalised metal nanoparticles and their surface enhancement effects, in particular, SEIRA in FTIR spectroscopy, which has so far been underestimated. Finally, the possibilities for a sensitive detection of various biospecific interactions using FTIR/SEIRA spectroscopy on gold nanoparticles, illustrated in this chapter, should be further developed for a range of nanoparticles of different metals, shapes, sizes and functionalising bio(macro)molecules.

References

1. Khlebtsov NG, Dykman LA (2010) Optical properties and biomedical applications of plasmonic nanoparticles. J Quant Spectrosc Radiat Transfer 111:1–35
2. Dykman LA, Khlebtsov NG (2011) Gold nanoparticles in biology and medicine: recent advances and prospects. Acta Naturae 3(2):34–55
3. Dykman LA, Khlebtsov NG (2012) Gold nanoparticles in biomedical applications: recent advances and perspectives. Chem Soc Rev 41(6):2256–2282
4. Hartland GV, Schatz G (2011) Virtual issue: plasmon resonances—a physical chemistry perspective. J Phys Chem C 115:15121–15123
5. Mahmoudi M, Lynch I, Ejtehadi MR, Monopoli MP, Bombelli FB, Laurent S (2011) Protein–nanoparticle interactions: opportunities and challenges. Chem Rev 111:5610–5637
6. Pérez-López B, Merkoçi A (2011) Nanoparticles for the development of improved (bio) sensing systems. Anal Bioanal Chem 399(4):1577–1590
7. Hamad-Schifferli K (2013) How can we exploit the protein corona? Nanomedicine 8(1):1–3
8. Omidfar K, Khorsand F, Azizi MD (2013) New analytical applications of gold nanoparticles as label in antibody based sensors. Biosens Bioelectron 43:336–347
9. Ravindran A, Chandran P, Khan SS (2013) Biofunctionalized silver nanoparticles: advances and prospects. Colloids surfaces B: Biointerfaces. doi:10.1016/j.colsurfb.2012.07.036)
10. You C–C, Chompoosor A, Rotello VM (2007) The biomacromolecule-nanoparticle interface. Nano Today 2(3):34–43
11. Thanh NTK, Green LAW (2010) Functionalisation of nanoparticles for biomedical applications. Nano Today 5(3):213–230
12. Feng J, Pandey RB, Berry RJ, Farmer BL, Naik RR, Heinz H (2011) Adsorption mechanism of single amino acid and surfactant molecules to Au 111 surfaces in aqueous solution: design rules for metal-binding molecules. Soft Matter 7(5):2113–2120
13. Roach P, Farrar D, Perry CC (2005) Interpretation of protein adsorption: surface-induced conformational changes. J Amer Chem Soc 127(22):8168–8173

14. Teichroeb JH, McVeigh PZ, Forrest JA (2009) Influence of nanoparticle size on the pH-dependent structure of adsorbed proteins studied with quantitative localized surface plasmon spectroscopy. Eur Phys J E 30(2):157–164

15. Shemetov AA, Nabiev I, Sukhanova A (2012) Molecular interaction of proteins and peptides with nanoparticles. ACS Nano 6(6):4585–4602

16. Rosi NL, Mirkin CA (2005) Nanostructures in biodiagnostics. Chem Rev 105(4):1547–1562

17. Dykman LA, Bogatyrev VA (2007) Gold nanoparticles: preparation, functionalisation and applications in biochemistry and immunochemistry. Russ Chem Rev 76(2):181–194

18. Gagner JE, Shrivastava S, Qian X, Dordick JS, Siegel RW (2012) Engineering nanomaterials for biomedical applications requires understanding the nano-bio interface: a perspective. J Phys Chem Lett 3(21):3149–3158

19. Gadogbe M, Ansar SM, He G, Collier WE, Rodriguez J, Liu D, Chu I-W, Zhang D (2013) Determination of colloidal gold nanoparticle surface areas, concentrations, and sizes through quantitative ligand adsorption. Anal Bioanal Chem 405(1):413–422

20. Daniel M-C, Astruc D (2004) Gold nanoparticles: assembly, supramolecular chemistry, quantum-size-related properties, and applications toward biology, catalysis, and nanotechnology. Chem Rev 104(1):293–346

21. Khlebtsov NG, Bogatyrev VA, Dykman LA, Melnikov AG (1996) Spectral extinction of colloidal gold and its biospecific conjugates. J Coll Interface Sci 180(2):436–445

22. Shipway AN, Lahav M, Gabai R, Willner I (2000) Investigations into the electrostatically induced aggregation of Au nanoparticles. Langmuir 16(23):8789–8795

23. Kelly KL, Coronado E, Zhao LL, Schatz GC (2003) The optical properties of metal nanoparticles: the influence of size, shape, and dielectric environment. J Phys Chem B 107(3):668–677

24. Willets KA, Van Duyne RP (2006) Localized surface plasmon resonance spectroscopy and sensing. Annu Rev Phys Chem 58:267–297

25. Amendola V, Meneghetti V (2009) Size evaluation of gold nanoparticles by UV − vis spectroscopy. J Phys Chem C 113(11):4277–4285

26. Dovbeshko GI, Fesenko OM, Shirshov YuM, Chegel VI (2004) The enhancement of optical processes near rough surface of metals. Semicond Phys Quant Electron Optoelectron 7(4):411–424

27. Aroca R (2006) Surface-enhanced vibrational spectroscopy. Wiley, Chichester, p 400

28. Larmour IA, Graham D (2011) Surface enhanced optical spectroscopies for bioanalysis. Analyst 136(19):3831–3853

29. Kneipp K, Kneipp H, Itzkan I, Dasari RR, Feld MS (1999) Ultrasensitive chemical analysis by Raman spectroscopy. Chem Rev 99(10):2957–2975

30. Talley CE, Huser T, Hollars CW, Jusinski L, Laurence T, Lane S (2005) Nanoparticle based surface-enhanced Raman spectroscopy. In: Wilson BC, Tuchin VV, Tanev S (eds) Advances in Biophotonics (NATO science series, I: life and behavioural sciences, vol 369, pp 182–195

31. Hering K, Cialla D, Ackermann K, Dörfer T, Möller R, Schneidewind H, Mattheis R, Fritzsche W, Rösch P, Popp J (2008) SERS: a versatile tool in chemical and biochemical diagnostics. Anal Bioanal Chem 390(1):113–124

32. Osawa M (2001) Surface-enhanced infrared absorption. In Kawata S (ed) Near-field optics and surface plasmon polaritons. Topics in applied physics, vol 81, Springer, Berlin, pp 163–187

33. Aroca RF, Ross DJ, Domingo C (2004) Surface-enhanced infrared spectroscopy. Appl Spectrosc 58(11):324A–338A

34. Ataka K, Heberle J (2007) Biochemical applications of surface-enhanced infrared absorption spectroscopy. Anal Bioanal Chem 388(1):47–54

35. Donaldson PM, Hamm P (2013) Gold nanoparticle capping layers: Structure, dynamics, and surface enhancement measured using 2D-IR spectroscopy. Angew Chem Int Ed 52:634–638

36. Schmitt J, Flemming H-C (1998) FTIR-spectroscopy in microbial and material analysis. Int Biodeterior Biodegrad 41(1):1–11

37. Dubois J, Shaw RA (2004) IR spectroscopy. Clinical and diagnostic applications. Anal Chem 76(19):361A–367A
38. Brown CW, Li Y, Seelenbinder JA, Pivarnik P, Rand AG, Letcher SV, Gregory OJ, Platek MJ (1998) Immunoassays based on surface-enhanced infrared absorption spectroscopy. Anal Chem 70(14):2991–2996
39. Seelenbinder JA, Brown CW, Pivarnik P, Rand AG (1999) Colloidal gold filtrates as metal substrates for surface-enhanced infrared absorption spectroscopy. Anal Chem 71(10):1963–1966
40. Kamnev AA, Dykman LA, Tarantilis PA, Polissiou MG (2002) Spectroimmunochemistry using colloidal gold bioconjugates. Biosci Rep 22(5–6):541–547
41. Dykman LA, Bogatyrev VA (1997) Colloidal gold in solid-phase assays. A review. Biochem (Moscow) 62(4):350–356
42. Wanzenbök HD, Mizaikoff B, Weissenbacher N, Kellner R (1997) Multiple internal reflection in surface enhanced infrared absorption spectroscopy (SEIRA) and its significance for various analyte groups. J Mol Struct 410–411:535–538
43. Dykman LA, Matora LYu, Bogatyrev VA (1996) Use of colloidal gold to obtain antibiotin antibodies. J Microbiol Meth 24(3):247–248
44. Iosin M, Toderas F, Baldeck PL, Astilean S (2009) Study of protein–gold nanoparticle conjugates by fluorescence and surface-enhanced Raman scattering. J Mol Struct 924–926:196–200
45. Burt JL, Gutiérrez-Wing C, Miki-Yoshida M, José-Yacamán M (2004) Noble-metal nanoparticles directly conjugated to globular proteins. Langmuir 20(26):11778–11783
46. Alvarez MM, Khoury JT, Schaaff TG, Shafigullin MN, Vezmar I, Whetten RL (1997) Optical absorption spectra of nanocrystal gold molecules. J Phys Chem B 101(19):3706–3712
47. Gole A, Dash C, Ramakrishnan V, Sainkar SR, Mandale AB, Rao M, Sastry M (2001) Pepsin-gold colloid conjugates: preparation, characterization, and enzymatic activity. Langmuir 17(5):1674–1679
48. Tsai Y-S, Chen Y-H, Cheng P-C, Tsai H-T, Shiau A-L, Tzai T-S, Wu C-L (2013) TGF-β1 conjugated to gold nanoparticles results in protein conformational changes and attenuates the biological function. Small. doi:10.1002/smll.201202755
49. Slocik JM, Stone MO, Naik RR (2005) Synthesis of gold nanoparticles using multifunctional peptides. Small 1(11):1048–1052
50. Dou X, Yamaguchi Y, Yamamoto H, Doi S, Ozaki Y (1998) NIR SERS detection of immune reaction on gold colloid particles without bound/free antigen separation. J Raman Spectrosc 29(8):739–742
51. Kamnev AA (2008) FTIR spectroscopic studies of bacterial cellular responses to environmental factors, plant-bacterial interactions and signalling. Spectrosc Int J 22(2–3):83–95
52. Kamnev AA, Dykman LA, Bogatyrev VA, Sadovnikova JN, Tarantilis PA, Polissiou MG (2007) Infrared spectroscopic detection of biospecific interactions using gold nanoparticles functionalised by biomacromolecules. In: Shtykov SN (ed) Proceedings of 10th Analytical Russian-German-Ukrainian symposium (ARGUS'2007—Nanoanalytics), Nauchnaya Kniga, Saratov (Russia), pp 10–13
53. Sadik OA, Yan F (2007) Electrochemical biosensors for monitoring the recognition of glycoprotein–lectin interactions. Anal Chim Acta 588(2):292–296
54. Lyu Y-K, Lim K-R, Lee BY, Kim KS, Lee W-Y (2008) Microgravimetric lectin biosensor based on signal amplification using carbohydrate-stabilized gold nanoparticles. Chem Comm 39:4771–4773
55. Peiris D, Markiv A, Dwek M (2011) A physiological approach to assess the affinity of lectin carbohydrate interactions using cancer cells immobilised on a biosensor surface. Glycobiology 21(11):1523
56. Gorityala BK, Lu Z, Leow ML, Ma J, Liu X-W (2012) Design of a "turn-off/turn-on" biosensor: Understanding carbohydrate-lectin interactions for use in noncovalent drug delivery. J Amer Chem Soc 134(37):15229–15232

57. Kamnev AA, Sadovnikova JN, Tarantilis PA, Polissiou MG, Antonyuk LP (2008) Responses of *Azospirillum brasilense* to nitrogen deficiency and to wheat lectin: a diffuse reflectance infrared Fourier transform (DRIFT) spectroscopic study. Microb Ecol 56(4):615–624

58. Bonnin S, Besson F, Gelhausen M, Chierici S, Roux B (1999) A FTIR spectroscopy evidence of the interactions between wheat germ agglutinin and *N*-acetylglucosamine residues. FEBS Lett 456(3):361–364

59. Kamnev AA, Dykman LA, Tarantilis PA, Polissiou MG (2002) Surface-enhanced Fourier transform infrared spectroscopy of protein a conjugated with colloidal gold. In: Khassanova L, Collery P, Maymard I, Khassanova Z, Etienne J-C (eds) Metal Ions in biology and medicine, vol 7. John Libbey Eurotext, Paris, pp 104–107

60. Chithrani BD, Ghazani AA, Chan WCW (2006) Determining the size and shape dependence of gold nanoparticle uptake into mammalian cells. Nano Lett 6(4):662–668

61. Kamnev AA, Dykman LA, Antonyuk LP, P.A. Tarantilis PA, Polissiou MG (2006) FTIR spectroscopic detection and study of biospecific interactions using functionalised gold nanoparticles. In: Akyüz S, Akalin E (eds) XXVIII European congress on molecular. spectroscopy, Sept 3–8, 2006, Istanbul, Turkey. Book of abstracts, Abstr. No. OA-07, p 31

Chapter 4
Formation of Nanoparticle Chains Within Liquid Crystal Defect Arrays

L. Pelliser, D. Coursault and E. Lacaze

One of the specific challenges in the study of nanomaterials is the assembly of nanometer-sized objects in macroscopic assemblies. Such materials can find new applications in both research and engineering according to the researcher's capability to interact with a large number of particles at once, while controlling their final state [1, 2]. Gold nanoparticles, thanks to their highly tunable optical properties, are thus one of the most studied nano-objects alongside carbon nanotubes (CNT). Their localized surface plasmon resonance (LSPR) offers numerous size- and environment-dependent measurable effects. This property leads to an interest in methods to manipulate the surroundings of such particles and, in particular, the neighboring nanoparticles, which highly influence the optical response of the observed NPs.

Here, we are studying the possibility of creating a large structure to guide the gold nanoparticles in forming a series of parallel chains of nanoparticles [3], with the final goal of having the particles being close enough to each other for an interaction to be detected. A promising solution to that goal was the use of liquid crystals (LC). They are indeed able to provide us with anisotropic structures [4–6] which could be used to trap the nanoparticles and, more importantly, could lead to an anisotropic optical response of the nanoparticles (NP).

Although both nematic and smectic liquid crystals can lead to linear structural topological defects, smectics appear to be more adapted to our requirements as they allow better trapping and alignment compared to nematics [7–9]. These defects are able to host impurities or, here, nanoparticles, and thus constitute a strong candidate for the goal of assembling these nanoparticles in long-range linear structures.

L. Pelliser · D. Coursault · E. Lacaze (✉)
CNRS, UMR 7588, Institut des Nano-Sciences de Paris (INSP), 4, place Jussieu, 75005 Paris, France
e-mail: emmanuelle.lacaze@insp.jussieu.fr

4.1 Oily Streaks in Liquid Crystal

The liquid crystal used in the experiments described in this paper is the 4-n-octyl-4$'$-cyanobiphenyl, more commonly called 8CB. At room temperature, this material is in a smectic A phase, and therefore, constituted of a series of parallel layers. Each of these layers is made of numerous 8CB molecules roughly parallel to each other and being normal to the layer itself. 8CB is characterized by an ordinary index perpendicular to the molecules, no = 1.52 and an extraordinary index, parallel to the molecules, ne = 1.67.

The smectic layer will be influenced by the two boundaries on each side of the liquid crystal; the contact surface with the air above the 8CB and the contact surface with the substrate under the 8CB. While there is no specific condition relating to the air (room temperature being the only one), the substrate must be prepared in a specific way to allow the creation of the oily streaks. In this paper, the substrate was made of a polymer, poly vinyl alcohol (PVA). Once the polymer has been deposited on a glass sample, the substrate is rubbed in order to create a planar anchoring of the 8CB molecules on it, which will in combination with the anchoring on air, lead to the correct boundary condition for the creation of the desired structures. The liquid crystal is then deposited with, if required for the experiment, nanoparticles.

The planar unidirectional anchoring implies that the layers of liquid crystal will have their director vector (the directional vector of the LC molecules inside a layer) parallel to the substrate itself, the rubbing ensuring that this direction will be the same all along the sample. On the second boundary (liquid crystal/air), the anchoring is homeotropic, with the director vector (and so the molecules) perpendicular to the boundary itself. The liquid crystal is therefore forced to have two different directions on each of its boundaries which leads to the structures studied in our work, the so-called oily streaks (Fig. 4.1a) [4, 5, 10].
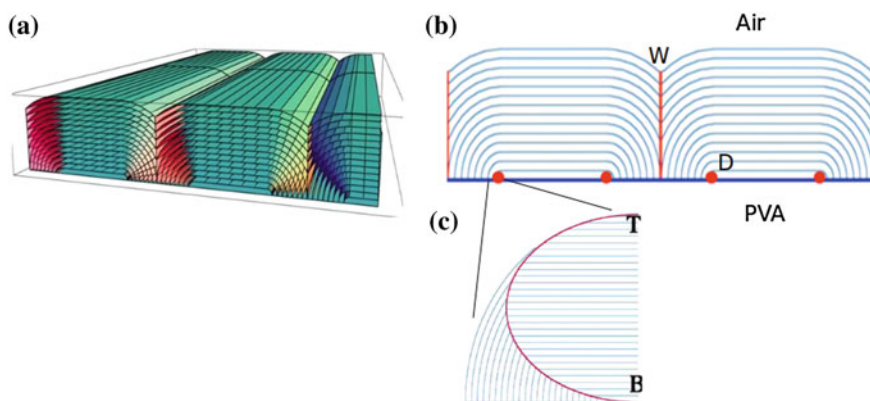

Fig. 4.1 **a**, **b** Oily streaks created by the deposition of LC on rubbed substrate (PVA), with defect areas (curvature planes between two consecutive hemicylinders—W on the picture—and curvature centers, the so-called disclinations—D on the picture) highlighted. **c** Structure of the inner layers of the LC, near the substrate, with a distortion under the form of a rotated grain boundary taking place close to the curvature center

Michel and coworkers dealt with such structures (on another substrate, MoS_2) and made a first set of experiments, observations, and analysis of these oily streaks [11]. It established a first model of the behavior of the layers, describing them as a series of parallel flattened hemicylinders (Fig. 4.1a) with, as shown in Fig. 4.1b, two types of defects: the curvature walls and disclinations. He has shown that the disclination corresponds to a substructure close to the substrate, associated with a rotating grain boundary which replaces the rotating layers too close from the curvature centers (Fig. 4.1c).

4.2 Nanoparticle Deposition

The trapping phenomenon was first studied through fluorescence microscopy illuminating and observing quantum dots, QD (CdSe-ZnS, diameter of 5 nm, purchased from Invitrogen, $\lambda_{ex} = 440$ nm, $\lambda_{em} = 565$ nm) deposited together with 8CB liquid crystal above a PVA substrate (30 μL of a solution with 10^{12} QD/ L and 5.10^{-3} M/L of 8CB diluted in toluene, leading to a 0.7 QD/μm^2 surface concentration). Fluorescence microscopy image evidences the alignment of QDs in chains as long as tens of micrometers (Fig. 4.2, bottom).

The presence of QDs was then observed in alignments separated by a distance similar to the one between various walls (between 0.64 and 7.5 μm for the PVA/ 8CB combination, with strong LC thickness variation explaining the large range of distances). This observation leads us to conclude that essentially one area per hemicylinder is occupied by a nanoparticles alignment. These alignments appear to be small segments of emitting nanoparticles, but the fluorescence microscopy does not allow the observation of further details of their organization, such as the length and width (expressed in number of particles in close distance to each other) of these segments.

Further observations done with gold nanoparticles (diameter of 3.8 nm, coated with dodecanethiol in toluene solution and purchased from Aldrich) were thus made in order to obtain more precise data about these apparent chains, constituted of multiple photoluminescence spots from the particles themselves. QDs are replaced by GNPs and the concentration is then increased by four orders of magnitude as extinction measurement is done on the new sample. The result as shown in Fig. 4.3 indicates the extinction peaks for incident light polarized parallel (red) and perpendicular (black) to the oily streaks.

It appears that the parallel light extinction peak is redshifted compared to the perpendicular one. The plasmon resonance in isotropic media is known to redshift in such a way that the refractive index increases [12, 13]. However, the index of the liquid crystal in the parallel orientation (1.52) is smaller than in the perpendicular one (from 1.52 to 1.67 according to the orientation of the smectic layer rotating within the hemicylinder). The influence of the liquid crystal should then have blueshifted the parallel light extinction peak instead of redshifting it, meaning
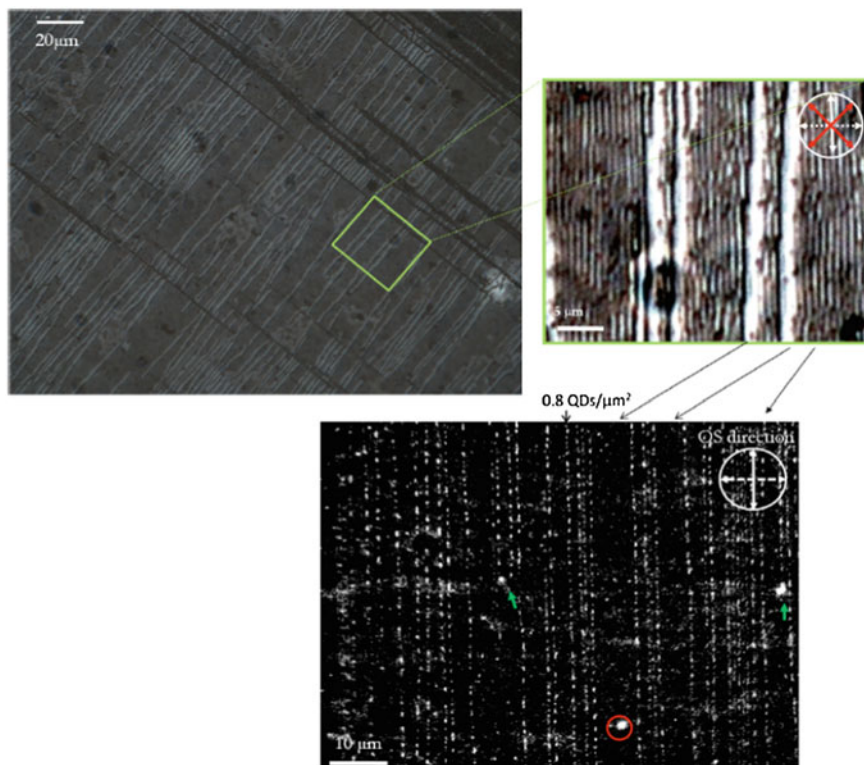
Fig. 4.2 (*top left*) Optical microscopy picture of 8CB deposited on rubbed PVA, polarizer/analyser crossed. (*top right*) Zoom on a series of oily streaks interrupted with large birefringent structures. (*bottom*) Quantum dots observed through fluorescence microscopy, showing the alignment of the particles in the direction of the streaks

that the displacement observed cannot be explained by the sole presence of the 8CB structures.

The other explanation is thus the only other interaction the particles have with each other, if they are close enough to experience an electromagnetic coupling [13]. The same coupling phenomenon happens when the particles are deposited on a substrate lacking the liquid crystal. In Fig. 4.3b can be seen the extinction spectra of various areas of GNP deposited on rubbed PVA deprived of LC. The particles there form networks of GNP close to each other, with the LSPR being redshifted due to the coupling phenomenon. Subsequent observations in that case showed no difference between the wavelengths of the surface plasmons in the two polarization angles parallel and perpendicular to the rubbing direction (Fig. 4.3a). This can be explained by the random orientation of the network formed by the coupled particles.

In Fig. 4.3c, the extinction of NPs diluted in toluene is superimposed to that of the NPs in smectic oily streaks for the perpendicular light extinction, while the
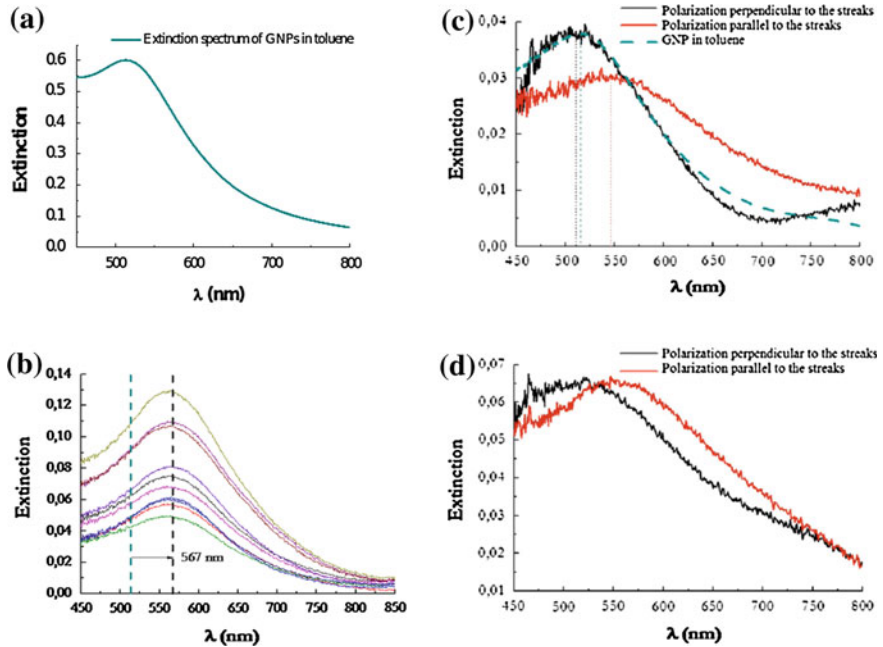
Fig. 4.3 a Extinction spectrum of GNPs in toluene. **b** Extinction spectra of GNPs deposited on PVA (3.10^{17} GNP L^{-1}) at various local concentrations, arranging themselves in networks of particles close to each other, showing the redshifting of the plasmon peak due to interparticle electromagnetic coupling. Highlight of the wavelengths of the plasmon peaks for this sample and for the isolated GNPs in toluene is made. **c** Extinction spectrum on the GNPs deposited on PVA with smectic 8CB (3.10^{16} GNP L^{-1}), divided in the polarizations parallel (*red curves*) to the oily streaks and perpendicular to them (*black curves*). The extinction of the GNPs in toluene is shown in *green dotted lines*. **d** Extinction spectra on another area of the same sample as **c**, divided in the polarizations parallel (*red curves*) to the oily streaks and perpendicular to them (*black curves*)

aforementioned redshift is visible between that reference measurement and the parallel light extinction. This allows us to conclude that the coupling phenomena only applies in the parallel direction, the plasmon properties in the perpendicular ones being left mainly untouched. The chains observed on this part of the sample can thus be considered to be straight, parallel to the oily streaks, and to have a width of a single nanoparticle. Indeed, a different shape or orientation would have led to a partial coupling being measured on the perpendicular polarization, then visible through a shift from the spectrum of GNP diluted in toluene.

The value of the redshift being dependent on the distance between the particles and on the number of particles coupled together [14], the more flattened nature of the parallel light extinction curve leads to argue that either this distance or the number of involved GNPs does vary among the deposited particles. When simulated through a DDA approximation [15] by our colleague G. Levi from

Itodys-Paris-France, chains of coupled GNP particles (separated by 1.5 nm of thiol each, in a material with the ordinary index of the 8CB) lead to redshifts valued between 17 and 40 nm with respect to isolated GNPs in toluene, increasing with the number of particles in a chain with equidistant particles. The value experimentally observed, in Fig. 4.3c, being 34 nm, thus indicates that the chains formed on the sample are more likely to be long ones (eight or more GNP) rather than short fragments. However, those chains should be of a limited size, as the analysis of Fig. 4.3d will show.

Also to be considered is the higher intensity of the 3.c black spectrum (perpendicular to the streaks), which can be explained by the presence of a second source of extinction at this wavelength, isolated particles inside the chains. They indeed lead to the presence of one band at this wavelength, either parallel or perpendicular to the oily streak. Their presence consequently increases the intensity of the perpendicular band's peak and enlarges that of the parallel band, which would have been of higher intensity in absence of the isolated nanoparticles.

These results show that gold nanoparticles deposited on these liquid crystal linear defect structures are assembling themselves in a mix of long, unidirectional chains all over the sample, composed of groups of electromagnetically coupled particles and isolated ones, possibly also trapped in smectic defects.

Nevertheless, an observation in another area shows a slightly varying optical extinction, see Fig. 4.3d. The global intensity is higher, indicating a larger local GNPs concentration. The extinction curve associated with the polarization perpendicular to the streaks has a lower intensity and a wider shape and that associated with parallel polarization is more redshifted than in Fig. 4.3c with respect to isolated GNPs in toluene, being redshifted to 44 nm instead of 34 nm. The reduction in the intensity of the perpendicular peak appears to be caused by a reduction of the isolated particles as more chains are being formed along the defects. The perpendicular peak's shape change is interpreted as being caused by a slight coupling between parallel chains when the concentration increases. However, the remaining large redshift between the two extinction curves (around 40 nm) indicates a largely higher coupling parallel to the oily streaks associated with even longer chains than in Fig. 4.3c. We have thus performed simulations of the extinction of infinite chains parallel to the oily streaks in a dipolar approximation. Figure 4.4 shows the corresponding evolution of the wavelength for the extinction band when the distance between GNPs increases, the calculation being performed in a homogeneous thiol index ($n = 1.458$). We obtain from this curve that for our GNPs of diameter 3.8 nm, a distance between GNPs of 4.5 nm is obtained. In other words, the dodecanethiol between the GNPs is highly compressed since its size varied between 1.5 nm for an extended molecule and 0.7 nm between two neighboring GNPs. This is interpreted as due to the large van der Waals attraction between gold GNPs when they are 1D localized within a smectic defect.

The observations realized on the various samples made during this study show finally that particles are clearly concentrating in thin and straight defect lines which force them to form unique straight chains if concentration is small enough, leaving vast empty areas in-between, as also shown by fluorescence microscopy
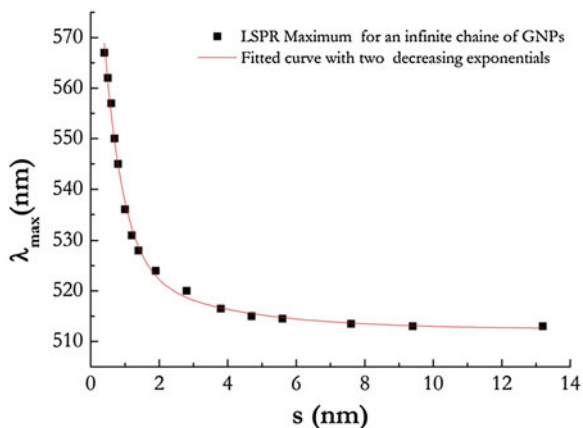
with QDs. This suggests the presence of a long-range interaction attracting the GNP toward the defect lines as the GNP could be causing an elastic distortion of the liquid crystal around them, while the defects themselves create a favorable area to trap the particles [16, 17]. When the concentration starts to increase, either thin ribbons are formed around the initial chains, or chains close to each other start to interact laterally.

The defects described previously appear to allow the trapping of foreign objects [3]. This phenomenon can be explained by the impurity behavior of the particles [18–21], as they will keep trying to reach the most energy-favorable areas of the oily streaks. These trapping areas, such as the walls of the hemicylinders and the centers of curvature, will allow the trapping as the deposition of the particle on them will result in an energy gain of the order of 60 times the thermal energy incurred by the phenomenon (elastic gain in presence of a nanoparticle which replaces part of the deformed area of a curvature wall, $a^2.K/l$, with K the curvature modulus for the wall—10^{-11} J/m, l the penetration length—1 nm—and a the size of the NP—4 nm) [9, 21, 22]. The defect must be of small size to induce formation of straight chains. We thus believe that it must be a dislocation which can be present at the basis of the curvature wall [23], or within the rotating grain boundary.

Once the particles are trapped into the defects, they would retain some mobility as they remain inside the defect, but could be affected by van der Waals interaction once close enough to other particles (distance equal or smaller to the diameter of the particle itself), leading to the formation of the chains.

In conclusion, it appears that, with the various experimentations presented in this paper, the oily streaks formed by the deposition liquid crystal on a substrate of rubbed PVA on glass can guide the positioning of gold NPs and QDs. The GNP used here assembled themselves in chains situated on the liquid crystal defects, in their dislocations. These chains, being unique, are then perfectly aligned with the axis of the oily streaks, with the particles close enough to each another to allow a coupling phenomenon to be detected through their extinction spectra.

A comparison of these spectra with theoretical models indicated that the thiol coatings of the particles forming the chains are being compressed, due to the van der Waals interactions.

This phenomenon opens interesting developments in both theoretical and practical research. As it should allow the production in large scale of chains or ribbons of coupled particles, this structure could for example, be used for plasmon signal guides, with obvious applications in signal transmission with potential Joule effect reduction and massive advantages in all technologies where electromagnetic compatibility is an issue (i.e., almost all modern microelectronics and especially air and space onboard systems).

Beyond this obvious engineering prospect, another logical development, here a theoretical one, shows itself in the study of this structure with other types of nanoparticles. As such, we are actually working with the positioning properties of anisotropic nanorods to study the possible orientation effect the linear defects could have on them.

4.3 Experimental Section

The optical properties of GNPs were investigated with a LOT Oriel MS260i spectrometer coupled to an upright optical microscope (Olympus BX 51) to probe a 40×40 μm area. QD fluorescence was observed with an inverted Olympus IX71 optical microscope with an oil-immersed objective (x100, NA = 1,4) connected to a CCD camera.

References

1. Grzelczak M, Vermant J, Furst EM et al (2010) Directed self-assembly of nanoparticles. ACS Nano 4:3591–3605
2. Whitesides GM, Kriebel JK, Mayers BT (2005) Nanoscale assembly. In: Huck WTS (ed) Springer, Cambridge, p 217
3. Coursault D, Grand J, Zappone B et al (2012) Linear self-assembly of nanoparticles within liquid crystal defect arrays. Adv Mat 24:1461–1465
4. Zappone B, Lacaze E (2008) Surface-frustrated periodic textures of smectic-A liquid crystals on crystalline surfaces. Phys Rev E 70:11709
5. Zappone B, Lacaze E, Ayeb H et al (2011) Self-ordered arrays of linear defects and virtual singularities in thin smectic-A films. Soft Matter 7:1161
6. Michel JP, Lacaze E, Alba M et al (2004) Optical gratings formed in thin smectic films frustrated on a single crystalline substrate. Phys Rev E 70:11709
7. Fleury JB, Pires D, Galerne Y (2009) Self-connected 3D architecture of microwires. Phys Rev Lett 103:267801

8. Pires D, Fleury JB, Galerne Y (2007) Colloid particles in the interaction field of a disclination line in a nematic phase. Phys Rev Lett 98:247801
9. Jakli A, Senyuk B, Liao G et al (2008) Colloidal micromotor in smectic A liquid crystal driven by DC electric field. Soft Matter 4:2471
10. Michel JP, Lacaze E, Goldmann M et al (2006) Phys Rev Lett 96:027803
11. Michel JP (2002) Films smectiques minces déposés sur un substrat monocristallin, PhD Thesis, University of Cergy-Pontoise
12. Rance GA, Marsh DH, Khlobystov AN (2008) Extinction coefficient analysis of alkanethiolate-stabilised gold nanoparticles. Chem Phys Lett 460:230–236
13. Mulvaney P (1996) Surface plasmon spectroscopy of nanosized metal particles. Langmuir 12:788
14. Khlebstov NG, Dykman LA (2010) Optical properties and biomedical applications of plasmonic nanoparticles. Quant Spectrosc Radiat Transfer 111:1
15. Johnson PB, Christy RW (1972) Optical constants of the noble metals. Phys Rev B 6:4370
16. Rozic B, Tzitzios V, Karatairi E, Tkalec U et al (2011) Theoretical and experimental study of the nanoparticle-driven blue phase stabilisation. Eur Phys J E 34:17
17. Prathiba R, Park K, Smmalyukh II (2009) Tunable optical metamaterial based on liquid crystal-gold nanosphere composite. Opt Express 17:19459
18. Yoshida H, Tanaka Y, Kawamoto K et al (2009) Nanoparticle-stabilized cholesteric blue phases. Appl Phys Express 12:121501
19. Karatairi E, Rozic B, Kutnjak Z et al (2010) Nanoparticle-induced widening of the temperature range of liquid-crystalline blue phases, Phys Rev E 81:041703
20. Ravnik M, Alexander GP, Yeomans JM et al (2011) Three-dimensional colloidal crystals in liquid crystalline blue phases. Proc Natl Acad Sci USA 108:5188
21. Voloschenko D, Pishnyak OP, Shiyanovskii SV et al (2002) Effect of director distortions on morphologies of phase separation in liquid crystals. Phys Rev E 65:060701
22. Kléman M (1983) In lines and walls: in liquid crystals, magnetic systems and various ordered media. In: Smectics A (ed) Wiley, Chichester
23. Williams C (1978) Défauts linéaires des mésophases smectiques a. J de Physique Colloques, 39, C2–48–C2–57

Chapter 5
Carbon Nanotubes Deagglomeration in Aqueous Solutions

E. O. Kovalska and Yu. I. Sementsov

5.1 Introduction

Since the discovery of carbon nanotubes (CNTs) [1] had attracted the interest of both the scientific and industrial community with a hope to develop various frontiers in the field of nanotechnology. The intriguing properties of CNT are believed to open new prospects in the material science, especially in the field of polymer-based composites. The various techniques of incorporation of CNT in polymer matrices were designed for the fabrication of new advanced materials with multifunctional properties [2].

The role of CNTs in polymer-based composites can be different [3–6]. For example, nanotubes provide strength and stiffness [7], as evidenced by the high tensile modulus ($\sim$1 TPA) [8]. The introduction of single-walled carbon nanotubes (SWCNTs) (2 wt.%) on polymer matrices increased the Vickers hardness by 3.5 times, and thermal conductivity with the introduction of 1 wt.% SWCNTs by two times. Adding of 1 wt.% of nanotubes increases the elastic modulus and tensile strength of polystyrene by 42 and 25 wt.%. The damping ability of polymers with the introduction of CNTs increases dramatically, which is connected to the interfacial sliding on the edge of the matrix filler. Thus, the modulus of loss of polycarbonate with the introduction of 2 wt.% SWNTs increases more than an order of magnitude and reaches 150 MPa [9]. Nanotubes could serve as a source of electromagnetic radiation with high efficiency, since the introduction of nanotubes significantly enhances the mechanical, electrical, and thermal properties of polymers. We can create antiradar coverage based on such composites. Adding of CNTs to expand a range of operating temperatures of composites due to higher transition temperature in the glassy state allows to change the structure of the matrix and increase the degree of crystallinity, etc.

E. O. Kovalska (✉) · Yu. I. Sementsov
O.O. Chuiko Institute of Surface Chemistry, NASU, 17, General Naumov street, Kiev 03164, Ukraine
e-mail: evgeniya1209@ukr.net

However, in order to exploit the exceptional properties of CNT one has to know a strategy for reproducible, stable, and uniform dispersion of CNT in the composites.

CNTs are often dispersed as aggregates in the matrix due to strong Van der Waals' interaction. In addition, certain properties of the host polymer matrix like wetting, polarity, crystallinity, melt-viscosity etc., add to the challenge of obtaining a percolative "network-like" structure of CNT in the composites.

In the past few years, several review articles have been published on various aspects of polymer/CNT composites including their preparation and CNT selection [10–18].

So, the problem is to prepare high stable CNT's dispersions for creation new material with new expected properties. CNTs are perspective material for creation new composites due to their unique structure and combination of high durability, electro-, and thermoconductivity [19]. In this work, we have studied a deagglomeration of CNTs in aqueous solutions of different compounds by a number of methods.

5.2 Materials and Methods

CNTs were obtained by the catalytic chemical vapor deposition (CCVD) method by pyrolysis of ethylene, propylene, or propane-butane on complex metal oxides catalysts [20].

Synthesis of CNTs using CCVD-process is carried out in flow reactors under inert environment at temperatures of 500–1,100 °C (Fig. 5.1). The first and crucial formation stage of CNTs is a heterogeneous reaction of decomposition of hydrocarbons or disproportionation of carbon monoxide on the surface of metal particles. Then carbon diffusion is lower and the nucleation and growth of nanocarbon take place from the region of high chemical potential to the part of metal catalyst particles. If the speed of carbon delivery on the working surface of the catalyst particles exceeds the diffusion speed, the carbonization of catalyst appears and, consequently, its decontamination and termination of growth of nanotubes take place [21, 22]. The most adequate to the conditions of CCVD process considered to "vertex" model (Fig. 5.2) of CNT's growth [23], but these methods do not provide the confident record kinetic parameters for CNT growth and fabrication.

For the production cycle (90 min), about 0.5 kg of nanocarbon product containing 20 % mineral impurities of the catalyst residue is needed. At the end of the loop, the reactor is filled with fluidized product for 1/2–2/3 volume. Removal of mineral impurities is produced by treatment with a mixture of ammonium bifluoride and hydrochloric acid [24].

The CCVD method gives the CNTs agglomerates in the form of tubes entangled with each other, with the size of 20–500 microns. Due to Van der Waals forces that hold the CNTs in agglomerates, they are extremely difficult to disperse
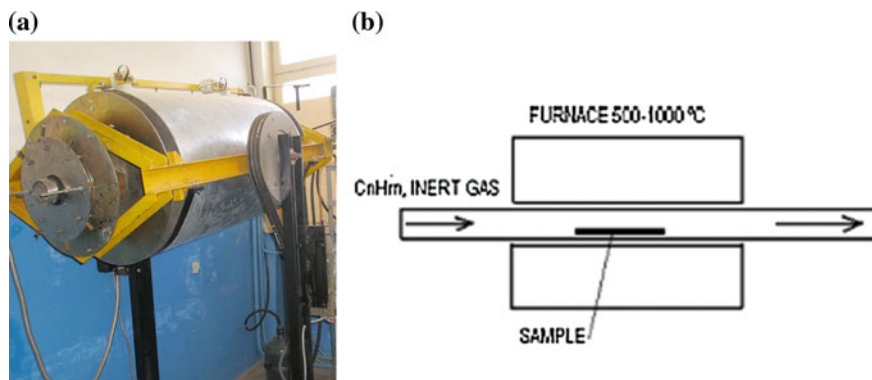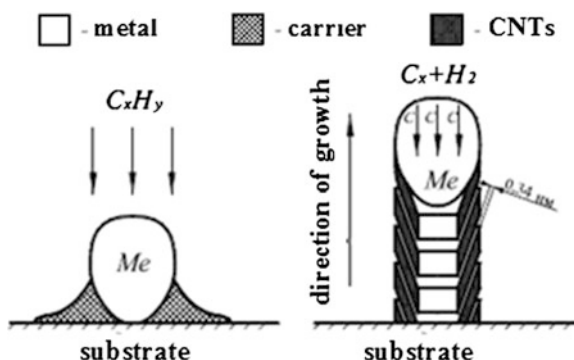
Fig. 5.1 Pilot plant synthesis of CNTs (**a**), scheme of reactor for synthesis of carbon nanotubes by Chemical Vapor Deposition (**b**)

Fig. 5.2 The "vertex" model of catalytic growth of CNTs [23]

and align in a polymer matrix. At the same time, high-performance composite materials filled with CNTs can be obtained under the condition of uniform distribution in the polymer matrix which leads to find an effective method of dispersing the agglomerates of CNTs.

The most common and widely used methods of homogenization are ultrasonic, vortex, and cavitation treatments. There are the following processes: instantaneous mixing without separation, destruction of aggregate state, activation of chemical bonds, dispersion, and depolymerization and, finally, homogenization. Treatment with ultrasound, mixing, and adding surfactants improves the properties of the composite, but does not improve the mechanical properties on the expected level.

In this paper, different methods were used for multi-wall carbon nanotubes (MWCNTs) dispersion: the deagglomeration process of MWCNTs in ultrasonic dispergator (UZDN-2T), the device which is working on the principle of cavitation and the universal rotating homogenizer. Previously, the CNT's dispersions were prepared: aqueous solution (glucose/CNTs), aqueous solution of CNTs; alcoholic

solution (ethanol/CNT's); water-soluble polymer; and ionic surfactant system/ CNT's [25]. Analysis of agglomerates was carried out by laser correlation spectroscopy (LCS). Distribution of particles' size was determined by laser correlation spectrometer « ZetaSizer-3 » (Malvern Instrument, UK) with the adaptor 7032 and Helium–Neon laser PH-111, 25 mW, $\lambda = 633$ nm. Studied suspension (1 ml) was put in cylindrical optical glass cell with 10 mm in diameter and placed in the thermostatically controlled cell of laser correlation spectrometer. Registration and statistical processing of the laser radiation were performed for 300–400 s. The resulting autocorrelation function (ACF) was treated using the PCS-Size mode [19].

5.3 Results and Discussions

The SEM and TEM images of CNT's agglomerates are presented on Fig. 5.3 [26]. The length of nanotubes is 20–500 microns, average diameter is 10–20 nm, external diameter is 20–50 nm, purity—about 99 %, specific surface area determined by argon desorption is 200–400 m^2/g, and bulk density is within 20–40 g/dm^3.

It is well known that size, structure, and form of the synthesized product are determined by catalyst in CCVD method [27]. Complex oxide catalysts ($Al_2FeMo_{0.21}$) containing iron for growth of CNTs have been synthesized by coprecipitation method [28]. As we can see, the size distribution of CNT's agglomerates replicates the distribution of catalyst particles (Fig. 5.4) [26].
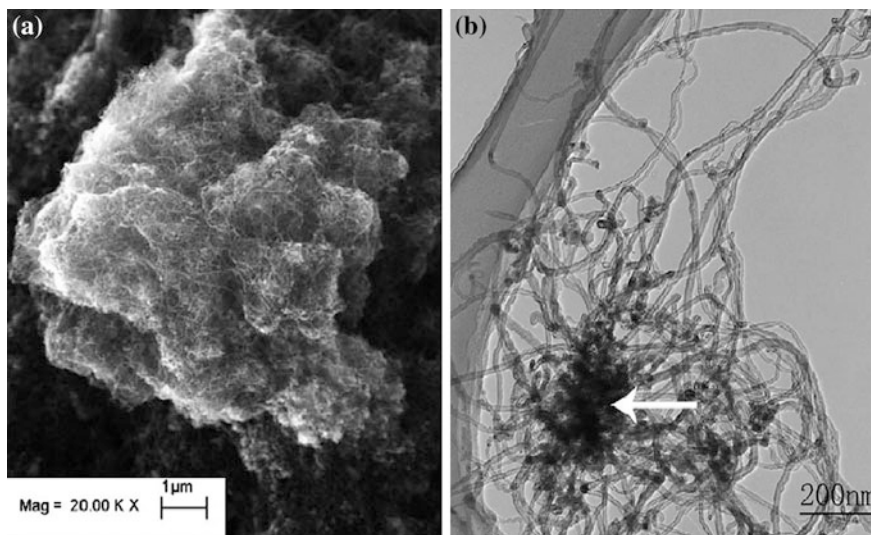

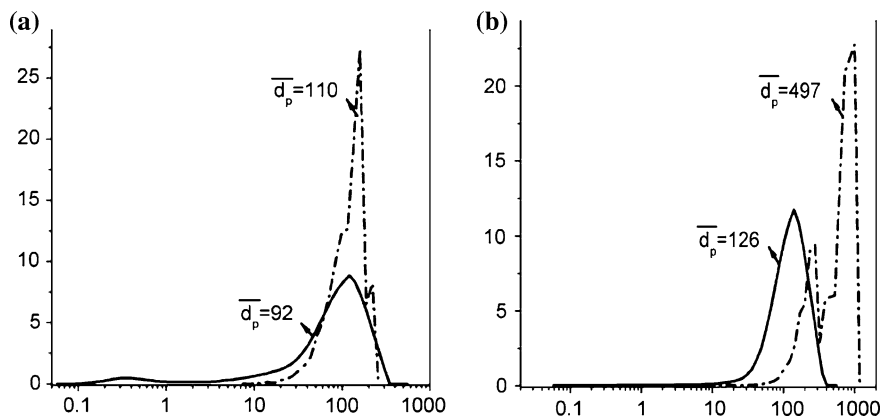**Fig. 5.3** SEM and TEM images of CNTs agglomerates are obtained by CCVD [26]

Fig. 5.4 Comparison of particle sizes determined by laser scanning method and statistical processing of microphotos (– *laser scanning*, - • - *statistics microphotos*): original catalytic particles (**a**); agglomerates of MWNTs (**b**) [26]

Synthesized agglomerates of CNT's were used for preparation of aqueous dispersions. The data about dispersions are collected in the Table 5.1: CNT's water systems that were studied, their time and type of treatment, the size of deagglomeration nanoparticles in water, and time of the existence of a stable system.

Published data show the following. That aqueous dispersion of CNTs could be stabilized through the addition of naturally occurring humic and fulvic acids [29, 30] acting in a similar fashion to surfactants [31]. Purified MWCNTs were shaken with an excess of MWNT-derived FAs in HCl solution, followed by centrifugation to remove any large aggregates. The dark gray supernatant is stable for at least 2 months. On contacting with 1.0 M NaOH solution, precipitation of the MWCNTs occurred due to leaching out of the surface adsorbed FAs. However, the solution is colorless due to a low concentration of FAs.

The dispersion test was conducted in ethanol solution for several concentrations of the MWCNTs [32]. Typical vials with samples in ethanol solution were

Table 5.1 The characterization of carbon nanotube dispersions

Water systems	Type of treatment	Time of treatment, min	Distribution of CNTs-size	The stability of dispersions
$C_6H_{12}O_6$/CNTs	Ultrasound	10–20	1–100 micron	Non
H_2O/CNTs	Cavitational	2–4	1–100 nm	Non
C_2H_5OH/CNTs	Rotary homogenizer	2–5	450 nm	Non
Water-soluble polymer and ionic surfactant system/CNTs	Rotary homogenizer	2–5	150–400 nm	Half year

sonicated for 20 min and then incubated at room temperature for a certain period of time. Due to the increasing of amount MWCNTs, the initial transparent gray color became dark and turbid. The highly dispersed MWCNTs were visually observed as black solutions without precipitation upon prolonged standing (2 months). At concentrations of 1.4 and 5.7 mg/dm^3 (MWCNTs/ethanol), the dispersion was apparently transparent without sedimentation. When the concentration of the MWCNTs in ethanol was 14 mg/dm^3, the dispersion became opaque black, but no precipitation was observed. At concentrations of more than 14 mg/dm^3, sediment was found at the bottom of the flask after two days. The dispersibility of the MWCNTs in ethanol was estimated to be $\sim$ 14 mg/dm^3, corresponding to the amount of MWCNTs dispersible in ethanol in this work. In addition, the MWCNTs revealed a higher dispersibility (40 mg/dm^3) in 1,2-dimethylformamide (DMF) than in ethanol.

In the work [33] was demonstrated the excellent dispersion of MWCNTs in aqueous sodium dodecyl sulfate (SDS) solutions. The minimum SDS to MWCNT ratio of 1.5–1 by weight is required to achieve dispersions with maximum achievable dispersion of MWCNTs in the aqueous SDS solution. The maximum concentration of MWCNTs that can be homogeneously dispersed is about 1.4 wt.%; for higher concentrations of MWCNTs, and accordingly of SDS, no valuable dispersion and stabilization of the MWCNT in the aqueous solution is achieved, most probably by the depletion-induced aggregation of the MWCNTs. The presented results allow control of the dispersion and stabilization process of MWCNTs in aqueous SDS solution.

LCS results have shown that treatment of dispersant gives the particles with different size for the system water/CNTs (with concentration of CNTs 0.05 wt.% by weight)—100–3,000 nm, and for concentration of 0.2 wt.%—10–100 nm and 1.000–5.000 nm. Dispersion in ultrasonic installation UZDN-2, within the same method of control allows for a system of water—0.2 wt.%. CNTs particle size 10–200 nm, and for the same system with glucose concentrations of 3 and 5 wt.% particle size 1–100 nm. In Fig. 5.5 is given the primary form of distribution function of particles size for various systems. It is shown that ultrasonic disintegration in aqueous medium at dispersant UZDN-2 does not give significant size changes of agglomerates (Fig. 5.5a). Since the initial particle size of 20–500 microns CNTs and CNTs take the form of dispersed oblong particles with diameters of order 0.5–1.0 microns and a length of 5–100 microns. Hydrogen system with glucose gives spherical particles with sizes of 1–100 microns. The level of homogenization in a facility that works on cavitation regime, significantly higher, and depends on the concentration of CNTs in hydrogen environment. Thus, for the concentration of 0.05 wt.% CNTs shares gain size in the range of 0.2–1.0 mm (Fig. 5.5b), and the processing system with a concentration of 0.2 wt.% CNTs observed the presence of such particles: 0.01–0.1 microns and 1.0–5.0 microns. Processing on a rotating homogenizer alcohol solution CNTs (Fig. 5.5c) leads to the formation of uniform particles with sizes of 450 nm.

As previously noted, adding surfactants improves the properties of the composite. Generally, hydrophobic interactions between the apolar hydrocarbon chains
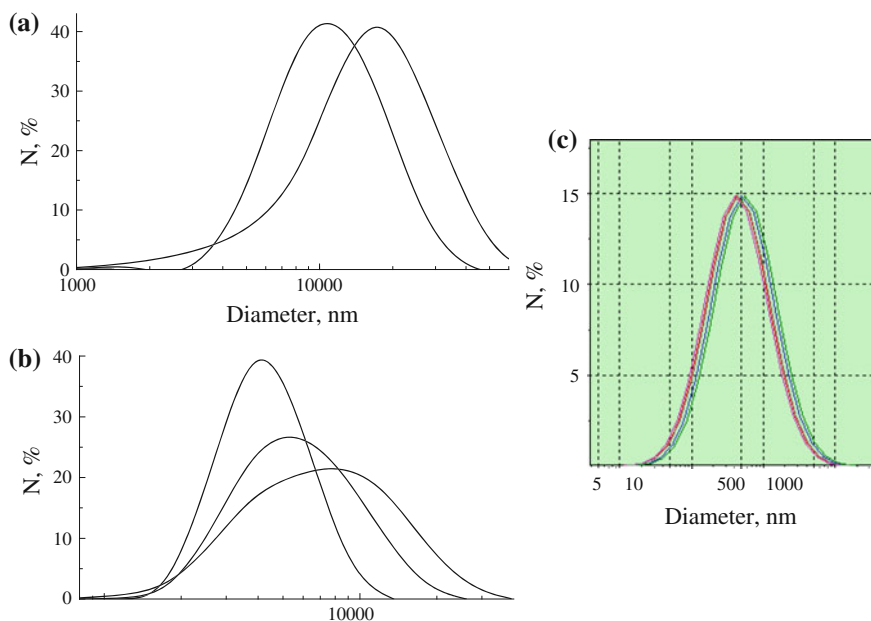
Fig. 5.5 The distribution of agglomerates CNTs size: ultrasound treatment 3 % aqueous solution of glucose with 0.067 wt.% CNTs (**a**); hydrogen cavitation processing system with 0.05 wt.% CNTs (**b**); processing on a rotating homogenizer solution alcohol solution (ethanol) CNTs (**c**)

of surfactants and the highly conjugated walls of MWCNTs enhance the electrostatic repulsive force and steric hindrance between individualized MWCNTs. Thus, they account for the stabilization of CNTs in aqueous systems. However, when it comes to the explanation of the distinct dispersion behavior of differently functionalized MWCNTs in the presence of different surfactants, no simple conclusion can be made. Nonetheless, based on the chemical structure of the surfactants and the differently functionalized MWCNTs, certain interactions, shown in Fig. 5.6 contribute to the observed behavior.

Chemical structures of the surfactants used are shown below the corresponding abbreviation. CTAB and Brij76 are above the critical micelle concentration (CMC), whereas the concentration of SDS is below CMC. For the sake of simplification, MWNTs are shown as a line instead of tubes (scheme not to scale) [34].

The influence of adding surfactant to the dispersion stability was investigated by other researchers. In this paper [35] was shown that the surfactants successfully stabilized the aqueous CNT dispersions, whereas in the absence of surfactants they rapidly sedimented. The concentration of each surfactant was approximately 0.3 wt.% and the concentration of CNTs used for their homogeneous dispersions in aqueous solution was 0.02 wt.%.

Comparative studies on dispersing of MWCNTs using two anionic surfactants (sodium dodecyl sulfate, SDS, and sodium dodecyl benzenosulfonate, SDBS) are
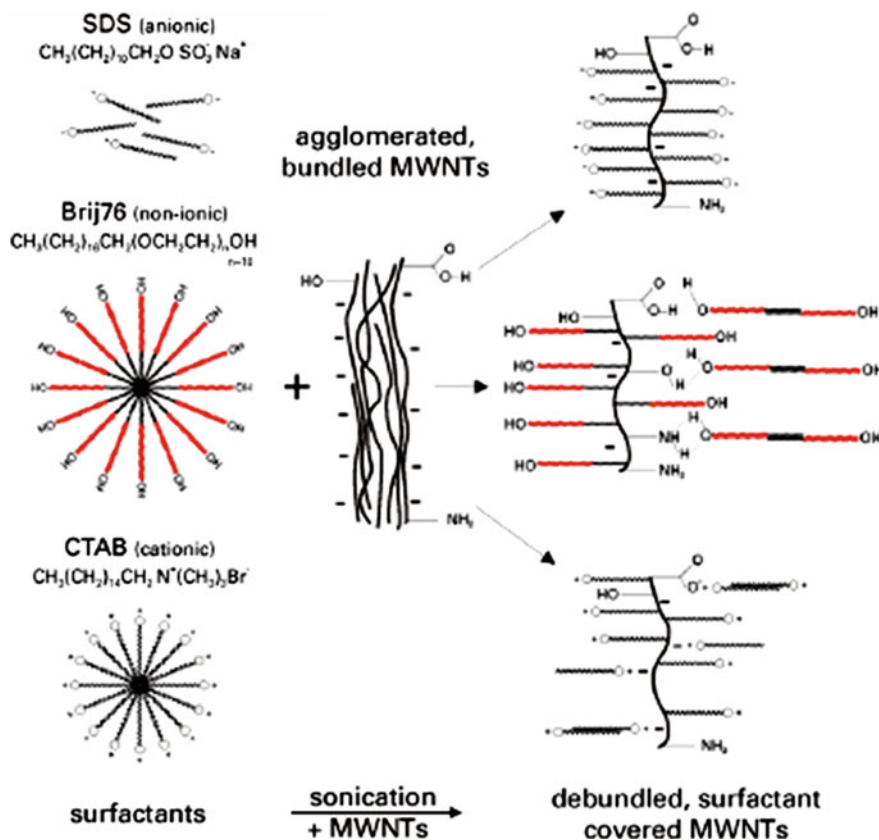
Fig. 5.6 Schematic representation of possible interactions between MWCNTs and different surfactants upon sonication [34]

presented [36]. The studies were conducted on the surfactant concentrations that were close to the CMC. The stability of CNTs suspensions obtained for surfactant solutions at concentrations lower than the CMC was investigated. It was also found that the surfactant structure influence on the diameter distribution of dispersed CNTs.

Suspension in the 1 wt.% concentration was stable used only 20 dmb % copolymer as dispersant [37]. An important factor contributing to the good dispersion of MWCNTs in ethanol solution was the affinity due to chemical intercalation between copolymer and MWCNTs. Steric stabilization was realized to impede the van der Waal's adherence between one MWCNT and other bundles of MWCNTs in the system; depletion stabilization would also exist which needed to be proved by further research. Consequently, the copolymer with basic groups which had strong affinity to the tubes was an efficient dispersant for MWCNTs in ethanol solution.
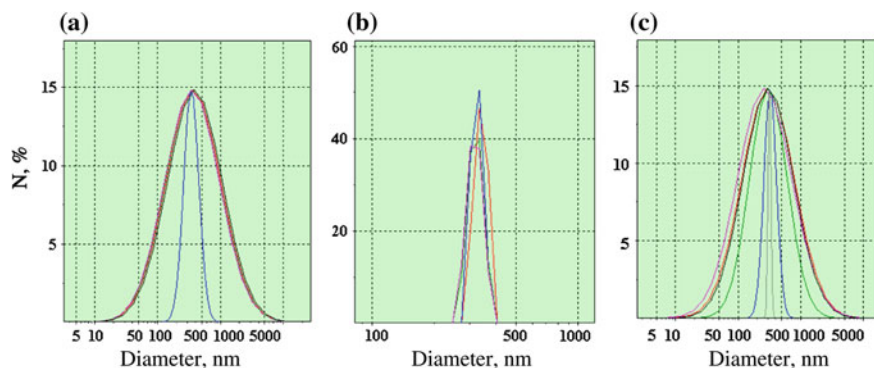
Fig. 5.7 Results of treatment of hydrogen system of water-soluble polymer and ionic surfactant system/CNTs on a rotating homogenizer: monodisperse distribution of sizes from 220 to 450 nm with an average size of 360 nm (**a**); solution diluted in 5 times, a stable suspension of nanoparticles with an average size of 300 nm (**b**); in polymodal approximation there of smaller fraction of the size about 150 nm (**c**)

We established that water-soluble polymer and ionic surfactant system/CNTs could obtain highly stable solution with a particle size from 150 to 400 nm during the process in universal homogenizer. Particle size depends on the concentration of components in the system. Figure 5.7 presents the results of treatment of the water-soluble polymer and ionic surfactant system/CNTs on a rotating homogenizer; monodisperse distribution of sizes from 220 to 450 nm with an average size of 360 nm (Fig. 5.7a); solution diluted five times, a stable suspension of nanoparticles with an average size of 300 nm (Fig. 5.7b); in polymodal approximation there of smaller fraction of the size about 150 nm (Fig. 5.7c). The appearance of particles on the glass after treatment is shown in Fig. 5.8.
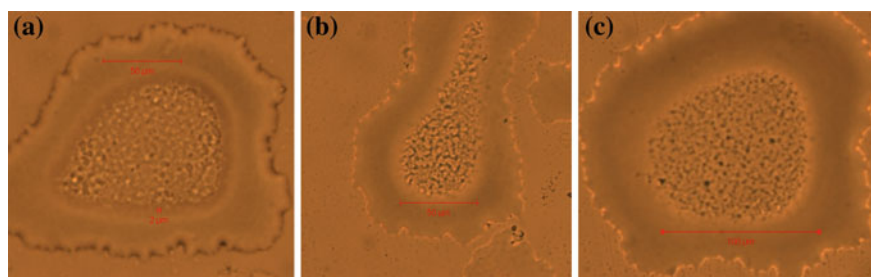

Fig. 5.8 Kind of film on glass in the optical microscope, respectively, to Fig. 5.7

5.4 Conclusions

Thus, deagglomeration of the carbon nanotube bundles were performed in an aqueous solutions of different chemical composition using ultrasound, cavitation, and rotating homogenizing treatment. Found that the degree of dispersion on the cavitation principle are strongly depends on the concentration of CNTs in the water. Using organic compounds ($C_6H_{12}O_6$) increase the efficiency of the dispersion. Ultrasound effect is manifested in the destruction of agglomerates CNTs and size. Processing in a universal homogenizer of water-soluble polymer and ionic surfactant system/CNTs had allowed obtaining highly stable solution with a particle size from 150 to 400 nm. The particle size depends on the concentration of components in the system.

Obtained results help to, firstly, explain the behavior of the CNTs agglomerates during the homogenizing procedure, secondly, underline the factors which help to homogenize CNTs in the aqueous solutions. Utilizing the CNT/water-soluble polymer/ionic surfactant mixture coupled with homogenizer machine shows the best results in terms of the solution stability, particles size, and their distribution. Developed method opens new branch in CNT/polymer composites preparation.

References

1. Iijima S (1991) Helical microtubules of graphitic carbon. Nature 354(6348):56–58 (London)
2. Suryasarathi B, Rupesh AKh, Paula M (2010) Assessing the strengths and weaknesses of various types of pretreatments of carbon nanotubes on the properties of polymer/carbon nanotubes composites: a critical review. Polymer 51:975–993
3. Du F, Winey KI (2006) Nanotubes in multifunctional polymer nanocomposites. In: Gogotsi Yu (ed.) Nanomaterials Handbook. CRC, Taylor&Francis, Boca Raton, London, pp 565–583
4. Breuer O, Sundararaj U (2004) Big returns from small fibers: a review of polymer/carbon nanotube composites. Polym Compos 25(6):630–645
5. Thostenson ET, Ren Z, Chou T-W (2001) Advances in the science and technology of carbon nanotubes and their composites: a review. Compos Sci Technol 61:1899–1912
6. Harris PJF (2004) Carbon nanotube composites. Int Mater Rev 49(1):31–43
7. Yu M, Lourie O, Dyer MJ et al (2000) Strength and breaking mechanism of multiwalled carbon nanotubes under tensile load. Science 287:637–640
8. Coleman JN, Khan U, Blau WJ, Gun'ko YK (2006) Small but strong: a review of the mechanical properties of carbon nanotube-polymer composites. Carbon 44(9):1624–1652
9. Koratkar NA, Suhr J, Joshi A et al (2005) Characterizing energy dissipation in single-walled carbon nanotube polycarbonate composites. Appl Phys Lett 87:063102
10. Treacy MMJ, Ebbesen TW, Gibson JM (1996) Exceptionally high young's modulus observed for individual carbon nanotubes. Nature 381:678–680
11. Wong EW, Sheehan PE, Lieber CM (1997) Nanobeam mechanisms: elasticity, strength and toughness of nanorods and nanotubes. Science 277:1971–1975
12. Berber S, Kwon Y-K, Tomarnek D (2000) Phys Rev Lett 84(20):4613–4616
13. Donnet J, Bansal R, Wang M (1993) Carbon black: science and technology. Marcel Dekker, New York

14. Garboczi EJ, Snyder KA, Douglas JF, Thorpe MF (1995) Intrinsic viscosity and the electrical polarizability of arbitrarily shaped objects. Phys Rev E 52:819–828
15. Potschke P, Bhattacharyya AR, Janke A et al (2005) Melt mixing as method to disperse carbon nanotubes into thermoplastic polymers. Fullerenes, Nanotubes, Carbon Nanostruct 13(1):211–224
16. Lin B, Sundararaj U, Potschke P (2006) Melt mixing of polycarbonate with multi-walled carbon nanotubes in miniature mixers. Macromol Mater Eng 291(3):227–238
17. Potschke P, Bhattacharyya AR, Janke A (2004) Melt mixing of polycarbonate with multiwalled carbon nanotubes: microscopie studies on the state of dispersion. Eur Polymer J 40(1):137–148
18. Dondero WE, Gorga RE (2006) Morphological and mechanical properties of carbon nanotube/polymer composites via melt compounding. J Polymer Sci Part B: Polymer Phys 44(5):864–878
19. Sementsov YuI, Alekseeva TA, Pyatkovsky ML et al (2009) Multiwall carbon nanotubes (CNT) deagglomeration and nanocomposite polymer/CNT production. In: Proceedings of mater. conference hydrogen materials science and chemistry of carbon nanomaterials ICHMS, 25–31 August. Yalta, p 784
20. Sementsov YuI, Melezhek OV, Prikhod'ko GP, et al (2007) Synthesis, structure, physicochemical properties of nanocarbon materials. In: Physical chemistry on nanomaterials and supramolecular structures, vol 2. Naukova dumka, Kyiv, pp 116–158
21. Fursikov MF, Tarasov BP (2004) Catalytic synthesis and properties of carbon nanotubes and nanofibers. Int Sci J Alternat Energy Ecology 10:24–40 (in Russian)
22. Alekseev NI (2006) About morphology of carbon nanotubes growing from the catalyst particles: formulation of the model. Solid State Phys 48(8):1518–1525 (in Russian)
23. Tkachev AG, Mishchenko E, Konovalov VF (2007) Catalytic synthesis of carbon nanotubes from gas-phase pyrolysis of hydrocarbons. Russ Nanotechnol 2(7–8):100–108 (in Russian)
24. Kovalska EA, Kartel NT, Prikhodko GP, Sementsov YuI (2012) Physical and chemical fundamentals of purification methods for carbon nanotubes (review). Chem phys technol surf 3(1):20–44 (in Ukrainian)
25. Kovalska EO, Prikhodko GP, Sementsov YuI (2012) Deaglomeration of carbon nanotubes in aqueous solutions of variety compounds. In: Proceedings of the international summer school nanotechnology: from fundamental researches to innovations, 26 Aug–2 Sep. Bukovel, Ukraine, pp 63–65 (in Ukrainian)
26. Hao Y, Qunfeng Z, Fei W et al (2003) Agglomerated CNTs synthesized in a fluidized bed reactor: Agglomerate structure and formation mechanism. Carbon 41:2855–2863
27. Kovalska EO, Sementsov YuI, Kartel NT, Prikhodko GP (2012) Synthesis of catalysts for growth of carbon nanotubes and testing their effectiveness. Chem Phys Technol Surf 3(3):335–340 (in Ukrainian)
28. Kovalska EO, Sementsov YuI, Prikhodko GP (2012) A method for producing catalysts for chemical vapor deposition of carbon nanotubes from gas phase. UA Patent 70847, 25 June 2012 (in Ukrainian)
29. Hyung H, Fortner JD, Hughes JB, Kim JH (2007) Natural organic matter stabilizes carbon nanotubes in the aqueous phase. Environ Sci Technol 41(1):179–184
30. Wang Zh, Shirley MD, Meikle ST et al (2009) The surface acidity of acid oxidised multi-walled carbon nanotubes and the influence of in situ generated fulvic acids on their stability in aqueous dispersions. Carbon 47:73–79
31. Bonard JM, Stora T, Salvetat JP et al (1997) Purification and size-selection of carbon nanotubes. Adv Mater 9(10):827–831
32. Chun K-Y, Choi SK, Kang HJ et al (2006) Highly dispersed multi-walled carbon nanotubes in ethanol using potassium doping. Carbon 44:1491–1495
33. Yu J, Grossiord N, Koning CE, Loos J (2007) Controlling the dispersion of multi-wall carbon nanotubes in aqueous surfactant solution. Carbon 45:618–623
34. Rausch J et al (2010) Surfactant assisted dispersion of functionalized multi-walled carbon nanotubes in aqueous media. Comp. Part A: Appl. Sci. Manuf 41:1038–1046

35. Kim H-S, Park WI, Kang M, Jin H-J (2008) Multiple light scattering measurement and stability analysis of aqueous carbon nanotube dispersions. J Phys Chem Solids 69:1209–1212
36. Bystrzejewski M, Huczko A, Lange H (2010) Dispersion and diameter separation of multi-wall carbon nanotubes in aqueous solutions. J Colloid Interface Sci 345:138–142
37. Zhao L, Gao L (2003) Stability of multi-walled carbon nanotubes dispersion with copolymer in ethanol. Colloids Surf A: PhysicochemEng Aspects 224:127–134

Chapter 6
Graphene-Like Autointercalated Niobium Diselenide Nanoparticles: New Possibility of 2D Nanomaterials Design

Liudmyla Mykolaivna Chepyga, Leonid M. Kulikov, Viktor M. Talash and Lev G. Akselrud

Layered or two-dimensional (2D) d-transition metal dichalcogenides ($2H–MCh_2$, M = Mo, W, Nb, Ta; Ch = S, Se), including autointercalated $2H–Nb_{1+y}Se_2$ ($0 \leq y \leq 0.29$, $2H–TaS_2$ structural type), are of interest to the scientific community because of their unique layered structure and related functional properties that may find use in different modern applications. As is well known, structures of 2D d-transition metal dichalcogenides comprises of covalent bond 2D sandwiched units that are separated by weak van der Waals spacing. These spacing can be intercalated by guest species to form a variety of compounds useful for scientific applications. A combination of constituent transition metal, chalcogen, or guest species can be selected to form a variety of intercalated compounds with desired architecture and functional properties. Particularly, the possibilities of using nanostructured $2H–MCh_2$ including graphene-like autointercalated $2H–Nb_{1+y}Se_2$ nanoparticles (inorganic graphene-like nanoparticles, 2D nanostructures; nanosheets) are following:

- energy converters: Li-ion chemical current sources, photo-intercalation solar energy converters;
- hydrogenous nanomaterials and sensors: hydrogen energetic;
- nanolubricants: multi-functional solid nanolubricant additives to industrial machine oils and greases for their tribotechnical parameters improvement; solid,

L. M. Chepyga (✉) · L. M. Kulikov · V. M. Talash
Frantsevich Institute for Problems of Materials Science of NASU, 3, Krzhyzhanovsky Street, Kiev-142 03680, Ukraine
e-mail: liudmylachepyga@ukr.net

L. M. Kulikov
e-mail: kulikovl@ipms.kiev.ua

V. M. Talash
e-mail: shtal@ipms.kiev.ua

L. G. Akselrud
Franko Lviv National University, 6, Cyril and Mefody Street, Lviv 79005, Ukraine
e-mail: akslev@googlemail.com

radiation-resistant, electro-conductive nanolubricants (antifriction composition nanomaterials, multi-functional nanostructured coatings) for space and ground-based operation conditions at high and low temperatures, hydrogen atmosphere and medical equipment: aerospace engineering, mechanical engineering, oil and gas complex, transport, military equipment, metallurgy, etc.;

- "nanoarmor": nanomaterials as super shock absorbers at very high pressures (to 40 GPa);
- magnetic 2D nanomaterials;
- nanoelectronics: 2D crystals can also be assembled in 3D heterostructures that do not exist in nature and have tailored properties, opening an entirely new chapter in condensed matter research [1–3].

Various techniques for nanostructured 2H–MCh_2 synthesis have been developed in the past decade or so. At this time, the possibility of synthesis of nano-crystalline layered 2H–MCh_2 (M = Nb, Ta; Ch = S, Se) are studied by many leading research centers in the world. The studies focused mainly on getting "fullerene-like" (IF, i.e., a mixture of nanotubes and onion-like nanoparticles) nanostructures 2H–MCh_2 (M = Nb, Ta; Ch = S, Se) during chemical vapor deposition (CVD) [4–6], thermal decomposition of 2H–MCh_3 (M = Nb, Ta; Ch = S, Se) [7]. Recently it has become clear that a range of inorganic-layered compounds (including 2H–$NbSe_2$) can be mechanically exfoliated in small quantities to give 2D nanosheets, for example [8]. Recently it became known about 2H–$NbSe_2$ nanosheets preparation: direct sonication of 2H–$NbSe_2$ micron powders in organic solvents [9] and sodium cholate/water solution [10] as well as an intercalation-assisted thermal cleavage method [11–13]. Also, earlier it was informed about successful use of activated electrochemical intercalation (Li^+/H_2O) of 2H–$NbSe_2$ micron powders for 2H–$NbSe_2$ layered nanoparticles synthesis [14].

Thereupon, we investigated the activated processes of electrochemical intercalation (Li^+/H_2O) of autointercalated 2H–$Nb_{1+y}Se_2$ micron particles and single crystals ($0 \leq y \leq 0.29$; 2H–TaS_2 structural type) in greater details. Here, we report that some results mentioned the activated processes of electrochemical intercalation that lead to prepare graphene-like autointercalated 2H–$Nb_{1+y}Se_2$ nanoparticles ($y = 0.02(1); 0.04(1); 0.09(1); 0.12(1); 0.22(1)$), as well as corresponding X-ray studies and SEM data.

The initial micron particles and single crystals of 2H–$Nb_{1+y}Se_2$ have been synthesized by low temperature CVD by interaction of components (corresponding stoichiometric ratio; the estimated weight of the final product—30 g) in evacuated quartz vials ($\sim 1 \cdot 10^{-3}$ Pa), to homogenize the product of interaction carried with additional annealing at 1,020–1,050 K for 24 h. For preparation single crystals (thin plates with an area of 1×1 mm^2) have been used to corresponding stoichiometric ratio of components and iodine as the carrier (about 5 mg cm^{-3}) (1,120 Ḱ → 1,090 Ḱ, 24 h) [15].

The nanosynthesis have been carried out by "top-down" activated processes of intercalation (Li^+/H_2O) of autointercalated 2H–$Nb_{1.02(1) \div 1.29(1)}Se_2$ micron particles and single crystals. We studied the timing data of galvanostatic processes of

intercalation with the potentiostat (PI-50-1, reference electrode—AgCl). The water solutions of $Li_2SO_4 \cdot H_2O$ (chemically pure) were used as electrolyte with concentration of 13 %.

After electrochemical treatment the nanoparticles were removed from solution, washed in water, and air-dried. The (XRD) was performed on a HZD-4A automatic X-ray diffractometer with $CuK\alpha$, $FeL\alpha$ radiation. The size and morphology of the $2H–Nb_{1+y}Se_2$ nanoparticles were performed using the software package of computer structural calculations WinCSD [16].

The scanning electron microscopy (SEM) images of graphene-like $2H–Nb_{1.02(1) \div 1.29(1)}Se_2$ nanoparticles were recorded on a REM-106I and JCM–5000 microscope at an accelerating voltages of 20 and 15 kV, respectively.

It is known that the cathodic reduction $2H–NbS_2$, $2H–TaS_2$ hydrated ions of alkali metals at intermediate stages there are different degrees of intercalation $(3 \rightarrow 2 \rightarrow 1)$ [17–19].

One would expect that the processes of electrochemical lithium intercalation are represents written as (Eq. 6.1):

$$xLi^+ + NbSe_2 + xe^- + H_2O \rightarrow Li_x^+(H_2O)_y[NbSe_2]^{x-} \quad 0 \leq x \leq 1, \, y = 2 \quad (6.1)$$
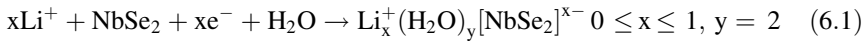
This means that the processes of intercalation of hydrated Li-ions occur in the interlayer space structure $2H–Nb_{1+y}Se_2$, where there are weak van der Waals forces. The growth of interlayer distance (≈ 1, 2 nm) is mainly due to the "thickness" bi-molecular layer of H_2O. This leads to an increase of elastic stresses potential energy and an increase in the drift contribution on the movement of intercalated phases. We note that relatively large currents lead to activation the processes of intercalation of Li-ions with bi-layers of H_2O in interlayer space $2H–Nb_{1.02(1)}Se_2$. Obviously, this leads to an intensification of motion of the intercalated phase $Li_x^+(H_2O)_y[NbSe_2]^x$ and dispersing micron particles along cleavage planes, where there are weak van der Waals forces, as a result of significant steric factors hydrated Li-ions in the interlayer space of the structure and mechanical stresses arising. It is assumed that voltage-dependent stage of process galvanostatic recovery $2H–MCh_2$ transport is intercalated ions in the solid phase.

Figure 6.1 shows the electrochemical lithium intercalation processes used to prepare the 2D nanosheets.

The intercalation of hydrated Li-ions, as the following dispersion, develop in the surface layers and, consequently, to a lesser number of van der Waals 'gaps' than the specified sequence of degrees of intercalation. This is also confirmed by the absence of intercalated hydrated Li-ions in the structure nanopowder: after dispersing hydrated ions deintercalation with new surfaces as possible embedded ions in the bulk of the particles. Note that to directly determine the number of intercalated hydrated Li-ions in the dispersion of the particles is difficult, especially since the process is accompanied by a significant increase in the surface, however, we can assume that the limiting composition corresponds $Li_{0.5}^+(H_2O)_y[NbSe_2]^{0.5-}$ (y = 2).

Layered bulk compound   Intercalated compound $Li^+_x(H_2O)_y$ [$NbSe_2$] $^{x-}$

≈1.2 nm

Isolated 2D nanosheets

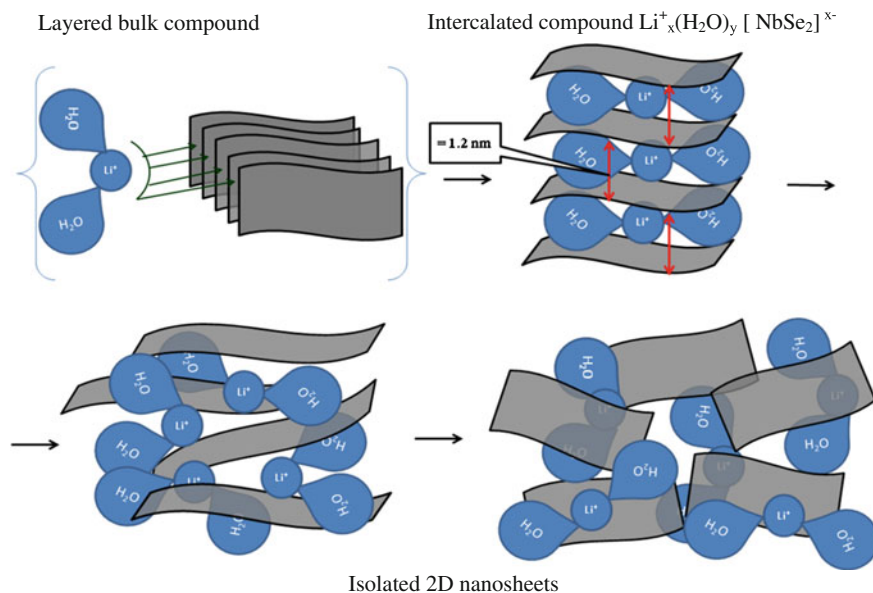**Fig. 6.1** The electrochemical lithium intercalation process to produce 2D nanosheets of $2H–Nb_{1+y}Se_2$ from the layered micron particles

It should be noted that the value of potential of $2H–Nb_{1.02(1)}Se_2$ in galvanostatic conditions depends on the current value, which characterizes the processes of intercalation of hydrated Li-ions in the layered structure of $2H–Nb_{1.02(1)}Se_2$ and dispersing micron particles. Note that the value of potential directly for the particles $2N–Nb_{1.02(1)}Se_2$ calculated as the difference between the values of potential of copper mesh with particles and without it were measured under similar conditions. We assume that the important role played the stage transfer of Li-ions with bi-layers of H_2O in the interlayer space structure $2H–Nb_{1.02(1)}Se_2$. It should be noted that the potential change in the electrochemical intercalation (Li^+/H_2O) particles $2H–Nb_{1+y}Se_2$ can be explained by the influence of reducing size of dispersed particles $2H–Nb_{1.02(1)}Se_2$ on the intensity of intercalation and dispersion.

From the results it follows that a significant impact on the intensity of intercalation and, accordingly, the dispersion has a value of current (Fig. 6.2). That is, the potential change indirectly characterizes the process of intercalation and dispersion of $2H–Nb_{1.02(1)}Se_2$.

Moreover, we explored the possibility of nanosynthesis of autointercalated diselenide niobium relatively similar to conditions using a mixture of single crystals of $2H–Nb_{1.02(1)}Se_2$ ($2H–TaS_2$ structural type). We can assume that as for micron particles of autointercalated $2H–Nb_{1.02(1)}Se_2$ and for single crystals is the process of intercalation of Li-ions with bi-layers of H_2O in the layered structure of $2H–Nb_{1.02(1)}Se_2$, which may lead to nanoparticles with size greater anisotropy compared with micron particles. We must point out that the process of passing the

Fig. 6.2 The value of potential for $2H-Nb_{1.02(1)}Se_2$ powder, U, depends on the time, t, at current, I: *1*—5 mA, *2*—7 mA, *3*—10 mA, *4*—20 mA, *5*—25 mA, *6*—30 mA, *7*—40 mA, *8*—50 mA

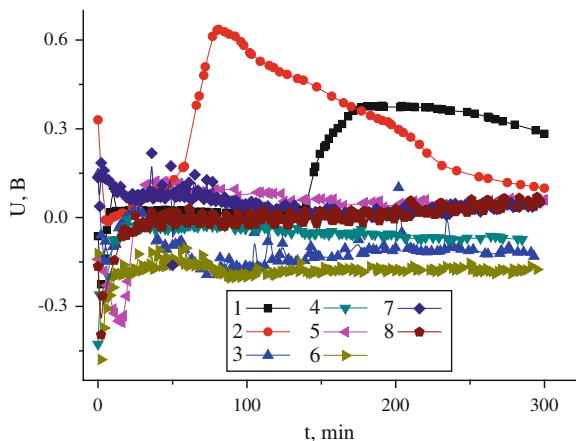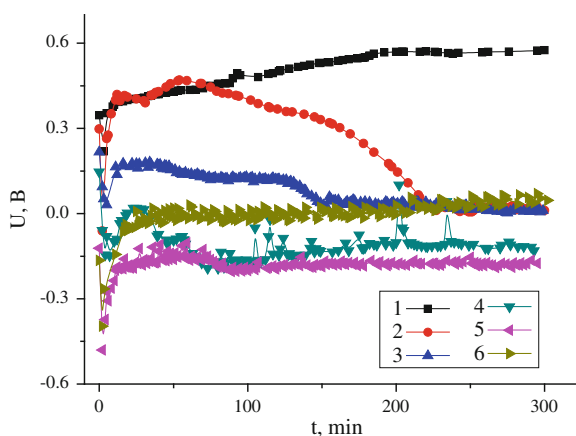**Fig. 6.3** The value of potential for $2H-Nb_{1.02(1)}Se_2$ micron particles and single crystals, U, depends on the time, t, at current, I: *1*—10 mA, *2*—30 mA, *3*—50 mA (*single crystals*), *4*—10 mA, *5*—30 mA, *6*—50 mA (*micron particles*)
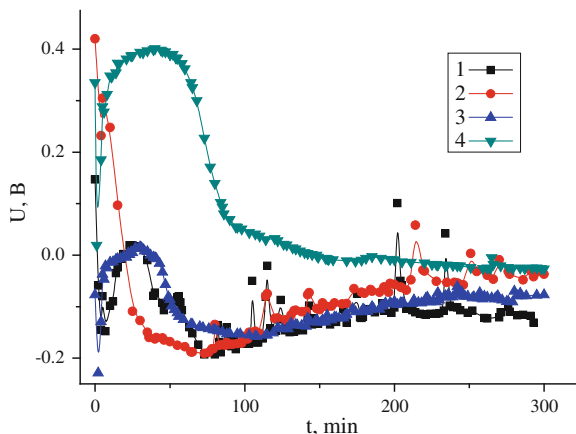
intercalation and dispersion of micron particles and single crystals have essential differences. The potential of initial micron particles $2H-Nb_{1.02(1)}Se_2$ shifted toward more negative values compared with the potential for single crystals (Fig. 6.3).

This can be explained by existing kinetic differences intercalation processes and thus dispersion due to the large difference in the size of the initial micron particles and single crystals ($\sim 1 \cdot 10^3$). Obviously for the effective synthesis of graphene-like nanoparticles $2H-Nb_{1.02(1)}Se_2$ should be used micron particles as an initial.

In connection with the above we compare the results of electrochemical intercalation (Li^+/H_2O) of autointercalated $2H-Nb_{1+y}Se_2$ (y = 0.02(1); 0.04(1); 0.09(1); 0.12(1); 0.22(1)) micron particles. It was shown that for the value of current 10 mA potential of $2H-Nb_{1.02(1)}Se_2$, $2H-Nb_{1.04(1)}Se_2$ and $2H-Nb_{1.09(1)}Se_2$ particles are shifted to the region of negative potential values in comparison with potential of $2H-Nb_{1.12(1)}Se_2$ (Fig. 6.4).

Fig. 6.4 The value of potential for 2H–Nb$_{1+y}$Se$_2$ powders, U, depends on the time, t: *1*—2H–Nb$_{1.02(1)}$Se$_2$, *2*—2H–Nb$_{1.04(1)}$Se$_2$, *3*—2H–Nb$_{1.09(1)}$Se$_2$, *4*—2H–Nb$_{1.12(1)}$Se$_2$ (I = 10 mA)

So, we note that the analysis above suggests three important points. The first is that significant impact on the processes of electrochemical intercalation and dispersion has the value of current. Obviously, increasing the value of current processes of intercalation leads to more intensive dispersion. The second important point is that to get graphene-like 2H–Nb$_{1+y}$Se$_2$ nanoparticles should use micron particles, but not single crystals. The third important point is that the potential depends on the content of autointercalated niobium atoms. The reason for these apparent dependences is that the autointercalated niobium affects the stability of the structure. Autointercalated Nb atoms statistically occupy octahedral cavities 2H–Nb$_{1+y}$Se$_2$ where weak van der Waals forces act (2H–TaS$_2$ structural type). As mentioned above, hydrated Li-ions also statically intercalated in the interlayer space and obviously also have to take emptiness as autointercalated niobium atoms. This leads to a deterioration of conditions kinetic movement hydrated Li-ions.

Structural studies involving X-ray studies were performed using of 2H–Nb$_{1.02(1)}$Se$_2$ nanoparticles. The results of X-ray studies of 2H–Nb$_{1.02(1)}$Se$_2$ are given in Table 6.1. According to the results of X-ray studies revealed that dispersed powders are nanocrystalline, homogeneous on the composition (NbSe$_2$), structural type (2H–TaS$_2$) and type nanostructures (graphene-like nanoparticles) and do not include other types of particles. So, it was prepared nanoparticles with average sizes of 22.7(7)–46.4(1.4) nm for [013] crystallographic direction and 61.9(1.7)–144(7) nm for [110] direction.

We should emphasize that the average size of 2H–Nb$_{1.02(1)}$Se$_2$ nanoparticles change in crystallographic directions [013], d$_{[013]}$, and therefore varies estimated number of nanolayers Se–Nb–Se nanoparticles. Significant changes in the size of nanoparticles suffer 2H–Nb$_{1.02(1)}$Se$_2$ in the crystallographic direction [110], d$_{[110]}$, which leads to differences in the d$_{[110]}$/d$_{[013]}$—index of anisotropy size of nanoparticles in crystallographic directions [013] and [110]. The nanoparticles size are controlled efficiently by kinetic parameters the processes of intercalation.

The parameters (a, c) of elementary cells of 2H–MCh$_2$ nanostructures correlate with average sizes of nanoparticles in the crystallographic directions [013] (a) and

Table 6.1 Results of X-ray studies 2H–Nb$_{1.02(1)}$Se$_2$ after electrochemical intercalation (Li$^+$/H$_2$O) and dispersion

Compound	Parameters of unit cells of initial particles, nm		Data for the powders after electrochemical processing					Amount nanolayers, n	Relation d$_{[110]}$/d$_{[013]}$
			Parameters of unit cells, nm		Average size of particles, nm, in the crystallographic directions [013] and [110]				
	a	c	a	c	d$_{[013]}$	d$_{[110]}$			
2H–Nb$_{1.02(1)}$Se$_2$	0.34449(2)	1.2554(1)	0.3447(2)	1.2597(9)	27.4(9)	75.0(1.9)		43	2.74
			0.3447(2)	1.2550(9)	41.6(1.4)	143.5(7.0) ≈ 144(7)		66	3.46
			0.3447(2)	1.2558(8)	46.4(1.6)	183.4(9.6) ≈ 180(10)		73	3.95
			0.3446(2)	1.2607(9)	25.4(8)	61.9(1.7)		40	2.44
			0.3444(2)	1.2563(9)	49.7(1.4)	164.8(7.4) ≈ 165(7)		79	3.32
			0.3447(2)	1.2550(9)	28.1(8)	135.0(6.4) ≈ 135(6)		44	4.80
			0.3448(2)	1.2551(9)	22.7(7)	132.4(4.2) ≈ 132(4)		36	5.81

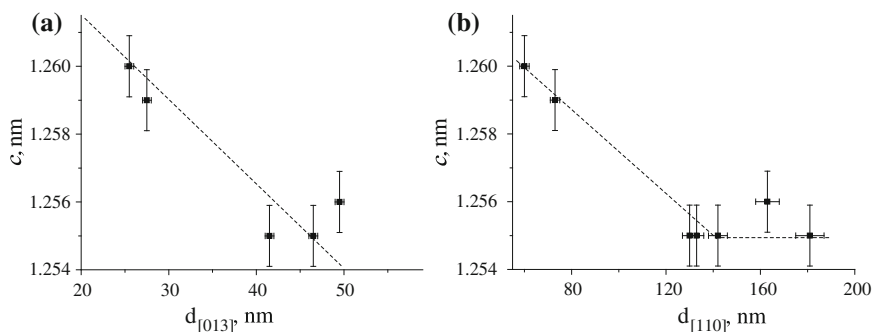**Fig. 6.5** The unit cell parameter c of graphene-like 2H–Nb$_{1.02(1)}$Se$_2$ nanoparticles depends on their average size, d, in the crystallographic directions [013], **a** and [110], **b**

[110] (b) and, as a rule, exceed the corresponding values for 2H–MCh$_2$ micron powders (Fig. 6.5a, b).

Figure 6.6a–d shows the SEM images of typical flakes observed after electrochemical intercalation (Li$^+$/H$_2$O) and dispersion. The nanoparticles have correct hexagonal form with considerable anisotropy sizes of length and thickness. It forms numerical conglomerates and does not include other types of particles. At present, the reason for formation of conglomerates is not clear. We suppose that this attributed to the highly reactive dangling bonds of both selenium and niobium atoms, which appear at the periphery of the nanoparticles.

Rightly noted that aqueous suspensions of dispersed particles in solution (Li$^+$/H$_2$O) are thermodynamically unstable. It is believed that the processes of hydrogen in the electrolysis of aqueous Li$_2$SO$_4$ intercalation and Li-ions are independent, although not eliminated their mutual influence through changes of pH near cathode region.

It can be assumed that the cathodic reduction of insoluble compounds in the aqueous environment participation adsorbed or atomic hydrogen in this process is highly problematic. Although it is known that the intercalation of some d-transition metal dichalcogenides from aqueous solutions of hydrogen under certain conditions is very likely due to the specific properties of hydrogen intercalation processes. For example, the cathodic reduction 1T–TiS$_2$ in Na$^+$/H$_2$O-electrolyte there are three stages of formation Na$_x$(H$_2$O)$_y$[TiS$_2$]^x: TiS$_2$ + H$_{0.16}$TiS$_2$, H$_{0.16}$TiS$_2$ + Na$_{0.27}^+$(H$_2$O)$_y$[TiS$_2$]$^{0.27-}$, Na$_x$(H$_2$O)$_y$[TiS$_2$]$^{x-}$, $0.27 \leq x \leq 0.4$, which is associated with changes of pH during the experiment [17]. So, here is the importance of the problem of stability of suspensions and control the size of nanoparticles in a wide range of anisotropic sizes.

Thus, it was investigated that the activated electrochemical intercalation (Li$^+$/H$_2$O) processes autointercalated 2H–Nb$_{1.02(1) \div 1.29(1)}$Se$_2$ micron particles and single crystals (2H–TaS$_2$ structural type) on their dispersion to graphene-like nanoparticles ("up-bottom"). It was shown that in galvanostatic mode electrochemical intercalation of hydrated Li-ions (Li$^+$/H$_2$O) in micron particles of
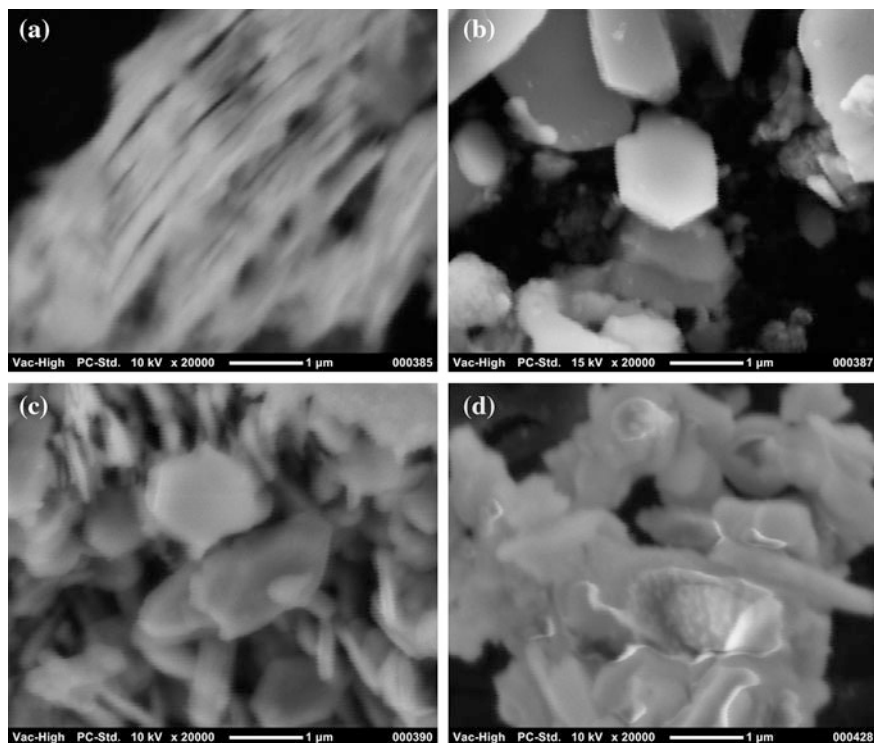
Fig. 6.6 The results of scanning electron microscopy of graphene-like $2H-Nb_{1.02(1) \div 1.29(1)}Se_2$ nanoparticles, the values of a current I = 30 mA (magnification—$\times 20,000$): **a** $2H-Nb_{1.02(1)}Se_2$, **b** $2H-Nb_{1.09(1)}Se_2$, **c** $2H-Nb_{1.12(1)}Se_2$, **d** $2H-Nb_{1.22(1)}Se_2$

autointercalated phases $2H-Nb_{1+y}Se_2$ ($0 \leq y \leq 0.29$, $2H-TaS_2$ structural type) is changing potential in time as a result of intercalation phases formation and dispersing micron particles to graphene-like nanoparticles. For intercalation and dispersion processes of micron particles and single crystals $2H-Nb_{1.02}Se_2$ are significant differences that related to existing kinetic differences intercalation processes. For the effective synthesis of graphene-like nanoparticles the micron particles of $2H-Nb_{1.02(1)}Se_2$ should be used as an initial.

The X-ray studies revealed that dispersed powders are nanocrystalline, homogeneous on the composition ($NbSe_2$), structural type ($2H-TaS_2$) and type nanostructures (graphene-like nanoparticles) and do not include other types of particles. So, it was prepared by the homogeneous, anisotropic graphene-like $2H-Nb_{1.02(1)}Se_2$ nanoparticles ($2H-TaS_2$ structural type) with average sizes of 22.7(7)–46.4(1.4) nm for [013] crystallographic direction and 61.9(1.7)–144(7) nm for [110] direction. From the results of SEM the nanoparticles have correct hexagonal form with considerable anisotropy sizes of length and thickness. It forms numerical conglomerates and does not include other types of particles.

References

1. Novoselov KS, Castro Neto AH (2012) Two-dimensional crystals-based heterostructures: materials with tailored properties. Phys Scr T146:014006. doi:10.1088/0031-8949/2012/T146/014006
2. Bhandavat R, David L, Sigh G (2012) Synthesis of surface functionalized WS nanosheets and performance as Li-ion battery anode. J Phys Chem Lett 3(11):1523–1530. doi:10.1021/jz300480w
3. Ogrin DC, Kissell KR, Lundberg KL, Tidrow JR (2012) Armor with transformed nanotube material. US Patent 8,225,704, 24 Jul 2012
4. Tsuneta T, Toshima T, Inagaki K et al (2003) Formation of metallic $NbSe_2$ nanotubes and nanofibers. Appl Phys 3(1):473
5. Liu Y, Li C, Li J et al (2008) Synthesis and characterisation of MS_2 (M = Nb, Ta) nanostructures. Int J of Mater Prod Tech 31(2–4):400
6. Toshima T, Inagaki K, Hatakenaka N et al (2006) Supercluster of electrons in ultrathin $TaSe_2$ nanocrystals. Phys Soc Japan. doi:10.1143/JPSJ.75.024706
7. Hor YS, Welp U, Ito Y et al (2005) Superconducting $NbSe_2$ nanowires and nanoribbons converted from $NbSe_3$ nanostructures. Appl Phys Lett. doi:10.1063/1.2072847
8. Novoselov KS, Jiang D, Schedin F, Geim AK et al (2005) Two-dimensional atomic crystals. Proc Natl Acad Sci USA 102:10451–10453
9. Coleman JN, Lotya M, ONeill A, Bergin SD et al (2011) Two-dimentional nanosheets produced by liquid exfoliation of layered materials. Science 331(6017):568-571. doi:10.1126/science.1194975
10. Smith RJ, King PJ, Lotya M, Wirtz C, Khan U et al (2011) Large-scale exfoliation of inorganic layered compounds in aqueous surfactant solutions. Adv Mater 23(34):3944–3948. doi:10.1002/adma.201102584
11. Zeng Z, Sun T, Zhu J, Huang X et al (2012) An effective method for the fabrication of few-layer-thick inorganic nanosheets. Angew Chem Int Ed 51(36):1–6. doi:10.1002/anie.201204208
12. Sekar P, Greyson EC, Barton JE, Odom TW (2005) Synthesis of nanoscale $NbSe_2$ materials from molecular precursors. J Am Chem Soc 127(7):2054–2055. doi:10.1021/ja0428006
13. Li JM (2010) Mass production of graphene-like single-crystalline $NbSe_2$ (004) nanosheets via intercalant-assisted thermal cleavage. Appl Phys A-Mat Sci Process 99(1):229–235
14. Kulikov LM, Semenov-Kobthar AO, Akselrud LG, Romaka LP (2001) Sposib otrymannya nanocrystalichnyx poroshkiv dyxalkohenidiv niobiu (The method for producing nanocrystalline powders of niobium chalcogenides). Ukraine Patent 98074044, 15 Aug 2001
15. Lieth RMA, Terhell JCJM (1977) Transition metal dichalcogenides. In: Lieth RMA (ed) Preparation and crystal growth of materials with layered structures. Reidel, Dordrecht, pp 141–223
16. Akselrud LG, Grin YuP, Pecharsky VK, Zavalij PYu et al (1993) Use of the CSD program package for structure determination from powder data. In: Proceedings of 2nd Europ Powder Diffraction Conference Pt 1.—Enschede. Trans Tech Pub, The Netherlands, pp 335–340
17. Schölhorn R (1981) Physics of intercalation compounds. In: Pietronero L, Tossatti E (eds). Springer, Berlin, p 33
18. Schölhorn R (1986) Proc.NATO Adv Res. D.Reidel Publishing Company, Dordrecht, p 323
19. Lerf A, Schölhorn R (1977) Solvation reactions of layered ternary sulfides A_xTiS_2, A_xNbS_2 and A_xTaS_2. Inorg Chem 16(11):2950–2956

Chapter 7
Optical Manifold of Spatial Localization of Dyes Molecules Self-Organized in the Body of Silica Thin Films

German Telbiz, Evgen Leonenko, Dezhiv Goer and Petro Manoryk

7.1 Introduction

The incorporation of dye molecules into solid matrixes is an attractive and widely investigated method to prepare dye-doped solid-state devices [1–5]. Large quantum yield of organic dye molecules combined with the advantages offered by the solid host matrix with respect to liquid solutions (bulky volume, flammable, toxic solvents, and difficult to be manageable) indicate that these materials can be good candidates, for solid-state dye laser applications [5, 6]. It has been shown that the lifetime and thermal stability of dyes are enhanced when they are entrapped in solid matrices [5]. Solid matrix offers a larger mechanical and thermal stability, reduces the risks of environmental and operator hazards, and allows to increase achievement of larger concentrations of the dye, reducing the formation of H-aggregates responsible for the quenching of the luminescence. Among the investigated possibilities, the embedding of dye molecules into silica materials prepared via sol-gel methods can offer the highest physical and chemical performances.

Two different approaches [2] can be used to prepare dye-doped silica materials: post-doping method (the impregnation), where the selected dye is incorporated into the sol-gel prepared porous silica and the pre-doping method, where the dye molecule is introduced at the sol stage in situ of solgel procedure. Post-doping method has disadvantage and some limits: difficult to determine the exact location of the dye molecules, dimension pores, presence of sorption center or defects on the surface, what induce untimely aggregation of the dye molecules. The main

G. Telbiz · E. Leonenko (✉) · P. Manoryk
LV Pisarzhevsky Institute of Physical Chemistry National Academy of Sciences of Ukraine, 31 Nauki pr, Kiev 03128, Ukraine
e-mail: scorpion5d@rambler.ru

D. Goer
Institute of Electron Physics National Academy of Sciences of Ukraine, 21 Universitetska St, Uzhgorod 88017, Ukraine

advantages of the pre-doping method with respect to the post doping one can be homogeneous distribution of the dye molecules due to mixing of the components at a molecular level, the possibility of introducing larger amounts of dye, and reducing the fluorescence quenching because of dye self-aggregation.

Main disadvantage to the realization of such hybrid materials remains the limited photostability of the confined dye inside the solid matrix, the consequently fast degradation of the dye molecules, and their luminescent properties. The aim of this work is a choice of method to obtain hybrid mesostructured sol-gel silica films with high concentration of dye and increased photostability. Rhodamine 6G, the most frequently used dye, with high quantum yield in fluorescence in the 500–600 nm range was selected as guest molecule.

Here, we present the analysis and comparison of the optical characteristics of dye molecules self-organized in the body of mesostructured silica thin films. Samples with different concentration of the dye were prepared by sol-gel method as homogeneous and transparent films deposited by spin and dip coating on the substrate.

7.2 Experimental

A colored mesostructured SiO_2 films were prepared by the template sol-gel technique using as precursor material composed of matrix tetraethoxysilane (TEOS), ethanol, distilled water, HCl and Pluronic 123 (1:8:2:0,5:0,01 molar ratios), and dye. This sol composition has proven to give good quality SiO_2 coatings [7]. The TEOS was dissolved in the ethanol using magnetic stirring for 15 min. For preparation of starting composition 0.003–0.72 g of Rhodamine 6G was dissolved in 10 ml sol. The dye concentration was in the range of 6×10^{-4}–1.5×10^{-1} mol/l. This solution was mixed at 60 °C for 120 min to form sol that was used in all of the following operations. The colored films were obtained on substrates (glass, mica, and silica) using a hand-made spin and dip coating apparatus and various rotation and withdrawal speed (1,500–2,500 rev./min. or 5–12 cm/min, respectively). Standard procedure of substrates (cleaned in hot chromic mixture, followed by a rinse with distilled water) was adopted before coating. After that the coating films were dried at ambient temperature for 48 h at atmospheric air conditions. The coating thickness measured by AFM was 200–800 nm.

The optical (absorption and transmission) spectra were measured at room temperature with a Specord 210 spectrophotometer. Steady state photoluminescence spectra measured with Hitachi MPF-4 and a Perkin Elmer LS55 spectrophotometer. Fluorescence spectra and decay kinetics of Rh6G/SiO_2 films were measured using the Edinburgh Instruments: TCSPC Fluorescence Spectrometer F900. The diode laser EPL-375 emitting 50-ps pulses with 0.15 mW average power was used for the sample excitation [8]. The surface relief and thickness of the films was revealed by atomic force microscopy using NanoScope D 300

(Digital instrument). Optical properties of a doped film were calculated using envelope method proposed by Swanepoel [10].

7.3 Result and Discussion

In designing the film for optical application, a number of factors need to be taken into account. Main is the ability of the film's matrix to effectively solubilize relatively high concentrations (10^{-3}–10^{-1} M) of the dye molecules. Such high concentrations are necessitated for the films to exhibit appreciable absorbance, even when their thickness is even 150–300 nm. Under the assumption that molecules are not effectively dispersed within the host matrix, the optical as well as the physical properties of the films tend to be negatively influenced. For example, broadening of the dye's absorption band, loss its intensity, and decrease light transmission through the film, is some of the adverse effects that might result. The method of production, optical, and physicochemical quality of the resultant films are the essential factors to be considered when deciding upon the film's composition. Film fabrication needs to be conducted with relative ease, using the proven deposition techniques such as dip coating or spin coating. This would allow obtaining films containing a variety of dyes within different concentration and desired optical properties.

It is known that applications in which rhodamine is used, abused its strong absorption and fluorescence in the visible region that often taken to minimize the self assembly aggregation process between individual dye molecules. With other side, formation of aggregates significantly reduces the quantum yield of fluorescence that leads to intensity decrease and to a lesser extent, broadening of the absorption band [11–13]. Rhodamine 6G shows a strong tendency to form aggregates when dissolved in concentrated solutions or after incorporation into various different matrixes. Aggregation change of the absorption spectrum is due to ''reversible polymerization'' i.e., aggregation of the dye monomers into loosely bound polymers [11].

For comparison, on Fig. 7.1a–c is shown the evolution of absorption spectrum Rh6G in ethanol solution, started sol composition and hybrid film concentration is increased. At a initial concentration of 6×10^{-4} mol/l, spectrum of the sol-composition and film is almost identical to that in solution, where the main absorption band of Rh6G in visible region corresponds to a transition moment largely parallel to the long axis of the molecule due to π–π* transition. Corresponding absorption maximum at 527 nm and a shoulder at 500 nm are observed in the spectra. Increasing of concentration (Fig. 7.1a) to the 1×10^{-3} mol/l leads to the intermolecular interaction involved in the formation of the dimer, the intensity of the shoulder at $\sim$500 nm becomes much more well-defined and broadened relative to the 6×10^{-4} mol/l sample. These changes most likely most indicative of the formation of a greater number "sandwich" type H-aggregates, along with the formation of J-type aggregates according to a well-known exciton model.

Fig. 7.1 UV-visible absorption spectra of **a** rhodamine 6G in ethanol solution, **b** started sol composition, and **c** mesostructured silica films with different amounts of Rh 6G. The dye concentrations (mol/l) are as follows: (a) 1–1 × 10^{-5}; 2–1 × 10^{-4}; 3–5 × 10^{-4}; 4–1 × 10^{-3}; (b) and (c) 1–6 × 10^{-4}; 2–7.5 × 10^{-3}; 3–2.1 × 10^{-2}; 4–1.5 × 10^{-1}
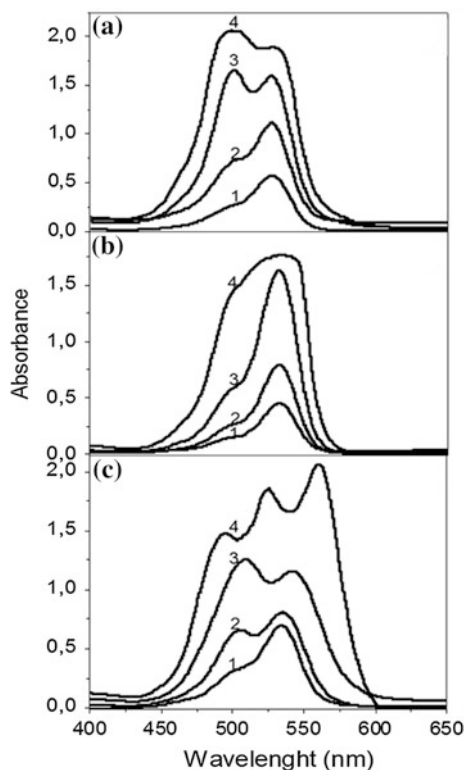
The evolution of the absorption spectrum, Rh6G of the started sol with its growth concentration is shown in Fig. 7.1b. When the concentration increased up to 0–2 mol/l, the spectrum is not identical to that in solution, the main difference being a slight shift to the red and the virtual absence of aggregation in sol. Red shift is most likely can be attributed to a weak ground state interaction between the Rh6G molecules and Pluronic P123 molecules in the host mesostructure [9]. Upon further increase in the concentration, the shoulder at ∼500 nm becomes much more defined.

In spectral data presented, in Fig. 7.1c we have evaluated the effect of the different amounts of dye introduced in mesostructured films. At the highest dye concentration H-dimer absorption band around 500 nm is observed in all the samples. This dimer band is overlapped to the vibronic band but can be clearly detected. The formation of J-type dimers cannot be evaluated from the absorption spectra because of the overlap with the monomer band. We therefore subtracted the absorption spectra of the films to separate the contributions of the different types of dimers. Figure 7.1c (curve 4) shows the spectra that resulted from the subtraction; as three different absorption bands are observed around 495, 525, and 560 nm, which can be assigned to H-dimers, molecular form, and J-type dimers, respectively [9]. It is interesting that the relative intensity of absorption bands
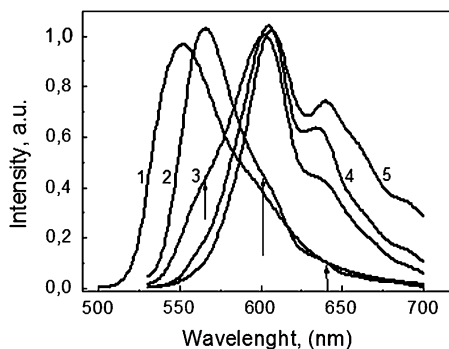
changes with a specific trend. The J-dimer band has the lowest relative intensity in
the silica films and the highest in the sample with the highest dye concentration,
monomer bands observed for concentration of Rh6G 0–2 mol/l.

To shed light to the effects of Rh6G aggregation on the optical properties of
films, we have measured fluorescence emission spectra using an excitation at
480 nm on samples with different concentrations of dye. We observed significant
differences in fluorescence spectra. The normalized fluorescence spectra of the film
samples are plotted in Fig. 7.2.

For films containing $7–5 \times 10^{-3}$ mol/l Rh6G, the increase of dye concentration
within the films has produced a broadening and red shift of the emission band
compared to the spectrum of film with concentration 6×10^{-4} mol/l. Since such
broadening is not observed in the absorption spectrum for this film, it is most likely
attributable to the formation of an excited state complex between the Rh6G and the
Pluronic P123 molecules [9]. When the concentration is increased to
2×10^{-2} mol/l, the spectrum further broaden, the shoulder in the absorption
spectra was observed (630 nm) and maximum is now shifted 5 nm to the red. The
broadening, in conjunction with the spectral shift is rather due to the presence of
J-type dimer aggregates, that confirmed by visualization of the shoulder in the
absorption spectrum for this film. Furthermore, the appearance of a shoulder at
~ 630 nm can be attributed to the fluorescence of "head to tail" aggregates
exclusively. At a concentration of $1–5 \times 10^{-1}$ mg/ml, the fluorescence spectrum
is very different from that of the low dye concentration such as even the previous
films. The maximum of band in this case we observed at 605 nm, compared to
565 nm for the 6×10^{-4} mol/l, where maximum of the shoulder shifted at
640 nm.

These changes can be the result of a high percentage of H- and J-type aggre-
gates, with various interaction angles, localized within the film after coating. The
existence of these aggregates can also account for the disappearance of the
monomer's fluorescence band at 564 nm.

These changes in the absorption and fluorescence spectra, still do not attest to
the applicability of these films. Time-resolved fluorescence studies help to show
the nature of the aggregates. According to [14], in ethanol the lifetime of Rh6G is

Fig. 7.3 The normalized fluorescence decay profiles for various concentrations of Rh6G-doped mesostructured silica film. Concentrationof dye (mol/l); 1–1 × 10^{-5}; 3–7.5 × 10^{-3}; 4–2.1 × 10^{-2}
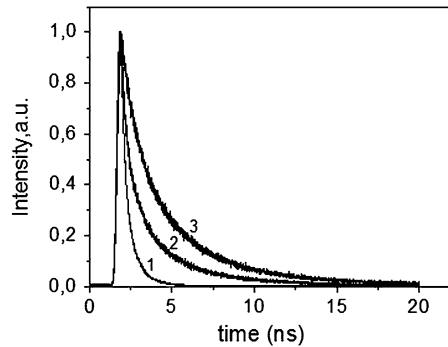
reported to be 3–8 ns, with a fluorescence quantum yield of 0.94, as well as good optical and thermal stability which determine its use as the lasing medium in both liquid and solid optically pumped dye lasers [14, 15]. The slight increase in lifetime of the dominant component further supports the above assertion that the excited state is somewhat stabilized through interactions with the Pluronic P123 molecules of the mesostructure (Fig. 7.3). The origin of the minor component cannot be ascertained at this point, but could be due to the excited state CT(charge-transfer) complex between Rh6G and surrounding Pluronic molecules.

Spin coating and dip coating are two basic techniques used to produce a thin film on a planar substrate. Both techniques are used to make different coatings and thin films with wide range thickness, surface morphology, and tuneable microstructure. We evaluated optical properties of doped films obtained from the same sol by spin coating and dip coating techniques. Typical fluorescence spectra with the concentration of the dye are shown in Fig. 7.4. As can be seen from the spectra, magnitude of the emission increases with the concentration of the dye in the films obtained by spin coating, while the films obtained by dip coating, at a certain concentration (∼0.01 mol/l), the quenching of fluorescence (curve 3, 3′). This can be explained by unequal time of consolidation of the structure of sol-gel film, which is functionally dependent on the deposition conditions on substrate. In case of dip coating, formation of structure continues more than a minute and

Fig. 7.4 Fluorescence spectra of the doped Rh6G mesostructured films obtained by spin (1–3) coating and dip (1′–3′) coating techniques with growth concentration of the dye: Concentration of Rh6G (mol/l): 1–7.5 × 10^{-3}; 2–2.1 × 10^{-2}; 3–1.5 × 10^{-1}
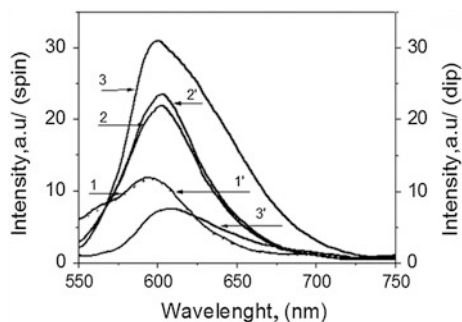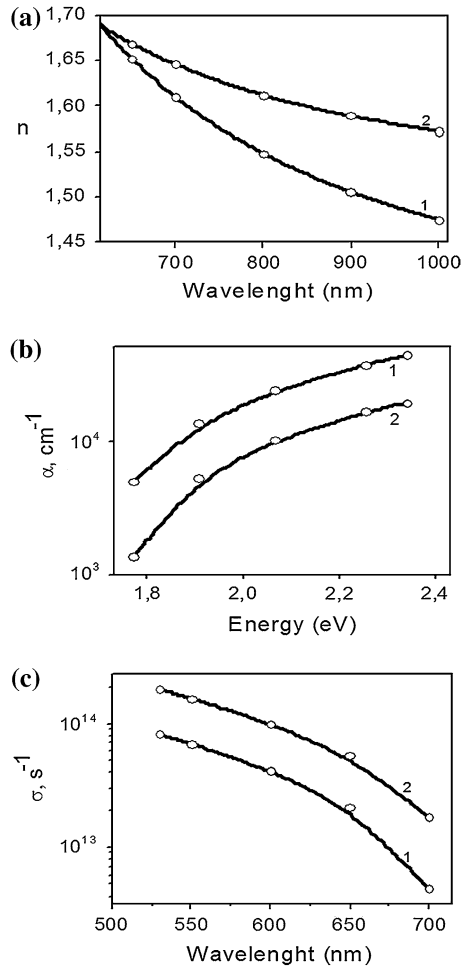
Fig. 7.5 Optical constants of doped Rh6G mesostructured films subject to method of their deposition on substrate: *1* spin-coating, *2* dip coating. **a** refractive index, **b** absorption coefficient, and **c** optical conductivity

aggregation of dye molecules will be spontaneous, while in case of spin coating, aggregation of dye molecules will be quickly stopped and formation of complex with fragment of Pluronic molecules can take place.

Therefore optical characteristic (refractive index, absorption coefficient, and optical conductivity), as key parameter their practical applicability, of spin and dip coating films were compared. Envelope method [10] was applied for calculating optical constant of thin films. Difference values of these constants (Fig. 7.5) can be evidence of various spatial organizations and directions of the aggregation of dye molecules within the body of hybrid films. Based on this data, the viability for these composite films to for excitation of lasing has been checked and ability of creation and design of waveguide nanolaser with all its featured beam parameters has been successfully tested.

7.4 Conclusion

Development of a simple sol-gel-based method for producing, by dip, or spin coating high quality inorganic/organic composite films using TEOS as the silica precursor, and a nonionic surfactant, Pluronic P123, as the organic template is reported. The observed manifold of the optical and fluorescence spectra shows the ability of dispersity and controlled aggregation of dye molecules (such as Rh6G) owing to time delay of their spontaneous transformation during the process of formation of mesostructured hybrid sol-gel films. Emission in films received by pre -doping method, observed even at high dye concentrations and characterize of long-term stability. A distribution of dye molecules in body of film corresponded to three extreme configurations, which we attribute to monomers, sandwich H-type dimers and head-to tail J-type aggregates. The formation of fluorescent aggregates most probably can be promoted of the amphiphilic triblock copolymers that favor the formation of hybrid micelles and the excited state CT complex between dye and surrounding Pluronic molecules. Variation of values of refractive index, absorption coefficient, and optical conductivity can be evidence of various spatial organizations of dye molecules within the body of generated films, subject to method of deposition on substrates. Preliminary experiments have shown viability of the composite films to for excitation of lasing that is perspective for design of waveguide nanolasers.

References

1. Brinker CJ, Sherer GW (1990) Sol–gel science: the physics and chemistry of sol–gel processing. Academic Press, New York
2. Wirnsberger G et al (2001) Mesostructured materials for optical applications: from low-k dielectrics to sensors and lasers. Spectrochimica Acta Part A 57:2049–2060
3. Hayward RC et al (2001) The current role of mesostructures in composite materials and device fabrication.Microporous Mesoporous Mater 44–45:619–662
4. Hoffmann F et al (2006) Silica-Based Mesoporous Organic-Inorganic Hybrid Materials. Angew Chem Int Ed 45:3216–325
5. Wu Y et al (2004) Composite mesostructures by nano-confinement. Nat Mater 3(11):816–822
6. Yang Y et al (2004) Opt Mater 24:621–628
7. Telbiz GM et al (2008) Sol-gel methods for materials processing, vol 12. Springer, pp 356–363
8. Telbiz GM et al (2010) Effect of nanoscale confinement on fluorescence of MEH-PPV/MCM–41 composite. Phys status solidi A 207:2174–2179
9. Gao F (2002) Photo-induced interaction of hydrophobic and hydrophilic dye molecules at nanometer distance. Dyes Pigm 52:223–230
10. Swanepoel R (1983) Determination of the thickness and optical constants of amorphous silicon. J Phys E, Sci Instrum 16:1214–1222

11. Fogel R et al (2002) Dimer-to-Monomer Transformation of Rhodamine 6G in Aqueous PEO−PPO−PEO Block Copolymer Solutions Macromolecules. 35:2063–2070
12. Martínez VM et al (2005) Characterization of Rhodamine 6G Aggregates Intercalated in Solid Thin Films of Laponite Clay. 2 Fluorescence Spectroscopy. J Phys Chem B 109:7443–7450
13. Malfatti L et al (2008) Aggregation States of Rhodamine 6G in Mesostructured Silica Films. J Phys Chem C 112:16225–16230
14. Rao AP, Rao AV (2003) Studies on the effect of organic additives on the monolithicity and optical properties of the rhodamine 6G doped silica xerogels. Mater Lett 57:3741–3747
15. Sharma S et al (2010) Spectroscopic and lasing properties of Xanthene dyes encapsulated in silica and polymeric matrices. Optik 121(1):11–18

Chapter 8
Nonlinear Optical Properties of New Nanocomposites: Metal Alkanoate Glasses with Semiconductor Quantum Dots

A. G. Lyashchova, D. V. Fedorenko, G. V. Klimusheva, T. A. Mirnaya and V. N. Asaula

Nonlinear optical properties of cadmium alkanoate composites with CdSe nanoparticles are investigated. The standard Z-scan technique with CW laser ($\lambda = 405$ nm) and CW laser with chopper was used for this purpose. The nonlinear characteristics of nanocomposites contained CdSe quantum dots (QDs) of different sized were measured. The process of self-defocusing in samples with nanoparticles was observed. The effects of thermal optical nonlinearity in new nanocomposites based on cadmium alkanoate were investigated for the first time. Whereas, nonlinear refraction and absorption in pure matrix were not observed at used excitation conditions the nonlinear response of the samples is caused exclusively by the presence of CdSe nanoparticles. The nonlinear absorption of nanocomposites weakens with particle size decreasing.

8.1 Introduction

The tendency to study nontraditional classes of liquid crystals and composites based on LC has grown during last years due to their specific physical properties. Their classes are presented by ionic, magnetic, inorganic liquid crystals, etc. Such kind of research essentially expands a field of fundamental knowledge about liquid crystals and opens new possibilities of their practical use.

There is a considerable interest in research, the optical nonlinearities of semiconductor quantum dots in stabilizing matrices for the leading investigations in different application areas such as nonlinear optics and photonics [1–3].

A. G. Lyashchova (✉) · D. V. Fedorenko · G. V. Klimusheva
Institute of Physics, National Academy of Science of Ukraine, Prospect Nauki 46,
Kiev 03680, Ukraine
e-mail: alina.zt@meta.ua

T. A. Mirnaya · V. N. Asaula
V. Vernadsky Institute of General and Inorganic Chemistry, National Academy of Science
of Ukraine, Palladina Avenue 32–34, Kiev 03142, Ukraine

Fig. 8.1 Model of nanocomposite: a spherical nanocrystal in metal alkanoate matrix
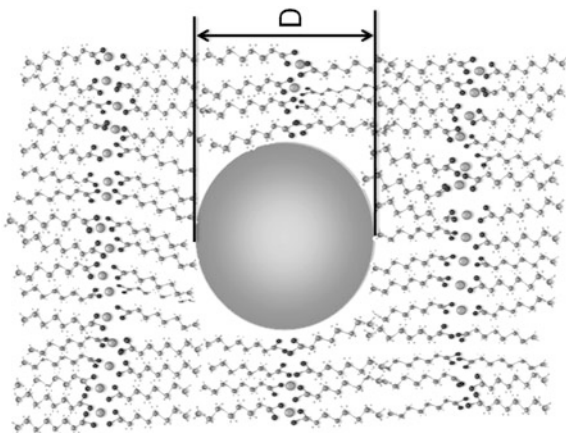
The first nanocomposites containing CdS semiconductor quantum dots were obtained [4] in metal alkanoate thermotropic ionic liquid crystalline matrices. Such nanocomposites can form layered anisotropic glasses at the room temperature.

Structural model of nanocomposite with CdS spherical particles in metal alkanoate matrix is depicted in the Fig. 8.1. The average diameter of nanocrystals is in the range D = 2 $\div$ 4 nm.

These new nanocomposites are attractive due to low dispersion of QDs size in anisotropic liquid crystal matrices and the ability of metal alkanoates to form ionic smectic glasses at room temperature [5].

8.2 Experimental Results

We studied the optical properties of nanocomposites with CdSe QDs with different sizes (1 nm–sample (1); 1.8 nm–sample (2); 2.6 nm–sample (3)) in cadmium caprylate matrix, pure cadmium caprylate matrix–sample (4). The absorption spectra of nanocomposites are presented on the Fig. 8.2. The nonlinear optical characteristics of these nanocomposites were studied by Z-scan method. The experimental setup is depicted in the Fig. 8.3. A CW diode laser operating at 405 nm wavelength was used as a light source. The power of the CW laser beam is 50 mW. The laser beam was focused on the sample by a convergent lens of 12 cm focal length. The sample was mounted on a translation stage and moved around the lens focus ($z = 0$) by a computer controlled stepper motor. The light transmittance was then measured by a closed-aperture photodetector as a function of the sample position. Typical peak-valley dependencies were received for the samples (2), (3) (Fig. 8.4). Nonlinear absorption measurements were performed using the same
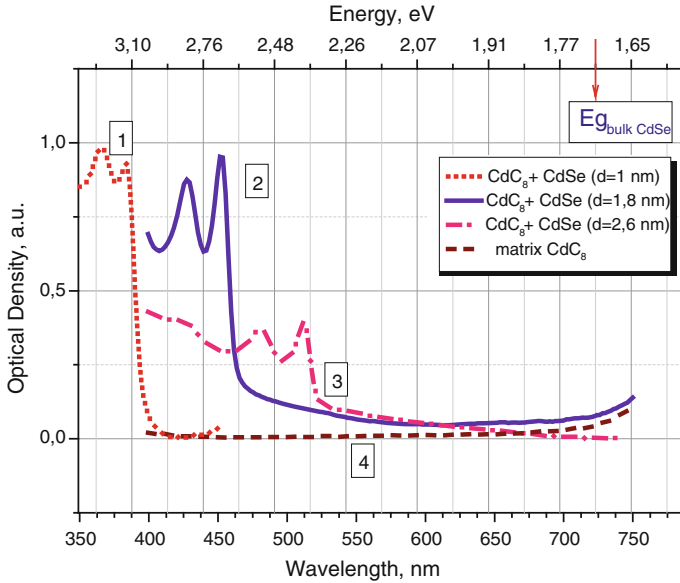
Fig. 8.2 The absorption spectra of nanocomposites for different size *d* (*curves 1, 2, 3*) of CdSe nanocrystals in cadmium caprilate matrix, pure cadmium caprilate matrix (*curve 4*)
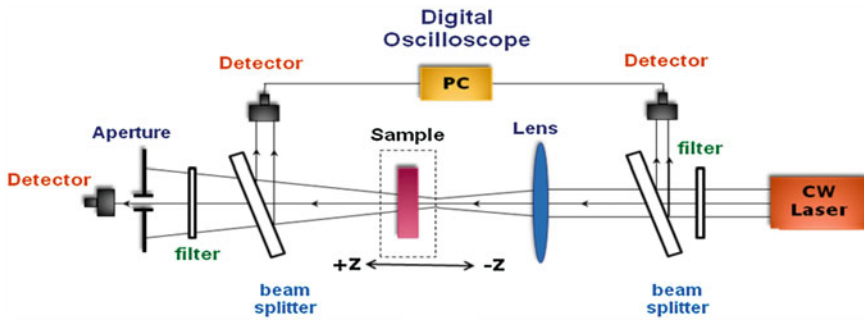

Fig. 8.3 Z-scan setup under CW diode laser for optical nonlinearity measurements

experimental setup with using an open aperture configuration. The normalized transmittance for this geometry is presented on the Fig. 8.5.

Analogical closed and open aperture experiments were made on Z-scan setup under CW diode laser with mechanical chopper operated at 50 Hz. The average power is 2 mW and pulse duration is 0.6 ms. Measured curves for closed aperture are presented on the Fig. 8.6. The normalized transmittance for open aperture geometry is presented on the Fig. 8.7.
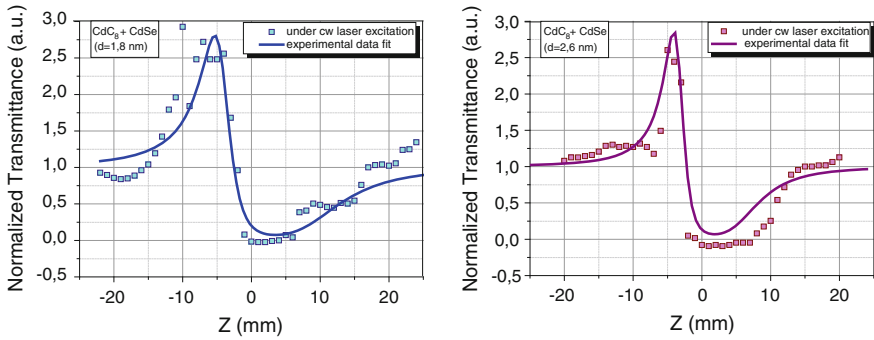
Fig. 8.4 Typical normalized transmittance dependence on the sample position for nanocomposite under continuous excitation. The *solid curve* corresponds to the photoinduced lens model (*PhLM*) fitting
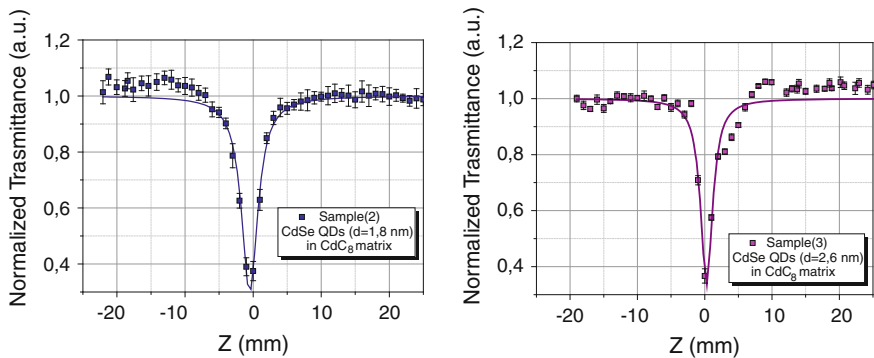

Fig. 8.5 Typical normalized transmittance dependence on the sample position for nanocomposite: cadmium selenium QDs in the cadmium caprilate matrix for different size of nanocrystals. The *solid curve* corresponds to the PhLM fitting

8.3 Discussion

The observed absorption belongs to cadmium selenide nanocrystals (Fig. 8.2, curves 1, 2, 3), cadmium caprylate matrix does not absorb light in this spectral range (Fig. 8.2, curve 4). The absorption bands of the samples are shifted in the high energy relative to energy of the band gap Eg of a cadmium selenide bulk crystal. We observed the larger blue shift for smaller nanoparticles [6] (compare curves 1, 2, 3). The bands are quite narrow, so the dispersion of nanoparticles size is relatively small. Our estimations of dispersion give the value 30 % from the mean.

The effects of local heating due to absorption of light on the propagation of a Gaussian CW laser beam through samples (2), (3) lead up to form nonlocal
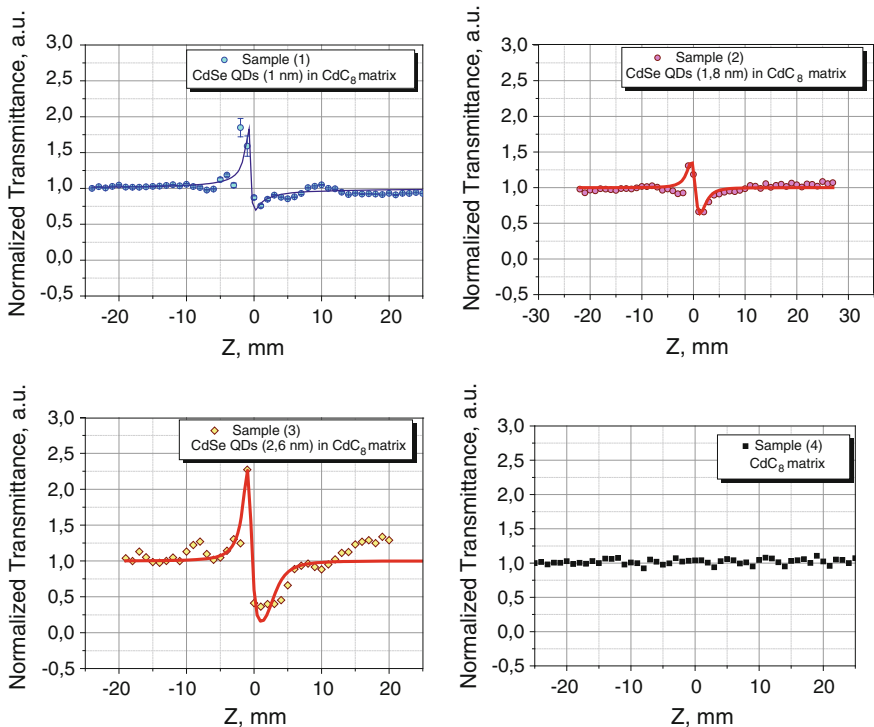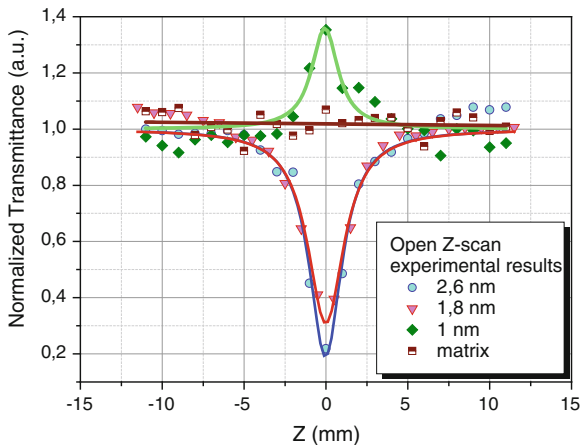
Fig. 8.6 Typical normalized transmittance dependence on the sample position for nanocomposite under pulsed excitation. The *solid curve* corresponds to the PhLM fitting

Fig. 8.7 Measured open Z-scan transmittance curves for nanocomposites. The *solid curve* corresponds to the PhLM fitting

thermal lens. Whereas maximum of transmittance curve appears before its mini-mum, the nonlinear refractive index has negative value. The process of self-defocusing is observed. Large values of nonlinear phase shift and nonlocal response of the nanocomposite media evoke asymmetry of peak-valley depen-dencies, see Fig. 8.4. Consequently, the standard model of Sheik-Bahae et al. [7] cannot be applied for the analysis of the results.

There are several models, which allow analyzing the experimental data in the case of large nonlinear phase shift, no local response and thermal lens effect [7–9]. We used the model proposed by Reynoso Lara et al. [8]. In the frame of this model, the nonlinear response of an illuminated part of the sample is modeled as photoinduced thin lens (PhTL). A focal length of photoinduced lens is a function of the incident beam radius w to the integer power m:

$$F = a_m w^m(z) \tag{8.1}$$

where a_m is a constant (includes the material parameters). This model describes the case of large phase change with typical asymmetry. Different integer values of parameter m correspond to various mechanisms of photoinduced lens development.

The model could be applied, when the maximum value of the normalized transmittance is 5, because greater values means phase changes on axis greater than 2π, then light from different radial distances of the beam could interfere losing the beam its Gaussian distribution [8].

The normalized transmittance is given by:

$$T = 1 - \frac{4x}{(1+x^2)^2}\left(\frac{z_0}{2F_{0m}}\right) + \frac{4}{(1+x^2)^3}\left(\frac{z_0}{2F_{0m}}\right)^2, \quad (x = z/z_0), \tag{8.2}$$

and can be reproduced in terms of the nonlinear phase shift by using the next relation:

$$\Delta\Phi_{0m} = \frac{z_0}{2F_{0m}}. \tag{8.3}$$

So, nonlinear refractive index can be calculated as,

$$n_2 = \frac{\Delta\Phi}{kI_0 L_{\text{eff}}}, \tag{8.4}$$

where $L_{\text{eff}} = (1 - e^{-\alpha_0 L})/\alpha_0$, $k = 2\pi/\lambda$, with L sample thickness, I_0 on-axis irradiance at focus ($z = 0$) and α_0 linear absorption coefficient.

In the case of thermal lens the focal length photoinduced by a Gaussian beam is given as [10]

$$F_{\text{ther}} = \frac{\pi k}{P_{\text{abs}}\left(\frac{\partial n}{\partial T}\right)} w^2 \tag{8.5}$$

In expression (8.5) k is the thermal conductivity, P_{abs} is the change of power after propagating through the sample due to the light absorption, $(\partial n/\partial T)$ is the change of refractive index with the temperature. Then the expression for material parameter a_m from (8.1) can be found out and $\frac{\partial n}{\partial T}$ can be estimated using (8.3):

$$a_m = \frac{\pi k}{P_{abs}\left(\frac{\partial n}{\partial T}\right)} \tag{8.6}$$

$$\frac{\partial n}{\partial T} = \frac{\pi k w_0^2}{P_{abs}}\frac{2\Delta\Phi}{z_0} \tag{8.7}$$

Phase shift, Rayleigh length were obtained from fitting experimental dependence by function (8.2). Parameters calculated by the formulae (8.3–8.7) of photoinduced thermal lens of the samples (2), (3) are presented in the Table 8.1.

We also made the Z-scan experiment with mechanical chopper for CW laser. The average power of laser beam was 2 mW and pulse duration was 0.6 ms. We estimated the time of thermal diffusion as $t_0 = \frac{w_0^2}{4D} \approx 3$ ms using the thermal diffusivity $D = 1.7 \times 10^{-7}$ m/s [11] and beam waist $w_0 = 45.5$ μm. The local media heating has been dissipating during intervals between pulses (time between pulses is 18 ms). As one can see, the time of thermal diffusion is greater than pulse duration. Thereby, thermal diffusion is negligible and the response of the media gets more local character. Consequently, the experimental dependencies (see Fig. 8.6) become symmetrical.

Therefore, applying of chopper for CW laser allowed reducing thermal lens effect and, respectively, the delocalization of refractive index distribution.

One can see from the Figs. 8.4, 8.6 that peak-valley differences of normalized transmittance greatly decreased in the case of pulsed excitation. Then the phase shift became much smaller: $\Delta\Phi \sim \Delta T$, hence the Sheik-Bahae model can be applied [7].

Fitting of experimental data allowed estimation of induced lens parameters and nonlinear coefficient n_2 (see Table 8.1). It should be noted, that the focal length and phase shift of induced lens in last case are changed.

Table 8.1 Linear and nonlinear optical parameters

Parameters	Sample (1)	Sample (2)		Sample (3)	
	Pulsed excitation	Continuous excitation	Pulsed excitation	Continuous excitation	Pulsed excitation
$\triangle\phi$	0.8	3.5	0.6	3.6	2.2
F, mm	1.1	0.9	1.2	0.5	0.3
I_0, W/m^2	3.15×10^5	7.86×10^6	3.15×10^5	7.86×10^6	3.15×10^5
n_2, cm^2/W	1.09×10^{-4}	3.17×10^{-5}	4.00×10^{-4}	1.46×10^{-5}	2.27×10^{-4}
n_2, esu	3.89×10^{-2}	1.13×10^{-2}	1.37×10^{-1}	5.23×10^{-3}	8.13×10^{-2}
$\partial n/\partial T$, K^{-1}	2.48×10^{-3}	4.95×10^{-2}	1.36×10^{-2}	5.11×10^{-2}	6.01×10^{-2}

Different observed values of optical nonlinearities of nanocomposites were connected with difference nanoparticles absorption at laser excitation. Nonlinear refraction and absorption in pure matrix were not observed at used excitation conditions (Figs. 8.6, 8.7). Hence, the nonlinear response of the samples is caused exclusively by the presence of nanoparticles. The nonlinear absorption weakens with particle size decreasing [samples (2) and (3)] and saturated absorption is observed for nanocomposite with quantum dots size 1 nm (Fig. 8.7). Large values of nonlinear refractive index (comparable with giant orientation nonlinearity of liquid crystals) might explain due to local thermal transition from the anisotropic glass to smectic A mesophase of cadmium caprylate at laser excitation.

8.4 Conclusions

It was shown, that nonlinear refraction and absorption in pure matrix were not observed at used excitation conditions, whereas the nonlinear response of the samples is caused exclusively by the presence of CdSe nanoparticles. The process of self-defocusing in samples with nanoparticles was observed. Obtained magnitudes and signs of nonlinear refractive index are of the same order with orientation nonlinearity of nematic liquid crystals. The nonlinear absorption weakens with particle size decreasing. Fast self-defocusing together with nonlinear absorption make studied nanocomposites to be an attractive media for optical limiters. The nonlinear response of nanocomposites can be extremely fast what must be investigated in the close feature.

References

1. Jia W, Douglas EP, Guo F, Sun W (2004) Optical limiting of semiconductor nanoparticles for nanosecond laser pulses. Appl Phys Lett 85:6326–6328
2. Shoute LCT, Kelley DF (2007) Spatial organization of GaSe quantum dots: organic/semiconductor liquid crystals. J Phys Chem C 111(28):10233–10239
3. Basu R, Lannacchione GS (2009) Evidence for direct self-assembly of quantum dots in a nematic liquid crystals. Phys Rev E80:010701-1–010701-4
4. Asula VM, Mirnaya TA, Yaremchyk HH (2010) Synthesis peculiarities of CdS nanocomposites in ionic liquid crystalline melt based on cadmium alkanoate. Ukrainian Chem J 76(3)
5. Mirnaya TA, Volkov SV (2002) In: Rogers RD, Seddon KR, Volkov SV (eds) Green industrial applications of ionic liquids. Kluwer Academic Publishers, London, pp 439–456
6. Gusev AI (2009) Nanomaterials, nanostructures, nanotechnology. Fizmatlit, Moscow
7. Sheik-Bahae M, Said AA, Wei TH, Hagan DJ, Van Stryland EW (1990) Sensitive measurement of optical nonlinearities using a single beam. IEEE J Quantum Electron QE-26:760–769
8. Reynoso Lara E, Navarrete Meza Z, Iturbe Castillo MD, Treviño Palacios CG, Marti Panameño E, Arroyo Carrasco ML (2007) Influence of the photoinduced focal length of a thin nonlinear material in the Z-scan technique. Opt Express 15:2517–2529

9. Cuppo FLS, Figueiredo Neto AM, Gómez SL, Palffy-Muhoray P (2002) Thermal-lens model compared with Sheik-Bahae formalism in interpreting Z-scan experiments on lyotropic liquid crystals. J Opt Soc Am B 19:6

10. Gordon JP, Leite RCC, Moore RS, Porto SPS, Whinnery JR (1965) Long-transient effects in lasers with inserted liquid sample. J Appl Phys 36:3–8

11. Bugaychuk S, Garbovskii Yu, Klimusheva G, Tolochko A, Kolesnik O, Vakhnin A, Mirnaya T, Jaremchyk G, Ishchenko A Nonlinear effects in ionic smectics with nanosized dye impurities. Proc SPIE 6023:602309-1–602309-6

Chapter 9
Surface Plasmon Retardation in Graphene Bilayer

Konstantin Batrakov and Vasil Saroka

9.1 Introduction

In recent years, an enormous interest has been surrounding the field of plasmonics, because of the variety of tremendously exciting and novel phenomena it could enable. Plasmonics seems to be the only viable path toward realization of nano-photonics; control of light at scales substantially smaller than the wavelength [1]. Accessing subwavelength optical length scales introduce the prospect of compact optical devices with new functionalities by enhancing inherently weak physical processes, such as fluorescence, Raman scattering of single molecules [2], and nonlinear phenomena [3]. An optical source that couples electronic transitions directly to strongly localized optical modes is highly desirable because it would avoid the limitations of delivering light from a macroscopic external source to the nanometer scale, such as low coupling efficiency and difficulties in accessing individual optical modes [4]. On the other hand, plasmonics is a crucial ingredient in the reverse process, namely the generation of coherent radiation [5].

The one of mechanisms of the generation was suggested in the work [6]. The idea utilizes the effect of wave slowing down in waveguides [7–9] and uses the analogy between carbon nanotubes (CNT) and traveling-wave tubes. Three basic properties of carbon nanotubes: the strong slowing down of surface electromagnetic waves [10], the ballisticity of the electron motion over typical CNT length [11, 12], and the extremely high electron current density reachable in CNTs [13], allow proposition of them as the candidates for the development of the nanoscale

K. Batrakov · V. Saroka (✉)
Institute for Nuclear Problems, Belarusian State University, Bobruyskaya 11,
220030 Minsk, Belarus
e-mail: 40.ovasil@gmail.com

K. Batrakov
e-mail: kgbatrakov@gmail.com

Čerenkov-type emitters. Theoretical treatment showed the possibility of such devices operation. But requirements that are put forward to the parameters of the devices operation are very strict, such as electron current density $\approx 10^9$ A/cm^2, nanotube length ≈ 10 μm, and so on. The main problem is that the retardation is not strong enough in nanotubes both single wall and multiwall. In fact, the retardation of surface modes is higher for multiwall nanotubes [14] and it can be interpreted in terms of the subtraction of plasmon oscillations frequencies of adjacent layers [14]. But in nanotubes, the frequencies of plasmon oscillations differ from layer to layer because of the changes of layers radii. This obstacle can be eliminated in planar systems. This greatly motivates us to explore the plasmon dispersion and the plasmon phase speed in a newly available material with unique properties: graphene and graphene multilayer.

The paper is organized as follows. In Sect. 9.2, a self-consistent problem is stated and the basic equation for the electromagnetic wave propagating in the n-layer graphene electron plasma is derived. A solution of this equation describing confined to graphene surface electromagnetic wave is presented in Sect. 9.3. The dispersion equations describing the slowing effect in graphene (graphene bilayer) are derived and discussed in Sect. 9.4. Analysis and concluding remarks are given in Sect. 9.5.

9.2 Self-Consistent Problem Basic Equation

Let us consider the electromagnetic wave propagating and interacting with electron system in an n-layer graphene. To describe such system Maxwell's equations for electromagnetic wave and quantum mechanical equations should be used. The former can be reduced to the wave equation for a scalar potential:

$$\left(\frac{\partial^2}{c^2 \partial t^2} - \Delta\right)\Phi(\mathbf{r}, t) = 4\pi\rho(\mathbf{r}, t), \tag{9.1}$$

where $\Phi(\mathbf{r}, t)$ is the scalar potential and $\rho(\mathbf{r}, t)$ is an electron charge density. Equation (9.1) should be supplemented by equation for the electron charge density. Many-body formalism is very useful for this purpose. Within the framework of this formalism the electron charge density takes the following form:

$$\rho(\mathbf{r}, t) = e\langle 0|\widehat{\rho}|0\rangle, \tag{9.2}$$

where e is the elementary charge, $|0\rangle$ is the ground state of the system under consideration, $\widehat{\rho}$ is referred to as the density operator, having the following form:

$$\widehat{\rho} = \widehat{\Psi}^\dagger \widehat{\Psi}, \tag{9.3}$$

where $\widehat{\Psi}$ is referred to as $\widehat{\Psi}$-operator or the secondary quantized electron wave function, and symbol $\dagger$ denotes Hermitian conjugation. The function is a decomposition over a full set of the possible stationary states of the system:

$$\widehat{\Psi} = \sum_{\mathbf{k}s} \psi_s(\mathbf{r}, \mathbf{k})\widehat{b}_{\mathbf{k}s}(t), \tag{9.4}$$

where summation is performed over the stationary states with a quasimomentum $\mathbf{k}$ as well as over all energy bands numbered with index s, $\psi_s(\mathbf{r}, \mathbf{k})$ is the wave function of the electron with the quasimomentum $\mathbf{k}$, in the sth energy band, and $\widehat{b}_{\mathbf{k}s}(t)$ is the time-dependent annihilation operator for the electron in the state corresponding to subscript indexes. The time evolution of the creation and annihilation operators is governed by the Heisenberg equation, which is an analog of the Schrödinger one, and has the following form:

$$\frac{d\widehat{b}_{\mathbf{k}s}(t)}{dt} = -\frac{1}{i\hbar}\left[H, \widehat{b}_{\mathbf{k}s}(t)\right], \tag{9.5}$$

where H is the Hamiltonian that can be written in the form:

$$\widehat{H} = \widehat{H}_0 + \widehat{H}_{\text{int}}, \tag{9.6}$$

here $\widehat{H}_0$ is an operator of the energy of the n-layer graphene electron plasma, for the case when the electromagnetic wave is absent, and $\widehat{H}_{\text{int}}$ is the interaction Hamiltonian. Operator $\widehat{H}_0$ has the form:

$$\widehat{H}_0 = \sum_{\mathbf{k}s} E_{\mathbf{k}s}\widehat{b}_{\mathbf{k}s}^{\dagger}(t)\widehat{b}_{\mathbf{k}s}(t) , \tag{9.7}$$

where $E_{\mathbf{k}s}$ is the unperturbed energy of the electron having quasimomentum k in the sth energy band, the product of the creation and annihilation operators in Eq. (9.7) is usually called occupation number operator. The interaction Hamiltonian can be written as:

$$\widehat{H}_{\text{int}} = \sum_{\mathbf{k}_1 s_1} \sum_{\mathbf{k}_2 s_2} H_{\mathbf{k}_1 s_1, \mathbf{k}_2 s_2}^{\text{int}}(t)\widehat{b}_{\mathbf{k}_1 s_1}^{\dagger}(t)\widehat{b}_{\mathbf{k}_2 s_2}(t), \tag{9.8}$$

where $H_{\mathbf{k}_1 s_1, \mathbf{k}_2 s_2}^{\text{int}}(t)$ is the matrix element, having the following form:

$$H_{\mathbf{k}_1 s_1, \mathbf{k}_2 s_2}^{\text{int}}(t) = e \int \Phi(\mathbf{r}, t)\psi_{s_1}^*(\mathbf{r}, \mathbf{k}_1)\psi_{s_2}(\mathbf{r}, \mathbf{k}_2)\, d\mathbf{r}, \tag{9.9}$$

From the Eqs. (9.3–9.9), the following two systems describing dynamics of creation and annihilation operators can be obtained:

$$\frac{d\widehat{b}_{\mathbf{k}s}(t)}{dt} = -\frac{i}{\hbar}\left(E_{\mathbf{k}s}\widehat{b}_{\mathbf{k}s}(t) + \sum_{\mathbf{k}_1 s_1} H_{\mathbf{k}s, \mathbf{k}_1 s_1}^{\text{int}}(t)\widehat{b}_{\mathbf{k}_1 s_1}(t)\right), \tag{9.10}$$

$$\frac{\mathrm{d}\widehat{b}_{\mathbf{k}s}^{\dagger}(t)}{\mathrm{d}t} = \frac{i}{\hbar}\left(E_{\mathbf{k}s}\widehat{b}_{\mathbf{k}s}^{\dagger}(t) + \sum_{\mathbf{k}_1,s_1} H_{\mathbf{k}_1s_1,\mathbf{k}s}^{\mathrm{int}}(t)\widehat{b}_{\mathbf{k}_1s_1}^{\dagger}(t)\right). \qquad (9.11)$$

If one considers electromagnetic wave as a small perturbation, solution for creation (annihilation) operators in zero-order approximation has the following form:

$$\widehat{b}_{\mathbf{k}s}(t) = \widehat{b}_{\mathbf{k}s}^{A}\exp\left(-\frac{i}{\hbar}E_{\mathbf{k}s}\,t\right), \qquad (9.12)$$

where $\widehat{b}_{\mathbf{k}s}^{A}$ can be referred to as an "amplitude" of the annihilation operator, which is independent on time. Then in the first-order approximation, we can add a time dependence to the amplitude:

$$\widehat{b}_{\mathbf{k}s}^{A}(t) = \widehat{b}_{\mathbf{k}s}^{(0)} + \widehat{b}_{\mathbf{k}s}^{(1)}(t), \qquad (9.13)$$

where $\widehat{b}_{\mathbf{k}s}^{(0)}$ is a time-independent part of the amplitude, and $\widehat{b}_{\mathbf{k}s}^{(1)}(t)$ is a time-dependent one. Substituting Eq. (9.13) into the Eq. (9.12) and further into Eq. (9.10), one can derive:

$$\frac{\mathrm{d}\widehat{b}_{\mathbf{k}s}^{(1)}(t)}{\mathrm{d}t} = -\frac{i}{\hbar}\sum_{\mathbf{k}_1s_1} H_{\mathbf{k}s,\mathbf{k}_1s_1}^{\mathrm{int}}(t)\,\widehat{b}_{\mathbf{k}_1s_1}^{(0)}\exp\left(-\frac{i}{\hbar}\left(E_{\mathbf{k}_1s_1} - E_{\mathbf{k}s}\right)\right), \qquad (9.14)$$

$$\frac{\mathrm{d}\widehat{b}_{\mathbf{k}s}^{(1)\dagger}(t)}{\mathrm{d}t} = \frac{i}{\hbar}\sum_{\mathbf{k}_1s_1} H_{\mathbf{k}_1s_1,\mathbf{k}s}^{\mathrm{int}}(t)\,\widehat{b}_{\mathbf{k}_1s_1}^{(0)\dagger}\exp\left(\frac{i}{\hbar}\left(E_{\mathbf{k}_1s_1} - E_{\mathbf{k}s}\right)\right). \qquad (9.15)$$

Performing the temporal Fourier transform of (9.14–9.15) it is produced:

$$\widehat{b}_{\mathbf{k}s}^{(1)}(\omega) = \frac{1}{\hbar\omega}\sum_{\mathbf{k}_1s_1} \widetilde{H}_{\mathbf{k}s,\mathbf{k}_1s_1}^{\mathrm{int}}\left(\omega - \frac{E_{\mathbf{k}_1s_1} - E_{\mathbf{k}s}}{\hbar}\right)\widehat{b}_{\mathbf{k}_1s_1}^{(0)}, \qquad (9.16)$$

$$\widehat{b}_{\mathbf{k}s}^{(1)\dagger}(\omega) = -\frac{1}{\hbar\omega}\sum_{\mathbf{k}_1s_1} \widetilde{H}_{\mathbf{k}_1s_1,\mathbf{k}s}^{\mathrm{int}}\left(\omega + \frac{E_{\mathbf{k}_1s_1} - E_{\mathbf{k}s}}{\hbar}\right)\widehat{b}_{\mathbf{k}_1s_1}^{(0)\dagger}, \qquad (9.17)$$

where $\widehat{b}_{\mathbf{k}s}^{(1)}(\omega) = \int \widehat{b}_{\mathbf{k}s}^{(1)}(t)\exp(i\omega t)\,t$ and similarly for time-dependent part of the amplitude of creation operator, $\widetilde{H}_{\mathbf{k}_1s_1,\mathbf{k}_2s_2}^{\mathrm{int}}(\omega)$ is the temporal Fourier transform of matrix element from Eq. (9.9):

$$\widetilde{H}_{\mathbf{k}_1s_1,\mathbf{k}_2s_2}^{\mathrm{int}}(\omega) = e\int\left(\int \Phi(\mathbf{r},t)\exp(i\omega t)\,\mathrm{d}t\right)\psi_{s_1}(\mathbf{r},\mathbf{k}_1)\psi_{s_2}(\mathbf{r},\mathbf{k}_2)\,\mathrm{d}\mathbf{r}. \qquad (9.18)$$

Substitution of Eqs. (9.12–9.13) in the Eq. (9.4) gives for the electron charge density (9.2):

$$\rho(\mathbf{r}, t) = \rho_0(\mathbf{r}) + \rho_1(\mathbf{r}, t), \tag{9.19}$$

where $\rho_0(\mathbf{r})$ is the negative equilibrium charge density completely compensated by positive charges of atom cores, and $\rho_1(\mathbf{r}, t)$ is an additional charge density generated by the perturbation. The second one should be substituted in the right hand side of Eq. (9.1).

Performing Fourier transform on x, y, and t, it is produced:

$$\widetilde{\rho}_1(\mathbf{k}_\|, z, \omega) = e \sum_{\mathbf{k}_1 s_1} \sum_{\mathbf{k}_2 s_2} \mathcal{F}_{\mathbf{k}_1 s_1}^{\mathbf{k}_2 s_2}(\mathbf{k}_\|, z) \widetilde{H}_{\mathbf{k}_2 s_2, \mathbf{k}_1 s_1}^{\text{int}}(\omega) \mathcal{R}_{\mathbf{k}_1 s_1}^{\mathbf{k}_2 s_2}(\omega), \tag{9.20}$$

$$\mathcal{F}_{\mathbf{k}_1 s_1}^{\mathbf{k}_2 s_2}(\mathbf{k}_\|, z) = \int \exp\left(-\mathrm{i}\mathbf{k}_\|\mathbf{r}_\|\right) \psi_{s_1}^*(\mathbf{r}, \mathbf{k}_1) \psi_{s_2}(\mathbf{r}, \mathbf{k}_2) \, \mathrm{d}\mathbf{r}_\|, \tag{9.21}$$

$$\mathcal{R}_{\mathbf{k}_1 s_1}^{\mathbf{k}_2 s_2}(\omega) = \frac{(n_{\mathbf{k}_1 s_1} - n_{\mathbf{k}_2 s_2})}{\hbar\omega + E_{\mathbf{k}_1 s_1} - E_{\mathbf{k}_2 s_2}}, \tag{9.22}$$

in the equations above $\mathbf{k}_\| = (k_x, k_y)$ is the component of wave vector along graphene surface, $\mathbf{r}_\| = (x, y)$ is a radius vector, laying in the graphene plane, $n_{\mathbf{k},s} = \langle 0|\widehat{b}_{\mathbf{k}s}^{(0)\dagger}\widehat{b}_{\mathbf{k}s}^{(0)}|0\rangle$ is the occupation number of the state $\mathbf{k}, s$. Fourier transformation applied to the left hand side of Eq. (9.1) gives:

$$\left(-\frac{\omega^2}{c^2} + k_\|^2 - \frac{\partial^2}{\partial z^2}\right) \widetilde{\Phi}(\mathbf{k}_\|, z, \omega), \tag{9.23}$$

where $k_\| = |\mathbf{k}_\||$, and $\widetilde{\Phi}(\mathbf{k}_\|, z, \omega)$ is the Fourier transform of the scalar potential $\Phi(\mathbf{r}, t)$:

$$\widetilde{\Phi}(\mathbf{k}_\|, z, \omega) = \int \int \Phi(\mathbf{r}, t) \exp\left(\mathrm{i}\left(\omega t - \mathbf{k}_\|\mathbf{r}_\|\right)\right) \mathrm{d}\mathbf{r}_\| \, \mathrm{d}t. \tag{9.24}$$

However, for a slowed down electromagnetic waves the following inequality is fulfilled: $\frac{\omega}{c} \ll k_\|$. That is why (9.23) can be replaced by:

$$\left(k_\|^2 - \frac{\partial^2}{\partial z^2}\right) \widetilde{\Phi}(\mathbf{k}_\|, z, \omega). \tag{9.25}$$

Finally we have the following equation:

$$\left(k_\|^2 - \frac{\partial^2}{\partial z^2}\right) \widetilde{\Phi}(\mathbf{k}_\|, z, \omega) = 4\pi e \sum_{\mathbf{k}_1 s_1} \sum_{\mathbf{k}_2 s_2} \mathcal{F}_{\mathbf{k}_1 s_1}^{\mathbf{k}_2 s_2}(\mathbf{k}_\|, z) \widetilde{H}_{\mathbf{k}_2 s_2, \mathbf{k}_1 s_1}^{\text{int}}(\omega) \mathcal{R}_{\mathbf{k}_1 s_1}^{\mathbf{k}_2 s_2}(\omega). \tag{9.26}$$

9.3 Self-Consistent Problem Solution

In the previous section, the basic Eq. (9.26) for the self-consistent problem was derived. For analyzing the graphene system with the help of this equation, the wave functions $\psi_s(\mathbf{r}, \mathbf{k})$ and the energies of electron states $E_{\mathbf{k},s}$ should be defined. Tight-binding method can be used to determine these quantities. Within a framework of this method, the wave functions are linear combinations of the Bloch functions:

$$\psi_s(\mathbf{r}, \mathbf{k}) = \sum_{i=1}^{\sigma} C_{is}(\mathbf{k}) \psi_i^{(B)}(\mathbf{r}, \mathbf{k}), \tag{9.27}$$

where σ is a number of carbon atoms in the unit cell of the n-layer graphene system, $C_{i,s}$ are the unknown coefficients to be found and $\psi_i^{(B)}(\mathbf{r}, \mathbf{k})$ are the Bloch functions:

$$\psi_i^{(B)}(\mathbf{r}, \mathbf{k}) = \frac{1}{\sqrt{N}} \sum_{j=1}^{N} \phi_i(\mathbf{r} - \mathbf{r}_{ij}) \exp(i\mathbf{k}\mathbf{r}_{ij}), \tag{9.28}$$

where N is a number of unit cells in the system, $\mathbf{r}_{ij}$ is the radius vector that points out position of ith atom in the jth unit cell, $\phi_i(\mathbf{r})$ is π-electron atomic orbital.

The unknown coefficients $C_{is}(\mathbf{k})$ are determined by solving eigenproblem for the n-layer graphene system:

$$MC_s = 0 , \tag{9.29}$$

where M is a $\sigma \times \sigma$ matrix, and $C_s = (C_{1s}(\mathbf{k}), \ldots, C_{\sigma s}(\mathbf{k}))^{\mathrm{T}}$ is a column vector. For the case of graphene bilayer the matrix M has the form:

$$\begin{pmatrix} E_0 + \Delta - E_{\mathbf{k}} & \gamma_0 f(k_x, k_y) & \gamma_1 & \gamma_4 f^*(k_x, k_y) \\ \gamma_0 f^*(k_x, k_y) & E_0 - E_{\mathbf{k}} & \gamma_4 f^*(k_x, k_y) & \gamma_3 f(k_x, k_y) \\ \gamma_1 & \gamma_4 f(k_x, k_y) & E_0 + \Delta - E_{\mathbf{k}} & \gamma_0 f^*(k_x, k_y) \\ \gamma_4 f(k_x, k_y) & \gamma_3 f^*(k_x, k_y) & \gamma_0 f(k_x, k_y) & E_0 - E_{\mathbf{k}} \end{pmatrix}, \tag{9.30}$$

and for graphene single layer:

$$\begin{pmatrix} E_0 + \Delta - E_{\mathbf{k}} & \gamma_0 f(k_x, k_y) \\ \gamma_0 f^*(k_x, k_y) & E_0 - E_{\mathbf{k}} \end{pmatrix}, \tag{9.31}$$

where E_0, Δ, γ_i are the tight-binding model parameters taken from [15]. Function $f(k_x, k_y)$ has the form:

$$f(k_x, k_y) = \exp\left(\frac{ik_x a}{\sqrt{3}}\right) + 2\exp\left(\frac{ik_x a}{2\sqrt{3}}\right)\cos\left(\frac{k_y a}{2}\right), \tag{9.32}$$

where k_x, k_y are projections of the momentum onto x and y axis, respectively, a is modulus of vectors $\mathbf{a}_1$ and $\mathbf{a}_2$, see Fig. 9.1.

Fig. 9.1 Graphene single layer crystal lattice. Vectors $\mathbf{a}_1$, $\mathbf{a}_2$ are the basis vectors of the lattice. Carbon atoms inequivalent due to symmetry of the lattice are depicted with different colors (*red* and *blue*)
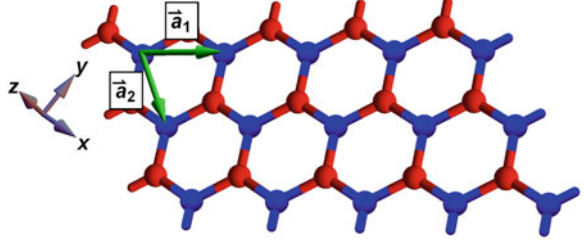
In general, the eigenproblem (9.29) has nonzero solution if determinant of its matrix is equal to zero:

$$\det M = 0. \tag{9.33}$$

Equation (9.33) is the polynomial equation of the σth order, and it has σ roots for each value of $\mathbf{k}$. These solutions can be numbered by index s varying from 1 to σ.

Assuming smallness of overlapping of atomic orbitals, the all terms in the left hand side of the Eq. (9.26) can be written in the form:

$$\int g_{\mathbf{k}_\parallel, \mathbf{r}_\parallel} \, \phi_i^*(\mathbf{r} - \mathbf{r}_{ij}) \phi_m(\mathbf{r} - \mathbf{r}_{mn}) \, d\mathbf{r}_\parallel = \delta_{im,jn} \int g_{\mathbf{k}_\parallel, \mathbf{r}_\parallel} \, |\phi_i(\mathbf{r} - \mathbf{r}_{ij})|^2 \, d\mathbf{r}_\parallel, \tag{9.34}$$

where $g_{\mathbf{k}_\parallel, \mathbf{r}_\parallel}$ is an arbitrary bounded function of arguments $\mathbf{k}_\parallel$ and $\mathbf{r}$, $\delta_{im,jn}$ is the Kronecker delta. Using (9.34), one can transform (9.21) to the following form:

$$\mathcal{F}_{\mathbf{k}_1 s_1}^{\mathbf{k}_2 s_2}(\mathbf{k}_\parallel, z) = \sum_{i=1}^{\sigma} C_{i s_1}^*(\mathbf{k}_1) C_{i s_2}(\mathbf{k}_2) F_i(\mathbf{k}_\parallel, z) \delta_{\mathbf{k}_\parallel, \mathbf{k}_2 - \mathbf{k}_1}, \tag{9.35}$$

where $\delta_{\mathbf{k}_\parallel, \mathbf{k}_2 - \mathbf{k}_1}$ is a Kroneker delta that provides the quasimomentum conservation during electron–photon interaction, $F_i(\mathbf{k}_\parallel, z)$ is a function that can be referred to as the atomic orbital form factor having the next form:

$$F_i(\mathbf{k}_\parallel, z) = \int \exp\left(-i\mathbf{k}_\parallel \mathbf{r}_\parallel\right) |\phi_i(\mathbf{r}_\parallel, z - z_i)|^2 \, d\mathbf{r}_\parallel. \tag{9.36}$$

Again using the tight-binding condition (9.34) and additionally Eqs. (9.27–9.28), one can present matrix elements (9.18) as follows:

$$\widetilde{H}_{\mathbf{k}_1 s_1, \mathbf{k}_2 s_2}^{\text{int}}(\omega) = \sum_{i=1}^{\sigma} C_{i s_2}^*(\mathbf{k}_2) C_{i s_1}(\mathbf{k}_1) A_i(\mathbf{k}_2 - \mathbf{k}_1, \omega), \tag{9.37}$$

where

$$A_i(\mathbf{k}_2 - \mathbf{k}_1, \omega) = \int F_i(\mathbf{k}_1 - \mathbf{k}_2, z) \frac{e}{S} \widetilde{\Phi}(\mathbf{k}_2 - \mathbf{k}_1, z, \omega) z, \tag{9.38}$$

here S is a square of the n-layer graphene sheet.

Substitution of Eqs. (9.37), (9.35) into the Eq. (9.26) gives:

$$\left(k_{\parallel}^2 - \frac{\partial^2}{\partial z^2}\right)\widetilde{\Phi}(\mathbf{k}_{\parallel}, z, \omega) = \sum_{i=1}^{\sigma} f_i(\mathbf{k}_{\parallel}, z, \omega)A_i(\mathbf{k}_{\parallel}, \omega) , \qquad (9.39)$$

where

$$f_i(\mathbf{k}_{\parallel}, z, \omega) = 4\pi e \sum_{\mathbf{k}_1 s_1, \mathbf{k}_2 s_2} \mathcal{D}_{\mathbf{k}_1 s_1, i}^{\mathbf{k}_2 s_2}(\mathbf{k}_{\parallel}, z)\delta_{\mathbf{k}_{\parallel}, \mathbf{k}_2 - \mathbf{k}_1}\mathcal{R}_{\mathbf{k}_1 s_1}^{\mathbf{k}_2 s_2}(\omega), \qquad (9.40)$$

and

$$\mathcal{D}_{\mathbf{k}_1 s_1, i}^{\mathbf{k}_2 s_2}(\mathbf{k}_{\parallel}, z) = \sum_{m=1}^{\sigma} C_{ms_1}^*(\mathbf{k}_1)C_{ms_2}(\mathbf{k}_2)C_{is_2}^*(\mathbf{k}_2)C_{is_1}(\mathbf{k}_1)F_i(\mathbf{k}_{\parallel}, z). \qquad (9.41)$$

In the long wave approximation inequality $k_{\parallel}a \ll 1$ is fulfilled. Therefore, the approximation $\exp(-i\mathbf{k}_{\parallel}\mathbf{r}_{\parallel}) \to 1$ in the expressions for atomic form factor can be used. We shall use approximation $\int |\phi_i(\mathbf{r}_{\parallel}, z - z_i)|^2 \, d\mathbf{r}_{\parallel} \to \delta(z - z_i)$ which corresponds to the electron wave functions concentrated on graphene monolayers. Applying these approximations one can reduce Eq. (9.38) to the form:

$$A_i(\mathbf{k}_{\parallel}, \omega) = \frac{e}{S}\widetilde{\Phi}(\mathbf{k}_{\parallel}, z_i, \omega), \qquad (9.42)$$

where the quasimomentum conservation law has been used. Smallness of the photon momentum leads to possibility of the following replacement:

$$D_{\mathbf{k}_1 s_1, i}^{\mathbf{k}_2 s_2}(\mathbf{k}_{\parallel}, z) \to D_{s_1, i}^{' s_2}(z), \qquad (9.43)$$

where

$$D_{s_1, i}^{' s_2}(z) = \sum_{m=1}^{\sigma} \delta_{s_1, s_2}|C_{ms_1}|^2|C_{is_1}|^2\delta(z - z_i) \qquad (9.44)$$

δ_{s_1, s_2} is the Kronecker delta arisen from the consideration of the eigenproblem (9.29), also note that the absolute value of the coefficients $C_{ij}(\mathbf{k})$ does not depend on $\mathbf{k}$, $\delta(z - z_i)$ is the Dirac delta corresponding to the new form of the atomic orbital form factor.

Applying the replacement rule (9.43) to the Eq. (9.40) and taking into account Eq. (9.42), one can obtain the new form of (9.39):

$$\left(k_{\parallel}^2 - \frac{\partial^2}{\partial z^2}\right)\widetilde{\Phi}(\mathbf{k}_{\parallel}, z, \omega) = \frac{4\pi e^2}{S} \sum_{\mathbf{k}_1 s_1, s_2} \mathcal{R}_{\mathbf{k}_1 s_1}^{\mathbf{k}_1 + \mathbf{k}_{\parallel}, s_2}(\omega)\mathcal{P}_{s_1}^{s_2}(\mathbf{k}_{\parallel}, z, \omega), \qquad (9.45)$$

where

$$\mathcal{P}^{s_2}_{s_1}(\mathbf{k}_\parallel, z, \omega) = \sum_{i=1}^{\sigma} \mathcal{D}'^{s_2}_{s_1,i}(z) \widetilde{\Phi}(\mathbf{k}_\parallel, z_i, \omega). \tag{9.46}$$

For Eq. (9.45), the following boundary conditions can be stated:

$$\widetilde{\Phi}\Big|_{z\to\pm\infty} = 0 , \tag{9.47}$$

$$\widetilde{\Phi}\Big|_{z=z_i^{(l)}-0} = \widetilde{\Phi}\Big|_{z=z_i^{(l)}+0} , \tag{9.48}$$

$$\frac{\mathrm{d}\widetilde{\Phi}}{\mathrm{d}z}\Big|_{z=z_i^{(l)}-0} - \frac{\mathrm{d}\widetilde{\Phi}}{\mathrm{d}z}\Big|_{z=z_i^{(l)}+0} = \frac{4\pi e^2}{S} \sum_{s_1} \mathcal{P}'_{s_1}(\mathbf{k}_\parallel, \omega) \sum_{\mathbf{k}_1} \mathcal{R}^{\mathbf{k}_1+\mathbf{k}_\parallel, s_1}_{\mathbf{k}_1 s_1}(\omega), \tag{9.49}$$

where

$$\mathcal{P}'_{s_1}(\mathbf{k}_\parallel, \omega) = \sum_{m,i=1}^{\sigma} |C_{ms_1}|^2 |C_{is_1}|^2 \widetilde{\Phi}(\mathbf{k}_\parallel, z_i, \omega). \tag{9.50}$$

Boundary condition (9.47) means finiteness of the scalar potential throughout the space. Conditions (9.48) and (9.49) correspond to the continuity of the scalar potential and the discontinuity of electric field strength on each sheet of the n-layer graphene system, respectively. The third boundary condition (9.49) was obtained by integration of Eq. (9.45) in the vicinity of each graphene plane.

For the regions $z \neq z_i$ solution of the Eq. (9.45) has the next form

$$\widetilde{\Phi}(k_\parallel, z, \omega) = \sum_{i=1}^{n} c_{1,i}(k_\parallel, \omega) \exp\left[k_\parallel(z - z_i^{(l)})\right] + c_{2,i}(k_\parallel, \omega) \exp\left[-k_\parallel(z - z_i^{(l)})\right] ,$$

$$\tag{9.51}$$

where n is the number of layers, $z_i^{(1)}$ is the position of the ith layer, $c_{j,i}(k_\parallel, \omega)$ are coefficients to be defined. A homogeneous system of algebraic equations for $c_{j,i}(k_\parallel, \omega)$ can be obtained if one applies the boundary conditions (9.47–9.49) to the solution specified above. Such system has nonzero solution when determinant of its matrix equals to zero. This equality gives the dispersion equation. Further it will be reduced to two particular cases: graphene single layer and bilayer.

9.4 Dispersion Equations for Graphene Single Layer and Bilayer

Dispersion equation for the n-layer graphene system derived in the way described in the previous section is too cumbersome to analyze in a general form. Its complexity strongly increases with the number of graphene layers in the system.

From practical point of view, two cases have huge attraction. They are graphene single layer and bilayer. The former is interesting because of linear dispersion of electrons [16], the latter—due to controllable energy gap in the band structure [17]. Besides, the second case is interesting, because of opportunity to investigate the dependence of electromagnetic wave dispersion on interaction between adjacent layers.

Let begin analysis from the more simple case of graphene single layer. We consider doped graphene with injected electron in the conduction band and take into account transition in conduction band only. Low temperature limit is considered in what follows. From mathematical point of view, it results in the step function form of the Fermi–Dirac distribution describing the average occupation numbers $n_{\mathbf{k},s}$. Moreover, long-wave approximation is applied again in calculations. This time it means that the denominator of the resonance factor should be expand to first-order terms with respect to $\mathbf{k}_\parallel$. Producing that, one can obtain the following dispersion equation for the graphene single layer:

$$\frac{4\pi^2 e^2}{\hbar v_F} k_F \frac{\omega - \left(\omega^2 - v_F^2 k^2\right)^{1/2}}{k(\omega^2 - v_F^2 k^2)^{1/2}} = 1, \tag{9.52}$$

where k_F is the momentum of an electron on the Fermi surface in the graphene single layer. Dependence of electromagnetic wave frequency on wave vector is shown on the Fig. 9.2.

Dependence of the plasmon phase speed on wave vector is presented on the Fig. 9.3.

It can be seen that plasmon phase speed in graphene single layer is 3–6 times smaller than the speed of light in the vacuum and it increases with the density of doped electrons.

Fig. 9.2 The dependence of plasmon frequency (THz) on wave vector (cm^{-1}). Density of doped electrons is taken to be 10^{12} cm^{-2}. *Dashed curve* shows the light cone (logarithmic scale is used)
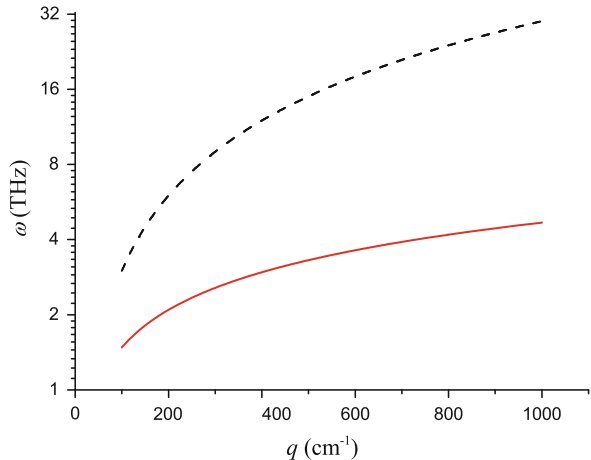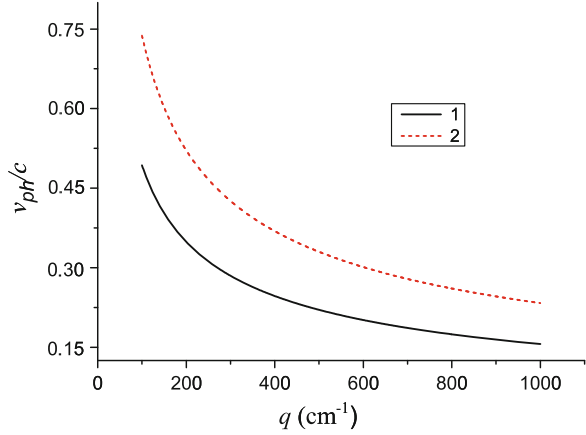
Fig. 9.3 The dependence of plasmon phase speed ($1/c$, where c is the speed of light in the vacuum) on wave vector (cm^{-1}). The *curves* (*1*) and (*2*) are plotted for densities of doped electrons 10^{12} cm^{-2} and 5×10^{-12} cm^{-2}, respectively

Another case of our interest is the graphene bilayer. Using the same assumptions as for the graphene single layer, we obtain the following dispersion equation:

$$\left(1 - \frac{2\pi e}{k}\Pi_1\right)\left(1 - \frac{2\pi e}{k}\Pi_2\right) - \frac{4\pi^2 e^2}{k^2}\Pi_1\Pi_2 \exp(-2kd) = 0 \ . \qquad (9.53)$$

where d is the distance between graphene sheets in graphene bilayer, $\Pi_{1,2}$ is referred to as irreducible polarizability, having the form:

$$\Pi_i = \sum_{k_1 < k_F} \left(\frac{1}{\hbar\omega + E_{\mathbf{k}_1 - \mathbf{k},i} - E_{\mathbf{k}_1,i}} - \frac{1}{\hbar\omega + E_{\mathbf{k}_1,i} - E_{\mathbf{k}_1 + \mathbf{k},i}}\right) , \qquad (9.54)$$

There are two irreducible polarizabilities corresponding to two different conduction bands.

In long wave approximation irreducible polarizability can be presented in the form $\Pi_i = \Gamma_i/\omega^2$, where Γ_i depends on $\mathbf{k}$ and does not depend on the frequency ω. Solution for the frequency has very simple analytical form in that case:

$$\omega_{1,2}^2(k) = \frac{\Gamma_1 + \Gamma_2}{2} \pm \sqrt{\left(\frac{\Gamma_1 + \Gamma_2}{2}\right)^2 - \Gamma_1\Gamma_2[1 - \exp(-2kd)]} , \qquad (9.55)$$

The sing "$-$" in the solution (9.55) corresponds to the acoustic plasmon mode, having phase speed considerably smaller than plasmons in graphene single layer. Let us remind that this solution is obtained within the assumption that electron wave functions concentrated on graphene layers. Such situation should be observed for spatially separated two graphene monolayers. In this system, the distance between layers can be turned. As a result the plasmon frequency and phase speed can also be controlled, that is clearly seen on Fig. 9.4.

Fig. 9.4 The dependence of the plasmon frequency ω on the wave number q for two spatially expanded graphene monolayers: the distance d between layers is (A) 4 nm, (B) 30 nm, (C) 100 nm, (D) 200 nm for doping electron densities $n_1 = n_2 = 10^{12}$ cm^{-2}
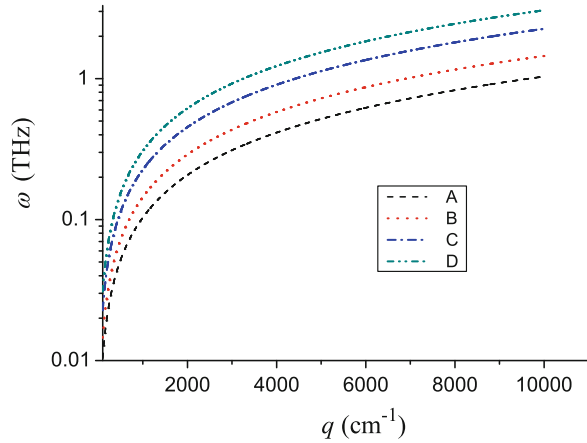
9.5 Conclusions

General method of obtaining dispersion equations for surface plasmons in the n-layer graphene system was developed. This method along with long-wave and tight-binding approximations was applied to derive dispersion equations for graphene single layer and bilayer. It was shown that in the case of single-layer graphene the phase speed of plasmon is only 3–6 times smaller than the speed of light in the vacuum that is not enough for Čerenkov synchronization with π electrons. Meanwhile, graphene bilayer demonstrates desired possibility of phase speed retardation up to the Fermi velocity of π-electrons in graphene. That paves the way to the synchronization with nonrelativistic π-electrons, e.g., inner currents of the graphene bilayer. Thus, graphene bilayer seems to be challenging material for nanoscale Cerenkov-type emitters in the terahertz region.

References

1. Barnes WL, Ebbesen TW (2003) Surface plasmon subwavelength optics. Nature 424:824–830
2. Anker JN, Ebbesen TW (2008) Biosensing with plasmonic nanosensors. Nat Matter 7:442–453
3. Liu Y, Bartal G, Genov DA, Zhang X (2007) Subwavelength discrete solitons in nonlinear metamaterials. Phys Rev Lett 99:153901
4. Stockman MI (2004) Nanofocusing of optical energy in tapered palsmonic waveguides. Phys Rev Lett 93:137404
5. Ren-Min M, Oulton RF, Sorger VJ, Guy B, Zhang X (2011) Room-temperature sub-diffraction-limited plasmon laser by total internal reflection. Nat Mater 10:110–113
6. Batrakov KG, Kuzhir PP, Maksimenko SA (2006) Radiative instability of electron beam in carbon nanotubes. Proc SPIE 6328:63280Z

 7. Batrakov KG, Maksimenko SA, Kuzhir PP, Thomsem C (2009) Carbon nanotube as a Cherenkov-type light emitter and free electron laser. Phys Rev B 70:125408–125420
 8. Batrakov KG, Kuzhir PP, Maksimenko SA (2008) Toward the nano-FEL: undulator and Cherenkov mechanisms of light emission in carbon nanotubes. Physica E 40:1065–1068
 9. Batrakov KG, Kuzhir PP, Maksimenko SA (2008) Stimulated emission of electron beam in nanotube bundles. Physica E 40:2370–2374
10. Slepyan GY, Maksimenko SA, Lakhtakia A, Yevtushenko O, Gusakov AV (1999) Electrodynamics of carbon nanotubes: dynamic conductivity, impedance boundary conditions and surface wave propagation. Phys Rev B 60:17136–17149
11. Frank S, Poncharal P, Wang ZL, de Heer WA (1998) Carbon nanotube quantum resistors. Science 280:1744
12. Berger C, Yi Y, Wang ZL, de Heer WA (2002) Multiwalled carbon nanotubes are ballistic conductors at room temperature. Appl Phys A 74:363–365
13. Wei BQ, Vajtai R, Ajayan PM (2001) Reliability and current carrying capacity of carbon nanotubes. Appl Phys Lett 79:1172
14. Batrakov KG, Kuzhir PP, Maksimenko SA (2010) Cherenkov synchronism: non-relativistic electron beam in multi-walled carbon nanotube and multi-layer graphene. Phys B: Phys Condens Matter 405:3050–3053
15. Partoens B, Peeters FM (2006) From graphene to graphite: electronic structure around the K points. Phys Rev B 74:075404
16. Saito R, Dresselhaus G, Dresselhaus M (1998) Physical properties of carbon nanotubes. Imperial College Press, London
17. Zhang Y, Tang T, Girit C, Hao Z, Martin MC, Zettl A, Crommie MF, Shen YR, Wang F (2009) Direct observation of a widely tunable bandgap in bilayer graphene. Nature 459:820

Part II
Interface Studies and Techniques

Chapter 10
Goniometric Setup for Plasmonic Measurements and Characterization of Optical Coatings

A. Loot, L. Dolgov, S. Pikker, R. Lõhmus and I. Sildos

10.1 Introduction

Reflection of light from the metal-dielectric films of subwavelength thicknesses varies by means of molecules adsorbed on the metal surface. This effect is used for optical plasmonic sensors of different organic and nonorganic species [1]. High refractive index prism with a metallized side face is one of the most typical optical elements of such sensors [2]. The side face of the prism is usually chemically modified for binding and sensing only certain type of molecules [3]. Devices suitable for detection of different molecular species can be realized on the basis of several microprisms [4] and sensors adapted for optical microscopes [5].

Universalization of sensors means not only compatibility with different analytes but also multi-functionality of the sensor. Minor modifications of the prism scheme allow detection of the optical parameters of liquids [6] and gases [7], analysis of microroughnesses on the metal surfaces [8] and nonlinear properties of the metal-dielectric layers [9]. Thus, the prism scheme used not only for sensing but also for characterization of optical media is vital. At certain resonant angle wave vector of light passing through the prism is favorable for excitation of surface plasmon-polariton wave on the metal surface. The medium in contact with the metal changes the resonant conditions. Experimentally it manifests in the changes in wavelength, polarization or resonant reflection angle of the testing light. Therefore, precise control of the light incidence and polarization is especially important for applications. In view of this, we represent here an original multifunctional goniometric setup for characterization of optical coatings and plasmonic measurements.

The structure of the current chapter is following. The introductory part (Sect. 10.1) emphasizes importance of the multifunctional plasmonic devices for characterization of metal-dielectric interfaces. Section 10.2 describes the resonance conditions for induction of surface plasmon-polaritons and presents a transfer matrix

A. Loot (✉) · L. Dolgov · S. Pikker · R. Lõhmus · I. Sildos
Institute of Physics, University of Tartu, Riia 142, Tartu 51014, Estonia
e-mail: ardi.loot@ut.ee

method (TMM) applied for analysis of an attenuated total internal reflection. Section 10.3 considers the general optical scheme of the goniometric setup. Section 10.4 treats practical application aspects of the proposed goniometric setup for analysis of refractive indices, thicknesses, and roughness of optical coatings. Control of spectral shape, intensity, direction, and polarization of plasmon-coupled emission in case of fluorescent $TiO_2:Sm^{3+}$ films is demonstrated. Details about program control of the setup and smart procedures used for its calibration are collected in the Sect. 10.5. The last resumptive Sect. 10.6 summarizes the previous ones and describes potential applications of the presented goniometric device.

10.2 Definition and Properties of Propagating Surface Plasmon-Polaritons

Surface plasmon-polaritons (SPPs) are electromagnetic waves which can propagate on the metal-dielectric interface [10]. SPPs are originated from collective oscillation of free electrons in the metal. They are characterized by exponential decay of the electric field amplitude in metal faster than in the dielectric media. Properties of SPPs can be derived from four Maxwell equations and the existence of only p-polarized SPPs is verified [11]. Indeed, let us consider two infinite media having an interface in xy plane: dielectric ($z > 0$) and metal ($z < 0$) (Fig. 10.1). Assume that SPPs propagate toward the positive values of the x-axis and have a propagation constant β. Then the dispersion relationship is

$$\beta = k_0 \sqrt{\frac{\varepsilon_d \varepsilon_m}{\varepsilon_d + \varepsilon_m}}, \tag{10.1}$$

where k_0 is the free space light wavevector, ε_d is the relative permittivity of dielectric, and ε_m is the complex relative permittivity of metal.

Applying Drude's model [12] for the complex permittivity of metal, it is possible to analyze the dispersion relation of SPPs. According to Drude's model the complex permittivity of metal equals to

$$\varepsilon(\omega) = 1 - \frac{\omega_p^2}{\omega^2 + i\Gamma\omega}, \tag{10.2}$$
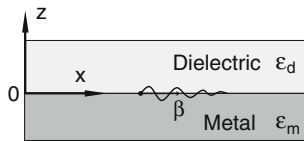
Fig. 10.1 Scheme of SPPs propagation at the metal-dielectric interface. Dielectric permittivities are marked as ε_d and ε_m respectively. β represents propagation constant of SPPs

where ω is the angular frequency, ω_p is the plasma frequency of metal, i is the imaginary unit, and Γ is the damping term. In case of silver, which together with gold is the most exploited metal in plasmonic experiments, the plasma frequency is $\omega_p \approx 1.2 \times 10^{16}$ rad s^{-1} and the damping term $\Gamma \approx 1.45 \times 10^{13}$ s^{-1}. The dispersion relation is plotted in Fig. 10.2 using Drude's model with silver parameters and dielectric permittivity $\varepsilon_d = 2.25$.

As it is shown in Fig. 10.2, the SPPs are created outside of the light line $\omega = ck$. Thus, it is impossible to induce SPPs by just shining light on the metal interface because of conservation of energy and momentum law. This is the main problem for inducing SPPs. There are several methods to overcome this issue: coupling of light by means of prism, grating, defect, or waveguide [11]. We emphasize here only methods based on prism coupling.

10.2.1 Resonance Conditions for Light-Induced Surface Plasmon-Polaritons: Prism Coupling Schemes

The most widely used prism coupling technique is elaborated by Kretschmann [2] and Raether [13]. At the critical incident angle the light energy near the metallized side face of the prism redistributes between the reflected beam and so-called surface evanescent wave. This evanescent wave activates SPPs in the metal when wave vectors of the light and SPPs are matched at the proper angle of total internal reflection. The simplest geometry engages a semicylindrical glass prism and a thin metal film (usually 40–60 nm thick) on the prism side face (Fig. 10.3). It can be demonstrated that for induction SPPs the refractive index of the prism n_p must exceed the surroundings. The prism allows to make the tangential component k_0 $\sin(\theta_i)$ of the light wave vector n_p times higher to match with the SPPs wave vector on the metal–air interface:

Fig. 10.2 SPPs and light dispersion relations
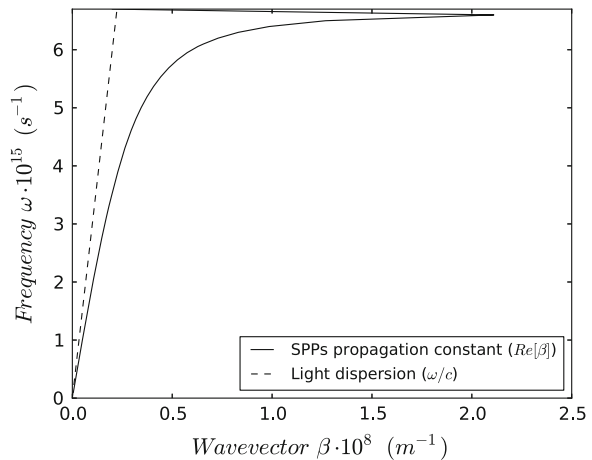
Fig. 10.3 Kretschmann
(*solid lines*) and reverse
Kretschmann (*dashed lines*)
excitation of surface
plasmons. Angle of incidence
is θ_i, n_p is refractive index of
prism. k_x and k_{SP} are
projected wavevector of light
and wavevector of SPPs
respectively
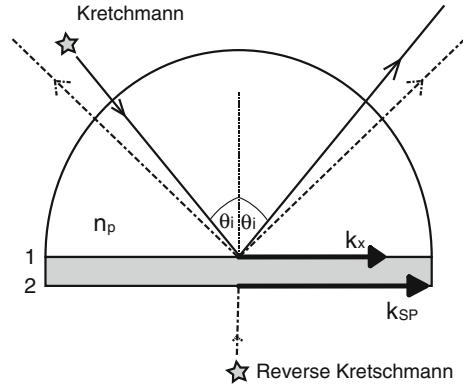
$$n_p k_0 \sin(\theta_i) = \mathrm{Re}(\beta + \Delta\beta). \tag{10.3}$$

Equation (10.3) describes the surface plasmon resonance conditions for the
light-induced SPPs on the interface 2 (Fig. 10.3). The SPPs dispersion relationship
for two infinite media with one interface is given by Eq. (10.1). Correction $\Delta\beta$ in
Eq. (10.3) is considered as an additional interface appearing in the system prism—
metal—surrounding [13]. Such correction is sufficient, if $\exp(2i\beta d) \ll 1$, where β
is the propagation constant of the SPPs from Eq. (10.1) and d is the thickness of
the metal film. Precise dispersion relationship for the smooth multilayered medium
can be found in Ref. [14].

One other prism coupling technique is called Otto configuration [15]. In this
case, three layer system prism-dielectric gap-metal is used. In phase matching
aspect, Otto configuration is very similar to Kretschmann's ones. Thus, the
refractive index of the prism is higher than the gap's refractive index to achieve a
needed enhancement of the wave vector. In practice, Kretschmann configuration is
more frequently applied because precise control of the gap thickness (usually
around ~ 200 nm) in Otto scheme is complicated. However, Otto configuration
has several advantages. For example, Otto scheme allows excitation of SPPs on the
surface of bulk metals. In contrast with this, Kretschmann configuration supports
only plasmons in thin films [13].

10.2.2 Transfer Matrix Method for Description of Surface Plasmon-Polaritons

Excitation of SPPs is considered in the previous paragraph. Here we turn to the
methods which allow detection of SPP waves. Since dispersion relationship of
SPPs is outside of the light line, and SPPs are confined to the interface, it is hard to
see them directly. Still, it is possible to detect SPPs owing to their influence on the
light reflection. There is a constant reflection of all light after the critical angle in

case of the total internal reflection. However, if a thin metal film is attached to the side face of the prism, a minimum in reflected light intensity will appear at the angle where phase matching with SPPs occurs. Angular dependences of reflectivity curves can be obtained by the manual adjustment of the detection angles using motorized goniometric setup or CCD array etc. Reflectivity can be described by Fresnel formulas supporting complex refractive index [2]. However, vast amount of reflections and refractions data complicates Fresnel calculations in case of multilayered systems. Transfer matrix method (TMM) solves the problem in more elegant way [15a]. Every layer of the system can be characterized by a 2×2 matrix which depends only on the layer thickness and the complex refractive index. The whole stratified system is characterized by the system matrix which is obtained as a result of the multiplication of all the layer's matrices. Finally, reflectance from the multilayered coating is calculated from the resultant matrix. With a little effort, the method can be modified for prisms with various shapes [16]. We applied TMM method for a theoretical fitting of the reflectivity data measured by means of our goniometric setup.

10.3 Optical Scheme of Goniometric Setup

Precise measurement of the light reflected from the sample at different angles is essential for the detection of SPPs. The proposed setup enables variation of the light incident angle and consistent rotation of detector. Measurement cycle implies automatized change of the light incident angles simultaneously with consecutive registration of the light intensity. In our case, a configuration with a fixed light source is favorable compared to others (Fig. 10.4). The prism with the attached sample and a detector is arranged as rotatable parts (Fig. 10.5a). Two coaxial precise rotational stages (8MR190 V-2-VSS42) from Lithuanian company STANDA are used (Fig. 10.5b). The bottom stage rotates the prism, and the upper one moves a sensor around it. These rotational stages are driven by the stepper motors with torque 0.6 nm, voltage 42 V, and current up to 1.2 A. Full step precision of those rotational stages is 0.01°. Movement in special microstepping regime enhances resolution up to 0.0013° in particular cases. Two axis stepper motor controller 8SMC1-USBhF-B2-MC2 from STANDA manages the rotation of the step motors by means of LabVIEW and C/C++ program facilities.

10.4 Applications of Goniometric Setup

SPPs are extremely sensitive to the thickness and permittivity of the metal-dielectric coatings. It gives a possibility for investigation of the surface plasmon-polariton waves themselves; their propagation length and penetration depth in
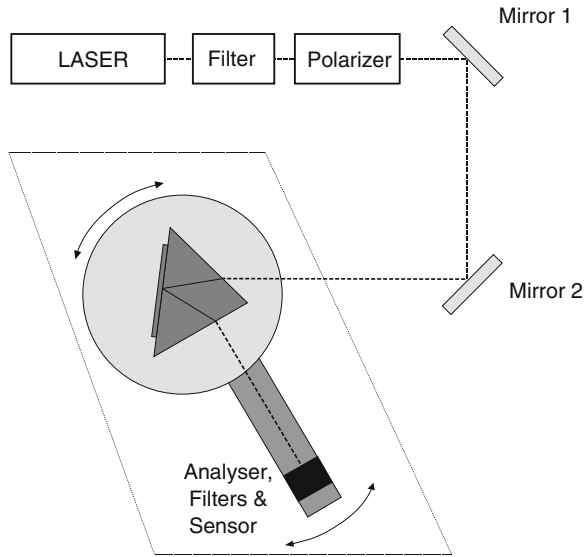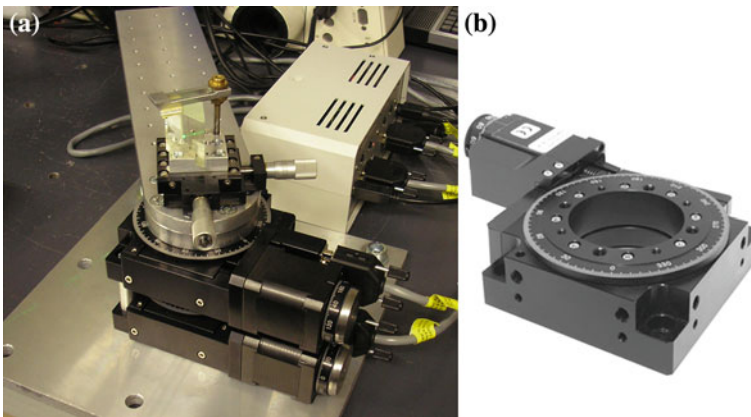
Fig. 10.4 General scheme of goniometric setup

Fig. 10.5 Assembled coaxial goniometer (**a**), based on two precise rotational stages (**b**)

cases of different metals and dielectrics [17]. On the other hand, SPPs can be used as a powerful tool for precise characterization of thin films: their thicknesses, complex refractive indices, and even surface roughness [17a].

10.4.1 Characterization of Thin Gold Films

Here we demonstrate that assembled goniometric setup can be successfully exploited for characterization of commercial optical coatings. Usually, we use

commercial gold-plated glass substrates from Phasis company as plasmonically active substrates. Thorough characterization of these substrates is essential for our further experiments. Results were compared with the data about gold and intermediate adhesive titanium layers provided by Phasis company.

A gold-coated glass sample was attached with immersion oil ($n = 1.516$) to the glass prism base (Fig. 10.6). Nd: YAG (532 nm) and HeNe (593 nm) lasers were used as the light sources. An optical filter eliminated laser undesired wavelengths of the laser source. Two mirrors directed the laser beam to the common axis of rotational stages. P-polarization of the light was controlled by an additional polarizer. Thorlabs PM100 photodiode was used as a detector (Fig. 10.4).

Angular dependence of reflectivity was measured between 10 and 70 °C with a step varying from 0.05 to 1° (Fig. 10.7). If reflected light intensity changed a lot, then the step size was decreased and vice versa. Reflection from the prism and substrate was taken into account. Since the prism and substrate have slightly different refractive indices, refraction from their interface was also included in calculations. As input parameters for fitting the measured curves and complex refractive indices for gold and titanium available from Palik's handbook of optical constants were used [18]. Theoretical fitting of experimental angular reflectivity was carried out using the TMM described in the paragraph 2.2. Initial and fitted parameters of the system are summarized in the Table 10.1. Simulated and measured angular reflection coefficients are in excellent agreement (Fig. 10.7). It turns out that the thickness of the adhesion layer is near 6 nm and the gold layer's thickness is near 49 nm. Optimized real part of the complex refractive index is comparable to initial input values but optimized imaginary parts deviate slightly from the initial ones (Table 10.1).

Fig. 10.6 Scheme of measured multilayered system: prism (*1*), immersion oil (*2*), cover glass (*3*), gold film (*4*). Reflected I_r and scattered I_e beams are marked, respectively
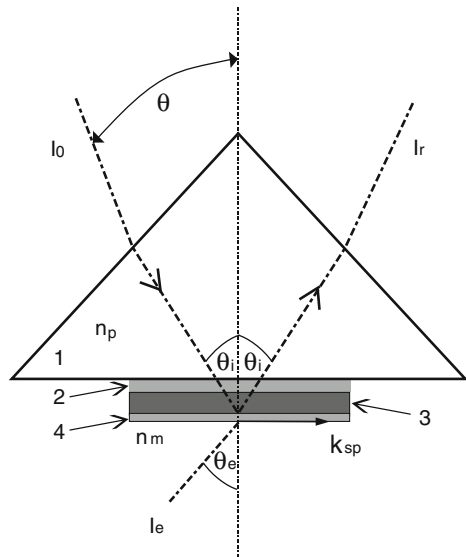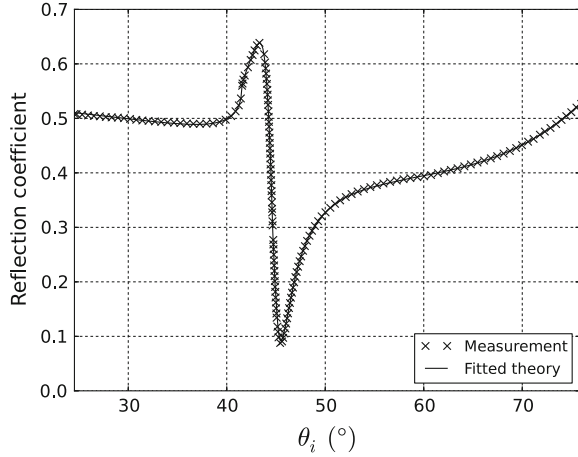
Analysis of the surface roughness is based on the transformation of SPPs to light on the surface inhomogeneity. This part of the light is scattered behind the prism (Fig. 10.6). Angular distribution of the light scattered behind the prism was measured and fitted via the theoretical model developed by Kretschmann [2]. According to the theory, the angular distribution of scattered light intensity is given by the formula

$$I_{\text{rel}} = \frac{\mathrm{d}I_e}{I_0 \mathrm{d}\Omega} = 4\left(\frac{\pi}{\lambda}\right)^4 \frac{n_s}{\cos(\theta_i)} \left|t_p(\theta_i)\right|^2 |W(\theta_e)|^2 |S(\Delta k)|^2, \qquad (10.4)$$

where I_e represents intensity of light scattered to solid angle $d\Omega$. I_0 represents intensity of incident light. I_{rel} is relative intensity of light scattered to the unit solid angle. Angles θ_i and θ_e are marked in Fig. 10.6. n_s is the refractive index of substrate. $\left|t_p(\theta_i)\right|^2$ is Fresnel coefficient for totally transmitted p-polarized light, $|W(\theta_e)|^2$ is the dipole function of a single emitter and $|S(\Delta k)|^2$ is Fourier transform of the roughness correlation function. Δk is Fourier component of the roughness spectrum. For simplicity, a Gaussian correlation function is used to represent surface roughness. So, the Fourier transform of roughness correlation function is

$$|S(\Delta k)|^2 = \frac{1}{4\pi} \sigma^2 \delta^2 \exp\left(-\frac{\sigma^2 \Delta k^2}{4}\right), \qquad (10.5)$$

where σ and δ are correlation length and root mean square (RMS) of roughness, respectively. Using this theory, it is possible to model angular distribution of the scattered light by finding the parameters σ and δ. As shown in Fig. 10.8, measured film roughness can be characterized by four roughness components, pairs of the correlation length, and RMS roughness. It turns out, that more than half of the scattered light is caused by a component $\sigma = 994$ nm and $\delta = 3.3$ nm. Same film was also measured with an atomic force microscope and RMS roughness around 3.5 nm was obtained.

Table 10.1 Real n and imaginary k parts of refractive index, thickness h for the layers of stratified system represented in Fig. 10.6

Medium	Initial parameters			Fitted parameters		
	h (nm)	n	k	h (nm)	n	k
Cover glass	∞	1.51		∞	1.51	
Titanium	5.0	2.02	2.78	5.8	2.11	3.72
Gold	50.0	0.26	2.97	48.8	0.28	2.86
Air	∞	1.0		∞	1.0	

Fig. 10.8 Angular distribution of scattered light intensity. δ_i and σ_i are RMS roughness and correlation length of component i respectively
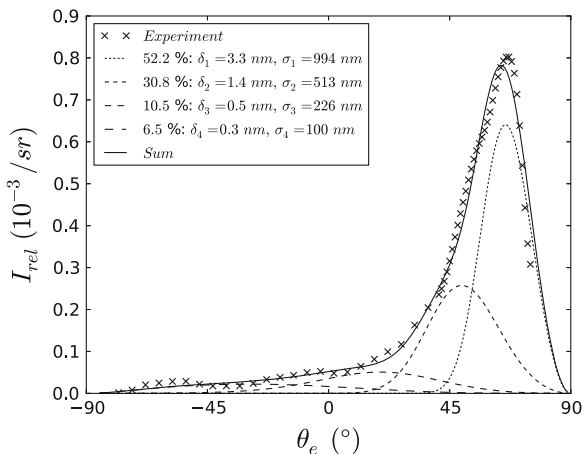
10.4.2 Application of Goniometric Setup to the Measurements of Directional Emission of Chromophores

Metallized prism can provide plasmon resonance conditions not only for the reflected but also for the fluorescent light. It opened new perspectives in field of so-called surface plasmon-coupled fluorescence [19].

There are several variants of possible placements for fluorescent molecules near the metal. Fluorophores can be incorporated inside the dielectric film deposited on the metal [20] or dissolved in the liquid in contact with the metallized prism [21]. Excitation of fluorophore can be realized from the side face of the prism (Kretschmann configuration) or from its metallized face with sample (reverse Kretschmann scheme) (Fig. 10.3). The main difference between these two cases is that Kretschmann scheme allows excitation of plasmon-polariton directly by incident light, but in reverse Kretschmann case plasmon-polariton wave appears not for the exciting but only for the fluorescent light.

Usually, researchers use organic dyes as fluorescent markers. Plasmon resonant conditions allow concentration of the almost all useful fluorescence in the narrow

angular range, which is beneficial for sensing minute amount of the matter down to the single molecules [19]. Here we demonstrate plasmonically assisted control of the fluorescence for nonorganic $TiO_2:Sm^{3+}$ fluorescent films. Rare earth Sm^{3+} ions have four spectral fluorescent bands assigned to the 4f–4f transitions of the Sm^{3+} ion. Each band can be coupled with plasmons at proper detection angle (Fig. 10.9). Excitation of $TiO_2:Sm^{3+}$ film deposited on the gold layer and attached to the prism was realized in reverse Kretschmann scheme (Fig. 10.3) by third harmonic (355 nm) of the Nd:YAG laser. It was so-called indirect photoexcitation of Sm^{3+} emission [22]. Plasmon-coupled reddish fluorescence of Sm^{3+} ions is directed at the angles at which wave vector of fluorescent light becomes equal to the plasmon wave vector [see Eq. (10.3)]. Therefore, the resonance angles in the angular dependences of directional fluorescence and reflectance are the same; maxima of emission correspond to plasmonic dips in reflectance (compare a, b in Fig. 10.10). Fluorophore-plasmon coupling appears for the Sm^{3+} ions situated at the distance <60 nm from the gold layer, which is too large for Förster quenching of emission but sufficiently small to be covered with plasmon field penetration depth. Directional plasmon-coupled Sm^{3+} fluorescence is strongly p-polarized because light of such polarization interacts with plasmons. It is worth to note that directional emission can also be s-polarized in case of thick ($\geq$100 nm) TiO_2 films. In this case, fluorescence is coupled with waveguide modes propagating in such films. An enhanced local field in the last case is not plasmonic but interference by nature. So the maximal intensity of the local field (dark areas in Fig. 10.11) is more concentrated in the dielectric and less connected with the metal nanolayer. Polarization changes in Sm^{3+} directional emission versus the TiO_2 film thickness are considered in our paper [23] in detail.

Fig. 10.9 Fluorescent spectra of $TiO_2:Sm^{3+}$ film (47 nm) deposited on the gold layer (50 nm) detected in reverse Kretschmann geometry at angles 20° (a), 60° (b), and 70° (c)
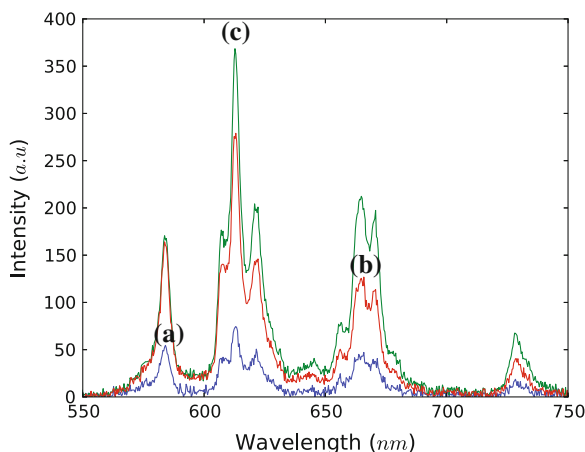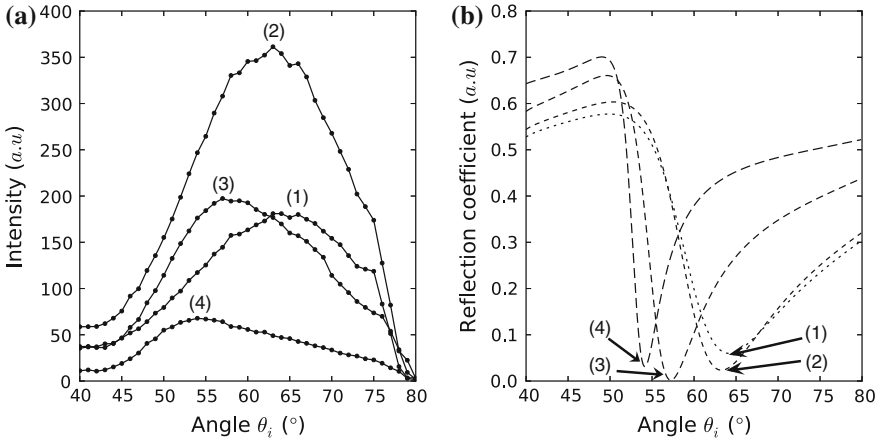
Fig. 10.10 Measured angular dependences of fluorescence (**a**), and calculated reflectance (**b**) for the $TiO_2:Sm^{3+}$ film (47 nm) deposited on the gold layer (50 nm). Data for different spectral bands of Sm^{3+} are plotted: (*1*) 583 nm; (*2*) 616 nm; (*3*) 665 nm; (*4*) 728 nm
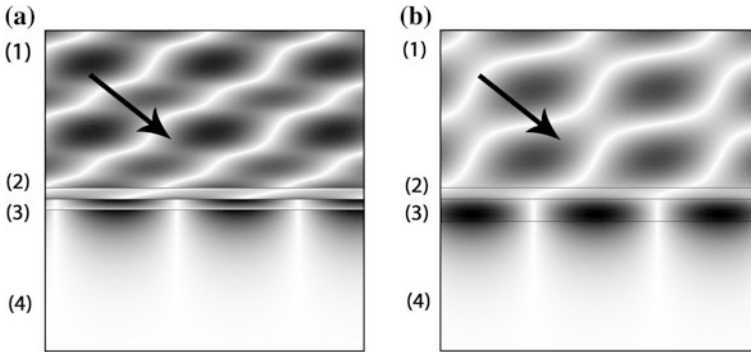

Fig. 10.11 Calculated distribution of light-induced local electric field inside the stratified structure: prism (*1*), glass (*2*), gold (*3*), $TiO_2:Sm^{3+}$ (*3*), air (*4*). The thicknesses of TiO_2 layer are different: 47 nm (**a**), and 100 nm (**b**). *Arrows* indicate the light incidence direction

10.5 Fine Points of Goniometric Setup Realization: Control Logic and Calibration

Control logic and graphical user interface code were written in programming language Python supported by additional libraries like NumPy, SciPy, MatPlotLib, PyUsb, and PySide. Small parts of code were written in C++ language because motors' controller does not have explicit Python support. All elements in the code are object-oriented. Control logic code can be divided into three parts: control of the rotational stages, communication with the sensors, and calibration algorithms.

Communication with the sensors is organized in a flexible way permitting photodiode and CCD spectrometer interchangeability. A new sensor does not require rewriting of the above-stated program code. It means just an appearance of the new object class usable by all above-stated program methods: GetName(), Start(), Stop(), Measure(), etc. Such universal interface of sensors allows processing of data obtained both in case of the light reflection and fluorescence. Intensity of the reflected light was detected by Thorlabs PM100 optical power meter with silicon sensor S130A. Fluorescence was measured with Ocean Optics 2000+ spectrometer with Sony ILX511B CCD.

Most of the calibration algorithms implemented in the program code are based on precise and fast determination of the light beam position, whether it is reflected or refracted from the sample. In a sense it is an automatic focusing procedure. The symmetric beam profile assumption is used as shown in the Fig. 10.12. Such dependence of the light intensity on the sensor angle is physically caused by the finite effective area of sensor. Thus, in the region 1 the whole beam fits to the effective area of the sensor. However, in regions 2 some part of the beam is absorbed or reflected by the sensor cover, and therefore not registered. A method implemented in the program code locates points A and B at the half-width of the beam (Fig. 10.12). If the location of A and B points is known, the beam center will be positioned in the middle of them. The sensor can be positioned at the calculated beam center with an accuracy $\Delta\phi$.

Identification of A and B points was realized by recursive search method. The first big step scanning rotation of the detector was aimed to locate the beam position and define its half-width intensity roughly (solid dots in Fig. 10.12). Then the recursive scan for the point A was initiated. The step size was divided by two and angular region of the search was halved as well (crosses in Fig. 10.12).

Fig. 10.12 Experimentally measured intensity inside the light beam versus the sensor angle
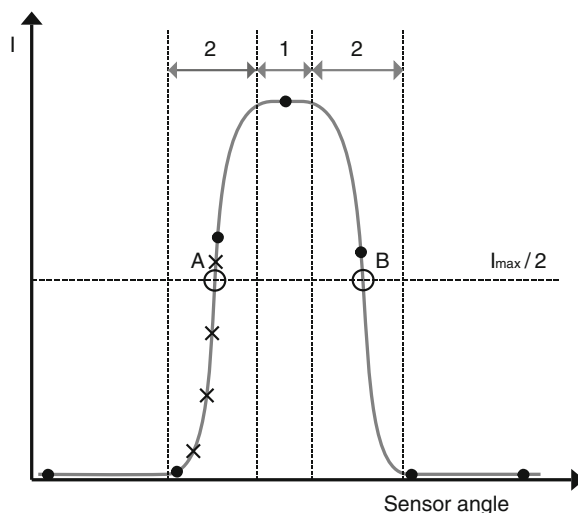
Such dichotomic procedure was repeated until the smallest possible scanning step. Afterwards the location of the point B was found in the same way.

The right-angle prism usually used in our setup can be substituted for the prism with other size and shape. In this case, a new prism together with a sample must be set on the rotational axis of supporting stages. Otherwise rotation will cause an undesirable shift of the light beam on the sample surface [24]. Thus, discrepancy in rotation angles of the prism and the detector complicates the measuring procedure (Fig. 10.13).

Proper positioning of the prism is possible, when the location of the light incident point O on the prism side face is defined relatively to the rotation axis A (Fig. 10.14). The angles of incidence and reflection for the light beams (Fig. 10.13b) are influenced by the accuracy in the beam position $\Delta\phi$ and the distance between the rotational axis and the reflecting surface Δx (Fig. 10.15). These parameters are independent. Change in $\Delta\phi$ causes only the parallel shift of the line and term Δx influences its slope. So, we can conclude about the distance between the rotational axis and the reflecting side face of the prism from the slope of the measured line. The second distance Δy (Fig. 10.14) can be found from the similar graph measured in the same way for another side face of the triangular prism.

Semicylindrical or hemispherical prisms are also possible in our setup. Some authors [3] prefer such prisms because of low refraction on the rounded facets. However, such prisms can have undesired focusing effects and disturb collimation of the light beams.

Graphical user interface (Fig. 10.16) of the controlling program provides fast and convenient measurements. It is made on the basis of Qt Project Libraries from PySide module. Qt graphical user interface works on every widespread operating system.

Fig. 10.13 Light reflection from the sample at the angle α. **a** Rotational axis (*black circle*) goes through sample's face. **b** Rotational axis is at distance Δx from the sample's face. γ denotes apparent angle of reflection
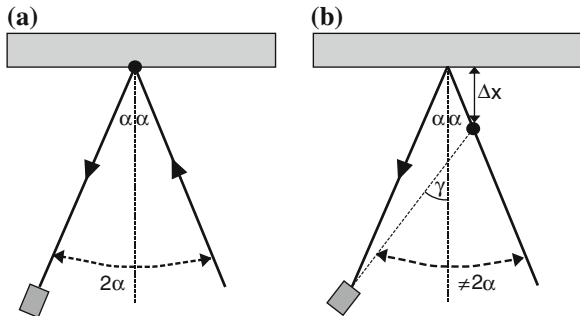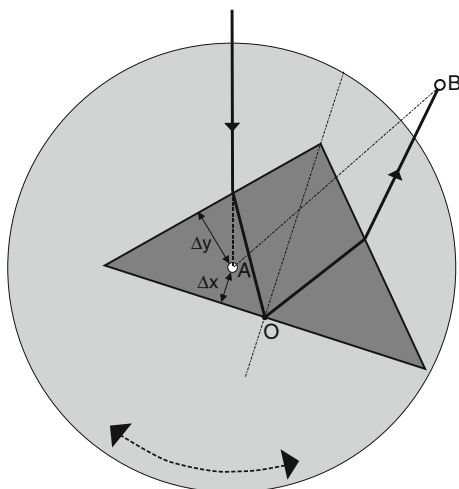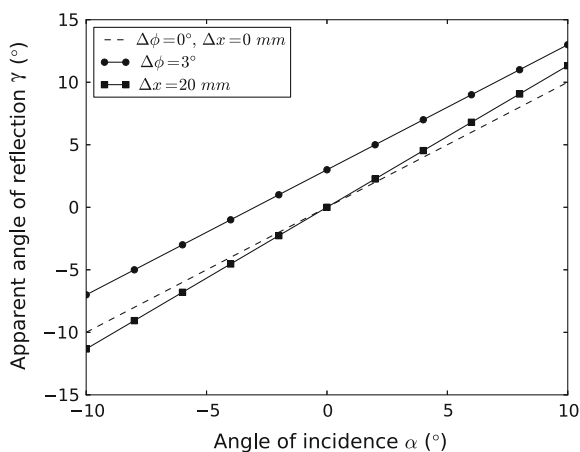
Fig. 10.14 Prism position relatively to the rotational axis A

Fig. 10.15 Dependence of apparent angle of reflection γ (from Fig. 10.13b) on the accuracy of incident angle $\Delta\phi$ and distance Δx between the sample and rotational axis

10.6 Conclusions

Light-induced SPPs are introduced in a manner emphasizing practical applications of surface plasmon resonance. Resonance is obtained as a result of the attenuated total internal reflection from the metal-dielectric sample attached to the prism. Smart solutions for optical goniometric measurements are realized, such as: recursive algorithm for detector positioning and adjustment of the sample on the rotational axis of setup. The accuracy of the assembled setup allows estimation of the film thicknesses and surface roughnesses with accuracy of several nanometers. Refractive index of each layer of stratified medium can be determined down to second decimal digit. It was demonstrated that proposed goniometric setup operates successfully not only with reflected but also with plasmon-coupled fluorescent
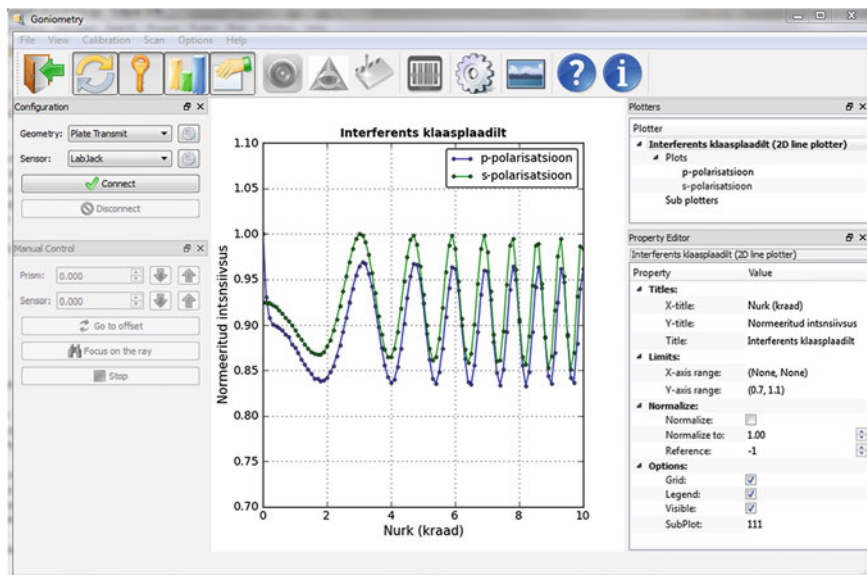
Fig. 10.16 Graphical user interface of the goniometric setup

light. It enables transformation of the isotropic rare earth fluorescence into the strongly polarized and directional one which is perspective for the sensing applications and induction of low loss coherent surface plasmon-polaritons.

References

1. Homola J (ed) (2006) Surface plasmon resonance based sensors. Springer, Berlin Heidelberg
2. Kretschmann E (1971) Die Bestimmung optischer Konstanten von Metallen durch Anregung von Oberflächenplasmaschwingungen. Z Phys 241:313–324
3. Schasfoort R, Tudos A (eds) (2008) Handbook of surface plasmon resonance. RSC Publishing, Cambridge
4. Yuk JS et al (2010) Surface plasmon-coupled emission (SPCE)-based immunoassay using a novel paraboloid array biochip. Biosens Bioelectron 25:1344–1349
5. Hoff M, Sars V, Oheim M (2008) A programmable light engine for quantitative single molecule TIRF and HILO imaging. Opt Express 16(22):18495–18504
6. Sathish RS, Kostov Y, Rao G (2010) Low-Cost Plastic Plasmonic Substrates for Operation in Aqueous Environments. Appl Spectrosc 64(11):1234–1237
7. Manera MG et al (2008) Optical gas sensing of TiO_2 and TiO_2/Au nanocomposite thin films. Sens Actuators, B 132:107–115

8. Velinov T et al (2011) Influence of the surface roughness on the properties of Au films measured by surface plasmon resonance and X-ray reflectometry. Thin Solid Films 519:2093–2097

9. Rako JG et al (1984) Optical second-harmonic generation with surface plasmons in noncentrosymmetric crystals. Phys Rev B 30(10):5552–5559

10. Ritchie RH (1957) Plasma losses by fast electrons in thin films. Phys Rev 106:874–881

11. Maier SA (2007) Plasmonics: fundamentals and applications. Springer Science, USA

12. Drude P (1900) Zur Elektronentheorie der Metalle. Ann Phys 1:566–613

13. Raether H (1988) Surface plasmons on smooth and rough surfaces and on gratings. Springer, New York

14. Ward CA, Bhasin K, Bell RJ et al (1974) Multimedia dispersion relation for surface electromagnetic waves. J Chem Phys 62:1674–1676

15. Otto A (1968) Excitation of nonradiative surface plasma waves in silver by method of frustrated total reflection. Z Phys 216:398–410

15a. Abeles F (1956) Optical properties of thin absorbing films. J Opt Soc Am 47:473–482

16. Chilwell J, Hodgkinson I (1984) Thin-films field-transfer matrix theory of planar multilayer waveguides and reflection from prism-loaded waveguides. J Opt Soc Am 1:742–753

17. Dawson P, Puygranier BAF (2001) Surface plasmon polariton propagation length: a direct comparison using photon scanning tunneling microscopy and attenuated total reflection. Phys Rev B 63:205410

17a. Bruijn HE, Altenburg BSF, Kooyman RPH, Greve J (1991) Determination of thickness and dielectric constant of thin transparent dielectric layers using surface plasmon resonance. Opt Commun 82:425–432

18. Palik ED (1998) Handbook of optical constants of solids. Academic Press, New York

19. Ray K et al (2009) Plasmon-controlled fluorescence towards high-sensitivity optical sensing. In Rao G (ed) Optical sensor systems in biotechnology. Springer series: advances in biochemical engineering/biotechnology, vol 116. Springer, Berlin, Heidelberg, pp 29–73

20. Gryczynski I et al (2004) Effects of sample thickness on the optical properties of surface plasmon-coupled emission. J Phys Chem B 108:12073–12083

21. Seidel J et al (2005) Stimulated emission of surface plasmons at the interface between a silver film and an optically pumped dye solution. Phys Rev Lett 94:177401

22. Kiisk V et al (2005) Photoluminescence characterization of pure and Sm^{3+}-doped thin metaloxide films. Appl Surf Sci 247(1–4):412–417

23. Dolgov L et al (2012) Tailoring of the spectral–directional characteristics of rare-earth fluorescence by metal–dielectric planar structures. Appl Phys B 107:749–753

24. Horn N, Kreiter M (2010) Plasmon spectroscopy: methods, pitfalls and how to avoid them. Plasmonics 5:331–345

Chapter 11
Effects of Surface and Interface in Oxide Nanoparticle System

T. Konstantinova, I. Danilenko and V. Varyukhin

11.1 Introduction

Understanding the possibility of significant changes in the properties of materials with decreasing particle size, grains, second phases, etc, less 100 nm, which emerged in the 1980s of last century [1], it was the key to the development of new technologies and materials in the coming decades. Further researches in this area were found a number of different effects, when the changes of material properties turn out a significant and nonmonotonic, depending on the size of their constituent elements [2–7].

Analysis of the scientific literature shows that in the range of nanoscale significant effects of the influence of the nanoparticles size on the properties of the materials are identified. For example, for materials and nanoelectronics devices such effects are observed at very small sizes, at least, <10 nm. This effect of the influence of the particle size is very strong in the process of catalysis and can be expressing the dependence with an extremum of certain nanoscale. Most of the work which involves the effect of particle size is publishing in the field of biology and medicine. Recent works in the field of agriculture and ecology are considerably active.

At the same time, works that consider the influence of nanoparticle size on the functional and structural properties of materials for technical use is relatively small. However, in recent years, a lot of works on nanostructured composite materials were appeared, as in the form of multiphase systems of nanoparticles, films, and as the voluminous matrix with nanoparticles.

In this case, the fundamental aspects of the effect of its own surface of nanoparticles and surfaces of their interaction with the environment and other phases in the behavior of systems of nanoparticles under the influence of various factors

T. Konstantinova (✉) · I. Danilenko · V. Varyukhin
Donetsk Institute for Physics and Engineering named after O.O.Galkin, NASU,
R.Luxembourg 72, Donetsk 83114, Ukraine
e-mail: matscidep@aim.com

were considered insufficiently. But these features of the response to external action are influencing the character of the reaction of the dispersed systems by way of self-organization of nanoparticles and determine the further evolution of the structure of the nanopowder, and ultimately the properties of the final product.

In this paper, the effects of the influence of the surface of nanoparticles (and the corresponding particle size) and the effects of their interaction at the temperature and pressure will be considered by the example of the system ZrO_2–Y_2O_3.

Doped zirconia exhibits persistent interest as engineering material because of its outstanding combination of properties such as: strength, toughness, high melting point, chemical inertness, electrical, optical properties, and biocompatible. These qualities provide wide range of applications for this material in the capacity of functional and structural, ceramics, and also for catalyst, in electrochemical devices, in medicine etc. Yttrium is used most frequently, stabilizing tetragonal (t) and cubic (c) phases with addition of 3 and 8 mol %, respectively.

Zirconia-related materials have attracted in the last decades increasing attention of both researches and manufactures, because development of new technology begin to product oxide nanopowders. Most of the above-mentioned applications of zirconia-based materials, especially of nanopowders, are related to their surface state, such as Gibbs energy, electrode potential, kind of active centers and their relation, level of segregation of doped, impurity ions, and others. The surface state is depended strongly from preparation conditions and that surface characterization is an evident need. And the interaction of nanoparticles in the system, what is one of the most phenomena in dispersed system is determined by surface state.

For the recent 15–20 years, mesoscopic approach has been widely used to describe different phenomena in solid state. Mesoscopic scale is considered to be intermediate between atomic scale and microscopic one. Significant progress in mesoscopic physics during last few years was carried out in the works of Ymry and described in [8] and connected with the development of theoretical background for electronic transport in metals, halfmetals, and semiconductors. These investigations have given answers to many fundamental questions about the transformation of quantum laws during transition into macroscopic level. Arkharov in 1980 [9] has shown the necessity of mesoscopic approach for description of the whole number of phenomena in condensed matter. He proposed the definition of mesoscopic phenomena as phenomena characterized by collective interaction of system elements. The elements of the system can be impurity atoms, dislocations, vacancies etc., and in majority of cases exactly the mesoscopic phenomena determine materials properties. From this point of view, self-organization phenomena in nanoparticle systems during synthesis, compaction, and sintering can be considered mesoscopic. It is also should be noted that description of self-organization phenomenon is often hard or even impossible without the use of this approach.

In this paper, we will discuss experimental results on the nanoparticles size influence in nanoparticles interaction in heating process and tetragonal-monoclinic transformation under high pressure.

11.2 Self-Organization of Nanoparticles in Calcination Process

Nanopowders of zirconia hydroxide were prepared by modified co-precipitation technique. (Solutions of high purity $ZrO(NO_3)_2$ and $Y(NO_3)_3$ salts taken at stoichiometric composition (3 mol % Y_2O_3) were used as starting materials. This precursor solution was mixed with ammonia solution. Precipitation pH was retained at the level of nine. After reaction stopped, the sediment was repeatedly washed with water in order to remove NO_3- ions. The precipitates were then dried in a microwave furnace. Nanopowders were calcined using 3 °C/min heating rate in a temperature range of 350–1,000 °C and naturally cooled with furnace. X-ray diffractometer (XRD) with nickel-filtered Cu Ka radiation was used to determine phase composition and crystalline size of calcined powder. Crystalline size was estimated using Scherrer formula [10]. Morphology of nanopowders was investigated using TEM on Jeol JEM 200A instrument and HRTEM on FEI F206 instrument.

The peculiarities in growth process of zirconia nanoparticles were considered in [11]. Nanoparticles obtained by our technology are single crystals with soft and easily destroyed agglomerates. They have low degree of size dispersion (20 %) and homogeneous dopants distribution and are 100 % tetragonal. The morphology of these nanopowders is shown in Fig. 11.1.
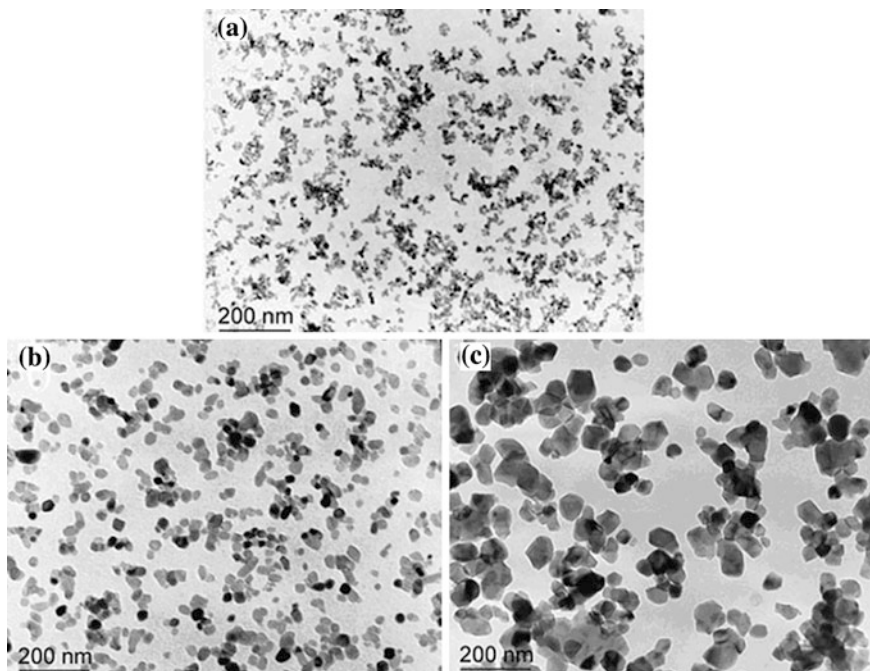
Fig. 11.1 Morphology of nanopowders ZrO_2 − 3 mol % Y_2O_3 calcined at different temperatures (**a**) −500 °C, (**b**) −700 °C, (**c**) −1,000 °C
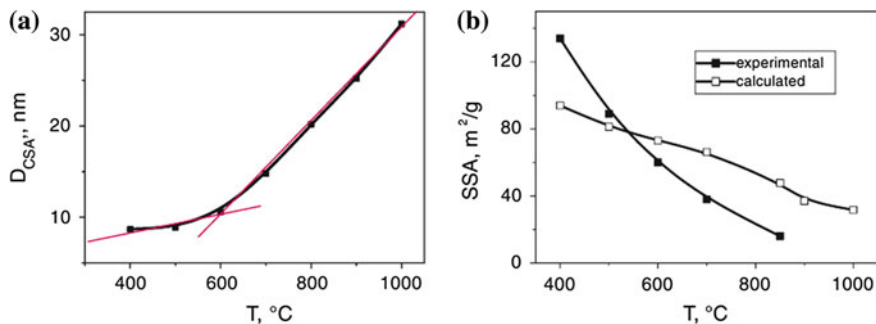
Fig. 11.2 Dependence of (**a**) nanoparticle size (coherent scattering area – CSA) and (**b**) specific surface area (SSA) measured and calculated for spherical particle via calcination temperature

On the dependence of particle size from calcination temperature (Fig. 11.2a), we see two stages of nanoparticles growth with different growth rate, that demonstrated two different mechanisms in this synthesis process, specific surface area (SSA) measured and calculated for spherical particle are shown in Fig. 11.2b.

Past decade investigations have shown that nanoparticles growth during synthesis proceeds not by connection of separate atoms or ions but by coarsening growth which is also known as ostwald ripening [12], oriented aggregation, oriented attachment, or oriented consolidation [13, 14]. Ribeiro in 2005 [13] proposed kinetic model for description of nanocrystal growth by oriented attachment mechanism during initial stages of nanoparticle synthesis and during growth induced by hydrothermal treatment.

The peculiarity of mesoscopic system is relatively weak bonding between primary particles ensuring cooperative rearrangement under external influence still being bonded to each other. This peculiarity makes the understanding of mechanisms and building of physical models a very complex task, as many factors should be taken into consideration. The difference of particles behavior in suspensions (liquid medium) and in powder state (gaseous medium) is of great importance. Liquid medium is undoubtedly facilitating particles movement under the influence of Brownian motion of liquid molecules thanks to big freedom for movement and to suspension state of particles. It makes collision and oriented attachment possible.

Our investigation with use HRTEM [14] in first demonstrated the really consolidation of zirconia nanoparticles calcinated at 500 °C (Fig. 11.3a) and on Fig. 11.3b the scheme of that mechanism is shown. In the 400–600 °C interval there is no diffusion in zirconia, anion diffusion activity begin >600 °C, and cation moving above 1,000 °C. Nevertheless, particles of nanopowders are in the state of continuous motion ensured by small translations and rotations. First of all, the mass of a single particle at middle interval of calcination temperature is very small (the mass of 10 nm particle is $3 \times 10 - 18$ g) and comparable with the one for the air molecule which has higher mobility than water. Second, nanoparticles being weakly bonded are in direct contact with each other experiencing mutual
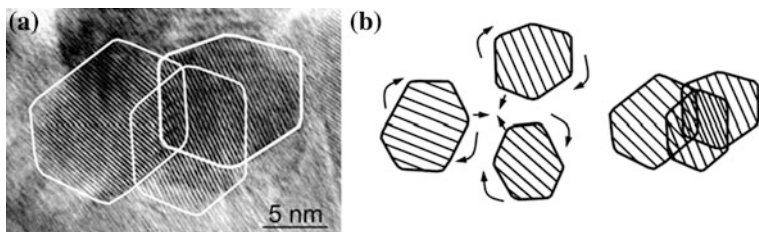
Fig. 11.3 Oriented attachment of nanoparticles. **a** HRTEM image, calcination temperature 500 °C. **b** Scheme of mechanism

attraction and repulsion. Under the influence of above layers, they can reach equilibrium state at the expense of consolidation. Third, it should be noted that zirconia is an ionic crystal with clearly defined surface relief and particles consolidate directly along its orientation.

Calcination in the temperature range of 600–1,000 °C leads to significant increase of grain growth, according to the slope of crystallite size temperature dependence (Fig. 11.2). Indeed, usual sintering of oxide powders assumes diffusion of both components. In the case of oxygen-containing crystals, in particular zirconium dioxide, oxygen diffusion according to impedance spectroscopy starts at temperatures higher 600 °C and cations (Zr and Y) diffusion starts only after reaching 1,100 °C [15]. The cause of such behavior is a great difference in activation energies: $\sim$0.8–1.2 eV for oxygen and $\sim$4.4 eV for zirconium [16].

Our investigations show that at temperatures higher than 600 °C surface state of nanoparticles changes dramatically. According to ESR data [17], amount of Zr^{3+} and F-centers (oxygen vacancy with trapped electron) [18] on the surface of nanoparticles significantly rise at 600 °C. For understanding the mechanisms of transport phenomena, the computer simulation was carried out [19]. Simulation used the strong coupling theory applied to the tetragonal zirconia plate with S-impurity consisting of four planes (111) and oxygen vacancy in the near-surface layer. Energy barriers of oxygen atom migration for different cells (Fig. 11.4a, b) were obtained for the surface migration of oxygen and migration of oxygen in near-surface layer by vacancy mechanism. It is shown [20, 21] that energy barrier of oxygen migration in the near-surface layer with vacancy is lower than energy barrier for the surface migration of the oxygen.

HRTEM investigation of structure of the powders calcined at 700 °C have shown that oriented attachment mechanism also works in this case forming the particles two times bigger in size and in addition to this considerable amount of particles with perfect and imperfect boundaries (Fig. 11.4c).

These experimental results in combination with computer simulation support the notion that on second stage oxygen diffusion by vacancy mechanism is the main process assisting the increase of growth rate of particles. We suppose that oriented attachment also takes place on this stage, but more efficient lacing of particles together occurs due to oxygen diffusion by vacancy mechanism between adjacent particles. This mechanism also facilitates the joining of nanoparticles
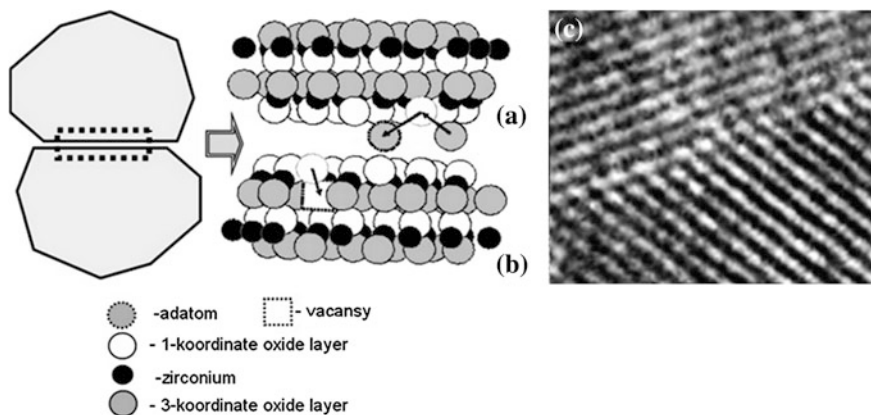
Fig. 11.4 Scheme of contact of two crystal surfaces: (**a**) oxygen migration along the surface (111) of zirconia plate and (**b**) in near-surface (111) layer with vacancy and (**c**) perfect boundary between two nanoparticles, HRTEM

with different orientation with the necessary angle due to cooperative displacements and rotations, making the formation of boundaries with minimum excess energy possible. Described mechanism can be called oxygen-vacancy lacing consolidation.

11.3 Evolution of Zirconia Nanoparticle System Under Hydrostatic Pressure

Usually, oxide particles are only consolidated under pressure without any transformations, if pressure is $<P_{crit}$, which appropriate phase transition on P–T scheme. Zirconia has stress-induced martensitic transition from stabilized high temperature tetragonal phase to low temperature monoclinic phase.

The phase transformation of metastable tetragonal phase to monoclinic phase (referred as t–m transformation) in zirconia plays important role in the formation of relatively high mechanical properties of zirconia ceramics [15, 22, 23]. Zirconia ceramics ($ZrO_2 - 3$ mol % Y_2O_3) in the tetragonal modification was called by Harvie, Hannik, and Pascoe "Ceramic Steel" for the most high among ceramic material strength and fracture toughness.

The process of stabilization of tetragonal phase in zirconia depends on concentration oxygen vacancies in crystal structure. The oxygen vacancies can be generated via doping, for example, trivalent cations within ZrO_2 lattice [24, 25]. It was shown that a decrease in the oxygen ion vacancy concentration decreases the tetragonal phase stability and promotes its transformation to the monoclinic phase. Garvie [26] demonstrated the role of crystalline size and agglomeration degree in stabilization of tetragonal phase without doping any impurities.

The physical factors also have strong influence on tetragonal phase stabilization in ZrO_2. Such factors are the strain and interfacial energy, external and internal hydrostatic pressure [27]. Variations of these factors play a great role of tetragonal phase stabilization and evolution during pressure compaction and heating. Effect of pressure on the phase transformations in zirconia nanopowder systems is not as widely studied [28–31].

But the behavior of nanopowders under pressure is more complex, because powders may be agglomerated or not, particles can have surface shell of adsorbed molecules or not. The questions about agglomerate type ("hard" or "soft") are important.

The powders were prepared by the same methods of synthesis that was described in the part 2 of this paper. Calcination temperature was 400, 500, 700, 800, 900, and 1,000 °C what ensured 8, 12, 18, 20, 23, and 30 nm cylindrical specimens of 20 mm diameter and 2–3 height were uniaxially pressed at 50 MPa, and after that samples in elastic container were subjected by isostatic pressure in oil. The treatment of specimens under isostatic pressure conditions was carried at different pressures from 100 to 750 MPa. The phase compositions of samples after isostatic pressure were determined by XRD.

Our technology ensures soft agglomerates [32], because first effect of high pressure influence is self-organized in nanoparticle system with the arising of granules and the granule size vastly depended from particle size (Fig. 11.5). The second effect is martensitic tetragonal-monoclinic transformation. In some papers [32, 33] were shown that the phase transformation from tetragonal to monoclinic phase in ZrO_2-3 mol $\%Y_2O_3$ nanopowders took place after isostatic pressure treatments, but detailed investigations of particle size influence on degree of tetragonal-monoclinic transformation have not been carried out. Our results on the hydrostatic treatment of zirconia nanopowder are shown in Fig. 11.6. The maximum amount of monoclinic phase in the samples treated with the same pressure is at particle size 23 nm, calcinated at 800 °C. The maximum values of monoclinic phase are reached after compaction at 750 MPa. The monoclinic phase, what
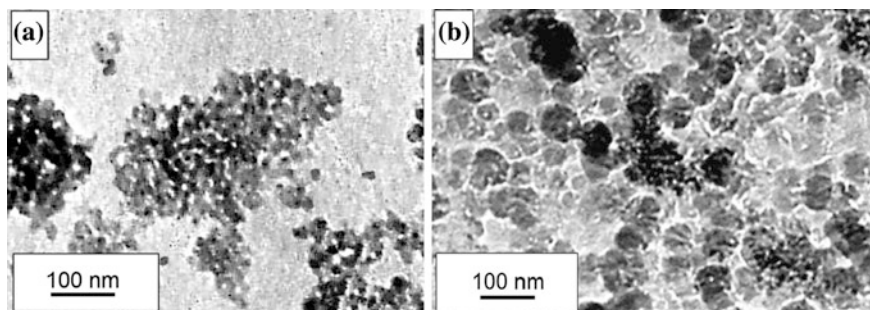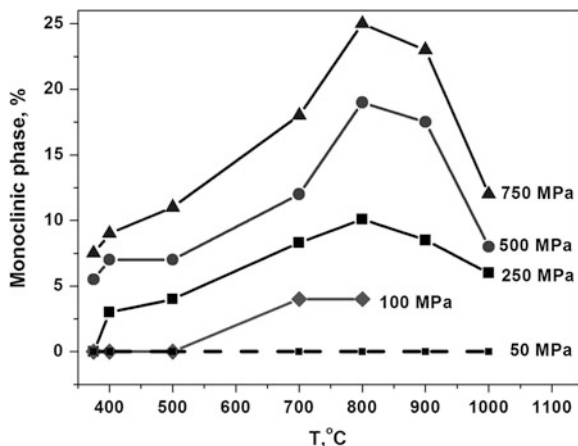

Fig. 11.5 The granule arising under high hydrostatic pressure: (**a**) initial nanoparticle, d = 10 nm and (**b**) their granule structure (d = 50 nm), in green ceramic after high hydrostatic pressure 500 MPa. TEM, two-step replica

Fig. 11.6 The monoclinic phase part versus particle sizes for different values of hydrostatic pressure

created under high pressure in zirconia nanoparticles has volume of elementary crystal cell on ∼4 % more than initial tetragonal cell and that are positive, because this transformation lead to destroy agglomerate. But in the case, when monoclinic part will be >30 %, the compacted specimen will be destroyed. It is more important to consider in region of small size (<25 nm). When we have initial size >25 nm the monoclinic part decreases. It may be due to more high stability of T-phase with increasing particle size or influence of agglomerate hard degree.

11.4 Conclusions

The described phenomenon in zirconia nanoparticle system demonstrated strong influence of surface and interface, and interface of evolution of structure nanoparticle under heating and hydrostatic pressure and have important role at application of nanopowders. Proposed conception on mesoscopic processes of nanoparticles formation made the understanding and theoretical description of significant amount of experimental data possible and open the way for purposeful governing by oxide nanopowder system on the stages of obtaining, compaction, and sintering.

References

1. Gleiter H (2000) Nanostructured materials: basic concepts and microstructure. Acta Mater 48(1):1–29
2. Hilger A, Von Hofe T, Kreibig U (2005) Recent investigations of size and interface effects in nanoparticle composites. Nova Acta Leopoldina NF 92. Nr. 340:9–19

 3. Paramsothy M, Chan J, Kwok R, Gupta M (2012) Nanoscale electro negative interface density (NENID) in magnesium alloy nanocomposites: effect on mechanical properties. J Nanopart Res 14(6):1–14

 4. Liu W-S, Peng Yu-H, Shiung C-E, Shih Y-H (2012) The effect of cations on the aggregation of commercial ZnO nanoparticle suspension. J Nanopart Res 14:1259–1265

 5. Leitch ME, Casman E, Lowry GV (2012) Nanotechnology patenting trends through an environmental lens: analysis of materials and applications. J Nanopart Res 14:1283–1291

 6. Wang W-N, Tarafdan JC, Biswas P (2013) Nanoparticle synthesis and delivery by an aerosol route for watermelon plant foliar uptake. J Nanopart Res 15:1417

 7. Akbarzadeh A, Samiel M, Davaran S (2012) Magnetic nanoparticles: preparation, physical properties, and applications in biomedicine. Nanoscale Res Lett 7:144

 8. Imry Y (2002) Introduction to mesoscopic physics, 2nd edn. Oxford University Press, New York

 9. Arharov VI (1980) Mesoscopic phenomena in solid state and their microstructure. Problems of modern physics, Moscow, Russia, Science, pp 609–617

10. Klug A, Alexander L (1974) X-ray diffraction procedures. Wiley Interscience, New-York

11. Konstantinova T, danilenko I, Glazunova V, Volkova G, Gorban O (2011) Mesoscopic phenomena in oxide nanoparticles systems: processes of growth. J Nanopart Res 13:4015–4023

12. Roldughin V (2004) Self-assembly of nanoparticles of interfaces. Rus Chem Rev 73:115–121

13. Ribeiro C, Lee E, Longo E, Leite E (2005) A kinetic model to describe nanocrystal growth by the oriented attachment mechanism. Chem Phys Chem 6(4):690–696

14. Konstantinova T, Ragulya A, Doroshkevich A, Volkova G, Glazunova V (2006) The mechanisms of particle formation in Y doped ZrO2. Int J Nanotechnol 3(1)

15. Chevalier J, Gremillard L, Virkar Anil V, Clarke David R (2009) The tetragonal to monoclinic transformation in zirconia: lessons learned and future trends. J Am Ceram Soc 92(9):1901–1920

16. Brossmann U, Wurschum R, Sodervall U, Schaefaefer H (1999) Oxygen diffusion in ultrafine grains monoclinic ZrO2. J Appl Phys 85:7646–7654

17. Konstantinova T, Danilenko I, Dobrikov A, Volkova G, Tokyy V, Gorban S (2002) TEM. ESR and XRD studies of thermally induced formation nanocrystalline zirconia, CIMTEC

18. Liu H, Feng L, Zhang X, Xue Q (1995) ESR characterization of ZrO2 nanopowders. J Phys Chem 99:332–334

19. Tokiy N, Tokiy V, Savina D, Konstantinova T (2007) Transport phenomena in surficial layers of zirconia proceedings of X-international conference. Hydrogen Mater Sci Chem Carbon Nanomat 172:499–508

20. Tokiy N, Konstantinova T, Tokiy V, Savina D (2003) Influence of oxygen vacancies and 26-d impurity on electronic and transport properties of zirconia. Electrochem Soc proc 7:181–186

21. Savina DL, Tokiy VV, Konstantinova TE, Tokyy NV (2008) Transport phenomena in near-surface layers of zirconia. Rus Nanosyst Nanomater Nanotechnol 6(3):725–730

22. Lange FF (1982) Transformation toughening. J Mater Sci 17:225–265

23. Hannink RH, Kelly PM, Muddle BC (2000) Transformation toughening in zirconia-containing ceramics. J Am Ceram Soc 83:461–487

24. Li P, Chen I (1994) Effect of dopants on zirconia stabilization—An X-ray absorption study: I, trivalent dopants. J Am Ceram Soc 77:118–128

25. Lu X, Liang K, Gu S, Zheng Y, Fang H (1997) Effect of oxygen vacancies on transformation of zirconia at low temperatures. J Mater Sci 32:6653–6656

26. Garvie RC (1965) The occurrence of metastable tetragonal zirconia as a crystallite size effect. J Phys Chem 69:1238–1243

27. Shukla S, Seal S (2005) Mechanisms of room temperature metastable tetragonal phase stabilization in zirconia. Int Mater Rev 50:1–20

28. Skovgaard M, Ahniyaz A, Sorensen BF, Almdal K, Lelieveld A (2010) Effect of microscale shear stresses on the martensitic phase transformation of nanocrystalline tetragonal zirconia powders. J Eur Ceram Soc 30:2749–2755

29. Subarao ES, Maiti HS, Srivastava KK (1974) Martensitic transformation in zirconia. Physica Status Solidi (a) 21:9–40
30. Alzyab B, Perry CH, Ingel RP (1987) High pressure phase transition in zirconia and yttria-doped zirconia. J Am Ceram Soc 70:760–765
31. Kabanova MI, Dubok VA, Nochevkin CA (1991) The structure and porosity of zirconia compacts under pressure to 6 GPa. Powder Metall Met Ceram 9:69–74
32. Danilenko I, Konstantinova T, Pilipenko N, Volkova G, Glasunova V (2011) Estimation of agglomeration degree and nanoparticles shape of zirconia nanopowders. Part Syst Charact 28:1–6
33. Danilenko I, Konstantinova T, Volkova G, Glazunova V (2013) A martensitic phase transition in nanocrystalline 3Y-TZP powders under hydrostatic pressure conditions. Phase Transitions. doi:10.1080/01411594.2012.749988

Chapter 12
Surface Sites of Nanomaterials: Investigation of Local Structures by In Situ IR Spectroscopy

Valentina Aina, Gabriele Alberto, Chiara Deiana, Yuriy Sakhno, Alessandro Damin and Gianmario Martra

12.1 Introduction

12.1.1 Nanomaterials

Since the late twentieth century, research in the field of nanotechnology and nanomaterials has certainly become a key pillar of modern science due to the potential heavy impact on technological, industrial, and medical fields. Although the term "nanotechnology" has been used for the first time by Japanese scientist Norio Taniguchi in 1974 [1], the basics of the subject were first expressed in 1959 by the physicist Richard Feynman, Nobel Prize in Physics in 1965, during his famous speech on "There's Plenty of Room at the Bottom" at an American Physical Society meeting at the California Institute of Technology. In his speech Feynman, many years before the invention of the scanning tunneling microscope allowed even to see a material at the atomic level, perfectly described the importance of studying and manipulating materials in the nanoscale because "…we have a lot of new things that would happen that represent completely new opportunities for design. Atoms on a small scale behave like nothing on a large scale, for they satisfy the laws of quantum mechanics. So, as we go down and fiddle around with the atoms down there, we are working with different law…we have new kinds of forces and new kinds of possibilities, new kinds of effects". In fact, physical and chemical properties of materials (such as optical and magnetic properties, electrical conductivity, surface energy and reactivity) significantly changed from the bulk form to nanoparticles (NPs) in the range of 1–100 nm size scale, where their behaviors are ruled by the so-called quantum effects. Moreover, in the nanoscale, most of these properties are size-dependent, and a wide range of

V. Aina · G. Alberto · C. Deiana · Y. Sakhno · A. Damin · G. Martra (✉)
Dipartimento di Chimica and Interdipartimental Centre of Excellence
"Nanostructured Interfaces and Surfaces—NIS", University of Torino,
Via P. Giuria 7, 10125 Turin, TO, Italy
e-mail: gianmario.martra@unito.it

possibilities is provided in terms of manipulation, in order to obtain nanomaterials with precise and peculiar features. Depending on their composition, nanomaterials can be employed in a wide range of applications, such as photo-catalysis and catalysis (e.g., TiO_2 [2] and Pd [3]-based NPs, respectively), energy conversion and storage devices (e.g., TiO_2 [2] and ZnO [4] based solar cells), biological and chemical sensing (e.g. fluorescent silica NPs [5] Au NPs [6], Fe_2O_3 based magnetic NPs [7] drug delivery (silica; [8] and polymer-based nanocomposites [9], biocompatible materials for bones regeneration (e.g., hydroxyapatite HA [10] and substitution (e.g., titanium-based materials) and SERS and SEIRA (coinage metal nanostructures) [11–13].

12.1.2 Properties of Nanomaterials

One of the most spectacular (and well known in the past) examples due to the "*nano-sizing*" of materials is constituted by the variation of the optical properties of coinage metals (Cu, Ag, and Au NPs), when compared to their bulk counterparts. In fact, colloidal solutions of these metals (obtained by chemical reduction of salt precursors like $CuSO_4$, $AgNO_3$, and, $HAuCl_4$) containing NPs ranged from 2 to 100 nm interval are characterized by a very intense coloration (typically dark yellow for Cu, yellow for Ag, and ruby red for Au) quite different with respect to that observed for bulk materials. It should be noted that Ag and Au at nanoscale were already applied in the past to give intense coloration (even at very low concentration) to glasses (yellow or red, respectively), Lycurgus cup is one of the most famous examples for intense coloration (Roman artifact in fourth Century A.D.), and now it is conserved at the British Museum of London. In 1600 Paracelsus described the preparation of "*aurum potabile*" (a ruby red solution) obtained by the reduction of $HAuCl_4$ by alcoholic extract of plants, and 200 years later Michael Faraday (1857) started the first scientific investigation of such colloidal Au solutions. It is now well understood that the origin of the strong coloration of these solutions (or materials like Ag and Au doped glasses) is due to the interaction between light (more generically an electromagnetic wave) and the electronic cloud of the NPs. In particular, the oscillating electric field of the impinging radiation exerts a force that displaces the electronic cloud from nuclei, originating an oscillating net dipole (plasmon) and causing a strong absorption of the light. The energy at which such absorption reaches its maximum (the so-called plasmonic peak) depends on several factors, such as element constitution, size, shape, aggregation state, and the dielectric environment of the NP [13]. In particular, for Cu, Ag, and Au nanospheres ranged from 2 to 70 nm interval, the plasmonic peak falls in the visible region (in the range between 400 and 600 nm). In the recent years, there was an incredible development of nanotechnology [14, 15] and it is now possible to obtain (by adopting several top-down or bottom-up preparation methods) NPs characterized by several shapes (spheres, rods,

triangles, and stars) and size, both in solution and supported/embedded in several materials (e.g., SiO_2) [16].

One important application which is directly derived from the confinement to the nanoscale of these materials, is SERS (Surface Enhanced Raman Spectroscopy). This intriguing technique (able to reach single-molecule sensitivity) originates by the observation that Raman signals of a molecule interacting with a NP (or an aggregate of NPs) are several times more intense if the Raman spectrum is recorded with an exciting laser line with energy matching the plasmonic peak. Without entering deeply into details, it is argued that this effect (the so-called electro-magnetic effect) is reconducible to the light-induced dipole moment in the NP [13].

Another major consequence in decreasing the size of a material to the nanoscale is the increase in the ratio of (surface atoms)/(bulk atoms) increases. In this case, the material acquires some new properties (suggesting that surface atoms are characterized by peculiar features with respect to bulk atoms) with respect to the interaction with the environment. One important example of this is gold in which the bulk phase is well known to be chemically inactive, becoming instead a very active catalyst for several kind of reactions (the most popular being the CO oxidation to CO_2) when prepared as NPs [17].

The fact that properties of surface atoms change with respect to bulk atoms have been well demonstrated by studying MgO NPs by means of absorption (in the diffuse reflectance mode) and photoluminescence UV–Vis spectroscopy, which provided direct information on electronic states peculiar of surface terminations [18, 19]. The surface morphology of these NPs, representative of materials with a high ionic character, results from the intersection of nano {001} planes, which leads to the exposure of five, four, and three-coordinated ions on facelets, whereas in the bulk they are octahedrally six-coordinated. Such surface coordinative unsaturations resulted in an increase in the Lewis acid and basic strength of cations and anions, respectively, progressively increasing as the level of unsaturation increased, with the appearance of a peculiar reactivity toward adsorbed molecules (e.g., heterolytic splitting of H_2, C–H bonds of organic molecules, with the formation of carbanions, nucleophylic attack to CO) [20–22].

12.2 IR Spectroscopy of Adsorbed Probe Molecules

To study the surface sites of nanomaterials, investigation tools sensitive to (1) the nature of surface sites, (2) the oxidation state, and (3) the local structure, are needed to have a chemical and physical "ultra high resolution" [23].

IR spectroscopy of adsorbed probe molecules provides the required structural and qualitative sensitivity to study the nature of powder samples' surface [24, 25]. In particular, the surface sites, having a lower coordination than the bulk ones, are available for the interaction with probe molecules: as a consequence of adsorption,

the spectral features of probe molecules change, indirectly providing information on surface centers [26].

The surface investigation with IR spectroscopy of adsorbed probe molecules requires a proper preparation of the powder samples that are usually compressed in self-supporting pellets and placed in gold frames to hold the samples. The selective adsorption/desorption of molecules can be obtained by inserting the pellets in proper homemade IR cells, equipped with CaF_2 or KBr windows [27].

The IR cells are then connected to a conventional vacuum line (residual pressure $\sim 10^{-5}$ mbar), where both thermal pretreatments and dosing of gas/vapor molecules can be carried out; the as-prepared materials are then ready for the in situ IR measurements of adsorbed probe molecules.

Hereinafter, the use of CO, CD_3CN, and H_2O for in situ *IR spectroscopy* of adsorbed molecules will be reported in order to investigate different nanomaterials' surfaces.

12.2.1 Carbon Monoxide: A Probe Molecule for Surface Lewis Acid Sites

The ideal probe molecule should be (1) small (to avoid sterical hindrance), (2) with spectral features sensitive to the surface state, and the surface should not be modified as a consequence of the interaction with the probe molecule [28]. Possessing all these features, carbon monoxide is one of the most frequently employed molecule for probing the Lewis acid sites exposed at nanomaterials' surface [29].

In Fig. 12.1, a schematic representation of CO, highest occupied molecular orbital (HOMO) and lowest unoccupied molecular orbital (LUMO), is shown.

When CO is adsorbed on the surface cationic centers, its frontier orbitals are perturbed. In particular, the HOMO, because of its slightly antibonding character, the interaction with surface sites causes a stabilization of the entire CO molecule, thus strengthening the carbon–oxygen bond and the CO stretching frequency (νCO) of adsorbed molecule increases with respect to the CO gas one (2,143.16 cm^{-1}). Conversely, when the electronic density is added to the LUMO

Fig. 12.1 CO HOMO and LUMO molecular orbitals
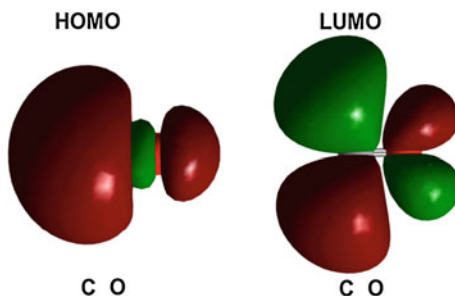
of CO the vCO of adsorbed molecules decreases with respect to the CO gas one, because of the weakening of the C–O bond [26].

Depending on the nature of metal-cation sites exposed at the surface, three different types of CO interactions can be established, which can affect the CO stretching frequency, and are summarized in Table 12.1.

1. *Electrostatic*
   This can be described as an interaction between the surface cation field (like for alkaline metal ions) and the CO charge distribution, and does not imply an electron transfer; the electrostatic interaction causes an increase in the CO stretching frequency than that of CO gas.
2. *σ bond $M^{n+} \leftarrow CO$*
   This kind of interaction is favored for metal ions with empty d orbitals and is established between the HOMO of CO and LUMO of metal ion; the σ bond formation causes a shift to higher frequency with respect to vCO gas.
3. *π bond $M^{n+} \rightarrow CO$*
   When the electron density is transferred from the HOMO (d_{xy}, d_{xz}) of metal ion to the LUMO ($2\pi^*$) of CO, the π back-donation is established. This interaction causes a decrease in the CO stretching frequency.
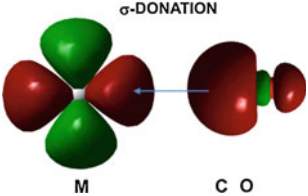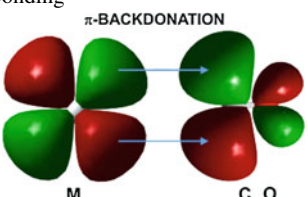
The CO stretching frequency adsorbed on metals with occupied d orbitals is therefore the result of synergic effect of σ bonding and π back-donation [23, 26, 30]. Hence, the kind and the strength of the CO-surface interaction influences the CO

Table 12.1 Effect of CO-surface and adsorbate–adsorbate interactions [23, 26, 30]

CO-surface interactions	Effect on vCO
Electrostatic	Increase
σ bonding	Increase
π bonding	Decrease
Adsorbate–adsorbate interactions	*Effect on vCo*
Dynamic shift	increase with θ
Static shift through space	Increase with θ
Static shift through solid	Decrease with θ

stretching frequency, but it is not the only factor that can cause a shift of the νCO. Indeed, also the interactions among adsorbed oscillators (adsorbate-adsorbate interactions) contribute to the frequency shift and can be of the dynamic and the static type.

The *Dynamic shift* is due to the coupling of vibrating dipoles of adsorbed molecules, parallel to each other. It is experienced only among identical oscillators, with the same stretching frequency, and hence also the same isotopes. The effect of this coupling is a shift of the νCO, with the coverage (θ), to higher frequency than for the isolated adsorbed molecule (singleton) [31].

Static shift. This contribution to the shift includes the following: (1) the interaction through space that is related to the electrostatic interactions of static dipoles and causes a shift of the νCO to higher frequency with θ; (2) the through solid contribution affects the surface centers by the adsorbing influence transmitted though the solid from another site and lowers the stretching frequency with respect to the singleton. The static shift is influenced by the type of solid, the distance between the adsorbed oscillators and the coverage [31].

Proper isotopic mixture of ^{12}CO and ^{13}CO could be used to establish the shift extent [32, 33].

12.2.1.1 IR Spectroscopy of CO Adsorbed on TiO$_2$ P25

Titanium dioxide is widely employed in different fields (1) as photocatalyst for the pollutants abatement [34, 35], (2) for solar energy production [36–38] with Grätzel solar cells [39, 40], or (3) as biomaterial [41].

Concerning the first application, the surface properties of TiO_2 nanomaterials have been proved to play an important role for the photocatalytic activity. Therefore, the disclosure of the surface structure-reactivity relationship represents a fundamental point for understanding and improving the photocatalytic performances.

In particular, several experimental and theoretical studies have been devoted to the surface investigation of TiO_2 P25 (Evonik, formerly Degussa) [33, 42–45], considered a landmark for photocatalytic applications because of its unsurpassed activity in several processes [46]. Among the different spectroscopic methods, IR spectroscopy of adsorbed CO is a useful tool to explore the local structure of sites exposed at the TiO_2 surface.

In Fig. 12.2 the IR spectra of CO adsorbed at 100 K on TiO_2 P25 sample are reported. Before CO adsorption, the sample was thermally treated at 873 K to completely remove H_2O molecules adsorbed and most of the OH groups from the surface [44, 45].

In the IR spectra, obtained for the adsorption of CO at 100 K on TiO_2 P25, several signals can be observed, and most of these spectral features are related to the internal stretching mode of CO (νCO) interacting with the Ti^{4+} surface sites; since their electronic configuration is d^0, only the electrostatic interaction and the σ bond formation with adsorbed CO would be possible.

Fig. 12.2 IR spectra of CO adsorbed at ca. 100 K on TiO$_2$ P25 outgassed at 873 K. Spectra acquired at decreasing coverages (θ), from 45 mbar CO to outgassing for 10 min at ca. 100 K. Adapted from Supporting Information of Ref. [45]
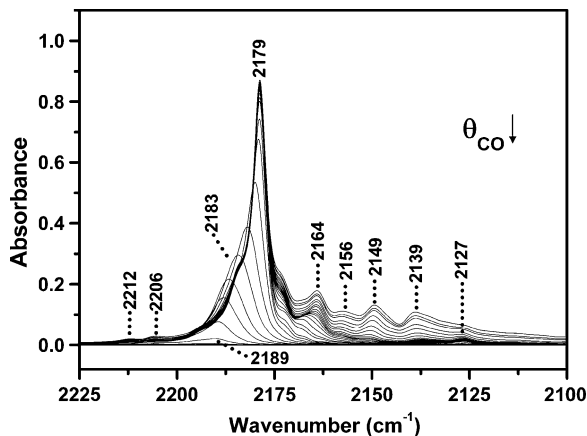
The most intense peak at 2,179 cm^{-1} is related to νCO adsorbed on the five-coordinated Ti^{4+}(Ti$^{4+}_{5c}$) sites exposed at the most abundant facets (101) of the TiO$_2$ P25 NPs. This signal shifts to 2,189 cm^{-1} by decreasing the CO coverage, as a result of the weakening of the adsorbate-adsorbate interactions, of both static and dynamic types. Two other signals are related to the same surface centers: the band at 2,127 cm^{-1}, due to the internal stretching mode of ^{13}CO molecules, present in natural abundance , and experiencing only the static interaction between adsorbed ^{13}CO oscillators; the other weak signal is located at 2,212 cm^{-1}, initially assigned to a combination of νCO and a low-frequency CO-surface mode [43]. Additionally, a shoulder at $\sim$2,183 cm^{-1} can be distinguished, which has been assigned to internal stretching mode of CO molecules adsorbed on Ti$^{4+}_{4c}$ exposed at the (110) facets [45].

The component at 2,206 cm^{-1} shows a lower reversibility than for the main peak with the decrease in the CO coverage, thus indicating a stronger interaction of CO molecules with these surface terminations, assigned to CO adsorbed on cationic sites in low coordination [33, 47, 48].

The component at 2,164 cm^{-1} has been previously associated with (001) surface [47, 49], but our recent theoretical data suggest [45] that the internal stretching mode of CO adsorbed on other surfaces could contribute to this signal. The remaining signals at 2,156 and 2,149 cm^{-1} are due to internal stretching mode of CO adsorbed on residual hydroxy groups and on rutile phase [50], respectively; the sub-band at $\sim$2,139 cm^{-1} is due to CO adsorbed in a liquid-like form [33, 47].

The combination of the IR spectroscopic data, obtained by using CO as molecular probe, with the reactivity studies could be relevant for a deeper knowledge of the photocatalytic processes and for the improvement of the TiO$_2$ photocatalytic performances.

12.2.2 Acetonitrile: A Probe Molecule for Surface Lewis Acid/Base Sites

Acetonitrile has been often used as a specific probe molecule for in situ IR spectroscopic studies, because of its medium-strength Lewis base character, which allows interaction with both hydroxy groups and Lewis acid/base surface sites. For IR spectroscopic measurements of acetonitrile adsorption, the perdeuterated form of acetonitrile (CD_3CN) is used, because in CH_3CN the analytical stretching vibration of the C–N group (the ν_{CN} mode) is split into two components by a Fermi resonance effect [51] that renders the spectra of adsorbed species difficult to read, especially when more than one adsorbed species is formed.

The fundamental vibrations of CH_3CN in the liquid state and their assignments are summarized in Table 12.2 [51].

Acetonitrile is a Lewis base of medium strength (gas phase proton affinity $= 779$ kJ mol^{-1}), which can interact both with hydroxy groups (by H-bonding or, in extreme cases, by proton extraction), and with coordinatively unsaturated (cus) surface cations (by acid–base coordination); [24, 52–54] moreover, acetonitrile can be used to monitor the presence of strongly basic surface centers, yielding reasonably well recognizable surface anionic species [55].

The shift of the $C \equiv N$ stretching vibration frequency is a function of the type of interaction [54, 56, 57]. Nitrogen electron doublet can be used as the base or electron donor. The $\nu(C \equiv N)$ wavenumber increases when electron donor/acceptor complexes $CD_3CN \cdots A$ are formed, A being a Lewis [58, 59] or a Brönsted acid site [60, 61]. With strong Brönsted acids, protonation occurs giving rise to a high $\Delta\nu(C \equiv N)$ shift (~ 75 cm^{-1}), however, still less important than that observed (~ 110 cm^{-1}) when CD_3CN is complexed with carbocations [62].

Deuterium atoms of CD groups in α of the $C \equiv N$ bond, as those of the methyl group of acetonitrile, present a proton donor character, in such a way that the formation of the CD_2CN^- carbanion can be observed from the breaking of a C-D bond. On a metal oxide, the following reaction can occur:

$$O^{2-}(surf) + CD_3CN \rightarrow OD^-(surf) + CD_2CN^-(ads) \qquad (12.1)$$

Table 12.2 IR bands of liquid CH_3CN and their assignments (Adapted from [51])

Description	Designation	Symmetry species	Wavenumber/cm^{-1}
Symmetric **C–H** stretching	ν_1	A$_1$	2,942
C $\equiv$ **N** stretching	ν_2	A$_1$	2,254
Symmetric **CH$_3$** deformation	ν_3	A$_1$	1,375
C–C stretching	ν_4	A$_1$	914
Antisymmetric **CH$_3$** deformation	ν_5	E	1,442
Antisymmetric **C–H** stretching	ν_6	E	3,001
CH$_3$ rocking	ν_7	E	1,047
C–C $\equiv$ **N** bending	ν_8	E	380
	$\nu_3 + \nu_4$	A$_1$	2,292

The reaction involves the acid/base character of the OD/O^{2-} and CD_3CN/CD_2CN^- couples; moreover, it requires the participation of cationic adsorption sites to stabilize the CD_2CN^- carbanion.

The $\nu(C \equiv N)$ wavenumber of the carbanion characterizes the cationic site; as an example, on ZnO [63], it is at 2,121 cm^{-1}, on MgO, at 2,190 cm^{-1}; [64] on CeO_2 it depends on the state of the adsorption site: 2,098 (Ce^{4+}) or 2,028 cm^{-1} (Ce^{3+}).

CH_2CN^- can be also solvated by a CH_3CN molecule. The characteristic wave numbers of CH_2CN^- (CH_3CN) complex are $\nu(NH) = 3,260$ cm^{-1} and $\nu(C \equiv N) = 2,110$ cm^{-1} [65].

Another type of species can result from the acetonitrile interaction with hydroxy groups: it is of the acetamide type. Therefore, on basic sites, adsorption of CH_3CN leads either to the amide or to the CH_2CN^- species formation.

12.2.2.1 IR Spectroscopy of CD$_3$CN Adsorbed on Bioactive Glasses

Bioactive glasses are silica-based glassy systems that are used for biomedical applications, mostly as bone prostheses. When bioactive glasses are immersed in a physiological solution, they can induce the deposition on their surface of a layer of hydroxycarbonate apatite (HCA), a mineral phase quite similar to the one that bones are actually made of [66]. To understand the nature of surface sites active in HCA deposition, the study of the availability of surface hydroxy groups and/or basic/acid centers is a crucial factor that determines bioactive glasses reactivity, since some surface functional groups and/or cations are likely to be sites for HCA deposition. For this reason, the adsorption/desorption of a highly specific probe molecule, like acetonitrile, in order to characterize the surface of two sol–gel bioactive glasses (named 58S and 77S) was resorted to [67]. 58S glass is made of 60 % SiO_2, 36 % CaO, and 4 % P_2O_5 whereas the chemical composition of 77S glass is 80 % SiO_2, 16 % CaO, and 4 % P_2O_5 (data are reported as % mol).

In Fig. 12.3a the adsorption isotherms on bioactive glasses activated at 573 K are shown.

The IR spectral patterns reported in Fig. 12.3a, clearly indicate that CD_3CN is able to interact with bioactive glasses in different ways. In particular, pattern (a) relative to CD_3CN uptake on 58S shows that the first nitrile dose (~ 1 mbar) generates two bands centered at $\sim 2,286$ and $\sim 2,275$ cm^{-1}, respectively. The bands correspond to the νCN mode of CD_3CN involved in a medium–strong coordinative interaction with Lewis acid sites and in a weaker H-bonding interaction with surface OH species. On the basis of the composition of bioactive glass 58S, it seems quite obvious that the only surface species that can act as Lewis acid centers are surface exposed cus Ca^{2+} cations.

Further, CD_3CN admissions induce intensity changes in the mentioned bands and eventually yield an additional band at $\sim 2,266$ cm^{-1}. The latter band, which is present at first only as a shoulder and becomes clearly visible when a pressure close to half the vapor pressure of the adsorptive ($p^0 \sim 100$ mbar at 298 K) is allowed to reach equilibrium, corresponds to the formation at the surface of the bioactive glass
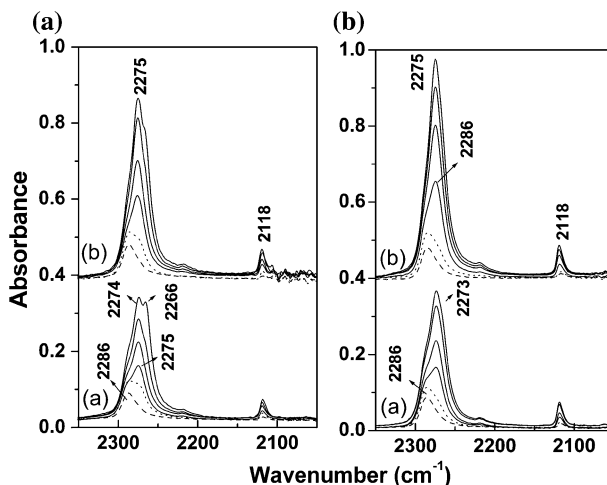
Fig. 12.3 CD_3CN adsorption/evacuation on bioactive glasses activated 1 h at 573 K (**a**) and at r.t. (**b**). All absorbance spectra are presented as differentials, (normalized against the background spectrum of the corresponding bare bioactive glass). *Solid-line* spectra: adsorption of successive doses (1–30 Torr) of CD_3CN on 58S (spectral sets a) and on 77S (spectral sets b); *dotted-line* spectra: after d3- CD_3CN evacuation at r.t. for 1 min; *broken-line* spectra: after CD_3CN evacuation at r.t. for 30 min (Adapted from [67])

of a liquid-like CD_3CN (physisorbed) phase. The weak band observed in all spectra at $\sim 2,118$ cm^{-1} is due to the $\nu_s(CD_3)$ mode of CD_3CN and, being virtually insensitive to the type of solid–gas interaction, it is somehow representative of the total amount of adsorbed CD_3CN. Outgassing at room temperature (r.t.) causes, as expected not only both, the removal of the liquid-like phase, and a decrease in the H-bonded species, but also after prolonged evacuation, part of the Lewis-interacting species absorbing at $\sim 2,286$ cm^{-1} persists on the surface.

Spectral set (b) in the upper part of Fig. 12.3a indicates that, upon CD_3CN adsorption/desorption on bioactive glass 77S treated at 573 K, only minor differences of band relative intensities are noted in the νCN spectral region with respect to 58S. In spite of the difficulty of obtaining weak differential spectra in the lower frequency regions (1,700–1,300 cm^{-1}), due to the presence of Si–O overtone/combination bands and of bands due to surface carbonate-like species, no clear evidence for the formation of new species was ever obtained during the CD_3CN adsorption/evacuation process on the bioactive glasses activated at 573 K. In that spectral region, various CD_3CN hydrolysis products (like, for instance, acetamide or acetate anions), and/or various anionic dehydrogenation products are known to be present. The formation of all these species is known to be catalyzed by basic surface sites. From the absence of evident absorptions in the low ν region, it is deduced that the presence on bioactive glass surface of some cus Ca^{2+} ions is not sufficient per se to induce the presence of basic anionic centers (OH$^-$, O^{2-}) capable of transforming spectroscopically appreciable amounts of coordinated CD_3CN into anionic reaction products.

In order to investigate whether, and to what extent, nitrile uptake on bioactive glasses may depend on the surface dehydration degree, similar CD_3CN adsorption/ desorption experiments were also run on the two bioactive glass specimens after a plain vacuum activation at room temperature. In this respect, it is important to recall that bioactive glasses are bound to operate in vitro in contact with aqueous solutions with a fully hydrated surface.

Figure 12.3b shows that all main vCN peaks, observed on samples treated at 573 K, are still present at virtually coincident frequencies on samples treated at room temperature. In particular, it is noted that: (1) on both bioactive glasses, there is an early formation of a vCN band at ~2,286 cm^{-1}, due to Lewis-coordinated CD_3CN. The vCN band at ~2,286 cm^{-1} resists evacuation at r.t. with only a moderately decreased intensity; (2) only on sample 58S activated at r.t. (set a of Fig. 12.3b), the vCN peak relative to CD_3CN adsorption on hydroxy groups seems to be shifted to marginally lower v (~2,273 cm^{-1}). More importantly, for both 58S and 77S, the band of H-bonded CD_3CN turns out to be definitely more intense with respect to the band due to CD_3CN coordinated to Lewis acid sites (~2,286 cm^{-1}); (3) on both bioactive glasses activated at r.t., the band at ~2,267 cm^{-1} ascribed to physisorbed nitrile is hardly visible, also under high adsorptive pressures. The latter two aspects can be easily explained if it is considered that, at r.t., the process of surface dehydroxylation has not begun yet, whereas that process certainly occurs to some extent at 573 K. This means that, after treatment at r.t., more hydroxyl-bearing species are present at the surface, and thus, the ~2,275 cm^{-1} vCN band due to H-bonded species is bound to be more intense. At the same time, a higher surface concentration of OH groups implies the presence of a higher concentration of specific adsorptionn sites for CD_3CN uptake, so that the formation of a liquid-like CD_3CN phase at nonspecific sites (vCN band at ~2,267 cm^{-1}) will be less favored.

From these data it is possible to conclude that Ca^{2+} cations are present at the surface of bioactive glasses, and are readily available for a Lewis acid–base interaction with bases (of medium strength). This derives from the fact that (most of the) surface Ca^{2+} cations, not involved in the formation of stable surface carbonate-like species, are preferably "screened" by coordinated water molecules that can be displaced ligand by bases as strong as acetonitrile. This means that surface Ca^{2+} cations are available for interaction with many Lewis-basic species that they can come into contact with when immersed in a physiological solution.

12.2.3 Adsorbed Water Molecules: Study of Water Structure at the Surface

Water adsorption on the surface of finely divided materials has been the objective of IR studies, since the research works were carried out in the field of surface science of high surface area materials [68].

Many efforts have been taken to study the state of adsorbed water on different oxide surfaces, with the use of IR transmission and reflectance spectroscopy [68]. However, in most of these studies, the interest was focused on the first layer of water molecules directly interacting with solid surface, conversely less attention was paid to the investigation of multilayers formation. The careful control of the amount of adsorbed or desorbed water vapor with in situ *IR spectroscopy* is a powerful tool to investigate not only the nature and surface structure of solids with high specific surface area (SSA), but also the structure of water adlayers, which play an important role in interfacial phenomena in biomedical applications [69]. In the MIR region, two fundamental H_2O vibrations are observed, i.e., OH-stretching (νOH) and H_2O bending (δH_2O) modes. In the case of water-surface interaction, the shift in frequency of the previously mentioned water vibrational modes, with respect to H_2O liquid-like state, can give very important information about hydrogen bond donor and acceptor behavior and about the strength of the coordinative bond with adsorbing sites [70]. Concerning the $\delta(H_2O)$ mode, when a water molecule interacts through the oxygen atom with surface cations or acts as an H-bond acceptor, the $\delta(H_2O)$ is shifted to lower wavenumber; conversely, when it acts as H-bond donor, the $\delta(H_2O)$ is blue-shifted: hence, the water-bending frequency is the result of both contributions. For this reason, the information that can be obtained from the analysis of this vibrational mode might be equivocal and the combined effects of strong H-bond and coordinative interactions could lead to $\delta(H_2O)$ unshifted frequency. On the other hand, the frequency variation of the OH-stretching mode mainly depends on the strength of the H-bond: stronger the hydrogen bond, lower the νOH frequency. The study of this feature is the main aim of the IR investigation of the interactions that water molecules experience at the surface dependent on the coverage. Moreover, a quantitative evaluation of the amount of adsorbed water molecules at the nanomaterials surface is also possible.

12.2.3.1 IR Spectroscopy of Water Adsorbed on HA

HA is the main component of hard tissues such as bones and teeth of vertebrate animals and humans. Consequently HA is readily considered as a bioactive material for artificial bone substitution because of its biocompatibility and chemical and biological affinity with bony tissue [71]. In vivo biomineralization process is an organized assembly of organic macromolecules that regulate nucleation, growth, morphology and aggregation of inorganic NPs of calcium phosphates [72]. To mimic the native tissue architecture, several crystals parameters must be controlled such as: size, chemical composition, morphology, and surface structure. At present, there is a great variety of methods designed to reproduce nano-HA [73]. When HA NPs are in contact with the biological environment they first interact with water molecules that are the main component of the body fluid. Further, when a biomolecule converges towards HA NPs surface, it should surmount the barrier of water layers initially surrounding the HA NPs as a

shell. Thus, in order to achieve a good osseointegration of HA NPs to native tissue, the HA NPs surface and hydration must be investigated.

Here, the results of IR spectroscopic studies of adsorbed H_2O molecules from vapor phase at the surface of HA crystalline NPs are reported.

Figure 12.4a shows the spectra of HA in the presence of 20 mbar of H_2O vapor (curves a), after outgassing at b.t. (curves b), and after the outgassing step at the end of a series of D_2O adsorption/desorption cycles (curves c). The low-frequency region of the displayed spectral range was limited to 1,350 cm^{-1} and this value is the onset of the cutoff due to the fundamental absorptions of the lattice phosphate groups.

The absorbance bands are assigned as follows.

1. Overtone and combination modes of the fundamental phosphate absorptions produced the 2,200–1,900 cm^{-1} weak pattern. Another signal due to bulk species is the sharp peak at 3,570 cm^{-1}, due to the stretching of OH^- groups and arranged to form like "columns" in the bulk. The set of components in the 1,550–1,350 cm^{-1} range is related to the stretching modes of carbonate groups [74]. Such components exhibited some change in shape and relative intensity depending on the amount of adsorbed water, indicating that part of the carbonate groups was located at the surface.
2. Adsorbed water molecules were responsible for the band at 1,642 cm^{-1} (δH_2O) and most part of the complex absorption in the 3,500–2,500 cm^{-1} range, resulting from the superposition of the lattice (in phase) and surface (out of phase) H_2O stretching bands as well as the stretching of surface and bulk
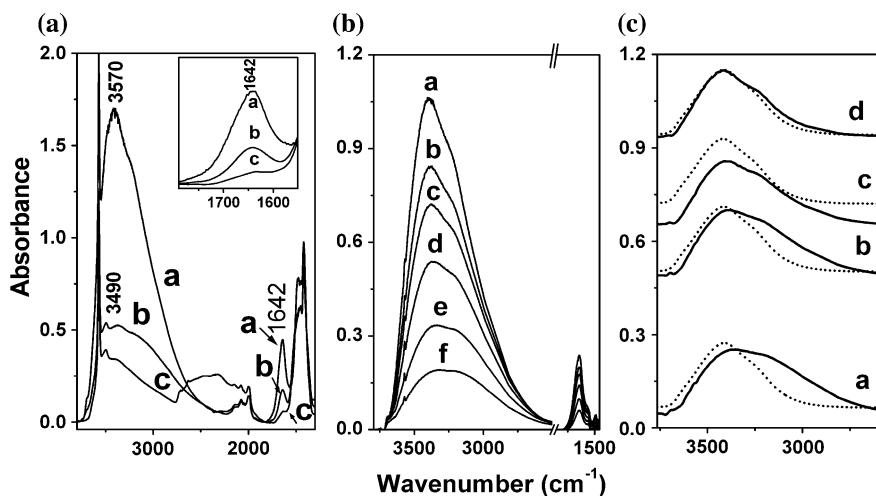
Fig. 12.4 IR spectra of HA section (**a**) "*a*" in the presence of 20 mbar of H_2O, "*b*" after 60 min of outgassing at b.t., "*c*" after exchange with D_2O and subsequent 60 min of outgassing at b.t.. Spectra in section (**b**) were obtained by subtracting the spectrum "*c*" section (**a**) from those collected at interim increment of decreasing H_2O coverage from "*a*" to "*b*". Results of spectra subtraction in section (**b**) "*c*"-"*d*", "*b*"-"*c*" and "*a*"-"*b*" are reported in section (**c**). (Section **a**: adapted from [74]; section **b** and **c** adapted from [75])

hydroxy groups involved in H-bonding. Passing from the presence of 20 mbar of water vapor (curves a section a) to vacuum (by outgassing at b.t., curve b section a), the amount of adsorbed H_2O was decreased from a multilayer state (also exposing dangling $-OH$, responsible for the very weak signal at 3,695 cm^{-1} [70] to a hydration layer constituted by isolated molecules left adsorbed on surface cations through a coordinative interaction.

3. After subsequent exchange with D_2O, followed by outgassing at b.t. (curve c section a), a weak component due to the bending mode of H_2O molecules entrapped in the bulk was observed. The stretching modes of these molecules contributed to a part of the broad and asymmetric absorption spread over the 3,500–2,500 cm^{-1} range, which contained the signal due to bulk hydroxy groups involved in hydrogen bonding as well. The broad band in the 2,800–2,000 cm^{-1} range was due to the stretching mode of surface -OD groups and adsorbed D_2O molecules, whereas band related to the bending mode of these latter, expected at $\sim$1,200 cm^{-1}, was outside the transparency window of the materials.

To obtain the information related to the interface water only, the spectrum "c" (Fig. 12.4 section a) was subtracted from series of spectra at increasing coverage (not shown), and results are reported in Section b. In order to avoid negative band at vOD range, the contribution of vOD-stretching mode was mathematically simulated and then subtracted allowing further treatment of data elaboration; such performance allows distinguishing the OH vibrations in a bulk from those organized at/over HA surface. The resulting absorption spectra of water layers are shown in Fig. 12.4 Section b. At low coverage, where only H_2O molecules in direct contact with the surface are present, a very broad band extended over the 3,700–2,600 cm^{-1} spectral range and centered at about 3,300 cm^{-1} can be observed. As the coverage increases, the band appears to be structured in two components (centered at $\sim$3,400 and 3,200 cm^{-1}, respectively). Their relative intensity shows significant difference increasing the coverage.

The analysis of the data shown in (Section b) was refined in order to relate the evolution of the spectral profiles with the number of H_2O molecules adsorbed per surface Ca^{2+} cations. To this aim, on the basis of the correspondence between the integrated intensity of the δH_2O band, amount of adsorbed water per nm^2 and number of Ca^{2+} ions per nm^2 [75], spectra corresponding to 1, 2, 3, 4 H_2O molecules per surface Ca^{2+} cation were selected. Thus, the contributions due to the second, third, and fourth water molecule per cationic site were obtained by subtracting the spectra corresponding to n H_2O molecules/Ca^{2+} (n = 1–3) from those related to n + 1 H_2O molecules/Ca^{2+} cation. The results of spectra elaboration are reported in Section c. The $v(H_2O)$ band appeared significantly broader at low water coverage, indicating the occurrence of stronger H-bonding among water molecules adsorbed on cations. Thus, the full set of data suggests the following picture:

1. H_2O molecules in direct contact with the surface, forming the first hydration layer, are apart enough from each other for preventing intermolecular interactions/structuring;

2. When additional H_2O molecules are adsorbed, they interact with the first hydration layer, exhibiting a pattern of the underlying surface. Such a pattern affects the H-bonding network progressively built-up, then "transmitting" to the multilayer an "imprinting" dependent on the surface structure of HA.

The next step in analyzing the spectra was the attainment of a quantitative evaluation of water molecules adsorbed at the surface, comparing the integrated intensity of water-bending mode, obtained for the sample here described, with the quantitative data resulting from a combined IR spectroscopic and microgravimetric analysis on another HA sample previously investigated.

To this aim, all acquired spectra were normalized both to the intensity of the 2,200–1,900 cm^{-1} pattern due to overtone and combination modes of bulk phosphates (to refer to the spectra to the same amount of sample) and to the SSA (to refer to the spectra to the same surface extension) so that, in the resulting spectra, differences in intensity should reflect actual differences in the amount of surface hydration species. Then the spectrum obtained after complete isotopic exchange (Fig. 12.4 Section a curve c) was subtracted as a background from those recorded in the presence of water vapor pressure (w.v.p.) and outgassed one (Fig. 12.4 curves a, b section a). This process produced patterns that contained only signals due to surface hydration species, i.e., water molecules and hydroxy groups. Because the δH_2O bands in the 1,750–1,550 cm^{-1} range were due to H_2O only, their integrated intensity was unequivocally related to the amount of adsorbed water molecules. In a previous study [76], the combination of IR and microgravimetric data allowed to evaluate the number of H_2O molecules coordinated to surface cations after outgassing at b.t. ($\sim$4.5/nm^2) [76]. The proportionality between the number of water molecules per surface unit and the integrated intensity of the δH_2O band was then established. On this basis, the amount of water adsorbed in multilayers (in the presence of 20 mbar of H_2O vapor) and those coordinated to surface cations after outgassing at b.t. was 12.2 and 3.7 molecules/nm^2 respectively. It is interesting to note that the coverage of $\sim$4.5 H_2O molecules/nm^2 for material described in Reference [76] should correspond to the occupancy of each surface Ca^{2+} ions by one water molecule.

The IR study of H_2O adsorbed on HA NPs allowed to establish that not only the first layer but also the multilayers of adsorbed H_2O are influenced by the surface structure; this has a fundamental role in the prediction/investigation of the interactions occurring at the biomaterial/biological fluids interface.

12.3 Conclusions

The collection of examples reported here proved that IR spectroscopy can be effectively employed to investigate the interaction of nanomaterials surfaces and molecules, leading to unique information on their surface structure and interfacial behavior. A synergistic combination of the results of this kind of investigation with

those provided by other complementary techniques (Raman and UV–Vis spectroscopies, X-Ray powder diffraction, high resolution transmission electron microscopy, SSA and porosity measurements) and by reactive/catalytic studies, could actually represent a source of innovative knowledge to refine and/or disclose the links among nanomaterials design, synthesis/preparation, and expected surface functional behavior. If it is successful, this integrated approach could represent a significant step toward the frontier of precisely tailored and highly effective nanomaterials.

References

1. Taniguchi N (1974) On the basic concept of 'nano-technology', Japan Society of Precision Engineering
2. Chen X, Mao SS (2007) Titanium dioxide nanomaterials: Synthesis, properties, modifications, and applications. Chem Rev 107:2891
3. Zhou ZY, Tian N, Li JT, Broadwell I, Sun SG (2011) Nanomaterials of high surface energy with exceptional properties in catalysis and energy storage. Chem Soc Rev 40: 4167
4. Weintraub B, Zhou ZZ, Li YH, Deng YL (2010) Solution synthesis of one-dimensional ZnO nanomaterials and their applications. Nanoscale 2:1573
5. Alberto G, Caputo G, Viscardi G, Coluccia S, Martra G (2012) Molecular engineering of hybrid dye-silica fluorescent nanoparticles: influence of the dye structure on the distribution of fluorophores and consequent photoemission Brightness. Chem Mat 24:2792
6. Murphy CJ, Gole AM, Stone JW, Sisco PN, Alkilany AM, Goldsmith EC, Baxter SC (2008) Gold nanoparticles in biology: beyond toxicity to cellular imaging. Accounts Chem Res 41:1721
7. Laurent S, Forge D, Port M, Roch A, Robic C, Elst LV, Muller RN (2008) Magnetic iron oxide nanoparticles: synthesis, stabilization, vectorization, physicochemical characterizations, and biological applications. Chem Rev 108:2064
8. Vallet-Regi M, Colilla M, Izquierdo-Barba I (2008) Bioactive mesoporous silicas as controlled delivery systems: application in bone tissue regeneration. J Biomed Nanotechnol 4:1 and references therein
9. Cabane E, Zhang XY, Langowska K, Palivan CG, Meier W (2012) Stimuli-responsive polymers and their applications in nanomedicine. Biointerphases 7:1
10. Cardoso DA, Jansen JA, Leeuwenburgh SCG (2012) Synthesis and application of nanostructured calcium phosphate ceramics for bone regeneration. J Biomed Mat Res B 100B:2316
11. Damin A, Usseglio S, Agostini G, Bordiga S, Zecchina A (2008) Au nanoparticles as SERS probes of the silica surface layer structure in the absence and presence of adsorbates. J Phys Chem C 112:4932
12. Budnyk AP, Damin A, Agostini G, Zecchina A (2010) Gold nanoparticle aggregates immobilized on high surface area silica substrate for efficient and clean SERS applications. J Phys Chem C 114:3857
13. Aroca R (2006) "Surface-Enhanced Vibrational Spectroscopy", Wiley, Chichester, Ch. 6
14. Pastoriza-Santos I, Alvarez-Puebla RA, Liz-Marzan LM (2010) Synthetic routes and plasmonic properties of noble metal nanoplates. Eur J Inorg Chem 2010:4288
15. Daniel MC, Astruc D (2004) Gold nanoparticles: assembly, supramolecular chemistry, quantum-size-related properties, and applications toward biology, catalysis, and nanotechnology. Chem Rev 104:293

16. Guerrero-Martinez A, Perez-Juste J, Liz-Marzan LM (2010) Recent progress on silica coating of nanoparticles and related nanomaterials. Adv Mater 22:1182
17. Stratakis M, Garcia H (2012) Catalysis by supported gold nanoparticles: beyond aerobic oxidative processes. Chem Rev 112:4469
18. Garrone E, Zecchina A, Stone FS (1980) An experimental and theoretical evaluation of surface states in MgO and other alkaline earth oxides. Phil Mag B 42:683
19. Coluccia S (1985) Surface structure and energy transfer on oxides investigated by photoluminescence spectroscopy. In: Che M, Bond GC (eds) Adsorption and catalysis on oxides surfaces, Elsevier, Amsterdam, p 59
20. Coluccia S, Boccuzzi F, Ghiotti, G, Morterra C (1982) Infrared study of hydrogen adsorption on MgO, CaO and SrO. Possible mechanism in promoting O–2 formation. J Chem Soc Faraday Trans 1 78:2111
21. Zecchina A, Coluccia S, Spoto G, Scarano D, Marchese L (1990) Revisiting MgO-CO Surface-Chemistry—an IR investigation. J Chem Soc Faraday T 86:703
22. Coluccia S, Chiorino A, Guglielminotti E, Morterra C (1979) Adsorption of 2,2'-bipyridyl on magnesium oxide and calcium oxide. Infrared spectra of neutral and anionic surface species. J Chem Soc Faraday Trans 1 75:2188
23. Marchese L, Martra G, Coluccia S (1997) Microcrystalline materials characterized by infrared spectroscopy. In: Catlow CRA, Cheetham A (eds) New trends in materials chemistry, Kluwer Academic Press, New York
24. Busca G (1998) Spectroscopic characterization of the acid properties of metal oxide catalysts. Catal Today 41:191
25. Busca G (2009) The use of infrared spectroscopic methods in the field of heterogeneous catalysis by metal oxides. In: Jackson D, Hargreaves JSJ (eds) Metal oxide catalysis, vol. 1. Wiley Weinhein, Germany, pp 95–175
26. Hadjiivanov KI, Vayssilov GN (2002) Characterization of oxide surfaces and zeolites by carbon monoxide as an IR probe molecule. Adv Catal 47:307–511
27. Morterra G, Aina V, Sakhno Y, Bertinetti L, M. C (2012) Surface characterization of inorganic nanobiomaterials at a molecular scale: use of vibrational spectroscopies. In: Surface tailoring of inorgainc materials for biomedical applications Rimondini L, Bianchi B, Verné E (eds) Bentham E-books, Oxford
28. Kustov LM (1997) New trends in IR-spectroscopic characterization of acid and basic sites in zeolites and catalysts. Top Catal 4:131
29. Yates JT (1994) Chemisorption on surfaces—an historical look at a representative adsorbate - carbonmonoxide. Surf Sci 299:731
30. Lamberti C, Zecchina A, Groppo E, Bordiga S (2010) Probing the surfaces of heterogeneous catalysts by in situ IR spectroscopy. Chem Soc Rev 39:4951
31. Platero EE, Scarano D, Zecchina A, Meneghini G, DeFranceschi R (1996) Highly sintered nickel oxide: surface morphology and FTIR investigation of CO adsorbed at low temperature. Surf Sci 350:113
32. Morterra C, Bolis V, Fubini B, Orio L, Williams TB (1991) A FTIR and HRTEM study of some morphological and adsorptive properties of monoclinic ZrO2 microcrystals. Surf Sci 251:540
33. Spoto G, Morterra C, Marchese L, Orio L, Zecchina A (1990) The morphology of TiO_2 microcrystals and their adsorptive properties towards CO—a HRTEM and FTIR study. Vacuum 41:37
34. Henderson MA (2011) A surface science perspective on TiO_2 photocatalysis. Surf Sci Rep 66:185–297
35. Hoffmann MR, Martin ST, Choi WY, Bahnemann DW (1995) Environmental applications of semiconductor photocatalysis. Chem Rev 95:69–96
36. Bowker M (2011) Sustainable hydrogen production by the application of ambient temperature photocatalysis. Green Chem 13:2235–2246
37. Fujishima A, Zhang XT, Tryk DA (2008) TiO_2 photocatalysis and related surface phenomena. Surf Sci Rep 63:515–582

38. Matsuoka M, Kitano M, Takeuchi M, Tsujimaru K, Anpo M, Thomas JM (2007) Photocatalysis for new energy production - recent advances in photocatalytic water splitting reactions for hydrogen production. Catal Today 122:51–61
39. Grätzel M (2001) Photoelectrochemical cells. Nature 414:338
40. Grätzel M, Photoch J (2003) Dye-sensitized solar cells. Photobio C 4:145
41. Sittig C, Textor M, Spencer ND, Wieland M, Vallotton PH (1999) Surface characterization of implant materials cp Ti, Ti-6Al-7Nb and Ti-6Al-4V with different pretreatments. J Mater Sci-Mater M 10
42. Martra G (2000) Lewis acid and base sites at the surface of microcrystalline TiO_2 anatase: relationships between surface morphology and chemical behaviour. App Catal A-Gen 200:275
43. Minella M, Faga MG, Maurino V, Minero C, Pelizzetti E, Coluccia S, Martra G (2010) Effect of fluorination on the surface properties of titania P25 powder: an FTIR study. Langmuir 26:2521
44. Deiana C, Fois E, Coluccia S, Martra G (2010) Surface structure of TiO_2 P25 nanoparticles: infrared study of hydroxy groups on coordinative defect sites. J Phys Chem C 114:21531
45. Deiana C, Minella M, Tabacchi G, Maurino V, Fois E, Martra G (2013) Shape-controlled TiO_2 nanoparticles and TiO_2 P25 interacting with CO and H_2O_2 molecular probes: a synergic approach for surface structure recognition and physico-chemical understanding. Phys Chem Chem Phys 15:307
46. Ryu J, Choi W (2008) Substrate-specific photocatalytic activities of TiO_2 and multiactivity test for water treatment application. Environ Sci Technol 42:294
47. Hadjiivanov K, Lamotte J, Lavalley JC (1997) FTIR study of low-temperature CO adsorption on pure and ammonia-precovered TiO_2 (anatase). Langmuir 13:3374
48. Morterra C (1988) An infrared spectroscopic study of anatase properties. J Chem Soc Faraday Trans 1 84:1617
49. Hadjiivanov KI, Klissurski DG (1996) Surface chemistry of titania (anatase) and titania-supported catalysts. Chem Soc Rev 25:61
50. Mino L, Spoto G, Bordiga S, Zecchina A (2012) Particles morphology and surface properties as investigated by HRTEM, FTIR, and periodic DFT calculations: from pyrogenic TiO_2 (P25) to nanoanatase. J Phys Chem C 116:17008
51. Knozinger H, Krietenbrink H (1975) Infrared spectroscopic study of the adsorption of nitriles on aluminium oxide. Fermi resonance in coordinated acetonitrile. J Chem Soc Faraday Trans 71:2421
52. Sempels RE, Rouxhet PG (1976) Infrared study of the adsorption of benzene and acetonitrile on silica—alumina gels: acidity properties and surface heterogeneity. J Colloid Interface Sci 55:263
53. Pelmenschikov AG, Vansanten RA, Janchen J, Meijer E (1993) CD_3CN as a probe of Lewis and Bronsted Acidity of Zeolites. J Phys Chem 97:11071
54. Chen JS, Thomas JM, Sankar G (1994) IR spectroscopic study of CD_3CN adsorbed on Alpo-18 molecular-sieve and the solid acid catalysts Sapo-18 and Meapo-18. J Chem Soc Faraday T 90:3455
55. Aboulayt A, Binet C, Lavalley JC (1995) IR study of acetonitrile adsorption on hydroxylated zirconium zioxide—mechanism of acetonitrile hydrolysis. J Chem Soc Faraday T 91:2913–2920
56. Pelmenschikov AG, Morosi G, Gamba A, Coluccia S, Martra G, Paukshtis EA (1996) Single and multiple Lewis sites of MgO: a combined IR and ab initio study with CD_3CN as a molecular probe. J Phys Chem 100:5011
57. Janchen J, Peeters MPJ, Anwolput MHMC, Wolthuizen JP, Vanhooff JHC, Lohse U (1033) CoApo molecular-sieve acidity investigated by adsorption calorimetry and IR spectroscopy. J Chem Soc Faraday T 1994:90
58. Angell C, Howell M (1969) Infrared spectroscopic investigation of zeolites and adsorbed molecules. IV. Acetonitrile. J Phys Chem A 73:2251

59. Purcell K (1967) An Investigation into the Source of C[UNK]N Vibrational Frequency Shifts. J Am Chem Soc 89:247
60. Eaton G, Pena-Numez A, Symons M (1988) Solvation of cyanoalkanes [CH_3CN and $(CH_3)_3CCN$]. An infrared and nuclear magnetic resonance study. J Chem Soc Farad Trans 1:2181
61. Olah G, Kiovsky T (1968) Stable carbonium ions. LXV. Protonation of hydrogen cyanide and alkyl nitriles in FSO_3HSbF5- SO2 solution. Comparative study of Meerwein's N-alkylnitrilium ions. J Am Chem Soc 90:4666
62. Bystrov DS (1992) A usual explanation of the unusual mechanism of Lewis acidity manifestation in Hzsm-5 zeolites. Zeolites 12:328
63. Lavalley, JC (1996) Infrared spectrometric studies of the surface basicity of metal oxides and zeolites using adsorbed probe molecules. Catalysis Today 27:377
64. Koubowetz F, Latzel J, Noller H, Colloid J (1980) Adsorption of acetonitrile on magnesia, an IR and TPD study. Interf Sci 74:322
65. Buchel E, Durot T (1980) Comprehensive carbanion chemistry. Elsevier, Amsterdam
66. Hench LL (2006) The story of Bioglass ®. J Mater Sci-Mater M 17:967
67. Cerruti M, Bolis V, Magnacca G, Morterra C (2004) Surface chemical functionalities in bioactive glasses. The gas/solid adsorption of acetonitrile. Phys Chem Phys 6:2468
68. Takeuchi M, Bertinetti L, Martra G, Coluccia S, Anpo M (2006) States of H_2O adsorbed on oxides: an investigation by near and mid infrared spectroscopy. Appl Catal a-Gen 307:13
69. Jena KC, Hore DK (2010) Water structure at solid surfaces and its implications for biomolecule adsorption. Phys Chem Phys 12:14383
70. Takeuchi M, Martra G, Coluccia S, Anpo M (2005) Investigations of the structure of H_2O clusters adsorbed on TiO_2 surfaces by near-infrared absorption spectroscopy. J Phys Chem B 109:7387
71. Dorozhkin SV (1975) Nanodimensional and nanocrystalline apatites and other calcium orthophosphates in biomedical engineering, biology and medicine. Materials 2009:2
72. Nakamoto K (1970) Infrared spectra of inorganic and coordination compounds, 2nd edn. Wiley, New York
73. Delgado-Lopez JM, Iafisco M, Rodriguez I, Tampieri A, Prat M, Gomez-Morales J (2012) Crystallization of bioinspired citrate-functionalized nanoapatite with tailored carbonate content. Acta Biomater 8:3491
74. Sakhno Y, Bertinetti L, Iafisco M, Tampieri A, Roveri N, Martra G (2010) Surface hydration and cationic sites of nanohydroxyapatites with amorphous or crystalline surfaces: a comparative study. J Phys Chem C 114:16640
75. Bolis V, Busco C, Martra G, Bertinetti L, Sakhno Y, Ugliengo P, Chiatti F, Corno M, Roveri N (2012) Coordination chemistry of Ca sites at the surface of nanosized hydroxyapatite: interaction with H_2O and CO. Philos T R Soc A 370:1313
76. Bertinetti L, Tampieri A, Landi E, Ducati C, Midgley PA, Coluccia S, Martra G (2007) Surface structure, hydration, and cationic sites of nanohydroxyapatite: UHR-TEM, IR, and microgravimetric studies. J Phys Chem C 111:4027

Chapter 13
Method to Produce Suspensions Using Encapsulated Nanopowders of 3-d Metals as Precursors

Kira V. Liapina, Peter G. Dulnev, Andrej I. Marinin, Tatyana V. Melnichenko and Anatolii I. Ustinov

13.1 Introduction

Highly dispersed and nanostructured metal containing materials are widely applied in various fields of engineering, including development and manufacture of electronic and optoelectronic instruments and devices, manufacture of composite materials for various applications, current conducting adhesives, sealants, films, protective lacquer paint coatings, and shields for protection from various environmental factors (corrosion, electromagnetic fields, and ionizing radiation), in chemical industry, in membrane and catalytic technologies, in biomedical, pharmaceutical, sensor, analytical and diagnostic technologies, in manufacture of finishing agents, and in other fields.

It is known that with reduction of characteristic dimensions of materials to the nanolevel, material properties can undergo essential changes. One of the main causes for these changes is a large specific surface and, therefore, high energy activity of both the individual particles, and their ensembles, owing to a considerable area of interfaces, that leads to appearance of new properties, important for practical application [1–6]. In practical terms, the most important is preservation of properties of nanomaterials in time, namely, stabilization of the dimensions and phase composition of nanoparticles and their ensembles. Such stabilization can be achieved both by creation of protective shells on the nanoparticle surface during its synthesis (encapsulation), and by introducing synthesized nanoparticles into the stabilizing medium (forming a nanosuspension using surfactants). The paper proposes a comprehensive approach to stabilization of metal nanoparticles:

K. V. Liapina (✉) · T. V. Melnichenko · A. I. Ustinov
E.O.Paton Electric Welding Institute, Kyiv, Ukraine
e-mail: kirulya@mail.ru

P. G. Dulnev
Institute of Bioorganic Chemistry and Petrochemistry, Kyiv, Ukraine

A. I. Marinin
National Institute of Food Technologies, Kyiv, Ukraine

forming metal nanopowders encapsulated in NaCl matrix with subsequent production of a suspension of organic–inorganic nanostructures, made in the form of a polycomplex, including organic molecules and nanoparticles of 3-d metals.

13.2 Method to Produce Encapsulated Nanopowders of Metals

Method to produce nanopowders of metals with encapsulation of particles in a chemically inert medium is described in detail in [7–10]. It is based on simultaneous deposition of metal and alkali metal halogenide (NaCl) from the vapor phase. Presence of salt ions in the vapor phase, on the one hand, limits metal particle growth, and on the other—ensures formation of a protective shell on their surface. Presence of a shell on particle surface prevents the processes of their consolidation during storage and protects them from interaction with the atmosphere. Application of such an approach allowed producing nanosized particles of copper (Fig. 13.1), in which metal particles are encapsulated in a chemically inert matrix based on sodium chloride. Figure 13.2 gives particle distribution by size.

Such a composite structure allows long-term storage of encapsulated nanoparticles in regular atmosphere, and, if required, removing the salt shell, placing these powders, for instance, into liquid, in which this salt dissolves.

Fig. 13.1 Electron-microscopic image (*light* field) of condensate formed at simultaneous deposition of vapor flows of copper and sodium chloride
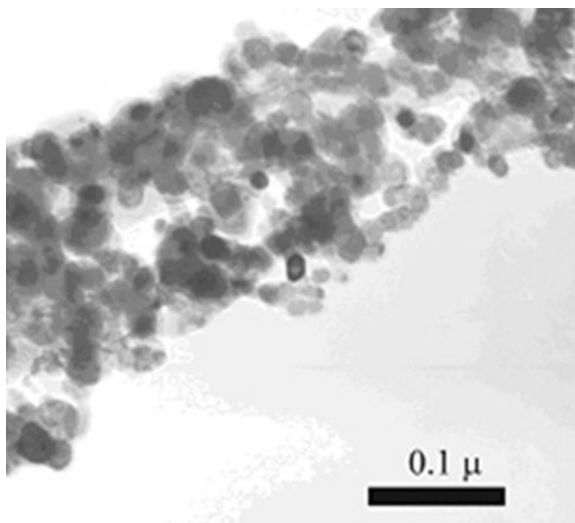
Fig. 13.2 Distribution of copper particles by size
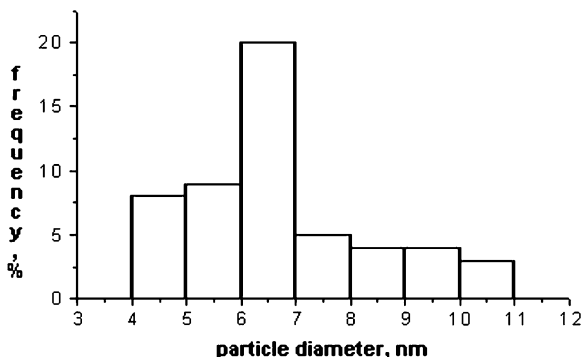
13.3 Suspension Preparation, Using Encapsulated Metal Nanopowders as Precursors

Suspensions based on encapsulated nanoparticles of 3-d metals were prepared by nanoparticle stabilization in aqueous medium through introduction of organic molecules into the coordinating solution, which have two or more amides in their composition. Obtained solution was subjected to dispersion with application of ultrasonic treatment for 60 min at the temperature of 60–80 °C. During dispersion the salt shell is removed from the nanoparticle surface and at the same time an organic shell is formed by creating new nanostructured organic–inorganic complexes based on polyamines containing metal nanoparticles that provide their stabilization.

Figure 13.3 shows the scattering of light by colloidal particles. On the right bulb with the colloidal solution, based on the encapsulated copper nanoparticles; on the left the bulb with water.

Properties of the prepared suspensions were studied by the method of dynamic dissipation of light, using Malvern Zetasizer Nano S instrument, Ver. 6.20, of Malvern Instruments Ltd., Great Britain. Volume distribution of particles by dimensions in the suspension is given in Fig. 13.4a. The distribution is monomodal

Fig. 13.3 The scattering of light by colloidal particles (Tyndall effect)
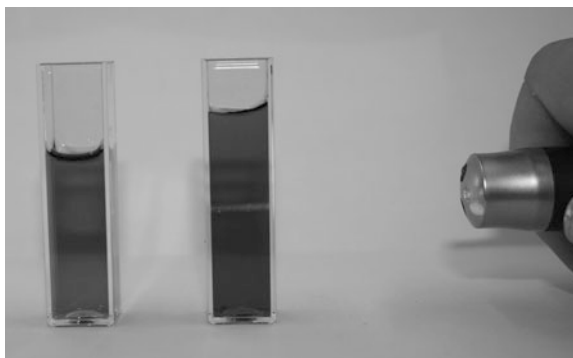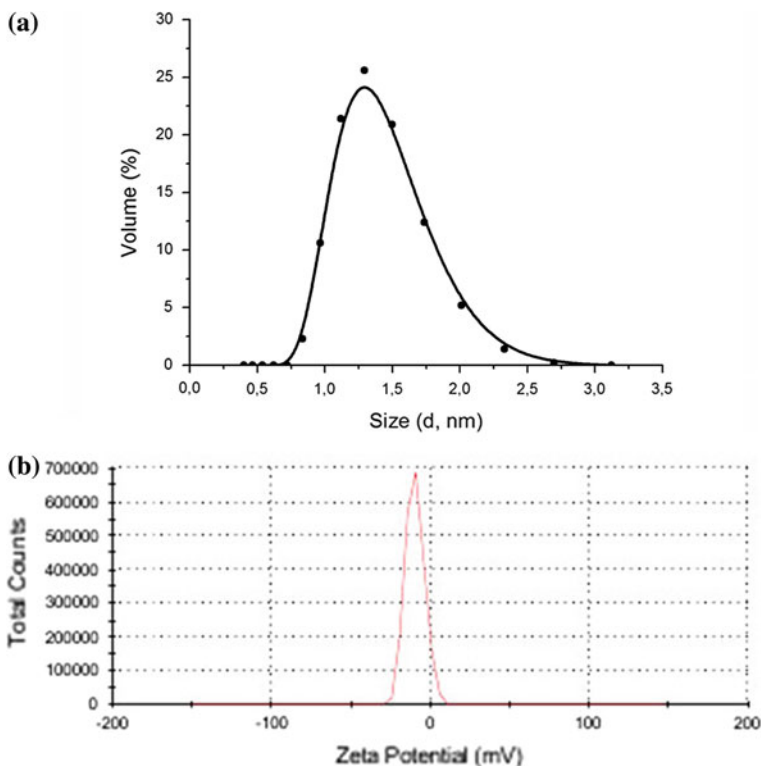
Fig. 13.4 a Distribution of copper particles by dimensions in the suspension based on amines. **b** Zeta-potential of copper particles

with a mode falling into the size range of ∼1 nm. In order to characterize the suspension stability and ability of particles to agglomerate, the zeta potential (particle surface charge that characterizes the degree and nature of interaction of particles of the disperse system) was determined. Obtained results are presented in Fig. 13.4b. Zeta potential for copper particles is equal to ∼30 mV that is indicative of a lack of compensation of particle surface charge, and potentially high surface activity, respectively.

Studying the suspension properties after its soaking at room temperature for 100 days showed no change in its dispersity and stability characteristics.

Thus, the possibility of producing a stable suspension based on nanostructured organic–inorganic complexes, consisting of polyamines and copper nanoparticles of up to 5 nm size, having a large specific surface and characterized by a narrow dispersion of dimensions, was established. The proposed method of preparing suspensions provides a high density of particle packing in organic–inorganic structures and high effectiveness of transformation of metal containing precursor into metal nanoparticles.

Fig. 13.5 Distribution of copper particles by size in glycerin-based suspension
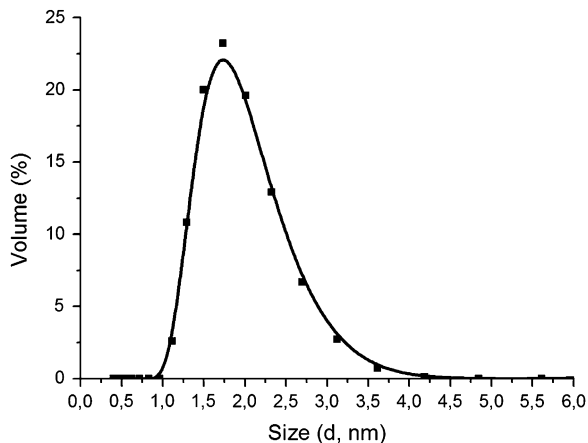
Glycerin-water system was selected as a stabilizing medium to check the effectiveness of the proposed complex method of preparing stable suspensions, containing nanoparticles of metals. Suspensions were prepared by the procedure described above. Colloidal solution of metal nanoparticles was subjected to dispersion by ultrasound at the temperature of 80–90 °C for 60 min Volume fraction of encapsulated nanopowder of copper, added to the solution, was not less than 60 vol %. Volume distribution of copper particles in the suspension is given in Fig. 13.5. It is seen that the average size of copper particles is close to 1 nm, whereas size dispersion is small.

Thus, results of performed investigations showed the possibility of preparing stable suspensions of metal particles on nanoscale by dissolution of salt shells of nanopowders, using both water soluble organic complexes based on amine derivatives, and glycerin–water system solution. An advantage of this method is the achievement of a high degree of uniformity of metal nanoparticles by dimensions, and the possibility of adding biogenic or bioactive components to the suspension which allows making such a material biocompatible or bioactive.

References

1. Gubin SP, Kateva NA et al (2005) Nanophase materials in electronics—materials, technology, device. Nonlinear World 3:10–26
2. Henglein A (1989) Small-particle research: physicochemical properties of extremely small colloidal metal and semiconductor particles. Chem Rev 89(8):1861–1873
3. Moriarty P (2001) Nanostructured materials. Rep Progr Phys 64:297–381
4. Rotello V (ed) (2004) Nanoparticles: Building blocks for nanotechnology. Kluwer Academic/ Plenum Publishers, New York
5. Ismagilov RR, Khasanov RA (2005) Quality and technology of production of baking quality wheat grain. Gilem, Ufa
6. Sergeev GB (2003) Nanochemistry. MGU, Moskow

7. Ustinov AI, Melnichenko TV, Liapina KV, Chaplyuk VI (2008) Method to produce encapsulated nanopowders and unit for its implementation. Patent of Ukraine #82448
8. Burda C, Chen X, Narayanan R, El-Sayed MA (2005) Chemistry and properties of nanocrystals of different shapes. Chem Rev 105(4):1025–1102
9. Puntes VF, Krishnan KM, Alivisatos AP (2001) Colloidal nanocrystal shape and size control: the case of cobalt. Science 291:2115–2117
10. Sandia corporation (2003) US Patent 6,929,675, 24 April 2003

Chapter 14
Metal Nanostructures and Active Materials

Thomas A. Klar

14.1 Fluorescent Species and Metal Nanoparticles in the Weak Coupling Limit

14.1.1 Ways to Influence Fluorescence Output by Metallic Nanoparticles

The interaction of a fluorophore and a proximate noble metal nanostructure is generally threefold. First, there will be a resonant energy transfer from the molecule to the nanoparticle, similar to the well-known Förster resonant energy transfer (FRET) [1, 2], second, the rate of spontaneous radiative emission may be influenced, and third, the effective excitation cross-section will be manipulated. At this point, we assume that neither the electronic levels of the fluorophore will be shifted by the presence of the metallic nanostructures nor will the presence of the fluorophore change the plasmonic resonances of the metallic nanostructures. With other words, we assume the weak coupling limit. As we are restricted in space, we cannot cover this topic in full breadth, but we refer the interested reader to more detailed reviews written by Metiu [3], Leung and George [4], Klimov et al. [5], Lakowicz et al. [6, 7], or Klar and Feldmann [8].

Let us assume that the fluorescent species (such as fluorophores, quantum dots, π-conjugated molecules, color centers etc.) induces a "mirror" dipole in the metallic nanostructure. Importantly, the electromagnetic interaction of the original dipole and the mirror dipole may lead to both, a reduction [9, 10] or an increase [10–14] of the radiative rate of the fluorophore Γ_{rad}, depending on whether the

T. A. Klar (✉)
Johannes Kepler University Linz, Institute of Applied Physics, Altenberger Straße 69, 4040 Linz, Austria
e-mail: thomas.klar@jku.at

molecular dipole is oriented perpendicular or tangential with respect to the surface of the metallic nanostructure and whether the fluorescence emission occurs on the short- or the long wavelength side of a plasmonic resonance [15–18]. Because the spacing between both dipoles is assumed to be much shorter than the wavelength, the overall effective dipole moment of the hybrid system, which is responsible for the strength of radiation, may be reduced in the case of out of phase oscillation of both dipoles or is increased in the case where the molecular dipole radiates in phase with the image dipole.

The nonradiative rate will, however, increase in any case because the intrinsic nonradiative channel, denoted by the intrinsic nonradiative rate Γ^0_{nonrad}, will be supplemented with another loss-channel, namely the energy transfer from the active molecule to the metallic nanostructure. This process is denoted by the energy transfer rate Γ_{ET}. It is not easy to predict whether the total quantum efficiency

$$\eta = \frac{\Gamma_{rad}}{\Gamma_{rad} + \Gamma^0_{nonrad} + \Gamma_{ET}} \tag{14.1}$$

will increase or decrease if an active molecule is brought into close proximity of a noble metal nanoparticle. For a fluorophore emitting on the red side of the plasmon resonance, the situation is illustrated in Fig. 14.1.

To the best of our knowledge, Chance et al. [19] were the first to include energy transfer from a fluorophore to a flat metallic surface correctly into the theory of fluorophore—metal interaction and they gave formulas for both the change of the radiative rate due to the mirror effect and the increase of the nonradiative rate due to losses via energy transfer into the metal. The validity of their theory has been impressively proven by a much better fit to the experimental data of Drexhage et al. [20–22] compared to the fit of theories neglecting the energy transfer.
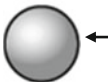
Molecular Dipole Orientation	Γ_{rad}	Γ_{nonrad}	η	
tangential	**decreasing** (molecule and NPPR out of phase)	**increasing** (due to energy transfer)	decreasing	
vertical	**increasing** (molecule and NPPR in phase)	**increasing** (due to energy transfer)	**decreasing** if energy transfer dominates	
			increasing if increased Γ_{rad} dominates	

Fig. 14.1 Table of changes of the radiative rate Γ_{rad}, the nonradiative rate Γ_{nonrad}, and the quantum efficiency η in case of a fluorophore being brought from infinite distance to a finite distance to a metallic nanoparticle, assuming the case of a fluorophore emitting at the red side of the nanoparticle plasmon resonance (NPPR)

While Chance et al. have assumed an infinitely large flat metal surface, the interaction of fluorophores with metallic nanostructures needs a more elaborate theory. In a "first order approximation", both, the molecule and the metallic nanoparticle are considered as point dipoles. In this limit, the interaction is similar to a Förster-type dipole–dipole interaction [1, 2] that turns into a Dexter type energy transfer for decreasing distances where higher order electric and magnetic multipole- and exchange interactions need to be considered [23]. According to Förster, the nonradiative resonant energy transfer rate depends on the inverse sixth power of the distance between the two dipoles. It is also proportional to the spectral overlap integral of the emission spectrum of the donor of energy and the absorption spectrum of the acceptor. While the Förster or Dexter models indicate that the interaction between an active molecule and a metal nanoparticle is expected to depend strongly on the mutual distance and the overlap integral of the fluorophore's emission and the nanoparticle's absorption spectrum, it fails to give the correct transfer rates because of two reasons: First, the nanoparticle's extension is usually in the range or even larger than the Förster radius (the distance of 50 % fluorescence quenching) and can therefore not be considered as a point-like object. Second, the metallic nanoparticle influences the radiative rate of the fluorescing molecule.

Gersten and Nitzan introduced a model that considers both effects [24]. The molecule-nanoparticle system is modeled in the framework of a dipole model which it is based on the static Maxwell equations. The moment of the image dipole inside the metallic nanoparticle is induced by the electric field of the originally excited molecule. The image dipole subsequently influences the electric field in its nanoenvironment, which acts back on the molecular dipole of the fluorophore. The total radiative rate is determined by considering the overall total dipole moment of the fluorophore–nanoparticle hybrid and inserting it into the Hertzian radiation formula. The power loss of the Hertzian dipole leads to a radiative rate despite the fact that the model is basically an electrostatic one. The nonradiative rate is derived by calculating Ohmic losses induced by the electric field inside the particle.

While Gersten and Nitzan considered this electrostatic model, Ruppin suggested a fully electrodynamic model [25]. He derived the radiative and nonradiative rates from a linear decomposition of the electromagnetic field into plane wave components. This decomposition ansatz is similar to the scattering theory of Mie [26]. Therefore, the Ruppin model should be considered as the "fluorescence quenching analogue" to Mie's electrodynamic scattering theory, whereas the Gersten-Nitzan model can be considered as the analog to the electrostatic scattering theory by Rayleigh. Both models have been compared and regimes were defined where the mathematically simpler static Gersten-Nitzan model can be safely applied without major loss of accuracy [27–31]. This is the case as long as the dimensions of the metallic nanostructure and the distance between the fluorophore and the metallic nanostructure are in the range of or smaller than the electromagnetic skin depth inside the nanoparticle, which typically measures a few tens of nanometers. A more comprehensive discussion on this topic can be found, e.g., in Mertens et al. [17]. However, if the dimensions are getting too small, specifically when the distance between the fluorophore and the metallic

nanostructure gets into the range of one nanometer, the local theories of Chance-Prock-Silbey, Gersten-Nitzan and Ruppin may fail [3]. Garcia de Abajo has recently studied nonlocal effects in the coupling of plasmons of strongly interacting nanoparticle dimers [32]. He demonstrates that the plasmon–plasmon interactions are weakened due to nonlocal dielectric constants. Similar effects are certainly expected for plasmon–fluorophore interactions. A quantum mechanical treatment with similar results has been given by Zuloaga and coworkers [33].

So far, we have only considered the influence of metallic nanostructures on the quantum efficiency of proximate fluorophores, derived from the radiative and nonradiative decay rates. However, in order to answer the question whether the total fluorescence output of a fluorophore close to a metallic nanostructure is increased or decreased, a consideration of the effective excitation cross-section is of equal importance. The total fluorescence yield is given by

$$F(\lambda_{ex}, \lambda_{em}) = \frac{\lambda_{ex} \cdot I(\lambda_{ex})}{h \cdot c} \cdot \sigma_{abs}^{eff}(\lambda_{ex}) \cdot \eta(\lambda_{em}) \tag{14.2}$$

λ_{ex} denotes the excitation wavelength, λ_{em} the emission wavelength, $I(\lambda_{ex})$ the intensity of the excitation light, $\eta(\lambda_{em})$ the quantum efficiency (Eq. 14.1), and $\sigma_{abs}^{eff}(\lambda_{ex})$ the effective absorption cross-section. The latter is changed with respect to the intrinsic absorption cross-section $\sigma_{abs}^{0}(\lambda_{ex})$ of a fluorophore far away from any metallic nanostructure. When the molecule is situated in the vicinity of a metallic nanostructure, the electric field $E(\lambda_{ex})$ is changed in the neighborhood of the metallic nanostructure with respect to the electric field without the metallic nanostructure $E^{0}(\lambda_{ex})$. Therefore, we can derive an effective absorption cross-section

$$\sigma_{abs}^{eff}(\lambda_{ex}) = \frac{\left| \overrightarrow{p} \circ \overrightarrow{E}(\lambda_{ex}) \right|^2}{\left| \overrightarrow{p} \circ \overrightarrow{E}^{0}(\lambda_{ex}) \right|^2} \cdot \sigma_{abs}^{0}(\lambda_{ex}) \tag{14.3}$$

whereby $\overrightarrow{p}$ is the molecular dipole moment of the active species. It is important to note that the electric field can be increased or decreased or reoriented in the presence of the metallic nanostructure $\overrightarrow{E}(\lambda_{ex})$ as compared to the electric field without the metallic nanostructure $\overrightarrow{E}^{0}(\lambda_{ex})$. Consequently, the molecular absorption might be increased or decreased. This situation is similar to the previously discussed change of the radiative emission rate of the molecule in the vicinity of a metallic nanostructure (Fig. 14.1). This is, however, not surprising because the Einstein A parameter, responsible for spontaneous emission, and hence the radiative rate, and the Einstein B parameter, responsible for the stimulated process of absorption, are strictly proportional in a strict two level system and still closely related in a multilevel system such as an organic molecule [34]. Due to the Stokes shift between the absorption and the emission spectra, it might well be possible that the effective absorption cross-section is enhanced but the radiative rate is, for instance, decreased via the interaction with a nanoparticle plasmon.

A very instructive demonstration that both, an increase and a decrease of the overall fluorescence output of fluorophores may happen, depending on the detailed parameters of the metallic nanostructure, was given by Matveeva et al. [35]. They have compared pure gold and silver-enhanced gold nanoparticles in their ability to manipulate the fluorescence from Rhodamine dyes in an immunoassay. They found that bare gold nanoparticles induced fluorescence quenching, while silver-enhanced nanoparticles increased the fluorescence output.

14.1.2 Time-Resolved Measurements to Determine Radiative and Nonradiative Rates

Clearly it is difficult to determine all above mentioned rates. Time-resolved measurements are an elegant tool to determine not only the overall fluorescence lifetime but also to determine the radiative and nonradiative rates in detail [9, 16, 36]. It is educational to consider the change of the radiative rate, of the nonradiative rate, and of the absorption cross-section separately [37]. Figure 14.2 exemplifies three extreme cases: The solid lines represent the fluorescence decay of a molecule far away from any metallic nanostructure, while the dashed lines show the fluorescence decay of a fluorophore close to metallic nanostructures.

Figure 14.2a sketches the example where the absorption cross-section is the only parameter to be changed (in this case: increased), while the radiative is kept constant and no nonradiative channel (also no energy transfer) is allowed. Hence, the slope of the decay curve on the semi-logarithmic plot must remain constant, and the fluorescent transient is parallel shifted to overall higher count rates because of the increased excitation rate. The totally detected fluorescence intensity can be calculated by integrating the curves from times 0 to infinity. A reduced absorption cross-section (with all other parameters in Eq. 14.2 being kept constant) would lead to a fluorescence transient parallel shifted below the original fluorescence
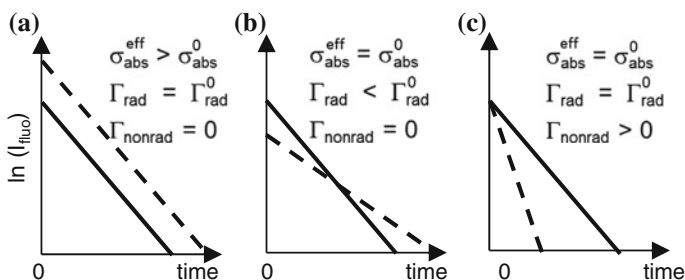
Fig. 14.2 Change of the fluorescence transients due to: **a** a change of the effective absorption cross-section only, **b** a decrease of the radiative rate only, and **c** a change of the nonradiative rate only. Solid lines show the transients of the fluorophore without any metallic nanostructure, dashed lines show the transients of fluorophores close to a metal nanostructure

transient. Figure 14.2b illustrates the situation where the effective absorption cross-section is kept constant but the radiative rate is decreased when the fluorophore is approached to a metal nanostructure ($\Gamma_{rad} < \Gamma_{rad}^0$; Γ_{rad}^0 being the radiative rate of the unperturbed fluorophore). No nonradiative losses are allowed in this model case ($\Gamma_{nonrad} = 0$), specifically, no energy transfer is allowed. Now, the fluorescence decays slower because the radiative rate is decreased. Because the integrated fluorescence intensity must remain unchanged (we excluded nonradiative processes !), the time-integrated fluorescence intensity must remain constant. As a consequence, the fluorescence must be less intensive at t = 0 for the fluorophore-metal composite system (dashed curve) as compared to the fluorescence from the unperturbed fluorophore (solid line). Hence, the intercept of the fluorescence transient with the ordinate at time 0 is a direct measure for the change of the radiative rate. Therefore it is imperative to plot time-resolved fluorescence transients of fluorophores close to metal nanostructures *without* any normalization. By normalization, the information of the fluorescence strength at time zero is lost and the radiative rate cannot be recovered. Figure 14.2c shows the situation, where the excitation cross-section and the radiative rate are unchanged, but a nonradiative channel, for example due to energy transfer to a nanoparticle, is introduced. While at time 0 the fluorescent transient starts at the same intensity as the fluorescence signal from an unperturbed fluorophore, the transient drops off more quickly due to the reduced lifetime. In summary, we see that a change in the slope of the logarithmically plotted fluorescence transient could be due to a change of the radiative or of the nonradiative rate (Fig. 14.2b, c) and a change of the intensity at time 0 could be due to a change of the excitation cross-section or due to a change of the radiative rate (Fig. 14.2a, b). In order to solve these ambiguities, a third bit of information needs to be gathered. This could be the measurement of the quantum yield. With the triple of (quantum yield, fluorescence lifetime, intensity at time 0) in hand, the triple (effective absorption cross-section, radiative rate, nonradiative rate) can be determined uniquely. Techniques of time-resolved fluorescence spectroscopy which allow for the determination of lifetimes of singlet emitters close to metallic nanostructures include time-correlated single photon counting [38–40], frequency domain fluorescence measurements [41, 42], streak camera measurements [9, 37, 43, 44], or femtosecond pump SHG-probe [45].

14.1.3 Example: Quenching of Cy3 at Varying Distances from Gold Nanoparticles

According to simple Förster theory, the energy transfer between a point-like donor of fluorescence and a point-like acceptor falls off with the inverse sixth power of the distance between them. As it should have become clear from the above discussion, the situation is not that simple if the acceptor is a noble metal nanoparticle. The metallic nanoparticle can usually not be considered as point like anymore and it does not only open a nonradiative channel for the de-excitation of the donor due to
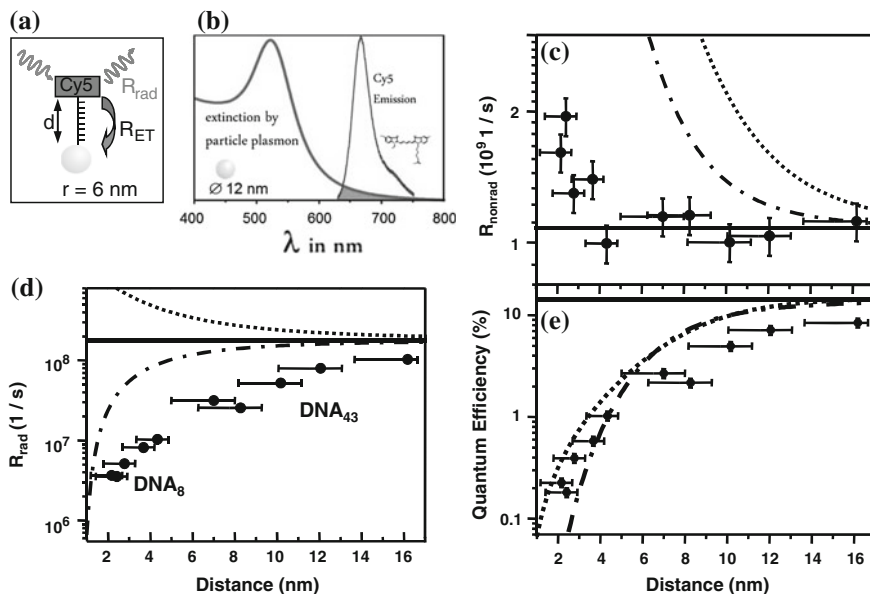
Fig. 14.3 **a** Sketch of a Cy5 dye molecule attached via a thiol-functionalized DNA to a gold nanoparticle of radius r = 6 nm. **b** The spectral overlap of the Cy5 emission and the nanoparticles' extinction spectrum is weak. **c** Nonradiative rate, **d** radiative rate, and **e** quantum efficiency of Cy5 molecules as a function of their distance to the gold nanoparticle surface. Simulated radiative and nonradiative rates and the resulting quantum efficiencies are shown for molecular dipole orientations perpendicular (*dotted lines*) or tangential (*dash dotted lines*) to the nanoparticle surface. Adopted in part from Ref. [36]. © 2005 The American Chemical Society

energy transfer but it also changes the radiative rate of the donor and its effective excitation cross-section. In the following, we would like to focus on the change of the radiative rate rather than the energy transfer rate. To do so, fluorescent molecules (Cy5) and gold nanoparticles were chosen where the spectral overlap of the fluorescence emission and the nanoparticles' absorption is small (Fig. 14.3b) [36]. Such a small spectral overlap renders energy transfer inefficient and hence, we can focus on the radiative rate. Further, we used DNA spacers of different length to bind the fluorophores to the gold nanoparticles (radius 6 nm) at different distances (Fig. 14.3a). The distance was further fine-tuned by the amount of DNA loading. A larger DNA coverage leads to steric hindrance and hence to DNA stretching. The result is shown in Fig. 14.3c–e. As expected, the nonradiative rate Γ_{nonrad} increases only moderately with decreasing distance of the fluorophores to the gold nanoparticles (Fig. 14.3c), while the radiative rate Γ_{rad} is decreased by 1.5 orders of magnitude (Fig. 14.3d), leading to a severe reduction of the quantum efficiency with decreasing distance (Fig. 14.3e). Therefore, the system of Cy5 molecules and gold nanoparticles is a nice demonstration of fluorescence quenching by gold nanoparticles not so much because of a radiative energy transfer, but because of a suppression of the radiative rate.

14.2 More Complex Interactions of Fluorophores and Metallic Nanostructures

14.2.1 Strong Coupling

If the active materials and the metallic nanostructures are in intimate contact and if the fluorophore's absorption coincides spectrally with the plasmon resonance, strong coupling between these two originally very different species may occur [46]. Strong coupling can be observed when two resonators interact so strongly that the eigenfrequencies of the coupled system start to shift away from the degenerate eigenfrequencies of the uncoupled entities. This is sometimes also called energetic "anti-crossing." Recently, the expression "plexciton" has been coined for the coupled resonance of a fermionic molecular excitation with a bosonic plasmonic resonance [47, 48]. The situation turns a little bit more complicated when multiple fluorophores are in ultimate vicinity of a metallic nanoparticle [49]. In this case, all molecular dipoles and the plasmon resonance need to be coupled. It has been found that also the cross talk between the molecules is supported by the plasmonic modes, even dipole forbidden dark plasmonic modes contribute [49].

To the best of our knowledge, the first experimental report on strong coupling between dye molecules and rough, sub-monolayer silver films dates back to 1980 (Fig. 14.4) [46]. Silver nanoparticles were prepared by sub-monolayer evaporation. As long as the substrate is covered with Ag nanoparticles only sparsely, the extinction spectrum looks more or less like the extinction spectrum of isolated silver nanoparticles (Fig. 14.4a). With increasing nominal thickness, the plasmons of the growing and more densely packed silver nanoislands start to couple and the plasmon spectra redshift until, finally, a broad and featureless extinction spectrum is observed in the case of a continuous silver film (dashed line in Fig. 14.4a). A pure Rhodamine B film without silver nanoislands shows an emission spectrum as indicated by line "0" in Fig. 14.4b. When Rhodamine B is brought into contact with sub-monolayer silver nanoisland films, a double-peaked extinction is observed (Fig. 14.4b), whereby one peak is blue shifted as compared to both, the plasmon peak and the Rhodamine B absorption and the second peak is red shifted. More recent observations of the strong coupling effect include: J-aggregates of a Cyanine dye have been strongly coupled to silver films [50], to silver films punctuated by a two dimensional hole array [51], or comprising nanovoids [52]. Quantum dots which are sandwiched between a metallic surface and a metallic STM tip couple with plasmonic modes [53]. Rhodamine 6G [54] or porphyrin [55] molecules show strong coupling to silver triangles [56]. The strength of the strong coupling effect is quantized by the Rabi splitting of the two resonances. Rabi splittings of up to 400 meV have been reported in the case of Rhodamine 6G molecules on sub-monolayer silver films [57]. It has also been shown that H- and J- aggregates of fluorophores can both couple to plasmonic nanostructures [54, 58–62]. Strong coupling has also been reported in case of fluorophores bound to silver and
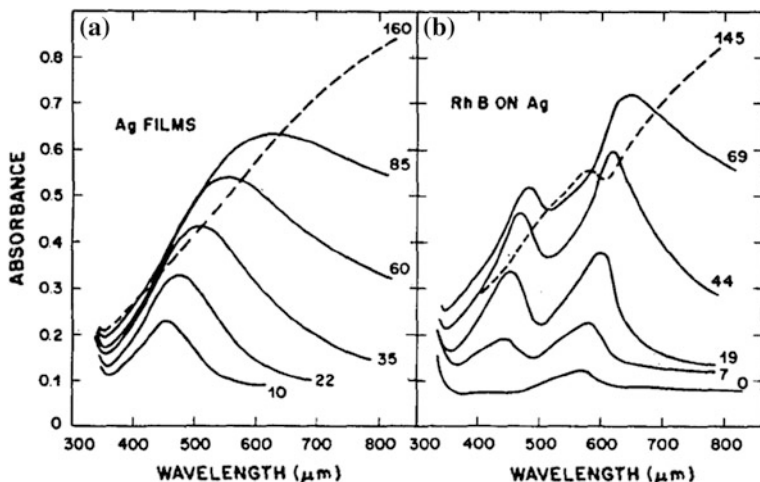
Fig. 14.4 Strong coupling of Rhodamine B with silver nanoparticles. **a** Extinction spectra of nanoparticular sub-monolayer silver films (nominal mass thickness given in Å). The nanoplasmonic resonances redshift with increasing nanoparticle density. **b** Extinction spectra of thin silver films in contact with Rhodamine B. Line "0" shows the absorption of a Rhodamine B film without silver. A clear double-peaked structure is visible, indicating an anticrossing of the Rhodamine B absorption and the plasmon resonance. In the case of the thick and smooth silver film which shows a broad and featureless extinction spectrum (a, dashed line), a more Fano-shaped interaction is observed (b, dashed line). Reprinted with permission from [46] © 1980 The Optical Society of America

gold particles in solution [63–66], in case of organic semiconductors bound to plasmonic resonances [50] or in case of organic molecules and holes or voids in metallic films [51, 52]. In an extreme case of strong coupling, triple resonances are predicted for the case of a single molecule resonating with a plasmonic nanostructure [67]. Strong coupling effects have even been reported in case of scattering spectra taken from *single* gold nanoparticles in close contact to dye molecules [68, 69] and the optically active protein cytochrome c [70].

14.2.2 Fano Resonances

Strong coupling is closely related to the Fano effect [71] where actually a sharp resonator couples to a broad continuum. In case of fluorophores where the fluorescence emission shows a similar spectral width as nanoplasmonic resonances, the strong coupling picture is more appropriate [46], while in the case of an atomic transition or a spectrally sharp quantum dot emission, coupling to a nanoparticle plasmon may be described better by a Fano resonance [72]. Theoretical work on this issue has been published recently by Neuhauser and Lopata [73] and by Kelley [74].

Zhang et al. theoretically investigated the nonlinear Fano effect [72] and Yan et al. included multipole effects [75]. The coupling of quantum dots and metallic rods has also been investigated [76].

14.2.3 Purcell Effect

In Sect. 14.1, we have discussed the changes of the excitation cross-section, of the radiative rate and of the nonradiative rate due to energy transfer of a fluorophore close to metallic nanostructures. We have assumed, however, that the absorption and emission lines of the fluorophores are spectrally sharp (quasi δ-functions), specifically that the emission can take place only to a single frequency. This is, however, only the case when atomic emission lines are considered. In contrast, a typical fluorophore shows several emission lines where a transition from the lowest vibronic level of the electronically excited state takes place to different vibronic or rotational levels of the electronic ground state. Typically, these transition are termed (0,0), (0,1), (0,2), and so forth, meaning that the transition originates from the "0" vibronic level in the upper state and ends at the "0", "1", "2" and so forth level of the electronic ground state. Further, each of these transitions is thermally broadened at room temperature so that a typical emission spectrum with two to three or even more broad and overlapping maxima and shoulders evolves. The total width of the fluorophore's emission spectrum is in the same order or sometimes even exceeds the spectral width of the plasmon resonance of metallic nanoparticles. Consequently, the plasmon may influence the radiative and energy transfer rates very differently over the range of the fluorescence spectrum. The problem is similar to the Purcell effect observed in macro- or microscopic mirror based resonators [20, 77], where some part of the emission band can be enhanced or suppressed if in- or out of resonance with the cavity, respectively. Traditionally, a cavity consists of two mirrors, separated by at least half the wavelength of light. The mode density and therefore the emission rate is increased if an integer multiple of half of the wavelength of the emitted light fits into the resonator. Otherwise, modes are excluded and the emission is suppressed. This may lead to the enhancement of one vibronic progression of a fluorescence emission spectrum to the detriment of the other ones [78]. This way, the emission spectra of fluorophores can be reshaped.

While far field micro-resonators must show a minimal size of half of the wavelength, plasmonic nanoresonators overcome this limitation. This has been early pointed out by Ritchie and Burstein [79], who reported a spectral reshaping of the fluorescence emission of Rhodamine 6G molecules close to a silver nano-island film. More recently, spectral shaping of fluorescence emission has been reported for semiconductor quantum dots [80–82], semiconductor quantum wells [83], and fluorophores [84–89] in close proximity of metallic nanostructures.

Figure 14.5 shows an example, how the fluorescence emission of Cy3 dye molecules can be spectrally reshaped by a pair of gold nanoparticles [86].
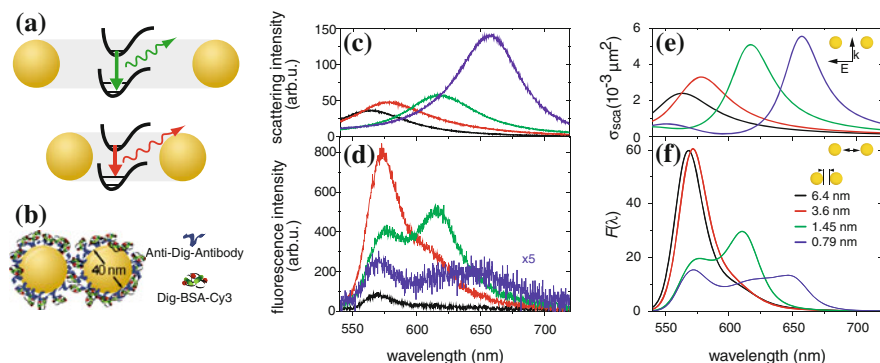
Fig. 14.5 **a** Radiative transitions to different ground state sublevels are enhanced in resonators formed by Au nanoparticle dimers of different distances. **b** Plasmonic nanoresonators with Cy3 fluorescent molecules. **c** Experimental scattering spectra and **d** experimental fluorescence spectra of individual dimers; spectra with same colors in (**c**) and (**d**) are measured on the same dimer. **e** Theoretical scattering cross-sections of nanoparticle dimers whose interparticle distance is chosen such that the resonance wavelengths reproduce the spectra in (**c**). **f** Calculated fluorescence spectra for Cy3 molecules located in the center of the dimers. An excellent agreement of the calculated and the measured spectral shapes of fluorescence is achieved. Reprinted with permission from Ref. [86] © 2008 The American Physical Society

Cy3 fluorophores are sandwiched between a pair of gold nanoparticles with the help of antigen–antibody recognition (Fig. 14.5b). The dimer of gold nanoparticles forms a nanoscopic resonator (note that the longest dimension of the total hybrid is in the range of 85 nm, which is clearly below half of a visible light wavelength). The distance between the gold nanoparticles varies from dimer to dimer due to different linker geometries. However, each single dimer shows a stable Mie scattering spectrum (Fig. 14.5c) and hence it is possible to ascribe a specific distance between the gold nanoparticles (Fig. 14.5e). After the determination of the surface-to-surface distance of a single, specific dimer, the microscope is switched from the dark field mode to a fluorescence mode, keeping the same individual pair of nanoparticles in focus. Hence, the Mie scattering spectra of one dimer and the fluorescence from Cy3 molecules on the same dimer can be directly compared. This allows a detailed study of the influence of a Mie resonator on the fluorescence emission. Experimental and theoretical fluorescence spectra are displayed in Fig. 14.5d and f, respectively. The surface-to-surface distances of the individual dimers on display amount to 6.4 nm (black line), 3.6 nm (red line), 1.45 nm (green line), and 0.79 nm (blue line). The fluorescence spectra from Cy3 molecules are displayed in Fig. 14.5d. The color coding of the emission spectra and the colors of the Mie scattering spectra are the same for one and the same specific gold nanoparticle pair. In case of the large surface-to-surface distances, the emission spectrum is very similar to the emission spectrum of Cy3 molecules in aqueous solution. The situation dramatically changes in case of the shorter distances between the nanoparticles. In case of a 1.45 nm interparticle spacing, the (0,1) vibronic

progression becomes the dominant mode and in case of 0.79 nm even the (0,2) vibronic progression is of similar strength as the (0,0) and the (0,1) emission lines.

An extended Mie theory allows for the calculation of radiative (Γ_{rad}) and nonradiative (Γ_{nonrad}) rates of a dipole in the center of a gold nanoparticle aggregate [86, 90–92]. When considering the fluorescence emission of a fluorophore with multiple emission lines (such as multiple, and thermally broadened vibronic sidebands, see above), care has to be taken to calculate the spectral dispersion of the quantum efficiency correctly. All different radiative and nonradiative decay channels compete with each other [85, 86, 93] and consequently, all those channels need to be summed up in the denominator of the quantum efficiency. In case of a continuous emission spectrum, the sums turn into integrals:

$$\eta(\lambda) = \frac{\Gamma_{rad}(\lambda)}{\int\limits_0^\infty f(\lambda')\Gamma_{rad}(\lambda')d\lambda' + \int\limits_0^\infty f(\lambda')\Gamma_{ET}(\lambda')d\lambda' + \Gamma_{nonrad}^0} \tag{14.4}$$

$f(\lambda)$ is the integral normalized fluorescence spectral density of the isolated molecule. Details can be found in Ref. [86, 94]. The theoretical fluorescence spectra calculated by using Eq. 14.4 and taking into account the correct effective excitation cross-section are shown in Fig. 14.5f. The spectral shapes of the theoretical and the experimental curves match almost perfectly, although no fitting parameters were used in the calculated spectra except the surface-to-surface distance, which was determined by comparing the measured Mie scattering spectra (Fig. 14.5c) with theory (Fig. 14.5e).

While in the publications discussed so far the emission of the fluorophores originates from dipole allowed electronic transitions, we will now discuss the possibility that also triplet transitions may couple to dipole resonances in plasmonic nanoparticles. Recently, we have shown, that the emission of Platinum-Porphyrin molecules can be spectrally reshaped by neighboring gold nanorods due to the plasmonic Purcell effect [95]. The triplet emitter 5,10,15,20-Tetrakis-(4-Sulfonatophenyl)porphyrin-Pt(II) (Pt-TSPP) was electrostatically attached to gold nanorods of different aspect ratio. Depending on the aspect ratio, the long axis plasmon resonance can be shifted from the visible up to the far red. This allows for the design of hybrid systems of Pt-TSPP and gold nanorods of tailored spectral overlap. Figure 14.6 shows the emission spectrum of Pt-TSPP (solid line) and the extinction spectra of the gold nanorods (dashed lines). Upon an increase of the aspect ratio, the long axis, long wavelength plasmon resonance redshifts. For nearly spherical nanorods, it does not overlap with one of the two major emission lines denoted as P1 and P2 (Fig. 14.6a). Upon spectral redshift, the plasmon subsequently becomes resonant with the P1 or the P2 emission (Fig. 14.6b–e). A clear spectral reshaping effect is visible for the emission lines form the Pt-TSPP. It is less pronounced as in the case of the Cy3 emission coupling to the gold nanoparticle dimer (Fig. 14.5) probably for two reasons: First, the Cy3 was (partially) placed also in between the gold nanoparticles, i.e., where the electric field is strongest due to the hot spot effect. Such strong field enhancements are not
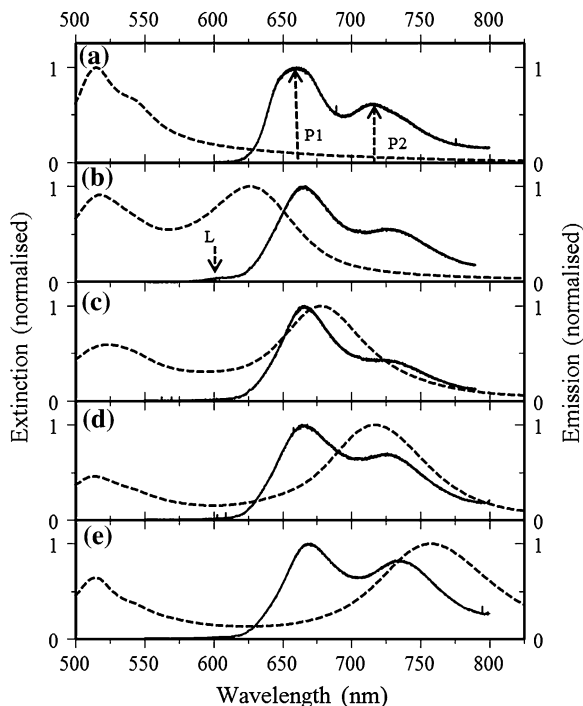
possible with rods. And second, the Cy3 is a singlet emitter, i.e., the fluorescence emission and the gold nanoparticles plasmon have the same dipole-like character. In the case of the porphyrin, however, a triplet emitter couples to the dipole-like long axis plasmon resonance. Hence, it must be emphasized that, although Pt-TSPP is an at least partially dipole forbidden emitter, it still shows a Purcell like spectral reshaping when placed close to plasmonic metal nanoparticles.

14.3 Applications in Biosensing

14.3.1 Oligonucleotide Sensing

Förster-type fluorescence quenching can be used for probing oligonucleotides such as DNA or RNA. A typical sensor format is the so called molecular beacon [96], where a donor fluorophore is attached to one end of a single-stranded DNA and a quencher molecule is attached to the other end. A short piece of both ends is self-complimentary so that those two ends hybridize and the single-stranded DNA forms a loop. In this closed geometry, the fluorescence is quenched. The oligo-nucleotide sequence of the open part of the loop is designed as a complimentary strand to the target oligonucleotide to be detected. If such target molecules are
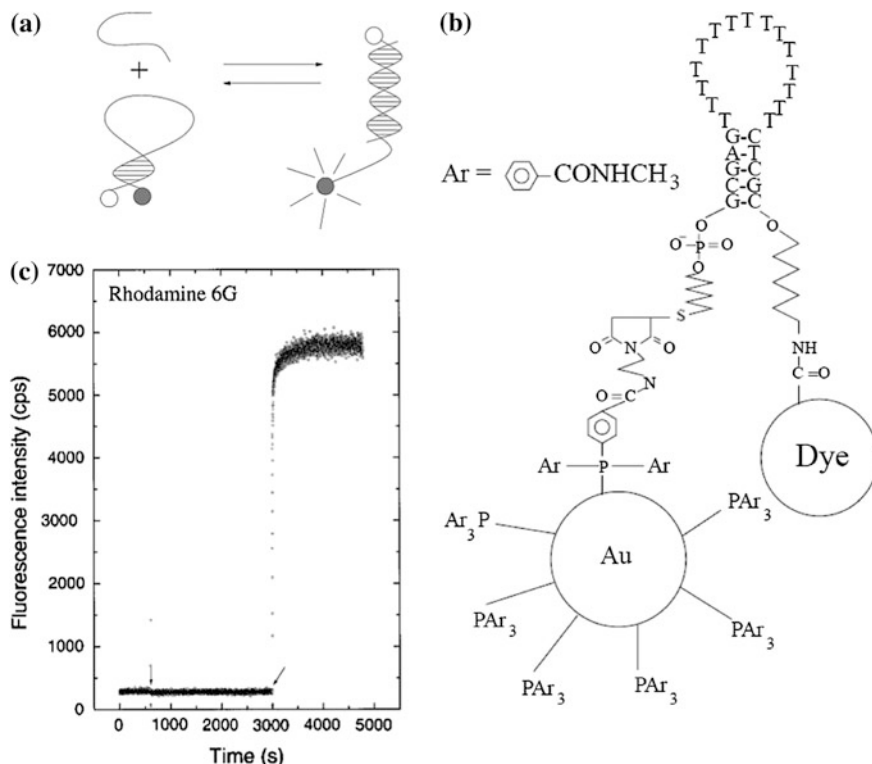
Fig. 14.7 a A molecular beacon possesses a fluorophore on one end of a single-stranded DNA and a quencher (in this case a gold nanoparticle) at the other end. The two ends of the beacon DNA are self-complimentary, so that the fluorophore is presented to the quencher and fluorescence is suppressed. If a target that matches the loop part of the DNA is present, the beacon opens and fluorescence emerges. **b** Details of the molecular beacon comprising a gold nanoparticle. **c** Fluorescence: 0–500 s: background, at 500 s the closed and hence quenched beacon is added. At 3,000 s the target is added. The beacon opens and fluorescence emerges. (**a,b**) taken from [97]; (**c**) taken from [98] with permission. © 2001 Nature Publishing Group

present in the analyte solution, the loop will hybridize with the target and due to steric hindrance and a finite persistence length of the DNA, the two ends will open up and the acceptor will be removed from the donor fluorophore. Hence, the "beacon" will now emit photons at the wavelength of the donor fluorophore and the presence of the target is revealed. Dubertret and coworkers [97, 98] have now replaced the organic acceptor by a gold nanoparticle (Fig. 14.7a, b). They showed that the fluorescence from a Rhodamine 6G molecules is quenched by 99.97 % when the beacon is closed (Fig. 14.7c). By using metal nanoparticles instead of organic molecules, the parasitic fluorescence left over in the closed form of the beacon (0.03 %) is two orders of magnitude less compared to a molecular beacon where Rhodamine 6G is quenched by the typical organic quencher DABCYL (2.33 % residual fluorescence). This high quenching efficiency renders molecular

beacons with gold nanoparticles sensitive even to single base mismatches in a 20-mer oligonucleotide target [97, 98].

Almost at the same time, Maxwell et al. [99] designed a "molecular beacon" comprising only a loop but no stem of self-complimentary DNA. They utilized the natural affinity of fluorophores (Rhodamines and Fluoresceins) to metallic nanoparticles. Such a beacon without a stem is "closed" in absence of the target. Single-stranded DNA was anchored on a gold nanoparticle with a linker at one of its ends and was functionalized with a fluorophore at the other end. Without the target, the DNA is back-folded to the nanoparticle due to the fluorophore's affinity to noble metals. This leads to quenching of fluorescence. However, the affinity of the fluorophores toward the nanoparticle is not strong enough to prevent hybridization with the target DNA which leads to a stiffening of the DNA and the fluorophore is displaced from the gold nanoparticle and starts to fluoresce. Li et al. have applied this technique in micro channel flow cells [100]. Further developments have revealed several other geometries of oligonucleotide sensors utilizing fluorescence quenching via noble metal nanoparticles [101–106]. A commonly used format is a sandwich-type sensor [107]. In this case, two different probe sequences are used, where each of them is complimentary to some part of the target oligonucleotide. One type of probes is attached to the donor fluorophore and the other type of probes is attached to metal nanoparticles. If the target is present in the analyte solution, the target hybridizes with both probes and therefore presents the fluorophore to the quenching metallic nanoparticle.

14.3.2 Immunosensor

Fluorescence quenching by metal nanostructures can be utilized for immunoassays, as well. Oh and coworkers [108] have reported on an avidin assay based on a competitive format. Semiconductor quantum dots were functionalized with streptavidin while gold nanoparticles were functionalized with biotin. Without further avidin in the analyte solution, the gold nanoparticles cluster around the semiconductor quantum dots, and effectively quench their luminescence. In the presence of avidin, however, the biotin on the gold nanoparticles is saturated with this free avidin and attachment of the semiconductor quantum dots to the gold nanoparticles is prohibited. Therefore, the quantum dots start to luminesce. While this assay of Oh et al. used only the "dummy" system biotin–avidin but no real antibodies, Grant et al. [109] functionalized an immune globulin G (IgG) antibody with a gold nanoparticle. The same antibody was also labeled with the fluorophore Alexa Fluor 594. Upon recognition of the antigen, the IgG changes its conformation which alters the distance between the fluorophore and the nanoparticle. The resulting change of the fluorescence yield indicated the presence of the antigen. Two other rather complex immunoassays based on the fluorescence quenching by gold nanoparticles have been reported by Ao et al. [110] and by Peng et al. [111].
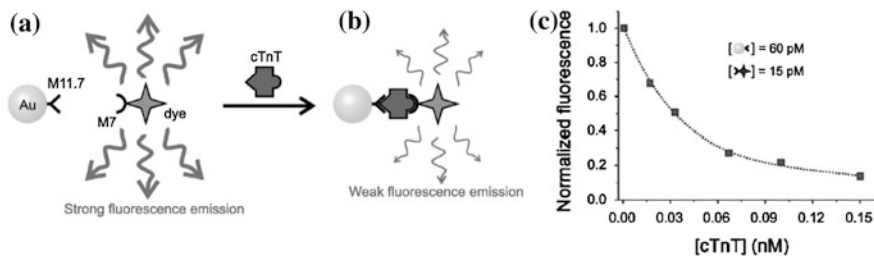
Fig. 14.8 **a** Gold nanoparticles and dye molecules are both functionalized with IgG antibodies against cTnT. **b** Upon addition of cTnT, the sandwich forms and the fluorescence are quenched. **c** Fluorescence quenching upon an increasing concentration of cTnT. Reprinted with permission from [112]. Copyright (2009) by the American Chemical Society

Recently, we reported a much simpler immunoassay based on a straight forward sandwich system, which was apt to sense the medically relevant cardiac Troponin T (cTnT) [112]. cTnT is a protein released into the blood stream upon heart muscle damage and therefore allows for diagnosing myocardial infarctions. Gold nanoparticles of 20 nm diameter were labeled with bivalent monoclonal antibody fragments F(ab')$_2$ anti-cTnT M11.7 which bind to the amino acids 136–147 of cTnT [113, 114]. The dye Cy3B was functionalized with the monoclonal F(ab')$_2$ fragment M7 which binds to the amino acids 125–131 (Fig. 14.8a). In presence of cTnT, a sandwich forms and the fluorescence is quenched (Fig. 14.8b, c). A limit of detection of 20 pM was obtained for cTnT [112]. One remarkable fact of this kind of immunosensor is its apparently long range Förster distance, i.e., the distance between the donor fluorophores and the metal nanoparticles at which half of the fluorescence is quenched. Typical organic quenchers achieve Förster distances only in the range of 5 nm. This is obviously too short for most sandwich-type immunoassays as the size of an antibody is in the range of 8 nm. Metallic nanoparticles, however, quench the fluorescence not only via energy transfer, but also via a manipulation of the radiative rate and a manipulation of the excitation cross-section (see Sect. 14.1). Some other reports on immunoassays utilizing this huge quenching ability (leading to huge Förster radii) in immunosensing have been published recently. The alpha fetoprotein cancer marker was detected with a limit of detection of 2.5ng/ml [115]; BSA was detected with a limit of detection of 5 pM [116]. Protease assays were reported in [117, 118].

14.3.3 Hapten Sensing

Besides oligonucleotides and proteins, much smaller molecules such as drugs or environmental poisons need to be detected, which are frequently termed haptens. Barker and Kopelman [119] have shown that the fluorescence yield of fluorescein attached to gold nanoparticles is further reduced upon the addition of nitric acid.

A biotin sensor was reported by Kato and Caruso [120] or also by Aslan and Perez-Luna [121]. They have functionalized gold nanoparticles with biotin, which was recognized by fluorescently labeled anti-biotin IgGs. In this "closed" formation, the probes where not fluorescent. After addition of competing biotin the fluorescently labeled anti-biotin IgGs left the surfaces of the gold nanoparticles, which lead to an increase of the fluorescence signal. As described above in Sect. 14.1, it depends on many factors whether metallic nanoparticles increase or decrease the fluorescence yield of dye molecules in their nanoenvironment. A specific case of an hapten sensor with an increase of fluorescence close to metallic nanostructures was reported by Wilson and Nicolau [122].

While biotin is usually used as a dummy system for an hapten sensor, a medically relevant drug has been sensed recently: digitalis glycoside digoxin, used to treat cardiac arrhythmia. Therapeutic drug monitoring of digoxin is mandatory because the therapeutic window is very narrow and toxicity is high. It was shown that digoxigenin, the aglycon of digoxin, can be detected by fluorescence quenching by gold nanoparticles [123]. The design of the competitive sensor format is shown in Fig. 14.9. The dye Cy3B and digoxigenin (Dig) are both attached to BSA. Gold nanoparticles are functionalized with anti-digoxigenin antibodies. If no digoxigenin is present in the analyte solution, the fluorescence is quenched because the double-functionalized BSA molecules bind to the antibodies (Fig. 14.9a). Upon the presence of digoxigenin in the analyte solution, the paratopes of the antibodies on the gold nanoparticles are occupied by the digoxigenin. Consequently, the Cy3B molecules are unquenched (Fig. 14.9b). A concentration series is shown in Fig. 14.9c. The linear range of the competitive digoxigenin assay ranges from 0.5 to 3 ng/mL. The limit of detection (LOD) was determined to be 0.2 ng/ml (LOD = $3 \times$ SD/m, where SD its standard deviation, and m the slope of the calibration curve). The limit of quantization (equal to $10 \times$ SD/m) was estimated to be 0.6 ng/ml.

Strong coupling (see Sect. 14.2.1) can also be used as a facile tool for hapten sensing based on fluorophore—metal nanoparticle interaction. Zhao et al. have functionalized silver nanoparticles with cytochrome P450cam proteins [124]. Cytochrome plays an important role in drug discovery because it can bind several haptens. As examples, Zhao et al. used camphor which binds to cytochrome, initiating a 26 nm spectral blueshift of the absorption band of cytochrome. Because strong coupling is an interaction of the absorption band of the fluorophore and the plasmon resonance, a change of the absorption of the cytochrome due to hapten binding immediately affects the plasmon resonance as well. The latter is easily detected and hence, the plasmonic structure acts as something like an "amplifier" of the binding event, mediated by strong coupling of the plasmon resonance to the absorption line of the cytochrome. In a more recent study, the same group extended this technique to detect a dozen of other important drugs [125].
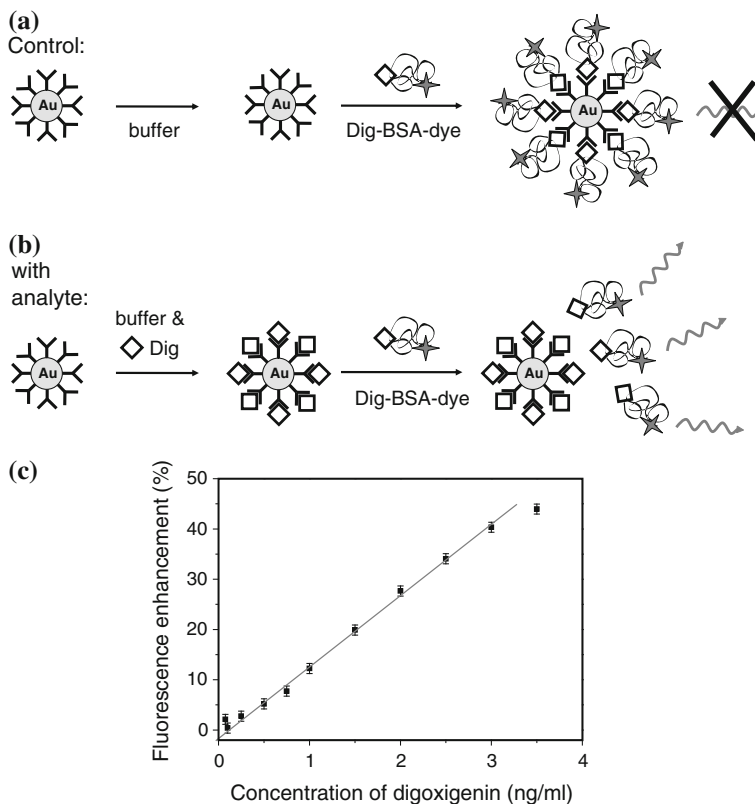
Fig. 14.9 **a** Control assay without analyte. Plain buffer solution is added in the first step. In the second step, BSA functionalized with Cy3B dye and digoxigenin molecules is added. The latter are recognized by the anti-Dig antibodies on the Au nanoparticles and the fluorescence is quenched. **b** If the analyte solution added in the first step contains digoxigenin, the digoxigenin occupies the paratopes of anti-Dig. Dig-BSA-Cy3B added in the second step cannot bind to the gold nanoparticles anymore. Hence, fluorescence from the Cy3B will be detected. **c** Fluorescence enhancement as a function of the concentration of digoxigenin. The fluorescence enhancement depends approximately linearly on the digoxigenin concentration from 0.5 to 3 ng/mL. Reprinted from Ref. [123] © 2009, with permission from Elsevier

14.3.4 Ion Sensing

Many heavy metal ions are severe environmental pollutants, but some can be important trace elements in biological systems. Fluorescence quenching by metal nanoparticles has been demonstrated to be also apt to detect metal ions. He et al. [126] have used pyridyl functionalized fluorophores which weakly coordinate to the nanoparticles. Fluorescence is quenched in this "closed" state. If however Cu^{2+} ions are present in the analyte solution, they coordinate much stronger to the pyridyl moieties, the fluorophores are detached from the nanoparticles and

unquenched. He et al. also demonstrated that this sensor shows not only sensitivity to Cu^{2+} ions but selectivity with respect to other ions was also demonstrated.

Mercury (II) detectors based on the manipulation of fluorescence by gold nanoparticles were reported by Huang and Chang [127], by Chen and coworkers [128, 129] and by Wang et al. [130]. More details on ion sensing with semiconductor and noble metal nanoparticles can be found in Ref. [131].

14.4 Lasers Comprising Nanometallic Resonators

14.4.1 Metallic DFB Gratings

The two indispensable ingredients of a laser are an active material and a resonator. Different resonator geometries have been established beyond the simplest setup of the two-mirror-cavity. One of them is the distributed feedback (DFB) grating, which is particularly useful for organic semiconductor lasers [132] because it allows for lasing in thin film waveguides. Specifically, DFB gratings have been used in optically pumped conjugated polymer lasers [133–136]. Dielectric DFB gratings guarantee low losses and a low lasing threshold. Unfortunately, dielectric DFB gratings elude the possibility to electrically contact the conjugated polymers. Metallic DFB gratings which could also serve as metallic contacts were supposed to increase the lasing threshold substantially due to energy transfer to the metal [137–139]. Despite this less promising forecast, it has been found that metallic DFB gratings are indeed able to serve as resonators for thin-film organic semiconductor lasers [138, 140], and they can do so even without any severe increase of the laser pumping threshold [141, 142].

An example, taken from Ref. [141] is shown in Fig. 14.10. The demonstrator consists of a glass substrate coated with a 110 nm thick ITO layer which is covered by a 2D grating of gold nanodiscs (Fig. 14.10a). The pitch is 300 nm, the diameter of the gold nanodiscs is 110 nm and their height is 30 nm. A $\sim$ 460 nm thick film of the polymer methyl-substituted ladder-type poly-(para)-phenylene (LPPP) was spin coated onto the sample from toluene solution. Figure 14.10a shows a sketch of the sample and illustrates the DFB resonator which utilizes the second order diffraction for feedback and the first order diffraction for out-coupling the light normal to the film surface. Figure 14.10b shows the photoluminescence spectrum for three different excitation pulse energies between 1.5 nJ and 2.7 nJ. While an excitation pulse energy of 1.5 nJ is well below the lasing threshold, a small additional peak is visible at 492 nm at an excitation energy of 1.9 nJ. A clear lasing mode is observed at a pump pulse energy of 2.7 nJ.
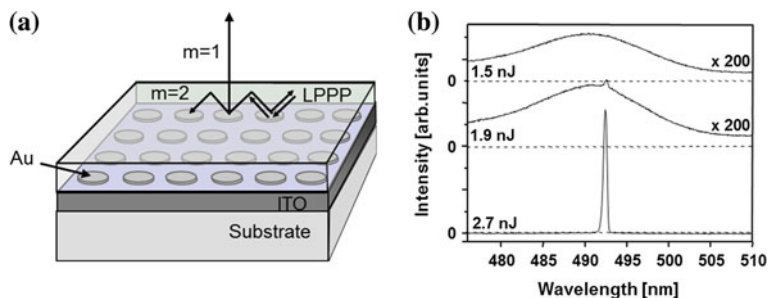
Fig. 14.10 **a** Schematic drawing of the polymer film on top of a gold nanodisc photonic crystal template. Feedback is accomplished by second order (m = 2) Bragg scattering, while the first order (m = 1) scattering couples the lasing mode out in vertical direction. The ITO thickness is 110 nm, the gold nanodiscs measure 110 nm in diameter and 30 nm in height, the grating constant is 300 nm and the LPPP film is approx. 460 nm thick. **b** Emission spectrum in the spectral region of the first vibronic sideband of LPPP below, at, and above lasing threshold. The pump pulse energies are indicated. Reprinted from Ref. [141] © 2003, with permission from Wiley–VCH Verlag GmbH & Co KG, Weinheim

14.4.2 Random Lasers Comprising Metallic Nanoparticles

It has been put forward by Anderson 1958 that particles like electrons can be localized in random media [143, 144]. Subsequently, it has been shown that Anderson localization does also apply for photons in random dielectric media [145–148]. A later report on Anderson localization of photons [149] has been questioned, because "it is difficult to distinguish localized light from absorbed light" [150]. This controversy, however, points to an interesting application: What if the randomly distributed scatterers are embedded in an active medium, not only capable of compensating absorption, but also being apt to provide a net gain. Would it be possible to use the random scattering as a laser resonator? And if so, could randomly distributed metallic nanostructures be used as a Anderson-like laser cavity? Both questions seem to be positively answered in the meantime. Amplified spontaneous emission and laser action with randomly distributed dielectric spheres as resonators have been predicted [151], observed [152, 153], and theoretically modeled [154–157]. The differences between rather weak scattering random cavities, which often lead to amplified spontaneous emission rather than coherent lasing, and strong scattering random cavities which show true lasing has been investigated in detail by Wiersma et al. [155], and by Cao et al. [158, 159] in theory and experiment, respectively. More recently, coherent lasing modes in the weak scattering media have also been discussed [160].

When metallic scatterers such as gold or silver nanoparticles are used, both incoherent and coherent random lasing has been demonstrated. Metal nanoparticle-induced incoherent random lasing, which occurs in weakly scattering media and is sometimes argued to be nothing else as amplified spontaneous emission, has been observed by Dice and coworkers [161, 162] and shortly after also by Popov
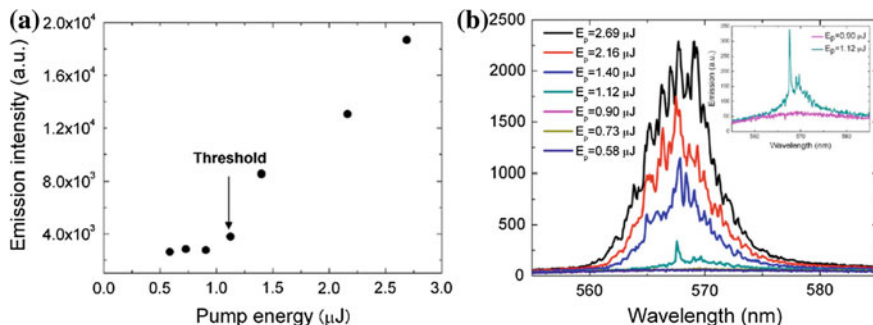
Fig. 14.11 Random laser emission from a Rhodamine 6G doped polymer thin film, embedded with silver nanoparticles. **a** Evolution of emission intensity as a function of pump energy. **b** Emission spectra as a function of pump energy. The inset shows the emission spectra just below and just above the pump threshold. Adapted from Ref. [168], reprinted with permission, © 2008 The American Institute of Physics

et al. [163, 164] and more recently by El-Dardiry and Lagendijk [165] and by Murai et al. [166]. In these incoherent random lasers, a spectral narrowing of the fluorescence is observed down to a few nanometers spectral width. Typically, only one peak is observed with a width of 3–5 nm indicating emission of low coherence. However, the intensity of the peak grows exponentially above a threshold.

In contrast to the single peak of about 4 nm width as observed in incoherent lasing, coherent feedback by random, but in-phase scattering leads to very sharp laser peaks (typically far less than 1 nm in width), whereby each individual laser peak is usually attributed to one closed path of coherent feedback. Using noble metal nanoparticles as randomly distributed scatterers, narrow laser-like emission peaks have first been reported by Kang [167] and have extensively been researched by the Meng and coworkers [168–172] and by others [173–175].

In their seminal paper [168], Meng and coworkers had embedded silver nanoparticles in a polyvinyl alcohol film which was doped with Rhodamine 6G, a well-known laser dye. They found that ultra-sharp coherent laser peaks were evolving at a pump fluence of only 1 μJ per pump pulse (Fig. 14.11b). The pump laser used was a 532 nm Nd:YAG laser, 10 Hz repetition rate, 25 ps pulse width, which was focused down to a stripe of 17 μm width and 2.4 mm length. The emission intensity of the laser spikes showed a clear pumping threshold (Fig. 14.11a).

14.4.3 Spaser

The term SPASER is an acronym for Surface Plasmon Amplification by Stimulated Emission and has been coined by Bergman and Stockman in 2003 [176]. The "R" is, strictly speaking, added to make a noun out of the verbum "to SPASE".

"Of Radiation" was added in the title of the original publication, in analogy to the LASER which is an acronym for Light Amplification by Stimulated Emission of Radiation. However, radiation is not necessarily produced in a SPASER as plasmons can be emitted via stimulated emission directly, because a plasmon-polariton, taken as a quasi-particle, behaves like a boson. Further, plasmon oscillations do not necessarily need to radiate, or in other words, they do not need to decay radiatively. Prominent examples are the surface plasmon-polariton which cannot decay radiatively into the vacuum if no specific coupling mechanism such as the Otto-[177] or the Kretschmann [178] configuration is applied. Another example of nonradiating plasmons are nanoparticle plasmons of higher order electric or magnetic symmetry (only electric-dipole-like nanoparticle plasmons radiate effectively). The essence is that, if one wants to use the spasing mechanism to produce a coherent beam of light (a laser beam), a two-step process needs to take place. First, the active material must coherently excite a plasmon-polariton and in a second step the plasmon decays to a radiating, free space photon. This has been discussed by Protsenko et al. in their article "Dipole Nanolaser"[179] and in detail by Zheludev and coworkers in their article "Lasing Spaser" [180]. More theoretical considerations have been published meanwhile on this topic [181, 182]. Recently, Mark Stockman theoretically showed that a plasmonic nanostructure can not only be used as a spaser, but also as an ultrafast amplifier [183]. Plasmonic structures with nonspherical geometry such as a bowtie nanoantenna [184] or nanocups [185] have been proposed as spasing structures, as well.

First experiments where surface plasmon polaritons were used in lasing devices date back to the late 90'ies. Capasso and his group showed that quantum cascade deep IR lasers profit from the use of surface plasmons [186, 187]. Stimulated emission of surface plasmons using a solution of dye molecules as the active medium was reported by Seidel and coworkers [188]. Capasso and coworkers placed a plasmonic nanoantenna on top of the entrance facet of a semiconductor laser [189]. However, in this case the plasmonic antenna is rather a focusing element of the laser radiation produced by a traditional edge emitting semiconductor laser.

An interesting concept is also to encapsulate subwavelength scale semiconductor heterostructures by metallic nanocavities. A heterostructure pillar of roughly 1,500 nm in height and 200 nm in diameter, covered by gold, was shown by Hill and coworkers to lase at 1,400 nm when the InGaAs laser-active region was pumped electrically [190–192]. Device improvement was found by Y. Fainman and coworkers if a silica spacer between the active InGaAs layer and the metallic coating was introduced [193–195]. This leads to a reduced loss of excitation energy via quenching of excitons by the metal. A size reduced version of a sub-micron semiconductor nanolaser covered by a metallic layer has recently been demonstrated: An InP disc was covered by a Ag "nanopan". This allowed for a subwavelength mode volume of only $0.56 \left(\lambda/(2n) \right)^3$, n being the refractive index of the semiconductor disc [196]. An "inverse" structure, where the active medium is outside and the metallic layer is inside has been reported by Flynn et al. [197].

An even more purist laser comprising a subwavelength modal volume has been introduced by the group of Zhang. They put a CdS nanowire on top of a silver film which was covered by an insulating MgF_2 layer of miniscule thickness [198]. This lead to a modal volume which is confined to just a few nanometers in the direction perpendicular to the semiconductor rod and also only a few nanometers in the direction vertical to the silver film, but the rods were micrometers long in the third dimension. A similar laser (of, however, much shorter rods) has been demonstrated by Lu et al. [199]. Most important, this group showed that the photon statistics of the laser output above threshold behaves as expected from a coherent laser beam: the second order photon correlation function is strictly one. However, semiconductor nanowires or nanorods used in these studies possess one elongated axis. An even more confined lasing spaser should, however, show the same nanoscale extensions in all three directions. A team around Noginov, Shalaev and Wiesner has recently reported on such a three dimensional nanoscale laser [200]. Gold nanoparticles with a diameter of 14 nm were covered by a silica shell of 15 nm thickness (Fig. 14.12, inset). The silica shell of each nanolaser contained approximately $2.7 \cdot 10^3$ molecules of the laser dye OG-488. The lasing spectra of a suspension of these nanolasers are shown in the main panel of Fig. 14.12 for different pumping powers. Pumping was achieved by a 488 nm pulsed laser with 5 ns pulse width and pulse energies up to 22.5 mJ. The lasing threshold was at about 5 μJ. Using a 100-fold diluted suspension showed the same lasing characteristics apart from a reduced overall output intensity. Because of this, the authors concluded that the stimulated emission stemmed from single nanolasers.

References

 1. Förster T (1948) Zwischenmolekulare Energiewanderung und Fluoreszenz. Ann Phys
    2:55–75
 2. Förster T (1949) Experimentelle und theoretische Untersuchung des zwischenmolekularen
    Übergangs von Elektronenanregungsenergie. Z Naturforsch 4a:321–327
 3. Metiu H (1984) Surface enhanced spectroscopy. Prog Surf Sci 17:153–320
 4. Leung PT, George TF (1995) Molecular fluorescence spectroscopy in the vicinity of a
    microstructure. J Chim Phys Phys- Chim Biol 92:226–247
 5. Klimov VV, Ducloy M, Letokhov VS (2001) Spontaneous emission of an atom in the
    presence of nanobodies. Quantum Electron 31:569–586
 6. Lakowicz JR (2001) Radiative decay engineering: biophysical and biomedical applications.
    Anal Biochem 298:1–24
 7. Lakowicz JR, Shen Y, D'Auria S et al (2002) Radiative decay engineering 2: effects of
    silver island films on fluorescence intensity, lifetimes, and resonance energy transfer. Anal
    Biochem 301:261–277
 8. Klar TA, Feldmann J (2012) Fluorophore—metal nanoparticle interactions and their
    applications in biosensing. In: Sau TK, Rogach A (eds) complex-shaped metal
    nanoparticles. Wiley-VCH, Weinheim, pp 395–427
 9. Dulkeith E, Morteani AC, Niedereichholz T et al (2002) Fluorescence quenching of dye
    molecules near gold nanoparticles: radiative and nonradiative effects. Phys Rev Lett
    89:203002
10. Anger P, Bharadwaj P, Novotny L (2006) Enhancement and quenching of single-molecule
    fluorescence. Phys Rev Lett 96:113002
11. Tam F, Goodrich GP, Johnson BR et al (2007) Plasmonic enhancement of molecular
    fluorescence. Nano Lett 7:496–501
12. Biteen JS, Pacifici D, Lewis NS et al (2005) Enhanced radiative emission rate and quantum
    efficiency in coupled silicon nanocrystal-nanostructured gold emitters. Nano Lett
    5:1768–1773
13. Kühn S, Hakanson U, Rogobete L et al (2006) Enhancement of single-molecule
    fluorescence using a gold nanoparticle as an optical nanoantenna. Phys Rev Lett 97:017402
14. Gerber S, Reil F, Hohenester U et al (2007) Tailoring light emission properties of
    fluorophores by coupling to resonance-tuned metallic nanostructures. Phys Rev B
    75:073404
15. Thomas M, Greffet JJ, Carminati R et al (2004) Single molecule spontaneous emission to
    absorbing nanostructures. Appl Phys Lett 85:3863–3865
16. Soller T, Ringler M, Wunderlich M et al (2007) Radiative and nonradiative rates of
    phosphors attached to gold nanoparticles. Nano Lett 7:1941–1946
17. Mertens H, Koenderink AF, Polman A (2007) Plasmon-enhanced luminescence near noble-
    metal nanospheres: comparison of exact theory and an improved Gersten and Nitzan model.
    Phys Rev B 76:115123
18. Chowdhury MH, Pond J, Gray SK et al (2008) Systematic computational study of the effect
    of silver nanoparticle dimers on the coupled emission from nearby fluorophores. J Phys
    Chem C 112:11236–11249

19. Chance RR, Prock A, Silbey R (1978) Molecular fluorescence and energy transfer near interfaces. In: Prigogine I, Rice SR (eds) Advances in chemical physics. Wiley, New York, pp 1–65

20. Drexhage KH, Fleck M, Kuhn H et al (1966) Beeinflussung der Fluoreszenz eines Europium-Chelates durch einen Spiegel. Berichte der Bunsengesellschaft für Physikalische Chemie 20:1179

21. Drexhage KH, Kuhn H, Schäfer FP (1968) Variation of the fluorescence decay time of a molecule in front of a mirror. Berichte der Bunsen-Gesellschaft für Physikalische Chemie 72:329

22. Kuhn H (1970) Classical aspects of energy transfer in molecular systems. J Chem Phys 53:101–108

23. Dexter DL (1953) A theory of sensitized luminescence in solids. J Chem Phys 21:836–850

24. Gersten J, Nitzan A (1981) Spectroscopic properties of molecules interacting with small dielectric particles. J Chem Phys 75:1139–1152

25. Ruppin R (1982) Decay of an excited molecule near a small metal sphere. J Chem Phys 76:1681–1684

26. Mie G (1908) Beiträge zur Optik trüber Medien, speziell kolloidaler Metallösungen. Ann Phys 330:377–445

27. Leung PT, George TF, Lee YC (1987) Limit of the image theory for the classical decay rates of molecules at surfaces. J Chem Phys 86:7227–7229

28. Leung PT, George TF (1987) Dynamical analysis of molecular decay at spherical surfaces. J Chem Phys 87:6722–6724

29. Leung PT, Kim YS, George TF (1988) Radiative decay rates for molecules near a dielectric sphere. J Phys Chem 92:6206–6208

30. Kim YS, Leung PT, George TF (1988) Remark on the morphology-dependent resonance in the decay rate spectrum for molecules near a spherical surface. Chem Phys Lett 152:453–456

31. Kim YS, Leung PT, George TF (1988) Classical decay rates for molecules in the presence of a spherical surface: a complete treatment. Surf Sci 195:1–14

32. Garcia de Abajo FJ (2008) Nonlocal effects in the plasmons of strongly interacting nanoparticles, dimers, and waveguides. J Phys Chem C 112:17983–17987

33. Zuloaga J, Prodan E, Nordlander P (2009) Quantum description of the plasmon resonance of a nanoparticle dimer. Nano Lett 9:887–891

34. Strickler SJ, Berg RA (1962) Relationship between absorption intensity and fluorescence lifetime of molecules. J Chem Phys 37:814–822

35. Matveeva EG, Shtoyko T, Gryczynski I et al (2008) Fluorescence quenching/enhancement surface assays: Signal manipulation using silver-coated gold nanoparticles. Chem Phys Lett 454:85–90

36. Dulkeith E, Ringler M, Klar TA et al (2005) Gold nanoparticles quench fluorescence by phase induced radiative rate suppression. Nano Lett 5:585–589

37. Aussenegg FR, Leitner A, Lippitsch ME et al (1987) Novel aspects of fluorescence lifetime for molecules positioned close to metal surfaces. Surf Sci 189:935–945

38. Imahori H, Norieda H, Nishimura Y et al (2000) Chain length effect on the structure and photochemical properties of self-assembled monolayers of porphyrins on gold electrodes. J Phys Chem B 104:1253–1260

39. Imahori H, Arimura M, Hanada T et al (2001) Photoactive three-dimensional monolayers: porphyrin-alkanethiolate-stabilized gold clusters. J Am Chem Soc 123:335–336

40. Geddes CD, Cao H, Gryczynski I et al (2003) Metal-enhanced fluorescence (MEF) due to silver colloids on a planar surface: potential applications of indocyanine green to in vivo imaging. J Phys Chem A 107:3443–3449

41. Lakowicz JR, Shen B, Gryczynski Z et al (2001) Intrinsic fluorescence from DNA can be enhanced by metallic particles. Biophys Biochem Res Commun 286:875–879

42. Gryczynski I, Malicka J, Holder E et al (2003) Effects of metallic silver particles on the emission properties of $Ru(bpy)_3^{2+}$. Chem Phys Lett 372:409–414

43. Aussenegg FR, Draxler S, Leitner A et al (1984) Picosecnond investigations on the fluorescence properties of adsorbed dye molecules. J Opt Soc Am B 1:456–457

44. Leitner A, Lippitsch ME, Draxler S et al (1985) Fluorescence properties of dyes adsorbed to silver islands, investigated by picosecond techniques. Appl Phys B 36:105–109

45. Kuhnke K, Becker R, Epple M et al (1997) C60 exciton quenching near metal surfaces. Phys Rev Lett 79:3246–3249

46. Glass AM, Liao PF, Bergman JG et al (1980) Interaction of metal particles with adsorbed dye molecules: absorption and luminescence. Opt Lett 5:368–370

47. Fofang NT, Park TH, Neumann O et al (2008) Plexcitonic nanoparticles: plasmon-exciton coupling in Nanoshell-J-Aggregate complexes. Nano Lett 8:3481–3487

48. Manjavacas A, Garcia de Abajo FJ, Nordlander P (2011) Quantum plexcitonics: strongly interacting plasmons and excitons. Nano Lett 11:2318–2323

49. Pustovit VN, Shahbazyan TV (2009) Cooperative emission of light by an ensemble of dipoles near a metal nanoparticle: the plasmonic Dicke effect. Phys Rev Lett 102:077401

50. Bellessa J, Bonnand C, Plenet JC et al (2004) Strong coupling between surface plasmons and excitons in an organic semiconductor. Phys Rev Lett 93:036404

51. Dintinger J, Klein S, Bustos F et al (2005) Strong coupling between surface plasmon-polaritons and organic molecules in subwavelength hole arrays. Phys Rev B (Condensed Matter) 71:035424

52. Sugawara Y, Kelf TA, Baumberg JJ et al (2006) Strong Coupling between Localized Plasmons and Organic Excitons in Metal Nanovoids. Phys Rev Lett 97:266808

53. Romero MJ, Van de Lagemaat J, Mora-Sero I et al (2006) Imaging of resonant quenching of surface plasmon by quantum dots. Nano Lett 6:2833–2837

54. Zhao J, Jensen L, Sung J et al (2007) Interaction of plasmon and molecular resonances for rhodamine 6G adsorbed on silver nanoparticles. J Am Chem Soc 129:7647–7656

55. Haes AJ, Zou S, Zhao J et al (2006) Localized surface resonance spectroscopy near molecular resonances. J Am Chem Soc 128:10905–10914

56. Fischer UC, Zingsheim HP (1981) Sub-microscopic pattern replication with visible-light. J Vac Sci Technol 19:881–885

57. Cade NI, Ritman-Meer T, Richards D (2009) Strong coupling of localized plasmons and molecular excitons in nanostructured silver films. Phys Rev B 79:241404

58. Gülen D (2010) Numerical spectroscopic investigation on the functionality of molecular excitons in tuning the plasmonic splitting observed in core/shell hybrid nanostructures. J Phys Chem C 114:13825–13831

59. Wurtz GA, Evans PR, Hendren W et al (2007) Molecular plasmonics with tuneable exciton-plasmon coupling strength in J-aggregate hybridized Au nanorod assemblies. Nano Lett 7:1297–1303

60. Ni W, Yang Z, Chen H et al (2008) Coupling between molecular and plasmonic resonances in freestanding dye-gold nanorod hybrid nanostructures. J Am Chem Soc 130:6692–6693

61. Vasa P, Pomraenke R, Cirmi G et al (2010) Ultrafast manipulation of strong coupling in metal-molecular aggregate hybrid nanostructures. ACS Nano 4:7559–7565

62. Vasa P, Pomraenke R, Schwieger S et al (2008) Coherent exciton-plasmon-polariton ineractions in hybrid metal-semiconductor nanostructures. Phys Rev Lett 101:116801

63. Kometani N, Tsubonishi M, Fujita T et al (2001) Preparation and optical absorption spectra of dye-doped Au, Ag, and Au/Ag colloidal nanoparticles in aqueous solutions and in alternate assemblies. Langmuir 17:578–580

64. Sato T, Ichikawa T, Ito T et al (1995) Nonlinear-optical properties of silver sols prepared by photoreduction method. Chem Phys Lett 242:310–314

65. Wiederrecht GP, Wurtz GA, Hranisavljevic J (2004) Coherent coupling of molecular excitonic polarisations of noble metal nanoparticles. Nano Lett 4:2121–2125

66. Ambjörnsson T, Mukhopadhyay G, Apell SP et al (2006) Resonant coupling between localized plasmons and anisotropic molecular coatings in ellipsoidal metal nanoparticles. Physical Review B 73:085412

67. Gu Y, Huang L, Martin OJF et al (2010) Resonance fluorescence of single molecules assisted by a plasmonic structure. Phys Rev B 81:193103
68. Uwada T, Toyota R, Masuhara H et al (2007) Single particle spectroscopic investigation on the interaction between exciton transition of cyanine dye J-aggregates and localized surface plasmon polarisation of gold. J Phys Chem C 111:1549–1552
69. Ni W, Ambjörnsson T, Apell SP et al (2010) Observing plasmonic-molecular resonance coupling on single gold nanorods. Nano Lett 10:77–84
70. Liu GL, Long YT, Choi Y et al (2007) Quantized plasmon quenching dips nanospectroscopy via plasmon resonance energy transfer. Nat Methods 4:1015–1017
71. Fano U (1961) Effects of configuration interaction on intensities and phase shifts. Phys Rev 124:1866
72. Zhang W, Govorov AO, Bryant GW (2006) Semiconductor-metal nanoparticle molecules: hybrid excitons and the nonlinear fano effect. Phys Rev Lett 97:146804
73. Neuhauser D, Lopata K (2007) Molecular nanoplasmonics: cross manipulation of near-field plasmons and molecules. I. Theory and application to junction control. J Chem Phys 127:154715
74. Kelley AM (2007) A Molecular spectroscopic description of optical spectra of J-aggregated dyes on gold nanoparticles. Nano Lett 7:3235–3240
75. Yan JY, Zhang W, Duan S et al (2008) Optical properties of coupled metal-semiconductor and metal-molecule nanocrystal complexes: role of multipole effects. Phys Rev B 77:165301
76. Cheng MT, Liu SD, Zhou HJ et al (2007) Coherent exciton-plasmon interaction in the hybrid semiconductor quantum dot and metal nanoparticle complex. Opt Lett 32:2125–2127
77. Purcell EM (1946) Spontaneous emission probabilities at radio frequencies. Phys Rev 69:681
78. Yokoyama H, Nishi K, Anan T et al (1990) Enhanced spontaneous emission from GaAs quantum wells in monolithic microcavities. Appl Phys Lett 57:2814–2816
79. Ritchie G, Burstein E (1981) Luminescence of dye molecules adsorbed at a Ag surface. Phys Rev B 24:4843–4846
80. Biteen JS, Lewis NS, Atwater HA et al (2006) Spectral tuning of plasmon-enhanced silicon quantum dot luminescence. Appl Phys Lett 88:131109
81. Biteen JS, Sweatlock LA, Mertens H et al (2007) Plasmon-enhanced photoluminescence of silicon quantum dots: simulation and experiment. J Phys Chem C 111:13372–13377
82. Fedutik Y, Temnov VV, Schöps O et al (2007) Exciton-plasmon-photon conversion in plasmonic nanostructures. Phys Rev Lett 99:136802
83. Wu CY, He CL, Lee HM et al (2010) Surface-plasmon-mediated photoluminescence enhancement from red-emitting InGaN coupled with colloidal gold nanocrystals. J Phys Chem C 114:12987–12993
84. Kühn S, Hakanson U, Rogobete L et al (2006) Enhancement of single-molecule fluorescence using a gold nanoparticle as an optical nanoantenna: supplementary information. Phys Rev Lett 97:017402
85. Le Ru EC, Etchegoin PG, Grand J et al (2007) Mechanisms of spectral profile modification in surface-enhanced fluorescence. J Phys Chem C 111:16076–16079
86. Ringler M, Schwemer A, Wunderlich M et al (2008) Shaping emission spectra of fluorescent molecules with single plasmonic nanoresonators. Phys Rev Lett 100:203002
87. Bakker RM, Yuan HK, Liu Z et al (2008) Enhanced localized fluorescence in plasmonic nanoantennae. Appl Phys Lett 92:043101
88. O'Carrol DM, Hofmann C, Atwater HA (2010) Conjugated polymer/metal nanowire heterostructure plasmonic antennas. Adv Mater 22:1223–1227
89. Zhao L, Ming T, Chen H et al (2011) Plasmon-induced modulation of the emission spectra of the fluorescent molecules near gold nanorods. Nanoscale 3:3849–3859
90. Xu Y-L (1995) Electromagnetic scattering by an aggregate of spheres. Appl Opt 34:4573–4588

91. Xu Y-L (1998) Electromagnetic scattering by an aggregate of spheres: errata. Appl Opt 37:6494
92. Xu H, Aizpurua J, Käll M et al (2002) Electromagnetic contributions to single-molecule sensitivity in surface-enhanced Raman scattering. Phys Rev E 62:4318–4324
93. Enderlein J (2002) Spectral properties of a fluorescing molecule within a spherical metallic nanocavity. Phys Chem, Chem Phys 4:2780–2786
94. Ringler M, Schwemer A, Wunderlich M et al (2008) Shaping emission spectra of fluorescent molecules with single plasmonic nanoresonators. Phys Rev Lett, Support Inf 100:203002
95. Djiango M, Ritter K, Müller R et al (2012) Spectral tuning of the phosphorescence from metalloporphyrins attached to gold nanorods. Opt Express 20:19374–19381
96. Tyagi S, Kramer FR (1996) Molecular beacons: probes that fluoresce upon hybridization. Nat Biotechnol 14:303–308
97. Dubertret B, Calame M, Libchaber AJ (2001) Single-mismatch detection using gold-quenched fluorescent oligonucleotides. Nat Biotechnol 19:365–370
98. Dubertret B, Calame M, Libchaber AJ (2001) Single-mismatch detection using gold-quenched fluorescent oligonucleotides, Erratum. Nat Biotechnol 19:680–681
99. Maxwell DJ, Taylor JR, Nie S (2002) Self-assembled nanoparticle probes for recognition and detection of biomolecules. J Am Chem Soc 124:9606–9612
100. Li YT, Liu HS, Lin HP et al (2005) Gold nanoparticles for microfluidics-based biosensing of PCR products by hybridization-induced fluorescence quenching. Electrophoresis 26:4743–4750
101. Mo ZH, Yang XC, Guo KP et al (2007) A nanogold-quenched fluorescence duplex probe for homogeneous DNA detection based on strand displacement. Anal Bioanal Chem 389:493–497
102. Li H, Rothberg LJ (2004) DNA sequence detection using selective fluorescence quenching of tagged oligonucleotide probes by gold nanoparticles. Anal Chem 76:5414–5417
103. Ray PC, Darbha gK, Ray A et al (2007) A gold-nanoparticle-based fluorescence resonance energy transfer probe for multiplexed hybridization detection: accurate identification of bio-agents DNA. Nanotechnology 18:375504
104. Kim CK, Kalluru RR, Singh JP et al (2006) Gold-nanoparticle-based miniaturized laser-induced fluorescence probe for specific fluorescence probe for specific DNA hybridization detection: studies on size-dependent optical properties. Nanotechnology 17:3085–3093
105. Xu Q, Liu J, He Z et al (2010) Superquenching acridinium ester chemiluminescence by gold nanoparticles for DNA detection. Chem Commun 46:8800–8802
106. Li H, Liang R, Turner DH et al (2007) Selective quenching of fluorescence from unbound oligonucleotides by gold nanoparticles as a probe of RNA structure. RNA 13:2034–2041
107. Wu ZS, Jiang JH, Fu L et al (2006) Optical detection of DNA hybridization based on fluorescence quenching of tagged oligonucleotide probes by gold nanoparticles. Anal Biochem 353:22–29
108. Oh E, Hong MY, Lee D et al (2005) Inhibition assay of biomolecules based on fluorescence resonance energy transfer (FRET) between quantum dots and gold nanoparticles. J Am Chem Soc 127:3270–3271
109. Grant SA, Heits B, Kleiboeker S (2006) Development of an optical biosensor utilizing gold nanoparticles to detect porcine reproductive and respiratory syndrome virus. Sensor Lett 4:246–252
110. Ao L, Gao F, Pan B et al (2006) Fluoroimmunoassay for antigen based on fluorescence quenching signal of gold nanoparticles. Anal Chem 78:1104–1106
111. Peng Z, Chen Z, Jiang JH et al (2007) A novel immunoassay based on the dissociation of immunocomplex and fluorescence quenching by gold nanoparticles. Anal Chim Acta 583:40–44
112. Mayilo S, Kloster MA, Wunderlich M et al (2009) Long-range fluorescence quenching by gold nanoparticles in a sandwich immunoassay for cardiac troponin T. Nano Lett 9:4558–4563

113. Ricchiuti V, Voss EM, Ney A et al (1998) Cardiac troponin T isoforms expressed in renal diseased skeletal muscle will not cause false-positive results by the second generation cardiac troponin T assay by Boehringer Mannheim. Clin Chem 44:1919–1924
114. Nichtl A (2004) Gold conjugates containing detergent. US Patent 6,833,275
115. Huang X, Ren J (2011) Gold nanoparticles based chemiluminescenct resonance energy transfer for immunoassay of alpha fetoprotein cancer marker. Anal Chim Acta 686:115–120
116. Freddi S, D'Alfonso L, Collini M et al (2009) Excited-state lifetime assay for protein detection on gold colloids—fluorophore complexes. J Phys Chem C 113:2722–2730
117. Kim YP, Daniel WL, Xia Z et al (2010) Bioluminescent nanosensors for protease detection based upon gold nanoparticle-luciferase conjugates. Chem Commun 46:76–78
118. Kim JH, Chung BH (2010) Proteolytic fluorescent signal amplification on gold nanoparticles for a highly sensitive and rapid protease assay. Small 6:126–131
119. Barker SLR, Kopelman R (1998) Development and cellular application of fiber optic nitric oxide sensors based on a gold-adsorbed fluorophore. Anal Chem 70:4902–4906
120. Kato N, Caruso F (2005) Homogeneous, competitve fluorescent quenching immunoassays based on gold nanoparticle/polyelectrolyte coated latex particles. J Phys Chem B 109:19604–19612
121. Aslan K, Perez-Luna VH (2006) Nonradiative Interactions between biotin-functionalized gold nanoparticles and fluorophore-labelled antibiotin. Plasmonics 1:111–119
122. Wilson R, Nicolau DV (2011) Separation-free detection of biological molecules based on plasmon-enhanced fluorescence. Angew Chem Int Ed 50:2151–2154
123. Mayilo S, Ehlers B, Wunderlich M et al (2009) Competitive homogeneous digoxigenin immunoassay based on fluorescence quenching by gold nanoparticles. Anal Chim Acta 646:119–122
124. Zhao J, Das A, Zhang X et al (2006) Resonance surface plasmon spectroscopy: low molecular weight substrate binding to cytochrome P450. J Am Chem Soc 128:11004–11005
125. Das A, Zhao J, Schatz GC et al (2009) Screening of type i and type II drug binding to human cytochrome P450–3A4 in nanodiscs by localized surface plasmon resonance spectroscopy. Anal Chem 81:3754–3759
126. He X, Liu H, Li Y et al (2005) Gold nanoparticle-based fluorimetric and colorimetric sensing of copper(II) Ions. Adv Mater 17:2811–2815
127. Huang CC, Chang HT (2006) Selective gold-nanoparticle-based "turn-on" fluorescent sensors for detection of mercury(II) in aqueous solution. Anal Chem 78:8332–8338
128. Chen J, Zheng AF, Chen A et al (2007) A functionalized gold nanoparticles and Rhodamine 6G based fluorescent sensor for high sensitive and selective detection of mercury (II) in environmental water samples. Anal Chim Acta 599:134–142
129. Zheng AF, Chen J, Wu G et al (2009) Optimisation of a sensitive method for the "switch-on" determination of mercury(II) in waters using Rhodamine B capped gold nanoparticles as a fluorescence sensor. Microchim Acta 164:17–27
130. Wang H, Wang Y, Jin J et al (2008) Gold nanoparticle-based colorimetric and "turn-on" fluorescent probe for mercury(II) ions in aqueous solution. Anal Chem 80:9021–9028
131. de Aberasturi DJ, Montenegro JM, de Larramendi IR et al (2012) Optical sensing of small ions with colloidal nanoparticles. Chem Mater 24:738–745
132. Shank CV, Bjorkholm JE, Kogelnik H (1971) Tunable distributed feedback dye laser. Appl Phys Lett 18:395
133. Kallinger C, Hilmer M, Haugeneder A et al (1998) A flexible conjugated polymer laser. Adv Mater 10:920–923
134. McGehee MD, Díaz-García MA, Hide F et al (1998) Semiconducting polymer distributed feedback lasers. Appl Phys Lett 72:1536–1538
135. Riechel S, Kallinger C, Lemmer U et al (2000) A nearly diffraction limited surface emitting conjugated polymer laser utilizing a two-dimensional photonic band structure. Appl Phys Lett 77:2310–2312
136. Riechel S, Lemmer U, Feldmann J et al (2000) Laser modes in organic solid-state distributed feedback lasers. Appl Phys B 71:897–900

137. McGehee MD, Heeger AJ (2000) Semiconducting (conjugated) polymers as materials for solid-state lasers. Adv Mater 12:1655
138. Andrew P, Turnbull GA, Samuel IDW et al (2002) Photonic band structure and emission characteristics of a metal-backed polymeric distributed feedback laser. Appl Phys Lett 81:954–956
139. Andrew P, Barnes WL (2001) Molecular fluorescence above metallic gratings. Phys Rev B 64:125405
140. Okamoto T, H'Dhili F, Kawata S (2004) Towards plasmonic band gap laser. Appl Phys Lett 85:3968–3970
141. Stehr J, Crewett J, Schindler F et al (2003) A low threshold polymer laser based on metallic nanoparticle gratings. Adv Mater 15:1726
142. Reufer M, Riechel S, Lupton JM et al (2004) Low-threshold polymeric distributed feedback lasers with metallic contacts. Appl Phys Lett 84:3262
143. Anderson PW (1958) Absence of diffusion in certain random lattices. Phys Rev 109:1492–1505
144. Abrahams E, Anderson PW, Licciardello DC et al (1979) Scaling theory of localization: absence of quantum diffusion in two dimensions. Phys Rev Lett 42:673–676
145. John S (1984) Electromagnetic absorption in a disordered medium near a photon mobility edge. Phys Rev Lett 53:2169–2172
146. Kuga Y, Ishimaru A (1984) Retroreflectance from a dense distribution of spherical particles. J Opt Soc Am A 1:831–835
147. Van Albada MP, Lagendijk A (1985) Observation of weak localization of light in a random medium. Phys Rev Lett 55:2692–2695
148. Wolf PE, Maret G (1985) Weak localization and coherent backscattering of photons in disordered media. Phys Rev Lett 55:2696–2699
149. Wiersma DS, Bartolini P, Lagendijk A et al (1997) Localization of light in a disordered medium. Nature 390:671–673
150. Scheffolld F, Lenke R, Tweer R et al (1999) Localization or classical diffusion of light? Nature 398:206–207
151. Lethokov VS (1968) Generation of light by a scattering medium with negative resonance absorption. Sov Phys JETP 26:835–840
152. Lawandy NM, Balachandran RM, Gomes ASL et al (1994) Laser action in strongly scattering media. Nature 368:436–438
153. Wiersma DS, Van Albada MP, Lagendijk A (1995) Coherent backscattering of light from amplifying random media. Phys Rev Lett 75:1739–1742
154. John S, Pang G (1996) Theory of lasing in a multiple-scattering medium. Phys Rev A 54:3642–3652
155. Wiersma DS, Lagendijk A (1996) Light diffusion with gain and random lasers. Phys Rev E 54:4256–4265
156. Jiang X, Soukoulis CM (2000) Time dependent Theory for random lasers. Phys Rev Lett 85:70–73
157. Vanneste C, Sebbah P (2001) Selective excitation of localized modes in active random media. Phys Rev Lett 87:183903
158. Cao H, Zhao YG, Ho ST et al (1999) Random laser action in semiconductor powder. Phys Rev Lett 82:2278–2281
159. Cao H, Xu JY, Chang SH et al (2000) Transition from amplified spontaneous emission to laser action in strongly scattering media. Phys Rev E 61:1985–1989
160. Polson RC, Vardeny ZV (2005) Organic random lasers in the weak-scattering regime. Phys Rev B 71:045205
161. Dice GD, Mujumdar S, Elezzabi AY (2005) Plasmonically enhanced diffusive and subdiffusive metal nanoparticle-dye random laser. Appl Phys Lett 86:131105
162. Dice GD, Elezzabi AY (2007) Random lasing from a nanoparticle-based metal-dielectric-dye medium. J Opt A 9:186–193

163. Popov O, Zilberstein A, Davidov D (2006) Random lasing from dye-gold nanoparticles in polymer films: enhanced gain at the surface-plasmon-resonance wavelength. Appl Phys Lett 89:191116

164. Popov O, Zilberstein A, Davidov D (2007) Enhanced amplified emission induced by surface plasmons on gold nanoparticles in polymer film random lasers. Polym Adv Technol 18:751–755

165. El-Dardiry RG, Lagendijk A (2011) Tuning random lasers by engineered absorption. Appl Phys Lett 98:161106

166. Murai S, Tokuda Y, Fujita K et al (2012) Tuning the wavelength of amplified spontaneous emission coupled to localized surface plasmons. Appl Phys Lett 101:031117

167. Kang JU (2006) Observation of random lasing in gold-silica nanoshell/water solution. Appl Phys Lett 89:221112

168. Meng X, Fujita K, Zong Y et al (2008) Random lasers with coherent feedback from highly transparent polymer films with nanoparticles. Appl Phys Lett 92:201112

169. Meng X, Fujita K, Murai S et al (2009) Coherent random lasers in weakly scattering polymer films containing silver nanoparticles. Phys Rev A 79:053817

170. Meng X, Fujita K, Murai S et al (2011) Plasmonically controlled lasing resonance with metallic-dielectric core-shell nanoparticles. Nano Lett 11:1374–1378

171. Meng X, Fujita K, Murai S et al (2009) Coherent random lasers from weakly scattering polymer films embedded with superfine silver nanoparticles. Phys Status Solidi C 6:S102–S105

172. Murai S, Fujita K, Meng X et al (2010) Random dispersion of metal nanoparticles can form a laser cavity. Chem Lett 39:532–537

173. Dominguez CT, Maltez RL, dos Reis RMS et al (2011) Dependence of random laser emission on silver nanoparticle density in PMMA films containing rhodamine 6G. J Opt Soc Am B 28:1118–1123

174. Nakamura T, Hosaka T, Adachi S (2011) Gold-nanoparticle-assisted random lasing from powdered GaN. Opt Express 19:467–475

175. Zhai T, Zhang X, Pang Z et al (2011) Random laser based on waveguided plasmonic gain channels. Nano Lett 11:4295–4298

176. Bergman DJ, Stockman MI (2003) Surface plasmon amplification by stimulated emission of radiation: quantum generation of coherent surface plasmons in nanosystems. Phys Rev Lett 90:027402

177. Otto A (1968) Excitation of nonradiative surface plasma waves in silver by the method of frustrated total reflection. Zeitschrift für Physik 216:398–410

178. Kretschmann E (1972) Untersuchungen zur Anregung und Streuung von Oberflächenplasmaschwingungen an Silberschichten (doctoral thesis). Universität Hamburg, Hamburg

179. Protsenko IE, Uskov AV, Zaimidoroga OA et al (2005) Dipole nanolaser. Phys Rev A 71:063812

180. Zheludev NI, Prosvirin SL, Papasimakis N et al (2008) Lasing spaser. Nat Photonics 2:351–354

181. Gordon JA, Ziolkowski RW (2007) The design and simulated performance of a coated nano-particle laser. Opt Express 15:2622–2653

182. Fang A, Koschny T, Soukoulis CM (2010) Lasing in metamaterial nanostructures. J Opt 12:024013

183. Stockman MI (2010) The spaser as a nanoscale quantum generator and ultrafast amplifier. J Opt 12:024004

184. Chang SW, Ni CYA, Chuang SL (2008) Theory for bowtie plasmonic nanolasers. Opt Express 16:10580

185. Pan J, Chen Z, Chen J et al (2012) Low-threshold plasmonic lasing based on high-Q dipole void mode in a metallic nanoshell. Opt Lett 37:1181–1183

186. Sirtori C, Gmachl C, Capasso F et al (1998) Long-wavelength ($\lambda = 8$–11.5 μm) semiconductor lasers with waveguides based on surface plasmons. Opt Lett 23:1366–1368

187. Tredicucci A, Gmachl C, Capasso F et al (2000) Single-mode surface-plasmon laser. Appl Phys Lett 76:2164–2166
188. Seidel J, Grafström S, Eng L (2005) Stimulated emission of surface plasmons at the interface between a silver film and an optically pumped dye solution. Phys Rev Lett 94:177401
189. Cubukcu E, Kort EA, Crozier KB et al (2006) Plasmonic laser antenna. Appl Phys Lett 89:093120
190. Hill MT, Oei YS, Smalbrugge B et al (2007) Lasing in metallic-coated nanocavities. Nat Photonics 1:589–594
191. Hill MT, Marell M, Leong ESP et al (2009) Lasing in metal-insulator-metal sub-wavelength plasmonic waveguides. Opt Express 17:11107–11112
192. Ding K, Liu ZC, Yin LJ et al (2012) Room-temperature continuous wave lasing in dep-subwavelength metallic cavities under electrical injection. Phys Rev B 85:041301
193. Mizrahi A, Lomakin V, Slutsky BA et al (2008) Low threshold gain metal coated laser nanoresonators. Opt Lett 33:1261–1263
194. Nezhad MP, Simic A, Bondarenko O et al (2010) Room-temperature subwavelength metallo-dielectric lasers. Nat Photonics 4:395–399
195. Lee JH, Khajavikhan M, Simic A et al (2011) Electrically pumped sub-wavelength metallo-dielectric pedestal pillar lasers. Opt Express 19:21524–21530
196. Kwon SH, Kang JH, Seassal C et al (2010) Subwavelength plasmonic lasing from a semiconductor nanodisc with silver nanopan cavity. Nano Lett 10:3679–3683
197. Flynn RA, Kim CS, Vurgaftman I et al (2011) A room-temperature semiconductor spaser operating near 1.5 μm. Opt Express 19:8954–8961
198. Oulton RF, Sorger VJ, Zentgraf T et al (2009) Plasmon lasers at deep subwavelength scale. Nature 461:629–632
199. Lu YJ, Kim J, Chen HY et al (2012) Plasmonic nanolaser using epitaxially grown silver film. Science 337:450–453
200. Noginov MA, Zhu G, Belgrave AM et al (2009) Demonstration of a spaser-based nanolaser. Nature 460:1110–1112

Part III
Nanocomposites and Applications of Nanotechnologies

Chapter 15
Hopping Model of Charge-Carrier Transport in Organic Nanoparticle Systems

I. I. Fishchuk, A. Kadashchuk, X. Li and J. Genoe

15.1 Introduction

Molecular and nanoelectronics are corner stones of technology in the twenty first century. Nanoscale technology has clear advantages to be gained from exploiting self-organized growth, as it avoids the need for highly sophisticated patterning of surfaces with nanometer-sized objects. Ideally, the functional properties can be obtained essentially in one self-assembled molecular layer, so that molecular electronics in principle would offer a maximum degree of miniaturization. On the other hand, organic semiconductor films offer a huge potential for the emerging flexible large area electronics because they allow for low-cost device fabrication and a low-temperature processing of semiconductor layers compatible with flexible plastic substrates [1, 2]. In typical amorphous or polycrystalline organic films, the charge-carriers move much more slowly than in perfect molecular crystals because they hop among localized states that are distributed in space and energy. The charge-carrier mobility, μ, is thus a critical parameter for the operating speed of a device, notably, in an organic field-effect transistor (OFET). Therefore, apart from the endeavor to optimize the structure–property relations of organic functional layers, it is of paramount importance to improve the understanding of *conceptual premises* of the electrical transport mechanisms in realistic organic electronic devices.

I. I. Fishchuk
Institute for Nuclear Research, NAS of Ukraine, Prospekt Nauky 47, Kyiv 03680, Ukraine

A. Kadashchuk (✉) · J. Genoe
IMEC, Kapeldreef 75, B-3001 Leuven, Belgium
e-mail: kadash@imec.be

A. Kadashchuk
Institute of Physics, NAS of Ukraine, Prospekt Nauky 46, Kyiv 03028, Ukraine

X. Li
Department of Chemical Engineering and Chemistry, Eindhoven University of Technology,
P.O. Box 513, 5600 MB, Eindhoven, The Netherlands

It is believed that charge-carrier transport in disordered organic semiconductors occurs via incoherent thermally activated hopping [3–6] within a manifold of states commonly described by a Gaussian density of states (DOS) distribution of energetic width σ. Charge-carrier transport studies in such materials have most often been described for the last two decades within the framework of the Gaussian Disorder formalism originally suggested by Bässler et al. [3]. Recently, the formalism was further advanced to account for the charge-carrier concentration effects [7–12], and one should distinguish charge transport regimes at *small-* and *high-*carrier concentrations that can be realized in the same organic material. An inherent feature of a Gaussian-shaped DOS is that at *small carrier concentrations*, when charge-carriers are noninteracting, the majority of equilibrated carriers mostly occupy weakly filled states well above the Fermi level. In this case, the equilibrium occupational DOS (ODOS) is also a Gaussian with width σ, but off-set from the center of the intrinsic DOS by an energy $\varepsilon_{eq} = -\sigma^2/k_B T$. The charge transport in this case is controlled by carrier jumps from states around the energy level ε_{eq} to the so-called effective transport energy level ε_t (described below). Therefore, at *low carrier concentration* the position of the Fermi level, in case of an empty DOS is irrelevant for the charge-carrier mobility [3, 12]. This case is typically realized in time-of-flight (ToF) experiments to measure charge-carrier mobility in the bulk of organic semiconducting films [3, 4].

However, the conditions described above are no longer valid at *high carrier concentrations* when the deep tail states of the DOS are completely filled by charge-carriers and the Fermi level rises above the mean quasi-equilibrium energy level ε_{eq} [8–13]. At sufficiently high carrier densities (as in an organic thin-film transistor where the current is confined to a very thin conductive layer near the interface with the gate dielectric, and in chemically doped organic semiconductors), carrier jumps from the Fermi level dominating the charge-carrier transport, giving rise to an Arrhenius-type $\ln(\mu) \propto T^{-1}$ temperature dependence of the mobility [12, 13] with a virtually constant (yet dependent on carrier concentration) activation energy. It was found that charge-carrier mobility in the same material can differ up to three orders of magnitude depending on whether the mobility is measured in a diode or a transistor device geometry [7, 8, 10]. This demonstrates that the concentration dependence of the mobility must be taken into account to describe the charge transport in realistic organic electronic devices. The latter transport regime has recently been described within the so-called extended Gaussian disorder model (EGDM) using numerical computer simulations by Pasveer and Coehoorn [8, 9], which predict an increase of μ with increase in both charge-carrier concentration and electric field. This model was also corroborated by analytic theories which were first formulated for a zero-field limit [10–12] and recently extended for arbitrary electric fields [14, 15].

The disorder formalism was also invoked to explain the electric field dependence of the charge-carrier mobility conventionally, as observed in disordered organic semiconducting materials. In contrast to perfect organic single crystals where the charge-carrier mobilities are normally electric field independent at room

temperature [16, 17], in disordered organic semiconductors μ increases with electric field, typically in a Poole–Frenkel (PF) fashion, $\ln \mu \propto F^{1/2}$ [3, 4], which is a consequence of charge hopping within the DOS distribution. The applied electric field tilts the DOS and thus lowers the average barrier height for energetic uphill jumps in the field direction. The initial Gaussian disorder model (GDM) [3] predicts the $\ln \mu \propto F^{1/2}$ dependence yet for a rather high electric field only [3]. Subsequent works [18, 19] showed that by introducing spatial correlation of the energies of transport sites, experimentally observed PF-type dependence at lower fields is recovered. The electric field dependence of μ is also predicted by the EGDM for a large charge-carrier concentration transport regime [20, 21].

In a number of experimental studies [22–24] it was commonly observed that charge-carrier mobility in OFET devices shows Arrhenius-type $\mu(T)$ temperature dependences which intersect at a given finite temperature T_0 when measured at different gate voltages (V_G), thus suggesting that the Meyer-Neldel rule (MNR) [25] is obeyed. The MNR is an empirical relation [25], originally derived from chemical kinetics and describes the fact that enthalpy and entropy of a chemical reaction are proportional. Generally, it states that in a thermally activated process an increase of the activation energy E_a is partially compensated by an increase of the prefactor:

$$\mu = \mu_0 \exp\left(-\frac{E_a}{k_B T}\right) \tag{15.1}$$

where E_a is the activation energy, T is the absolute temperature, and k_B is the Boltzmann constant. It is empirically found that the prefactor μ_0 increases exponentially with E_a:

$$\mu_0 = \mu_{const} \exp\left(\frac{E_a}{k_B T_{MN}}\right) \tag{15.2}$$

where μ_{const} is a constant prefactor and T_{MN} is the so-called Mayer-Neldel temperature. A combination of Eqs. (15.1) and (15.2) gives the general form:

$$\mu = \mu_{const} \exp\left[-E_a\left(\frac{1}{k_B T} - \frac{1}{k_B T_{MN}}\right)\right] \tag{15.3}$$

Equation (15.3) shows the MNR relation between the OFET charge-carrier mobility μ and the activation energy "E_a", which is, in the case of OFET measurements, gate voltage dependent. Equation (15.3) implies an isokinetic temperature $T = T_{MN}$ determined by the Meyer-Neldel energy $E_{MN} = k_B T_{MN}$, at which charge-carrier mobility values coincide in one value.

The aim of the present chapter is to review the current achievements regarding theoretical description of the charge-carrier transport in disordered organic semiconductors, with particular attention on charge-carrier transport behavior at large carrier concentration as realized in OFETs. Our consideration is focused on effective medium approximation (EMA) analytic theory which was applied to

describe the charge-carrier concentration-, electric field-, and temperature-dependent charge-carrier transport in organic materials that are used as active layers in OFET devices. In particular, we show that the establishment of the MNR is a characteristic signature of hopping transport in a random system with variable charge-carrier concentration irrespective of their polaronic character. Finally, we compare our theory with alternative models suggested before to explain the MNR for the charge-carrier transport in OFETs.

15.2 EMA Approach to Hopping Charge Transport at Large Charge-Carrier Concentrations

15.2.1 General EMA Theory Formulation

Recently, Fishchuk et al. [14, 15] formulated an analytic theory which is able to describe the drift charge-carrier mobility in a disordered organic solid as a function of *carrier concentration*, *temperature*, and applied *electric field*, and is based on the EMA method using the concept of effective transport energy. A key point of this model compared to the previous EMA treatment [11, 12] is that it is extended for *arbitrary electric fields* and is able to describe consistently both the carrier density and field dependences of charge-carrier mobility. Another important modification of the previous EMA formalism [15] is using a method of configurational averaging of hopping *transition times*. Initially suggested for zero-field—and low carrier concentration—limits according to Ref. [26], it has been now generalized to calculate the drift mobility at finite electric field and for the high carrier concentration transport regime.

Within this approach, a disordered organic system is replaced by an effective three-dimensional (3D) manifold of localized sites with an average intersite distance $a = N^{-1/3}$, where N is the density of the localized states. The theory considers an energetically disordered organic system of localized states characterized by the DOS distribution $g(\varepsilon)$ in the framework of the EGDM [8, 11] which accounts for the dependence of the charge-carrier mobility on the relative carrier concentration n/N, where n is the density of charge-carriers. Positional disorder is neglected.

In general, the effective drift hopping mobility μ_e in a random 3D hopping transport system under an applied electric field can be obtained as

$$\mu_e = a k_0 \frac{W_e^+ - W_e^-}{F} \qquad (15.4)$$

where W_e^+ and W_e^- describe the effective jump rates along-, and opposite- to the electric field direction, respectively, for an arbitrary electric field $\mathbf{F} = \{F, 0, 0\}$. An additional coefficient k_0 emerges in Eq. (15.2) to include the generalized Einstein equation as recently suggested by Tessler [27], relating the mobility and

diffusion coefficient at arbitrary carrier concentration. This coefficient is essential at large carrier concentrations, while in the case of vanishing carrier density $k_0 \rightarrow 1$. Within the average-hopping-times method [26], the effective jump rates W_e^+ and W_e^- can be calculated using the effective transport energy ε_t level as

$$W_e^\pm = \left\langle \tau_{12}^\pm \right\rangle^{-1}, \quad \left\langle \tau_{12}^\pm \right\rangle = \frac{\int_{-\infty}^{\varepsilon_t} P(\varepsilon) \left\{ W_{12}^\pm(\varepsilon_t, \varepsilon) \right\}^{-1} d\varepsilon}{\int_{-\infty}^{\varepsilon_t} P(\varepsilon) d\varepsilon}, \tag{15.5}$$

where W_{12}^+ and W_{21}^- are effective jump rates between two neighboring localized sites along—and opposite—to the electric field direction, respectively. We use Miller–Abrahams (MA) jump rate [28]

$$W_{12}^\pm(\varepsilon_t, \varepsilon) = W_0 \exp\left[-\frac{|\varepsilon_t - \varepsilon \mp eaF| + (\varepsilon_t - \varepsilon \mp eaF)}{2k_B T} \right] \tag{15.6}$$

to describe an elementary charge transfer under an applied electric field between sites with energy ε and ε_t being defined in the limit of zero field. Here $W_0 = v_0 \exp(-2r_t/b)$, where v_0 is the attempt-to-escape frequency, r_t is the jump distance below the effective transport energy ε_t, and b is the localization radius of the charged site.

As it was shown in [26, 29, 30], the major contribution to the drift time is determined by the upward hops of carriers from states located below the transport energy to the state ε_t. Therefore, configurational averaging of the hopping transitions times in Eq. (15.5) has to be done over the energy distribution of empty localized states, viz. by using the function

$$P(\varepsilon) = g(\varepsilon)[1 - f(\varepsilon, \varepsilon_F)], \tag{15.7}$$

where $f(\varepsilon, \varepsilon_F)$ is given by the Fermi–Dirac statistics

$$f(\varepsilon, \varepsilon_F) = \frac{1}{1 + \exp\left(\frac{\varepsilon - \varepsilon_F}{k_B T} \right)}. \tag{15.8}$$

The Fermi level ε_F position can be determined from the following transcendental equation for the carrier concentration n

$$n = \int_{-\infty}^{\infty} d\varepsilon \, g(\varepsilon) f(\varepsilon, \varepsilon_F). \tag{15.9}$$

The coefficient k_0 (cf. Eq. 15.4) in this case is determined as

$$k_0 = 1 - \frac{\int_{-\infty}^{\infty} d\varepsilon \, g(\varepsilon) f^2(\varepsilon, \varepsilon_F)}{\int_{-\infty}^{\infty} d\varepsilon \, g(\varepsilon) f(\varepsilon, \varepsilon_F)}. \tag{15.10}$$

The DOS distribution $g(\varepsilon)$ is assumed be a Gaussian with width σ, which is generally accepted to be appropriate for disordered organic media

$$g(\varepsilon) = \frac{N}{\sigma\sqrt{2\pi}}\exp\left[-\frac{1}{2}\left(\frac{\varepsilon}{\sigma}\right)^2\right], \quad -\infty < \varepsilon < \infty. \tag{15.11}$$

A combination of Eq. (15.4) with Eqs. (15.5–15.10), and (15.11) gives the effective charge-carrier mobility μ_e as

$$\mu_e = \mu_0 k_0 \left(\frac{r}{a}\right)^2 \exp\left(-2\frac{r_t}{b}\right)\frac{\left(Y_e^+\right)^{-1} - \left(Y_e^-\right)^{-1}}{f}, \tag{15.12}$$

where

$$Y_e^{\pm} = \frac{\int_{-\infty}^{x_t} dt\, \frac{\exp\left\{-\frac{t^2}{2} + \frac{1}{2}[|x_t - t \mp f| + (x_t - t \mp f)]x\right\}}{1 + \exp[-(t - x_F)x]}}{\int_{-\infty}^{x_t} dt\, \frac{\exp\left\{-\frac{t^2}{2}\right\}}{1 + \exp[-(t - x_F)x]}}. \tag{15.13}$$

Here

$$Y_e^{\pm} = \frac{W_e^{\pm}}{W_0}, \quad f = \frac{eaF}{\sigma}, \quad x = \frac{\sigma}{k_B T}, \quad x_F = \frac{\varepsilon_F}{\sigma}, \quad x_t = \frac{\varepsilon_t}{\sigma}, \quad \mu_0 = \frac{ea^2 v_0}{\sigma}. \tag{15.14}$$

The concept of effective transport energy has been proved to be especially efficient for calculating the carrier mobility in disordered materials [29, 30, 31]. The effective transport energy ε_t in this method does not depend on the applied electric field F and hence for a Gaussian DOS distribution can be determined from the transcendental equation derived for zero-field mobility [11]

$$\frac{1}{\sqrt{2\pi}}\frac{\exp\left(-\frac{1}{2}x_t^2\right)}{1 + \exp[-(x_t - x_F)x]}\left\{\frac{1}{\sqrt{2\pi}}\int_{-\infty}^{x_t} dt\, \frac{\exp\left(-\frac{1}{2}t^2\right)}{1 + \exp[-(t - x_F)x]}\right\}^{-\frac{4}{3}} = \frac{3}{2}\left(\frac{4\pi}{3B}\right)^{\frac{1}{3}}x\frac{b}{a} \tag{15.15}$$

Here, the parameter $B = 2.7$ has been determined according to percolation criteria [31]. The factor r_t is calculated by

$$r_t = a\left\{\frac{4\pi}{3B}\frac{1}{\sqrt{2\pi}}\int_{-\infty}^{x_t} dt\, \frac{\exp\left(-\frac{1}{2}t^2\right)}{1 + \exp[-(t - x_F)x]}\right\}^{-\frac{1}{3}}. \tag{15.16}$$

It should be noted that percolative effects have been considered in Ref. [31] not-rigorously, in that the consideration was limited to the renormalization solely of the factor r_t. Since r_t and ε_t are quantities interrelated by definition, the accounting for the percolative effects must be done for the transport energy ε_t as well. A combination of Eqs. (15.15) and (15.16) takes this duly into account.

15.2.2 Spatial Energy Correlations

Energy correlations in organic disordered solids imply slowly varying static spatial fluctuation in the potential energy landscape and can arise due to charge-dipole [19] or charge-quadrupole interactions or fluctuations (inhomogeneity) in electronic polarization energy, resulting from molecular density fluctuations in an organic material due to microscopic regions that are under compression or dilation [32]. The energy correlation effects were mostly invoked to describe a $\ln \mu \propto \sqrt{F}$ Poole–Frenkel-type field dependence of charge-carrier mobility, typically observed in ToF measurements. The EGDM was originally suggested for energy *uncorrelated* systems and therefore it predicts a specific $\ln \mu \propto F$ field dependence [8, 9] that is in variance to available experimental data featuring a $\ln \mu \propto \sqrt{F}$ behavior in the experimentally accessible range of electric fields.

On the other hand, it is well established that a PF-type field dependence of the charge-carrier mobility can be reproduced over an extended interval of electric fields when some kind of correlated disorder is taken into account in the framework of the correlated disorder model (CDM) [19] or the extended correlated disorder model (ECDM) [20, 21]. Conventional noncorrelated disorder models ignoring the energy correlation effects, i.e., assuming that site energies are distributed independently, predict the PF-law only in a very narrow range of high electric fields $\left(F > 3 \times 10^5\,\text{V/cm}\right)$ [3]. Therefore, accounting for the energy correlation effects is necessary for an adequate description of the Poole-Frankel type of charge-carrier mobility dependence on electric fields, as experimentally observed down to moderate electric fields. This aspect is especially relevant in the case of the OFET mobility measurements, because in this configuration measurements are done at rather *low lateral electric fields* owing to typically large transistor channel length used in OFET devices, if compared to other organic electronic devices, e.g., in sandwich-type diodes.

Generally, accounting for the energy-correlated disorder effects could hardly be treated rigorously analytical, although it might be solved by numerical computer simulations [19, 20]. Therefore, in our analytical treatment [15], we have used some key ingredients from the numerical simulations studies performed before within the CDM [19, 20] for a low carrier concentration limit. The authors of this reference have shown [19, 20] that the size of an "energetic valley" (cluster) comprising many localized sites, scales algebraically with the depth of fluctuations. As suggested before [33], by using the simulations results of Parris et al. [34], one could account for the energy correlation effects by substituting the parameters $x = \sigma/k_\text{B}T$ and $f = eaF/\sigma$ (for noncorrelated disordered system) by $x_c = \sigma_c/k_\text{B}T$ and $f_c = h_c\sqrt{x_c/2}$, respectively, where $h_c = \sqrt{eaF/\sigma_c}$. The presence of energy correlations results also in some flattening of the local potential energy landscape within larger scale energetic structures. Therefore, the width of the so-called correlated DOS, σ_c, has to be somewhat smaller than the initial σ-value featuring in the noncorrelated GDM approximation. Coehoorn et al. [20] have

shown, that one can use $\sigma_c \cong 0.83\,\sigma$ due to the charge-carrier mobility under the presence of the energy correlations. In the limit of zero field and zero charge-carrier density the charge-carrier mobility follows a $\mu_e \propto \exp(-0.29x^2)$ temperature dependence instead of $\mu_e \propto \exp(-0.44x^2)$ inherent for the GDM.

Another important consequence of the energy correlation effects on the field dependence of the charge-carrier mobility $\mu(F)$ at *high* carrier concentrations relevant for OFET operation has been recently demonstrated by Bouhassoune et al. [20] and Novikov [21]. Based on their computer simulations, they found that the typical size of the jump length governing the charge-carrier mobility, does not depend only on electric field *but also on carrier concentration*. The typical jump length within ECDM was found to decrease with increasing carrier concentration. This leads to a decrease of the slope S of the electric field dependence of the charge-carrier mobility $\ln\mu$ vs $S \times \sqrt{F}$ compared to the slope S_0 in the case of zero-concentration limit $n/N \to 0$, as $S = S_0(1 - n/N)^m$, provided that the energy correlations have been taken into account. For a non-correlated disordered system within the EGDM, the slope remains the same upon varying carrier concentration [21]. This effect can be accounted [15] by the following expressions for the temperature dependence of S_0 and m: $S_0 = -5.42 + 2.995(\sigma/k_BT) - 0.115(\sigma/k_BT)^2$ and $m = -9.69 + 10.81(\sigma/k_BT) - 0.905(\sigma/k_BT)^2$. In the range $2.0 < \sigma/k_KT < 5.0$ the calculated parameter S_0 perfectly agrees with the relevant slope $S_1 = 0.78 \left[(\sigma/k_BT)^{3/2} - 2\right]$ obtained by numerical computer simulations [19] for the small carrier concentration limit.

Coulomb interactions between charge-carriers might start to play an essential role at large carrier concentrations [21, 35], which is not accounted for in the present theoretical description [15]. The recent Monte Carlo simulations by Zhou et al. [35] have, however, demonstrated that the effect of Coulomb interactions is not significant if the carrier density is below $n/N < 10^{-2}$. In accordance with that, charge mobility computer simulations (accounting for Coulomb interactions) by Novikov [21] show, that for charge-carrier concentrations $n/N \leq 10^{-1}$ the charge-carrier mobility increases with increasing n/N exactly in the same manner as in the case of non-interacting carriers (cf. Ref. [8]). Since our theoretical model does not go beyond the charge-carrier density limit given above, the present consideration disregards the Coulombic interaction effects.

Thus, the charge-carrier mobility in disordered organic semiconductors can be calculated by Eqs. (15.12–15.16) obtained within the EGDM approximation with accounting for energy correlation effects by substituting parameters σ, f by σ_c, f_c, respectively, as described above.

15.3 Calculations of the Charge-Carrier Concentration- and the Electric Field-Dependences of the Charge Mobility

15.3.1 Dependence of the Charge Mobility on Carrier Concentration

In the following, the EMA theory, formulated in Sect. 15.2, will be used to calculate the charge-carrier mobility in organic semiconductor materials as a function of *carrier concentration*, applied *electric field,* and *temperature*. The best verification of an analytical theory is a direct comparison with computer simulation results, as the simulation actually solves the model as it stands while a real experiment can include processes not accounted for. Relevant computer simulations of the charge-carrier transport in a random organic solid have been reported in Ref. [8], assuming an energy *uncorrelated system* and neglecting variable hopping range transitions. In this approximation Eq. (15.12), obtained within the above described analytical EMA model, transforms to

$$\mu_e = \mu_0 k_0 \exp\left(-2\frac{a}{b}\right) \frac{Y_e^+ - Y_e^-}{f}, \tag{15.17}$$

where the values $Y_e^{\pm}$ are given by Eq. (15.13). To employ Eq. (15.17) for calculating the charge-carrier mobility one has to define the effective transport energy level x_t. Recently, Fishchuk et al. [11] found, that this level is given by the relation $x_t = -x/18$ (cf. Eqs. 15.15, 15.16), which is valid for a broad range of charge-carrier densities relevant for practical applications (except for extremely high densities) and the Miller–Abrahams jump rate.

Charge-carrier concentration dependences of the charge-carrier mobility μ_e calculated by Eq. (15.17) at zero-field limit $(F \to 0)$ for different temperatures are presented in Fig. 15.1. The results of numerical simulations of the charge-carrier mobility by Pasveer et al. [8] for a system with an equivalent set of parameters are given by symbols in Fig. 15.1 for comparison. It is gratifying that the present EMA theory provides an excellent quantitative agreement with previous numerical simulations data for the charge-carrier mobility. The presented results are similar to calculations presented in Ref. [11], although they are obtained by a different calculation method. The presented EMA model describes also very well the results on concentration dependence of the charge mobility measured in different organic semiconducting films [11].

Thus, for energy *uncorrelated* hopping transport systems, calculations of the charge-carrier mobility by the present EMA theory are in excellent agreement with the relevant numerical computer simulation data.

Fig. 15.1 Carrier concentration dependence of the charge-carrier mobility in an organic disordered material calculated by Eq. (15.17) at different temperatures at zero electric field limit (*solid curves*) using the transport energy concept [14]. Numerical results from Ref. [8] obtained for the same parameters are given by symbols
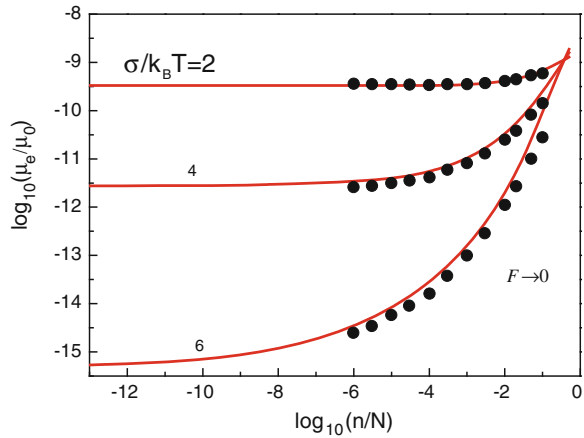
15.3.2 Dependence of the Charge-Carrier Mobility on Electric Field

The approximated Eq. (15.17) can also be used to calculate the electric field dependence of the charge-carrier mobility in *an energy uncorrelated* disordered system [14] and results could be compared which recent computer simulations [8] performed on the same system. Figure 15.2a shows the electric field dependences of the charge-carrier mobility μ_e (solid curves) calculated by Eq. (15.17) at different temperatures for *relatively small*-carrier-concentration $n/N = 10^{-5}$, which is typically realized at OLED device operation. These dependences differ little from that obtained for a vanishing charge-carrier concentration ($n/N \to 0$). The field dependence of μ_e for *relatively large* carrier concentration $n/N = 0.05$, which is typically realized in a conductive channel of an OFET, calculated at different temperatures by Eq. (15.17) is depicted in Fig. 15.2b (solid lines). Symbols in Fig. 15.2a and b shows results of the relevant recent computer simulations of Pasveer et al. [8] for comparison with the present theory [14] and one can see a good quantitative agreement between the EMA theory predictions and the numerical results for the same material parameters. One might note a slight decrease of the calculated mobility with increasing electric field at large temperatures (upper curves in Fig. 15.2a, b) while the numerical simulations show a slightly increasing/saturating mobility (symbols). This seemingly has no physical meaning and is due to a limitation of the present theoretical treatment at small $\sigma/k_B T$ values at which the transport energy approximation becomes less accurate.

The electric field dependences of the charge-carrier mobility $\mu(F)$ in *energy-correlated* organic disordered system can be calculated by the modified EMA theory described in Ref. [15]. with accounting for the energy correlation effects as suggested in Sect. 15.2.2. The corresponding EMA calculation results are depicted in Fig. 15.3a in $\ln \mu \propto \sqrt{F}$ representation. The curves (solid lines) were calculated

Fig. 15.2 (**a**) Electric field dependences of the drift charge mobility calculated by Eq. (15.17) in *an energy uncorrelated* disordered system at various temperatures for relatively small $n/N = 10^{-5}$ and (**b**) large carrier concentration $n/N = 0.05$ (**b**) (*solid curves*) using the transport energy concept [14]. Numerical results from Ref. [8] for the same parameters are given by symbols for comparison
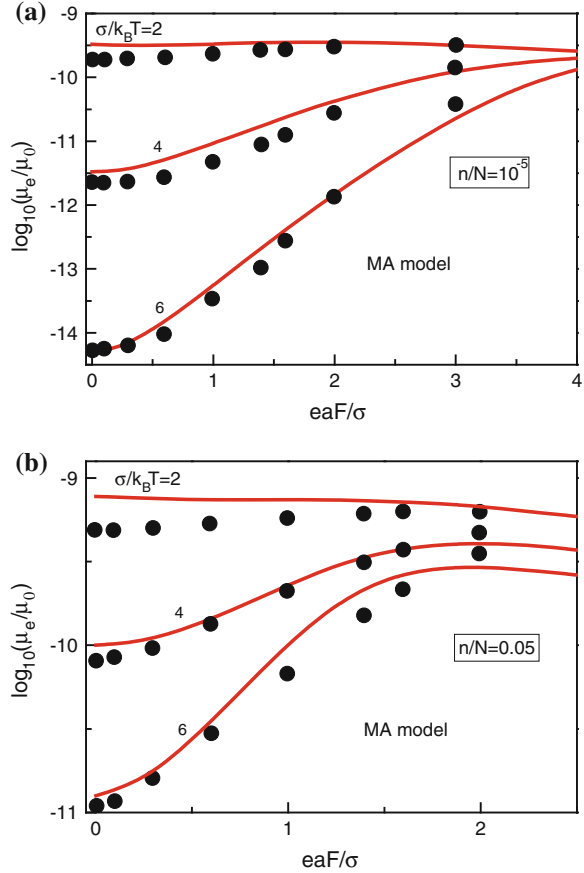
by Eqs. (15.12–15.16) for *different carrier concentrations* relevant to OFET operation, taking into account the dependence of the jump length on carrier concentration according to Ref. [20]. The same dependences were also calculated by ignoring the latter effect and are given for comparison (Fig. 15.3a, dashed curves). As one can see, the Poole–Frenkel field dependences are well reproducible in the range $0.4 < (eaF/\sigma)^{1/2} < 1.0$ for the considered charge-carrier concentrations and feature a clear decrease in the slope of the curves with increasing carrier concentration (Fig. 15.3a, solid lines), whereas the slope remains virtually the same if the carrier concentration dependence of the jump length is ignored (dashed curves in Fig. 15.3a). These analytically calculated dependences agree well with the relevant computer simulation results of Ref. [21]. Assuming representative material parameters for a disordered solid, viz. $\sigma = 0.07$ eV and $a = 1.4$ nm, one obtains a corresponding electric field range $8 \times 10^4 < F < 5 \times 10^6$ V/cm for which the PF-type field dependence is valid (shown by straight lines in Fig. 15.3a).

Fig. 15.3 **a** Poole–Frenkel plots of electric field dependences of the effective charge-carrier mobility $\ln(\mu_e/\mu_0)$ calculated by Eqs. (15.12–15.16) for an *energy-correlated* organic disordered system for several carrier concentrations ($n/N = 10^{-3.0}$, $10^{-2.5}$, and $10^{-2.0}$) at $a/b = 5$, and $\sigma/k_B T = 5$ with accounting (see text) for the carrier concentration dependence of the jump length (*solid curves*) and ignoring the latter effect (*dashed curves*) [15]; **b** electric field dependence of charge-carrier mobility calculated for a *non-correlated* disordered system
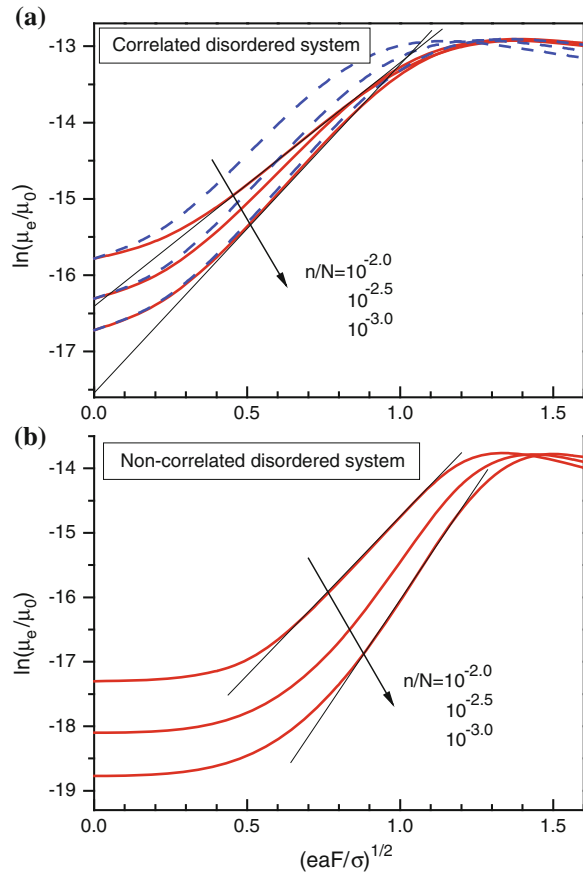
Figure 15.3b shows the electric field dependences of the charge-carrier mobility, calculated with the same parameters as in Fig. 15.3a, but for an energy *non-correlated* organic disordered system. As one can see from Fig. 15.3b, a $\ln \mu \propto \sqrt{F}$ dependence (straight lines in Fig. 15.3b) is revealed for such a system but only within a narrow range of strong electric fields, consistent with previous computer simulations by Bässler et al. [3]. In the present study, we used a representative ratio $a/b = 5$ for organic disordered semiconductors, which has extensively been employed before in Monte Carlo simulations studies of the charge-carrier transport [3].

The electric field dependences of the charge-carrier mobility calculated by Eqs. (15.12–15.16) for an *energy-correlated* system at different temperatures for a relatively small-carrier-density, $n/N = 10^{-5}$ and a very high carrier density, $n/N = 10^{-1.5}$ are shown in Fig. 15.4. As one can see, a $\ln \mu \propto \sqrt{F}$ dependence of the charge-carrier mobility has been revealed at both carrier concentration regimes. It is basically similar to the Poole–Frenkel field dependences conventionally observed in the limit of low carrier concentrations, i.e., in ToF mobility measurements.

Fig. 15.4 Poole-Frenkel plots of electric field dependences of the effective charge-carrier mobility $\ln(\mu_e/\mu_0)$ in an organic disordered system calculated by Eqs. (15.12–15.16) at different temperatures with accounting for *energy correlations* for two carrier concentrations: $n/N = 10^{-1.5}$ (*upper branch*) and 10^{-5} (*lower branch*). $a/b = 5$
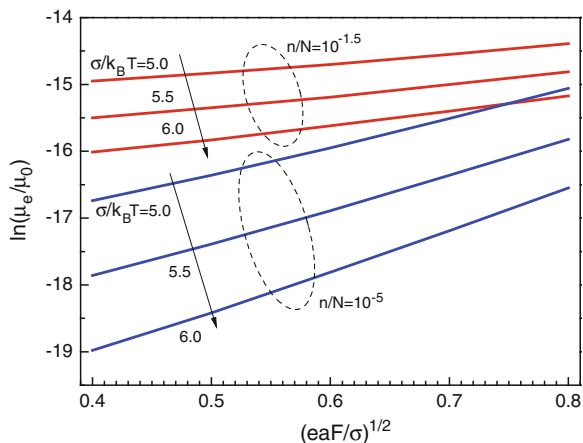
15.3.3 Effect of Strong Local Electric Fields on Charge Mobility in Inhomogeneous Materials

In order to verify predictions of the present EMA theory, we compared the results of our analytical calculations with experimental results on charge-carrier mobility in a C_{60}-based OFET [36, 37]. Figure 15.5 shows the lateral electric field dependence of the OFET mobility $\log_{10}(\mu) \propto \sqrt{F}$ (symbols) measured [15] at different temperatures in C_{60} film, and. The presented results prove, that the OFET mobility features a Poole–Frenkel-type dependence on lateral electric field in the range of very low electric fields of the order of $\sim 10^3$ V/cm generated by the applied source-drain voltage (V_{SD}) over the Conductive channel (length 35 µm) of the OFET device.

An important question arises, why the Poole–Frenkel field dependence the OFET mobility (Fig. 15.5) is observed at such lower electric field? Although the present analytic model [15] as well as previous computer simulation studies [20], does predict a PF-type dependence for the FET mobility, and the major problem is that the experimentally observed field dependences are usually beyond the field range where the PF-law is predicted. Note that the established hopping transport models predict that μ should saturate at electric fields $F \leq 10^4$ V/cm [15, 20, 21]. Here we should emphasize that the average lateral electric field in OFET devices is usually relatively small, being of the order of 10^3 V/cm due to normally long transistor channels, while a Poole–Frenkel ($\ln(\mu_e) \propto \sqrt{F}$) dependence is predicted to occur at much higher fields—around $F \approx 10^5$ V/cm. Therefore, neither available analytical theories nor computer simulations are able to reproduce the experimental observations even when the energy correlation effects are taken into account.

To solve the puzzle, we propose that in multiple-grain organic films the electric field is not necessarily homogenous—as is usually tacitly assumed—but it can be
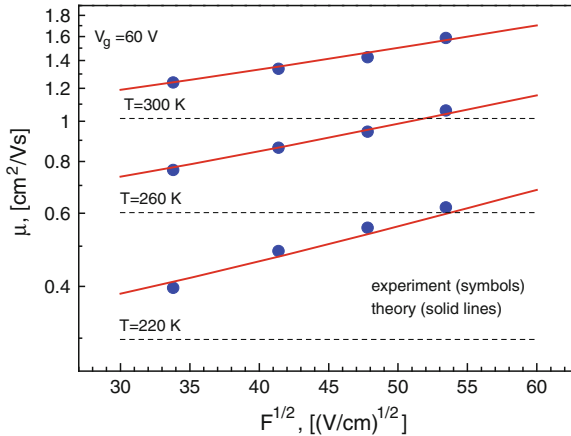
Fig. 15.5 Experimental (*symbols*) lateral field dependence of the charge-carrier mobility measured in C_{60}-based OFETs at different temperatures [15] and theoretical fitting by Eqs. (15.12–15.16) (*solid lines*) with accounting for energy correlations and using the following set of parameters: $\sigma = 0.07$ eV; $a/b = 5$; $a = 1.4$ nm; $n/N = 0.05$; and $q = 256$. *Dashed curves* were calculated at $q = 1$, i.e., assuming a homogenous lateral electric field

inhomogeneous. Indeed, the severe difference between local conductivities within grains and at grain boundaries (GB) results in redistribution of accumulated charges, which can create *very strong local lateral fields* [38] in the latter regions, as required for the current to be continuous in the channel. These strong local fields in the GB result in the carrier mobility in GB to become field dependent, and as the mobility in GB limits the overall mobility its field dependence translates to a field dependence of the average mobility.

Below, we present experimental verification of the concept of strong local fields confined to GB, which has recently been elucidated by studying the surface electrostatic potential distributions along the transistor channel by scanning Kelvin probe measurements (SKPM) during OFET device operation in a polycrystalline organic semiconductor layer [38]. Ink jet printable 6,13-bis(triisopropyl-silyle-thynyl) pentacene (TIPS-PEN) (for synthesis of this material see Ref. [39]) was chosen as the model system in this study, since previous studies have shown that pure TIPS-PEN films feature crystallite grains with dimensions compatible with the spatial resolution of SKPM, and have indicated that this material allows for the manipulation of film morphology within a transistor channel from multiple grains separated by GB to a single grain [40]. Two types of TIPS-PEN films were prepared: (1) pure TIPS-PEN forming irregular-shaped crystalline deposit with multiple-grain morphology within a transistor channel (namely "channel with GB"); (2) TIPS-PEN blended with polystyrene (PS) that features much larger TIPS-PEN crystallites with more homogenous film morphology throughout transistor channels. The films were checked by cross-polarized optical microscope to assure that in the latter case a large crystallite of TIPS-PEN covers the whole transistor channel under investigation (namely "channel without GB").

Charge-carrier mobility in this study was obtained from output characteristics (I_{SD} vs. V_D plots) at a constant average charge (Q) in a transistor channel. The average charge-carrier mobility $\mu(V_D)$ can be determined in linear regime as [38]:

$$\mu(V_D) = \frac{L}{W \cdot C_i(V_G - \frac{V_D}{2} - V_{th})} \cdot \left(\frac{\partial I_{SD}}{\partial V_D}\right) \cdot \left(\frac{\partial V_D}{\partial V_{D-channel}}\right) \qquad (15.18)$$

where L and W is the channel length and width, respectively, V_G and V_D is the source-gate and the source-drain voltage, respectively, C_i is the capacitance per unit area of the gate dielectric, and V_{th} is the threshold voltage. And $V_{D\text{-}channel}$ is the actual voltage drop within the channel region by subtracting the drops at the edges of source and drain contacts, measured by SKPM at difference applied V_D and the corresponding V_G assuring a constant Q in the channel. Constant Q here was assured by sweeping the gate voltage (V_G) at half of the rate for V_D sweeping (according to definition of $Q = C_i(V_G - \frac{V_D}{2} - V_{th})$).

Figure 15.6 (symbols) shows OFET mobility as a function of lateral electric field in two types of TIPS-PEN channels with- and without GB (circles and squares, respectively), calculated from the experimentally obtained output characteristics using Eq. (15.18) in linear regime with constant channel charges. The field dependences of mobility in the above two types of channels are found to differ drastically. In the TIPS-PEN channel with GB (circles in Fig. 15.6) μ
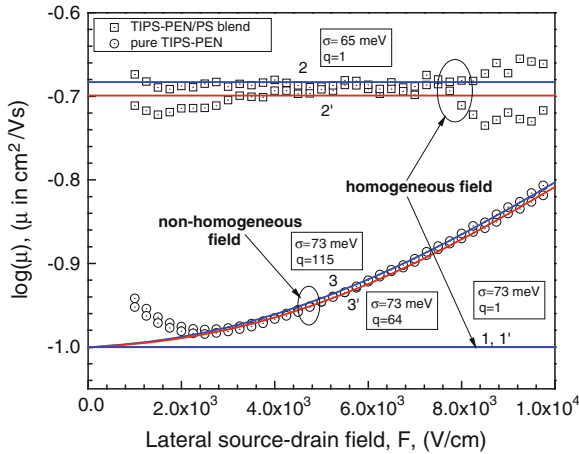
Fig. 15.6 Lateral-field dependences of the OFET mobility measured in TIPS-PEN channel with GB (*circles*) and without GB (*squares*) at $T = 300$ K. Charge mobilities calculated assuming homogenous electric field ($q = 1$) for $\sigma = 65$ meV and $\sigma = 73$ meV within Pasveer/Coehoorn model (*curve 2* and *1*, respectively, in *blue color*) and by Fishchuk model (*curve 2'* and *1'*, respectively, in *red color*). Other parameters used: $a = 0.7$ nm, $c = 10^{-3}$, and the ratio $a/b = 10$ and 5 for Pasveer/Coehoorn and Fishchuk model, respectively. The best-fit curve for the channel with GB calculated assuming strong local electric fields accounted for by the field magnification parameter $q = 115$ within Pasveer/Coehoorn model (*curve 3*, in *blue*) and by $q = 64$ within Fishchuk model (*curve 3'*, in *red*). Note that *curves 1* and *1'* coincide

increases with lateral electric field, while μ is virtually field independent in TIPS-PEN channels without GB (squares in Fig. 15.6). A slightly negative field dependence of μ was observed in the pure TIPS-PEN channels with GB at $F < 2 \times 10^3$ V/cm, however, the appearance of this behavior was sample dependent and ascribed to the possible influence of contact resistance at very low V_D.

To explain our observations, we first tried to fit the experimental field-dependent mobility (Fig. 15.6) with Pasveer/Coehoorn model [8, 9]. Most of the material parameters used for calculation were taken from experiments, viz., carrier concentration experimentally estimated as $c = 10^{-3}$; $a = 0.7$ nm taken as a typical intermolecular distance for pentacene [41]; $a/b = 10$ used according to Ref. [8]; for TIPS-PEN channels with GB the energetic disorder parameter $\sigma = 73$ meV was estimated from experimentally measured Meyer-Neldel temperature (T_{MN}) (not shown here) according to the method described recently [12], while for the blended TIPS-PEN channels $\sigma = 65$ meV was used as fitted parameter, the prefactor mobility μ_0 was chosen to match the zero-field mobility value. Note that activation energy (energetic disorder) for the OFET mobility in TIPS-PEN films was found to depend significantly on the fabrication procedure [42]. Mobilities calculated according to Refs. [8, 9] under the premise of *homogenous lateral electric field* are shown by solid blue curves 1 and 2 in Fig. 15.6 and they evidence that original Pasveer/Coehoorn model *predicts no field dependence* at such low fields and reasonable material parameters. This model can quantitatively describe well just the flat field dependence of μ observed in TIPS-PEN blend channels without GB, but it clearly fails to describe the data for pure TIPS-PEN channels with GB (circles in Fig. 15.6).

Next, the mobilities in the relevant lateral electric field range were calculated by Fishchuk analytic model [15] for the same set of material parameters and assuming homogenous electric field (curves 1′ and 2′ in Fig. 15.6). These calculation results are quite similar to those obtained by the Pasveer/Coehoorn model (cf. curves 1 and 2 in Fig. 15.6) and similarly fail to fit the experimental data for TIPS-PEN channels with GB (circles in Fig. 15.6).

Thus, the established hopping charge transport models, assuming homogenous electric field *are unable to provide a quantitative description* of the increasing OFET mobility in TIPS-PEN in the range of low lateral electric fields relevant for experiments. To solve the puzzle, we propose that in multiple-grain channels, the OFET mobility is controlled not by the lateral field averaged over the transistor channel (as conventionally assumed), but rather by the much stronger effective local electric fields generated in such inhomogeneous media. This is supported by measuring the surface electrostatic potential distributions along transistor channels by SKPM during device operation at applied lateral voltage $V_D = -5$ V and varying source-gate voltage V_G on the same TIPS-PEN samples as used for charge transport measurements in Fig. 15.6. Typical potential profiles obtained in the channel containing GB and that without GB, are shown in Fig. 15.7a and b, respectively. Both types of TIPS-PEN films show typical smooth parabolic potential profiles from source to drain electrodes (Fig. 15.7) in studied channels when *devices are in*
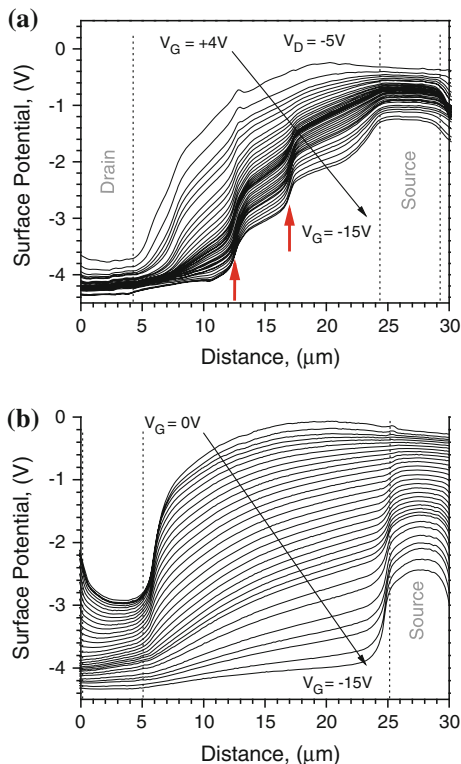
Fig. 15.7 Surface potential profiles of pure TIPS-PEN (**a**) and the TIPS-PEN/PS blend (**b**) measured by SKPM in the active layer of OFET devices at $V_D = -5$ V and for different V_G voltages. Positions of GB are indicated by *red arrows* in (**a**)
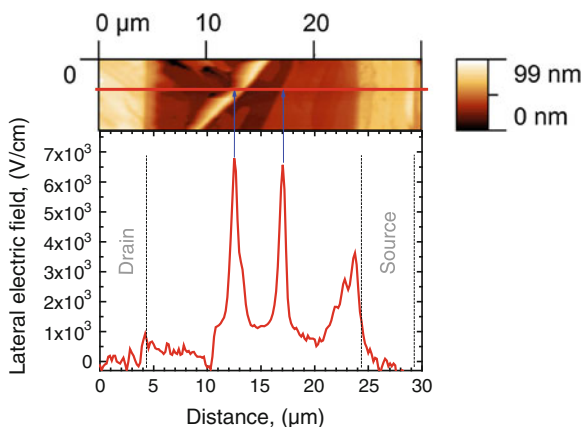
Fig. 15.8 *Lower panel* distribution of lateral electric field calculated from the surface potential distribution from Fig. 15.7a at $V_D = -5$ V and $V_G = -15$ V in pure TIPS-PEN channel. Positions of GB are indicated by *arrows*. *Upper panel* corresponding AFM topography image of the studied channel. *Red horizontal line* in the *upper panel* depicts the position where the cross-section of SKPM scan in Fig. 15.7a was taken

"OFF-state" (before V_G is reaching V_{th}), but *abrupt potential drops* occur within the channel of TIPS-PEN with GB (shown by the red arrows in Fig. 15.7a) when the device is in "ON-state", i.e., upon charge accumulation near the gate electrode.

The electrostatic field profile in Fig. 15.8 (lower panel) clearly reveals several sharp peaks. Note that these peaks could in reality be much bigger because of the limited spatial resolution of SKPM [43]. These spikes in the field distribution correlate with the locations of GB revealed by AFM topography image (cf. lower and upper panels in Fig. 15.8). TIPS-PEN blend channel devoid of GB (indicated by AFM and cross-polarized optical micrographs) shows rather smooth surface potential profiles within transistor channel irrespective of whether transistor is in *ON* or *OFF-state* (Fig. 15.7b) [38].

Strong inhomogeneity of lateral electric field in the conductive channel can be rationalized in terms of electrostatic screening due to different local conductivities within grains and at GB. GB are known to limit charge transport in polycrystalline films by establishing major potential barriers [44–47] between their more ordered domains. In such case, the OFET conductive channel can be considered as a series of resistors whose resistance is controlled by the "microscopic" charge mobility. In the off-state, the lateral field is homogenous because the dielectric constant is virtually isotropic. Therefore, μ is isotropic. Upon applying a gate voltage to a channel with GB, charges (holes) start to accumulate in the channel, and instantaneously the density of accumulated holes within an individual grain is redistributed along the *external* lateral field (source to drain) direction; at one side of the grain it generates a locally increased hole concentration, and at the other side a reduced (or close to locally "depleted") hole density. This creates an *internal* lateral electric field within the individual grain which compensates the applied external field. Note that this "charge-redistribution" effect stems from the *mobile* (not trapped) holes inside grains induced by V_G voltage, therefore here termed as a charge *accumulation* (rather than trapping) process at the GB. This effect generates high local field between the grains (i.e. at the GB), while the field inside the grains is screened. This would translate into an inhomogeneity of the lateral electric field. As long as the spatial extension of GB is much smaller than the average size of more ordered grains, the local fields could be much stronger than the average applied field.

The concept of inhomogeneous local fields [38] can describe *quantitatively* the experimentally observed lateral-field dependence of the OFET mobility with both the modified Pasveer/Coehoorn and Fishchuk models. The barrier heights due to GB are subject to distribution over the film, therefore, taking into account a huge variety of percolative passes present between the long source and drain electrodes, the charge transport in average could be considered as that occurring in an effectively random disordered system even though charge-carriers may experience just a few crossings over GB in a particular percolative pass. Since the actual ratio between local field at the GB and the averaged field is not amenable to analytical treatment, here we introduce a phenomenological field magnification parameter $q \gg 1$ as a fitting parameter. Evidently, the employment of q parameter just results in renormalization of the electric field F used in our calculations.

Figure 15.6 demonstrates that the experimental results on the field dependence of μ in TIPS-PEN channels with GB (Fig. 15.6, circles) can be well fitted using $q = 64$ and $q = 115$ for the Fishchuk (Fig. 15.6, red curve 3′) and the Pasveer/ Coehoorn (Fig. 15.6, blue curve 3) models, respectively, using the same $\sigma = 73$ meV. The flat lateral-field dependence observed in channels without GB (Fig. 15.6, squares) is also well described by our model assuming the absence of strong local fields ($q = 1$) in the homogenous film using a smaller energetic disorder parameter $\sigma = 65$ meV.

The above concept of inhomogeneous local fields can also be applicable for C_{60}-based OFETs with polycrystalline channels and describe *quantitatively* the experimentally observed lateral-field dependence of the OFET mobility in these devices by the extended EMA model. Figure 15.5 shows the theoretical fitting of the experimental data for C_{60} film (symbols) by Eqs. (15.12–15.16) (solid lines) using $q = 256$ [15]. The dashed curves in Fig. 15.5 were calculated assuming a homogeneous lateral electric field in the transistor channel and, as one can see, no electric field dependence is expected within the range of such low electric fields. This justifies the critical role of strong local fields in the theoretical description of electric field dependence of charge-carrier mobility in OFET structures.

Thus, the observed field dependence of charge-carrier mobility in an OFET at low electric fields is a signature of a phenomenon that could be termed as *electric field confinement effect* in a grainy organic film and this concept can *quantitatively* describe the experimentally observed lateral-field dependence of the OFET mobility with modified hopping transport models. It originates from a lateral redistribution of accumulated (gate-induced) mobile charges by the applied source-drain voltage, at the GB. It gives rise to strong local electric field and is relevant for organic films with inhomogeneous morphology caused by, e.g., sample annealing in order to improve charge transport, and for chemically doped organic polycrystalline films.

15.4 Calculations of Temperature Dependence of the Charge-Carrier Mobility: Influence of Carrier Concentration and Electric Field

Temperature dependence of the hopping charge-carrier mobility is of particular interest as it bears on the fundamental nature of hopping charge transport in disordered organic semiconductors. In this section, using the above EMA analytical formalism we consider thoroughly the temperature dependence of the charge-carrier mobility in disordered organic solids at large carrier concentration transport regime relevant in OFETs.

15.4.1 The Influence of the Carrier Concentration on μ(T) in Zero Electric Field Limit (Apparent Meyer-Neldel Compensation Rule)

The effective drift mobility μ_e for any jump rate model can be calculated in zero-field limit using the generalized Einstein equation, which can be written as suggested recently by Roichman and Tessler [27]

$$\mu_e = ek_0 r_t^2 W_e / k_B T, \tag{15.19}$$

where

$$W_e = \langle W_{12} \rangle \tag{15.20}$$

To calculate W_e for arbitrary carrier concentration n $(n < N)$ one should account for a many-particle nature of the charge-carrier transport process by a proper choice of the energy distribution functions for starting- and target-states: $P(\varepsilon_1)$ and $Q(\varepsilon_2)$ function, respectively. For the intrinsic Gaussian DOS distribution $g(\varepsilon)$, the normalized $P(\varepsilon_1)$ distribution can be presented as

$$P(\varepsilon_1) = \frac{g(\varepsilon_1) f(\varepsilon_1, \varepsilon_F)}{\int_{-\infty}^{\infty} d\varepsilon \, g(\varepsilon) f(\varepsilon, \varepsilon_F)}, \tag{15.21}$$

and the normalized $Q(\varepsilon_2)$ distribution as

$$Q(\varepsilon_2) = \frac{g(\varepsilon_2)[1 - f(\varepsilon_2, \varepsilon_F)]}{\int_{-\infty}^{\infty} d\varepsilon \, g(\varepsilon)[1 - f(\varepsilon, \varepsilon_F)]}. \tag{15.22}$$

The effective drift mobility Eq. (15.19) at arbitrary concentration of charge-carriers can also be calculated by employing the concept of the *effective transport energy* ε_t which depends on temperature and carrier concentration. The effective transport energy level implies the energy of a target site to which most of the localized carriers make thermally activated jumps and which does not depend on the energy of a starting state ε_1 when $\varepsilon_1 < \varepsilon_t$. This approach accounts for changing the jump distance with changing temperature in the two-site transitions. By employing this concept Eq. (15.22) reduces to

$$Q(\varepsilon_2) = \delta(\varepsilon_2 - \varepsilon_t) \tag{15.23}$$

Substituting Eqs. (15.6) at zero electrical field, (15.21), and (15.23) into Eq. (15.20), for the Miller–Abrahams jump rate model one obtains for an arbitrary carrier density

$$W_e = \frac{\int_{-\infty}^{\varepsilon_t} d\varepsilon \, W(\varepsilon, \varepsilon_t) \, g(\varepsilon) f(\varepsilon, \varepsilon_F)}{\int_{-\infty}^{\varepsilon_t} d\varepsilon \, g(\varepsilon) f(\varepsilon, \varepsilon_F)}, \tag{15.24}$$

where

$$W(\varepsilon, \varepsilon_t) = \nu_0 \exp\left(-2\frac{r_t}{b}\right) \exp\left(-\frac{\varepsilon_t - \varepsilon}{k_B T}\right), \tag{15.25}$$

here $r_t = r(\varepsilon_t)$ is the jump distance at and below the transport energy level ε_t. In Eq. (15.24) and further, only hopping transitions to the transport energy level from the states below the ε_t have been taken into account at the configuration averaging. Then Eq. (15.20) for the effective Miller–Abrahams jump rate can be rewritten as

$$W_e = \nu_0 \exp\left(-2\frac{r_t}{b}\right) \exp\left(-\frac{\varepsilon_t}{k_B T}\right) \frac{\int_{-\infty}^{\varepsilon_t} d\varepsilon \, \exp\left(\frac{\varepsilon}{k_B T}\right) g(\varepsilon) f(\varepsilon, \varepsilon_F)}{\int_{-\infty}^{\varepsilon_t} d\varepsilon \, g(\varepsilon) f(\varepsilon, \varepsilon_F)}. \tag{15.26}$$

Then one obtains the effective charge mobility

$$\mu_e = \mu_0 x k_0 \left(\frac{r_t}{a}\right)^2 \exp\left(-2\frac{r_t}{b}\right) \exp(-x x_t) \frac{\int_{-\infty}^{x_t} dt \, \frac{\exp\left(-\frac{1}{2}t^2 + xt\right)}{1+\exp[x(t-x_F)]}}{\int_{-\infty}^{x_t} dt \, \frac{\exp\left(-\frac{1}{2}t^2\right)}{1+\exp[x(t-x_F)]}}, \tag{15.27}$$

It should be noted that the effective transport energy concept is justified for a considerable degree of the energetic disorder, i.e., Eq. (15.15) is valid only at $\sigma/k_B T > 1$.

Here we limit our consideration of the charge-carrier transport to a region of relatively high temperatures only. For low temperature, charge-carrier transport is discussed in Ref. [12]. Figure 15.9a (thick curves) shows the calculated temperature dependences of the charge-carrier mobility, plotted in a $\ln(\mu_e/\mu_0)$ versus $\sigma/k_B T$ representation for different charge-carrier concentrations assuming $a/b = 10$. The calculations are restricted to a temperature regime defined by $\sigma/k_B T \geq 3$. The Arrhenius-type of the $\mu(T)$ dependence indicates that the ODOS is virtually temperature independent. This is quite in contrast to the case of $n/N \to 0$ characterized by the nonArrhenius-type temperature dependence $\ln(\mu_e/\mu_0) \propto (\sigma/k_B T)^2$, since in such a case charge-carrier transport is dominated by hopping from the equilibrium ODOS distribution which is temperature dependent as discussed in the introduction.

A remarkable result is that if one would—hypothetically—extend the above calculations to higher temperatures, the asymptotes (thin lines) would intersect at finite temperature $T_0 \cong 2\sigma/5k_B$. Note that the EMA approach [11] does not allow us to present the results in closed analytic form. However, the calculated results including their (hypothetical) extension toward infinite T can be parameterized in terms of an approximate analytical equation for the charge-carrier mobility μ_e as a function of $\sigma/k_B T$, a/b, and n/N,

Fig. 15.9 a Dependence of effective charge mobility $\ln(\mu_e/\mu_0)$ on $\sigma/k_B T$ at *different carrier concentrations* calculated by Eq. (15.27) (*red thick curves*) at $\sigma/k_B T \geq 3$ and $a/b = 10$. *Thin lines* present the approximation dependences calculated by approximated Eq. (15.29). The *inset shows* the intersection point $\sigma/k_B T_0$ versus a/b ratio. **b** $\ln(\mu_e/\mu_0)$ versus $1/T$ dependences at different width of the DOS, σ, calculated by Eq. (15.27) (*red thick curves*) at constant $n/N = 10^{-2}$ and $a/b = 10$. *Thin lines* present the approximation dependences calculated by approximated Eq. (15.29)
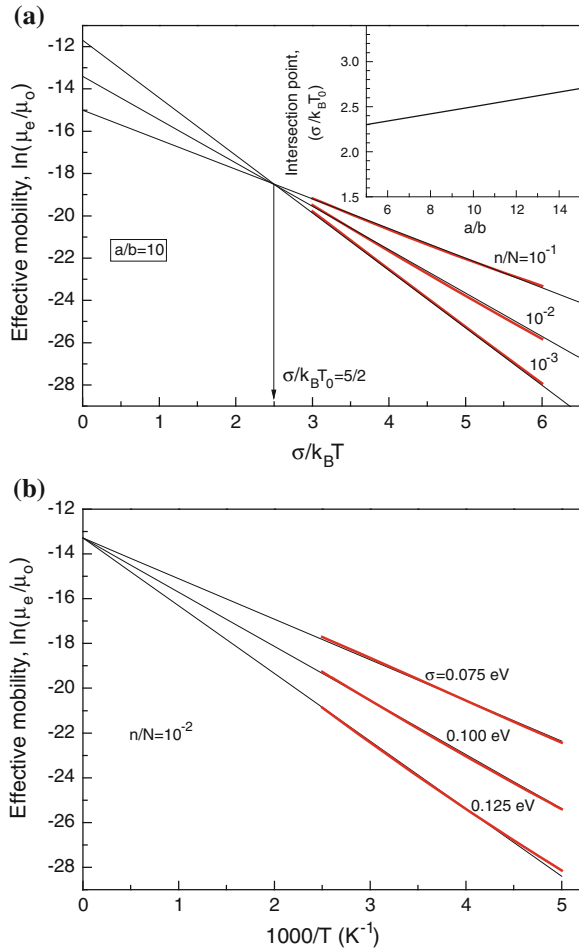
$$\mu_e = \mu_0 \exp\left[-2\frac{a}{b} + \frac{1}{2}\left(\frac{a}{b} - 7\right)\right] \exp\left\{-\left[\frac{3}{40}\frac{a}{b} - \frac{1}{15}\frac{a}{b}\log_{10}\left(\frac{n}{N}\right)\right]\left(\frac{\sigma}{k_B T} - y_0\right)\right\},$$

(15.28)

where $y_0 = 21/10 + (1/25)(a/b)$. It is appropriate for $8 < a/b < 12$ and for $10^{-3} \leq n/N \leq 10^{-1}$ which is relevant for OFET operation. The inset in Fig. 15.9a proves that the isokinetic temperature T_0, at which the $\ln(\mu) \propto T^{-1}$ graphs intersect, depends rather weakly on a/b. Rewriting Eq. (15.28) yields [12]

$$\mu_e = \mu_0 \exp\left[-2\frac{a}{b} + \frac{1}{2}\left(\frac{a}{b} - 7\right)\right] \exp\left[-E_a\left(\frac{1}{k_B T} - \frac{1}{k_B T_0}\right)\right],$$

(15.29)

where

$$E_a = \left[\frac{3}{40}\frac{a}{b} - \frac{1}{15}\frac{a}{b}\log_{10}\left(\frac{n}{N}\right)\right]\sigma; \quad T_0 = \frac{E_{MN}}{k_B} = \frac{\sigma}{k_B y_0}. \tag{15.30}$$

It turns out that Eq. (15.29) can be extended to lower carrier concentrations $10^{-5} \leq n/N < 10^{-3}$, if E_a is substituted by $E'_a = 0.85E_a$.

As one can note, Eq. (15.29) is nothing else than the conventional Meyer-Neldel relation (cf. Eq. 15.3), which has been verified by experiments on several OFET devices [22–24]. A certain compensation behavior is evident from Eq. (15.29) that is the essence of the MNR. The prefactor of the charge-carrier mobility is a product of parameter μ_0 and the temperature independent exponential term in Eq. (15.29). Let us rewrite Eq. (15.29) as

$$\mu_e = \mu_{00} \exp\left(-\frac{E_a}{k_B T}\right), \tag{15.31}$$

where

$$\mu_{00} = \mu_0 \exp\left[-2\frac{a}{b} + \frac{1}{2}\left(\frac{a}{b} - 7\right) + \frac{E_a}{k_B T_0}\right]. \tag{15.32}$$

Then one can obtain

$$\ln\left(\frac{\mu_{00}}{\mu_0}\right) = -2\frac{a}{b} + \frac{1}{2}\left(\frac{a}{b} - 7\right) + \frac{E_a}{k_B T_0}. \tag{15.33}$$

Equation (15.33) relates the prefactor μ_{00} with the activation energy E_a, namely predicts a linear relationship between $\ln \mu_{00}$ and E_a exactly as suggested by the MNR.

If one assumes $\sigma = 0.1\,\text{eV}$ and $a/b = 10$, a typical value for organic disordered materials, then Meyer-Neldel energy $E_{MN} = k_B T_0 = 0.04\,\text{eV}$ is obtained, the value which indeed has been typically observed in many relevant experiments. The activation energy E_a (Eq. 15.30) is temperature independent, varies linearly with σ and decreases with increasing charge-carrier concentration due to the shift of the Fermi level [11, 12, 22] toward the effective transport energy level. An important consequence of the presented theoretical model is, that it provides compact analytical relations (viz. Eqs. 15.29 and 15.30) which can be readily used to evaluate material parameters like the effective carrier concentration from experimentally accessible data on temperature dependence of the mobility measured in organic semiconductor-based devices [12]. The width of the DOS $\sigma = 5E_{MN}/2$ can be obtained from the experimentally determined quantity E_{MN} assuming a typical value $a/b = 10$, and Eq. (15.30) yields an estimate for the effective carrier concentration n/N from experimentally measured E_a at vanishing lateral electric field.

Interestingly, the structure of Eq. (15.29) predicts that if one extends a family of $\ln(\mu)$ versus T^{-1} graphs calculated at variable E_a, i.e., by changing the active organic semiconductor layer, yet constant carrier concentration, to $T \to \infty$, they

would intersect at $T \to \infty$ and not at a finite T_0 as MNR would imply. Figure 15.9b shows temperature dependences of the effective mobility calculated by Eq. (15.27) (thick lines) and approximated Eq. (15.29) (thin lines) for different energetic disorder parameter σ, yet constant carrier concentration $n/N = 10^{-2}$ and $a/b = 10$. These calculations are restricted to moderately high temperatures. As it is evident from Fig. 15.9b, the calculated temperature dependences in this case *do not show* any MNR compensation effect and intersect at infinite temperature. This is in disagreement with the conventional MNR that predicts a correlation between prefactor rate and activation energy regardless of how the change of E_a is accomplished, i.e., by either changing the width of the DOS itself or changing the degree of state filling. This implies that the observed compensation effect for OFET mobility (Eq. 15.29) is *not a true MNR*, but rather an apparent one, and it was fully proven by recent experimental studies of the OFET mobility in C_{60}-based OFETs [48].

15.4.2 The Influence of the Electric Field on Temperature Dependence μ(T)

Let us consider first the electric field-effect on $\mu(T)$ in the small carrier concentration transport regime. The charge-carrier mobility at low carrier concentration is conventionally measured by the ToF technique which has been applied extensively to study charge-carrier transport in disordered organic solids, for instance, in vapor-deposited molecular glasses [3, 4]. A small charge-carrier concentration is required in the ToF method to avoid any space charge inside the sample and, hence, a field redistribution, which can distort the ToF signal. To limit space charge effects it has become common practice to limit the number of migrating charge-carriers to 5 % of the capacitor charge, i.e., ca. 10^{10} charge-carriers/cm^2 in an electric field of 10^5 V/cm, equivalent to a concentration of $n = 10^{13}$ cm^{-3} in a 10 μm thick sample. Taking $N \approx 10^{22}$ cm^{-3} as a representative value for molecular glasses, one gets a relative carrier concentration of $n/N \approx 10^{-9}$. At such a carrier concentration, the charge-carrier mobility is independent on carrier concentration, because the Boltzmann statistic dominates the hopping transport; that is the reason why it is called the "small-carrier-concentration limit".

Figure 15.10a presents the temperature dependences of the charge-carrier mobility calculated by Eq. (15.12) with accounting for energy correlation effects at $n/N = 10^{-9}$ for different electric fields. As one could expect, the temperature dependences are nice straight lines in $\ln(\mu) \propto T^{-2}$ representation, which agrees with a number of previous theoretical and computer simulation data, as well as with ToF experiments [3, 4, 6]. The temperature dependences intersect at infinite temperature as suggested by the GDM [3], and no MNR (or Gill-type) behavior is observed. If one, hypothetically, replots these data in simple Arrhenius coordinates $\ln(\mu) \propto T^{-1}$ then, as one can see from Fig. 15.10b: (1) the calculated

Fig. 15.10 a Temperature dependences of the charge-carrier mobility $\ln(\mu_e) \propto 1/T^2$ calculated by Eq. (15.12) for an energy-correlated system at low carrier concentration $n/N = 10^{-9}$ parametric in electric fields and at $a/b = 5$; **b** The same data replotted in Arrhenius ($\ln(\mu_e) \propto 1/T$) representation
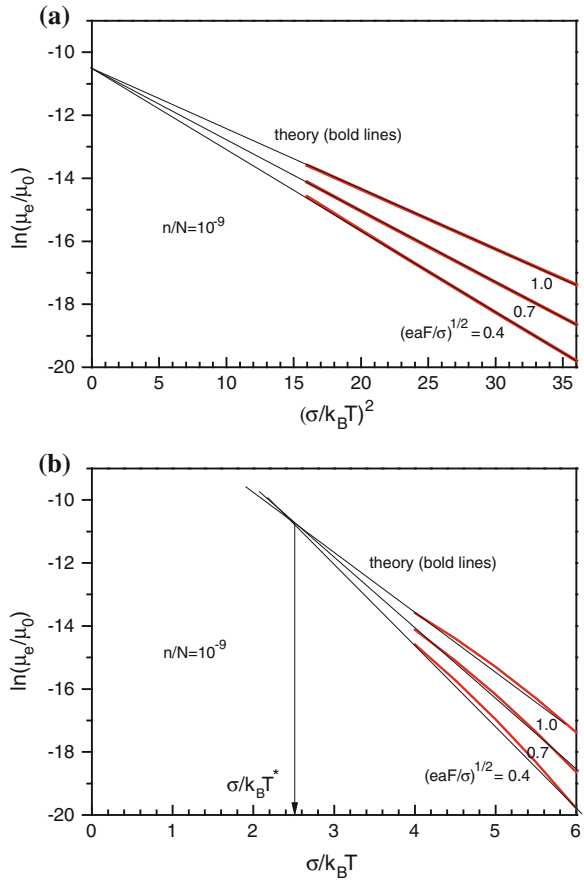
T-dependences are no longer perfect straight lines, and (2) their formal extrapolation to higher temperatures shows an apparent intersect at some intermediate temperature T^*. It is clear that the latter is just a simple consequence of *improper* $\ln(\mu) \propto T^{-1}$ representation of the data, which in reality feature functionally different temperature dependence. Thus, as already stated long ago [4], the Gill relation is not appropriate for the description of the ToF mobility data.

15.4.2.1 Meyer-Neldel Behavior at Finite Electric Field

Hereafter, we consider the transport regime of large carrier concentrations, which is typically realized in operating OFET devices. The temperature dependence of the charge-carrier mobility at large carrier densities differs from that for the low concentration limit: (1) It obeys an Arrhenius-type dependence as discussed already in literature [13, 14], and (2) while in the low carrier density limit the slope
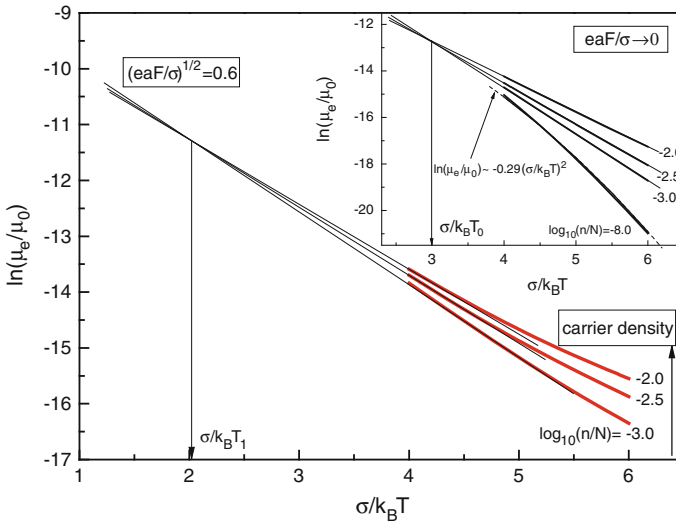
Fig. 15.11 Effective charge-carrier mobility $\ln(\mu_e/\mu_0)$ versus σ/k_BT calculated by Eq. (15.12) at finite electric field $((eaF/\sigma)^{1/2} = 0.6)$ for different effective carrier concentrations (*bold curves*) [15] with accounting for energy correlations and $a/b = 5$. *Inset* $\ln(\mu_e/\mu_0)$ versus σ/k_BT calculated at vanishing electric field $(F \to 0)$ for different effective carrier concentrations (*bold curves*) with accounting for energy correlations

of $\mu(T)$ depends on the electric field only, at large carrier densities, it depends not only on the electric field but also on the carrier concentration.

Figure 15.11 (bold curves) depicts the temperature dependences of the charge-carrier mobility calculated by Eq. (15.12) at a *finite* constant electric field taking into account the energy correlations for several large carrier concentrations relevant for OFET operation [15]. The calculated curves are virtually straight lines in Arrhenius representation and their asymptotes, due to an extension to higher temperatures (given by thin lines in Fig. 15.11), intersect at some finite temperature T_1 featuring, thus, a MNR-type behavior.

Temperature dependences of the charge-carrier mobility for *vanishing electric field* $(F \to 0)$ calculated by Eq. (15.12) taking into account the energy correlations at different carrier concentrations are shown in the inset in Fig. 15.11 for comparison. As one can see, the asymptotes to the calculated dependences at high carrier concentrations $(n/N = 10^{-3} \ldots 10^{-2})$ can be linearly extrapolated to higher temperatures and intersect at finite temperature T_0 demonstrating thus a MNR behavior. These results agree well with our previous calculations of the temperature-dependent charge-carrier mobility [12] parametric in carrier concentration using an EMA theory developed *solely* for zero-electric field and for a noncorrelated energy disordered system. This verifies that the present extended EMA model at vanishing electric field provides virtually the same results regarding the MNR behavior for $\mu(T)$ upon varying the charge-carrier concentration as the

model described before [12]. At a very low carrier concentration, $n/N = 10^{-8}$, the calculated temperature dependence of the charge-carrier mobility can be perfectly fitted by the relation $\ln(\mu_e) \propto -0.29(\sigma/k_B T)^2$ (inset in Fig. 15.11, dashed curve) which was obtained before from computer simulation studies [34], which supports the adequateness of the present analytical theory. Thus, accounting for energy correlations does result in a notably weaker temperature dependence of the charge-carrier mobility as compared to that for noncorrelated systems, notably for the charge-carrier mobility at vanishing electric field.

15.4.2.2 Gill Behavior Upon Varying the Electric Field

Temperature dependences of the charge-carrier mobility parametric in electric fields calculated by Eq. (15.12) are plotted in Fig. 15.12 for two different carrier concentrations: $n/N = 10^{-9}$ (dashed curves, lower branch) and 10^{-2} (bold curves, upper branch). These dependences were calculated within the present EMA model over a broad temperature range up to very high temperatures not accessible for experiments. As one can see from Fig. 15.12, at large carrier concentration asymptotes to the calculated $\ln(\mu) \propto T^{-1}$ dependences extrapolated to higher temperatures (thin straight lines) intersect at finite temperature T_2 implying that the MNR-type behavior *upon varying the electric field* (also called in the literature the Gill behavior, empirically suggested long ago [49]) is reproduced over a range of moderate temperatures. These EMA calculation results are in good agreement with
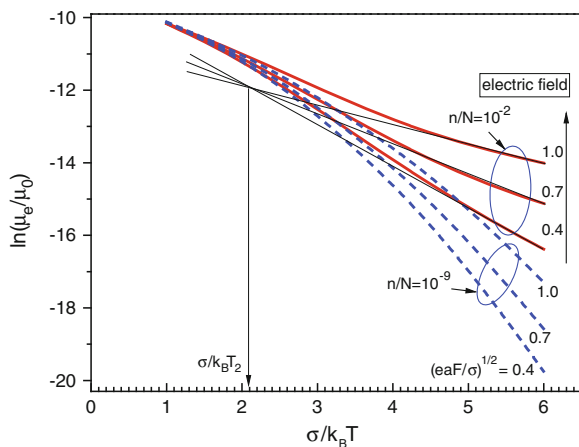
Fig. 15.12 Effective charge-carrier mobility $\ln(\mu_e/\mu_0)$ versus $\sigma/k_B T$ calculated by Eq. (15.12) parametric in electric fields for two different carrier concentrations $n/N = 10^{-9}$ and 10^{-2} (*dashed* and *bold curves*, respectively) at $a/b = 5$ in an energy-correlated hopping system. The *thin straight lines* show extrapolation of the calculated dependences at $n/N = 10^{-2}$ to higher temperatures

recent experimental observation of the Gill behavior in C_{60}-based OFET devices [36]. No Gill-type behavior occurs for very low carrier concentration, $(n/N = 10^{-9})$ (Fig. 15.12), because the charge-carrier mobility in this regime does not follow $\ln(\mu) \propto T^{-1}$ dependence as was discussed above.

At very high temperature, the calculated charge-carrier mobilities merge into the same value independent of electric field and carrier concentration (Fig. 15.12). This means that, according to the present treatment, there is no finite critical temperature above which the mobility would feature negative field dependence as follows from the empirical Gill equation. The reason for such $\mu(T)$ dependences is that at higher temperatures the average energy ε_m of the equilibrium occupational density-of-states (ODOS), which derives from $\varepsilon_m = \int_{-\infty}^{\infty} d\varepsilon \, \varepsilon \, g(\varepsilon) n(\varepsilon, \varepsilon_F) \Big/ \int_{-\infty}^{\infty} d\varepsilon \, g(\varepsilon) n(\varepsilon, \varepsilon_F)$, is no longer approached to the T-independent Fermi level ε_F, but is determined by the T-dependent shift of $\varepsilon_m \to \varepsilon_0 = -\sigma^2/k_B T$ toward the transport energy [12] and, concomitantly, toward the center of the DOS.

The electric field dependence of the charge-carrier mobility is consistent with the reasoning described above. Under the applied field, the average equilibrium energy ε_m increases and, as a consequence, the charge-carrier mobility determined by jumps from ε_m to ε_t should also increase with increasing electric field. At high carrier concentrations the EGDM formalism predicts a lowering of the barrier height for carrier jumps, because ε_m increases not only as a result of an increase of the carrier density but also due to an increase of the applied electric field (lateral field in the case of an OFET).

15.5 The Influence of Electric Field on Meyer-Neldel Temperature and the Influence of Charge-Carrier Concentration on Gill Temperature

For the sake of convenience, we discriminate between the isokinetic temperatures resulting from intersection of $\ln(\mu) \propto T^{-1}$ upon *varying carrier concentration* and that upon *varying applied electric field* and call them *Meyer-Neldel-* (denoted as T_1) and *Gill-* (denoted as T_2) temperature, respectively. Recent experimental studies [37, 50, 51] have revealed that the Meyer-Neldel temperature and Gill temperature are not constant but depend on the electric field F and on charge-carrier concentration n/N, respectively. This effect can be well reproduced within the present extended EMA model [15] provided that the carrier concentration dependence of the jump length is taken into account according to Ref. [20] as described in Sect. 15.2.2. The latter is responsible for changing the slope of the field dependences of the OFET mobility with increasing carrier concentration shown in Fig. 15.3a. Figure 15.13a (solid curves) shows the MN-temperature T_1 versus applied electric field calculated within the present model. Apparently, the MN-temperature shifts to lower values with increasing F. The field dependence of T_1 can be parameterized as follows [15, 37]

Fig. 15.13 Calculated
dependence of MN-
temperature T_1 (**a**) on electric
field, and the dependence of
Gill temperature T_2 on carrier
concentration (**b**) for an
energy-correlated disordered
hopping system [15]. The
same dependences calculated
upon ignoring the carrier
concentration dependence of
the jump length (*dashed
curves 2*) and upon ignoring
any energy correlation effects
(*dashed curves 3*). See text
for details
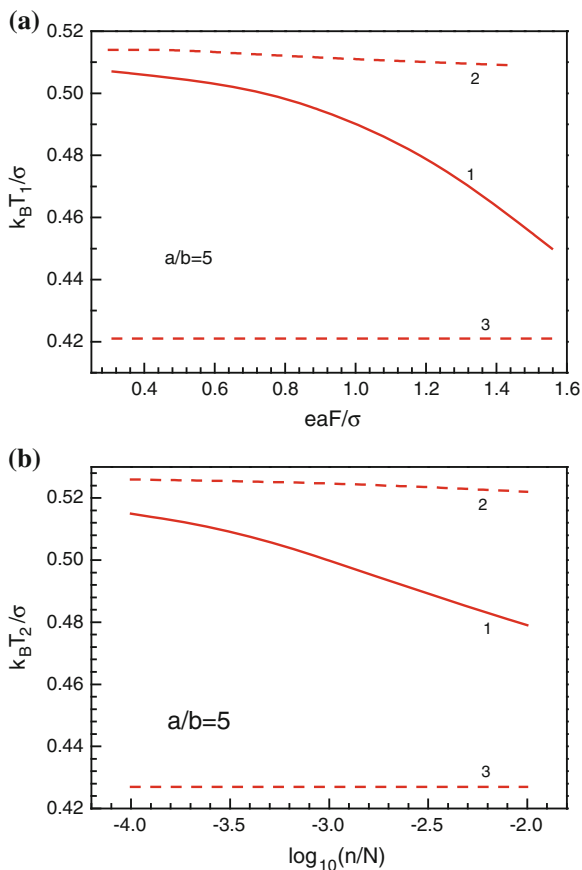
$$\frac{k_B T_1}{\sigma} = 0.5 + 0.029 \frac{eaF}{\sigma} - 0.039 \left(\frac{eaF}{\sigma}\right)^2. \qquad (15.34)$$

If the carrier concentration dependence of the jump length is ignored (cf.
dashed lines in Fig. 15.3a) the $k_B T_1/\sigma$ quantity demonstrates just a very weak field
dependence as given by the dashed curve 2 in Fig. 15.13a. Virtually, no field
dependence was found for $k_B T_1/\sigma$ calculated for an energy noncorrelated disor-
dered system and $k_B T_1/\sigma \cong 0.42$ (dashed curve 3 in Fig. 15.13a). Thus, we con-
clude that the change of the MN-temperature T_1 upon applied electric field results
from the presence of energy correlation effects, namely, due to the decrease of the
typical jump length with increasing carrier concentration.

Along this line, the Gill temperature T_2 tends to decrease with increasing carrier
concentration n/N (Fig. 15.13, solid curve 1). This carrier density dependence of
T_2 can be well approximated by

$$\frac{k_B T_2}{\sigma} = 0.416 - 0.037 \log_{10}\left(\frac{n}{N}\right) - 0.0031\left[\log_{10}\left(\frac{n}{N}\right)\right]^2. \qquad (15.35)$$

We found that $k_B T_2/\sigma$ shows a very weak concentration dependence (dashed curve 2 in Fig. 15.13b) if the carrier concentration dependence of the typical jump length is ignored. If energy correlations are absent, the Gill temperature is virtually independent on carrier concentration and reaches the constant value $k_B T_2/\sigma \cong 0.43$ (Fig. 15.13b, dashed curve 3). Both $k_B T_1/\sigma \cong 0.42$ and $k_B T_2/\sigma \cong 0.43$ values obtained for an energy uncorrelated system are slightly smaller than that obtained when energy correlations are taken into account because the formers ignore the decrease of σ due to the presence of the energy correlations. It should be pointed out that the above calculated dependences for T_1 and T_2 are only relevant to the range of electric fields where the Poole–Frenkel-type field dependence holds.

The results of the above calculated charge-carrier mobility in the high carrier concentration limit can be used to estimate the energetic disorder parameter σ from experimental data basically by two different methods:

1. Equation (15.34) allows calculating the parameter σ using the experimentally measured Meyer-Neldel temperature T_1 ($E_{MN} = k_B T_1$) at a given electric field F (within the field interval where a PF-type dependence is obeyed) according to the following relation

$$\sigma = E_{MN} A \left(1 + \sqrt{1 + \left(\frac{eaF}{E_{MN}}\right)^2 \frac{0.078}{A^2}}\right), \quad A = 1 - 0.029 \frac{eaF}{E_{MN}}. \qquad (15.36)$$

The present extended theoretical model [15] yields $E_{MN}/\sigma \cong 0.33$ for zero-field mobility. Previous theoretical treatment limited to the zero-field case [12], which disregarded the energy correlations and percolation effects, yielded a somewhat different ratio: $E_{MN}/\sigma \cong 0.40$.

2. In its turn, the experimentally measured Gill temperature T_2 ($E_G = k_B T_2$) at a given high carrier concentration n/N (being determined by a gate voltage (V_G) in an OFET) can also be used to calculate σ by Eq. (15.35), which yields

$$\sigma = \frac{E_G}{0.416 - 0.037 \log_{10}\left(\frac{n}{N}\right) - 0.0031\left[\log_{10}\left(\frac{n}{N}\right)\right]^2}. \qquad (15.37)$$

To use Eq. (15.37) one has, however, to know the effective carrier concentration in a thin conductive channel of an OFET, which demonstrates a highly nonuniform distribution—strongly decreasing from the semiconductor/insulator interface into the bulk [52].

Thus, the first of the above-mentioned methods seems to be more appropriate for estimating the energetic disorder parameter σ from experimental data. A big

advantage of the present extended theoretical model is that it *does not require an extrapolation* of experimental data to zero electric field. It allows fitting of experimental data, obtained at a given (not too low) electric field, in order to evaluate material parameters of organic semiconductors.

The present theory has been applied to fit experimental data (Fig. 15.14) on electric field dependence of the Meyer-Neldel energy and charge-carrier concentration dependence of the Gill energy measured in C_{60}-based OFETs [15, 37, 50]. Figure 15.14 demonstrates a remarkably good fitting of the experimental data by the present analytic model.

Finally, we should note that the above consideration suggests that the MN and Gill energies are inherently interrelated in disordered organic semiconductors. Indeed, combining Eqs. (15.34) and (15.35) one obtains

$$\frac{E_G}{E_{MN}} \equiv \frac{T_1}{T_2} = \frac{0.416 - 0.037\,z - 0.0031\,z^2}{0.5 + 0.029\,h - 0.039\,h^2}, \qquad (15.38)$$

where $z = \log_{10}(n/N)$ and $h = eaF/\sigma$, for $-4 \leq z \leq -2$ and $0.3 \leq h \leq 1.6$. Figure 15.15 presents a 3D plot of the ratio E_G/E_{MN} upon carrier concentrations and applied electric fields calculated by Eq. (15.38).

It is important to note that according to the presented EMA model the MN- and Gill-energies are interrelated but they are not identically equal—as can be seen from Fig. 15.15, E_{MN} and E_G values coincide only at certain electric fields and carrier concentrations.
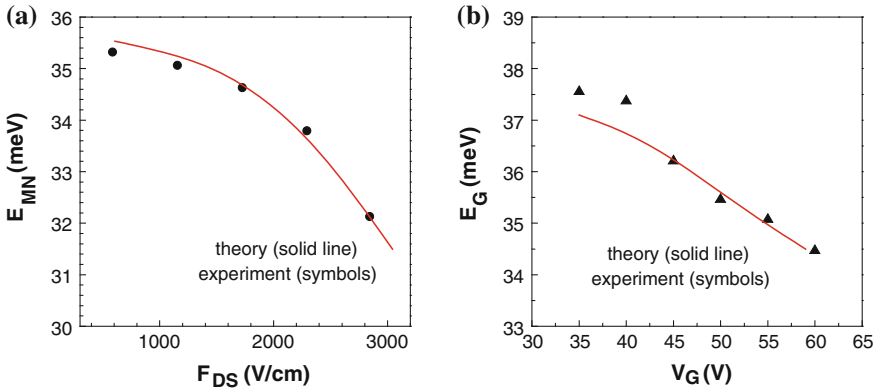
Fig. 15.14 Experimentally determined (**a**) MN-energy $E_{MN} = k_B T_1$ (*symbols*) versus the applied lateral electric field and (**b**) Gill energy $E_G = k_B T_2$ as a function of used gate voltage V_G. Fitting by Eqs. (15.36) and (15.37), respectively, using the following set of parameters: $\sigma = 0.07$ eV; $a/b = 5$; $a = 1.4$ nm and $q = 256$ are given by *solid lines*

Fig. 15.15 Ratio of E_G/E_{MN} calculated by Eq. (15.38) for different electric fields and carrier concentrations [15]
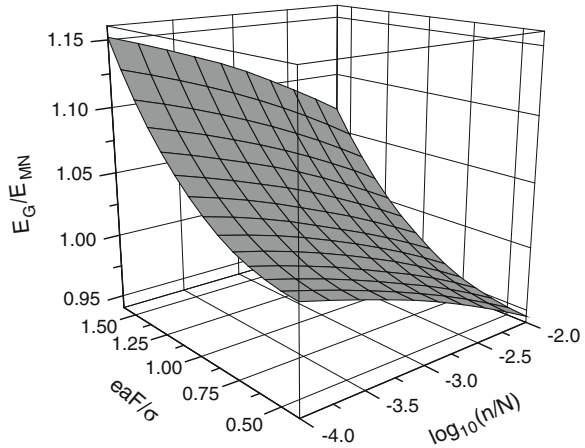
15.6 Concluding Remarks on the Comparison of Different Models for the MNR in OFETs

In this chapter, we have demonstrated that the establishment of the MNR behavior is a characteristic signature of conventional hopping charge transport in a disordered organic system with variable carrier concentration and can be rationalized within the recently suggested analytic EMA theory [11, 12, 15] based on disorder formalism. The latter was applied to describe the observed MNR behavior in C_{60}-based OFETs [12, 37, 48]. The presented theoretical model premised a Gaussian DOS distribution and Miller–Abrahams jump rate, and it ignores polaronic effects. It attributes the MNR behavior to disorder and predicts that the MNR energy E_{MN} in organic semiconductors is directly related to the width of the Gaussian DOS, σ, providing thus a method for evaluating the amount of energetic disorder in the material. An important experimental verification of the suggested model is that the MNR behavior for the OFET mobility is clearly observed in C_{60} films [12, 37, 48], i.e., in a system where polaron effects are negligible due to a very weak electron–phonon coupling found for this material [53], which is shown to be inversely proportional to the number of π-bonded atoms [53]. Indeed, C_{60} single crystals are normally characterized by a virtually temperature independent mobility [54], whereas polaron transport (Holstein polaron model) does require an activation energy equal to the half of the polaron binding energy [55]. Thus, polaron formation does not necessarily need to be involved to rationalize the MNR behavior.

Let us compare the presented EMA model by Fishchuk et al. [12, 15] with alternative models suggested before to explain the MNR phenomenon in different systems. The so-called multiexcitation entropy (MEE) model by Yelon and Movaghar [56, 57] was conventionally used to explain the MNR for thermally activated processes in general and it predicts a correlation between the prefactor rate and the activation energy E_a *regardless of how the change of E_a is accomplished.*

The latter is in clear disagreement with the experimental observation that the MNR behavior for the temperature dependences of the charge-carrier mobility in C_{60} films arises upon varying the carrier concentration, but not regarding varying the width of the DOS [48]. As demonstrated in Fig. 15.9b, the EMA calculated temperature dependences in the latter case do not show any MNR compensation effect and intersect at the infinite temperature [12]. This implies that for the OFET charge mobility there is in fact no genuine correlation between the prefactor and the Arrhenius factor that arises from activated jumps, and therefore the *MNR phenomenon in these materials is an apparent rather than true one*, exactly as predicted by the EMA theory of Fishchuk et al. [12]. Another drawback of the above MEE model is that it is not able to rationalize both the experimentally observed electric field dependence of the Meyer-Neldel temperature as well as the carrier concentration dependence of the Gill temperature, because these models predict that MN and Gill temperatures are constant, in contradiction to experimental results [37, 50]. On the other hand, the suggested disorder-based EMA model can explain the phenomena mentioned above (Figs. 15.14 and 15.15), and provides a qualitative fit of experimental data [37, 50]. Further, the experimentally observed shift in the Mayer-Neldel energy was found to clearly correlate with energetic disorder in C_{60} films grown at different growth conditions, which is in excellent agreement with the predictions of the above EMA theory [48]. In contrast, the MEE model by Yelon and Movaghar [56, 57] neglects the inherent energetic disorder in these materials and therefore cannot rationalize the observed significant change in the MNR energy with changing film morphology. Besides, this model is unable to account for the carrier concentration effects on charge mobility.

Moreover, the MEE model predicts that the exponential increase of the prefactor with increasing activation energy (to provide MNR behavior) can only occur at large values of the activation energies $E_a \sim 1$ eV [56]. In this case, the Debye energy $\hbar \omega_D \ll E_a$, so the thermal activation process can only occur via multiphonon excitations, which results in an exponential increase of the number of different activation paths and consequently in an exponential increase of the prefactor with increasing E_a. This can be interpreted also in terms of increasing entropy S, i.e., $S \propto E_a$. For two-site approximation in Refs. [56, 57] with a fixed difference in site energies $\varepsilon_2 - \varepsilon_1 = E_a$ the MNR behavior arises as a result of multiphonon activated transitions, while no such a behavior is expected for single phonon transitions. In the latter case there is just a single activation path that cannot lead to an exponential increase of the prefactor, which implies that the MNR behavior is not expected for the Miller–Abrahams transport in the framework of the MEE model suggested before [56, 57]. On the other hand, the activation energies of the charge mobility in C_{60}–based OFETs are found to be considerably smaller (i.e., between 0.05 and 0.25 eV depending on V_G and being comparable with phonon mode energies in C_{60} reaching the value of ~ 0.2 eV [58]) than that required by the MEE model, which in combination with negligible polaron effects in this material justifies the Miller–Abrahams jump rate approximation. The puzzle can be solved if one accounts for disorder effects and considers a random system with a Gaussian DOS distribution of site energies where a charge-carrier experiences a

large number of hops between sites with *different energies* before it reaches a collecting electrode. This is just the hopping transport within a manifold of localized states distributed in energy, which gives rise to the MNR behavior for the Miller–Abrahams hopping transport regime as recovered by analytical EMA calculations [12] and also confirmed by computer simulations [9]. In this case an increase of E_a can also be associated with an increasing entropy S, so that from $\mu_1 = \mu_0 \exp(S/k_B)$ [57] it follows that the entropy is given by $S = E_a/T_0$ and it depends on the energetic disorder parameter σ, as $E_a \propto \sigma$ according to Eq. (15.30). Experimental data on E_a and T_0 can provide an estimate for the entropy S and for its dependence on charge-carrier concentration (gate voltage). With increasing charge-carrier concentration, the part of the DOS between Fermi level and the effective transport energy level becomes narrower, which is equivalent to some ordering of the system and consequently to reducing entropy.

Finally, it should be noted that recently Emin [59] advanced an adiabatic polaron model that considers carrier-induced softening of the vibrations upon electron motion and includes the Fröhlich long-range polaron approach, and showed that this conditions bring up the MNR and Poole–Frenkel-type behavior for the charge mobility. Although this model recovers the above behaviors as good as the Fishchuk theory [12, 15], it seems to be irrelevant for the charge-carrier transport in C_{60}-based OFETs due to its contradictions and/or failing to explain a number of other essential experimental observations listed here:

1. As the Emin model ignores energy disorder, it clearly fails to explain the dependence of the charge-carrier mobility on carrier concentration (on V_G) in OFETs because the activation energy of the charge mobility is assumed to be determined solely by polaron formation and no tail state filling is expected within this approach. There is no charge-carrier concentration factor in this model.

2. For the above reason, the MNR behavior in OFETs *regarding changing the gate voltage* cannot be reproduced at all by the Emin model, because the model does not predict the dependence of the activation energy on V_G. In fact, the Emin model was suggested for the for a very low carrier concentration transport regime when mobility is independent on carrier concentration, realized for instance in ToF measurements.

3. Emin's theory predicts that the characteristic Meyer-Neldel temperature $T_{MN} \equiv t/k_B$ is determined by the electron-transfer energy t. Therefore, to rationalize an experimentally observed strong decrease of T_{MN} from 408 K to 250 K in C_{60}-films grown at substrate temperatures T_{sub} increasing from room temperature to $T_{sub} = 250\,°C$ [48], one has to assume a strong increase of average intermolecular distances in such C_{60} films because the Emin model relates the change in parameter t to the change of intermolecular distance in material. This would imply considerably less dense C_{60} films grown at $T_{sub} = 250\,°C$ compared to those grown at room temperature, which sounds highly unrealistic, especially, because such films are known to have better crystallinity and should be better packed.

4. The Fröhlich polaron approach implemented in Emin's model requires a polar medium that is difficult to justify for C_{60}-based OFET structures with nonpolar BCB dielectric layers.
5. The Emin model explains neither a weakening of the Poole–Frenkel field dependence in the same material at larger carrier concentration nor the electric field dependence of T_{MN} experimentally found in C_{60}-based OFET [37, 51].
6. Finally, the Emin model fails to explain why the charge mobility in C_{60} crystals is temperature independent [54] and thus featuring no MNR behavior, while the temperature dependent charge-carrier transport is typically observed in deposited thin C_{60} films. Ignoring the energy disorder in Emin model should result in identical charge transport properties in both cases, which is in clear contradiction to experiment.

Therefore, we have to conclude that the Emin model is not appropriate to describe the presented experimental results on the charge-carrier transport in C_{60} films. The temperature-dependent charge-carrier mobility measured at different carrier concentrations and electric fields in C_{60} films of different morphology can be consistently described within the EMA theory of Fishchuk et al. [12, 15, 37, 48] based solely on disorder arguments without necessity to invoke polaron formation. Nevertheless, we want to emphasize that our approach does not exclude the polaron formation in organic solids at all; the polaron effects are certainly present and might be readily incorporated into the present GDM via employing the polaron jump rate and the MNR behavior retains.

References

1. Klauk H (2006) Organic electronics: materials, manufacturing and applications. Wiley-VCH, Weinheim
2. Berggren M, Nilsson D, Robinson ND (2007) Organic materials for printed electronics. Nat Mater 6:3–5
3. Bässler H (1993) Charge transport in disordered organic photoconductors a monte carlo simulation study. Phys Stat Sol (b) 175:15
4. Borsenberger PM, Weiss DS (1998) Organic photoreceptors for xerography. Dekker, New York
5. Blom PWM, Vissenberg MCJM (2000) Charge transport in poly(p-phenylene vinylene) light-emitting diodes. Mater Sci Eng 27:53
6. Arkhipov VI, Fishchuk II, Kadashchuk A, Bässler H (2007) In: Hadziioannou G, Malliaras G (eds) Semiconducting polymers: chemistry, physics and engineering, 2nd edn. Wiley-VCH Verlag, Weinheim

7. Tanase C, Meijer EJ, Blom PWM, deLeeuw DM (2003) Unification of the hole transport in polymeric field-effect transistors and light-emitting diodes. Phys Rev Lett 91:216601

8. Pasveer WF, Cottaar J, Tanase C, Coehoorn R, Bobbert PA, Blom PWM, de Leeuw DM, Michels MAJ (2005) Unified description of charge-carrier mobilities in disordered semiconducting polymers. Phys Rev Lett 94:206601

9. Coehoorn R, Pasveer WF, Bobbert PA, Michels MAJ (2005) Charge-carrier concentration dependence of the hopping mobility in organic materials with Gaussian disorder. Phys Rev B 72:155206

10. Arkhipov VI, Heremans P, Emelianova EV, Adriaenssens GJ, Bässler H (2002) Weak-field carrier hopping in disordered organic semiconductors: the effects of deep traps and partly filled density-of-states distribution. J Phys: Condens Matter 14:9899–9911

11. Fishchuk II, Arkhipov VI, Kadashchuk A, Heremans P, Bässler H (2007) Analytic model of hopping mobility at large charge carrier concentrations in disordered organic semiconductors: Polarons versus bare charge carriers. Phys Rev B 76:045210

12. Fishchuk II, Kadashchuk AK, Genoe J, Ullah M, Sitter H, Singh TB, Sariciftci NS, Bässler H (2010) Temperature dependence of the charge carrier mobility in disordered organic semiconductors at large carrier concentrations. Phys Rev B 81:045202

13. Craciun NI, Wildeman J, Blom PWM (2008) Universal arrhenius temperature activated charge transport in diodes from disordered organic semiconductors. Phys Rev Lett 100:056601

14. Fishchuk II, Kadashchuk A, Poroshin VN, Bässler H (2010) Charge-carrier and polaron hopping mobility in disordered organic solids: Carrier-concentration and electricfield effects. Phil Mag 90:1229

15. Fishchuk II, Kadashchuk AK, Ullah M, Sitter H, Pivrikas A, Genoe J, Bässler H (2012) Electric field dependence of charge carrier hopping transport within the random energy landscape in an organic field effect transistor. Phys Rev B 86:045207

16. Warta W, Karl N (1985) Hot holes in naphthalene: high, electric-field-dependent mobilities. Phys Rev B 32:1172

17. Warta W, Stehle R, Karl N (1985) Ultrapure, high mobility organic photoconductors. Appl Phys A: Solids Surf A36:163–170

18. Gartstein YN, Conwell EM (1995) High-field hopping mobility in molecular systems with spatially correlated energetic disorder. Chem Phys Lett 245:351–358

19. Novikov SV, Dunlap DH, Kenkre VM, Parris PE, Vannikov AV (1998) Essential role of correlations in governing charge transport in disordered organic materials. Phys Rev Lett 81:4472

20. Bouhassoune M, van Mensfoort SLM, Bobbert PA, Coehoorn R (2009) Carrier-density and field-dependent charge-carrier mobility in organic semiconductors with correlated Gaussian disorder. Org Electron 10:437

21. Novikov SV (2008) Hopping transport of interacting carriers in disordered organic materials. Phys Stat Sol (c) 5:740

22. Meijer EJ, Meijer EJ, Matters M, Herwig PT, de Leeuw DM, Klapwijk TM (2000) The Meyer–Neldel rule in organic thin-film transistors. Appl Phys Lett 76:3433

23. Meijer EJ (2003) Charge transport in disordered organic field-effect transistors. PhD thesis. Technical University of Delft

24. Paloheimo J, Isotalo H, Kastner J, Kuzmany H (1993) Conduction mechanisms in undoped thin films of C60 and C60/70. Synth Met 56:3185

25. Meyer W, Neldel H (1937) Über die Beziehungen zwischen der Energiekonstanten ε und der Mengenkonstanten a in der Leitwerts-Temperaturformel bei oxydischen Halbleitern. Z Tech Phys (Leipzig) 12:588

26. Baranovskii SD, Cordes H, Hensel F, Leising G (2000) Charge-carrier transport in disordered organic solids. Phys Rev B 62:7934

27. Roichman Y, Tessler N (2002) Generalized Einstein relation for disordered semiconductors—implications for device performance. Appl Phys Lett 80:1948

28. Miller A, Abrahams E (1960) Impurity conduction at low concentrations. Phys Rev 120:745

29. Arkhipov VI, Heremans P, Emelianova EV, Adriaensses GJ, Bässler H (2003) Charge carrier mobility in doped semiconducting polymers. Appl Phys Lett 82:3245
30. Arkhipov VI, Emelianova EV, Heremans P, Bässler H (2005) Analytic model of carrier mobility in doped disordered organic semiconductors. Phys Rev B 72:235202
31. Rubel O, Baranovskii SD, Thomas P, Yamasaki S (2004) Concentration dependence of the hopping mobility in disordered organic solids. Phys Rev B 69:014206
32. Rakhmanova SV, Conwell EM (2000) Electric-field dependence of mobility in conjugated polymer films. Appl Phys Lett 76:3822
33. Fishchuk II, Hertel D, Bässler H, Kadashchuk AK (2002) Effective-medium theory of hopping charge-carrier transport in weakly disordered organic solids. Phys Rev B 65:125201
34. Parris PE, Dunlap DH, Kenkre VM (2000) Energetic disorder, spatial correlations, and the high-field mobility of injected charge carriers in organic solids. Phys Stat Sol (b) 218:47
35. Zhou J, Zhou YC, Zhou JM, Wu CQ, Ding XM, Hou XY (2007) Carrier density dependence of mobility in organic solids: A Monte Carlo simulation. Phys Rev B 75:153201
36. Pivrikas A, Ullah M, Sitter H, Sariciftci NS (2011) Electric field dependent activation energy of electron transport in fullerene diodes and field effect transistors:Gill's law. Appl Phys Lett 98:092114
37. Ullah M, Pivrikas A, Fishchuk II, Kadashchuk A, Stadler P, Simbrunner C, Sariciftci NS, Sitter H (2011) Effect of source-drain electric field on the Meyer–Neldel energy in organic field effect transistors. Appl Phys Lett 98:223301
38. Li X, Kadashchuk A, Fishchuk II, Smaal WTT, Gelinck G, Broer DJ, Genoe J, Heremans P, Bässler H (2012) Electric field confinement effect on charge transport in organic field-effect transistors. Phys Rev Lett 108:066601
39. Anthony JE, Brooks JS, Eaton DL, Parkin SR (2001) Functionalized pentacene: improved electronic properties from control of solid-state order. J Am Chem Soc 123:9482–9483
40. Li X, Smaal WTT, Kjellander C, van der Putten B, Gualandris K, Smits ECP, Anthony J, Broer DJ, Blom PWM, Genoe J, Gelinck G (2011) Charge transport in high-performance ink-jet printed single-droplet organic transistors based on a silylethynyl substituted pentacene/insulating polymer blend. Org Electron 12:1319–1327
41. Verlaak S, Heremans P (2007) Molecular microelectrostatic view on electronic states near pentacene grain boundaries. Phys Rev B 75:115127
42. Park JG, Vasic R, Brooks JS, Anthony JE (2006) Characterization of functionalized pentacene field-effect transistors and its logic gate application. J Appl Phys 100:044511
43. Charrier D, Kemerink M, Smalbrugge B, de Vries T, Janssen R (2008) Real versus measured surface potentials in scanning kelvin probe microscopy. ACS Nano 2:622–626
44. Teague LC, Hamadani BH, Jurchescu OD, Subramanian S, Anthony JE, Jackson TN, Richter CA, Gundlach DJ, Kushmerick JG (2008) Surface potential imaging of solution processable acene-based thin film transistors. Adv Mater 20:4513–4516
45. Horowitz G, Hajlaoui ME, Hajlaoui R (2000) Temperature and gate voltage dependence of hole mobility in polycrystalline oligothiophene thin film transistors J Appl Phys 87:4456
46. Kaake LG, Barbara PF, Zhu X-Y (2010) Intrinsic charge trapping in organic and polymeric semiconductors: a physical chemistry perspective. J Phys Chem Lett 1:628–635
47. Annibale P, Albonetti C, Stoliar P, Biscarini F (2007) High-resolution mapping of the electrostatic potential in organic thin-film transistors by phase electrostatic force microscopy. J Phys Chem A 111:12854–12858
48. Ullah M, Fishchuk II, Kadashchuk AK, Stadler P, Pivrikas A, Simbrunner C, Poroshin VN, Sariciftci NS, Sitter H (2010) Dependence of Meyer–Neldel energy on energetic disorder in organic field effect transistors. Appl Phys Lett 96:213306
49. Gill WD (1972) Drift mobilities in amorphous charge-transfer complexes of trinitrofluorenone and poly-n-vinylcarbazole. J Appl Phys 43:5033
50. Fishchuk II, Kadashchuk AK, Ullah M, Sitter H, Sariciftci NS, Bässler H (2012) Electric field dependence of charge-carrier hopping transport at large carrier concentrations in disordered organic solids: Meyer–Neldel and Gill energies. J Phys C 376:012011

51. Ullah M, Pivrikas A, Fishchuk II, Kadashchuk A, Stadler P, Simbrunner C, Sariciftci NS, Sitter H (2011) Electric field and grain size dependence of Meyer–Neldel energy in C60 films. Synth Met 161:1987
52. Tanase C, Meijer EJ, Blom PWM, de Leeuw DM (2003) Local charge carrier mobility in disordered organic field-effect transistors. Org Electr 4:33
53. Devos A, Lannoo M (1998) Electron-phonon coupling for aromatic molecular crystals: possible consequences for their superconductivity. Phys Rev B 58:8236
54. Frankevich E, Maruyama Y, Ogata H (1993) Mobility of charge carriers in vapor-phase grown C60 single crystal. Chem Phys Lett 214:39
55. Emin D (1992) Low-temperature ac conductivity of adiabatic small-polaronic hopping in disordered systems. Phys Rev B 46:9419
56. Yelon A, Movaghar B (1990) Microscopic explanation of the compensation (Meyer-Neldel) rule. Phys Rev Lett 65:618
57. Yelon A, Movaghar B, Crandall RS (2006) Multi-excitation entropy: its role in thermodynamics and kinetics. Rep Prog Phys 69:1145
58. Faber C, Janssen JL, Côté M, Runge E, Blase X (2011) Electron-phonon coupling in the C60 fullerene within the many-body GW approach. Phys Rev B 84:155104
59. Emin D (2008) Generalized adiabatic polaron hopping: meyer-neldel compensation and poole-frenkel behavior. Phys Rev Lett 100:166602

Chapter 16
Grain Growth Kinetics During Microwave Sintering of the Nanocrystalline Titanium Nitride

Dmytro Demirskyi and Andrey Ragulya

16.1 Introduction

Difficulties associated with densification of nitrides are due to the fact that they possess high surface energy but low self-diffusion constant. Therefore such sintering resistant materials are usually densified by liquid phase sintering [1]. The other possible route to promote self-diffusion is decrease in particle size used [2], as it is reported that decrease in particle size up to ~ 50 nm will result in increase in self-diffusion coefficient by three orders of magnitude, and decrease of the initial [3] and final [4] sintering temperatures. Alternatively, densification is enhanced under applied pressure. Titanium nitride was successfully densified by hot pressing and spark plasma sintering [5–7]. Microwave heating was also previously successfully used for synthesis and sintering of nanocrystalline TiN or its composites at relatively low temperatures [8–10]. Like the spark plasma sintering, microwave sintering is one of the unconventional rapid sintering techniques that exploit fast heating rates and cause minimal grain growth [11]. Microwave sintering provides fast and volumetric heating, providing high densification rates [12]. Aside an abovementioned advantage, there is a sufficient drawback—the lack of clear explanation upon acceleration of diffusion processes during microwave sintering [11, 12]. The aim of this paper is an investigation of grain growth process during microwave sintering of the nanocrystalline titanium nitride powder compacts, in order to clarify the contradicting statements upon the effect of microwave heating on the grain growth process during sintering [13–15].

D. Demirskyi (✉) · A. Ragulya
Department of Physics of Strength and Plasticity, Frantsevich Institute for Problems in
Material Science, 3 Krzhizhanovsky str, Kyiv 03680, Ukraine
e-mail: dmytro.demirskyi@gmail.com

A. Ragulya
e-mail: ragulya@ipms.kiev.ua

16.2 Materials and Methods

The TiN powders, ranging in size from 30 to 40 nm (US-Nano, USA), were ground for 15 min in an agate mortar and compacted into disks, 8 mm in diameter and 4 mm in thickness, at a pressure of 200 MPa. The later was followed by CIP at 320 MPa and resulted in samples with green density of 52 % of the theoretical value and weight of 0.3 g. The compacted disks were isothermally sintered at 1,173, 1,173, and 1,373 for various times, ranging from 0.1 to 2 h. The microwave sintering process was carried out using 2 kW 2.45 GHz multimode microwave applicator. For reference, the conventional sintering experiments were carried out in a rate-controlled dilatometer (Netzsch 402, Germany). The identical heating rate of 50 °C min^{-1} was used for heating samples to the sintering temperatures, in case of the conventional sintering process heating rate of 10 °C min^{-1} was used while heating to 120 °C, followed by 50 °C min^{-1} as mentioned above. The N_2 gas was used during sintering experiments with flow rate of 2 L min^{-1}. After sintering, samples were allowed to cool with the furnace. To avoid additional errors in electromagnetic field distribution and temperature measurements [16], the temperature was monitored from the samples' surface using infrared pyrometer OS35-20-MA (Omega, USA) for 20–500 °C and followed by Raytek Marathon Series (working temperature range 350–2,000 °C).

X-ray diffraction measurements of the samples before and after sintering were conducted with Dron-3 diffractometer with Cu Ka radiation source. The XRD data were analyzed using Jade5 software (MDI, USA), with grain size calculated according to the Scherrer formula. Density of all samples was determined using Archimedes principle (ASTM B963-08). The microstructure of the samples was observed using a Jeol JSM-7001F field emission scanning electron microscope (SEM).

16.3 Results and Discussion

16.3.1 Densification of Green Samples

Relative densities of the samples are shown in Fig. 16.1. The initial relative density of the compacted samples was 52 % of the theoretical density, which is 5.43 g cm^{-3}. The effect of dwell time on the sintering densities at different temperatures reveals the identical tendency; within 10 min, the relative density increases rapidly upto 86–88 % for the three temperatures. That is referred in the present article as the first stage. In the first stage, densification process was fast and temperature influence was not evident for the temperature region used. Therefore, this may take place due to the large porosity of green bodies, collapse of pores, surface diffusion, etc., [17]. The effect of the grain growth was overruled, because

Fig. 16.1 Effect of sintering time on relative density of samples sintered at 1,173, 1,273 and 1,373 K, respectively
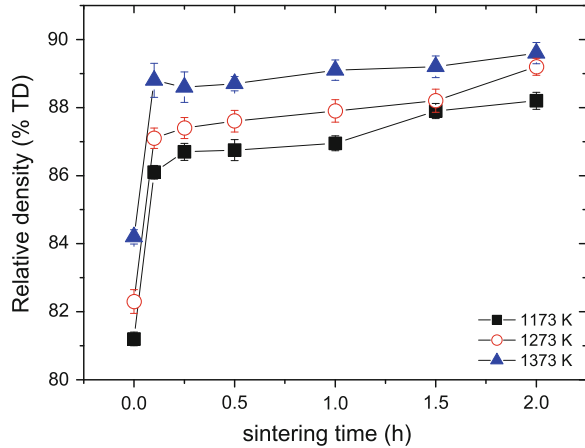
the grain size observed for the first stage is around 45 nm, which is slightly larger than that of the original crystalline size (30–40 nm).

The second stage, from 10 to 120 min, results in continuous increase of density with increasing of sintering time and temperature. However, the increase rate is much smaller than that for the first stage. The reason for this is that, unlike the first stage, the crystal growth. Sintering after 2 h did not cause evident increase in density (but yet resulted in further grain growth). There could be also an alternative explanation to this moderate increase in density for the second stage. Some previous works on pure metals, i.e., copper, showed that for microwave sintering the density of 92–95 % can be considered as critical in terms of "shielding effect" [18, 19]. As far as we did not use any external or internal susceptors during microwave sintering experiments, further densification during the second stage becomes impossible. Further increase in processing temperature to 1,250 and 1,300 °C resulted in decrease in final density to 88.6 and 88.2 %, respectively.

It is well understood that microwave energy is delivered directly to materials through molecular interaction with the electromagnetic field during the microwave irradiation. However, the electromagnetic fields decrease as the microwave passed through the material due to the absorption. The dissipation of electromagnetic energy is characterized by the loss factor (tan $\delta = \varepsilon''/\varepsilon'$, where ε' and ε'' stand for the dielectric constant and the dielectric loss factor, respectively). Also, the attenuation of the electromagnetic wave can be characterized by a penetration depth, on which the field strength is reduced by a factor of $e = 2.718...$ [19]:

$$l = \frac{c}{\omega} \sqrt{\frac{2\left[1 + \sqrt{1 + (\tan \delta)^2}\right]}{\varepsilon'(\tan \delta)^2}} \tag{16.1}$$

where c is the velocity of light, ε is the field frequency.

For metal and metallic conductor materials, the measured penetration depth of microwaves with a frequency of 2.45 GHz at a temperature of 20 °C is very small.
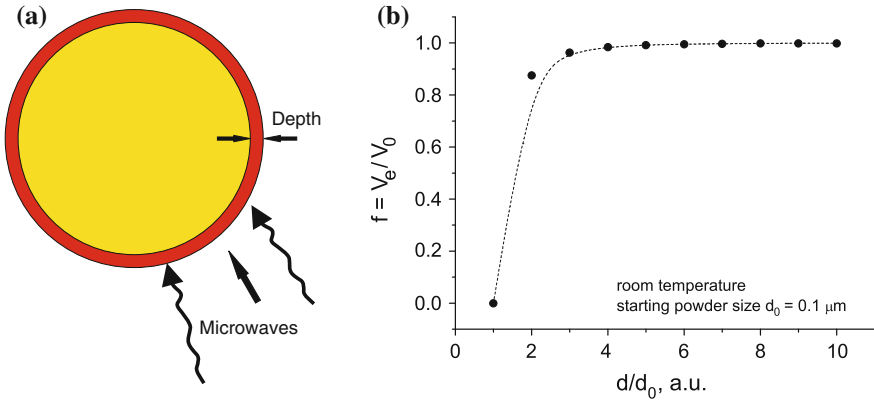
Fig. 16.2 **a** Schematic diagram of the penetration depth in a conductive powder particle. **b** Effective absorption volume in the powder particle versus increase in particle diameter

For example, the penetration depths of titanium and TiN material are 7.58 and 4.77 μm, respectively. These penetration values are too small for the materials to be prepared for products. However, the powder-metallurgical green parts have the unexpected large values. For instance, the penetration depth of TiN green part with 1 μm mean powder particle size can reach up to 7.5 cm, which is enough for fabricating a product. The powder compacts have greater penetration depth due to the effective absorption volume which commonly increases with the decreased particle size (Fig. 16.2). The effective absorption volume can be calculated with the following formula:

$$f = V_\varepsilon/V_0 = 1 - (d/d_0)^3 \tag{16.2}$$

where V_0 is the volume and d_0 is the diameter of the powder; $d = d_0 - 2l$, l is the penetration depth of the powder. Therefore, the smaller size of titanium nitride particle the green compaction has, the larger the penetration depth will be. However, the properties of powder compaction are weakened and disappeared with the densification. It means that the penetration depth decreases during the sintering processing, especially at high temperature when samples are close to the full density.

16.3.2 Grain Growth Kinetics

Figure 16.3 shows the microstructures of the samples sintered at 1,173 K for different times. Only the slight increase in grain size is apparent. Taking into account the slightly increase in density, appropriately expending the dwell time can be helpful for improving the quality of the sintered samples. Figure 16.4 shows microstructure of the samples using microwave sintering for 2 h at temperatures of

1,173 and 1,373 K, and also for the case of the conventional sintering (Fig. 16.4c) for 1,373 K. It can be seen that the average grain size increases rapidly with increasing the sintering temperature, suggesting that grain growth in the case of microwave sintering is more sensitive to temperature than dwell time. With increase in temperature (Fig. 16.4b), coarse-faced morphologies with evident size scattering are formed. In contrast, conventional sintering at 1,273 K (Fig. 16.4c) results much larger grains with more uniform size and shape.

In order to have a better understanding of the grain growth process, the analysis of grain growth kinetics was made using the grain growth equation [20]:

$$G_t^n - G_0^n = K \cdot t \qquad (16.3)$$

where

$$K = K_0 \cdot \exp\left(-\frac{Q}{RT}\right) \left[m^n s^{-1}\right] \qquad (16.4)$$

Fig. 16.3 Microstructures of the fractured sections of TiN nanocrystalline samples sintered at 1,173 K, **a** for 0.1 h, **b** 0.5 h, and **c** 1 h
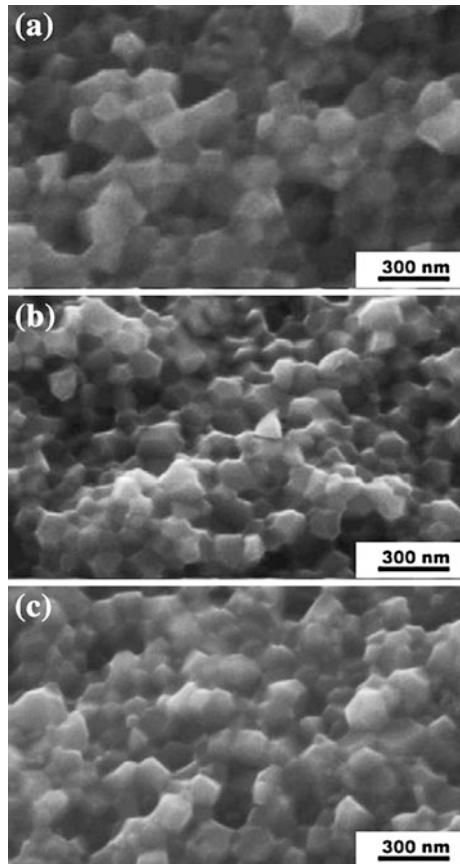
Fig. 16.4 Microstructures of
fractured sections of TiN
nanocrystalline sintered
samples for 2 h at **a** 1,173 K
with a mean grain size of
165 nm and relative density
of 88.2 % and **b** 1,373 K with
a mean grain size of 220 nm
and relative density of 89.6 %
using microwave sintering,
and **c** at 1,373 K using
conventional sintering with a
mean grain size of 335 nm
and relative density of 92 %
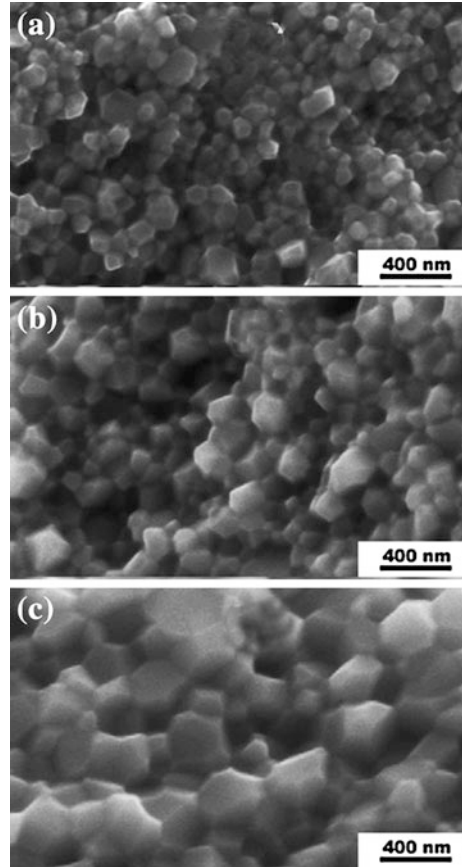
where G_t and G_0 are the grain sizes at time t and $t = 0$, respectively; n is the grain
growth exponent, K_0 is the pre-exponential constant of the diffusion coefficient,
Q is the activation energy for the grain growth, T is the absolute temperature and
R is the gas constant.

Equation 16.1 can be changed into the following form:

$$\log (G_t - G_0) = \frac{1}{n}\log t + \frac{1}{n}\left(\log K_0 - \frac{Q}{RT}\right) \qquad (16.5)$$

Thus from the slope of the line of log G versus log t, which is $1/n$, grain growth
kinetic exponent (n) is readily determined. Figure 16.5 illustrates the results for the
samples sintered at 1,173, 1,173, and 1,373 K for the microwave sintering and for
conventional sintering at 1,373 K. From the slopes of the lines, the grain growth
kinetic exponents, n, are 2.25, 2.1, and 2.05 for 1,173, 1,273, and 1,373 K,
respectively. Interestingly, in case of conventional sintering grain growth exponent
of 3.1 is determined for temperatures in the range 1,273–1,473 K. That should

correspond to the grain growth by volume (bulk) diffusion mechanism. In case of microwave sintering n suggests that grain growth by grain-boundary diffusion dominates ($n = 2$). The slight increase in grain growth exponent for the lower temperatures can be explained by the contribution of the surface diffusion, which does not contribute to the densification or grain growth [20, 21]. Alternatively, the slight contribution of volume diffusion is also possible. The shift in grain growth exponent value can be also explained difference between micro- and nanocrystalline materials [20]. However, this effect should influence both microwave and conventional sintering case. Importantly, for the coarse titanium nitride the grain growth by grain-boundary and volume diffusion was previously identified [22].

The grain size data obtained were analyzed according Eq. (16.4), using $n = 2$ and $n = 3$ for microwave and conventional sintering, respectively. Resulted Arrhenius plots are shown in Fig. 16.6. The data exhibited the high degree of fit to two lines ($R^2 = 0.9916$ for $n = 2$ and $R^2 = 0.98557$ for $n = 3$) and the corresponding activation energies derived from the line slopes were 230 ± 6 and 390 ± 26 kJ mol^{-1} for $n = 2$ and 3, respectively. Which in case of $n = 2$ is in good agreement with data obtained previously on grain growth of pure titanium nitride by mechanism of grain-boundary diffusion 230 kJ mol^{-1} [22]. In case of conventional sintering and $n = 3$ that is in reasonable agreement with the range (480 kJ mol^{-1}) reported for sintering of TiN in nitrogen [1] but differs by 1/3 from that for microwave sintering. Based on the volume self-diffusion value of 528 kJ mol^{-1} reported by Anglezio-Abautret et al. [23], the present value is suggestive of volume diffusion.

The decrease in activation energies of the sintering process during microwave-assisted sintering was reported previously for all stages of the sintering process, including grain growth [13, 24–28]. In the present case, we believe that the difference in activation energy can be solely explained by the difference in grain growth mechanisms. The origin of this difference in grain growth mechanisms could have pure microwave effect [26], but requires validation for other high-melting point compounds, and is considered as the next step in forthcoming

Fig. 16.5 Grain size versus time t for growth of nanocrystalline TiN sintered at three different temperatures by microwave sintering and for 1,373 in case of the conventional sintering
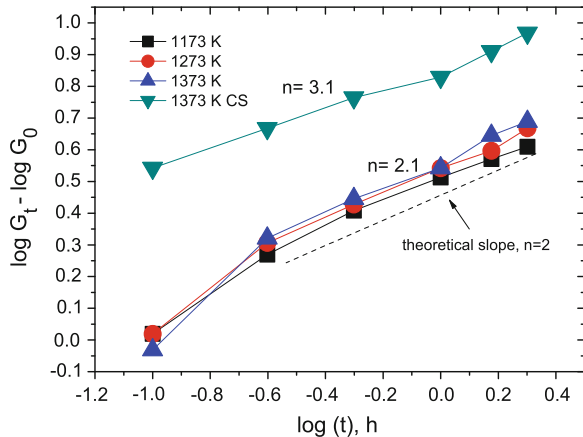
Fig. 16.6 Plot of log
K versus 1/*T* for growth of
nanocrystalline TiN
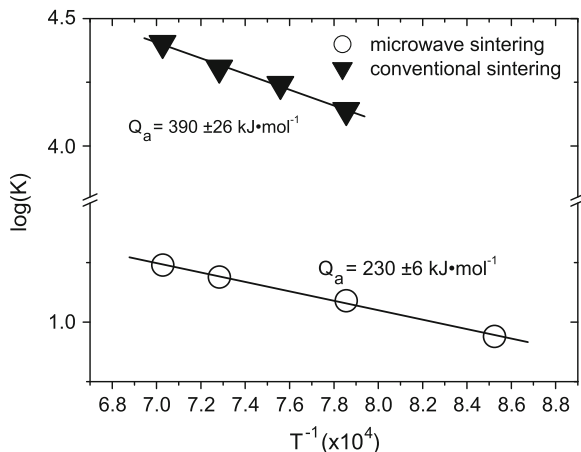
research. Taking into consideration high degree of fit, the grain growth by mechanism of grain-boundary diffusion seems to be active during intermediate stage of microwave sintering and resulting in moderate grain growth factor of 4.2–4.8.

16.4 Conclusions

Sintering behavior of nanocrystalline titanium nitride powder with a mean crystalline size of 30–40 nm was investigated using microwave-assisted sintering. The densification process during microwave sintered happened into two stages, with significant densification took place during the first one. That is followed with the slight increase in density and significant grain growth. In case of microwave sintering of TiN from 1,173 to 1,373 K, the grain growth exponent of 2.1 and the apparent activation energy for the grain growth is 230 ± 6 kJ mol^{-1} were obtained. The latter is suggestive of grain growth by grain-boundary diffusion mechanism. In contrast, conventional sintering resulted in much coarser grains, with grain growth exponent of 3 and activation energy of 390 kJ mol^{-1}.

References

1. Kuzenkova MA, Kislyi PS (1971) Vacuum sintering of titanium nitride. Powder Metall Met Ceram 10:125–128
2. Hosokawa M, Nogi K, Naito M, Yokoyama T (eds) (2007) Nanoparticle technology handbook. Elsevier, Amsterdam

3. Troitskii VN, Rakhmatullina AZ, Berestenko VI, Gurov SV (1983) Initial sintering temperature of ultrafine powders. Powder Metall Met Ceram 22:12–14

4. Ragulya AV (2008) Consolidation of ceramic nanopowders. Adv Appl Ceram 107:118–134

5. Themelin L, Desmaison-Brut M, Boncoeur M, Valin F (1988) Microstructure, mechanical properties and oxidation behaviour of hot-isostatic-pressed titanium nitride. L'Industrie Ceramique 828:426–433

6. Groza JR, Curtis JD, Kramer M (2000) Field-assisted sintering of nanocrystalline titanium nitride. J Am Ceram Soc 83:1281–1283

7. Sherif El-Sekandarany M, Omori M, Konno TJ, Sumiyama K, Hirai T, Suzuki K (1998) Syntheses of full-density nanocrystalline titanium nitride compacts by plasma-activated sintering of mechanically reacted powder. Metall Mater Trans A 29(7):1973–1981

8. Vaidhyanathan B, Agrawal DK, Roy R (2000) Novel synthesis of nitride powders by microwave-assisted combustion. J Mater Res 15:974–981

9. Venkateswarlu K, Saurabh S, Rajinikanth V, Sahu RK, Ray AK (2010) Synthesis of TiN reinforced aluminium metal matrix composites through microwave sintering. J Mater Eng Perform 19:231–236

10. Matsumoto T, Makino Y, Miyake S (2011) Synthesis of titanium-chromium nitride composites by millimeter-wave sintering. J Mater Sci 36:693–698

11. Agrawal DK (1998) Microwave processing of ceramics. Curr Opin Solid State Mater Sci 3:480–485

12. Binner J, Annapoorani K, Paul A, Santacruz I, Vaidhyanathan B (2008) Dense nanostructured zirconia by two stage conventional/hybrid microwave sintering. J Eur Ceram Soc 28:973–977

13. Janney MA, Kimrey HD (1990) Microstructure evolution in microwave-sintered alumina. In: Bieninger J, Handwerker C (eds) Advances in sintering. American Ceramic Society, Westerville

14. Nightingale SA, Worner HK, Dunne DP (1997) Microstructural development during the microwave sintering of yttria-zirconia ceramics. J Am Ceram Soc 80:394–400

15. Xu G, Lloyd IK, Carmel Y, Olorunyolemi T, Wilson OC Jr (2001) Microwave sintering of ZnO at ultra high heating rates. J Mater Res 16:2850–2858

16. Pert E, Carmel Y, Birnboim A, Olorunyolemi T, Gershon D, Calame J, Lloyd IK, Wilson OC (2001) Temperature measurements during microwave processing: the significance of thermocouple effects. J Am Ceram Soc 84:1981–1986

17. Ragulya AV, Skorokhod VV (2007) Consolidated nanostructured materials. Naukova Dumka, Kiev [in Russian]

18. Fang Y, Agrawal DK, Roy R (2003) Microwave sintering of nano-phase MgO, TiO2, and Cu metal powders. In: proceeding sintering, Penn State University, Pennsylvania, 15–17 Sep 2003

19. Gupta M, Leong W (2007) Microwaves and metals. Wiley, New York

20. Chaim R, Shlayer A, Estournes C (2009) Densification of nanocrystalline Y_2O_3 ceramic powder by spark plasma sintering. J Eur Ceram Soc 29:91–98

21. Averback RS, Hofler HJ, Hahn H, Logas JC (1992) Sintering and grain growth in nanocrystalline ceramics. Nanostruct Mater 1:173–178

22. Kuzenkova MA, Kislyi PS (1970) Sintering of titanium nitride in nitrogen. Powder Metall Ceram 9:379–382

23. Anglezio-Abautret F, Pellissier B, Miloche M, Eveno P (1991) Nitrogen self-diffusion in titanium nitride single crystals and polycrystals. J Eur Ceram Soc 8:299–304

24. Demirskyi D, Ragulya A (2012) Low-temperature microwave sintering of TiN–SiC nanocomposites. J Mater Sci 47:3741–3745

25. Vasylkiv O, Demirskyi D, Sakka Y, Ragulya A, Borodianska H (2012) Densification kinetics of nanocrystalline zirconia powder using microwave and spark plasma sintering—a comparative study. J Nanosci Nanotechnol 12(6):4577–4582

26. Janney MA, Kimrey HD, Schmidt MA, Kiggans J (1991) Grain growth in microwave-annealed alumina. J Am Ceram Soc 74:1675–1681
27. Demirskyi D, Ragulya A, Agrawal D (2011) Initial stage sintering of binderless tungsten carbide powder under microwave radiation. Ceram Int 37:505–512
28. Demirskyi D, Agrawal D, Ragulya A (2010) Densification kinetics of powdered copper under single-mode and multimode microwave sintering. Mater Lett 64:1433–1436

Chapter 17
Luminescent Imaging of Biological Molecules and Cells on the Photonic Crystal Surface

**V. V. Boiko, O. M. Fesenko, V. F. Gorchev, S. O. Karakhim,
L. Dolgov, V. Kiisk, I. Sildos, V. S. Gorelik and G. I. Dovbeshko**

17.1 Introduction

Contrast imaging of biological cells and tissues is an important part of vital medical and biological analyses. Optical transparency restricts microscopic imaging of cells. Various dyes, quantum dots, and metal nanoparticles can be used as luminescent labels [1] for improvement of visualization. This approach allows to judge the necessary molecules by distribution and brightness of markers attached to them. Coloration or imparting fluorescent properties can be realized, particularly, by means of 4',6-diamidino-2-phenylindole (DAPI) label applied for cell nuclei or DNA complexes. Marking of proteins including their cytoskeleton is possible, for example, by means of the green fluorescent protein (GFP) [2].

At the same time, the popularity of label-free methods has grown recently. Particularly, an enhancement of optical signals can be achieved if the analyte is deposited on the photonic structures. As a rule, structures in the form of multi-layered dielectric films are used for the coupling of light reflected from the analyte with waveguide or leaky modes [3]. Here, we propose a three-dimensional photonic structure for the label-free imaging of DNA molecules. Earlier, [4] we revealed that photoluminescence of DNA can be essentially enhanced if this

V. V. Boiko (✉) · O. M. Fesenko · G. I. Dovbeshko
Department of Physics of Biological Systems, Institute of Physics, National Academic
of Science of Ukraine, Prospect Nauki, 46 03680 Kyiv, Ukraine
e-mail: vb@iop.kiev.ua

V. F. Gorchev · S. O. Karakhim
O.V.Palladin Institute of Biochemistry, National Academic of Science of Ukraine,
Leontovicha street, 9 01601 Kyiv, Ukraine

L. Dolgov · V. Kiisk · I. Sildos
Institute of Physics, University of Tartu, Riia 142 51014 Tartu, Estonia

V. S. Gorelik
P.N. Lebedev Physical Institute of the Russian Academy of Sciences, Leninsky Prospect,
53 117924 Moscow, Russia

organic molecule is deposited on the photonic surface or confined inside synthetic opal . Here, we combine methods of confocal optical microscopy with analysis of optical spectra and fluorescent kinetics to specify the range of optical phenomena, which can be responsible for improved imaging of organic molecules on the opal surface.

17.2 Experimental Equipment

The experiments were done on a confocal laser scanning microscope Carl Zeiss LSM 510 META with a Plan Neofluar 10x/0.3 Korr and 40x/0.6 Korr objectives. The application of a confocal setup gives rise to the image contrast enhancement, because a small-size apperture is applied so that the "extraneous" light emitted by the neighbor points of the analyzed object does not arrive at a detector. The "cost" of a contrast enhancement is the necessity to use rather complicated schemes for the scanning of a specimen or light beam, which increases the time required to obtain complete information about the examined object.

We used different lasers with wavelengths of 405, 488, 543, and 633 nm to obtain images with this microscope. Fluorescence images were registered by using Zeiss AxioCam digital camera. PL excitation was carried out with the use of an ultraviolet lamp HBO 100 and by applying blue (FSet01 wf), green (Fset10 wf), and red (Fset20 wf) filters. Images in the visible range and in the "transmission" geometry were obtained using a halogen lamp. The scanning rate depends on the resolution, so it was equal to 1/5 s per layer for the microscope LCM-510 at a resolution of 512×512. The maximum resolution was 1048×1048 [5].

According to the Rayleigh criterion for the resolution limit (an intensity reduction by 26 % from its maximum value) in the case of a confocal microscope, $r_{conf} = 0.44 \frac{\lambda}{n \cdot \sin \theta} = 0.88 \frac{\lambda'}{D} F$, where $\lambda' = \lambda/n$. At the same time, for a conventional optical microscope, $r_{resel} = 0.61 \frac{\lambda}{n \cdot \sin \theta} = 1.22 \frac{\lambda'}{D} F$. The resolution of a confocal microscope is only 1.4 times better than that of an optical one [6]. Therefore, the main advantage of a confocal microscope is not an increase in the resolution, but a substantial increase in the contrast when the image is formed.

To estimate the photoluminescence (PL) spectral density, we scanned the sample over its surface in the "Lambda scan" mode, which allowed the PL spectrum to be registered with the use of a line of tiny photodetectors with a spectral resolution of 10.7 nm. For the quantitative analysis, we used the Region of interest (ROI) feature, which enabled us to obtain the plot of the PL intensity versus the wavelength, with the dependence being averaged over the selected region.

Fluorescent spectra of the samples were measured by means of Horiba Jobin–Yvon FluoroMax-4P spectrofluorometer using 150 W xenon sources. All spectra were automatically corrected to the instrumental response.

For the measurement of fluorescence decay kinetics, the samples were excited by 5 ns pulses from tunable Ekspla NT340 optical parametric oscillator at the repetition rate of 20 Hz. The fluorescence signal from the sample was detected by Hamamatsu photomultipliers. In the case of nanosecond kinetics, the photomultiplier current was first recorded with a Tektronix digital oscilloscope and then deconvoluted against the reference laser pulse recorded under similar conditions. In the case of microsecond kinetics, the single-photon pulses from photomultiplier were counted by using the FAST ComTec multichannel analyzer P7882.

17.3 Preparation of Samples

The samples of synthetic opal were produced by using the method of natural globule sedimentation, by evaporating the reaction mixture at a given rate. The modified Stober method [7] was applied for synthesis of silicon dioxide globules. The molar ratio of components in the reaction mixture was as follows: $NH_4OH:H_2O:C_2H_5OH:Si(OC_2H_5)_4 = 0:76:18:11:0.14$. To remove chemically bound water and the remnants of organic compounds, obtained crystals were annealed at a temperature of 800 °C.

DNA (Lando, Belarus) [8, 9] was dissolved in aqueous solution (pH 6.5) on cool bath under room temperature up to 1 mg/ml concentration, divided in 10 aliquots and put in refrigerator. This DNA contains less than 0.2 % proteins. For DNA staining, bisBenzimide H33342 trihydrochloride (Hoechst 33342) (Sigma) was applied [10]. Then, we took an aliquot quantity of a DNA solution and dropped it on opal, the same we did with DNA aliquot mixed with fluorescent label.

17.4 Results and Discussion

First, the luminescent properties of photonic crystal (PC) were studied with the confocal microscopy. It is known that opal has a domain structure of 20–250 μm in size with iridescent property. We obtained images of PC domains in luminescent mode under excitation of 365 nm from mercury lamp (Fig. 17.1). As usually, the imaging of domains in Fig. 17.1a has not enough contrast similarly as in Ref. [11]. It could be improved by infiltration of small amount of colloidal gold (10 μl with concentration 40 mg/l) that give a possibility to detect fine details on the surface of PC (Fig. 17.1b).

Visualization of the opal surface is caused by luminescent properties of silica. Usually, luminescent bands of silica situated in wide region starting from 350 to 700 nm [12–14]. Optimal wavelengths for excitation of photonic crystals can be selected from the luminescence emission excitation matrix (Fig. 17.2). The initial PC demonstrates PL with two intensive maxima at about 400 and 500 nm, and
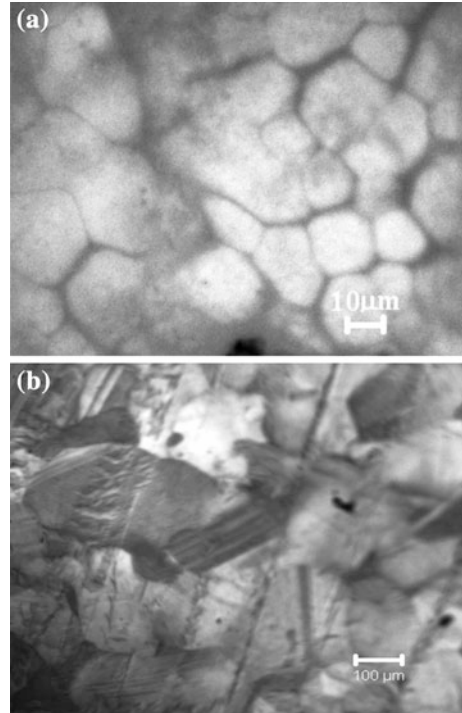
several weak bands in the interval of 600–700 nm. PL of synthetic opal is connected with the presence of defects and impurities. The band with a maximum at a wavelength near 520 nm is related to the surface states of Si-H (2.37 eV), whereas, the band with maxima at 652 and 692 nm to the bulk and surface states Si-O (1.9 and 1.79 eV, respectively) [4]. The nature of the band at about 400 nm was discussed in [13]. According to [13] this band is associated with the presence of various impurities such as zinc, calcium, sodium, iron, and zirconium oxides, which get into the specimens in the course of crystal fabrication. The fraction of these impurities is less than 10^{-5}. The PL intensity for the initial synthetic opal changed from point to point under the scanning over its surface [11]. For the PC with a well-ordered structure, the variation of PL intensity over the surface was observed with an identical coefficient for various frequencies. For the PC with a less-ordered structure, the luminescence intensity changed differently at different frequencies. Such a dependence of the synthetic opal luminescence intensity on the surface site can be connected with the inhomogeneity of the opal surface, the presence of a domain structure, the variation in the spectral position of the energy gap, and the nonuniform distribution of impurities. Since the size of domains in PCs is comparable with the wavelength of light in the visible range, one may expect a local increase of the electromagnetic field for the impurity-induced PL, so that a signal even from a very small number of impurities could be registered. The energy gap of PC reveals itself in a luminescence band; namely, a dip has to be
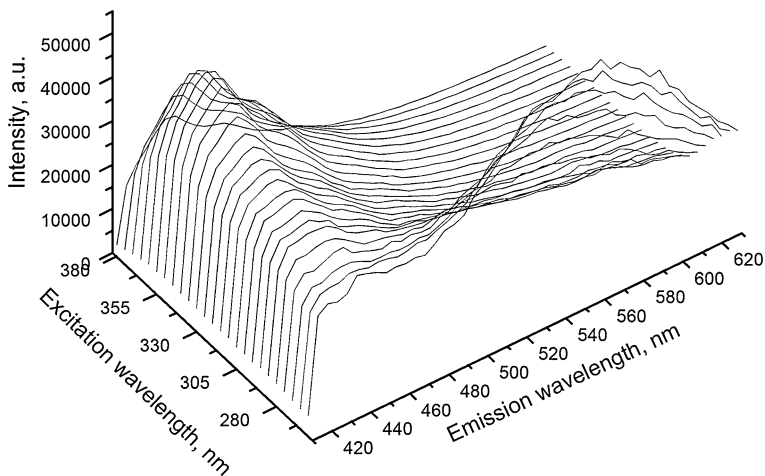
Fig. 17.2 Luminescence emission excitation matrix detected for the photonic crystal at the excitation region 260–380 nm and emission region 410–630 nm

observed in the luminescence band in the spectral region, where the PC energy gap is located [13]. For the studied crystals with a globule size of 240 nm, the Bragg reflection should take place at about 530 nm. In accordance with that, a dip was registered in the corresponding region of the opal PL spectra [13].

The most efficient excitation wavelengths λ_{exc} lies in 310–370 nm range for the blue luminescent band of silica and in 240–270 nm range for the greenish-red band (Fig. 17.2). Therefore we selected $\lambda_{exc} = 250$ nm and $\lambda_{exc} = 350$ nm excitations and applied them for measurement of fluorescent kinetics from photonic crystals. The fluorescent kinetics was measured also for amorphous quartz plates as a reference data.

The recorded fluorescence decay kinetics were not monoexponential generally. Therefore, for each emission wavelength we obtained several decay times, which can be associated with different types of defect centers in the samples (Table 17.1).

One can see that reference amorphous quartz sample has long decay time components of several tens or even one hundred microseconds, which are bigger, than microsecond times obtained from the photonic crystal samples. Photonic structure causes localization of optical modes. So, photonic arrangement of silica globules can be the reason for increase of radiation probability or acceleration of microsecond emission.

Spectra of PL were obtained from 2 points of a luminescene region on the surface of pure and doped by DNA synthetic opal in the Lambda Scan mode and got difference spectra between opal and opal with DNA (Fig. 17.3). Photoluminescence was excited with a laser at a wavelength of 405 nm and registered in the range of 422–754 nm by using beamsplitter 405/488. Difference spectrum demonstrates the increase of fluorescence for the DNA-doped opal in the region

Table 17.1 Lifetimes of fluorescence for photonic crystals

Sample	λ_{exc} nm	λ_{em} nm	Nanosecond time components
Photonic crystal 1	250	450	6 ns
	250	600	6 ns
	350	450	1 ns, 7 ns
	350	600	1 ns, 7 ns
Photonic crystal 2	350	450	4 ns, 20 ns
	250	550	6 ns
Amorphous quartz	250	450	6 ns
			Microsecond time components
Photonic crystal 1	250	450	0.49 µs, 12.1 µs
	250	550	0.44 µs, 26.1 µs
Photonic crystal 2	250	450	29.9 µs
Photonic crystal 2	250	550	42.5 µs
Amorphous quartz	250	450	15.1 µs, 104 µs
	250	650	14.4 µs, 48.6 µs

Fig. 17.3 Difference spectrum of fluorescence obtained from neat and infiltrated by DNA regions on the opal surface. Excitation wavelength is 405 nm, ChS filter: 422–754 nm
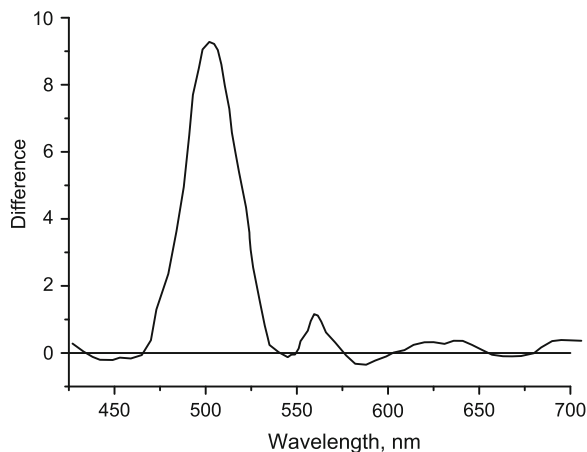
470–520 nm. This region coincides with triplet states in DNA excited in the system DNA opal near the stop zone of opal.

To confirm that the enhanced emission in the range 470–520 nm is caused by DNA, we additionally labeled it by Hoechst 33342 stain (Fig. 17.4). Figure 17.4b and d are the enlarged areas taken from Fig. 17.4a and c, correspondingly. Character of imaging for the unmarked and marked DNA is similar. Therefore, we can conclude that we registered namely DNA, but not some other extraneous admixtures. The same visualization of unmarked DNA by infiltration into photonic crystal is described in our early papers [4, 11]. There we got imaging of big amount of DNA and DNA clusters on the surface of PC. This amount of DNA was registered with FTIR spectroscopy [4]. Here we visualized much smaller amount
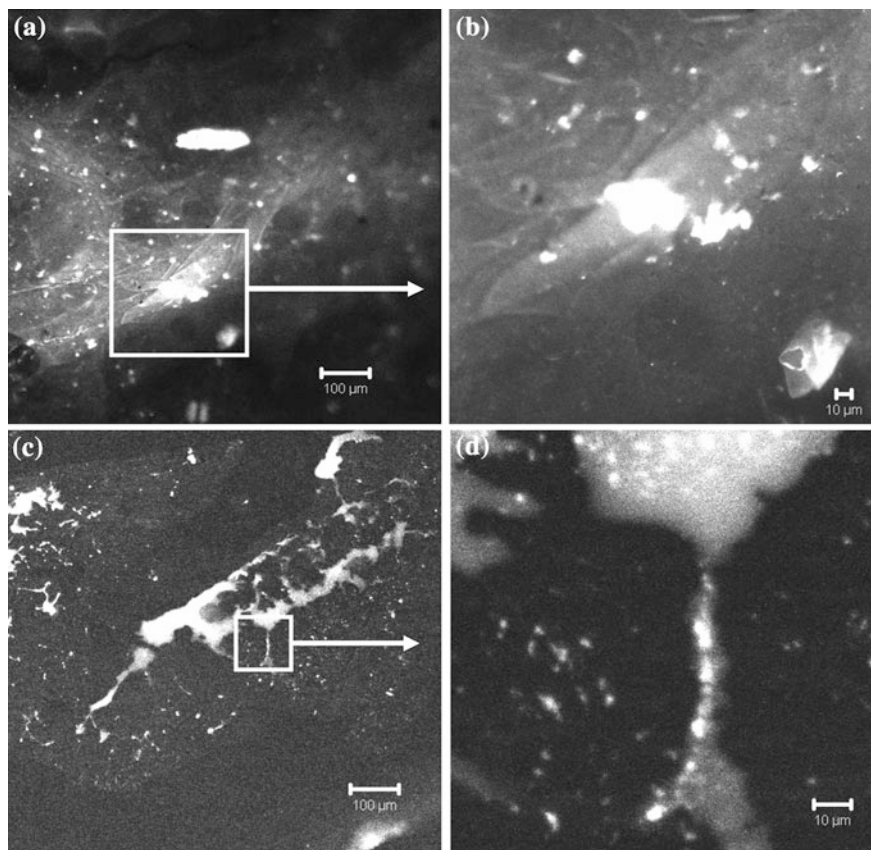
Fig. 17.4   Image of the synthetic opal surface infiltrated by DNA (**a**, **b**) and additionally stained by Hoechst 33342 (**c**, **d**). Excitation is 405 nm

of DNA (10 microliters of 1 mg/ml) dropped on the PC surface without additional staining. This amount of DNA on the surface of PC could not be registered with FTIR spectroscopy. Protein contamination of DNA used in this paper is 0.2 %, which is much less than 3 % used in our previous experiments [4, 11]. This gives us an additional proof that detected emission is caused by DNA, but not by protein part.

Enhancement of DNA fluorescence can be caused by several reasons. First, at the surface of PC, an incident electromagnetic field could be enhanced and localized due to multiple scattering by PC [15]. This effect for photons is similar to the well-known 'Anderson localization' for electrons [16]. In this case, an efficiency of light-photonic crystal interaction increases in many times as a result of intensive light scattering in strongly inhomogeneous medium.
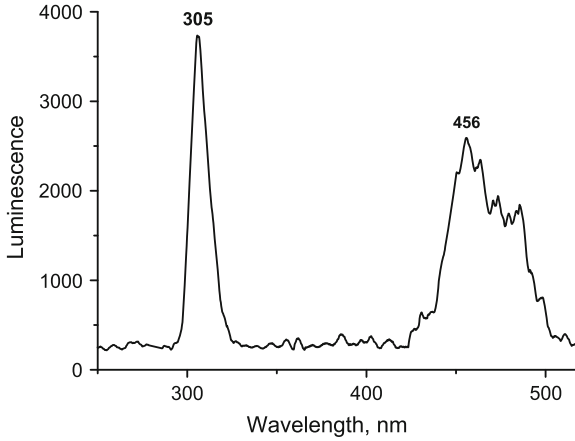
Fig. 17.5 Fluorescence spectra of water solution of DNA (from Lando [8, 9]), concentration 1 mg/ml excited by the fourth harmonics of Nd: YAG laser with 266 nm
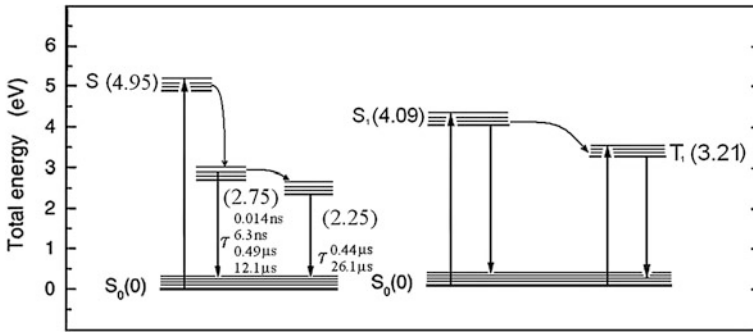
Fig. 17.6 Energy levels and scheme of defects of synthetic opal (*left*, our data) and DNA (*right*) [17]

Other reason could be connected with phonon processes in PC and DNA as well strong interaction between phonons and photons. Incident light excites numerous defect states in PC leading to luminescence and then irradiated light could cause reabsorption, emission, and scattering.

After infiltration of DNA in PC surface, the DNA is located inside and on the PC surface and more strong interaction between light and DNA on the PC occur and lead to the appearance of DNA luminescence. For comparison, we present the DNA luminescence under excitation of fourth harmonic of laser Nd:YAG with 266 nm. Due to high concentration of light in small frequency region of negligible average power density (10 mW), we obtained DNA luminescence under room temperature (Fig. 17.5) and increased the efficiency of process about 10^4 time and obtained two bands (305 and 456 nm). We suppose that the same mechanism (light localization) works in the case of appearance of DNA luminescence in PC.

Here we present state energy levels and scheme (Fig. 17.6) of PC defects and DNA luminescent states. They are located close to one another and in the case of close distance in real systems they could influence the process in both systems via photon–phonon interaction or other mechanisms.

So, we observe that the PC has luminescence in wide time region starting from tens of picoseconds to milliseconds or wider. DNA has lifetime of different states in wide region also. So, in this case, DNA and PC could exchange their energy or transfer energy from one to another. More detailed investigation of energy transfer processes will be realized in our next work by comparison of fluorescent kinetics for undoped and DNA-doped photonic crystals.

17.5 Conclusions

Imaging of unmarked DNA infiltrated into the silica photonic crystal at room temperature is achieved. Improved imaging of DNA could be connected with its enhanced fluorescence mediated by photonic crystal in the range 470–520 nm. Localization of light in photonic crystal can cause decrease of microsecond lifetimes in case of undoped opal in comparison with bulk amorphous silica and assist improved imaging of DNA.

References

1. Pawley JB (ed) (2006) Handbook of biological confocal microscopy. Springer, Berlin
2. Selivanov EV (2003) Stains in biology and medicine. Handbook (in Russian), Azbuka, Barnaul
3. Ganesh N, Mathias P, Zhang W, Chow E, Malyarchuk V, Cunningham B (2008) Leaky-mode assisted fluorescence extraction: application to fluorescence enhancement biosensors. Opt Express 16(26):21626
4. Boyko V, Dovbeshko G, Fesenko O, Gorelik V, Moiseyenko V, Romanyuk V, Shvets T, Vodolazkyy P (2011) New optical properties of synthetic opals infiltrated by DNA. Mol Cyst Liq Cryst 535:30
5. Paddock S (ed) (1998) Confocal microscopy methods and protocols. Humana Press, Newcastle
6. Webb RH (1996) Confocal optical microscopy Rep Prog Phys 59, 427
7. Stober W, Fink A, Bohn E (1968) Controlled growth of monodisperse silica spheres in the micron size range. J Coll Interf Sci 26:62
8. Lando D, Egorova VP, Krot VI, Akhrem AA (1996) Determination of protein admixture in highly purified DNA preparations. Mol Biol 30(3):418–421
9. Akhrem AA, Egorova VP, Egorov AS, Krot VI, Lando DY, Luka ZA (1989) Biopolymers and Cell, 5(5), 44

10. Sigma—ALDRICH, Data sheet, http://www.sigmaaldrich.com/catalog/product/sigma/14533
11. Dovbeshko GI, Fesenko OM, Moiseenko VN et al. (2012) Novel photoluminescence-enhancing substrates for image formation of biological objects. Ukr J Phys 57(7):732
12. Glinka YD, Lin S-H, Chen YT. Appl Phys Lett 75(6):778
13. Gruzintsev AN, Emel'chenko GA, Masalov VM, Yakimov EE (2009) Neorgan Mater 45:302
14. Dovbeshko GI, Fesenko OM, Boyko VV, Romanyuk VR, Gorelik VS, Moiseyenko VN, Sobolev VB, Shvalagin VV (2012) Secondary emission from synthetic opal infiltrated by colloidal gold and glycine. Ukr J Phys 57(2):154
15. Sajeev J (1987) Phys Rev Let, 58(23):2486
16. Osminkina LA et al. (2012) Optical properties of silicon nanowire arrays formed by metal-assisted chemical etching: evidences for light localization effect. Nanoscale Res Lett, 7:524
17. Yashchuk VM, Kudrya VY, Levchenko SM, Yevtushenko NV (2007) Scientific Notes (in Russian) 61:39

Chapter 18
Peculiarities of Liquid Crystal—Carbon Nanotube Dispersions Doped with a Minute Amount of Nanoparticles of Synthetic Clay

S. Tomylko, O. Yaroshchuk, O. Kovalchuk and N. Lebovka

Abstract It is shown that adding of a small amount (0.1 wt %) of organomodified laponite (LapO) nanoplatelets results in drastic changes in dielectric and electro-optical characteristics of the suspensions of carbon nanotubes (CNTs) in nematic liquid crystal E7. The addition of LapO leads to the absence of classical percolation of conductivity and dielectric constant, as well as reduction of Frederiks threshold and significant growth of contrast ratio of the E7-CNTs samples.

18.1 Introduction

Among the many nanoparticles used as fillers of liquid crystals (LC), carbon nanotubes (CNTs) are of particular interest. These particles, which can be considered as rolled graphene nanolayers are characterized by enormous value of length to diameter ratio (aspect ratio), which can be as high as several thousands. They exhibit extraordinary mechanical strength, highly anisotropic electrical and thermal properties.

Because of high aspect ratio and strong interaction with LC molecules ($E_{LC\text{-}CNT} \sim 2$ eV), CNTs well integrate in LC [1–3]. They bring new properties to LC hosts and allow one drastically reducing the intrinsic drawbacks of these materials that appear when using them in displays and other electro-optic devices.

S. Tomylko (✉) · O. Yaroshchuk · O. Kovalchuk
Institute of Physics, NASU, Prospekt Nauky 46, 03028 Kyiv, Ukraine
e-mail: tomulkosv@ukr.net

O. Kovalchuk
Kyiv National University of Technologies and Design, Nemirovich-Danchenko St. 2, 01011 Kyiv, Ukraine

N. Lebovka
Institute of Biocolloidal Chemistry, NASU, Vernads'koho Boulevard 42, 03142 Kyiv, Ukraine

Furthermore, introduction of CNTs may result in untypical responses of LC layers such as effect of electro-optical memory in the nematic [3–5] and isotropic [6] phase. On the other hand, LC is a unique host for CNTs allowing ones to obtain orientationally ordered ensembles of CNTs with readily controllable ordering axis.

The properties of LC-CNT composites strongly depend on structural organization of nanotubes. It is well known that CNTs tend to aggregate forming developed aggregates and even continuous network at higher concentration. Efficiency of this process can be affected by many factors. The most known of them is surface modification of CNT. In this study, we extend to the LC-CNT suspensions a more peculiar approach, known for more than a decade for dispersions [7]. This approach is that the particles of other sort and properties are brought in a studied composite.

As the additional particles we use the nanoplatelets of clay, which are proven to have high affinity to CNTs and well exfoliate in LCs. As those, we earlier utilized organically modified particles of natural clays (Montmorillonite (MMT)) [8]. However, the results appeared quite ambiguous and highly dependent on origin of clay minerals. In the present research, we apply a synthetic clay Laponite (Lap) mainly because of two reasons. First, the synthetic particles have identical chemical content and structure, which are well controlled in the course of synthesis. Second, the size of Lap platelets is much smaller than the size of MMT platelets (~ 10 nm versus ~ 10 μm), so they naturally belong to the category of nanoparticles. We demonstrate that addition of small amount of Lap cardinally changes dielectric and electro-optic properties of LC-CNT composites opening new horizons for application of these composites.

18.2 Experimental Section

18.2.1 Materials

We used a nematic LC E7 from Merck, which is the eutectic mixture of three cyanobiphenyl and one cyanotriphenyl compound. The temperature of its nematic-to-isotropic transition is 58 °C. At room temperature, the dielectric constants of this mixture in the directions parallel and perpendicular to the LC director are $\varepsilon_{//} = 19$ and $\varepsilon_{\perp} = 5.2$, respectively. As CNTs, we utilized the multi-walled carbon nanotubes from Spetsmash Ltd. (Kyiv, Ukraine), produced from ethylene by the chemical vapor deposition method [9]. These CNTs had an outer diameter 20–40 nm, and the length 5-10 μm. The specific electric conductivity σ of the powder of the compressed CNTs was about 10 S/cm.

The clay was Laponite from Rockwood Additives Ltd., UK Its formula is $Na_{0.7}$ $[(Si_8Mg_{5.5}Li_{0.4}) O_{20} (OH)_4]$. It is a powder, in which the disc-like nanoplates of the clay are packed into stacks. The thickness and diameter of these discs are about 1 nm and 25–30 nm, respectively. The faces of disks have a constant negative

charge, while the surface charge of their edges is pH-dependent and positive in acidic medium [10]. As described elsewhere [11], the platelets of original Laponite were modified by ion-exchange reactions with the surfactant cetyltrimethylammonium bromide (CTAB, $C_{16}H_{33}$-N(CH_3)$_3$Br, Fluka, Germany) with 99.5 % purity. The resultant material will be further called as the organomodified Laponite (LapO).

18.2.2 Samples

LCs filled by multi-walled CNTs, LapO, or their hybrid mixtures, were obtained by adding appropriate weights of the CNTs (c = 0.025–0.5 wt %) and LapO (0.1 wt %) to E7 at T = 60 °C with subsequent 10 min sonication of the mixture using an ultrasonic disperser at the frequency of 22 kHz. Then suspensions were kept at room temperature for 24 h, sonicated for 2 min and then loaded by capillary forces into the cells.

The cells for electro-optical and dielectric measurements were made from glass substrates, containing patterned ITO electrodes and aligning layers of polyimide AL3046 (JSR, Japan) for planar alignment. The polyimide layers were obtained by spin coating technique backed at 180 °C for 90 min and rubbed by a fleecy cloth in order to provide a uniform planar alignment of LC in the field-off state. The cells were assembled so that the rubbing directions of the opposite aligning layers were antiparallel or perpendicular, thus the antiparallel or twisted cells were obtained. The antiparallel cells were further used in dielectric studies, while the twisted cells were used for electro-optic measurements. The cell gap d was maintained by 20 μm glass spacers.

18.2.3 Methods

The dielectric studies were conducted by oscilloscopic method [12]. The experimentally measured values of the resistance R and capacitance C of the LC cells were used for calculation of dielectric constants ε' and ε'', respectively. The constants ε' and ε'' were determined in a wide frequency range, $f = 10^{-1}-10^6$ Hz, allowing one to plot dielectric spectra of the samples. The value of ε'' was further used for calculation of the sample conductivity σ from the formula $\sigma = 2\pi\varepsilon_0 \varepsilon''f$. Furthermore, the Cole–Cole diagrams $\varepsilon''(\varepsilon')$ were plotted to determine the width of the near-electrode dielectric layers λ and the time τ of the near-electrode relaxation [13].

The electro-optical measurements were carried out using setup described in [14]. In these experiments, the transmittance of the twist cells, T, placed between two parallel polarizers, was measured as a function of the applied AC voltage U ($f = 2$ kHz) ramped up from 0 to 30 V. The cells were operated in a waveguide

regime (the Mauguin's regime) [15], so that polarization of the testing light followed the LC director, which experienced rotation in 90°. The electro-optic contrast CR was calculated on the basis of $T(U)$ curve, according to formula $CR = T_s/T_0$, where T_0 and T_s are the transmittance values in the initial and saturated states, respectively. Also, the threshold voltage of electric switching (Frederiks's threshold) was estimated as the voltage corresponding to the transmittance value $T_0 + 0.1(T_s–T_0)$.

18.3 Results and Discussion

18.3.1 Dielectric Properties

The typical dielectric spectra, i.e., frequency dependences of the real ε' and imaginary ε'' parts of dielectric constant ε, are presented in Fig. 18.1 for pure LC, LC-CNT, and LC-CNT-LapO samples at 20 °C. The measured frequency range is divided into three areas. The low-frequency area A ($10^{-1} < f < 10$ Hz for pure LC) corresponds to first relaxation process, attributed to surface dipole polarization and space-charge polarization, which essentially changes the near-electrode concentration of free ions [13]. The moderate frequency area B ($10 < f < 10^4$ Hz for pure LC) reflects the processes of polarization and conduction in the bulk of the sample. In this area, there are no relaxation processes, thus the dielectric constant ε' and conductivity σ are independent of the frequency. The high-frequency area C ($10^4 < f < 10^6$ Hz for pure LC) is associated with another relaxation processes—dipole relaxation in the bulk, associated with rotation around the short molecular axis [15]. Further we consistently consider the dielectric properties of composites in the B and A areas of the frequency range.

18.3.1.1 Bulk Dielectric Properties

As it was said above, the permittivity ε' and electrical conductivity σ are frequency independent in B area. The σ (c) curves of LC-CNT and LC-CNT-LapO composites are presented in Fig. 18.2. These data were analyzed using the least-square fitting to the scaling equation

$$\sigma = a\,(c - c_c)^t \tag{18.1}$$

commonly used for characterization of percolation phenomena [16]. In this equation, c_c is the critical concentration of CNTs and t is the conductivity index. Figure 18.2 shows that Eq. (18.1) fits well to the σ (c) curves for LC-CNT series, but the fitting results are unusual compared to the dispersions of CNTs in other matrices. First of all, the critical concentration in all cases is close to 0 ($c_c < 0.02$ wt %). Apparently, this is due to small distance between the electrodes

Fig. 18.1 Complex
permittivity components ε'
and ε'' versus field frequency
f for LC E7 **a** E7-CNTs
(0.05 wt %) **b** and E7-CNT
(0.05 wt %)-LapO
(0.1 wt %) **c** samples
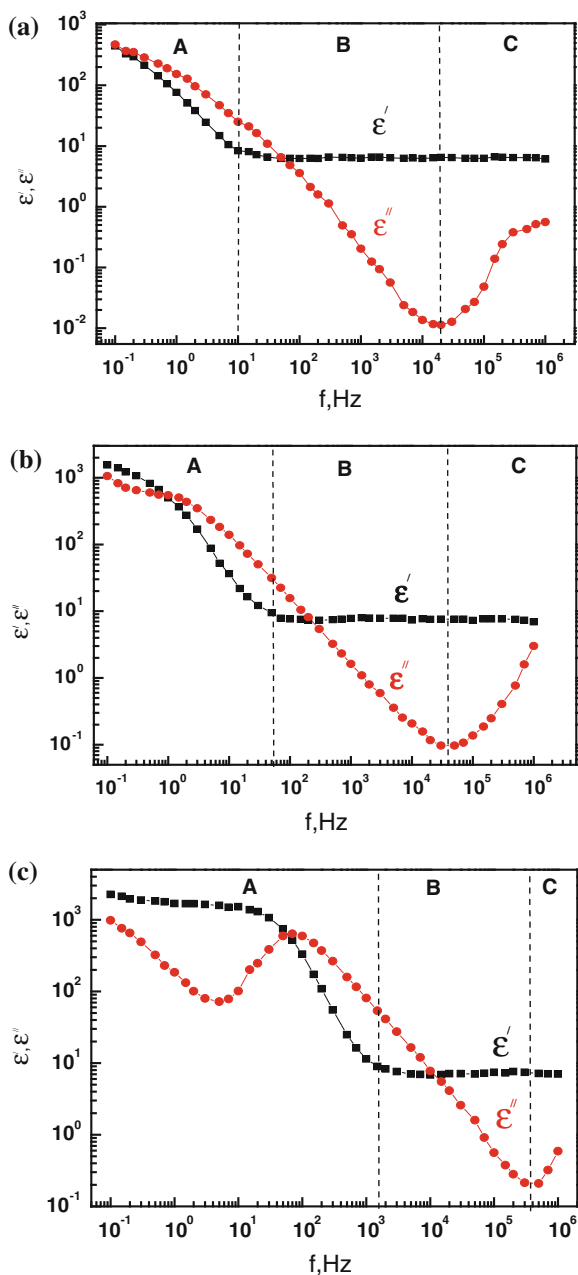
$(d = 20 \ \mu m)$, which is comparable to the length of the nanotubes (5–10 μm). This
means that the channels of high conductivity, associated with the nanotubes (single
nanotubes and their aggregates), start to form in the direction perpendicular to the

Fig. 18.2 Measured
(symbols) and fitted to
formula (18.1) (*lines*)
conductivity versus CNT
concentration *curves* for
E7-CNTs **a** and E7-CNT-
LapO **b** series. The data
corresponding to $c = 0$
(unfilled symbols) are
excluded from fitting
procedure
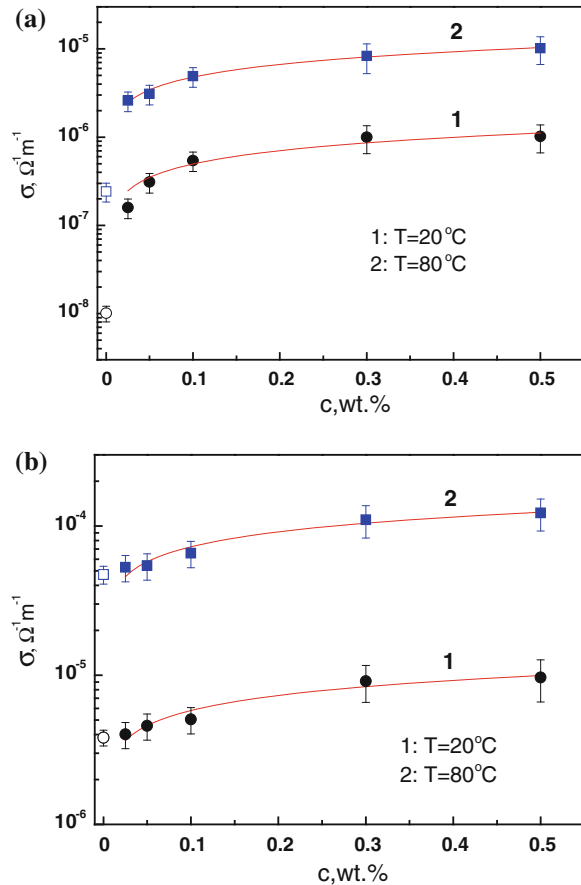
composite layer at a very low concentration of CNTs. In contrast to this direction, where the size of aggregates is limited by the cell thickness, in the plane of the composite layer the aggregates can be practically unlimited. In this sense, the aggregates formed in our cells are largely two-dimensional.

The conductivity index t of the samples of LC-CNT series was 0.63 ± 0.08 at 20 °C and 0.48 ± 0.03 at 80 °C. Note that $\sigma(c)$ dependences are essentially sublinear. This indicates that our case is far from the ordinary 3D percolation, characterized by $t \approx 2$ [16]. Indeed, since the length of the nanotubes is comparable to the thickness of the cell, the case of 2D–3D crossover, when the theory predicts the range of $4/3 < t < 2$ [17, 18], suits better for our samples. Nevertheless, even this assumption fails to describe sublinear character of $\sigma(c)$ curves. We believe that such behavior is due to increasing of ion concentration (releasing of the ions from nanoparticles) and solvation of CNTs by LC molecules.

It should be noted that (18.1) describes a $\sigma(c)$ curve for the LC-CNT-LapO series not as good as for the LC-CNT series (there is no clear jump in

Fig. 18.3 Permittivity versus CNT concentration *curves* for E7-CNTs **a** and E7-CNT-LapO **b** series. The *straight lines* are just for eye guidance
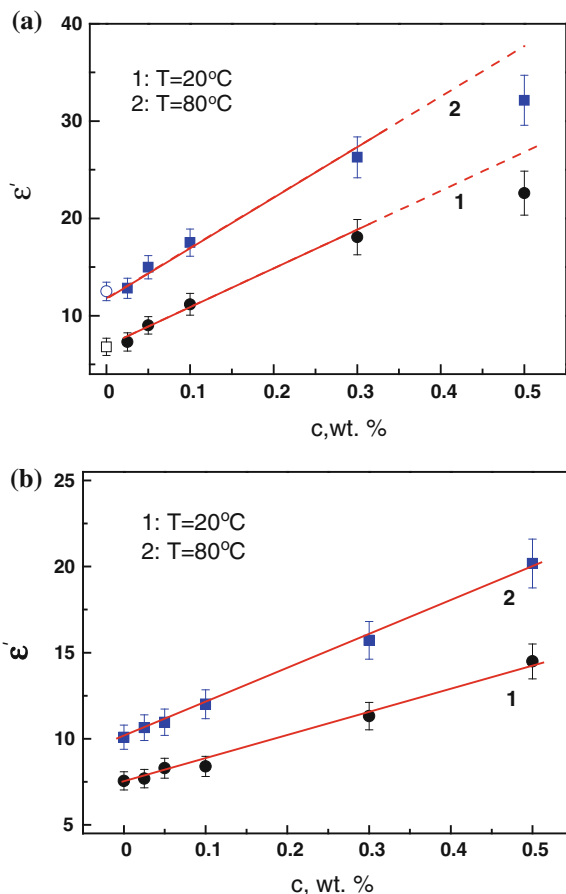
conductivity). However, we use it to compare the $\sigma(c)$ curves for these two series quantitatively. The parameter t for the LC-CNT-LapO series appeared to be two times smaller than for the LC-CNT series: $t = 0.32 \pm 0.04$ (at both 20 and 80 °C). Considerably reduced values of t in the LapO-assisted suspensions give an additional evidence of inhibition of CNT aggregation in an LC. Apparently, the LapO particles, having a great affinity to CNTs, actively surround them. Because of insulation properties of LapO particles, this effect leads to significant reduction in the number of electric contacts between the nanotubes.

The $\varepsilon'(c)$ dependences are shown in Fig. 18.3. It can be seen that ε' monotonically grows with c and increases by about three times with addition of 0.5 wt % of CNTs. The growth of ε' was observed in both nematic and isotropic phases, meaning that it is mainly due to the contribution of the polarizability of nanotubes rather than disturbance of LC orientation by the particles and their aggregates. This result is consistent with the earlier results indicating the increase in LC permittivity with addition of a minute amount of CNTs [19]. The $\varepsilon'(c)$ curve

Fig. 18.4 The time of the near-electrode dielectric relaxation **a** and the width of the near-electrode layers **b** as functions of CNT concentration for E7-CNT (curves 1 and 2) and E7-CNT-LapO (curves 3 and 4) series. The curves 1 and 3 correspond to $T = 20\ °C$ and the curves 2 and 4 correspond to $T = 80\ °C$. The *lines* are just for eye guidance
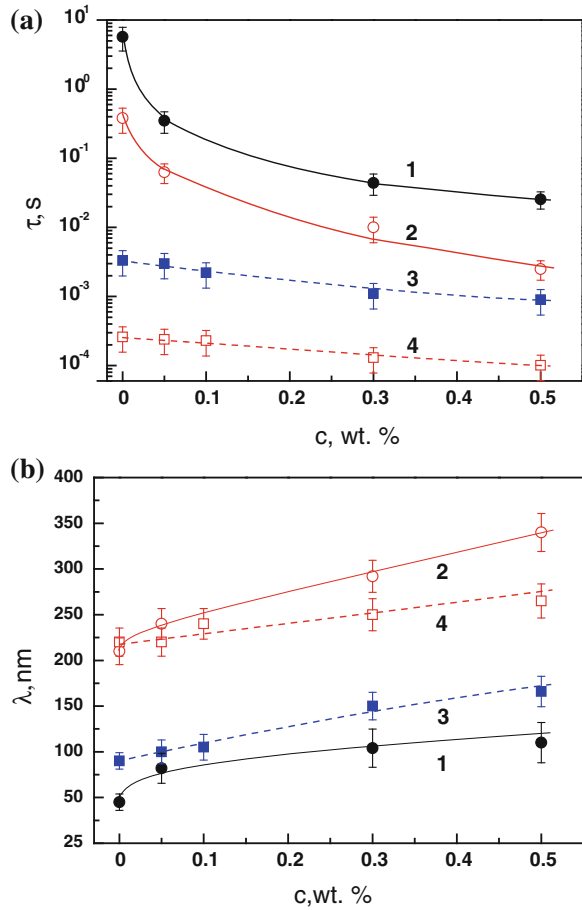
for the LC-CNT series is quasi-linear up to 0.3 wt %. The deviation at higher concentrations c from the linear law can be caused by incomplete filling of CNTs in the cell, since big aggregates are unable to enter the cell. The $\varepsilon'(c)$ curve for the LC-CNT-LapO series is linear over the entire range of CNT concentrations studied in this work. This might reflect improved dispersion of CNTs in the composites containing LapO. The linearity of the $\varepsilon'(c)$ curves suggests that they can be fitted to Maxwell–Wagner mixing equation

$$\varepsilon' = \varepsilon'_{LC} + Kc \tag{18.2}$$

derived in $c \ll 1$ approximation [20]. Here, K is a constant combining permittivity of LC, $\varepsilon'_{LC,}$ and CNT, ε'_{CNT}. Thus, despite the fact that our system is above the percolation threshold of conductivity, the Maxwell–Wagner theory still describes effective permittivity. This interesting fact needs further study.

Fig. 18.5 Transmittance versus voltage curves for the E7 *1*, E7-CNT (0.1 wt %) *2* and E7-CNT (0.1 wt %)-LapO (0.1 wt %) *3* samples
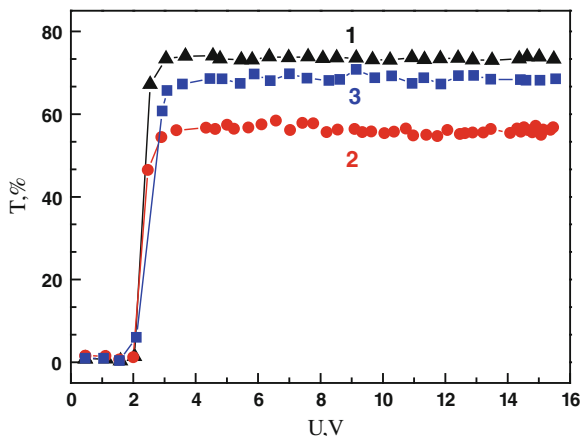
Fig. 18.6 Contrast ratio versus CNT concentration curve for the E7-CNTs *1* and E7-CNTs-LapO *2* series
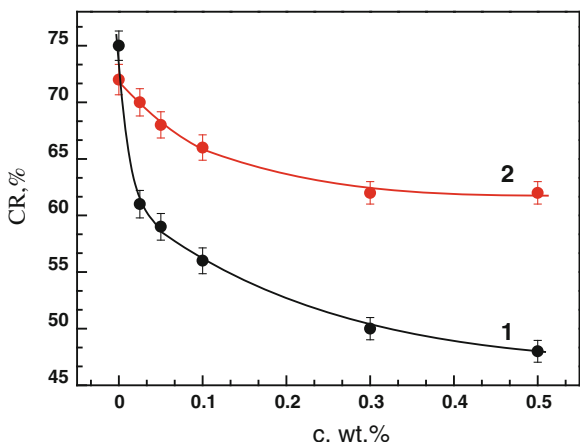
18.3.1.2 Dielectric Peculiarities in the Near-Electrode Layers

Figure 18.4 presents the effect of addition of CNTs and CNT-LapO particles on the time of dielectric relaxation τ and the width of the near-electrode layers λ of LC cells. In the absence of LapO, the increase in CNT concentration results in a sharp decay of τ at both $T = 20$ and $T = 80$ °C (Fig. 18.4a). Concurrently, a noticeable increase in λ is observed (Fig. 18.4b). A similar tendency was previously described for the LC 5CB doped with CNTs [3]. It was explained by reconfiguration of near-electrode dielectric layers in the presence of CNTs and shunting of these layers by the nanotubes acting as elements of the percolation network. The described effects are weaker in the LapO-assisted LC-CNTs suspensions. For these samples, the $\tau(c)$ curve decays, while the $\lambda(c)$ curve grows according to the exponential law. As it was said above, this may indicate significant interaction of insulating LapO platelets with CNTs. Apparently, it reduces

Fig. 18.7 Frederiks threshold voltage versus CNT concentration curves for the E7-CNTs *1* and E7-CNTs-LapO *2* series
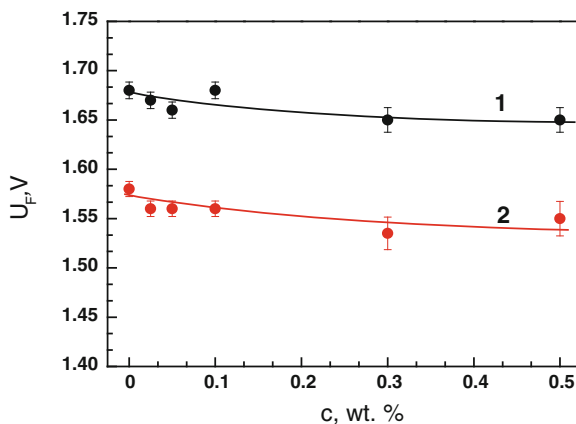
efficiency of electrical contacts between the nanotubes and electrodes, as well as between the different nanotubes. It weakens the shunting capability of CNTs and, probably, their interaction with ionic impurities forming the near-electrode layers.

18.3.2 Electro-Optic Properties

The doping by LapO nanoparticles significantly improves electro-optical characteristics of LC-CNT suspensions. The transmittance T versus applied voltage U curves for the twisted cells filled with pure LC E7, E7-CNT (0.1 wt %), and E7-CNT (0.1 wt %)–LapO (0.1 wt %) suspensions are presented in Fig. 18.5. This Figure shows that CNTs mostly affect the saturation value of T. This is mainly due to absorption of testing light by bulky CNT aggregates. However, introduction of a small amount of LapO platelets minimizes this effect, making the $T(U)$ characteristic of LC-CNTs sample close to that of pure LC. Due to improvement of the saturation value of T, the samples containing LapO show higher electro-optic contrast than their LC-CNT counterparts (Fig. 18.6). Finally, we detected inessential decrease in Frederiks's threshold ($\Delta U_F \sim 0.1$ V) in the LapO-assisted LC-CNT suspensions (Fig. 18.7).

18.4 Conclusions

The effect of nanoparticles of organically modified laponite on dielectric and electro-optic properties of the dispersions of multi-walled carbon nanotubes in a nematic LC E7 is investigated. It is found that introduction of a small amount (0.1 wt %) of LapO platelets in an LC-CNT suspension results in essential changes in dielectric properties. In particular, the introduced LapO particles

considerably suppress the percolation character of conductivity and extend the range of linearity of the permittivity versus CNT concentration curve. Furthermore, addition of LapO particles weakens the effect of CNTs on the parameters of the near-electrode layers: changes in the time of dielectric relaxation and thickness of the near-electrode layers become more gradual and thus more controllable with increase in CNT concentration. Finally, the LapO-assisted LC-CNTs dispersions demonstrate considerably improved electro-optic characteristics, such as better switching contrast and reduced threshold voltage. Thus, the proposed approach is rather effective for optimization and diversification of the properties of LC dispersions of CNTs.

References

1. Qi H, Hegmann T (2008) Impact of nanoscale particles and carbon nanotubes on current and future generation of liquid crystal displays. J Mat Chem 18:3288–3294
2. Lagerwall J, Scalia G (2008) Carbon nanotubes in liquid crystals. J Mat Chem 18:2890–2898
3. Dolgov L, Kovalchuk O, Lebovka N, Tomylko S, Yaroshchuk O (2010) Liquid crystal dispersions of carbon nanotubes: dielectric, electro-optical and structural peculiarities. In: Marulanda JM (ed) Carbon Nanotubes, INTECH, Croatia, pp 451–484
4. Dolgov L, Lebovka N, Yaroshchuk O (2009) Effect of electro-optic memory in suspensions of carbon nanotubes in liquid crystal. Colloid J 71(5):603–611
5. Dolgov L, Yaroshchuk O, Tomylko S, Lebovka N (2012) Electro-optical memory of liquid crystal doped by multi-walled carbon nanotubes. Cond Matter Phys 15(3):33401
6. Basu R, Iannacchione GS (2009) Dielectric hysteresis, relaxation dynamics, and nonvolatile memory effect in carbon nanotube dispersed liquid crystal. J Appl Phys 106:124312
7. Tohver V, Smay JE, Braem A, Braun PV, Lewis JA (2001) Nanoparticle halos: a new colloidal stabilization mechanism. PNAS 98(16):8950–8954
8. Lebovka N, Goncharuk A, Bezrodna T, Chashechnikova I, Nesprava V (2012) Microstructure and electrical conductivity of hybrid liquid crystalline composites including 5CB, carbon nanotubes and clay platelets. Liq Cryst 39(5):531–538
9. Melezhyk AV, Sementsov YuI, Yanchenko YV (2005) Synthesis of porous carbon nanofibers on catalysts fabricated by the mechanochemical method. Rus J Appl Chem 78(6):924–930
10. Lysenkov EA, Lebovka NI, Yakovlev YV, Klepko VV, Pivovarova NS (2012) Percolation behaviour of polypropylene glycol filled with multiwalled carbon nanotubes and laponite. Compos Sci Technol 72:1191–1195
11. Zebrowski J, Prasad V, Zhang W, Walker LM, Weitz DA (2003) Shake-gels: shear-induced gelation of laponite–PEO mixtures. Colloids and Surfaces A: Physicochem Eng Aspects 213:189–197
12. Twarowski AJ, Albrecht AC (1979) Depletion layer studies in organic films: low frequency capacitance measurements in polycrystalline tetracene. J Chem Phys 20(5):2255–2261
13. Sawada A, Tarumi K, Naemura S (1999) Effects of electric double layer and space charge polarization by plural kinds of ions on complex dielectric constant of liquid crystal materials. Jpn J Appl Phys 38(3A):1418–1422
14. Zakrevska S, Zakrevskyy Y, Nych A, Yaroshchuk O, Maschke U (2002) Electro-optics of liquid crystal-aerosil-photopolymer composites. Mol Cryst Liq Cryst 375:467–480
15. Blinov L (2011) Structure and properties of liquid crystals. Springer, Dordrecht
16. Stauffer D, Aharony A (1994) Introduction to percolation theory. (2nd ed.) CRC Press, USA
17. Lebovka NI, Manna SS, Tarafdar S, Teslenko N (2002) Percolation in models of thin film depositions. Phys Rev E 66:66134

18. Müller K-H, Wei G, Raguse B, Myers J (2003) Three-dimensional percolation effect on electrical conductivity in films of metal nanoparticles linked by organic molecules. Phys Rev B 68:155407
19. Basu R, Iannacchione GS (2010) Orientational coupling enhancement in a carbon nanotube dispersed liquid crystal. Phys Rev E 81:051705
20. Choy TC (1999) Effective medium theory. Oxford Clarendon Press, New York

Chapter 19
Comparison of Poly(rI) and Poly(rA) Adsorption on Carbon Nanotubes

M. V. Karachevtsev, G. O. Gladchenko and V. A. Karachevtsev

19.1 Introduction

Noncovalent functionalization of SWCNTs opens the possibility for overcoming their inherent insolubility and improving their processability, paving the way for different potential applications. This approach does not disrupt the large π-electronic surface of nanotubes, and, thus, it allows keeping their extraordinary mechanical, electronic, and optical properties. The polymer conjugation with SWCNT is an excellent solution on the path to nanotube noncovalent functionalization, which facilitate their promotion in the advanced technology [1]. Noncovalent binding of the polymer to carbon nanotube surfaces is very effective for dispersing SWCNTs in organic solvents [2] and water [3], for producing unusual nanohybrids used in medicine and biosensing.

It was shown that a strong nanohybrid is formed with the polymer and nanotubes when the polymer was wrapping around nanotubes [1–5]. The wrapping mechanism leads not only to a better interaction with the nanotube surface but also helps to reinforce mechanical properties of the bulk material due to the extraordinary strength of the individual nanotubes [5]. Polymer wrapping around the nanotube depends on the stiff or flexible backbone of the polymer [6–9], the chemical composition of the polymer and also on geometric parameters of constituents in the nanocomposite [6]. Polymers with stiff backbones tend to wrap around the nanotube with a more distinct conformation and form a helical configuration [9]. However, flexible polymer chains with bulky and aromatic side groups form an interchain stitching rather than a helical conformation [8]. On the contrary, the stiffness of these backbones decreases the intrachain coiling. It was also demonstrated that aromatic moieties along the backbone appear to dictate the

M. V. Karachevtsev (✉) · G. O. Gladchenko · V. A. Karachevtsev
B.I. Verkin Institute for Low Temperature Physics and Engineering,
Kharkov 61103, Ukraine
e-mail: mkarachevtsev@ilt.kharkov.ua

adsorption conformation which is likely due to the preference for optimizing π–π interactions.

Last time, DNA is exploited very intensively as a wrapping polymer around nanotubes [3, 10–23]. Due to its helical structure, DNA can wrap tightly around the nanotube in water spontaneously [3]. The strong DNA binding with SWCNT occurs when the hydrophobic nitrogen bases interact with the sidewall of SWCNT through π–π stacking whereas the hydrophilic sugar-phosphate backbone interacts with water. It is obvious that properties of these two nanostructures supplement each other, and, as a result, a hybrid with specific structural features is formed. DNA provides a high dispersion efficiency of nanotubes in water. As well, DNA also has the advantage over the other polymers as far as choosing the base type or their sequence gave an opportunity to separate nanotubes with certain chirality from the bulk material [18]. In addition, the well-developed DNA chemistry can facilitate the further functionalization of DNA: SWCNT hybrid.

Due to helical wrapping of the polymer around SWCNT sidewalls in combination with the strong binding through π-stacking, DNA keeps its adsorption on the nanotube after hybrid deposition onto the substrate. In such a film the nanotubes are individual in the polymer surrounding or isolated in bundles with the polymer among them, that provides emission from semiconducting SWCNTs [21].

π–π interaction between the nanotube sidewall and organic molecules or polymers possessing the π-aromatic polycyclic moiety plays an important role in the development of SWCNT applications. The stacking interaction influences the absorption spectrum of binding molecules the intensity of which decreases because of changes in electronic interactions between compounds. Such a decrease is known as the hypochromic effect [24, 25]. Theory considers hypochromism as a result of weak dipole–dipole interactions between stacking chromophores modified by the light wave. The well-known example is DNA, UV absorption of which decreases when the duplex structure is formed by two single strands and increases under the helix $\rightarrow$ coil transition [24, 25]. As DNA absorption spectrum is mainly conditioned with absorption of nucleic bases (NBs) (see, for example, [24]) in UV range from 200 to 300 nm, a significant transformation of absorption spectra of some homopolymers was observed after their adsorption onto the nanotube surface [22]. π–π stacking interaction between the nanotube and π-conjugated NBs was manifested not only in DNA absorption spectrum but was observed directly in the absorption spectrum of polymer-wrapped SWCNTs [23]. It was demonstrated that at the wavelength longer than 300 nm the absorption spectrum of the polymer-wrapped SWCNTs is of weaker absorption intensity than the spectrum of the unbound SWCNTs. The absorption decrease observed was explained by hypochromicity of nanotubes, which was induced by their interaction with NBs [23].

Molecular dynamics (MD) simulations are intensively exploited to clarify the mechanism of DNA adsorption onto SWCNT, to estimate energetic parameters, and to determine the structure of DNA: SWCNT. The simulations showed that ss-DNA of any sequence will spontaneously adsorb to SWCNT sidewall of arbitrary chirality. It was found that the formation of ss-DNA helix which arises from electrostatic and torsional interactions within the sugar-phosphate backbone results

in the polymer wrapping around SWCNT. The polymer adsorption is driven by the attractive π-π stacking interaction between DNA bases and SWCNT sidewall. Quantum-chemical methods applied for describing these interactions provided a quantitative characterization of the mechanism of DNA binding to the nanotube surface [19, 20]. As a result, the stability row of the bases binding to SWCNT has been established: guanine (G) > adenine (A) > cytosine (C) ≈ thymine (T) > uracil (U).

Recent MD simulation showed that the flexibility of ss-DNA enables right- and left-handed helices and the formation of U-shaped loops [14]. If we add to this that ss-DNA involves a set of polymers with slightly different physical properties (due to different types of NBs or their sequences), we should expect a wide range of polymer wrapping conformations around SWCNTs.

Here, we investigate adsorption of two relatively long homopolynucleotides: polyriboinosinic acid (poly(rI)) and polyriboadenylic acid (poly(rA)) on SWCNT surface, employing absorption spectroscopy and MD simulation. These two related polymers possess the same sugar-phosphate backbone but differ only in the structure of purine bases. It is known that these polymers have the different base ordering at room temperature and, therefore, different rigidity. So, poly(rA) is of high polymer ordering [26, 27] while the structure of poly(rI) is characterized with quite disordering [28, 29]. Thus the main purpose of this study was to compare binding of these two related polymers, differing in rigidity, with the tube surface.

19.2 Materials and Methods

19.2.1 Materials

Potassium salts of poly(rA) and poly(rI) acids were purchased from Sigma-Aldrich (USA) and used as received. The polymers were dissolved in aqueous buffer solution consisted of 5×10^{-3} M Na$^+$ cacodylate (pH6.9) (Serva, Germany) and 5×10^{-3} M NaCl. The buffer was prepared on ultra purified water with the resistance of 18 MΩ. The concentration of polynucleotides was determined optically, using the corresponding molar extinction coefficients: poly(rA), $\varepsilon_{259} = 10,100$ M^{-1} cm^{-1} [26], poly(rI), $\varepsilon_{248} = 10,100$ M^{-1} cm^{-1} [29].

Purified SWCNTs (produced by HIPCO method) were purchased from Unidym^{TM} (USA). In order to obtain SWCNT:RNA conjugates, carbon nanotubes were mixed with aqueous solution of polyribonucleotides and sonicated for 40 min (1 W, 44 kHz). The polymer concentration was 0.4–0.6 mM and SWCNT:polymer weight concentration ratio ranged from 1:1 to 1:1.2. After sonication the suspension was centrifuged at 70,000 g for 1 h. The supernatant was decanted and used as a stock solution in experiments. As follows from our former electrophoretic estimation, after 40 min ultrasonication the lengths of polymer fragments were within 100–150 nucleotides [11]. An aqueous suspension of SWCNT with an

anionic surfactant sodium dodecyl sulfate (SDS) (Sigma–Aldrich, USA) was prepared by the same method. The concentration of surfactant in the suspension was 1 %.

19.2.2 Methods

19.2.2.1 Absorption Spectroscopy

All UV-visible absorbance measurements were carried out on Specord M40 (Carl Zeiss, Jena, Germany) equipped with a thermoelectrically controlled cuvette holder. Quartz cuvettes with 1 mm path length were used in experiments. Absorption spectra were recorded in the range of 200–900 nm, at the room temperature. Temperature dependences of changes in the optical density ($\Delta A(T)$) of polynucleotides (the melting curves) were measured with the heating rate of 0.25 °C/min at $\lambda = 259$ nm (poly(rA)) and 248 nm (poly(rI)). In these measurements a two-cuvette arrangement was used: one cell with nanotube suspension (or polymer solution) was placed in the working channel of the spectrophotometer and the reference cuvette contained a buffer solution. The reference cell was thermostatted within (20 ± 0.5) °C.

19.2.2.2 Molecular Dynamics Simulation

Adsorption of homo oligonucleotides $r(I)_{25}$ and $r(A)_{25}$ on SWCNT surface was simulated by the Molecular dynamics method. For this purpose the program package NAMD [30] was employed with Charmm27 force field parameter set [31]. Periodic boundary conditions were applied in modeling. Sizes of boxes were 52 Å × 66 Å × 141 Å and 51 Å × 65 Å × 141 Å for SWCNT:$r(I)_{25}$ and SWCNT:$r(A)_{25}$, respectively. Each system was embedded in water (more than 13,200 H_2O molecules). Twenty five Na^+ ions were added to each system for neutralization of the charge on the sugar-phosphate backbone. SWCNT for both systems was selected as a zigzag (16,0) nanotube. Its length and diameter were 11.0 and 1.122 nm, respectively. In our simulation SWCNT atoms were uncharged. Before simulation starting, the oligonucleotides were located near the nanotube surface. Oligonucleotides were initialized in B-conformation. The system was minimized during 1,000 steps (with 1 fs time step) and then was modeled during 60 ns (the time step was also 1 fs). In our simulations NPT ensemble was used in which the number of molecules, pressure, and temperature were fixed. Temperatures and pressures in the periodic boxes were 343 K and 1 atmosphere, respectively. Interaction energies were calculated by NAMD Energy Plugin (Version 1.3) which was implemented in VMD program package [32].

19.3 Results and Discussion

19.3.1 Absorption Spectroscopy of SWCNT:Poly(rI) and SWCNT:Poly(rA)

Some homopolynucleotides at room temperature, at neutral pH and low ionic strength have the ordered helical structure which arises because of essential stacking interactions favoring parallel orientation of adjacent bases [33]. Stacking interactions are predicted to be a driving force for the formation of ordered helical conformations of homopolynucleotide single strands [24, 25, 33]. Such ordered structures have been observed at neutral pH for oligo- and poly(rA) [26, 27]. According to recent theoretical considerations, at room temperature poly(rA) consists of multiblocks with short helical domains interspaced with "melted" random-coil ones [33].

In the case of poly(rI) the situation is different, this polymer has no stable form of helices [28, 29] that indicates its flexibility. Earlier experiments on CD spectroscopy showed that poly(rI) at neutral pH and low ionic strength is a single-stranded poor base stacked helix [28].

The ordered structure of the polynucleotide manifests itself in the rise of the optical absorption intensity in UV-range upon the heating of polynucleotide aqueous solution from the room temperature to 90 °C as it was observed for poly(rA) (Fig. 19.1). This absorption intensity rise is related with the so-called hyperchromic effect. At polymer heating NBs are disordered, and, as a result, attenuation of light absorption is taken off. This attenuation (i.e., the hypochromic effect which is opposite to the hyperchromic one) appears due to the weak interaction between the dipole moment of the electronic transition of one molecule which absorbed photon and the dipole moment induced in neighboring molecules [24, 25].

In the double-stranded DNA (ds-DNA) π–π-stacked disordering of the bases occurred also when temperature of the polymer solution increases. This disordering

Fig. 19.1 Temperature effect on optical absorption of free poly(rA) and poly(rI) (measured at 259 and 248 nm, respectively). Structures of two nitrogen bases—adenine (*left*) and hypoxanthine (*right*)—show a difference in monomer structures
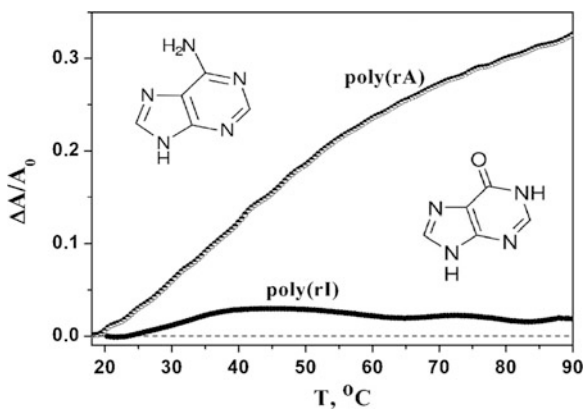
is accompanied with an increase in the optical absorption the temperature dependence of which has the characteristic S-like form (the so-called melting curve) due to high cooperativity of the helix-coil transition in ds-DNA [24]. For single-stranded polynucleotides such a S-like form is not observed, however, for some polymers the smooth increase of optical absorbance can be revealed that indicates a more gradual unfolding suggesting a predominantly noncooperative helix-coil transition. For poly(rA) the absorption increase with the temperature growth takes place in the wide temperature range and reaches 33 % at 90 °C (Fig. 19.1). It is supposed that at this temperature poly(rA) acquires a practically disordering conformation. However, in poly(rI) an absorbance increase with temperature is practically absent (Fig. 19.1) that points out the poor base ordering already at room temperature. This observation agrees with literature analysis of rigidity of these polymers: so, poly(rA) is characterized with a rather high degree of the base ordering at room temperature [26, 27] that points to its high rigidity and, on the contrary, poly(rI) is of high flexibility of the random coil [28, 29].

The π-π stacking interaction between the nanotube and π-conjugated nitrogen bases manifested directly in transformation of DNA absorption spectrum [22] and can be also observed in the absorption spectrum of polymer-wrapped SWCNTs [23]. The polynucleotide interaction with SWCNT induces the decrease of the carbon nanotube absorption intensity (the hypochromic effect) in 300–400 nm region, in comparison with absorption of SWCNT covered with SDS which has no π-conjugated system [23]. Earlier we observed this effect for SWCNT covered with poly(rC), poly(rG), ds-DNA, and ss-DNA [23]. It was shown that the magnitude of the so-called hypochromic coefficient may use for the comparison of π-π stacking interaction of different polymers with the nanotube surface.

In this work we performed similar analysis of absorption spectra of SWCNT:poly(rI) and SWCNT:poly(rA) hybrids in 200–600 nm region and compared them with those of SWCNT:SDS as well as with the unbound polymer (Figs. 19.2 and 19.3, respectively). As SDS absorption in UV region begins at the wavelength less than 200 nm, the spectrum of SWCNT:SDS aqueous suspension observed in 200–600 nm range is caused only by nanotubes absorption. On the contrary, the absorption spectrum of SWCNT:polymer suspension in the range of 200–300 nm is a result of superimposition of nanotube and polymer absorption spectra. Absorption spectra of the samples studied are similar in the range of 400–600 nm but differ in the intensity which is conditioned with different nanotube concentrations in aqueous suspensions. To compare the nanotube spectra obtained, the spectrum intensity of the polymer-wrapped nanotubes was scaled to their spectrum intensity in SDS environment (Fig. 19.2a), using the multiplier (wavelength independent). In this case, a possible small shift of nanotube spectral peaks, induced by various environments, can be neglected.

As the spectra of the polymer and nanotubes are superimposed in the range of 200–300 nm, the corrective extraction of the polymer spectrum from the common spectrum is not a simple procedure because of ambiguity in the polymer and nanotubes concentration determination. So, to take into account the SWCNT hypochromic effect correctly, we do not consider this spectral range.

Fig. 19.2 UV-visible
absorption spectra of
SWCNT:poly(rI) hybrids and
of its components in water
buffer suspension/solution:
a absorption spectra of
SWCNT:poly(rI) aqueous
suspensions (*bold line*), of
SWCNTs aqueous suspension
with SDS (1 % by weight)
(*dashed-line*) and differential
spectra (ΔA) of
SWCNT:poly(rI)-poly(rI)
(*thin line*); **b** absorption
spectrum of poly(rI) (*dash-
dotted line*), and
SWCNT:poly(rI)-
SWCNT:SDS (*solid line*).
Intensity of SWCNT:poly(rI)
spectrum was normalized to
SWCNT:SDS one in
500–600 nm spectral range
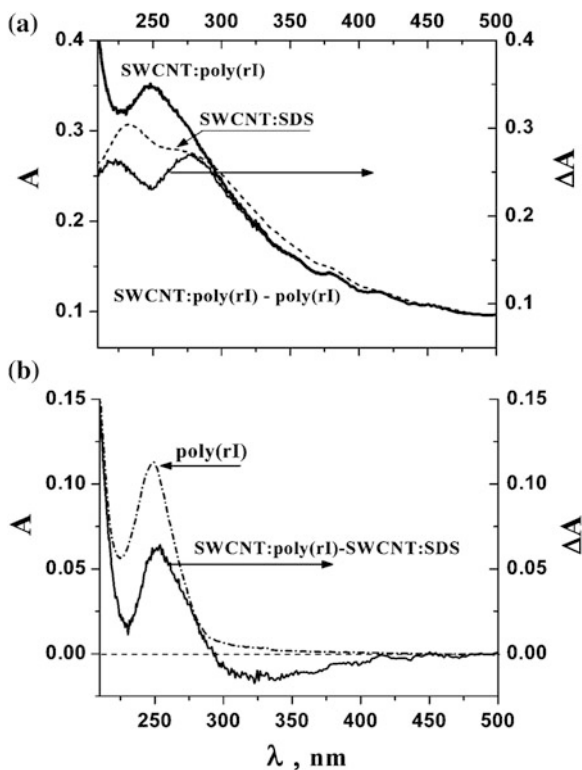
As follows from Fig. 19.2, the scaled optical density of SWCNT:poly(rI)
suspension in 300–400 nm range is somewhat lower than that for SWCNT:SDS
ones. It should be noted that the value of the spectra discrepancy decreases
monotonically with the wavelength increasing. We showed earlier [23], that the
absorption decrease is caused by hypochromism of nanotubes, induced by their
interaction with the polymer. The spectrum of nanotubes interacting with the
polymer is obtained by subtracting the poly(rI) spectrum from that of
SWCNT:poly(rI). The differential spectrum is also shown in Fig 19.2a.

Spectrum of the "bound" poly(rI) (Fig. 19.2b, solid line) was obtained by
subtraction of "pure" SWCNT absorbance (Fig. 19.2a, dashed-line) from
SWCNT:poly(rI) absorbance (Fig. 19.2a, bold line). To reveal the spectrum
transformation of poly(rI) after its adsorption, the spectra of free (Fig. 19.2b, dash-
dotted line) and "bound" polymers were compared. The hypoxanthine absorption
spectrum is conditioned with two main $\pi \rightarrow \pi^*$ electronic transitions observed
(according to data of various authors [29, 34]) at 266–276 nm and 246–250 nm.
On the comparison of the "bound" poly(rI) spectrum with that of the free polymer
(Fig. 19.2b, solid line and dash-dotted line, respectively), weak differences are
seen, namely, the bathochromic shift of the spectrum maximum (248 → 253 nm)
and the shoulder appearance in 266–276 nm region. A similar spectrum

Fig. 19.3 UV-visible absorption spectra of SWCNT:poly(rA) hybrids and of its components in water buffer suspension/solution: **a** absorption spectra of SWCNT:poly(rA) aqueous suspensions (*bold line*), of SWCNTs aqueous suspension with SDS (1 % by weight) (*dashed-line*) and differential spectra (ΔA) of SWCNT:poly(rA)-poly(rA) (*thin line*); **b** absorption spectrum of poly(rA) (*dash-dotted line*), and SWCNT:poly(rA)-SWCNT:SDS (*solid line*). Intensity of SWCNT:poly(rA) spectrum was normalized to SWCNT:SDS one in 500–600 nm spectral range
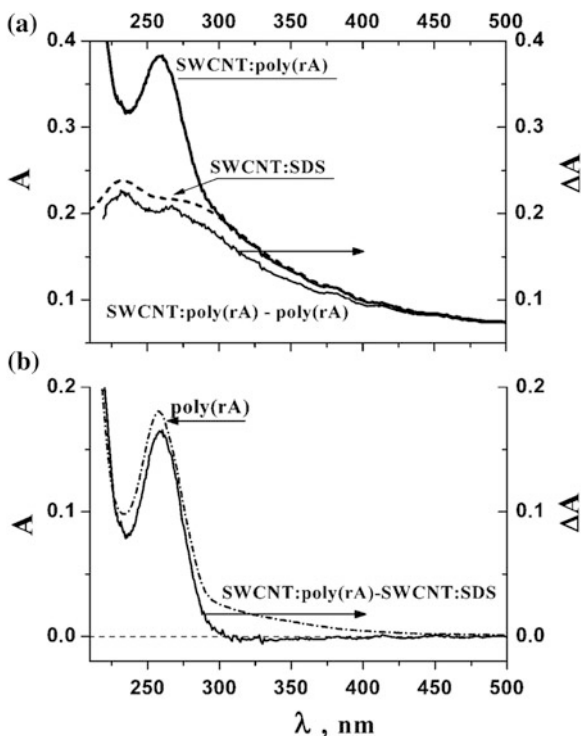
transformation was observed earlier for poly $d(G)_{30}$ adsorbed to the nanotube surface [22] with guanine as NBs which is similar in structure to hypoxanthine (the lack of the amino group at C2 position, as compared to guanine). As the data on the direction and spectral position of optical dipole transitions for hypoxanthine are absent in literature, we take the advantage of the similar structure with guanine and believe that the transition at ~ 248 nm corresponds to the long axis of hypoxanthine which aligns along the nanotube axis. The red-shift of this band indicates that hypoxanthines are stacked with the nanotube in such configuration to align with the direction of 248 nm transition moment along the nanotube axis.

The hypochromic effect of SWCNT can be described by the hypochromic coefficient determined as $K(\lambda) = (A_{NTi}(\lambda) - A_{NT}(\lambda))/A_{NT}(\lambda) = (A_{PNT}(\lambda) - A_P(\lambda) - A_{NT}(\lambda))/A_{NT}(\lambda)$ (where $A_{NT}(\lambda)$ and $A_{NTi}(\lambda)$ are the spectra of "unbound" nanotubes (in SDS environment) and nanotubes interacting with the polymer, respectively; $A_{PNT}(\lambda)$ is the spectrum of the nanotubes:polymer sample) [23]. As follows from Fig. 19.4, the coefficient $K(\lambda)$ begins to grow noticeably from 500 nm and reaches -0.08 value up to 340 nm. Such a monotonous growth of $K(\lambda)$ absolute value upon the wavelength decrease can be explained by the increasing interaction between electronic levels of nanotubes and hypoxanthine as the levels approach each other (see for detail Ref. [23]).

Fig. 19.4 Spectral
dependence of hypochromic
coefficient $-K(\lambda)$ of SWCNT
covered with poly(rA) (*bold
line*) and poly(rI) (*dash-
dotted line*)
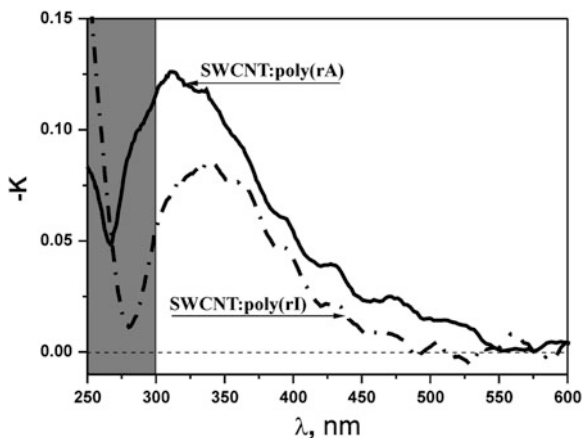
As in the case of poly(rI), poly(rA) interaction with SWCNT should induce hypochromicity in 300–500 nm region, in comparison with SWCNT:SDS. However, use of the above method for this sample to analyze the polymer interaction with the tube has a difficulty. Thus, the scaled spectrum of SWCNT:poly(rA) practically does not differ from that of SWCNT:SDS in 300–500 nm range. The situation with similarity of the spectra was clarified after analyzing the spectrum of poly(rA) solution without nanotubes, which was exposed by ultrasonication for 40 min (for the same time as for the nanotube suspension with poly(rA)). It turned out that, unlike the spectrum of poly(rI) being influenced with ultrasound, a long-wave "tail" in the poly(rA) absorption spectrum appeared in 300–450 nm range, which hinders the observation of the nanotube:polymer interaction in this spectral range (Fig. 19.3b). Evidently, such a transformation of the polymer spectrum upon ultrasound exposure is connected with the polymer disruption. It should be noted that clarification of possible reasons for appearing additional absorption just in this polymer requires special studies. Subtraction of the spectrum of the polymer being sonicated gave a decrease of nanotube absorption in 300–450 nm range with regard to SWCNT:SDS spectrum. As a result, the dependence of the hypochromic coefficient on the wavelength was also obtained for SWCNT:poly(rA) (Fig. 19.4).

For comparison, spectral dependences of hypochromic coefficients obtained were built in one figure (Fig. 19.4). Note, that a reliable determination of $K(\lambda)$ value can be deduced at wavelengths longer than 300 nm where absorption spectra of nanotubes and the polymer are not superimposed. It is seen from figure that the dependence $-K(\lambda)$ for SWCNT:poly(rI) in the range of 450–300 nm runs essentially lower than this dependence for SWCNT:poly(rA), and this points to a stronger energy of poly(rA) interaction with the nanotube surface than that observed for poly(rI).

19.3.2 Comparison of r(I)$_{25}$ and r(A)$_{25}$ Adsorption on Carbon Nanotubes: Molecular Dynamics Simulation

To compare poly(rI) and poly(rA) adsorption on carbon nanotubes, we have simulated this process, employing the molecular dynamics. Before simulation the self-ordered structure of each polymer with 25-nucleotides in length was created and located close to the tube surface (Fig. 19.5). The initial structure of oligomer r(I)$_{25}$ was selected as the ordered helix as the degree of its disordering is unknown. As a result, oligomer r(I)$_{25}$ disordering and its adsorption on the nanotube surface occurred simultaneously. First of all, we have analyzed the initial structures of r(I)$_{25}$ and r(A)$_{25}$ to find the difference in base self-stacking interaction for these polymers in order to explain the difference between polymers in base ordering that modulates polymer rigidity. At first, we tried to find additional H-bonds between neighbor bases in stack. Really, for r(A)$_{25}$ we found hydrogen bonding between the amino group and nitrogen of adjacent adenines while for r(I)$_{25}$ similar H-bonding between neighbor bases was not revealed. We believe that this additional hydrogen bonding strengthens the stacking interaction in poly(rA) that stabilizes the polymer rigidity. Similar conclusion has been made recently for poly(rC) which was stabilized by hydrogen bonding between the amino and carbonyl groups of adjacent cytosines [33].

The total simulation time of oligomer adsorption on carbon nanotubes was 60 ns. Every 10 ns we controlled the number of nitrogen bases which were stacked with the nanotube surface as well as self-stacked NBs. The bases are considered stacked with the nanotube surface if more than half of ring atoms were in van der Waals (vdW) contact with this surface. At each step of simulation interaction energies between the nanotube and oligomer were determined for both systems. Interaction energies between each oligomer and SWCNT as a function of simulation time are depicted in Fig 19.6.

During first 10 ns simulation oligomers contacted with the nanotube surface, the initial high ordered structure of oligomers disappears and some NBs begin to arrange on the tube surface in the stacking conformation. We note that the first 1–4 ns of simulation of r(I)$_{25}$ adsorption is characterized by a higher rise of the energy of oligomer interaction with the tube than r(A)$_{25}$ (Fig. 19.6). This can be explained by a lower base ordering in the former oligomer, which facilitates a quicker disordering of the oligomer helix. Note, that helix prevents the oligomer adsorption onto the tube. As well, poor bases ordering permits to bend the sugar-phosphate backbone significantly, and, as a result, to 10 ns r(I)$_{25}$ formed two loops being characterized with the appearance of H-bonds between two hypoxanthines, which are located on the opposite sides of this loop. Note, that such a strong loop strengthening is possible just as a result of the oligomer flexibility. On the contrary, the strong base ordering of r(A)$_{25}$ is accompanied with a lower adsorption rate, and up to 10 ns the loops being formed by the oligomer did not demonstrate the strong curvature of the sugar-phosphate backbone, that excludes the
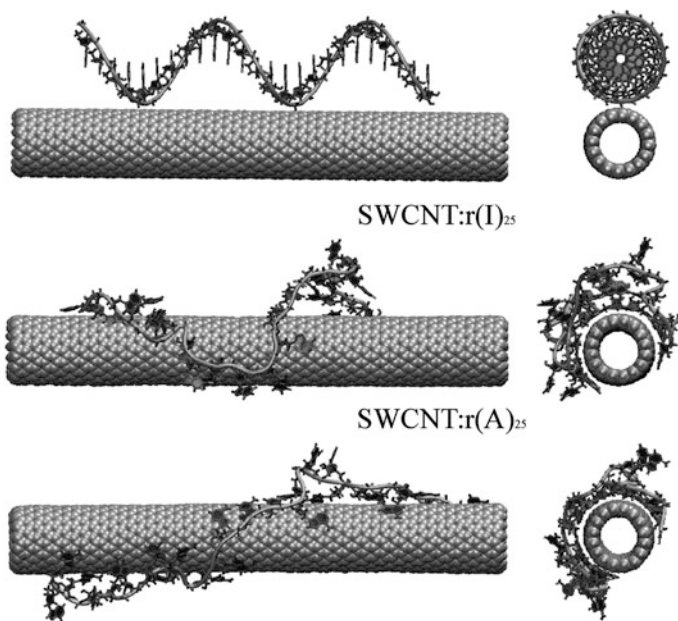
Fig. 19.5 Snapshot of r(I)$_{25}$ structure and SWCNT (16,0) in the initial simulation step, SWCNT:r(I)$_{25}$ and SWCNT:r(A)$_{25}$ hybrids after 60 ns simulation. Water molecules and Na$^+$ counterions were removed for better visualization. The phosphate backbone is depicted by *grey solid curves*

Fig. 19.6 Dependence of interaction energy between SWCNT and r(I)$_{25}$ (*grey*(1)), SWCNT and r(A)$_{25}$ (*black* (2)) on simulation time
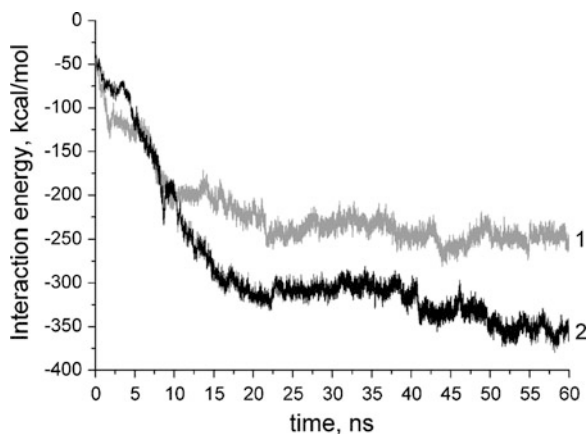
appearance of H-bonds between the opposite adenines inside the loop. As the next simulation showed, such loops are destroyed whereas the r(I)$_{25}$ loop does not disappear even after 60 ns simulation (Fig. 19.5). After 5 ns the rise of the interaction energy with the tube of two oligomers became comparable. So, after first 10 ns 9 adenines of r(A)$_{25}$ and 9 hypoxanthines of r(I)$_{25}$ are stacked to the

nanotube surface. For this time binding energies for both oligomers demonstrate the essential increase (Fig. 19.6) and till 10 ns they have approximately the same value (about 200 kcal/mol).

Next 10 ns simulation showed that there is a noticeable growth of the interaction energy of $r(A)_{25}$ while for $r(I)_{25}$ the energy increase was essentially weaker. After 20 ns simulation the binding energy reaches 315 and 220 kcal/mol for $r(A)_{25}$ and $r(I)_{25}$, respectively (Fig. 19.6). The difference in the energy values correlates with the number of bases stacked with the nanotube surface: 16 adenines and 10 hypoxanthines. An essential difference in the binding energy can be explained by appearance of the stable loop formed by $r(I)_{25}$ during the first 10 ns, which is spaced from the tube surface. Note, that after 20 ns modeling both oligonucleotides do not wrap around the nanotube.

After 40 ns simulation 16 adenines and 13 hypoxanthines were stacked with the nanotube (Table 19.1). Dependence of the binding energy of $r(I)_{25}$ with the tube on time shows a tendency with a small increasing of the energy and for SWCNT:$r(A)_{25}$ this energy changes slightly too. The loop formed by $r(I)_{25}$ on the nanotube is retained.

The number of adenines stacked with the tube increases to 18 after 50 ns simulation but the number of hypoxanthines stacked with the tube (13 bases) does not change up to 60 ns (Table 19.1). After 60 ns modeling the energy of $r(A)_{25}$ and $r(I)_{25}$ binding to the tube surface reaches 350 and 250 kcal/mol, respectively. Both oligomers do not wrap around the nanotube even after the maximal simulation time. It should be noted that essentially lower $r(I)_{25}$ binding energy with the nanotube is caused with the formation of the stable loop of 10 hypoxanthines, which is distant from the nanotube surface (Fig. 19.7). As well, detail analysis of this loop structure revealed that the stability of the loop on the nanotube is essentially conditioned with two H-bonds between hypoxantines located in different positions of the loop. This self-stacking and H-bond becomes possible as a result of rather strong curvature of the sugar-phosphate backbone in the loop and

Table 19.1 Number of nitrogen bases of oligonucleotides $r(A)_{25}$ and $r(I)_{25}$ which were in stack with tube surface and unstacked for different simulation time

Time	Type of nitrogen base stacking	$r(I)_{25}$	$r(A)_{25}$
10 ns	Stacked with tube	9 hypoxanthines	9 adenines
	Unstacked	Loop (10 hypoxanthines)	
20 ns	Stacked with tube	10 hypoxanthines	16 adenines
	Unstacked	Loop (9 hypoxanthines)	
30 ns	Stacked with tube	10 hypoxanthines	15 adenines
	Unstacked	Loop (10 hypoxanthines)	
40 ns	Stacked with tube	13 hypoxanthines	16 adenines
	Unstacked	Loop (9 hypoxanthines)	
50 ns	Stacked with tube	12 hypoxanthines	18 adenines
	Unstacked	Loop (9 hypoxanthines)	
60 ns	Stacked with tube	13 hypoxanthines	19 adenines
	Unstacked	Loop (10 hypoxanthines)	

Fig. 19.7 Snapshots of loop formed by r(I)$_{25}$ on the tube surface after 60 ns simulation. The phosphate backbone is depicted by *gray solid curve*, nucleoside showed by *black rings*, some of them form H-bonding dimers inside the loop
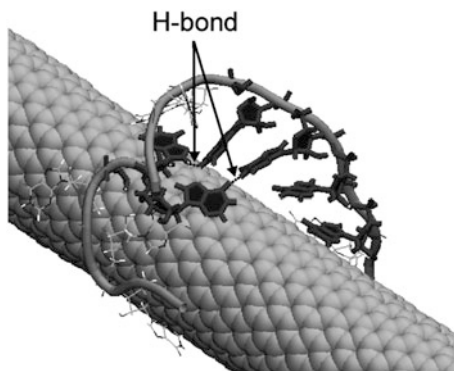
due to the tube surface which conditions this curvature and, in this way, stabilizes the loop. It should be noted that small loops formed with r(A)$_{25}$ disappear with simulation time, additional hydrogen bonds between adenine and ribose are not revealed. More ordered structure of r(A)$_{25}$ promotes stretching of the polymer along the nanotube surface and its wrapping around the nanotube. Upon r(A)$_{25}$ adsorption on the nanotube surface, domains (tetramers/trimers/dimers) of the polymer, consisting of ordered bases, are kept rather long. Most likely, just these domains promote keeping of the helix structure of the whole oligomer. In comparison with r(A)$_{25}$, disordered r(I)$_{25}$ is lesser elongated along the nanotube, and the loop formed assists its position on the tube more compact.

As well, it follows from Fig. 19.5 oligomer r(I)$_{25}$ undergoes higher distortion than that in comparison with r(A)$_{25}$. Thus, the distance between phosphate groups of the beginning and the end of r(I)$_{25}$ after adsorption onto the tube is about two times shorter than the same distance for r(A)$_{25}$, which extended by about 20 % in comparison with the initial value. Note, that the oligomer ends demonstrate the biggest curvature of the phosphate backbone.

The polymer helicity in DNA/RNA depends significantly on the balance between repulsive Coulomb forces among negatively charged phosphates, which tend to untwist the helix, and π-stacking interaction of the bases the optimized structure of which limits the helix untwisting. When π-stacking interaction weakens, the polymer stability decreased. Most likely, in poly(rI) weak stacking interaction between hypoxanthines lowers the polymer stability, on the one hand, and a possibility of forming an additional hydrogen bond between oxygen and the hydroxyl group of ribose, on the other hand, promotes fixing of the oligomer conformation with disordered bases. As a result, poly(rI) is significantly disordered at room temperature.

It should be noted that earlier modeling using molecular dynamics to calculate the energy of six different nucleotide monophosphates (NMPs) binding to (6,0) SWCNT in aqueous solution revealed that the binding energy of NMP inosine is much weaker than that of adenylic NMPs (2.1 vs. 10.3 kcal/mol) [10].

Thus, simulation of adsorption of two oligomers (r(I)$_{25}$ and r(A)$_{25}$) onto the nanotube surface showed that, although both the oligomers do not form the complete turn around the nanotube, nevertheless, it is seen that r(A)$_{25}$ conformation on the nanotube is of helical character and demonstrates a tendency of making the complete turn though with a rather big pitch. At the same time r(I)$_{25}$ conformation on the nanotube is of lesser ordered form for which the presence of loop is characteristic, which is located over some distance from the tube surface, and this lowers essentially the energy of this oligomer interaction with the tube.

The result obtained agrees with those of earlier modeling [8] which showed that, most probably, the flexible polymer does not form the helical structure on the tube and adsorbed without a stable conformation on SWCNT. At the same time, stiff polymer is of tendency to the helical conformation around the nanotube, which provides higher energy of such a polymer binding to the tube [9].

The principal difference between our polymers studied and earlier modeling of stiff or flexible polymer adsorption on the nanotube lays in their different structures. So, in previous studies rigidity or flexibility of the polymer was mainly provided by the polymer backbone. In our case the backbone of two biopolymers was the same (the sugar-phosphate one), and the polymer inflexibility depends on the value of the base stacking interaction. As adsorption of the polymer takes place mainly through bases, just the absorption reduces this difference in flexibility. This essential difference permits to distinguish adsorption of organic polymers onto the nanotube from DNA/RNA adsorption.

19.4 Conclusions

Employing spectroscopic and molecular dynamics methods, adsorption study of two related biopolymers (poly(rA) and poly(rI)) on the nanotube surface showed that the ordered polymer (poly(rA)) interacts stronger with tube surface than disordered one (poly(rI)). Polymer adsorption simulation demonstrated that the interaction energy of more flexible r(I)$_{25}$ with the tube is essentially lower than this energy of more ordered r(A)$_{25}$ (250 vs. 350 kcal/mol). Conformation analysis of oligomers on the nanotube surface revealed that the more ordered oligomer is of tendency to the helical structure around the nanotube, and this provides higher binding energy. At the same time a more disordered r(I)$_{25}$ forms a stable loop, which is away from the nanotube and oligomer is of lesser similarity with the helical structure. On the contrary, more ordered r(A)$_{25}$ takes the conformations with a larger number of bases stacked with the tube than the disordered polymer poly(rI) (19 adenines vs. 13 hypoxanthines of 25 nucleotides). As well, this conclusion is supported with spectral studies of the hypochromic effect of nanotubes interacting with these polymers, which become apparent due to π-π stacking interaction of nanotubes with NBs. Thus, the value of the hypochromic effect for nanotubes covered with poly(rA) is higher than that determined for nanotubes with poly(rI).

References

1. O'Connell MJ, Boul P, Ericson LM et al (2001) Reversible water solubilization of single-walled carbon nanotubes by polymer wrapping. Chem Phys Lett 342:265–271
2. Hasan T, Tan PH, Bonaccorso F et al (2008) Polymer-assisted isolation of single wall carbon nanotubes in organic solvents for optical-quality nanotube-polymer composites. J Phys Chem C 112:20227–20232
3. Zheng M, Jagota A, Strano M et al (2003) Structure-based carbon nanotube sorting by sequence-dependent DNA assembly. Science 302:1545–1548
4. Star A, Stoddart JF, Steuerman D et al (2001) Preparation and properties of polymer-wrapped single-walled carbon nanotubes. Angew Chem Int Ed 40:1721–1725
5. Rahmat M, Hubert P (2011) Carbon nanotube–polymer interactions in nanocomposites. A review. Compos Sci Technol 72:72–84
6. Kusner I, Srebnik S (2006) Conformational behavior of semi-flexible polymers confined to a cylindrical surface. Chem Phys Lett 430:84–88
7. Gurevitch I, Srebnik S (2008) Conformational behavior of polymers adsorbed on nanotubes. J Chem Phys 128:144901-1–144901-8
8. Tallury SS, Pasquinelli MA (2010) Molecular dynamics simulations of flexible polymer chains wrapping single-walled carbon nanotubes. J Phys Chem B 114:4122–4129
9. Tallury SS, Pasquinelli MA (2010) Molecular dynamics simulations of polymers with stiff backbones interacting with single-walled carbon nanotubes. J Phys Chem B 114:9349–9355
10. Frischknecht AL, Martin MG (2008) Simulation of the adsorption of nucleotide monophosphates on carbon nanotubes in aqueous solution. J Phys Chem C 112:6271–6278
11. Karachevtsev VA, Gladchenko GO, Karachevtsev MV et al (2008) Adsorption of poly(rA) on the carbon nanotube surface and its hybridization with poly(rU). Chem Phys Phys Chem 9:2872–2881
12. Martin W, Zhu W, Krilov G (2008) Simulation study of noncovalent hybridization of carbon nanotubes by single-stranded DNA in water. J Phys Chem B 112:16076–16089
13. Karachevtsev MV, Lytvyn OS, Stepanian SG et al (2008) SWCNT-DNA and SWCNT-polyC hybrids: AFM study and computer modeling. J Nanosci Nanotechnol 8:1473–1480
14. Johnson RR, Kohlmeyer A, Johnson ATC et al (2009) Free energy landscape of a DNA-carbon nanotube hybrid using replica exchange molecular dynamics. Nano Lett 9:537–541
15. Johnson RR, Johnson ATC, Klein ML (2010) The nature of DNA-base–carbon-nanotube interactions. Small 6:31–34
16. Roxbury D, Mittal J, Jagota A (2012) Molecular-basis of single-walled carbon nanotube recognition by single-stranded DNA. Nano Lett 12:1464–1469
17. Karachevtsev MV, Karachevtsev VA (2011) Peculiarities of homooligonucleotides wrapping around carbon nanotubes: molecular dynamics modeling. J Phys Chem B 115:9271–9279
18. Tu X, Manohar S, Jagota A et al (2009) DNA sequence motifs for structure-specific recognition and separation of carbon nanotubes. Nature 460:250–253
19. Stepanian SG, Karachevtsev MV, Glamazda AYu et al (2009) Raman spectroscopy study and first-principles calculations of the interaction between nucleic acid bases and carbon nanotubes. J Phys Chem A 113:3621–3629
20. Shukla MK, Dubey M, Zakar E et al (2009) Interaction of nucleic acid bases with single-walled carbon nanotube. Chem Phys Lett 480:269–272
21. Karachevtsev VA, Glamazda AYu, Dettlaff-Weglikowska U et al (2006) Spectroscopic and SEM studies of SWCNTs: polymer solutions and films. Carbon 44:1292–1297
22. Hughes ME, Brandin E, Golovchenko JA (2007) Optical absorption of DNA—carbon nanotube structures. Nano Lett 7:1191–1194
23. Karachevtsev VA, Plokhotnichenko AM, Karachevtsev MV et al (2012) Decrease of carbon nanotube UV light absorption induced by π-stacking interaction with nucleotide bases. Carbon 48:3682–3691

24. Cantor CR, Schimmel PR (1980) Biophysical Chemistry. W.H. Freeman and Company, San Francisco
25. Tinoco I Jr (1960) Hypochromism in polynucleotides. J Am Chem Soc 82:4785–4790
26. Holcomb DN, Timasheff SN (1968) Temperature dependence of the hydrogen ion equilibria in poly(riboadenylic acid). Biopolymers 6:513–529
27. Brams J, Michelson AM, van Holde KE (1966) Adenylate oligomers in single- and double-strand conformation. J Mol Biol 15:467–488
28. Thiele D, Guschlbauer W (1973) The structures of polyinosinic acid. Biophysik 9:261–277
29. Howard FB, Miles HT (1982) Poly(inosinic acid) helices: essential chelation of alkali metal ions in the axial channel. Biochemistry 21:6736–6745
30. Phillips JC, Braun R, Wang W et al (2005) Scalable molecular dynamics with NAMD. J Comp Chem 26:1781–1802
31. Foloppe N, MacKerell AD Jr (2000) All-atom empirical force field for nucleic acids: I. Parameter optimization based on small molecule and condensed phase macromolecular target data. J Comp Chem 21:86–104
32. Humphrey W, Dalke A, Schulten K (1996) VMD: Visual molecular dynamics. J Molec Graph 14:33–38
33. Seol Y, Skinner GM, Visscher K et al (2007) Stretching of homopolymeric RNA reveals single-stranded helices and base-stacking. Phys Rev Lett 98:158103-1–158103-4
34. Cech CL, Tinoco I Jr (1976) Circular dichroism calculations for polyinosinic acid in proposed multi-stranded geometries. Nucl Acids Res 3:399–404

Chapter 20
Non-Covalent Immobilization of Oligonucleotides on Single-Walled Carbon Nanotubes

Evgeny K. Apartsin, Marina Yu. Buyanova, Darya S. Novopashina, Elena I. Ryabchikova and Alya G. Venyaminova

20.1 Introduction

Carbon nanotubes (CNTs) have unique chemical and physical properties and are compatible with biomacromolecules and cells. Modern synthetic methods make it possible to obtain modified CNTs containing organic, inorganic, and hetero-organic fragments [1, 2]. Hybrids of CNTs with nucleic acids, proteins, and other biological molecules find a wide range of practical applications. CNT hybrids with nucleic acids are used in the systems of target molecule detection [3] as well as in nanomedicine as transporters of therapeutic nucleic acids [4–6]. The methods frequently used for obtaining the hybrids of nucleic acids (NA) with single-walled and multi-walled carbon nanotubes (SWCNTs and MWCNTs) are to be described below.

E. K. Apartsin · M. Y. Buyanova · D. S. Novopashina (✉) · E. I. Ryabchikova
A. G. Venyaminova
Institute of Chemical Biology and Fundamental Medicine SB RAS, 8 Lavrentiev ave,
Novosibirsk 630090, Russia
e-mail: danov@niboch.nsc.ru

E. K. Apartsin
e-mail: eka@niboch.nsc.ru

M. Y. Buyanova
e-mail: buyanova.marina@gmail.com

E. I. Ryabchikova
e-mail: lenryab@niboch.nsc.ru

A. G. Venyaminova
e-mail: ven@niboch.nsc.ru

M. Y. Buyanova
Novosibirsk State University, 2 Pirogov str, Novosibirsk 630090, Russia

20.1.1 Covalent Immobilization of NA to CNTs

There are several approaches of covalent attachment of NA onto CNT surface. The frequently used method employs a conjugation of 5′- or 3′-amino-terminated oligonucleotide with carboxy-functionalized CNTs (CNT-COOH) upon carbodi-imide activation resulting in formation of amide bond. The use of this method for modification of dispersed [7–11] and aligned CNTs [12–14] was reported. It is also possible to add the 5′-NH$_2$-terminated peptide nucleic acid oligomers to activated carboxylic groups of CNT-COOH [15]. It should be noted that unmodified oli-gonucleotide can be attached to CNT-COOH by interactions of amino-groups of heterocyclic bases with activated carboxylic groups [16], with the functional activity of oligonucleotide being retained. The inversed approach, i.e., conjugation of oligonucleotide to amino-modified SWCNTs [17] presumes activation of 5′-phosphate group in oligonucleotide followed by coupling with CNTs modified with ethylenediamine. In another method of covalent grafting of oligonucleotide onto CNTs [18] ethylenediamine-modified SWCNTs were treated by bifunctional reagent to form HS-groups on the SWCNT surface. The addition of 5′-SH-oli-gonucleotide was resulted in its covalent grafting to SWCNTs via disulfide bond.

A method of photomodification of CNT surface by azides of different structure followed by grafting of oligonucleotide from CNTs using standard NA synthesis procedure or by grafting of pre-synthesized oligonucleotide to modified CNTs was suggested [19, 20]. As a result, oligonucleotide molecules are attached to numerous sites of CNTs directly or via linker.

The principal advantage of covalent immobilization of NA to CNTs is strong binding between nanomaterial and biomolecule. However, such method does not permit to achieve high loading of oligonucleotide to CNTs.

20.1.2 Non-Covalent Immobilization of NA to CNTs

Oligonucleotides are known to interact with CNTs by means of π-π-stacking interactions of heterocyclic bases of oligonucleotide with aromatic system of nanotube [21, 22]. The selective affinity of oligonucleotide of definite sequence to the CNT of given chirality was also shown [23]. To obtain hybrids, sonication of mixed solution of oligonucleotide and CNTs are usually used. The hybrids formed are relatively stable in conditions of ion-exchange and site-exclusion chromatog-raphy [24–26] and also upon application of low voltage [27–31]. However, such kind of hybrids appear to decompose during electrophoresis [32–34] and after translocation into cells [35].

Addition of complementary strand to the solution of CNT-NA hybrid resulted in decomposition of the latter by withdrawal of NA duplex from CNT surface [36–38]. Nevertheless, the successful delivery of NA duplexes (including siRNA) adsorbed onto CNTs into cells has been shown [39–41]. When the oligonucleotide added is

complementary to the terminal region of another oligonucleotide adsorbed on CNTs, partial removal of the latter from SWCNT occurs, with displaced fragment taking part in duplex formation. This property was used for the construction of nano-structured materials [42–44].

The use of electrostatic interactions between oligonucleotide and functionalized CNTs appeared to be a very efficient method of construction of CNT-NA hybrids. To date, a wide number of approaches to obtain hybrids of single-strand and double-strand DNA and RNA with CNTs by means of electrostatic interactions have been reported [45–47]. CNTs are usually functionalized by amino-terminated linkers interacting with phosphate groups in oligonucleotide backbone. The most simple approach presumes the covalent attachment of amines to activated carboxylic groups in oxidized CNTs. Used for this purpose are aliphatic amines [8, 48–53], amino-terminated dendrimers [54, 55], diamino-oligo(ethylene glycols) [53] grafted to CNTs or poly-amines grafted from CNTs [56, 57]. Another approach consists of the electrostatic interaction of oligonucleotides and their complexes with MWCNTs or SWCNTs amino-functionalized by 1, 3-dipolar cycloaddition. Employing this approach, non-covalent hybrids of CpG oligonucleotides [58, 59], siRNA [60, 61] and plasmid DNA [62–64] with SWCNTs and MWCNTs bearing amino-oligo(ethylene glycol) and amino-terminated dendrons were obtained.

In an alternative method of electrostatic NA attachment to CNTs, the latters are non-covalently amino-functionalized by positively charged amino-bearing molecules. The substances most suitable for this purpose are surfactants and surfactant-like molecules consisting of hydrophobic part interacting with CNT surface and positively charged hydrophilic part interacting with NA fragments. The design of hybrids of siRNA, plasmid DNA and calf thymus DNA with CNTs functionalized with dodecyltrimethylammonium bromide [65], cetylpyridinium chloride [66], cationic cholesterol compounds [67–69], and positively charged pyrene compounds [70, 71] was reported. As an example of use of more complex non-polymeric molecules for the CNTs functionalization with NA, anchoring of lipid-amino acid denrdimer conjugates on SWCNTs followed by electrostatic attachment of siRNA shoud be mentioned [72]. Among the wide variety of cationic polymers, the frequently used for the obtaining of CNT-NA hybrids are polyethylenimine [66, 73–76], poly(L-lysine) [77], poly(diallyldimethylammonium chloride) [50, 78] and chitosan [79, 80]. The use of poly(2,6-pyridinedicarboxylic acid) [48, 81] and cationic glyco-polymers [82] was also reported.

Selective attachment of oligonucleotides directly to the sites of CNT functionalization can be achieved by using highly specific non-covalent streptavidin-biotin interaction. Typically, biotinylated oligonucleotide is immobilized on streptavidin-coated CNTs. Functionalization of CNTs with streptavidin can be done both by simple protein adsorption on CNTs surface [83, 84] and by covalent attachment of streptavidin to pre-functionalized CNTs [85]. According to another method, CNTs were biotinylated at first, then streptavidin molecules were attached specifically at the sites of biotinylation; finally, biotinylated oligonucleotide was

added to be attached to streptavidin molecules [86]. The approaches of obtaining NA-CNT hybrids based on streptavidin–biotin interaction are used to immobilize different oligonucleotides on CNT surface, such as DNAzymes, aptamers, oligonucleotide probes, and long double-stranded DNA fragments.

Non-covalent methods of NA immobilization to CNTs attract the attention of researchers due to their diversity and simplicity in use. The frequently appearing disadvantage of non-covalent methods is low stability of hybrids formed.

20.1.3 The Use of Anchor Groups for Attachment of NA to CNTs

Along with methods of covalent and non-covalent immobilization of NA to CNTs, the method combining them both should also be discussed. Usually, two alternative approaches are used. Oligonucleotide can be conjugated to a small molecule having high affinity to CNTs and then this conjugate interacts with CNTs to give CNT-NA hybrid. In an alternative approach, CNTs are functionalized by small molecules interacting with them with high affinity and bearing reactive groups followed by the addition of oligonucleotide also resulting in formation of hybrid. These small molecules that can be non-covalently bonded with CNT surface thus immobilizing oligonucleotide are referred to as anchor groups. As a rule, anchor groups are derivatives of hydrophobic molecules bearing reactive groups for the conjugation with oligonucleotides.

An efficient method combining the NA attachment and hydrophilic functionalization of CNTs utilizes phospholipid as an anchor group, with amino-terminated poly (ethylene glycol) being conjugated with lipid moiety. Upon functionalization, lipid tails cover CNT surface, and poly (ethylene glycol) makes them highly soluble. Terminal amino groups are treated by bifunctional reagent to form HS-groups on CNT surface, after that 5′-SH-oligonucleotide is conjugated to functionalized CNTs via disulfide bond. The approach described was used for obtaining hybrids of SWCNTs with antisense oligonucleotides [87] and siRNA [88–91]. After functionalization and NA attachment, SWCNT-NA hybrids formed were highly soluble and demonstrated high biocompatibility.

One of the most convenient methods for obtaining of NA-CNT hybrids is based on anchoring of oligonucleotides onto CNTs by means of pyrene residues. In contrary to the non-covalent immobilization of NA onto CNTs using positively charged pyrene derivatives mentioned above [70, 71], pyrene anchor groups are conjugated to oligonucleotides by amide or phosphoramide bond. This can be done either by interaction of 1-pyrenebutanoic acid succinimidyl ester with 5′- or 3′-amino-terminated oligonucleotide [92–95] or by introduction of 1-pyrenylmethylamine onto 5′-phosphate-terminated oligonucleotide followed by the interaction of pyrene conjugate obtained with CNTs [96, 97].

In general, the use of pyrene anchor groups for the immobilization of oligo-nucleotides and their complexes on CNTs is a very prospective approach. The main advantages of such kind of anchor groups are high synthetic flexibility, high density of functionalization and the possibility to both attach oligonucleotides to functionalized CNTs and functionalize CNTs with pre-formed oligonucleotide-anchor group conjugate. Nevertheless, the lack of systemic study of the effect of different factors on hybrids formation process is an obstacle for application of this approach. Here, the comparative study of the immobilization of 5′-pyrene conjugates homo-oligoribonucleotides and homo-oligodeoxyribonucleotides of different length onto SWCNT surface is done.

20.2 Materials and Methods

20.2.1 Materials

SWCNT-COOH (500–1,500 nm length, Aldrich, US) were used as a platform for the construction of hybrids. Oligoribo- and oligodeoxyribonucleotides were synthesized by the solid phase phosphoramidite method using an ASM-800 automated synthesizer (Biosset, Russia). The 5′-terminal phosphate groups were introduced into oligonucleotides at the last stages of the synthesis by means of a condensation of the polymer-bound protected oligonucleotide with [2-[2-(4,4′-dimethoxytrityl-oxy)ethyl]sulfonyl]ethanol H-phosphonate using pivaloyl chloride as activator. H-Phosphonate was synthesized as described in [98].

20.2.2 Instrumentation

Optical density of solutions of oligonucleotides and their derivatives was measured on a Nanodrop 1000 spectrophotometer (Thermo Fisher Scientific, US). Solutions of SWCNTs and their hybrids with oligonucleotides were prepared by sonication in a Sonorex Super RK 31 H ultrasonic bath (Bandelin Electronic, Germany). The fluorescence spectra were recorded on a Cary Eclipse spectrofluorometer (Varian Inc., US) in quartz cuvettes (optical path of 3 mm) at 25 °C. The temperature was maintained using a 2219 Multitemp II thermostatic circulator (LKB Bromma, Sweden). Mass spectra were recorded using a MALDI-TOF Autoflex Speed mass-spectrometer (Bruker Daltonics, Germany). ζ-Potential measurements of SWCNTs and their hybrids with oligonucleotides were conducted using a Nanosizer ZS particle analyzer (Malvern Instruments, UK). TEM images were obtained using a Veleta (SIS, Germany) digital camera mounted on a JEM 1400 transmission electron microscope (JEOL, Japan).

20.2.3 Synthesis of 5′-Pyrene Conjugates of Oligonucleotides

To a solution of 5′-phosphorylated oligonucleotide (cetyltrimethylammonium salt; approximately 0.03 μmol) and 4-N,N′-dimethylaminopyridine (5 mg, 41 μmol) in anhydrous DMSO (50 μl), triphenylphosphine (6.8 mg, 25 μmol), and 2,2′-dipyridyl disulfide (5.3 mg, 25 μmol) in anhydrous DMSO (25 μl each) were added. The reaction mixture was stirred for 15 min at 37 °C. The activated oligonucleotide was precipitated with 2 % $LiClO_4$ in acetone, washed quickly with acetone, and dissolved in water (5 μl), followed by addition of 1-pyrenylmethylamine hydrochloride (0.6 mg, 2.2 μmol) in the mixture of DMSO (25 μl) and triethylamine (5 μl). The reaction mixture was stirred for 2 h at 37 °C. The nucleotide material was precipitated with 2 % $LiClO_4$ in acetone and washed with acetone.

20.2.4 Procedure of the Preparation of SWCNT-COOH-Containing Solutions

To obtain solutions of hybrids, SWCNT-COOH were added to the buffered (10 mM Tris-HCl, pH 7.5, 1 mM Na_2EDTA, 0.1 M NaCl) solution of 1-pyrenylmethylamine or 5′-pyrene conjugate of oligonucleotide (1 μM) to the final concentration of 0.5–128 mg/L, sonicated for 30 min and centrifuged (5 min, 14,000 g).

20.2.5 Isotherms of Adsorption of Pyrene Conjugates of Oligonucleotides on SWCNTs

The fluorescence spectra of non-covalent hybrids of pyrene conjugates of oligonucleotides with SWCNT-COOH were recorded at $\lambda_{ex} = 345$ nm. The amount of oligonucleotide adsorbed on SWCNTs v_{ads} was calculated by the following formula:

$$v_{ads} = \left(1 - \frac{I_p}{I_p^0} \right) \cdot C(Pyr)_\Sigma \cdot V,$$

where I_p is the intensity of pyrene residues fluorescence at 378 nm in the solution of hybrid of oligonucleotide with SWCNTs, I_p^0 is the intensity of pyrene residues fluorescence at 378 nm in the reference solution of oligonucleotide in the same concentration (1 μM), $C(Pyr)_\Sigma$ is total concentration of pyrene conjugate of oligonucleotide (1 μM), V is sample volume.

20.2.6 TEM Examination of the Samples of SWCNTs and Their Hybrids with Oligonucleotides

A formvar-covered copper grid was placed on a drop of solution of a SWCNT-containing sample (SWCNT amount was 25 mg/L) for 90 s. The grid was then placed on a drop of aqueous solution of contrasting agent (0.5 % uranyl acetate) for 5 s. The excess of a liquid was removed by filter paper. The grids were examined in a JEM 1400 electron microscope at accelerating voltage of 80 kV. The images were collected by side-mounted Veleta digital camera (SIS, Germany).

20.3 Results and Discussion

20.3.1 5′-Pyrene Conjugates of Oligonucleotides

The 5′-pyrene conjugates of model oligoribo- and oligodeoxyribonucleotides were synthesized by the coupling of 1-pyrenylmethylamine with 5′-terminal phosphate group of oligonucleotide selectively activated by triphenylphosphine and 2,2′-dipyridyl disulfide in the presence of 4-N,N′-dimethylaminopyridine as a nucleophilic catalyst [99– 101]. Pyrene residues were conjugated to oligonucleotides *via* phosphoramide bond (Fig. 20.1).

The structure of the conjugates was confirmed by MALDI TOF mass-spectrometry (Table 20.1) and UV ($\lambda_{max} = 260$ nm, oligonucleotide; $\lambda_{max} = 330$, 345 nm, pyrene) and fluorescence spectroscopy ($\lambda_{ex} = 345$ nm, $\lambda_{em} = 378$, 390 nm, pyrene).
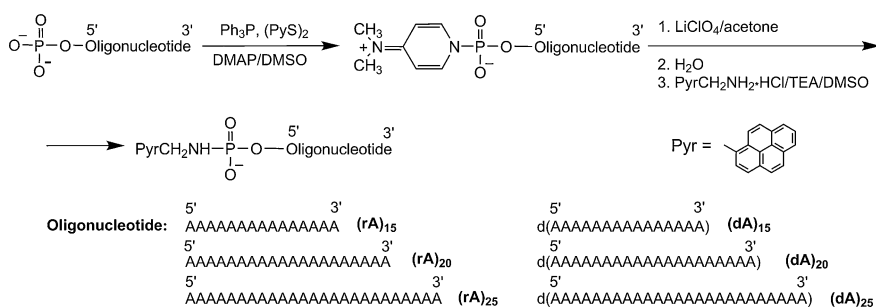
Fig. 20.1 Synthesis of 5′-pyrene conjugates of oligonucleotides

Table 20.1 5′-Pyrene conjugates of oligonucleotides

Abbreviation	Conjugate[a]	Molecular weight	
		Calculated	Found[b]
Pyr(rA)$_{15}$	5′-PyrCH$_2$NHpAAAAAAAAAAAAAAA	5169.4	5169.9
Pyr(rA)$_{20}$	5′-PyrCH$_2$NHpAAAAAAAAAAAAAAAAAAAA	6815.4	6819.7
Pyr(rA)$_{25}$	5′-PyrCH$_2$NHpAAAAAAAAAAAAAAAAAAAAAAAAA	8461.4	8467.1
Pyr(dA)$_{15}$	5′-PyrCH$_2$NHpd(AAAAAAAAAAAAAAA)	4929.4	4929.8
Pyr(dA)$_{20}$	5′-PyrCH$_2$NHpd(AAAAAAAAAAAAAAAAAAAA)	6495.4	6500.3
Pyr(dA)$_{25}$	5′-PyrCH$_2$NHpd(AAAAAAAAAAAAAAAAAAAAAAAAA)	8061.5	8063.2

[a] Pyr = pyrene residue; p = phosphate group.
[b] MALDI TOF mass-spectrometry.

20.3.2 Hybrids of SWCNTs with Oligonucleotides

The 5′-pyrene conjugates of oligoribo- and oligodeoxyribonucleotides were non-covalently immobilized on SWCNT-COOH (Fig. 20.2). Pyrene residues were adsorbed on defectless sites of SWCNT surface thus anchoring oligonucleotides. This process was carried out in relatively mild conditions (short-term sonication), with oligonucleotide remaining stable and undamaged [97].

A comparative study of the immobilization of 5′-pyrene conjugates of different oligonucleotides onto the surface of SWCNT-COOH was performed to evaluate the influence of oligonucleotide structure on the hybrid formation and to find conditions of the maximum loading of oligonucleotides on SWCNT-COOH. The efficacy of the adsorption of 5′-pyrene conjugates of oligonucleotides on the surface of SWCNT-COOH was evaluated by ζ-potential measurements and fluorescence titration. To examine the effect of oligonucleotides on hydrodynamic properties of SWCNTs, ζ-potential measurements were conducted at SWCNT-COOH concentration of 12–128 mg/L. The ζ-potential values graphs were shown to have minima at the points believed to correspond to the maximal amount of oligonucleotide adsorbed on individual SWCNTs (Fig. 20.3). It was interesting to find that in the plots of hybrids of SWCNT-COOH with oligoribonucleotides the minima were observed at SWCNT concentration about 60 mg/L, while in the plots
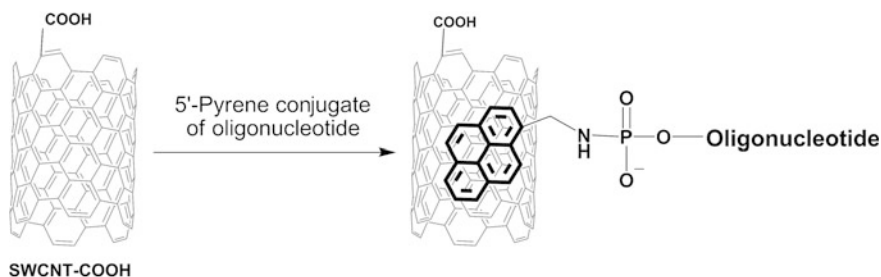
Fig. 20.2 Scheme of SWCNT-COOH non-covalent functionalization
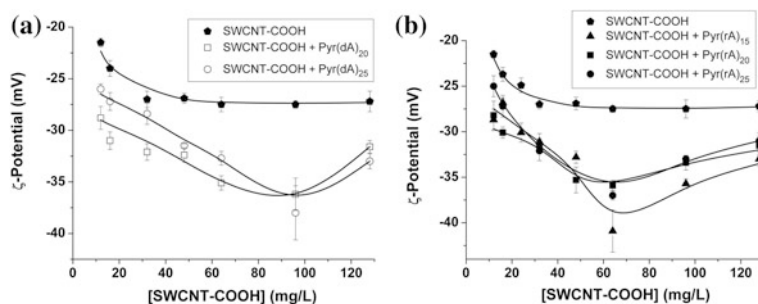
Fig. 20.3 ζ-Potential plots of SWCNT-COOH and their hybrids with oligoribonucleotides (**a**) and oligodeoxyribonucleotides (**b**). Conditions: 10 mM Tris–HCl, 1 mM Na_2EDTA, 0.1 M NaCl, pH 7.5; oligonucleotide concentration is 1 μM. Data represent mean ± S.D. (n = 5)

of hybrids of SWCNT-COOH with oligodeoxyribonucleotides of the same length the minima were observed at SWCNT concentration about 100 mg/L. This phenomenon can be explained by different hydratation of oligoribo- and oligodeoxyribonucleotides resulting in the formation of hybrids of different composition.

The efficacy of oligonucleotides adsorption on the surface of SWCNT-COOH was assessed by the fluorescence titration of the solutions of the pyrene conjugates of oligonucleotides by SWCNTs at concentrations from 0.5 to 128 mg/L according to [96]. The similar approach of the estimation of oligonucleotide adsorption efficacy employing gel electrophoresis has been reported recently [86], however, the use of fluorometry is believed to increase the accuracy of assay used. Presented in the Fig. 20.4a are the typical fluorescence spectra of pyrene residues during the titration by SWCNTs. Fluorescence intensity has been shown to decrease with the increasing of SWCNT concentration as a result of pyrene fluorescence quenching upon adsorption onto SWCNTs [102]. The comparison of isotherms of adsorbtion of 1-pyrenylmethylamine and conjugate $Pyr(rA)_{15}$ on SWCNT-COOH is presented in the Fig. 20.4b. The adsorption of pyrene conjugate of oligonucleotide is defined mostly by adsorption of pyrene residues but the adsorption process is hindered by oligonucleotide itself.

The amount of the adsorbed conjugates was calculated from the data on the fluorescence quenching. The isotherms of adsorption of the pyrene conjugates of oligoribo- and oligodeoxyribonucleotides of different length on the surface of SWCNTs are presented in Fig. 20.3c, d. The capacity values of SWCNTs for oligonucleotides were calculated from adsorption isotherms at the point of reaching a plateau by [96] as quantity of oligonucleotide (μmol) adsorbed onto SWCNTs. Pyrene residues adsorption efficacy slightly decreases with the increase of the oligonucleotide length due, probably, to stacking interactions of the heterocyclic bases of oligonucleotides with the SWCNT surface. The adsorption of oligodeoxyribonucleotides on SWCNT-COOH has been shown to be less effective than those of oligoribonucleotides. The capacity of SWCNTs was amounted to 20–35 μmol of oligonucleotide per gram for oligodeoxyribonucleotides and 30–50 μmol/g for oligoribonucleotides. SWCNT: oligonucleotide ratios resulting
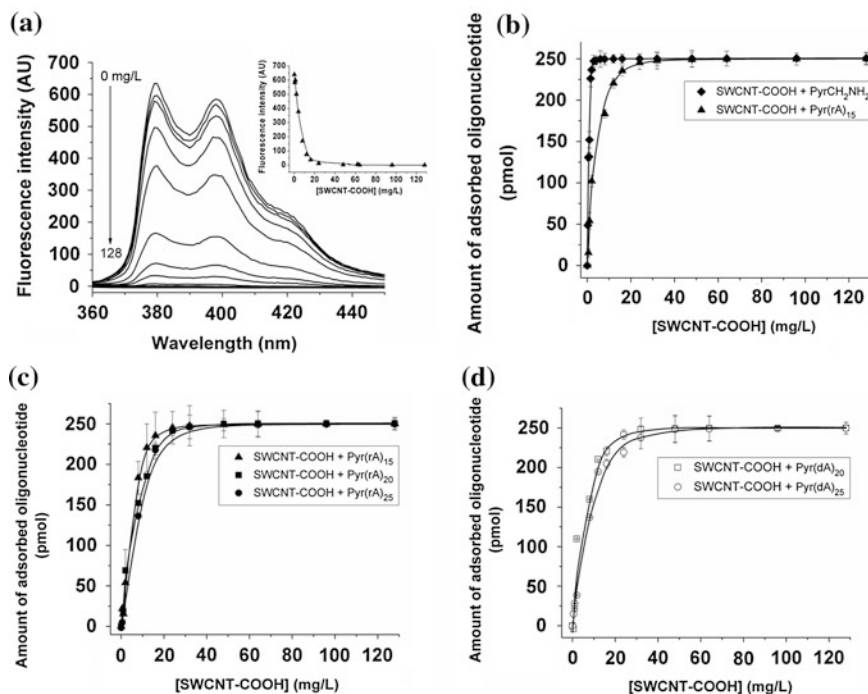
Fig. 20.4 Fluorescence spectra (λ_{ex} = 345 nm) of the hybrid of SWCNT-COOH with Pyr(rA)$_{15}$ at concentrations of SWCNT-COOH from 0 to 128 mg/L (Inset: dependence of fluorescence intensity at λ_{max} = 378 nm on concentration of SWCNTs) (**a**) and adsorption isotherms: 1-pyrenylmethylamine and conjugate Pyr(rA)$_{15}$ on SWCNT-COOH (**b**), pyrene conjugates of oligoribonucleotides on SWCNT-COOH (**c**), pyrene conjugates of oligodeoxyribonucleotides on SWCNT-COOH (**d**). The data in adsorption isotherm plots represent mean ± S.D., n = 3. Conditions: 10 mM Tris-HCl, 1 mM Na$_2$EDTA, 0.1 M NaCl, pH 7.5; 25 °C; oligonucleotide concentration is 1 μM

both in the minima in ζ-potential plots and in reaching a plateau in adsorption isotherms plots were considered optimal for the formation of hybrids.

20.3.3 TEM Observations of Modified SWCNTs and Their Hybrids with Oligonucleotides

The morphology of SWCNT-COOH and their hybrids with oligonucleotides prepared under the optimal conditions was examined using TEM after staining with uranyl acetate. The use of contrasting agents permitted the oligonucleotides on SWCNT surface to be visualized at a relatively low magnification (Fig. 20.5). Visualization is achieved due to electrostatic interactions of uranyl cations with the phosphate groups in the oligonucleotide backbone.

Bundles of SWCNTs with a diameter of 10–20 nm and length up to 1 μm were observed on electron micrographs. The sites of oligonucleotides adsorption were seen after staining as rounded structures with a diameter of about 2–5 nm on the surface of the nanotubes. Electron-dense stripes across SWCNT bundles were also observed. Such a finding is in agreement with the data of Chhikara et al. [68]. The study of the effect of oligonucleotide nature and length on their distribution on SWCNTs was attempted, but unfortunately, TEM observation did not reveal any significant differences in the distribution of electron-dense structures. It should be noted that in the absence of a contrasting agent no electron-dense structures were found on the SWCNT surface.

20.4 Conclusion

In summary, pyrene residues attached to the 5′-termini of oligonucleotides were used as the anchor groups to immobilize the latters onto the SWCNT surface. The formation of non-covalent hybrids of SWCNT-COOH with 5′-pyrene conjugates of oligoribo- and oligodeoxyribonucleotides was demonstrated. By means of fluorescence titration and ζ-potential measurements oligoribonucleotides were shown to interact with SWCNTs more efficiently than oligodeoxyribonucleotides. Both SWCNTs and their hybrids with oligonucleotides were characterized by physico-chemical methods. Since the approach based on the use of pyrene anchor groups is suitable for the attachment of different types of oligonucleotides onto SWCNTs, the regularities of interaction of pyrene conjugates of oligoribo- and oligodeoxyribonucleotides found in this work can be used for the rational design of multifunctional CNT-based constructions as a platform for future therapeutics and diagnostics.

References

1. Eder D (2010) Carbon nanotube-inorganic hybrids. Chem Rev 110:1348–1385. doi:10.1021/cr800433k
2. Tasis D, Tagmatarchis N, Bianco A, Prato M (2006) Chemistry of carbon nanotubes. Chem Rev 106:1105–1136. doi:10.1021/cr050569o
3. Cui D (2007) Advances and prospects on biomolecules functionalized carbon nanotubes. J Nanosci Nanotechnol 7:1298–1314. doi:10.1166/jnn.2007.654
4. Foldvari M, Bagonluri M (2008) Carbon nanotubes as functional excipients for nanomedicines: I. Pharmaceutical properties. Nanomedicine: NBM 4:173–182. doi:10.1016/j.nano.2008.04.002
5. Foldvari M, Bagonluri M (2008) Carbon nanotubes as functional excipients for nanomedicines: II. Drug delivery and biocompatibility issues. Nanomedicine: NBM 4:183–200. doi:10.1016/j.nano.2008.04.003
6. Vashist SK, Zheng D, Pastorin G et al (2011) Delivery of drugs and biomolecules using carbon nanotubes. Carbon 49:4077–4097. doi:10.1016/j.carbon.2011.05.049
7. Cai H, Cao X, Jiang Y et al (2003) Carbon nanotube-enhanced electrochemical DNA biosensor for DNA hybridization detection. Anal Bioanal Chem 375:287–293. doi:10.1007/s00216-002-1652-9
8. Yang X, Lu Y, Ma Y et al (2007) DNA electrochemical sensor based on an adduct of single-walled carbon nanotubes and ferrocene. Biotechnol Lett 29:1775–1779. doi:10.1007/s10529-007-9450-2
9. Duzgun A, Maroto A, Mairal T et al (2010) Solid-contact potentiometric aptasensor based on aptamer functionalized carbon nanotubes for the direct determination of proteins. Analyst 135:1037–1041. doi:10.1039/b926958d

10. Zhang QD, Piro B, Noel V et al (2011) Functionalization of single-walled carbon nanotubes for direct and selective electrochemical detection of DNA. Analyst 136:1023–1028. doi:10.1039/C0AN00486C

11. Zhao C, Qu K, Xu C et al (2011) Triplex inducer-directed self-assembly of single-walled carbon nanotubes: a triplex DNA-based approach for controlled manipulation of nanostructures. Nucleic Acids Res 39:3939–3948. doi:10.1093/nar/gkq1347

12. He P, Dai L (2004) Aligned carbon nanotube-DNA electrochemical sensors. Chem Commun 348–349. doi: 10.1039/B313030B

13. Wang SG, Wang R, Sellin PJ, Zhang Q (2004) DNA biosensors based on self-assembled carbon nanotubes. Biochem Biophys Res Commun 325:1433–1437

14. Berti F, Eisenkolbl C, Minocci D et al (2011) Cannabinoid receptor gene detection by electrochemical genosensor. J Electroanal Chem 656:55–60. doi:10.1016/j.jelechem.2011.01.021

15. Williams KA, Veenhuizen PTM, de la Torre BG et al (2002) Nanotechnology: carbon nanotubes with DNA recognition. Nature 420:761. doi:10.1038/420761a

16. Guo M, Chen J, Liu D et al (2004) Electrochemical characteristics of the immobilization of calf thymus DNA molecules on multi-walled carbon nanotubes. Bioelectrochemistry 62:29–35. doi:10.1016/j.bioelechem.2003.10.005

17. Tam PD, Van Hieu N, Chien ND et al (2009) DNA sensor development based on multi-wall carbon nanotubes for label-free influenza virus (type A) detection. J Immunol Methods 350:118–124. doi:10.1016/j.jim.2009.08.002

18. Baker SE, Cai W, Lasseter TL et al (2002) Covalently bonded adducts of deoxyribonucleic acid (DNA) oligonucleotides with single-wall carbon nanotubes: synthesis and hybridization. Nano Lett 2:1413–1417. doi:10.1021/nl025729f

19. Moghaddam MJ, Taylor S, Gao M et al (2004) Highly efficient binding of DNA on the sidewalls and tips of carbon nanotubes using photochemistry. Nano Lett 4:89–93. doi:10.1021/nl034915y

20. Moghaddam MJ, Yang W, Bojarski B et al (2012) Azide photochemistry for facile modification of graphitic surfaces: preparation of DNA-coated carbon nanotubes for biosensing. Nanotechnology 23:425503. doi:10.1088/0957-4484/23/42/425503

21. Zheng M, Jagota A, Semke ED et al (2003) DNA-assisted dispersion and separation of carbon nanotubes. Nat Mater 2:338–342. doi:10.1038/nmat877

22. Zheng M, Jagota A, Strano MS et al (2003) Structure-based carbon nanotube sorting by sequence-dependent DNA assembly. Science 302:1545–1548. doi:10.1126/science.1091911

23. Liu R, Chen Z, Zhao F et al (2011) Sorting the unique chirality, right handed single wall carbon nanotubes via the dye modified ssDNA. J Nanosci Nanotechnol 11:7587–7592. doi:10.1166/jnn.2011.4717

24. Tu X, Zheng M (2008) A DNA-based approach to the carbon nanotube sorting problem. Nano Res 1:185–194. doi:10.1007/s12274-008-8022-7

25. Tu X, Manohar S, Jagota A, Zheng M (2009) DNA sequence motifs for structure-specific recognition and separation of carbon nanotubes. Nature 460:250–253. doi:10.1038/nature08116

26. Yamamoto Y, Fujigaya T, Niidome Y, Nakashima N (2010) Fundamental properties of oligo double-stranded DNA/single-walled carbon nanotube nanobiohybrids. Nanoscale 2:1767–1772. doi:10.1039/c0nr00145g

27. Ovadekova R, Jantova S, Letasiova S et al (2006) Nanostructured electrochemical DNA biosensors for detection of the effect of berberine on DNA from cancer cells. Anal Bioanal Chem 386:2055–2062. doi:10.1007/s00216-006-0830-6

28. Viswanathan S, Radecka H, Radecki J (2009) Electrochemical biosensor for pesticides based on acetylcholinesterase immobilized on polyaniline deposited on vertically assembled carbon nanotubes wrapped with ssDNA. Biosens Bioelectron 24:2772–2777. doi:10.1016/j.bios.2009.01.044

29. Zeng G, Li Z, Tang L et al (2011) Gold nanoparticles/water-soluble carbon nanotubes/ aromatic diamine polymer composite films for highly sensitive detection of cellobiose dehydrogenase gene. Electrochim Acta 56:4775–4782. doi:10.1016/j.electacta.2011.03.035

30. Tian J, Zhao H, Liu M et al (2012) Detection of influenza A virus based on fluorescence resonance energy transfer from quantum dots to carbon nanotubes. Anal Chim Acta 723:83–87. doi:10.1016/j.aca.2012.02.030

31. Zhou P, He L, Gan G et al (2012) Fabrication and evaluation of [Co(phen)2L]3 + -modified DNA-MWCNT and SDS-MWCNT electrodes for electrochemical detection of 6-mercaptopurine. J Electroanal Chem 665:63–69. doi:10.1016/j.jelechem.2011.11.026

32. Li X, Peng Y, Ren J, Qu X (2006) Carboxyl-modified single-walled carbon nanotubes selectively induce human telomeric i-motif formation. Proc Natl Acad Sci USA 103:19658–19663. doi:10.1073/Proc.Natl.Acad.Sci.U.S.A.0607245103

33. Peng Y, Li X, Ren J, Qu X (2007) Single-walled carbon nanotubes binding to human telomeric i-motif DNA: significant acceleration of S1 nuclease cleavage rate. Chem Commun 5176–5178. doi: 10.1039/b710950d

34. Wu Y, Phillips JA, Liu H et al (2008) Carbon nanotubes protect DNA strands during cellular delivery. ACS Nano 2:2023–2028. doi:10.1021/nn800325a

35. Lu Q, Moore JM, Huang G et al (2004) RNA polymer translocation with single-walled carbon nanotubes. Nano Lett 4:2473–2477. doi:10.1021/nl048326j

36. Chen RJ, Zhang Y (2006) Controlled precipitation of solubilized carbon nanotubes by delamination of DNA. J Phys Chem B 110:54–57. doi:10.1021/jp055044e

37. Yang R, Jin J, Chen Y et al (2008) Carbon nanotube-quenched fluorescent oligonucleotides: probes that fluoresce upon hybridization. J Am Chem Soc 130:8351–8358. doi:10.1021/ja800604z

38. Chen H, Wang J, Liang G et al (2012) A novel exonuclease III aided amplification method for sensitive nucleic acid detection based on single walled carbon nanotube induced quenching. Chem Commun 48:269–271. doi:10.1039/c1cc16127j

39. Hazani M, Naaman R, Hennrich F, Kappes MM (2003) Confocal fluorescence imaging of DNA-functionalized carbon nanotubes. Nano Lett 3:153–155. doi:10.1021/nl025874t

40. Bartholomeusz G, Cherukuri P, Kingston J (2009) In vivo therapeutic silencing of hypoxia-inducible factor 1 alpha (HIF-1 alpha) using single-walled carbon nanotubes noncovalently coated with siRNA. Nano Res 2:279–291. doi:10.1007/s12274-009-9026-7

41. Kirkpatrick DL, Weiss M, Naumov A et al (2012) Carbon nanotubes: solution for the therapeutic delivery of siRNA? Materials 5:278–301. doi:10.3390/ma5020278

42. Li Y, Han X, Deng Z (2007) Grafting single-walled carbon nanotubes with highly hybridizable DNA sequences: potential building blocks for DNA-programmed material assembly. Angew Chem Int Ed 46:7481–7484. doi:10.1002/anie.200701748

43. Cheng E, Li Y, Yang Z et al (2011) DNA-SWNT hybrid hydrogel. Chem Commun 47:5545–5547. doi:10.1039/c1cc11028d

44. Han S, Maune HT, Barish RD et al (2012) DNA-linker-induced surface assembly of ultra dense parallel single walled carbon nanotube arrays. Nano Lett 12:1129–1135. doi:10.1021/nl201818u

45. Lacerda L, Bianco A, Prato M, Kostarelos K (2008) Carbon nanotube cell translocation and delivery of nucleic acids in vitro and in vivo. J Mater Chem 17–22. doi: 10.1039/b711554g

46. Prato M, Kostarelos K, Bianco A (2008) Functionalized carbon nanotubes in drug design and discovery. Acc Chem Res 41:60–68. doi:10.1021/ar700089b

47. Menard-Moyon C, Kostarelos K, Prato M, Bianco A (2010) Functionalized carbon nanotubes for probing and modulating molecular functions. Chem Biol 17:107–115. doi:10.1016/j.chembiol.2010.01.009

48. Yang J, Jiao K, Yang T (2007) A DNA electrochemical sensor prepared by electrodepositing zirconia on composite films of single-walled carbon nanotubes and poly(2,6-pyridinedicarboxylic acid), and its application to detection of the PAT gene fragment. Anal Bioanal Chem 389:913–921. doi:10.1007/s00216-007-1450-5

49. Yang XY, Liu ZF, Mao J et al (2007) The preparation of functionalized single walled carbon nanotubes as high efficiency DNA carriers. Chin Chem Lett 18:1551–1553. doi:10.1016/j.cclet.2007.10.006

50. Krajcik R, Jung A, Hirsch A et al (2008) Functionalization of carbon nanotubes enables non-covalent binding and intracellular delivery of small interfering RNA for efficient knock-down of genes. Biochem Biophys Res Comm 369:595–602. doi:10.1016/j.bbrc.2008.02.072

51. Wang X, Ren J, Qu X (2008) Targeted RNA interference of cyclin A2 mediated by functionalized single-walled carbon nanotubes induces proliferation arrest and apoptosis in chronic myelogenous leukemia K562 cells. ChemMedChem 3:940–945. doi:10.1002/cmdc.200700329

52. Zhao C, Peng Y, Song Y et al (2008) Self-assembly of single-stranded RNA on carbon nanotube: polyadenylic acid to form a duplex structure. Small 4:656–661. doi:10.1002/smll.200701054

53. Zhao C, Song Y, Qu K et al (2010) Luminescent rare-earth complex covalently modified single-walled carbon nanotubes: design, synthesis, and DNA sequence-dependent red luminescence enhancement. Chem Mater 22:5718–5724. doi:10.1021/cm101767c

54. Pan B, Cui D, Xu P et al (2007) Design of dendrimer modified carbon nanotubes for gene delivery. Chin J Cancer Res 19:1–6. doi:10.1007/s11670-007-0001-0

55. Pan B, Cui D, Xu P et al (2009) Synthesis and characterization of polyamidoamine dendrimer-coated multi-walled carbon nanotubes and their application in gene delivery systems. Nanotechnology 20:125101. doi:10.1088/0957-4484/20/12/125101

56. Liu M, Chen B, Xue Y et al (2011) Polyamidoamine-grafted multiwalled carbon nanotubes for gene delivery: synthesis, transfection and intracellular trafficking. Bioconjugate Chem 22:2237–2243. doi:10.1021/bc200189f

57. Wang L, Shi J, Zhang H et al (2013) Synergistic anticancer effect of RNAi and photothermal therapy mediated by functionalized single-walled carbon nanotubes. Biomaterials 34:262–274. doi:10.1016/j.biomaterials.2012.09.037

58. Bianco A, Hoebeke J, Godefroy S et al (2005) Cationic carbon nanotubes bind to CpG oligodeoxynucleotides and enhance their immunostimulatory properties. J Am Chem Soc 127:58–59. doi:10.1021/ja044293y

59. Partidos CD, Hoebeke J, Wieckowski S et al (2009) Immunomodulatory consequences of ODN CpG-polycation complexes. Methods 49:328–333. doi:10.1016/j.ymeth.2009.03.005

60. Herrero MA, Toma FM, Al-Jamal KT et al (2009) Synthesis and characterization of a carbon nanotube-dendron series for efficient siRNA delivery. J Am Chem Soc 131:9843–9848. doi:10.1021/ja903316z

61. Podesta JE, Al-Jamal KT, Herrero MA et al (2009) Antitumor activity and prolonged survival by carbon-nanotube-mediated therapeutic siRNA silencing in a human lung xenograft model. Small 5:1176–1185. doi:10.1002/smll.200801572

62. Pantarotto D, Singh R, McCarthy D et al (2004) Functionalized carbon nanotubes for plasmid DNA gene delivery. Angew Chem Int Ed 43:5242–5246. doi:10.1002/anie.200460437

63. Singh R, Pantarotto D, McCarthy D et al (2005) Binding and condensation of plasmid DNA onto functionalized carbon nanotubes: toward the construction of nanotube-based gene delivery vectors. J Am Chem Soc 127:4388–4396. doi:10.1021/ja0441561

64. Klumpp C, Lacerda L, Chaloin O, et al. (2007) Multifunctionalised cationic fullerene adducts for gene transfer: design, synthesis and DNA complexation. Chem Commun 3762–3764. doi: 10.1039/b708435h

65. Lee H, Mijovic J (2009) Bio-nano complexes: DNA/surfactant/single-walled carbon nanotube interactions in electric field. Polymer 50:881–890

66. Varkouhi AK, Foillard S, Lammers T et al (2011) SiRNA delivery with functionalized carbon nanotubes. Int J Pharmaceutics 416:419–425. doi:10.1016/j.ijpharm.2011.02.009

67. Cha T-G, Baker BA, Sauffer MD et al (2011) Optical nanosensor architecture for cell-signaling molecules using DNA aptamer-coated carbon nanotubes. ACS Nano 5:4236–4244. doi:10.1021/nn201323h

68. Chhikara BS, Misra SK, Bhattacharya S (2012) CNT loading into cationic cholesterol suspensions show improved DNA binding and serum stability and ability to internalize into cancer cells. Nanotechnology 23:065101. doi:10.1088/0957-4484/23/6/065101

69. Zhang H, Baker B a, Cha T-G, et al (2012) DNA oligonucleotide templated nanohybrids using electronic type sorted carbon nanotubes for light harvesting. Adv Mater 24:5447–5451. doi: 10.1002/adma.201201628

70. Chung C-L, Gautier C, Campidelli S, Filoramo A (2010) Hierarchical functionalisation of single-wall carbon nanotubes with DNA through positively charged pyrene. Chem Commun 46:6539–6541. doi:10.1039/C0CC00673D

71. Rege K, Viswanathan G, Zhu G et al (2006) In vitro transcription and protein translation from carbon nanotube-DNA assemblies. Small 2:718–722. doi:10.1002/smll.200500465

72. McCarroll J, Baigude H, Yang C, Rana TM (2010) Nanotubes functionalized with lipids and natural amino acid dendrimers: a new strategy to create nanomaterials for delivering systemic RNAi. Bioconjugate Chem 21:56–63. doi:10.1021/bc900296z

73. Galandová J, Ovádeková R, Ferancová A, Labuda J (2009) Disposable DNA biosensor with the carbon nanotubes-polyethyleneimine interface at a screen-printed carbon electrode for tests of DNA layer damage by quinazolines. Anal Bioanal Chem 394:855–861. doi:10.1007/s00216-009-2740-x

74. Liu Y, Wu DC, Zhang WD et al (2005) Polyethylenimine-grafted multiwalled carbon nanotubes for secure noncovalent immobilization and efficient delivery of DNA. Angew Chem Int Ed 44:4782–4785. doi:10.1002/anie.200500042

75. Luque GL, Ferreyra NF, Granero A et al (2011) Electrooxidation of DNA at glassy carbon electrodes modified with multiwall carbon nanotubes dispersed in polyethylenimine. Electrochim Acta 56:9121–9126. doi:10.1016/j.electacta.2011.07.036

76. Sanz V, Tilmacîu C, Soula B et al (2011) Chloroquine-enhanced gene delivery mediated by carbon nanotubes. Carbon 49:5348–5358. doi:10.1016/j.carbon.2011.08.001

77. Cai D, Doughty A. C, Potocky B. T, et al. (2007) Carbon nanotube-mediated delivery of nucleic acids does not result in non-specific activation of B lymphocytes. Nanotechnology 365101. doi: 10.1088/0957-4484/18/36/365101

78. Guo M, Chen J, Nie L, Yao S (2004) Electrostatic assembly of calf thymus DNA on multi-walled carbon nanotube modified gold electrode and its interaction with chlorpromazine hydrochloride. Electrochim Acta 49:2637–2643. doi:10.1016/j.electacta.2004.02.014

79. Galandova J, Ziyatdinova G, Labuda J (2008) Disposable electrochemical biosensor with multiwalled carbon nanotubes-chitosan composite layer for the detection of deep DNA damage. Anal Sci 24:711–716. doi:10.2116/analsci.24.711

80. Yang T, Zhou N, Zhang Y et al (2009) Synergistically improved sensitivity for the detection of specific DNA sequences using polyaniline nanofibers and multi-walled carbon nanotubes composites. Biosens Bioelectron 24:2165–2170. doi:10.1016/j.bios.2008.11.011

81. Yang T, Zhang W, Du M, Jiao K (2008) A PDDA/poly(2,6-pyridinedicarboxylic acid)-CNTs composite film DNA electrochemical sensor and its application for the detection of specific sequences related to PAT gene and NOS gene. Talanta 75:987–994. doi:10.1016/j.talanta.2007.12.049

82. Ahmed M, Jiang X, Deng Z, Narain R (2009) Cationic glyco-functionalized single-walled carbon nanotubes as efficient gene delivery vehicles. Bioconjugate Chem 20:2017–2022. doi:10.1021/bc900229v

83. Lyonnais S, Goux-Capes L, Escude C et al (2008) DNA-carbon nanotube conjugates prepared by a versatile method using streptavidin-biotin recognition. Small 4:442–446. doi:10.1002/smll.200700586

84. So HM, Park DW, Jeon EK et al (2008) Detection and titer estimation of Escherichia coli using aptamer-functionalized single-walled carbon-nanotube field-effect transistors. Small 4:197–201. doi:10.1002/smll.200700664

85. Yim TJ, Liu J, Lu Y et al (2005) Highly active and stable DNAzyme-carbon nanotube hybrids. J Am Chem Soc 127:12200–12201. doi:10.1021/ja0541581

86. Liu Z, Galli F, Waterreus W-J et al (2012) Single-walled carbon nanotubes as scaffolds to concentrate DNA for the study of DNA-protein interactions. ChemPhysChem 13:1569–1575. doi:10.1002/cphc.201100896

87. Delogu LG, Magrini A, Bergamaschi A et al (2009) Conjugation of antisense oligonucleotides to PEGylated carbon nanotubes enables efficient knockdown of PTPN22 in T lymphocytes. Bioconjugate Chem 20:427–431. doi:10.1021/bc800540j

88. Kam NW, Liu Z, Dai H (2005) Functionalization of carbon nanotubes via cleavable disulfide bonds for efficient intracellular delivery of siRNA and potent gene silencing. J Am Chem Soc 127:12492–12493. doi:10.1021/ja053962k

89. Lanner JT, Bruton JD, Assefaw-Redda Y et al (2009) Knockdown of TRPC3 with siRNA coupled to carbon nanotubes results in decreased insulin-mediated glucose uptake in adult skeletal muscle cells. FASEB J 23:1728–1738. doi:10.1096/fj.08-116814

90. Liu Z, Tabakman SM, Chen Z, Dai H (2009) Preparation of carbon nanotube bioconjugates for biomedical applications. Nat Protoc 4:1372–1382. doi:10.1038/nprot.2009.146

91. Liu Z, Winters M, Holodniy M, Dai H (2007) siRNA delivery into human T cells and primary cells with carbon-nanotube transporters. Angew Chem Int Ed 46:2023–2027. doi:10.1002/anie.200604295

92. Baek Y-K, Jung D-H, Yoo SM et al (2011) Label-free detection of DNA hybridization using pyrene-functionalized single-walled carbon nanotubes: effect of chemical structures of pyrene molecules on DNA sensing performance. J Nanosci Nanotechnol 11:4210–4216. doi:10.1166/jnn.2011.3663

93. Maehashi K, Katsura T, Kerman K et al (2007) Label-free protein biosensor based on aptamer-modified carbon nanotube field-effect transistors. Anal Chem 79:782–787. doi:10.1021/ac060830g

94. So HM, Won K, Kim YH et al (2005) Single-walled carbon nanotube biosensors using aptamers as molecular recognition elements. J Am Chem Soc 127:11906–11907. doi:10.1021/ja053094r

95. Taft BJ, Lazareck AD, Withey GD et al (2004) Site-specific assembly of DNA and appended cargo on arrayed carbon nanotubes. J Am Chem Soc 126:12750–12751. doi:10.1021/ja045543d

96. Apartsin EK, Novopashina DS, Nastaushev YV, Venyaminova AG (2012) Fluorescently labelled single-walled carbon nanotubes and their hybrids with oligonucleotides. Nanotechnol Russ 7:99–109. doi:10.1134/S1995078012020024

97. Novopashina DS, Apartsin EK, Venyaminova AG (2012) Fluorescently labeled bionanotransporters of nucleic acid based on carbon nanotubes. Ukr J Phys 57:718–722

98. Novopashina DS, Sinyakov AN, Ryabinin VA et al (2005) Sequence-specific conjugates of oligo(2′-O-methylribonucleotides) and hairpin oligocarboxamide minor-groove binders: design, synthesis, and binding studies with double-stranded DNA. Chem Biodiv 2:936–952. doi:10.1002/cbdv.200590071

99. Novopashina DS, Totskaya OS, Kholodar SA et al (2008) Oligo(2'-O-methylribonucleotides) and their derivatives: III. 5'-Mono- and 5'-bispyrenyl derivatives of oligo(2'-O-methylribonucleotides) and their 3'-modified analogues: synthesis and properties. Russ J Bioorg Chem 34:602–612. doi:10.1134/S1068162008050105

100. Zarytova V, Ivanova E, Venyaminova A (1998) Design of functional diversity in oligonucleotides via zwitter-ionic derivatives of deprotected oligonucleotides. Nucleosides Nucleotides 17:649–662. doi:10.1080/07328319808005207

101. Zarytova VF, Godovikova TS, Kutyavin IV, Khalimskaya LM (1987) Reactive oligonucleotide derivatives as affinity reagents and probes in molecular biology. In: Bruzik KS, Stec WS (eds) Biophosphates and their analogues, synthesis, structure, metabolism and activity. Elsevier, Amsterdam, pp 149–164

102. Wang L, Zhang L, Xue X et al (2012) Enhanced dispersibility and cellular transmembrane capability of single-wall carbon nanotubes by polycyclic organic compounds as chaperon. Nanoscale 4:3983–3989. doi:10.1039/c2nr30346a

Chapter 21
Sol–Gel Organic–Inorganic Hybrid Materials Containing Lanthanide Complexes with Polydentate Acyclic and Cyclic Ligands: Synthesis and Spectral-Luminescent Properties

S. S. Smola, O. V. Snurnikova, E. N. Fadeyev and N. V. Rusakova

Abbreviations

APTMS	(3-aminopropyl)trimethoxysilane
DMF	*N,N*-Dimethylformamide
DTPA	Diethylenetriaminepentaacetic acid
EDTA	Ethylenediaminetetraacetic acid
ESI	Electrospray ionization
ET	Energy transfer
FTIR	Fourier transform infrared spectroscopy
IR	Infrared
ISC	Intersystem crossing
Ln(III)	Lanthanide(III)
NMR	Nuclear magnetic resonance
OLED	Organic light-emitting diode
TBC	25,26,27,28-tetrahydroxy-*p-tert*-butylcalix[4]arene
TEOS	Tetraethyl orthosilicate
TESPIC	3-(triethoxysilyl)propyl isocyanate
THF	Tetrahydrofuran
UV	Ultraviolet
m	Multiplet (NMR-spectra)
s	Singlet
t	Triplet
I_{4f}	4f-Luminescence intensity
S_0	Ground singlet state
S_1	First excited singlet state

S. S. Smola · O. V. Snurnikova · E. N. Fadeyev · N. V. Rusakova (✉)
Department of Chemistry of Lanthanides, A.V. Bogatsky Physico-Chemical Institute,
National Academy of Sciences of Ukraine, Lustdorfskaya doroga, 86, Odessa 65080, Ukraine
e-mail: lanthachem@ukr.net

T_1 First excited triplet state
λ_{ex} Excitation wavelength
λ_{em} Emission wavelength
τ Excited state lifetime

Design and study of new luminescent compounds as active components of nanomaterials is one of the challenges for scientists working on light-emitting devices, luminescent thin films, OLEDs, optical amplifiers, solar energy conversion, alternative light sources, and other. Among a large number of luminescent compounds lanthanide-containing ones should be noted as unique luminescent probes. The emission spectra of lanthanide ions is described as narrow bands covering the wide range from the UV (Gd(III)) to visible (Pr(III), Sm(III), Eu(III), Tb(III), Dy(III), Tm(III)) and near-infrared (Pr(III), Nd(III), Ho(III), Er(III), Yb(III)). The lifetimes of lanthanide emission are rather large, e.g., 0.2–0.5 ms for Nd(III), 1–11 ms for Eu(III) [1–3]. These unique properties of the lanthanide emission (4f-emission) are the result of the forbidden transitions between f-orbitals of the inner 4f-shell, shielded by the filled 5s—and 5p-shells. Because of this shielding the influence of the local environment of the lanthanide ion is limited.

Since all lanthanide ions have low molar absorption coefficients (<10 L mol^{-1} cm^{-1}), the direct excitation in absorption bands of f–f-transitions leads to weak 4f-emission. One of the efficient method to improve 4f-luminescent characteristics is sensibilization of lanthanide luminescence in complexes with strongly absorbing organic ligands [3]. Under excitation at the absorption bands of organic ligands much more energy can be absorbed by the organic chromophores than the lanthanide ion itself. Then the excitation energy is transferred from the organic ligands to the lanthanide ion by intramolecular energy transfer mechanism. The scheme of the commonly accepted mechanism of energy transfer from the organic ligands to the lanthanide [4, 5] is presented in Fig. 21.1.

The organic ligands absorbing energy are excited to one of the vibrational levels of the first excited singlet state ($S_0 \rightarrow S_1$). The molecule undergoes fast internal conversion to the lowest vibrational level of the S_1-state. The excited singlet state can be deactivated radiatively to the ground state exhibiting molecular fluorescence ($S_1 \rightarrow S_0$) or go through nonradiative intersystem crossing from the singlet state S_1 to the triplet state T_1. The triplet state T_1 can be deactivated radiatively to the ground state S_0 by the spinforbidden transition $T_1 \rightarrow S_0$. This results in molecular phosphorescence. A nonradiative transition from the triplet state to an excited state of the lanthanide ion can occur. After this indirect excitation by energy transfer, the lanthanide ion may undergo a radiative transition to a lower 4f state by characteristic narrow band luminescence or may be deactivated by nonradiative or back transfer processes. Such indirect excitation leads to a large Stoke's shift and efficient 4f-luminescence and gives many advantages to lanthanide complexes as luminescent probes. On the other hand, studying the 4f-luminescence some information on the local structure around lanthanide ion can be gained: number of metal-ion sites,
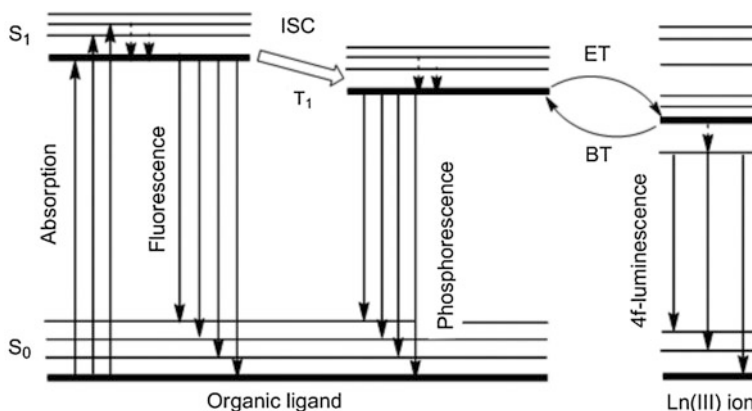
Fig. 21.1 Schematic energy diagram showing main photophysical processes in lanthanide complexes

composition and symmetry of the first coordination sphere, solution state of the Ln(III) ion, or donor–acceptor distances [6–10].

Design of highly luminescent lanthanide complexes implies the improvement of two main factors that determine the efficiency of 4f-luminescence: energy transfer and minimization of non-radiative processes. Concerning the first one there is an energy match criteria suggested on simplified model that the only existing pathway of energy transfer is from ligand triplet state. The energy difference between the singlet S_1 and triplet T_1 $\Delta E(S_1-T_1)$ should be at about 5000 cm^{-1} and between triplet state and emissive level $\Delta E(T_1-Ln^{3+})$—in the range of 2500–3500 cm^{-1} [11, 12]. A close match between the energy of the triplet state and the energy of the receiving 4f-level of the lanthanide ion is not desirable because energy back transfer of the lanthanide ion to the triplet state can occur [13, 14].

The main reason of deactivation processes of excited 4f-states is vibronic coupling with the ligand and solvent molecules. High energy vibrations, such as O–H, N–H, C–H, quench the lanthanide luminescence, especially for Nd(III), Er(III), and Yb(III) emitting in near IR range. There is a number of synthetic methods for elimination of radiationless losses of energy, such as perhalogenation (usually, perfluorination [15–17]) or deuteration [18–20] of ligand, confinement of coordination of solvent molecules to lanthanide ion: synthesis in deuterated media [21, 22], in presence of surfactants [23–25] or heteroligand chelation [26], insertion of the lanthanide ion in pre-organized environment, e.g., macrocyclic ligands (pophyrins [27–29], calix[n]arenes [30–33], for instance), metall-organic frameworks [34, 35]. Generally, the use of these methods sometimes requires difficult experimental technique and increases the cost of the lanthanide-based material for its practical use. Recent studies on organic–inorganic hybrids containing lanthanide ions have demonstrated their technological potential. In lanthanide-containing

hybrid materials usually the complex is embedded in an organic (e.g., poly(methyl methacrylate), poly(vinyl alcohol), poly (N-vinylcarbazole) [36–38]), or inorganic (e.g., SiO_2-, Al_2O_3-, TiO_2-based sol-gel materials [39–41]) polymeric host matrix. The benefit of such organic–inorganic materials is its superior mechanical and thermal stability and luminescence output than the molecular lanthanide complex. In this context, the sol–gel method is a powerful tool for embedding lanthanide complex into an inorganic host and processing of hybrid materials as well as nanocomposites, nanoparticles with interesting properties.

In this work, in order to obtain hybrid materials containing lanthanide complexes covalently bonded to a silica polymeric network the following strategy was applied. At first, the organic ligands were modified by reaction with amino- or isocyano-derivatives of trialkoxysilane. Then the stage of complex formation with Ln(III) ion was held. And finally a hybrid material was obtained by sol–gel process. As organic ligands aminopolycarboxylic (ethylenediaminetetraacetic (EDTA) and diethylenetriaminepentaacetic (DTPA)) acids and *p-tert*-butylcalix[4]arene (TBC) were used. The advantage of EDTA and DTPA is high stability of Ln(III) complexes [42], that is important for acid- or base-catalyzed sol–gel synthesis. The aminopolycarboxylic acids possess enough donor atoms to fill high coordination number of Ln(III) ions. The influence of the silica host on the 4f-luminescence can be also studied due to the absence of strong light-absorbing functional groups in EDTA and DTPA. In contrast with aminopolycarboxylates *p-tert*-butylcalix[4]arene (TBC) have strong absorption band in the UV-region and it is one of the suitable ligands for sensitization of Ln(III) luminescence due to aromatic fragments playing a role of "photoantenna" [43, 44]. Furthermore, *p-tert*-butyl radicals at the upper rim of calix[4]arene stabilize the "cone" conformation of the macrocycle and provide its conformational stability in chemical reactions. The hydroxyl groups on the lower rim of calix[4]arene quite easily undergo chemical modifications with substitution of mobile hydrogen atoms that allows to provide covalent bonding of ligand/complex species to an inorganic carrier.

All synthesized compounds and materials have been characterized by elemental analysis, ESI-mass spectrometry, IR- and ^{1}H NMR-spectroscopy. Elemental analysis (C, H, N) was carried out on Perkin–Elmer CHN-240 analyzer. The content of the lanthanide ions was determined by complexometric titration. ESI-Mass spectra of compounds were recorded on Waters ESI TOF Premier spectrometer. ^{1}H NMR spectra were obtained on Bruker Avance AV 400 (400 MHz) spectrometer in D_2O solutions at pH $\approx$ 10 (with the addition of NaOD) for aminopolycarboxylic acids and in $CDCl_3$ ion the case of calixarene and its complexes. IR spectra were recorded on Perkin–Elmer Frontier FT-IR spectrometer in KBr pellets.

Aminopolycarboxylic acids were modified by reaction of dianhydride of relevant acid with (3-aminopropyl)-trimethoxysilane (APTMS) according to modified method described in [45]. Aminopolycarboxylic acid dianhydride (5 mmol) was dissolved in 150 ml of anhydrous DMF with slight heating. Then an equimolar amount of APTMS was added dropwise. The reaction mixture was stirred at 80 °C for 48 h. Then 100 ml of THF were added, formed white precipitate was filtered

and recrystallized from solvent mixture DMF-benzene (1:1). EDTA-APTMS: Yield 83 %. M.p. > 250 °C (dec.). Elemental analysis: found for $C_{16}H_{31}N_3O_{10}Si$ %: C, 42.35; H, 6.91; N, 9.11; calculated, %: C, 42.37; H, 6.89; N, 9.27. ESI-MASS, m/z: 453 ($[M]^-$), 393 ($[M–2CH_3-OCH_3]^-$), 334 ($[M–2CH_3–OCH_3–CH_2COOH]^-$). ^1H NMR, δ (D_2O): 0.71 t (2H, $–CH_2-Si$, J = 8.29 Hz), 1.64 m (2H, $–CH_2–CH_2-Si$, J = 7.53 Hz), 3.00 t (2H, $–CH_2–H_2–CH_2–Si$, J = 7.15 Hz), 3.20–3.35 m (4H, $N–CH_2–CH_2–N$), 3.09 s (2H, $–CH_2–CONH–$), 3.52 s (6H, $–CH_2–COO^-$). DTPA-APTMS: Yield 79 %. M.p. > 250 °C (dec.). Elemental analysis: found for $C_{20}H_{38}N_4O_{12}Si$, %: C, 43.47; H, 6.79; N 10.31; calculated, %: C, 43.31; H, 6.91; N 10.10. ESI-MASS, m/z: 554 ($[M]^-$), 493 ($[M–2CH_3–OCH_3]^-$), 391 ($[M–(CH_2)_3Si(OMe)_3]^-$). ^1H NMR, δ (D_2O): 0.59 t (2H, $–CH_2-Si$, J = 7.79 Hz), 1.67 m (2H, $–CH_2–CH_2-Si$, J = 7.60 Hz), 2.90 t (2H, $–CH_2–CH_2–CH_2-Si$, J = 6.02 Hz), 2.97 t (4H, $N–CH_2–CH_2–N$, J = 5.77 Hz), 3.09 t (4H, $N–CH_2–CH_2–N$, J = 5.77 Hz), 3.33 c (8H, $–CH_2–COO^-$), 3.49 c (2H, $–CH_2–CONH–$).

The second step was synthesis of the lanthanide complexes with modified aminopolycarboxylic acids. Complex with paramagnetic ion Lu(III) was obtained for NMR spectroscopic studies. EDTA-APTMS (or DTPA-APTMS) (0.10 mmol) was dissolved in 10 ml of 0.01 M NaOH (pH = 8.0 ± 0.5) under heating. Then 0.10 mmol of lanthanide (III) chloride was added and stirred at 80 °C for 5 h. Then the solution was filtered, evaporated, and the solid residue was isolated by adding 20 mL of acetone, centrifuging and washing with ethanol and water several times. Elemental analysis: Nd-EDTA-APTMS, found for $C_{13}H_{25}N_3NaNdO_{12}Si$, %: C, 25.69; H, 4.27; N, 6.63; Nd, 23.78; calculated, %: C, 25.57; H, 4.13; N, 6.88; Nd, 23.62. Eu-EDTA-APTMS, found for $C_{13}H_{25}N_3NaEuO_{12}Si$, %: C, 25.39; H, 4.01; N, 6.97; Eu, 24.39; calculated, %: C, 25.25; H, 4.07; N, 6.80; Eu, 24.57. Tb-EDTA-APTMS, found for $C_{13}H_{25}N_3NaTbO_{12}Si$, %: C, 25.11; H, 3.93; N, 6.91; Tb, 25.57; calculated, %: C, 24.97; H, 4.03; N, 6.72; Tb, 25.41. Yb-EDTA-APTMS, found for $C_{13}H_{25}N_3NaYbO_{12}Si$, %: C, 24.29; H, 3.99; N, 6.77; Yb, 27.18; calculated, %: C, 24.42; H, 3.94; N, 6.57; Yb, 27.06. Lu-EDTA-APTMS, found for $C_{13}H_{25}N_3NaLuO_{12}Si$, %: C, 24.51; H, 3.81; N, 6.38; Lu, 27.35; calculated, %: C, 24.34; H, 3.93; N, 6.55; Lu, 27.28. ESI-MASS, m/z: 618 ($[M–Na]^-$), 518 ($[M–(CH_2)_3SiOONa]^-$). ^1H NMR, δ (D_2O): 0.79 t (2H, $–CH_2-Si$, J = 7.78 Hz), 1.81 m (2H, $–CH_2–CH_2-Si$, J = 7.71 Hz), 3.04 t (2H, $–CH_2–CH_2–CH_2–Si$, J = 7.61 Hz), 2.75 s (4H, $N–CH_2–CH_2–N$), 3.00-3.50 m (8H, $–CH_2–COO^-$, $–CH_2–CONH–$). Nd-DTPA-APTMS, found for $C_{17}H_{27}NdN_4NaO_{12}Si$, %: C, 30.34; H, 4.19; N, 8.13; Nd, 21.22; calculated, %: C, 30.26; H, 4.03; N, 8.30; Nd, 21.38. Eu-DTPA-APTMS found for $C_{17}H_{27}EuN_4NaO_{12}Si$, %: C, 29.83; H, 3.81; N, 8.39; Eu, 22.41; calculated, %: C, 29.92; H, 3.99; N, 8.21; Eu, 22.27. Tb-DTPA-APTMS, found for $C_{17}H_{27}TbN_4NaO_{12}Si$, %: C, 29.86; H, 3.77; N, 8.29; Tb, 22.89; calculated, %: C, 29.62; H, 3.95; N, 8.13; Tb, 23.05. Yb-DTPA-APTMS, found for $C_{17}H_{27}YbN_4NaO_{12}Si$, %: C, 29.22; H, 3.75; N, 7.79; Yb, 24.81; calculated, %: C, 29.02; H, 3.87; N, 7.96; Yb, 24.60. Lu-DTPA-APTMS, found for $C_{17}H_{27}LuN_4NaO_{12}Si$, %: C, 28.79; H, 3.99; N, 7.81; Lu, 24.99; calculated, %: C, 28.94; H, 3.86; N, 7.94; Lu, 24.80. ESI-MASS, m/z: 684

([M–Na]$^-$), 665 ([M–H$_2$O–Na]$^-$), 582 ([M–(CH$_2$)$_3$SiOONa]$^-$). ^{1}H NMR, δ (D$_2$O): 0.71 t (2H, –CH$_2$–Si, J = 8.02 Hz), 1.77 m (2H, –C*H$_2$*–CH$_2$-Si), 3.01 t (2H, –*CH$_2$*–CH$_2$–CH$_2$–Si), 2.55 t (2H, N–CH$_2$–, J = 6.28 Hz), 2.72 t (2H, N–CH$_2$–, J = 5.78 Hz), 2.94 t (2H, N-CH$_2$–, J = 6.78 Hz), 2.97 t (2H, N–CH$_2$–, J = 5.77 Hz), 3.29–3.70 m (10H, –CH$_2$–COO$^-$, –*CH$_2$*–CONH–).

The lanthanide-containing nanocomposites were synthesized using adapted Stöber method [46]. TEOS (5 mmol, 1.12 ml) was added to a mixture of absolute ethanol (7.2 ml) and distilled water (0.08 ml) and stirred for 30 min, followed by the addition of 0.1 mmol of the Ln(III) complex (Ln-EDTA-APTMS or Ln-DTPA-APTMS) in 5 ml of water (pH = 7.0–7.5). Then 2 ml of NH$_4$OH (25 %) was added. Stirring was continued at the same temperature during 30 min. The resulting samples were isolated by adding 20 ml of acetone, centrifuging and washing with ethanol and water several times to remove the unreacted materials that were dried at reduced pressure at 95–100 °C for 2 weeks. The molar ratio of the components in the synthesis was TEOS : Ln(III) complex = 50:1.

The modification of aminopolycarboxylic acids and formation lanthanide (III) complexes were confirmed by ESI-mass spectrometry, ^{1}H NMR and FT-IR-spectroscopy. In the ESI-mass spectrum of EDTA-APTMS peaks with m/z 453 [M], 393 [M–2CH$_3$O–CH$_3$] and 317 [M–CH$_2$Si(OCH$_3$)$_3$] are present. The spectrum of DTPA-APTMS displays peaks with m/z 493 ([M–2CH$_3$–OCH$_3$]$^-$), 447 ([M–Si(OCH$_3$)$_3$]) and 391 ([M–(CH2)$_3$Si–(OCH$_3$)$_3$]$^-$). In the spectra of Eu(III) and Lu(III) complexes the most intense peaks correspond to molecular ion without coordinated water molecules.

The presence of trimethoxysilyl-groups in EDTA- APTMS and DTPA-APTMS due to its unsymmetrical structure causes magnetical non-equivalence of some protons and complication of ^{1}H NMR spectra as compared to free EDTA and DTPA [47]. In the spectrum of DTPA-APTMS, for instance, the signals of N(CH$_2$)$_2$ N-protons appear as two triplets at 2.97 and 3.90 ppm, signals of NCH$_2$COO–fragments are two singlets at 3.33 and 3.49 ppm. There are three signals corresponding to three methylene groups of propyl fragment at 0.59, 1.67, and 2.90 ppm.

The formation complex of EDTA- APTMS and DTPA-APTMS with Lu(III) ions leads to similar changes in ^{1}H NMR spectra due to limitation of the con-formational rotation around single C–C and C–N bonds under the coordination of the metal. Such changes in the spectra are typical for aminopolycarboxylates. For example, in the spectrum of Lu-DTPA-APTMS there is a small low field shift (0.10–0.12 ppm) of propyl protons signals, four triplets at 2.55–2.97 ppm were observed instead of two triplets of ethylenediamine protons in DTPA-APTMS, multiplet at 3.25–3.50 ppm was registered instead of two singlets from N–CH$_2$–COO-fragments.

The comparison of the FTIR spectra of the modified ligands, complexes, and hybrid materials was made. The FTIR spectra of DTPA-APTMS, its Eu(III) complex and hybrid material are shown as an example in Fig. 21.2. In the spectrum of DTPA-APTMS a broad band at 1052–1144 cm^{-1} and the band at 911 cm^{-1} correspond to the asymmetric and symmetric vibrations of the Si–O–C

bonds, respectively. Peak at 480 cm^{-1} corresponds to the deformation vibrations O–Si–O, and the peak at 694 cm^{-1} probably caused by the stretching vibrations Si–C. Peaks at 1634 cm^{-1} and 1385–1398 cm^{-1} were attributed to v_{as} (COO^-) and v_s (COO^-), respectively. A shoulder at 1733 cm^{-1} corresponds to nonionized carboxyl group. Band of deformation vibrations of amino-group of APTMS at 1577 cm^{-1} [48] is absent in the spectrum of DTPA-APTMS, confirming the formation of amide bond. The direct observation of amide bond vibrations is complicated, probably, due to its overlay with the vibrations of carboxylic groups. The band at 2548 cm^{-1}corresponds to stretching vibrations of R_3N^+–H fragments. Peaks at 2936, 2972, 3026 cm^{-1} were attributed to stretching vibrations of –C–H groups located near nitrogen atom.

In the FTIR spectrum of the complex Eu-DTPA-APTMS (Fig. 21.2b) a shift of v_{as} (COO^-) ($\Delta v = 40$ cm^{-1}) is observed, which confirms the coordination with Eu(III). The vibrations of R_3N^+–H fragment disappears in spectrum of complex. Stretching vibration of-CH_2– groups are at 2855, 2927 and 2981 cm^{-1} and bending vibration are at 1328 and 1446 cm^{-1}. v_s(COO^-) are manifested in the form of signals at 1385 and 1410 cm^{-1}. The bands at 1094 and 1119 cm^{-1} are
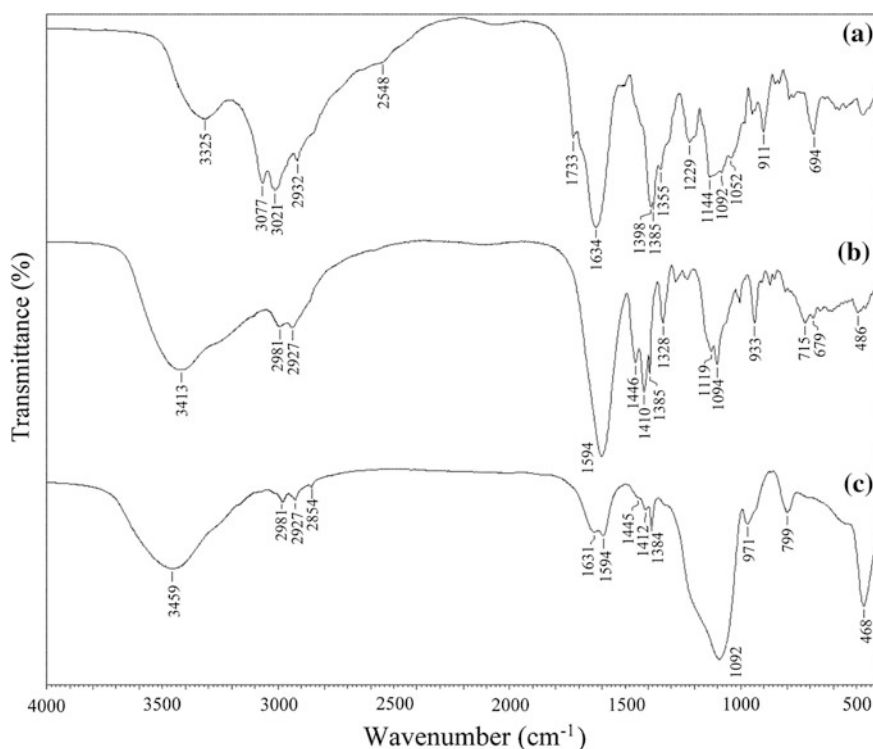
Fig. 21.2 FTIR spectra of DTPA-APTMS (**a**) Eu-DTPA-APTMS (**b**) and Eu-DTPA-APTMS-SiO_2 (**c**) in KBr pellets

assigned to the stretching vibrations of Si–OH, which arise as a result of hydrolysis. The IR spectra also confirm the absence of polycondenzation of hydrolyzed fragments: peak corresponding to bending vibrations Si–O–Si at 799 cm^{-1} is absent. The bands at 679, 715 cm^{-1} correspond to oscillation of C–Si bond.

The FTIR spectra of sol–gel materials represent a superposition of spectra of SiO$_2$ [49] and Ln-DTPA-APTMS (or Ln-EDTA-APTMS). The peaks at 468 and 799 cm^{-1} were attributed to O–Si–O and Si–O-Si bending vibrations, respectively; bands of symmetric and asymmetric stretching vibrations of Si–O–Si are located at 970 and 1088 cm^{-1}. Some hydroxyl groups remaining in structure of materials give the band at 1639 cm^{-1} (bending vibrations of Si–OH groups) and a broad band at 3459 cm^{-1} (stretching vibrations of O–H groups). It is worth noting that position of the main absorption bands of the complex does not change, confirming the preservation of its structure in synthesized hybrid.

The calix[4]arene-derived hybrid materials were also synthesized in several steps. The lower rim of the TBC ligand was modified by reaction with 3-(triethoxysilyl)propyl isocyanate (TESPIC), wherein active isocyanine group reacts with hydroxyl group of calix[4]arene on the mechanism of nucleophilic addition, according to similar method described in [50, 51]. *p-Tert*-butylcalix[4]arene (0.324 g, 0.5 mmol) was dissolved in 20 ml of pyridine, and 3-(ethoxysilyl)propyl isocyanate (0.124 g, 0.5 mmol) in 5 ml of pyridine was added dropwise with stirring. The reaction mixture was kept under stirring at 60–65 °C for 8–10 h. After the end of reaction, the solvent was removed. The obtained product was recrystallized from toluene. Elemental analysis, calculated for C$_{54}$H$_{77}$NSiO$_8$: C, 72.4, H, 8.6; found C, 72.6, H, 8.4. ^{1}H NMR (CDCl$_3$) δ, ppm: 0.63 (t, 2H, CH$_2$Si), 1.10 (t, 9H, C<u>H$_3$</u>CH$_2$), 1.22 (s, 9H, C(CH$_3$)$_3$), 1.27 (s, 27H, C(CH$_3$)$_3$), 1.62–1.68 (m, 6H, CH$_3$<u>CH$_2$</u>), 3.15–3.21 (m, 2H, <u>CH$_2$</u>CH$_2$CH$_2$), 3.51 (d, 4H, ArCH$_2$Ar), 3.75–3.81 (m, 2H, <u>CH$_2$</u>CH$_2$CH$_2$) 4.12 (d, 2H, ArCH$_2$Ar), 4.25 (d, 2H, ArCH$_2$Ar), 4.55 (s, 1H, NH), 7.06 (s, 6H, ArH), 7.23 (s, 2H, ArH), 10.35 (s, 1H, OH).

Ln-TBC-containing hybrid materials were prepared without isolation of Ln(III) complex. To a solution of TBC-TESPIC (0.0216 g, 0.024 mmol) in 5 ml of DMF an equimolar amount of lanthanide chloride was added. The reaction mixture was stirred for 3 h, tetraethoxysilane (TEOS) was added (0.250 g, 1.2 mmol) and stirring was continued for another 4 h. Then 0.02 ml of concentrated hydrochloric acid and 30 ml of distilled water was added to the resulting solution under careful stirring. The final hybrids were isolated by adding 20 mL of acetone, centrifuging, and washing with ethanol and water several times to remove the unreacted materials. The molar ratio of the components in the synthesis was TEOS:Ln(III) complex = 50:1.

The presence of TBC ligand covalently bonded to a silica polymeric host was identified by means of FTIR spectroscopy. In the spectrum of TBC-TESPIC stretching vibration bands of the hydroxyl groups is shifted to higher frequencies compared to TBC ($v_{(OH)}$ = 3163 cm^{-1}) and overlaps with the absorption band of the NH-vibrations forming a broad band with a peak at 3338–3345 cm^{-1}. Increasing the intensity of absorption bands with maxima at 2964 and 2913 cm^{-1} is more than twofold due to the superposition of vibration bands of substituent

CH$_2$-groups and signals of methylene bridge of calixarene macrocycle. The vibrations of N=C=O groups originating from TESPIC were not obserfed at 2270–2280 cm^{-1}, indicating the modification of TBC. In contrast to the initial calix[4]arene, there are also bands of stretching vibrations of the carbonyl group ($\nu_{(c=o)}$ = 1658 cm^{-1}) and ethoxysilylic fragment ($\nu_{(Si–O)}$ = 1112 cm^{-1}, $\nu_{(Si–C)}$ = 1210 cm^{-1}).

As in the case of aminopolycarboxylates the FTIR spectra of calix[4]arene-containing hybrids consist of bands of Ln(III)–TBC complex [52, 53] superimposed on absorption bands of SiO$_2$. The spectra reveal a red shift of the band of phenolic groups bending vibrations ($\Delta\delta_{c-O-H}$ = 18–20 cm^{-1}) and the shift in the low-frequency of bands of stretching vibrations of carbonyl fragments ($\nu_{(c=o)}$ = 1635 см$^{-1}$), these changes indicate the coordination of the se groups with lanthanide ion. Reduction of the frequency of Si–O-bonds oscillations ($\nu_{(Si–O)}$ = 1040 cm^{-1}) caused due to the hydrolysis of the fragments and the formation of SiO$_2$-skeleton matrix.

Thus sol–gel organic–inorganic hybrid materials Ln-EDTA-APTMS/SiO$_2$, Ln-DTPA-APTMS/SiO$_2$, and Ln-tBC-TESPIC/SiO$_2$ (Ln(III) = Nd, Eu, Tb, Yb, Er, Lu) were synthesized (Fig. 21.3). The scanning electron microphotographs demonstrate the microstructure of hybrids. The morphology of the Ln(III) aminopolycarboxylate-containing hybrids Ln-DTPA-APTMS/SiO$_2$ is rough and the intensive tendency of growing into inorganic polymer is observed with reservation of the coordinated positions in corresponding bulk materials. In the case of calix[4]arene-based hybrid the configuration of the organosilane is mixed up and it is difficult to form an organized structure under the weak interactions such as π–π-staking and because of the coordination between organic groups in TBC-TESPIC and lanthanide ions.

The microstructure of sol–gel materials significantly depends on conditions of the synthesis and the formation and the growth rates of the sol particles during the stage of sol formation [53]. Thus, at pH < 7 the rate of particles formation is greater than the rate of growth that leads to a large number of little particles (less than 10 nm) which form a three-dimensional structure. At pH = 7–10 the growth rate of particles dominates and their size can reach about 1000 nm, but further increase in size may lead to their deposition from solutions. On the photo the formation of spherical nanoparticles could not be observed that suggests their aggregation with forming of a three-dimensional matrix on the early stages of growth (up to 5 nm).

The emission spectra of silica-modified ligands were studied to estimate the position of singlet and triplet levels from the fluorescence and phosphorescence spectra and the possibility of the excitation energy transfer to Ln(III) ion. The emission spectra of Lu-EDTA-APTMS/SiO$_2$ (Fig. 21.4a) and Lu-DTPA-APTMS/SiO$_2$ at 298 K show fluorescence in the range of 400–600 nm with maximum at 421 and 413 nm, respectively. At 77 K the maxima of this band shift to 446 nm and 483 nm for EDTA-and DTPA-derived samples, respectively. In the case of Lu-TBC-TESPIC/SiO$_2$ the sample exhibits fluorescence at 406 nm and phosphorescence at
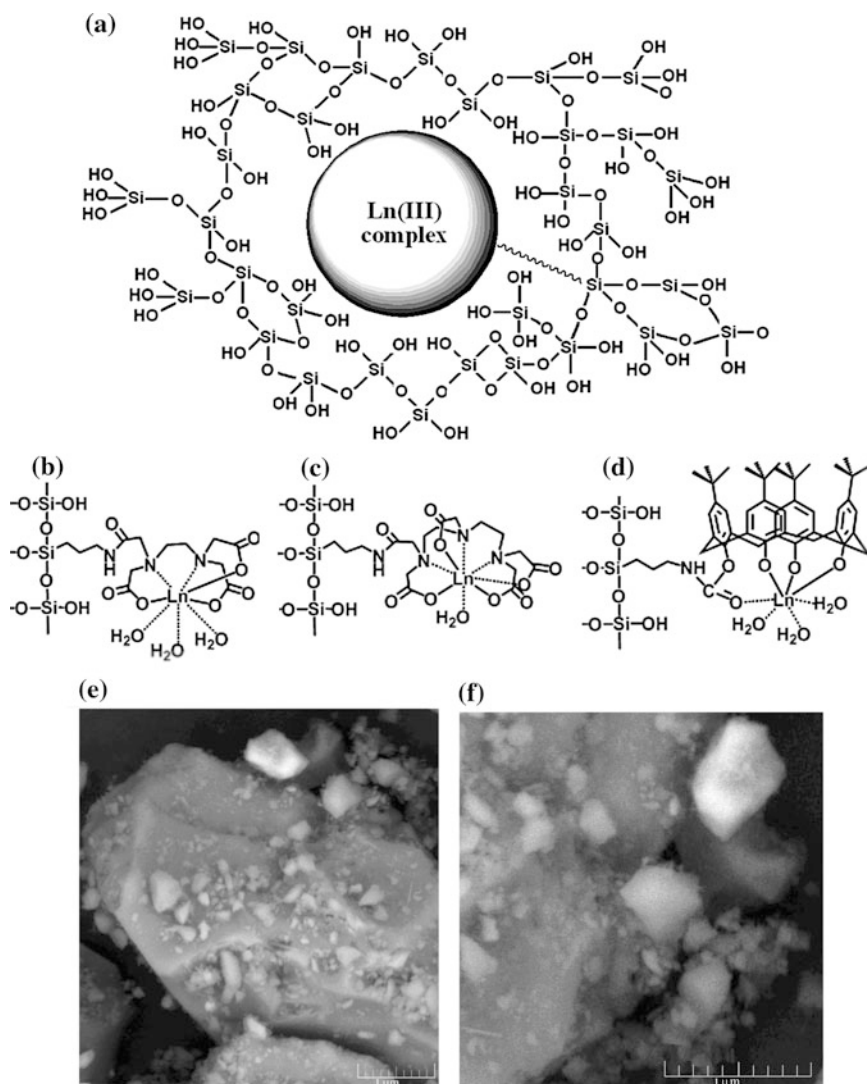
Fig. 21.3 Schematic structure of synthesized organic–inorganic hybrids (**a**) Ln-EDTA-APTMS/SiO$_2$ (**b**) Ln-DTPA-APTMS/SiO$_2$ (**c**) Ln-TBC-TESPIC/SiO$_2$ (**d**) and SEM-images of DTPA (**e**) and TBC-based samples (**f**)

419 nm in the form of broad bands in the range 380–520 nm (Fig. 21.4b). The maxima of these spectra are shift hypsochromically at 3 and 5 nm, respectively, compared with lutetium complexes with TBC and the same for samples in the solid state and in solution. Therefore, the energy of the singlet states of Lu-EDTA-APTMS/SiO$_2$, Lu–DTPA-APTMS/SiO$_2$, and Lu-TBC-TESPIC/SiO$_2$ amounts to
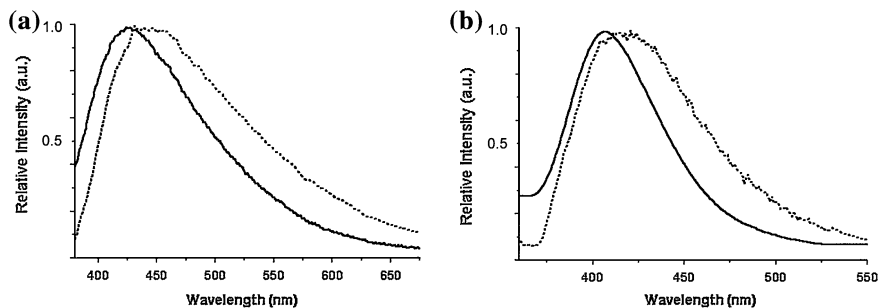
Fig. 21.4 Fluorescence (*solid line*) and phosphorescence (*dashed line*) spectra of Lu-EDTAAPTMS/SiO$_2$ (**a**) and Lu-TBC-TESPIC/SiO$_2$ (**b**)

23,750 cm^{-1}, 24,210 cm^{-1}, and 24,630 cm^{-1}, respectively, and the energy of the triplet states—22,420 cm^{-1}, 21,900 cm^{-1}, and 23,870 cm^{-1}, respectively.

The values of the triplet levels are suitable to realize the intramolecular excitation energy transfer to Ln(III) ions and to observe 4f-luminescence. The position of the energy levels of aminopolycarboxylate-derived organic–inorganic materials is more suitable for energy transfer to Eu(III) than Tb(III) ions. The energy gap between triplet state and the emissive $^5D_0$-level of Eu(III) (17280 cm^{-1}) is in the range of 4600–5100 cm^{-1}, while for $^5D_4$-level of Tb(III) (20500 cm^{-1})—1400–1920 cm^{-1} and the energy back transfer processes are expected in Tb-EDTA-APTMS/SiO$_2$ and Tb-DTPA-APTMS/SiO$_2$. The difference between triplet level of TBC-based material and Eu(III) and Tb(III) ions is at about 6600 and 3370 cm^{-1}, respectively, indicating more efficient energy transfer to Tb(III) ion in contrast to aminopolycarboxylates. The large energy gap for Eu-TBC-TESPIC/SiO$_2$ assumes the greater contribution of radiationless losses of the excitation energy on O–H-, C–H-vibrations in quenching of 4f-luminescence.

The excitation spectra of Eu-EDTA-APTMS/SiO$_2$ and Eu-DTPA-APTMS/SiO$_2$ (Fig. 21.5a) consist of symmetric and broad band ranging from 300 to 400 nm. As can be seen, the matrix—the organic ligand within silica polymeric host is able to transfer much more energy to europium ion than it absorbs at 394 nm (f–f-transition $^7F_0 \rightarrow {}^5L_6$). The corresponding emission spectrum contains $^5D_0 \rightarrow {}^7F_J$ (J = 0, 1, 2, 3, 4) transition lines of Eu(III) with the red emission $^5D_0 \rightarrow {}^7F_2$ as the most intensive one. The observed transitions are mainly of an electric dipole nature, except the $^5D_0 \rightarrow {}^7F_1$ line which has a predominant magnetic dipole contribution. It is worth noting that the fluorescence of matrix in the 390–450 nm region is quenched more than 75 % as compared to Lu(III) complexes. The emission spectrum of Eu-TBC-TESPIC (Fig. 21.5b) represents the band of matrix fluorescence and very poor 4f-luminescent signal of Eu(III), probably because of the efficient energy back transfer processes.

The 4f-luminescence intensity of obtained xerogels was compared with the corresponding molecular complexes (Eu-EDTA, Eu-DTPA) (Table 21.1).
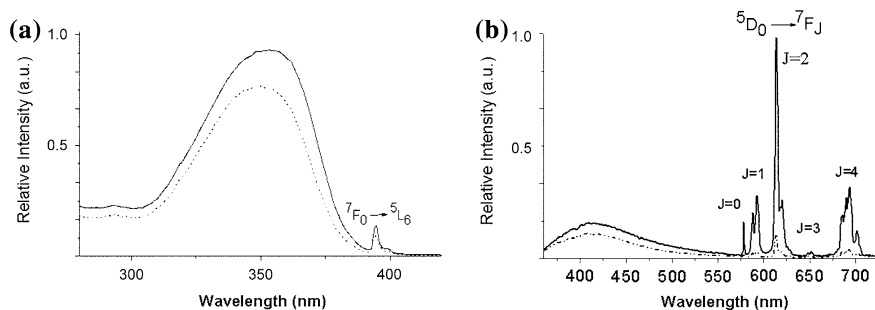
Fig. 21.5 Excitation **a** and emission **b** spectra of Eu-DTPA-APTMS/SiO$_2$ (*solid line*) and Eu-EDTA-APTMS/SiO$_2$ (*dashed line*)

The luminescence intensity of Eu-EDTA-APTMS/SiO$_2$ is about 63 % from Eu-EDTA intensity, and intensity of Eu-DTPA-APTMS/SiO$_2$ is 72 % from Eu-DTPA. When assessing these values the concentration of the ion-emitter in the sample should also be taken into account. The content of Eu(III) in Eu-DTPA-APTMS/SiO$_2$, for instance, is 6.7 times lower in comparison with the Eu-DTPA. The 4f-luminescence intensity of Eu-DTPA-APTMS/SiO$_2$ is 1.5 times higher than of Eu-EDTA-APTMS/SiO$_2$. A slight increase of Eu(III) excited state lifetime is observed in hybrids: from 329 μs in Eu-EDTA to 343 μs in Eu-EDTA-APTMS/SiO$_2$ and from 625 μs in Eu-DTPA to 672 μs in Eu-DTPA-APTMS/SiO$_2$.

The energy transfer from the hybrid matrix to Tb(III) is not as efficient as ion in Eu(III)-containing materials. The luminescence spectra of Tb-EDTA-APTMS/SiO$_2$ and Tb-DTPA-APTMS/SiO$_2$ (Fig. 21.6a) registered upon excitation wavelength at 350 nm show wide intensive band of fluorescence at 420 nm and series of peaks, corresponding to Tb(III) transitions $^5D_4 \rightarrow {}^7F_J$ (J = 3, 4, 5, 6). The intensity of the matrix fluorescence is two times larger than the 4f-luminescence. Thus, excitation at 350 nm leads both to luminescence of Tb(III) and fluorescence of hybrid matrix, which excitation energy is not completely transferred to the lanthanide ion. The reason is probably in the value of the energy levels of the

Table 21.1 Spectral-luminescent properties of hybrid materials

Sample	I_{4f}, %	τ, μs
Eu-EDTA	82.3	329
Eu-DTPA	100.0	625
Eu-EDTA-APTMS/SiO$_2$	52.5	343
Eu-DTPA-APTMS/SiO$_2$	72.3	672
Tb-EDTA	84.1	1162
Tb-DTPA	100.0	1930
Tb-EDTA-APTMS/SiO$_2$	10.9	1213
Tb-DTPA-APTMS/SiO$_2$	12.0	1973

Mass content of Ln(III) in Ln-EDTA was about 34.3–35.6 %, Ln-DTPA—28.0–29.0 %, Ln-EDTAAPTMS/SiO$_2$—4.3–4.5 % and in Ln-DTPA-APTMS/SiO$_2$—4.1–4.3 %
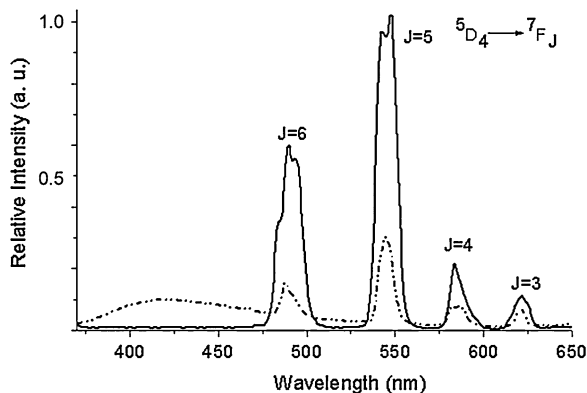
matrix and Tb(III) ion, that causes energy back transfer. In contrast to aminopolycarboxylates, the emission spectrum of Tb-TBC-TESPIC/SiO$_2$ shows very intensive 4f-luminescence (Fig. 21.6b),

In silica materials doped with lanthanide complexes with TBC 4f-luminescence of Nd(III), Er(III), and Yb(III) is realized in the IR-region. For erbium-containing compound 4f-luminescence is observed with the maximum at 1530–1532 nm (6540 cm^{-1}) corresponding to the transition $^4I_{13/2} \rightarrow {}^4I_{15/2}$ (Fig. 21.7a). It was found that in the silicate particles the intensity of Er(III) luminescence is 3.2–3.6 times higher than in the solution of the initial complex Er-TBC.

Upon excitation in the macrocycle absorption band (312–320 nm) particles containing complex Nd-TBC exhibit characteristic 4f-luminescence: bands with maxima at 889–895 nm (11,173–11,250 cm^{-1} transition $^4F_{3/2} \rightarrow {}^4I_{9/2}$), 1065–1069 nm (9350–9400 cm^{-1}) and 1073–1076 nm (9250–9300 cm^{-1}) corresponding to the splitting transition $^4F_{3/2} \rightarrow {}^4I_{11/2}$.
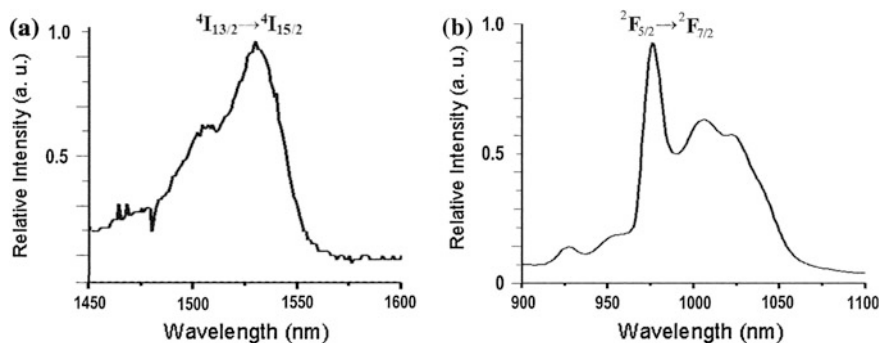
Fig. 21.7 Emission spectra of **a** Er-TBC-TESPIC/SiO$_2$ and **b** YB-TBC-TESPIC/SiO$_2$

The spectrum of 4f-luminescence of Yb-TBC-TESPIC/SiO$_2$ represents a band, corresponding to the band split to three peaks with maxima at 976, 1006 and 1022 nm (Fig. 21.7b). Such splitting is a consequence of reducing the symmetry of the coordination polyhedron of the ytterbium complex in silica matrix.

In a series of synthesized compounds EDTA - and DTPA-APTMS are more suitable precursors for obtaining Eu(III) complexes and hybrids with effective 4f-luminescence in visible and TBC-TESPIC—for Tb(III) and Lanthanides emitting in near IR-range. Despite the inefficient energy transfer in Tb(III) aminopoly-carboxylate-containing hybrids they could be useful objects for research as wide-range dual-wave emitters due to simultaneous fluorescence and 4f-luminescence. It may be concluded that sol–gel organic–inorganic hybrids with covalently bonded Ln-EDTA, Ln-DTPA and Ln-TBC complexes are promising materials for further research in practical application. This work was supported by the National Academy of Sciences (DCNTP "Nanotechnology and nanomaterials", project 6.22.7.43).

References

1. Albrecht M, Osetska O, Klankermayer J et al. (2007) Enhancement of near-IR emission by bromine substitution in lanthanide complexes with 2-carboxamide-8-hydroxyquinoline Chem Commun 18:1834–1836
2. Glover P, Basett A, Nockemann P et al (2007) Fully fluorinated imidodiphosphinate shells for visible- and NIR-emitting lanthanides: hitherto unexpected effects of sensitizer fluorination on lanthanide emission properties. Chem Eur J 13:6308–6320
3. Eliseeva S, Bünzli J-C (2010) Lanthanide luminescence for functional materials and bio-sciences. Chem Soc Rev 39:189–227
4. Weissman S (1942) Intramolecular energy transfer the fluorescence of complexes of europium. J Chem Phys 10:214–217
5. Crosby G, Whan R, Alire R (1961) Intramolecular energy transfer in rare earth chelates. Role Triplet State J Chem Phys 34:743–748
6. Crosby G, Whan R, Freeman J (1962) Spectroscopic studies of rare earths chelates. J Phys Chem 66:2493–2499
7. Muller G, Kean S, Parker D et al (2002) Temperature and pressure dependence of excitation spectra as a probe of the solution structure and equilibrium thermodynamics of a Eu(III) complex containing a modified dota ligand. J Phys Chem A 106:12349–12355
8. Frey S, Horrocks W Jr (1995) On correlating the frequency of the $^7F_0 \rightarrow {}^5D_0$ transition in Eu^{3+} complexes with the sum of 'nephelauxetic parameters' for all of the coordinating atoms Inorg Chim Acta 229: 383–390
9. Bünzli J-C, Klein B, Wessner D (1982) Crystal structure and emission spectrum of tris(nitrato)-1,4,7,10-tetraozacyclododecane-Europium(III) Inorg Chim Acta 59:269–274
10. Bünzli J-C (2010) Lanthanide luminescence for biomedical analyses and imaging. Chem Rev 110:2729–2755
11. Samuel A, Xu J, Raymond K (2009) Predicting efficient antenna ligands for Tb(III) emission. Inorg Chem 48:687–698
12. Archer R, Chen H, Thompson L (1998) Synthesis, characterization, and luminescence of europium(III) schiff base complexes. Inorg Chem 37:2089–2095

13. Latva M, Takalo H, Mukkala V et al (1997) Correlation between the lowest triplet state energy level of the ligand and lanthanide(III) luminescence quantum yield J. Luminescence 75:149–169

14. Dadabhoy A, Faulkner S, Sammes P (2002) Long wavelength sensitizers for europium(III) luminescence based on acridone derivatives. J Chem Soc Perkin Trans 2:348–357

15. Dang S, Yu JB, Wang X et al (2010) A study on the NIR-luminescence emitted from ternary lanthanide [Er(III), Nd(III) and Yb(III)] complexes containing fluorinated-ligand and 4,5-diazafluoren-9-one. J Photochem Photobiol A Chem 214:152–160

16. Monguzzi A, Tubino R, Meinardi F et al (2009) Er^{3+} perfluorinated complexes for broadband sensitized near infrared emission. Chem Mater 21:128–135

17. dos Santos E, Freire R, da Costa N et al (2010) Theoretical and experimental spectroscopic approach of fluorinated Ln^{3+}-diketonate complexes. J Phys Chem A 114:7928–7936

18. Hasegawa Y, Murakoshi K, Wada Y et al (1996) Enhancement of luminescence of Nd^{3+} complexes with deuterated hexafluoroacetylacetonato ligands in organic solvent. Chem Phys Lett 248:8–12

19. Hasegawa Y, Murakoshi K, Wada Y, et al. (1996) Characteristic emission of β-diketonato Nd^{3+} complexes dressed with perfluoroalkyl groups in DMSO-d_6 Chem Phys Lett, 260: 173–177

20. Bischof C, Wahsner J, Scholten J et al (2010) Quantification of C − H quenching in near-IR luminescent ytterbium and neodymium cryptates. J Am Chem Soc 132:14334–14335

21. Glover P, Bassett A, Nockemann P et al. (2007) Fully fluorinated imidodiphosphinate shells for visible- and NIR-emitting lanthanides: hitherto unexpected effects of sensitizer fluorination on lanthanide emission properties. Chem–Eur J, 13: 6308–6320

22. Iwamuro M, Adachi T, Wada Y, et al. (2000) Photosensitized Luminescence of Neodymium(III) Coordinated with 8-Quinolinolates in DMSO-d_6 Bull Chem Soc Japan 73: 1359–1363

23. Binnemans K, Gnrller-Walrand C (2002) Lanthanide containing liquid crystals and surfactants. Chem Rev 102:2303–2345

24. Peter S, Panigrahi B, Viswanathan K et al (1992) Fluorescence enhancement of dysprosium, europium and terbium using sodium benzoate-trioctylphosphine oxide-triton X-100 Anal Chim Acta 260: 135–141

25. Wenlian L, Weili L, Gui Y, et al. (1993) Enhanced luminescence and energy transfer of Eu(III) and Tb(III) in chelates in micelle solutions J Alloys and Compounds 191: 107–110

26. Ermolaev V, Gruzdev V (1984) Novel spectral-kinetic methods for investigation of ligand exchange in labile metal complexes in solutions. Inorg Chim Acta 95:179–185

27. Asano-Someda M, Kaizu Y, (2001) Hot bands of (f,f*) emission from ytterbium(III) porphyrins in solution J Photochem Photoboil A: Chem 139: 161–165

28. Korovin Yu, Rusakova N (2001) Infrared 4f-luminescence of lanthanides in the complexes with macrocyclic ligands Rev. Inorg Chem 21:299–329

29. Beeby A, Dickins R, Fitzgerald S et al (2000) Porphyrin sensitization of circularly polarised near-IR lanthanide luminescence: enhanced emission with nucleic acid binding J Chem Soc Chem Commun: 1183–1184

30. Steemers F, Verboom W, Reinhoudt D et al (1995) New sensitizer-modified calix[4]arenes enabling near-UV excitation of complexed luminescent lanthanide ions. J Am Chem Soc 117:9408–9414

31. Ramírez F, Charbonnière L, Muller G et al (2001) A p-tert-butylcalix[4]arene functionalised at its lower rim with ether-amide pendant arms acts as an inorganic–organic receptor: structural and photophysical properties of its lanthanide complexes J Chem Soc, Dalton Trans 3205–3213

32. Kajiwara T, Katagiri K, Hasegawa M et al (2006) Conformation-controlled luminescent properties of lanthanide clusters containing p-tert-butylsulfonylcalix[4]arene. Inorg Chem 45:4880–4882

33. Skripacheva V, Mustafina A, Rusakova N et al (2008) Novel heterometallic Co(III)-Ln(III) (Ln = Gd, Tb, Dy) complexes on *p*-sulfonatothiacalix[4]arene platform exhibiting redox-switchable metal-to-metal energy transfer Eur J. Inorg Chem 2008:3957–3963

34. Eddaoudi M, Moler D, Li H et al (2001) Modular chemistry: secondary building units as a basis for the design of highly porous and robust metal—organic carboxylate frameworks. Acc Chem Res 34:319–330

35. Daiguebonne C, Kerbellec N, Bernot K et al (2006) Synthesis, crystal structure, and porosity estimation of hydrated erbium terephthalate coordination polymers. Inorg Chem 45:5399–5406

36. Misra V, Mishra H (2008) Photoinduced proton transfer coupled with energy transfer: Mechanism of sensitized luminescence of terbium ion by salicylic acid doped in polymer J Chem Phys 128: 244701-1-244701-8

37. Raj D, Francis B, Reddy M et al (2010) Highly luminescent poly(methyl methacrylate)-incorporated europium complex supported by a carbazole-based fluorinated *β*-diketonate ligand and a 4,5-bis(diphenylphosphino)-9,9-dimethylxanthene oxide co-ligand. Inorg Chem 49:9055–9063

38. O'Riordan A, O'Connor E, Moynihan S et al (2005) Narrow bandwidth red electroluminescence from solution-processed lanthanide-doped polymer thin films. Thin Solid Films 491:264–269

39. Binnemans K (2009) Lanthanide-based luminescent hybrid materials Chem Rev 109:4283–4374

40. Feng J, Zhang H (2012) Hybrid materials based on lanthanide organic complexes. Rev Chem Soc Rev. doi:10.1039/C2CS35069F

41. Anderegg G, Arnaud-Neu F, Delgado R et al (2005) Critical evaluation of stability constants of metal complexes of complexones for biomedical and environmental applications. Pure Appl Chem 77:1445–1495

42. Alpha B, Lehn J-M, Mathis G (1987) Energy transfer luminescence of europium(III) and terbium(III) cryptates of macrobicyclic polypyridine ligands Angew Chem Int Ed 26: 266–267

43. Sabbatini N, Perathoner S, Balzani V, Alpha B, Lehn J-M (1987) Supramolecular photochemistry. Reidel, Dordrecht

44. Qiaoyu N, Jianxin M, Haiming W et al (2006) Novel terbium chelate doped fluorescent silica nanoparticles. J Rare Earths 24:193–196

45. Rieter W, Kim J, Taylor K et al (2007) Hybrid silica nanoparticles for multimodal imaging. Angew Chem Int Ed 46:3680–3682

46. Stöber W, Fink A (1968) Controlled growth of monodisperse silica spheres in the micron size range. J Colloid Interface Sci 26:62–69

47. Choppin G, Baisden P, Khan S (1979) Nuclear magnetic resonance studies of diamagnetic metal-diethylenetriaminepentaacetate complexes. Inorg Chem 18:1330–1332

48. Kim J, Seidler P, Wan L et al (2009) Formation, structure, and reactivity of amino-terminated organic films on silicon substrates. J Colloid Interface Sci 329:114–119

49. Yan B, Zhang H, Wang S et al (1997) Luminescence properties of the ternary rare earth complexes with *β*-diketones and 1,10-phenanthroline incorporated in silica matrix by a sol-gel method. Mater Chem Phys 51:92–96

50. Lu H-F, Yan B, Liu J-L (2009) Functionalization of calix[4]arene as a molecular bridge to assemble luminescent chemically bonded rare-earth hybrid systems. Inorg Chem 48:3966–3975

51. Li Y-J, Yan B, Wang L (2011) Rare earth(Eu^{3+}, Tb^{3+}) mesoporous hybrids with calix[4]arene derivative covalently linking MCM-41:Physical characterization and photoluminescence property J Solid State Chem 184: 2571–2579

52. Katsyuba S, Kovalenko V, Chernova x et al (2005) Vibrational spectra, co-operative intramolecular hydrogen bonding and conformations of calix[4]arene and thiacalix[4]arene molecules and their para-tert-butyl derivatives. Org Biomol Chem 3:2558–2565

53. Leyton P, Domingo C, Sanchez-Cortes S et al (2007) Reflection–absorption IR and surface-enhanced IR spectroscopy of tetracarboethoxy t-butyl-calix[4]arene, as a host molecule with potential applications in sensor devices. Vib Spectrosc 43:358–365
54. Brinker CJ, Scherer GW (1990) Sol-gel science: the physics and chemistry of sol-gel processing. Academic Press, New York

Chapter 22
Study of Nanocomposites of Amino Acids and Organic Polyethers by Means of Mass Spectrometry and Molecular Dynamics Simulation

V. G. Zobnina, M. V. Kosevich, V. V. Chagovets and O. A. Boryak

22.1 Introduction

Nanocomposites made of biomolecules and organic components are promising for biomedical and pharmaceutical applications [1], drug delivery in particular [2]. Organic nanoparticles composed of proteins and polyether polymers are currently under development [2]. Knowledge on parameters of intermolecular interactions of proteins with polyethers is necessary for elaboration of advanced materials and technological procedures. The complexity and heterogeneity of such systems, however, hampers obtaining information on their structure. In this connection, so-called monomeric approximation in which interactions of the building blocks of macromolecules are modeled may be helpful.

In the present communication, we address self-organization of organic nano-particles composed of amino acids and oligomers of organic polyethers, which mimic structural motives of pegylated proteins. Systems composed of representatives of amino acids which differ in their polarity, charge state, hydrophilicity/hydrophobicity, and polyethylene glycol PEG-400 or oxyethylated glycerol OEG-5 are studied.

An efficient tool in studies of noncovalent complexes of organic and biological molecules is mass spectrometry [3], electrospray ionization (ESI) mass spectrometry in particular [4]. Computer experiment based on molecular dynamics simulation permits to model structures of the complexes observed in mass spectrometric experiments.

V. G. Zobnina (✉) · M. V. Kosevich · V. V. Chagovets · O. A. Boryak
B. Verkin Institute for Low Temperature Physics and Engineering of the National Academy
of Sciences of Ukraine, 47, Lenin Avenue, Kharkov 61103, Ukraine
e-mail: zobnina@ilt.kharkov.ua

M. V. Kosevich
e-mail: mvkosevich@ilt.kharkov.ua

O. A. Boryak
e-mail: boryak@ilt.kharkov.ua

An assumption concerning the structure of amino acids-polyether complexes can be made on the basis of the results of previous studies of polyethers interactions with monoatomic ions [5–8]. It is known that polyether chains assemble around monoatomic cations forming crown ether-like structures [5, 6]. Recently, it was shown that the polyether chains can form stable gas-phase complexes with monoatomic chlorine anion [7, 8] as well. It can be proposed, that the polyether chains will self-assemble in similar manner around the charged groups of amino acids.

22.2 Experimental

22.2.1 Electrospray Mass Spectrometry

Electrospray (ESI) mass spectra measurements were performed using Perkin-Elmer SCIEX API 2000 Triple Quadrupole LC/MS/MS mass spectrometer (PE Sciex, Toronto, Canada). Standard experimental settings were applied, as described in our previous papers [7–9].

For sample preparation, equal volumes (5–10 μL) of 10^{-2} M stock solutions of amino acids and polyethers PEG-400 or OEG-5 were mixed and then diluted by methanol to 10^{-4} M concentration.

Sources of reagents were as follows: amino acids were purchased from "Reachem" (Saint Petersburg, Russian Federation); methanol was supplied by "Reanal" (Budapest, Hungary); PEG-400 was produced by "Loba-Chemie" (Vienna, Austria). Oxyethylated glycerol OEG-5 was synthesized at the Institute for Problems of Cryobiology and Cryomedicine of the National Academy of Sciences of Ukraine (Kharkov, Ukraine).

22.2.2 Molecular Dynamics Simulations

Molecular dynamics simulations of associates of polyether oligomers with amino acids were performed with CHARMM 32 force field [10, 11] using NAMD program [12]. Integration step was 1 fs. The 10^3 integration steps for optimization of the initial structure took 1 ps. The simulation was continued for 0.2 ns at 300 K. Visualization of the structures obtained was performed by ChemCraft program [13]. The computer experiments were performed using the facilities of the computer grid-cluster of the B. Verkin Institute for Low Temperature Physics and Engineering of the NAS of Ukraine.

22.3 Experimental Results

Here we present the results of ESI mass spectrometric study of systems composed of polyether oligomers OEG-5 or PEG-400 and amino acids which differ in polarity, hydrophilicity/hydrophobicity, and charge state. Formation of supramolecular amino acid-polyethers complexes is observed for all systems. The abundance, distribution, and charge state of the complexes, however, vary with the type of the amino acid component. Modeling of amino acids-oligomer complexes by molecular dynamics simulation has confirmed our assumption concerning assembling of the polyethers' chains around the charged groups of amino acids.

22.4 Polyethers

Polyether polymers are polydispersed compounds characterized by molecular mass distribution and index of polydispersity [5]. Such a distribution is reflected in their mass spectra as a bell-shaped set of peaks [14, 15]. The oligomers are recorded either in the protonated form or as complexes with alkali metal ions Na^+ or K^+ present in trace quantities in all polymer samples. Mass spectra of PEGs of different molecular weights are well-known from the literature [6, 14]. The ESI mass spectral pattern of oligomers of OEG-5 [15] is presented in Fig. 22.1. It contains three bell-shaped sets of peaks $OEG_n \cdot H^+$, $OEG_n \cdot Na^+$, $OEG_n \cdot K^+$ (where n is a degree of polymerization of the oligomers).

Similar sets of peaks characteristic of polyethers are present in the mass spectra of amino acid-polyether systems.
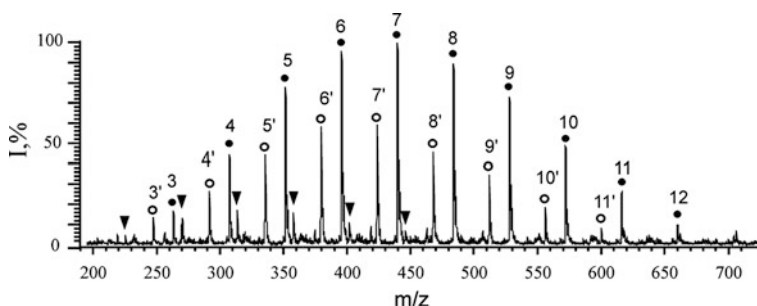
Fig. 22.1 Positive ion ESI mass spectrum of oligomers of OEG-5. Symbols: $\blacktriangledown$–$OEG_n \cdot H^+$, $\bigcirc$–$OEG_n \cdot Na^+$, $\bullet$ –$OEG_n \cdot K^+$. Numbers above the peaks correspond to degree of polymerization n. (Adapted from work [15] with permission of "Mass-Spektrometriya" journal)

22.5 Proline-Polyether System

Proline (Pro) is a hydrophobic heterocyclic imino acid which differs from all other protein-forming amino acids by its nitrogen atom being in the form of secondary amine.

In Fig. 22.2 both positive and negative ion ESI mass spectra of (proline – OEG-5) system are presented. The spectra contain peaks characteristic of the individual components of the system and products of their noncovalent interactions.

The main experimental result consists in the recording of the sets of peaks of both protonated and deprotonated clusters of proline with OEG-5, $OEG_n \cdot Pro \cdot H^+$ and $[OEG_n \cdot (Pro-H)]^-$, in the corresponding ion modes. Qualitatively similar sets of peaks were recorded for (proline–PEG-400) system. Observation of such pair clusters means that proline forms stable complexes with polyether oligomers.

Two distinctive features of the ESI mass spectra of the (proline–OEG-5) system are worth of discussion. First, the relative abundances of the peaks of both deprotonated proline $[Pro-H]^-$ and its clusters with OEG-5 in the negative ion mass spectra (Fig. 22.2b) are higher than those of the peaks of the protonated proline $Pro \cdot H^+$ and $OEG_n \cdot Pro \cdot H^+$ clusters in the positive ion mass spectra (Fig. 22.2a). Literature data show that pH value for OEG-5 is 6.5, while the isoelectric point for proline is at pH value 6.3, which means that the deprotonated form of proline must dominate in the OEG-5 solute. This is in agreement with the above-indicated higher abundance of the negatively charged species. Second, proline-OEG-5 clusters in the cationized form are absent in spite of the presence of

Fig. 22.2 ESI mass spectra of (proline–OEG-5) system: **a** positive ions; **b** negative ions. Symbols: ▼–$OEG_n \cdot H^+$, ○–$OEG_n \cdot Na^+$, ●–$OEG_n \cdot K^+$, ■—$OEG_n \cdot Pro \cdot H^+$, ◆—$[OEG_n-H]^-$, *—$[OEG_n \cdot (Pro-H)]^-$. Numbers above the peaks correspond to degree of polymerization n. (Adapted with permission of "Biofizichnii Visnik" [16])
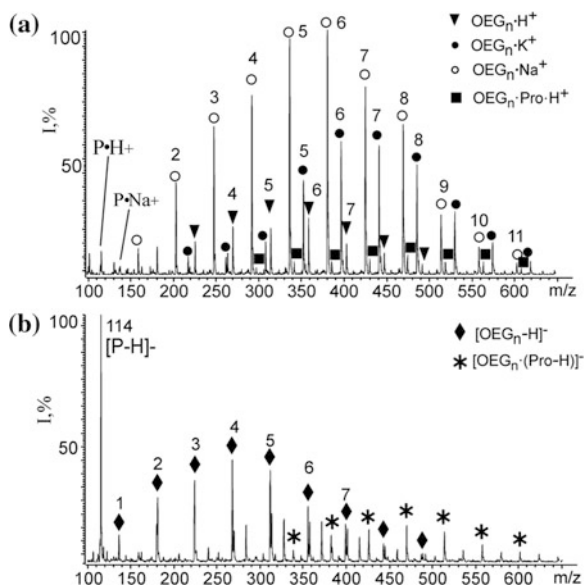
the cationized form of the both individual components—Pro·Na$^+$ and OEG$_n$·Na$^+$, OEG$_n$·K$^+$—in the positive ion mass spectra. This effect may find the following explanation. Anionic COO$^-$ group of deprotonated proline can bind to the stable quasi-cyclic complex of an oligomer with alkali metal cation. The resulting triple cluster is neutral and thus it is not recorded in the mass spectra. Similar associates are known for amino acids and crown ethers with trapped alkali metal ion. As to a possibility of the polyethers binding to the cationized proline, there is obviously a competition for its binding with alkali metal ions, which is resolved in favor of the latter [16].

Molecular dynamics simulation was performed for clusters of proline in zwitterionic, protonated, and deprotonated form with oligomers of different chain length. A self-organization or assembling of the initially extended polyether chain around the amino acid was observed in the course of simulation. In Fig. 22.3 snapshots of equilibrated structures of complexes of the zwitterionic proline (a) and deprotonated proline (b) with OEG oligomers are presented.

It can be seen that in OEG$_9$·Pro complex positively charged $= NH_2^+$ moiety of the zwitterionic proline (Fig. 22.3a) is surrounded by the polyether chain in quasi-cyclic conformation resembling a crown-ether structure; the nucleophilic ether oxygen atoms of the chain are turned to this positively charged group. At the same time, hydrogen atoms of the rest of the OEG$_9$ chain are turned to the negatively charged COO$^-$ group of proline. Ionic hydrogen bond is formed between COO$^-$ group and terminal OH group of the oligomer. In the case of the complex with deprotonated proline ([OEG$_{10}$·(Pro–H)]$^-$, Fig. 22.3b) an "inversed" conformation (in relation to the crown-ether-like conformation) is adopted by the polyether chain structured around the anionic proline, that is oxygen atoms of the quasi-cyclic structure are turned outwards, while hydrogen atoms are directed to the anion. Thus, the quasi-cyclic structure of the polyether chain formed around the organic cationic group (Fig. 22.3a) is similar to that formed around the mono-atomic cations Na$^+$ and K$^+$, while the chain structure around the organic anion
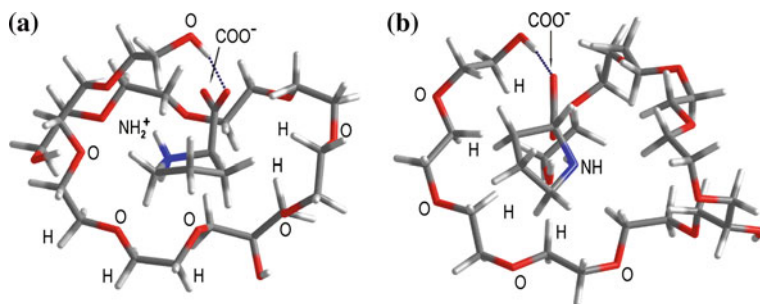
Fig. 22.3 Snapshots of equilibrated structures of complexes of proline and oligomers of OEG, obtained by molecular dynamics simulation: **a** complex of the zwitterionic proline with OEG$_9$ oligomer; **b** complex of deprotonated proline with OEG$_{10}$ oligomer. Sticks representation [13] is applied. (Here and further color scheme for atoms is as follows: hydrogen—*white*, carbon—*dark grey*, nitrogen—*blue*, oxygen—*red*)

Fig. 22.4 A structure of a neutral cluster of deprotonated proline with potassium cation trapped by the OEG$_{10}$ oligomer
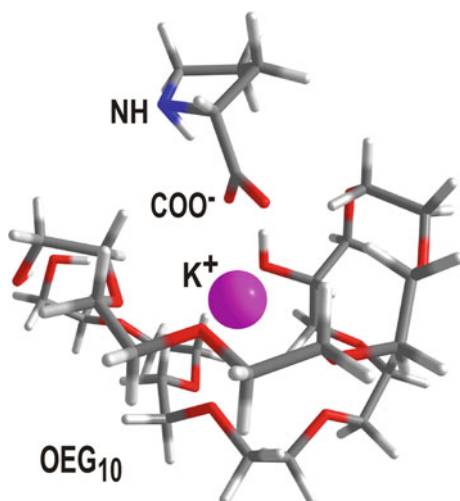
(Fig. 22.3b) is similar to that formed around the monoatomic chlorine anion [7, 8]. It may be concluded that the polyether chain tends to wind around the charged groups of proline amino acid.

To check our assumption concerning formation of neutral complexes of deprotonated amino acid anion with alkali metal cation tightly bound with a polyether, three-component system composed of (Pro–H)$^-$ and OEG$_{10}$·K$^+$ complex was subjected to molecular dynamics procedure. In the course of simulation a stable triple cluster was formed (Fig. 22.4), as it was anticipated. COO$^-$ group of proline became bound to potassium cation, while the latter remained trapped within the polymeric quasi-helical surrounding.

22.6 Valine-Polyether System

Valine (Val) belongs to essential nonpolar amino acids; it contains a hydrophobic alkyl side radical.

In Fig. 22.5 positive ion ESI mass spectrum of (valine–OEG-5) system is presented. The mass spectrum contains a set of OEG$_n$·Val·H$^+$ protonated associates which evidence the formation of complexes of the amino acid with oligomers of various chain length. A set of deprotonated associates [OEG$_n$·(Val-H)]$^-$ of comparable abundance is present in the negative ion mass spectrum. There are no triple clusters of valine and oligomers with alkali metal ions.

Molecular dynamics simulation of clusters of oligomers with valine in various charge states is performed. In Fig. 22.6, a snapshot of the complex of OEG$_8$ with valine in neutral zwitterionic form is shown. It can be seen that the polyether chain is located near the charged COO$^-$ and NH$_3^+$ groups of the zwitterionic amino acid. Terminal OH-groups of the polyether form hydrogen bonds with these groups.

Fig. 22.5 Positive ion ESI mass spectrum of (valine–OEG-5) system. Symbols: ▼–$OEG_n \cdot H^+$, ○–$OEG_n \cdot Na^+$, •–$OEG_n \cdot K^+$, ■–$OEG_n \cdot Val \cdot H^+$
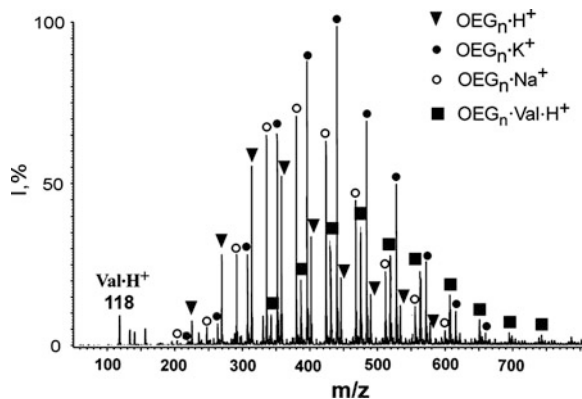
Fig. 22.6 Snapshot of equilibrated structure of a complex of zwitterionic valine with polyether oligomer OEG_8, obtained by molecular dynamics simulation
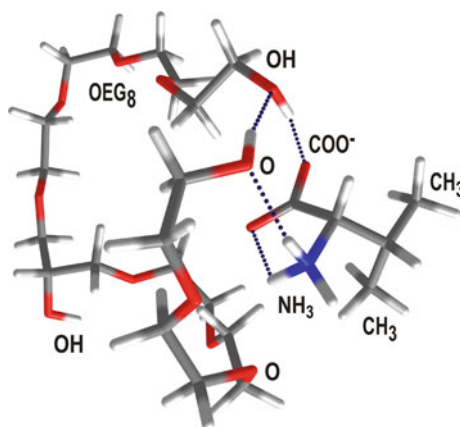
The hydrophobic alkyl side chain of valine is excluded from the interactions. Clusters of oligomers with neutral unionized valine appeared to be unstable.

In the clusters with protonated or deprotonated valine winding of an oligomer around NH_3^+ or COO^- groups, respectively, is observed. It agrees with a possibility of observation of valine-polyether clusters both in the positive and negative ESI ion modes; efficiency of cluster formation is not affected by the neutral hydrophobic side chain of valine.

22.7 Histidine-Polyether System

Histidine (His) is an essential hydrophilic amino acid which contains heterocyclic imidazole functional group in the side chain. The latter is responsible for weak basic properties of histidine; it is protonated at pH below 6 providing the cationic state of the amino acid.

Fig. 22.7 ESI mass spectra of (histidine–OEG-5) system: **a** positive ions; **b** negative ions. Symbols: ▼–$OEG_n \cdot H^+$, ○–$OEG_n \cdot Na^+$, ●–$OEG_n \cdot K^+$, ■–$OEG_n \cdot His \cdot H^+$, □–$OEG_n \cdot OEG_m \cdot His \cdot H^+$, ◆–$OEG_n \cdot Cl^-$. Numbers above the peaks correspond to degree of polymerization n. (Reproduced from work [9] by permission of John Wiley & Sons)
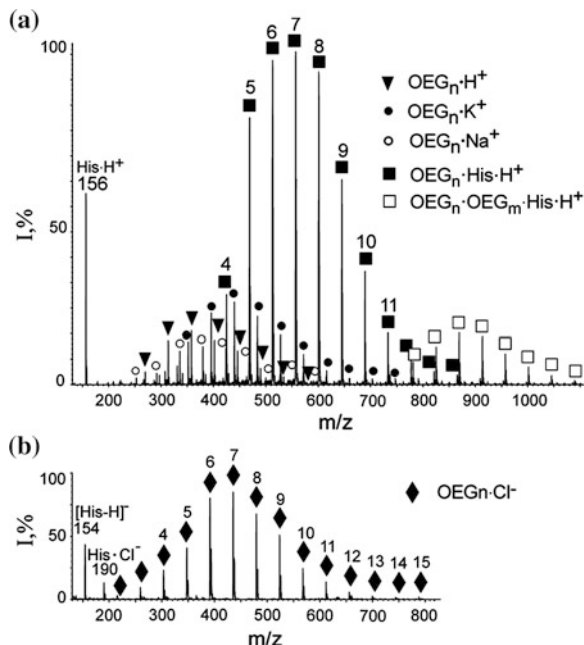
Hydrochloride His·HCl form of histidine was used in the present study. The salt state of the amino acid was responsible for the distinctions of the ESI mass spectral patterns of the (histidine-polyether) system from the spectra of the systems containing other amino acids [9].

In Fig. 22.7 both positive and negative ion mass spectra of (histidine–OEG-5) system are shown; the mass spectral patterns of (histidine–PEG-400) system are similar. A set of very abundant peaks of protonated pair complexes $OEG_n \cdot His \cdot H^+$ are recorded in the positive ion mode (Fig. 22.7a). In contrast to other amino acids, histidine can form triple complexes $OEG_n \cdot OEG_m \cdot His \cdot H^+$ with two oligomers at a time. There are no cationized clusters of histidine with oligomers. There are no clusters of deprotonated histidine with oligomers in the negative ion mode (Fig. 22.7b). A set of clusters of oligomers with the chlorine anion of the salt, $OEG_n \cdot Cl^-$ or $PEG_n \cdot Cl^-$, are recorded instead. Observation of stable gas-phase clusters of polyethers with chlorine anion was a novel experimental fact, which was discussed in the above-mentioned publications [7, 8].

Remarkably, high yield of $OEG_n \cdot His \cdot H^+$ and $PEG_n \cdot His \cdot H^+$ protonated complexes is in agreement with our assumption about winding of the polyether chains around charged atoms or groups of atoms. Collisionally induced dissociation of $OEG_n \cdot His \cdot H^+$ complexes has confirmed the location of the proton on histidine molecule in the gas-phase complexes. Protonated form of histidine, formed on dissociation of its hydrochloride salt in solution, attracts polyethers and provides domination of its positively charged associates in the ESI mass spectra.
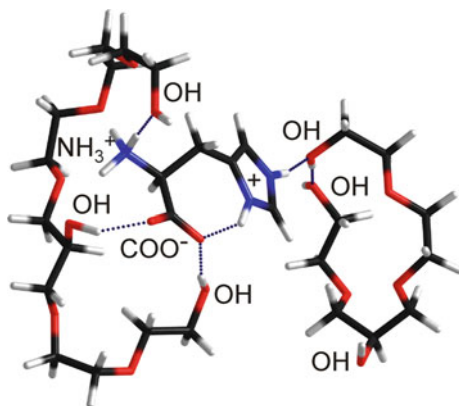
Molecular dynamic simulation of OEG$_n$ and PEG$_n$ complexes with histidine in neutral, zwitterionic, and protonated forms has demonstrated the wrapping of charged groups present in certain forms of histidine by the polyether oligomers [9]. Presence of three spatially separated charged centers in the zwitterionic protonated histidine facilitates its interaction with two oligomers in a triple complex (Fig. 22.8). In the pair protonated complexes single oligomers either assemble in a quasi-cyclic structure around the positively charged imidazole ring, or form H-bonds and wrap around the NH$_3^+$ and COO$^-$ groups, similarly to the case presented in Fig. 22.8.

22.8 Systems of Polyethers with Aspartic Acid and Glutamic Acid

Aspartic acid (Asp) and glutamic acid (Glu) are representatives of hydrophilic anionic amino acids. They are negatively charged at physiological conditions.

ESI mass spectra of the (glutamic acid–OEG-5) system are presented in Fig. 22.9. Mass spectra of the (aspartic acid–OEG-5) system and the systems with PEG-400 were similar to those shown in Fig. 22.9. Comparison of the mass spectra obtained in positive (Fig. 22.9a) and negative (Fig. 22.9b) ion modes reveals that, as it could be expected, the abundances are much more higher for the polyether clusters with deprotonated form of the amino acids, [OEG$_n$·(Glu-H)]$^-$, in the negative ion mode as compared to the low-abundant clusters with the protonated amino acid, OEG$_n$·Glu·H$^+$, in the positive ion mode. The binding of the polyethers with the deprotonated amino acid which is dominant in solution confirms formation of the complexes in the initial solution. Thus formed complexes are transferred to the gas phase under the electrospray procedure and reflect adequately the composition of the solution under study.

Fig. 22.9 ESI mass spectra of (glutamic acid–OEG-5) system: **a** positive ions, **b** negative ions. Symbols: ▼– $OEG_n \cdot H^+$, ○–$OEG_n \cdot Na^+$, ●– $OEG_n \cdot K^+$, ■–$OEG_n \cdot Glu \cdot H^+$, ◆–$OEG_n \cdot Cl^-$, Δ–$[OEG_n-H]^-$, *–$[OEG_n \cdot (Glu-H)]^-$
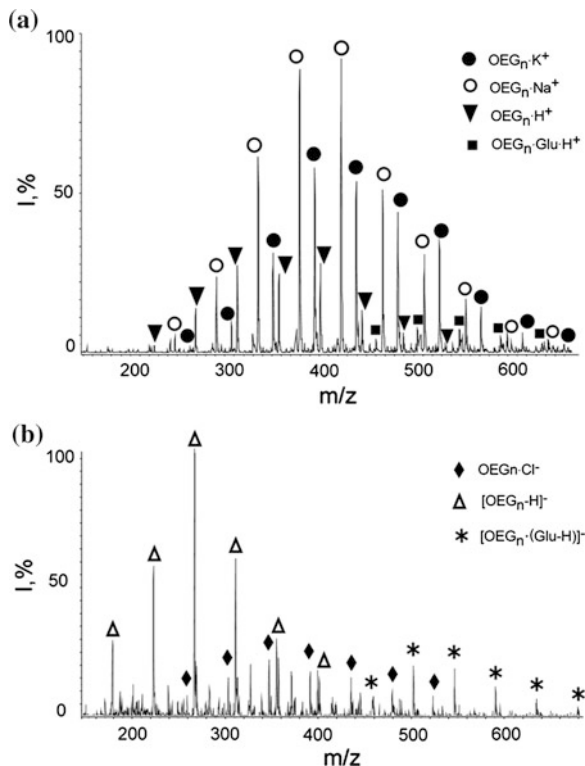
Molecular dynamics simulation for polyethers' oligomers complexes with glutamic acid in the deprotonated zwitterionic form (Fig. 22.10) have confirmed the rules established earlier for other amino acids.

Relatively short chains, as in the $[OEG_6 \cdot (Glu-H)]^-$ complex (Fig. 22.10a), wrap the negatively charged groups of the amino acid; hydrogen atoms of the chain are turned to the acidic COO^- groups. Further stabilization of the structure is achieved due to formation of ionic hydrogen bonds between three OH-groups of the oligomer and two COO^- groups of the amino acid. Longer chain in $[OEG_7 \cdot (Glu-H)]^-$ complex (Fig. 22.10b) start to assemble into a helical structure
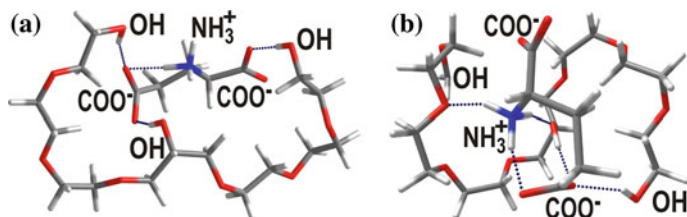
Fig. 22.10 Snapshots of equilibrated structures of the complexes of polyether oligomers with zwitterionic deprotonated glutamic acid: **a** $[OEG_6 \cdot (Glu-H)]^-$; **b** $[OEG_7 \cdot (Glu-H)]^-$

around the amino acid. When the chain length is sufficient, the NH_3^+ group of the zwitterionic glutamic acid is also wrapped by the polyether.

It may be speculated that the structural motives revealed for short polyethers complexes with individual amino acids may occur in the complexes of polyethers with proteins in the case of exposure of charged side chains of amino acids at the protein surface.

22.9 Conclusions

In the framework of a problem of characterization of nanomaterials based on organic polyethers and biomolecules, formation of complexes of amino acids building blocks of proteins and polyethers is addressed. Combined approach uniting experimental ESI mass spectrometric technique and computer modeling by means of molecular dynamics allowed us to reveal stable complexes of amino acids with polyether oligomers.

It is shown that the abundance and charge state of the complexes recorded in the ESI mass spectra depend on the type of amino acid. The most abundant complexes are observed for polar ionic amino acids. For cationic histidine positively charged protonated clusters $PEG_n \cdot His \cdot H^+$ or $OEG_n \cdot His \cdot H^+$ only are recorded. For anionic glutamic and aspartic acids the clusters with deprotonated amino acid $[OEG_n \cdot (Glu-H)]^-$, $[OEG_n \cdot (Asp-H)]^-$ dominate. For nonpolar proline and valine clusters of oligomers with the amino acids both in protonated form $OEG_n \cdot Pro \cdot H^+$, $OEG_n \cdot Val \cdot H^+$ and deprotonated form $[OEG_n \cdot (Pro-H)]^-$, $[Val_n \cdot (Pro-H)]^-$ are present.

Molecular dynamics simulation of the amino acid-polyether clusters demonstrates that a polyether chain tends to self-organize around the charged groups of amino acids. Positively charged HN_3^+ group of zwitterionic form of all amino acids and protonated imidazole ring of histidine are wrapped by oligomers in quasi-cyclic conformation similar to that adopted by crown ethers in their complexes with alkali metal cations. Negatively charged COO^- group of zwitterionic and anionic amino acids are wrapped by the oligomers in the "inversed" conformation. Long enough chain can organize in a quasi-helical structure around the charged groups. Hydrophobic side radicals are excluded from interactions.

It is demonstrated that both ESI mass spectrometry and molecular dynamics simulation are efficient methods in characterization of organic nanomaterials.

The results obtained are necessary for better understanding of the assembling and structure of nanomaterials based on pegylated proteins. The structural motives revealed for amino acid-polyether complexes may occur in the relevant domains of the protein-polyether nanoparticles.

References

1. Zhong W-H, Li B, Maguire RG et al (2012) Nanoscience and nanomaterials—synthesis, manufacturing and industry impacts. DEStech Publications Inc., Lancaster
2. Veronese FM, Pasut G (2005) PEGylation, successful approach to drug delivery. Drug Discov Today 10(21):1451–1458. doi:10.1016/S1359-6446(05)03575-0
3. Schalley CA, Springer A (2009) Mass spectrometry of non-covalent complexes: supramolecular chemistry in the gas phase. Wiley, Hoboken
4. Cole RB (ed) (1997) Electrospray ionization mass spectrometry: fundamentals, instrumentation, and applications. Wiley-Interscience, New York
5. Harris JM, Zalipsky S (1997) Poly(Ethylene Glycol): chemistry and biological applications. American Chemical Society, Washington
6. Wyttenbach T, Helden G, Bowers MT (1997) Conformations of alkali ion cationized polyethers in the gas phase: polyethylene glycol and bis[(benzo-15-crown-5)-15-ylmethyl] pimelate. Int J Mass Spectrom Ion Proc 165–166:377–390. doi:10.1016/S0168-1176(97)00179-1
7. Zobnina VG, Kosevich MV, Chagovets VV et al (2010) Stable associates of polyether oligomers with chlorine anion as revealed by electrospray mass spectrometry and molecular dynamics. Mass-Spektrom 7(3):225–231
8. Kosevich MV, Zobnina VG, Chagovets VV et al (2011) Observation of poly (ethylene glycol) clusters with the chlorine anion in the gas phase under electrospay conditions. Rapid Commun Mass Spectrom 25(6):713–718. doi:10.1002/rcm.4919
9. Zobnina VG, Kosevich MV, Chagovets VV et al (2012) Interactions of oligomers of organic polyethers with histidine amino acid. Rapid Commun Mass Spectrom 26(5):532–540. doi:10.1002/rcm.5342
10. Brooks BR, Brooks CL III, Mackerell AD Jr et al (2009) CHARMM: the biomolecular simulation program. J Comput Chem 30(10):1545–1614. doi:10.1002/jcc.21287
11. Lee H, Venable RM, MacKerell AD Jr et al (2008) Molecular dynamics studies of polyethylene oxide and polyethylene glycol: hydrodynamic radius and shape anisotropy. Biophys J 95(4):1590–1599. doi:10.1529/biophysj.108.133025
12. Phillips JC, Braun R, Wang W et al (2005) Scalable molecular dynamics with NAMD. J Comput Chem 26(16):1781–1802. doi:10.1002/jcc.20289
13. ChemCraft (2012) http://www.chemcraftprog.com. Accessed 3 Sep 2012
14. Hart-Smith G, Barner-Kowollik C (2010) Contemporary mass spectrometry and the analysis of synthetic polymers: trends, techniques and untapped potential. Macromol Chem Phys 211(14):1507–1529. doi:10.1002/macp.201000107
15. Kosevich MV, Zobnina VG, Zhivotova EN et al (2009) Mass spectrometric study of cryoprotectors, based on oxyethylated glycerol derivatives. Mass-Spektrom 6(1):7–20
16. Zobnina VG, Boryak OA, Kosevich MV et al (2009) Mass spectrometric study of interactions of amino acids with cryoprotectors. Proline and oxyethylated glycerol derivatives. Biofiz Visn 22(1):103–115

Chapter 23
Application of Baculovirus Technology for Studies of G Protein-Coupled Receptor Signaling

Olga Mazina, Lauri Tõntson, Santa Veiksina, Sergei Kopanchuk and Ago Rinken

23.1 Introduction

G protein-coupled receptors (GPCR), also referred to as 7 transmembrane spanning receptors (7TM), constitute the largest superfamily of receptors in vertebrates and invertebrates. These receptors respond to a wide range of signaling compounds such as bioamines, lipids, peptides, hormones, odorants, and even photons. They mediate the majority of cell-to-cell communication in the human body and are targets for nearly one-third of the prescription drugs on the market [1].

The classic paradigm of the GPCR signal transduction is a linear model (Fig. 23.1): upon agonist binding, conformational changes in the receptor protein activate a heterotrimeric G protein, which can activate or inhibit a variety of downstream effector molecules [2]. GPCRs act as guanine-nucleotide exchange factors for the heterotrimeric G proteins. Activated receptor induces a conformational change in the associated G protein α-subunit leading to release of bound guanosine diphosphate (GDP) followed by binding of guanosine triphosphate (GTP) [3]. GTP binding to the α-subunit induces conformational changes, which cause dissociation of the α-subunit and the $\beta\gamma$-complex from each other and from the GPCR. The GTP bound α-subunit as well as the $\beta\gamma$-dimer is now able to interact with various effector-proteins along the signaling pathway. One such is adenylate cyclase (AC), a membrane spanning enzyme that catalyzes cyclic adenosine monophosphate (cAMP) formation from adenosine triphosphate (ATP). cAMP is a second messenger molecule activating several cellular proteins thereby amplifying the receptor-mediated signal. The slow inherent GTPase activity of the α-subunit hydrolyzes the bound GTP to GDP, leading to inactivation of the α-subunit. The resultant α-GDP complex reassociates with the $\beta\gamma$-heterodimer and

O. Mazina · L. Tõntson · S. Veiksina · S. Kopanchuk (✉) · A. Rinken
Institute of Chemistry, University of Tartu, Ravila 14a, 50411 Tartu, Estonia
e-mail: sergei.kopanchuk@ut.ee

O. Mazina · S. Veiksina · S. Kopanchuk · A. Rinken
Competence Centre on Reproductive Medicine and Biology, 50411 Tartu, Estonia
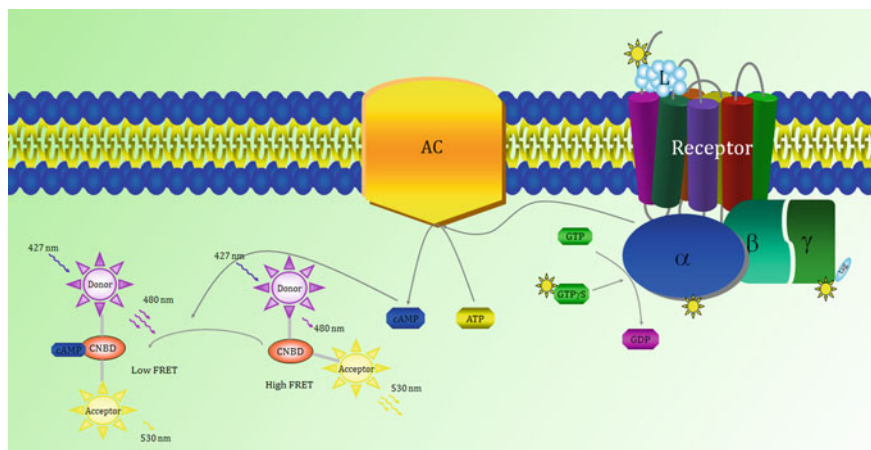
Fig. 23.1 The classic paradigm of the GPCR signal transduction. An illustrative scheme of the basic GPCR signaling components together with the fluorescent tools used to monitor signal propagation at three different stages of the signaling cascade. Abbreviations: *L* ligand (e.g., neurotransmitter, drug); *sun-shape* fluorescent label; *α, β, γ* subunits of the heterotrimeric G protein; *GTP*, and *GDP* guanosine tri and diphosphate respectively; *GTPγS* guanosine-5′-O-[gamma-thio]triphosphate, a nonhydrolyzable GTP analog; *AC* adenylate cyclase; *ATP* adenosine triphosphate, *cAMP*—3′-5′-cyclic adenosine monophosphate; *FRET* Förster resonance energy transfer, *Donor* and *Acceptor*—two fluorescent proteins forming a FRET pair; *CNBD* cyclic nucleotide binding domain of the cAMP biosensor

the G protein returns to resting state. Efficient coupling of the heterotrimeric G protein to receptor requires all three subunits to be present and initiates conformational changes in the receptor with increase of affinity for agonists [4].

More and more evidences point to the fact that the cellular GPCR mediated signaling has to be described by a more complex model accounting for the reactions taking place in addition to the linear signal transduction. Receptor homo—[5–7] and heterodimerization [5], receptor phosphorylation, desensitization, and internalization have been revealed [8]. The necessity of various bivalent metal ions for receptor binding and modulating agonistic response has been demonstrated [7, 9, 10]. Traditionally, the development of novel biologically active ligands in GPCR drug discovery has been focused on targeting the orthosteric binding site of the receptor, which is defined as the site where the endogenous ligand binds during signal transduction. Compounds that bind to an allosteric binding site of the receptors could modulate the binding properties of the orthosteric ligand. This phenomenon poses great potential in drug development and the search for specific selectivity of drug action [11].

Given the importance of GPCR in modern therapeutics, the understanding of the specificity of receptor activation and signal propagation is vital for designing new selective compounds targeting the receptor of choice with high potency.

23.2 Three Strategies to Study the GPCR Signaling at Different Locations

The general aim of our work is to approach the GPCR system from different directions. Using data from ligand binding to receptors, G protein activation studies and measurements of the second messenger levels, we try to combine these three different readouts into new meaningful information about the signal transduction mechanism. In order to access the different levels of GPCR mediated signal transduction we need to use different strategies.

There are very different approaches to study GPCR systems, starting from animal tissue preparations up to purified native or recombinant proteins, from muscle contraction studies to radioligand binding studies in vitro. Our research strategies rely on the two basic properties, experiments are being performed using baculovirus constructs and the detected signals are based on molecular fluorescence.

Baculovirus expression vector system (BEVS) is well known as a feasible and safe technology that has been successfully used for the expression of many target proteins and can also be used to develop cell-based assays in infected insect cells [12]. The basis of BEVS lies in large enveloped DNA viruses *Autographa californica multicapsid nucleopolyhedrovirus* (AcMNPV) derived from insects. Infection of insect cells (e.g., *Spodoptera frugiperda*, Sf9) with a virus encoding the desired transgene under a powerful baculovirus promoter, leads to the production of the recombinant protein in high quantities.

During replication in insect cells baculoviruses are budded from the host cell. Viruses take on a part of the cell membrane while exiting the cell. Using BEVS the Sf9 cells can be programmed to express a recombinant GPCR and by collecting the budded viruses from such cells baculoviral particles (40–50 nm in diameter and 200–400 nm in length) carrying the receptor of interest can be obtained.

Although the replication of AcMNPV is highly insect specific in nature, it can penetrate and transduce a wide range of cells of other origin [13]. After replacing the baculovirus promoter with a strong mammalian promoter (e.g., *cytomegalovirus*, CMV) the modified baculovirus particles are now able to deliver transgenes to a wide variety of mammalian cells, where they can be transcribed and the desired proteins can be expressed. This technology is known as BacMam [14].

23.3 Fluorescent Ligand Binding

For the development of fluorescence-based ligand binding studies we have chosen the labeled peptide NDP-α-MSH, agonist of the melanocortin receptors. We have compared two red-shifted fluorophores with high fluorescence quantum yields, cyanine derivative Cy3B, and rhodamine derivative TAMRA, to be coupled with NDP-α-MSH. Although we have used two different labels, after the comparative

analysis of ligands with the given labels we found that Cy3B has superior physical characteristics (brighter, more photostable, low hydrophobicity, etc.) and thus outperforms TAMRA-coupled ligand in our experimental setup [15]. The assay works well using the cell-membrane preparations to characterize fluorophore-bound ligands as well as its competition with non-labelled ligand (Fig. 23.2).

For additional improvements in assay quality and for decreasing the complexity of measured signals, we proposed to use sample preparations where receptors are produced using the Baculovirus Surface Display technology. Using the receptors on the surface of the viral nanoparticle greatly increases the quality of signal in the ligand-binding assay (signal/noise ratio, stability in time, etc.) and provides additional flexibility of experimental format that is necessary for implementation of HTS.
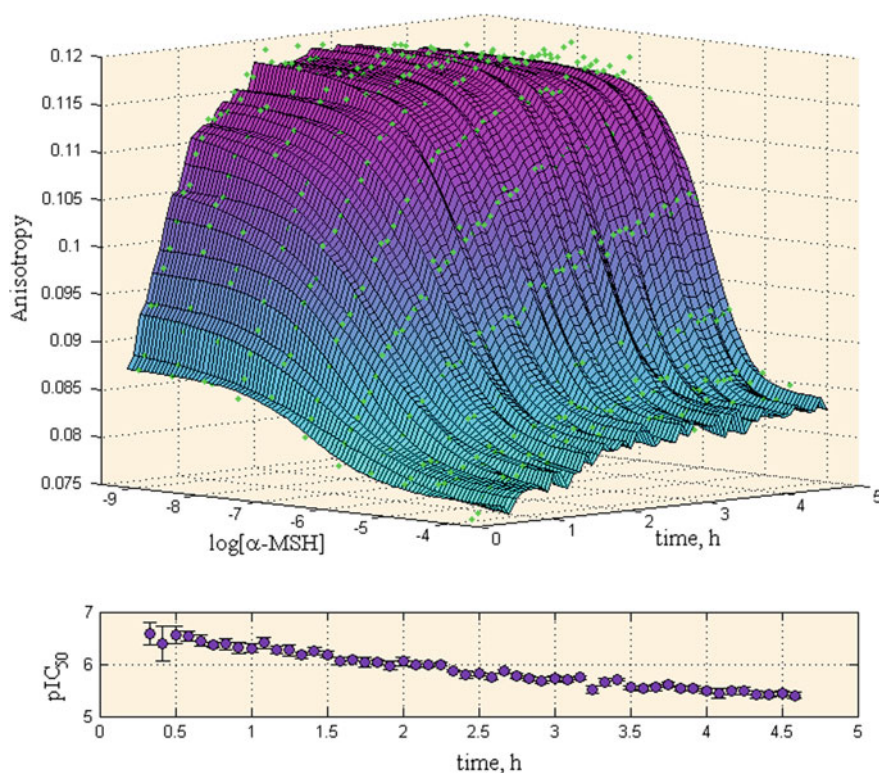
Fig. 23.2 Time courses of changes in fluorescence anisotropy signal of Cy3B labeled NDP-α-MSH (1 nM) binding to MC$_4$ receptors in the presence of different concentrations of α-MSH. Fluorescence anisotropy of the fluorophore was measured at 590(20) nm over 5 h period and indicated as *green dots*. Fitting these data to the logistic function corresponding to the phenomenological model allowed the extraction of the apparent IC$_{50}$ values at different time points (presented in the inset)

23.4 G-Protein Activation

Baculoviral expression systems are advantageous for the expression and purification of mammalian heterotrimeric G-proteins due to low levels of endogenous insect G-proteins, which interact poorly with their mammalian counterparts [16]. We have employed this technology for the tandem affinity purification of mammalian G-proteins using StrepII tagged $\gamma 2$ subunits [17]. We have also used BEVS for the expression of tetracysteine tagged α subunits of i, s, and q subtype and $\gamma 2$ subunits. Simultaneous infection of insect cells with multiple baculoviruses was required in the case of $\beta\gamma$ subunits, as they dimerize immediately after they have been synthesized and would otherwise result in poor yields or non-functional protein preparations.

Purification of heterotrimeric G-proteins from insect cells using StrepII-tagged γ subunits is rapid and simple, with 90–95 % homogeneity attainable in a single chromatographic step. We have used such purified protein preparations to verify the functionality of our tetracycsteine tagged G-proteins by displacing fluorophore-labeled nucleotides from G-protein α subunits. An example of nucleotide binding to CCPGCC tagged and wild type G-protein heterotrimers is provided in Fig. 23.3. Additional confirmation of functionality is provided by the tandem affinity chromatographic procedure itself: if tetracysteine or StrepII tagging would significantly interfere with heterotrimer formation, we would not be able to purify heterotrimeric functional proteins. Instead only $\beta\gamma$-subunits, or even only γ subunits, would be caught by affinity purification techniques.

Fluorescent nucleotides such as Bodipy-FL-GTPγS are found not to be optimal for the use in cellular environments due to high level of nonspecific binding and membrane-impermeability [18]. Baculoviral particles can yield higher specific signal amplitudes than many mammalian cell lines due to their relatively higher ratios of heterologously expressed proteins over endogenous proteins and membrane lipids. However, even here fluorescent nucleotides were not suitable for direct

Fig. 23.3 Displacement of Bodipy-FL-GTPγS (5 nM) from G-protein $\alpha_{i2}\beta_1\gamma_2$ heterotrimers by GTPγS, as determined by changes in fluorescence anisotropy. Data is from a representative experiment with either wild type α-subunits (*blue open symbols*) or mutated (*red filled symbols*) α-subunits
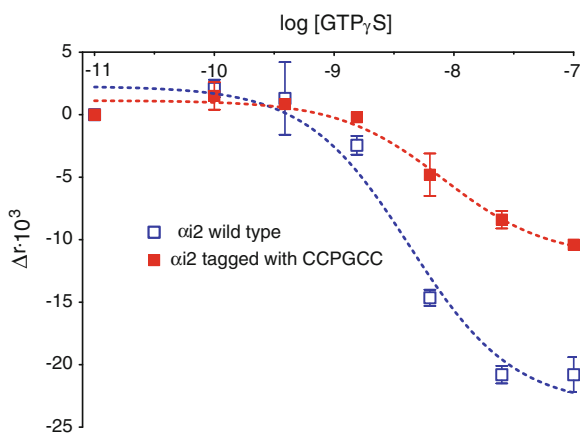
characterization of different G-proteins and other methods, such as those based on Förster resonance energy transfer (FRET), have to be used. Thus, real time in vivo observation of G-protein activation remains a challenge, unless specific genetically engineered G-protein constructs are employed [19]. We have verified the expression and functionality of our tetracysteine tagged G-proteins in purified protein preparations and labeled them orthogonally with fluorophores such as F2FlAsH and ReAsH in baculoviral particles alongside GPCRs. Preliminary results suggest that these fluorescent arsenical hairpin binders suffer from similar nonspecific binding problems as fluorescent nucleotides, which limits signal amplitude and complicates specific labeling. On the other hand, the high sensitivity of the fluorescence of such fluorophores to their molecular environment can be used to measure protein conformational changes in vitro [20] without the need for a partner fluorophore, as is required for resonance energy transfer-based measurements. We have noticed similar sensitivity in some of our tetracysteine-tagged G-protein subunits labeled with FlAsH-analogues (unpublished observations).

23.5 Monitoring the Changes in Cellular cAMP Level

For monitoring the GPCR mediated signal propagation, it is possible to look at the change in the cellular level of a second messenger molecule. For many GPCR-s such second messenger is cyclic adenosine monophosphate. The concentration of cAMP can be modulated either by activation or inhibition of the enzymes adenylate cyclases by G protein α subunits. To measure the changes in cAMP level inside the cells in real time different FRET-based biosensors have been used, e.g., Epac2-camps [21] and $^{T}Epac^{VV}$ [22].

The use of the BacMam system for cAMP biosensor expression enabled us to establish an easy and reproducible assay for monitoring elevation of cAMP in live cells [10]. Importantly, this technology is compatible with a broad range of cell lines and can be used to study different GPCR-s in several cellular environments. Both of the biosensors at our disposal are expressed in the cell cytosol and respond to changes in cAMP concentrations in the physiological range (0.1–100 µM) [21, 22]. The expression of recombinant biosensor proteins is well tolerated by cells and the amount of the expressed protein can be adjusted by viral dose depending on the cell line and the experimental design.

Using the cAMP sensor BacMam expression system, both G_s and G_i protein coupled receptor mediated signal transduction can be measured (Fig. 23.4). As an example it allows us to distinguish between agonist and antagonist effects on different subtypes of dopamine receptors (D1R family is coupled to G_s and D2R family is coupled to G_i proteins). Such assays enable us to screen for new receptor subtype selective compounds [23]. The biological effect of bivalent cations on receptor activation can also be assayed using the above mentioned sensor system. The ligand potencies on melanocortin receptor 1 (MC_1R) activations were positively modulated by Ca^{2+} and Mg^{2+} ions [10].
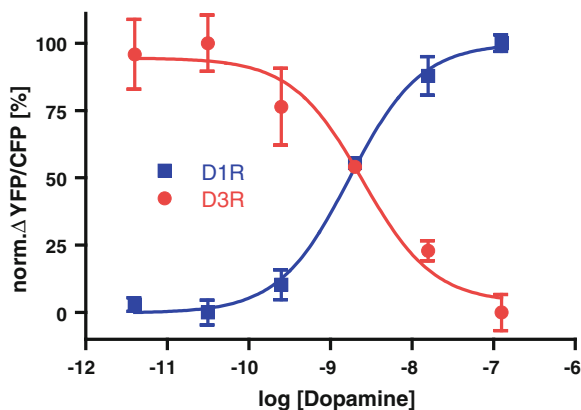
Fig. 23.4 Inhibition and activation of cAMP synthesis with dopamine. Dopamine was added to the HEK293 cells expressing either dopamine D1 receptor (*blue*) or D3 receptor (*red*) and the response as change in FRET signal was measured 10 min after agonist treatment. For D3 receptor 10 μM forskolin (direct activatior of adenylate cyclase) was added together with the agonist. Measurements performed in triplicates at 37 °C. Cells were transduced with $^{T}Epac^{VV}$ BacMam virus for 3 h and further incubated for 21 h in complete growth media supplemented with 5 mM sodium butyrate

Often the biological effect of receptor antagonists is hard to measure because these compounds by definition do not pass along the mediated signal coming from the extracellular part via the receptor. With our system we can measure both GPCR agonist and antagonist effects on a second messenger level. The agonist displacement experiments performed on MC_1 receptors in B16F10 cells have shown potencies in agreement with the data from ligand binding experiments (unpublished observations).

The cAMP sensor BacMam system has been optimized for the use on a 96-w cell assay plate in a fluorescence plate reader with simultaneous dual emission for FRET measurements. The data analysis relies on the change in the fluorescence intensity ratio of the FRET donor and acceptor fluorophores upon cAMP binding to the sensor protein. Using Fluorescence-lifetime imaging microscopy (FLIM) it is possible to improve the signal to noise ratio in FRET measurements even further using the $^{T}Epac^{VV}$ biosensor [22]. This third generation cAMP sensor uses a very bright and single-exponentially decaying cyan florescent protein variant mTurquoise [24] as FRET donor and is developed to perform optimal in both FLIM and fluorescence intensity change detection schemes.

23.6 Discussion

The application of three different fluorescence-based strategies to monitor GPCR signaling revealed three distinct signal readouts. Combining those signals provides an opportunity to get a better picture of the GPCR system and characterize it in

more detail. Although the cellular signaling system is very complex often connected with different pathways we propose a possible approach to characterize at least part of it.

Fluorescence-based assays make it possible to study the systems of interest from different aspects with precision and high sampling rate. This has led to the adoption of a "systems" approach in studies of entire GPCR signaling pathways. This, however, leads to an explosive increase of raw data. Usage of ordinary differential equation based on mechanistic models that describe ligand-receptor interaction processes could allow getting deeper insight into the studied processes. The recognition of the increasing complexity of the studied systems has proven the necessity to use global numerical approaches in data analysis based on mechanistic models [25]. Due to the inherent multiplexing properties of fluorescence, different types of signals could differ with changes in the underlined processed (quantum yield, fluorescence lifetime, and rotational diffusion of fluorophores). To account for this, we propose the application of second-generation global analysis [26].

The technical developments at present have blessed us with an emerging amount of novel spectroscopic and microscopic techniques. As an example the use of total internal reflection fluorescence (TIRF) microscopy can filter out much of the noise coming from cell cytosol and make monitoring ligand binding to receptors at single molecule level possible. Also, future applications for fluorescence correlation spectroscopy (FCS) are to be developed using the well-characterized baculovirus nanoparticles. Monitoring the fluctuation of the fluorescence intensity upon the interaction between the fluorescently labeled ligand and the receptor on the baculovirus surface can be the average ligand binding experiment of tomorrow.

23.7 Summary

In the long term, understanding the signal transduction mechanisms (particularly ligand receptor interactions) will improve strategies for the search and development of new therapeutics with more selective action that will be safer for patients. Much research is going on the pharmacological field of receptor signaling. There are over 800 different GPCRs in human organism; many of their endogenous activators are still unknown. Here, we have proposed an approach with means of fluorescence detectors and the versatile aid of the baculovirus expression system, to systematically monitor three separate stages of cellular signaling: ligand binding to the receptor, G protein activation, and second messenger cAMP production as a result of the binding event.

References

1. Overington JP, Al-Lazikani B, Hopkins AL (2006) How many drug targets are there? Nat Rev Drug Discovery 5(12):993–996
2. Neer EJ (1995) Heterotrimeric G proteins: organizers of transmenbrane signals. Cell 80(2):249–257
3. Iiri T, Farfel Z, Bourne HR (1998) G-protein diseases furnish a model for the turn-on switch. Nature 394(6688):35–38
4. Yasuda H, Lindorfer MA, Woodfork KA, Fletcher JE, Garrison JC (1996) Role of the prenyl group on the G protein γ subunit in coupling trimeric G proteins to A1 adenosine receptors. J Biol Chem 271(31):18588–18595
5. Mandrika I, Petrovska R, Wikberg J (2005) Melanocortin receptors form constitutive homo- and heterodimers. Biochem Biophys Res Commun 326(2):349–354
6. Elsner A, Tarnow P, Schaefer M, Ambrugger P, Krude H, Grüters A, Biebermann H (2006) MC4R oligomerizes independently of extracellular cysteine residues. Peptides 27(2):372–379
7. Kopanchuk S, Veiksina S, Petrovska R, Mutule I, Szardenings M, Rinken A, Wikberg JE (2005) Co-operative regulation of ligand binding to melanocortin receptor subtypes: evidence for interacting binding sites. Eur J Pharmacol 512(2):85–95
8. Claing A, Laporte SA, Caron MG, Lefkowitz RJ (2002) Endocytosis of G protein-coupled receptors: roles of G protein-coupled receptor kinases and ß-arrestin proteins. Prog Neurobiol 66(2):61–79
9. Holst B, Elling CE, Schwartz TW (2002) Metal ion-mediated agonism and agonist enhancement in melanocortin MC1 and MC4 receptors. J Biol Chem 277(49):47662–47670
10. Mazina O, Reinart-Okugbeni R, Kopanchuk S, Rinken A (2012) BacMam system for FRET-based cAMP sensor expression in studies of melanocortin MC1 receptor activation. J Biomol Screen 17(8):1096–1101
11. Keov P, Sexton PM, Christopoulos A (2011) Allosteric modulation of G protein-coupled receptors: a pharmacological perspective. *Neuropharmacology*
12. A Kost, T., Patrick Condreay, J, S Ames R (2010) Baculovirus gene delivery: a flexible assay development tool. Current gene therapy, 10(3), 168–173
13. Kost TA, Condreay JP (2002) Recombinant baculoviruses as mammalian cell gene-delivery vectors. Trends Biotechnol 20(4):173–180
14. Condreay JP, Witherspoon SM, Clay WC, Kost TA (1999) Transient and stable gene expression in mammalian cells transduced with a recombinant baculovirus vector. Proc Natl Acad Sci 96(1):127–132
15. Veiksina S, Kopanchuk S, Rinken A (2010) Fluorescence anisotropy assay for pharmacological characterization of ligand binding dynamics to melanocortin 4 receptors. Anal Biochem 402(1):32–39
16. Kozasa T (2003) Purification of G Protein Subunits from Sf9 Insect Cells Using Hexahistidine-Tagged alpha and betagamma Subunits. Methods Molecular Biology-Clifton Totowa 237:21–38
17. Tõntson L, Babina A, Võsumaa T, Kopanchuk S, Rinken A (2012) Characterization of heterotrimeric nucleotide-depleted Gαi-proteins by Bodipy-FL-GTPγS fluorescence anisotropy. Arch Biochem Biophys
18. Gille A, Seifert R (2003) Low-affinity interactions of BODIPY-FL-GTP? S and BODIPY-FL-GppNHp with Gi-and Gs-proteins. Naunyn-Schmiedeberg's Arch Pharmacol 368(3):210–215
19. Kimple RJ, Jones MB, Shutes A, Yerxa BR, Siderovski DP, Willard FS (2003) Established and emerging fluorescence-based assays for G-protein function: heterotrimeric G-protein alpha subunits and regulator of G-protein signaling (RGS) proteins. Comb Chem High Throughput Screen 6(4):399–407
20. Nakanishi J, Maeda M, Umezawa Y (2004) A new protein conformation indicator based on biarsenical fluorescein with an extended benzoic acid moiety. Anal Sci 20(2):273–278

21. Nikolaev VO, Bünemann M, Hein L, Hannawacker A, Lohse MJ (2004) Novel single chain cAMP sensors for receptor-induced signal propagation. J Biol Chem 279(36):37215–37218
22. Klarenbeek JB, Goedhart J, Hink MA, Gadella TW, Jalink K (2011) A mTurquoise-based cAMP sensor for both FLIM and ratiometric read-out has improved dynamic range. PLoS ONE 6(4):e19170
23. Reinart-Okugbeni R, Ausmees K, Kriis K, Werner F, Rinken A, Kanger T (2012) Chemoenzymatic synthesis and evaluation of 3-azabicyclo [3.2. 0] heptane derivatives as dopaminergic ligands. European J Med Chem
24. Goedhart J, Van Weeren L, Hink MA, Vischer NO, Jalink K, Gadella TW (2010) Bright cyan fluorescent protein variants identified by fluorescence lifetime screening. Nat Methods 7(2):137–139
25. Dyson RM, Kaderli S, Lawrance GA, Maeder M (1997) Second order global analysis: the evaluation of series of spectrophotometric titrations for improved determination of equilibrium constants. Anal Chim Acta 353(2):381–393
26. Otto MR, Lillo MP, Beechem JM (1994) Resolution of multiphasic reactions by the combination of fluorescence total-intensity and anisotropy stopped-flow kinetic experiments. Biophys J 67(6):2511–2521

Chapter 24
Interplay of Quadratic and Cubic Nonlinear Optical Responses in KDP Single Crystals with Incorporated TiO$_2$ Nanoparticles

V. Ya. Gayvoronsky, M. A. Kopylovsky, M. S. Brodyn, A. S. Popov, V. O. Yatsyna and I. M. Pritula

24.1 Introduction

The single crystals (SCs) of potassium dihydrogen phosphate (KDP, KH$_2$PO$_4$) family is widely used in modern optoelectronics and nonlinear optics. In particular, optical crystals with lower impurity and higher laser damage threshold are required in industrial laser systems. In fact, these types of crystals have low magnitude of d_{36} nonlinear coefficient which determines second harmonic generation (SHG) efficiency in comparison to borate crystals family.

An effective method to improve properties of KDP crystals is organic/inorganic admixtures incorporation into pure matrix when the growth process is performed. Research targeted at the design of composite materials based on dielectric matrices with incorporated organic impurities [1, 2] and nanoparticles (NPs) [3–5] are being actively carried out nowadays. Composite media of "dielectric matrix/nanoparticles" type are promising for the development of nonlinear optical (NLO) elements for applications in laser radiation conversion and control. However, nonisomorphic inclusions of dopants can cause essential local deformation of the crystal lattice. Recently, potassium dihydrogen phosphate matrix has been used as a host of dielectric SiO$_2$ [5] and semiconductor CdTe NPs [6] in order to design novel lasing media.

Promising results were obtained for KDP SCs with incorporated TiO$_2$ NPs of anatase modification (KDP:TiO$_2$) [4]. The series of as grown KDP:TiO$_2$ SCs with different concentrations of TiO$_2$ NPs in growth solution in range $10^{-5} \div 10^{-3}$ wt.% is presented on the Fig. 24.1a–c. The study of grown KDP:TiO$_2$ crystals revealed their high optical quality and homogeneity, high laser damage

V. Ya. Gayvoronsky (✉) · M. A. Kopylovsky · M. S. Brodyn · A. S. Popov · V. O. Yatsyna
Institute of Physics NAS of Ukraine, Pr. Nauki, 46, Kiev 03680, Ukraine
e-mail: vlad@iop.kiev.ua

I. M. Pritula
Institute for Single Crystals NAS of Ukraine, Pr. Lenin, 60, Kharkov 61001, Ukraine

threshold and low scattering losses in optical range, as well as new interesting properties. Electron paramagnetic resonance (EPR) spectra study of KDP:TiO$_2$ demonstrated that the concentration of noncontrolled impurities in KDP:TiO$_2$ is several times lower than in nominally pure KDP samples [7]. Besides, the concentration values of NPs in {010} prismatic (Pr) growth sector is twice as large as in the {101} pyramidal (P) sector, the schematic representation of which is presented in Fig. 24.1d. The effect of enhancement and sign inversion of nonlinear refractive index in KDP:TiO$_2$ relatively to pure KDP crystals was observed under self-action of picosecond range laser pulses [3]. Besides, under resonant continuous wave (CW) laser excitation we have shown the possibility of characterization of KDP matrix intrinsic defects and surface defect states of anatase NPs due to significant nonlinear refractive index variation $\Delta n \sim 10^{-5}$ [8].
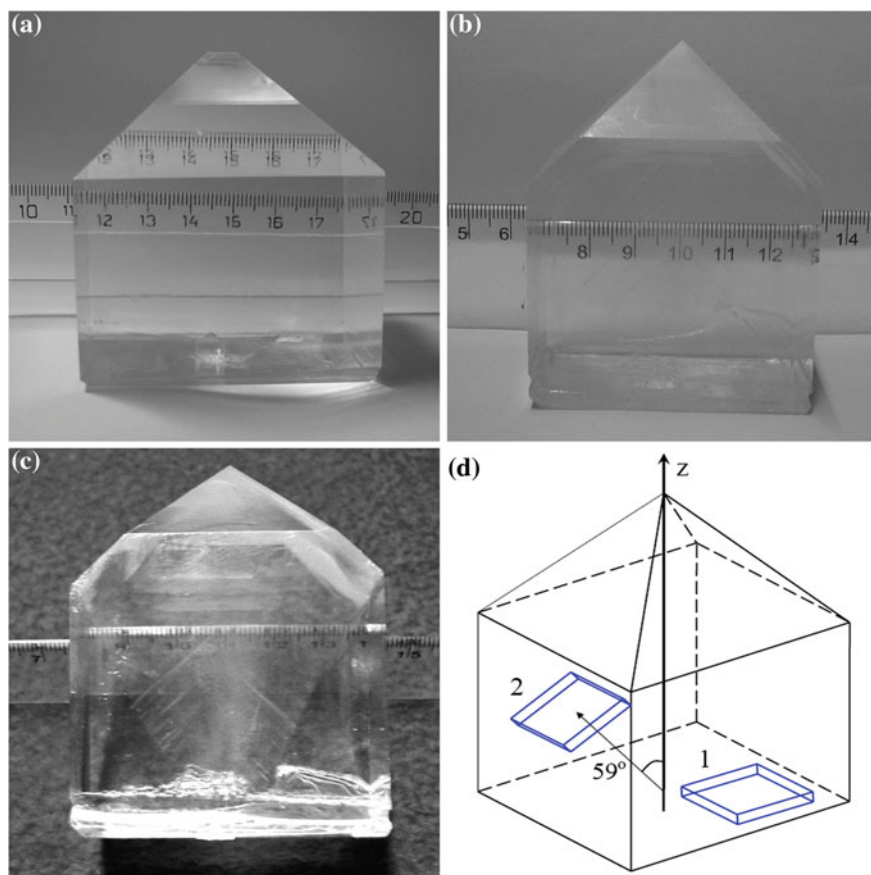
Fig. 24.1 Series of as grown KDP:TiO$_2$ single crystals with different concentrations of TiO$_2$ NPs in mother liquor solution: 10^{-5} (**a**), 10^{-4} (**b**) and 10^{-3} wt.% (**c**); **d** schematic representation of the KDP crystal pyramidal (P) and prismatic (Pr) growth sectors and types of the samples cut: 1st is perpendicular to the crystal Z-axis (Z-cut); 2nd—to the II type phase-matching (PM) direction for the SHG at 1064 nm

24.2 Experimental Technique and Samples Characterization

Crystals growth. Pure KDP and KDP:TiO$_2$ crystals were grown by the temperature reduction method onto point seed ($10 \times 10 \times 10$ mm^3). As a raw material, we used potassium dihydrogen phosphate salt with impurities (Fe, Cr, Al, Sb, Bi, Cu, Hg, Ag, Pb) not exceeding 0.5–1 ppm. The mother liquors (pH = 4.0–4.1) were prepared in accordance with the solubility curve at a saturation temperature of 50 °C, passed through fluoroplastic filters with a pore diameter of 0.05 mm, and then overheated during 24 h at T = 80 °C. TiO$_2$ NPs (15 nm) were synthesized by the sol-gel method: TiCl$_4$ were precipitated using ammonia, the resulting suspension was washed and subjected to super high-frequency heating that led to the formation of pyrotitanic acid H$_2$Ti$_2$O$_5$ transformed into TiO$_2$ after annealing at 600 °C. The peculiarities of KDP:TiO$_2$ SCs growth are explained in detail in [9]. Samples notation and optical properties of KDP and KDP:TiO$_2$ SCs are presented in Table 24.1.

It was shown that the NPs with adsorbed H$_2$PO$_4^-$ and (H$_2$PO$_4$)$_4^{2-}$ anions were incorporated predominantly in the positively charged face (101) of the P sector of KDP [9]. High resolution X-ray three-crystal diffractometry investigation of the as-grown KDP SCs with TiO$_2$ NPs revealed the presence of the turns of the growth layer "stacks" up to 3 arcsec for the growth sectors {010} and {101}. The observed thickness of these "stacks" is of the order of 20–30 μm. For KDP:TiO$_2$ crystals a relative change of the crystal lattice parameter ($\Delta d/d$) was found to be caused by incorporation of TiO$_2$ NPs into the boundaries of the growth layers. This gave rise to the formation of a semicoherent binding on the interface between the captured TiO$_2$ and the matrix. No essential influence of the NPs on the laser damage threshold of KDP with 10^{-5} wt.% of TiO$_2$ was established.

The linear optical and NLO studies were performed for two kinds of the SC samples for each growth sector presented at Fig. 24.1d. The first one corresponds

Table 24.1 Optical properties of Z-cut plates of KDP and KDP:TiO$_2$ crystals

Growth sector	Sample notation	TiO$_2$ conc., wt.%	NPs conc. in SCs, cm^{-3}	Scattering losses, %		Re($\chi^{(3)}$), 10^{-4} esu	
				633 nm	532 nm	1064 nm	532 nm
{101}	P	–	–	1.0	1.0	−0.7	10
	P5	10^{-5}	$3.2 \cdot 10^{10}$	1.7	1.7	−1.3	−1.7
	P4	10^{-4}	$3.3 \cdot 10^{11}$	1.8	2.5	−1.6	−0.8
{010}	Pr	–	–	1.1	1.1	−1.7	−1.5
	Pr5	10^{-5}	$1.6 \cdot 10^{10}$	2.6	1.7	−1.5	5.3
	Pr4	10^{-4}	$1.6 \cdot 10^{11}$	2.6	1.3	−1.3	6.2
	Pr3	10^{-3}	$1.6 \cdot 10^{12}$	2.6	2.8	−0.5	3.7

Growth sector, samples notation, TiO$_2$ concentration in growth solution, NPs concentration in grown single crystals (SCs), scattering losses at 532 nm and 633 nm wavelengths [17], and real part of cubic nonlinear susceptibilities Re($\chi^{(3)}$) under 532 and 1064 nm CW laser self-action [8]

to the Z-cut plates cut perpendicular to the SC axis, the second one—cut perpendicular to the II type phase-matching (PM) direction for the SHG at 1064 nm. Both kinds of samples were prepared with two typical dimensions: so-called "thin" $10 \times 10 \times 0.8$ mm^3 and "thick" $10 \times 10 \times 10$ mm^3 plates. It is worth to note that the layers of the incorporated TiO$_2$ NPs in Z-cut samples are tilted to Z-axis in case of P sector and are parallel to the axis in Pr ones. All the surfaces of the studied samples were finished with optical polishing, without antireflective coatings.

Scattering measurements. The experimental setup for the measurements of spatial distribution cross-section of the scattered intensity is based on the goniometer G-5. The technique is described in detail in [10]. The laser source (DPSS laser with $\lambda = 532$ nm, $P = 50$ mW or He–Ne laser with $\lambda = 633$ nm, $P = 10$ mW) and the sample is mounted on the fixed arm of goniometer. The registration device is fixed on its movable arm at the distance $l = 200$ mm from the sample and consists of CCD array (AMKO LTI MuLTI-ray with 1024 px and pixel size 25×200 μm^2, 12-bit digital resolution) with lens attached to it. The lens with diameter 9.6 mm controls the solid angle for the scattered radiation collection.

The estimation of scattering losses p_{scat} is based on the integration of the scattered light power $\Delta P(\theta)$ in the solid angle $\Delta\Omega$ of the lens over the part of the forward hemisphere [10]:

$$p_{\text{scat}} = \frac{2\pi}{P_0} \int_{\theta_{\min}}^{\pi/2} \frac{\Delta P(\theta)}{\Delta\Omega} \sin\theta \mathrm{d}\theta \qquad (24.1)$$

where P_0 is total power transmitted, $\theta_{\min} \approx 1.8°$ exceeds the lens angular aperture $\sim 1.4°$ due to the finite size of the transmitted beam at the registration plane. The technique allowed to measure the spatial distribution of scattered intensity for KDP:TiO$_2$ SCs with six orders of magnitude dynamic range.

Spatial profile analysis technique. We used the CW DPSS lasers with 532 nm and 1064 nm wavelengths as well as the mode-locked pulsed YAG:Nd laser (42 ps FWHM, repetition rate 5 Hz, $\lambda = 1064$ nm) with the Gaussian spatial profile as laser sources. Neutral attenuator A (see Fig. 24.2a) with transmission from 1 to 50 % allowed to vary the laser beam intensity and control the reversibility of the NLO response. The crystals S were positioned after the focal point of the focusing lens L^I or L^{II} with focal distance 8/11 cm for the CW/pulsed excitation regimes. The photodiodes (PD) 1, 2, 3 provide a power/energy acquisition: of input laser beam (PD1), of the beam transmitted through the sample (PD2) and passed the finite aperture ($\varnothing = 2$ mm) of on-axis diaphragm (PD3) in the far field. The lens L with wide aperture collects scattered radiation onto the PD2.

The total transmittance of the studied crystals is determined by the signals ratio of the photodiodes PD2 to PD1 corrected to the apparatus function. In the framework of the cubic NLO response, the photoinduced variation of the total transmittance $T(I_0)$ versus the incident intensity I_0 of the plane light wave can be derived analytically $T(I_0) = T_0/(1 + q(I_0))$. Typically, the effect is attributed to the two-photon absorption (TPA) process. In the expression above T_0 is the linear (spectral)
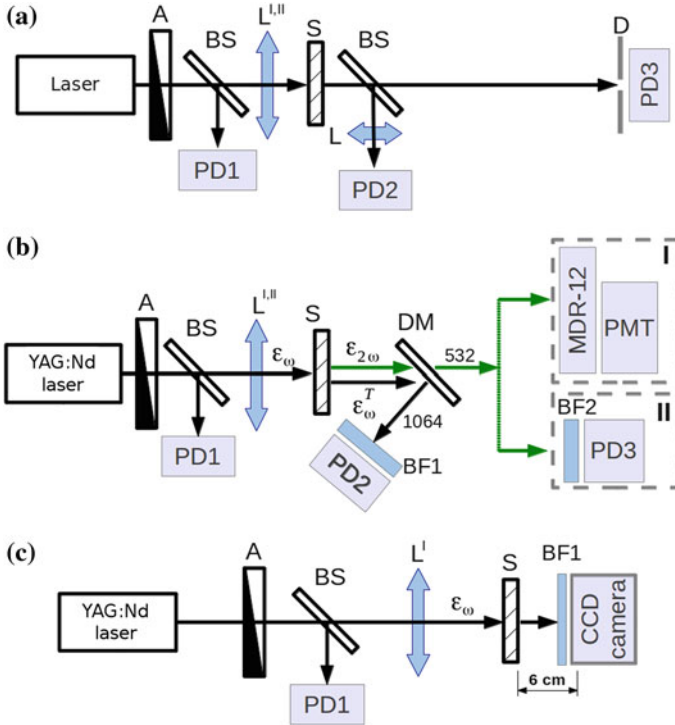
Fig. 24.2 Scheme of experimental setup for: **a** laser beam self-action technique, **b** the SHG efficiency measurements without phase-matching (PM) conditions (inset I) and with PM conditions (inset II), **c** spatial laser beam profile transformation analysis. *A* attenuator, *BS* beam splitter, $L^{I,II}$ lens with focal distance 8 cm (*I*) or 11 cm (*II*), *S* sample, *DM* dichroic mirror, *BF1*, *BF2* bandpass filters, *D* finite diaphragm, *PD1*, *PD2*, *PD3* photodiodes, *PMT* photomultiplier, *MDR-12* monochromator, $\varepsilon_\omega, \varepsilon_\omega^T, \varepsilon_{2\omega}$ energies of incident, transmitted and SH pulses, respectively

transmission coefficient, $q(I_0) = \beta I_0 L_{eff} \sim \mathrm{Im}\left(\chi^{(3)}\right) I_0$, $L_{\mathrm{eff}} = (1 - \mathrm{e}^{-\alpha L})/\alpha$-self-action effective length, α—linear absorption coefficient, L—the thickness of the media, β—TPA coefficient, $\chi^{(3)}$—cubic NLO susceptibility. Spatial averaging across the Gaussian beam profile transforms $T(I_0)$ into $T^{CW}(I_0) = T_0 \cdot \ln(1 + q(I_0))/q(I_0)$ for TEM$_{00}$ CW laser beam excitation [11].

For the pulsed laser excitation regime it is impossible to obtain the exact expression for the spatial and temporal averaging across the beam and pulse Gaussian profiles. We applied the approximate formulae

$$T^p(I_0) = T^{CW}(I_0)\left[\frac{1 + 0.228q(I_0)}{1 + 0.136q(I_0)}\right], \qquad (24.2)$$

where a fraction in brackets provides the proper contribution of the temporal averaging [12].

The signals ratio of PD3 and PD1 allows us to interpret the on-axis transmittance in the far field. It is sensitive to convergence/divergence of the laser beam which is caused by self-focusing/defocusing phenomena in the media [12, 13]. According to the model for the cubic nonlinearity with negligible nonlinear absorption described in [13], the peak photoinduced phase shift at the exit surface of the sample is proportional to the photoinduced refractive index $\Delta\varphi(I_0) = kL_{eff}\Delta n(I_0) \sim \mathrm{Re}(\chi^{(3)})I_0$ (k—the wave vector). For the pulsed excitation regime taking into account the Gaussian decomposition approach [13] and the spatial and temporal averaging of the transmitted pulse, the on-axis transmittance in the far field can be presented as an expansion into $\Delta\varphi$:

$$T_a(I_0) = S\Big((1 + C_1\Delta\varphi(I_0) + C_2(\Delta\varphi(I_0))^2 + \cdots\Big), \tag{24.3}$$

where coefficients C_n are determined by the geometry of the experiment:

$$
\begin{aligned}
C_1 &= \frac{1}{S\sqrt{2}}\exp\left[\frac{-4r_0^2(3+b^2)}{\omega^2(9+b^2)}\right]\sin\left[\frac{8br_0^2}{\omega^2(9+b^2)}\right],\\
C_2 &= \frac{1}{3S\sqrt{3}}\left(\exp\left[\frac{-6r_0^2(5+b^2)}{\omega^2(25+b^2)}\right]\cos\left[\frac{24br_0^2}{\omega^2(25+b^2)}\right] - \exp\left[\frac{-6r_0^2(1+b^2)}{\omega^2(9+b^2)}\right]\right),
\end{aligned}
\tag{24.4}
$$

where S—is the aperture linear transmittance, ω—the beam radius and b—the ratio of the geometric focusing to the diffraction broadening (see Ref. [12]). In the case of the CW laser excitation, the coefficients C_n^{CW} are in following relation with one for the pulsed: $C_n^{CW} = C_n \cdot \sqrt{n}$ [12, 14]. In order to compensate the impact of the photoinduced transmittance variation on refractive NLO response, we normalize the on-axis transmittance in the far field on total transmittance of the sample. The verification of such approach is described in [13] for extraction of purely refractive Z-scan from closed aperture one by division it on open aperture Z-scan. Thus, the fitting of the experimental total and on-axis transmittances by Eqs. 24.2, 24.3 for chosen laser intensity range allows us to obtain the magnitudes of $\Delta\alpha$ and $\Delta\varphi$ as well as Δn, $\mathrm{Im}(\chi^{(3)})$ and $\mathrm{Re}(\chi^{(3)})$ values.

SHG measurement technique. We have used phase-matched (PM) method [15, 16] for the SHG efficiency measurements and estimations of quadric NLO coefficient d_{36} of mentioned crystals. We have also performed the study of the impact of the NPs on laser frequency conversion efficiency for the Z-cut samples. In the last case the SHG process takes place without PM conditions.

The experimental setup is shown on the Fig. 24.2b. The inset I corresponds to the measurements without PM conditions, inset II—to the PM conditions [15]. The picosecond laser pulses with Gaussian spatial and temporal profiles (pulse width 42 ps FWHM at 1064 nm, repetition rate 5 Hz) were used as fundamental

excitation. The neutral attenuator A allowed to vary the incident pulses energy up to 300 μJ. Under PM conditions, the sample was positioned at 2 cm after the beam waist of focusing lens L^{II} ($f = 11$ cm). The diagonal of the crystal faces was adjusted along the incident beam polarization in order to obtain equal energy splitting between o- and e-waves. The acquisition of the input/transmitted $\left(\varepsilon_\omega/\varepsilon_\omega^T\right)$ pulse energies was provided by photodiodes PD1/PD2 as well as SH ($\varepsilon_{2\omega}$) one with PD3. The dichroic mirror (DM) and proper bandpass filters (BF1/BF2) were used to separate fundamental and SH output pulses. All registration channels were absolutely calibrated with a power/energy meter VEP-1L. To minimize the impact of diffraction effects on the parametric and self-action phenomena, we used robust transverse spatial averaging of the NLO response, with typical laser beam aperture adjusted to be about 1 mm.

The energy conversion efficiency η into the SH in the given pump field approximation was derived from the power conversion efficiency [15] by taking into account the temporal averaging across the incident Gaussian pulse profile and reflection losses at the crystal/air interfaces [16]:

$$\eta \equiv \frac{\varepsilon_{2\omega}}{\varepsilon_\omega} = \frac{8\sqrt{2\pi}L^2|d_{\text{eff}}|^2\exp(-L(\alpha_\omega + \alpha_{2\omega}/2))}{c\tau\varepsilon_0\left\{\lambda_{2\omega}a\left(1 + n_\omega^0\right)\left(1 + n_\omega^e\right)\left(1 + n_{2\omega}^e\right)\right\}^2}\varepsilon_\omega, \qquad (24.5)$$

where $n_{\omega,2\omega}^{o,e}$ are the refractive indices of the ordinary and extraordinary beams at corresponding wavelengths, $d_{\text{eff}} = d_{36}\sin(2\theta)$ is the effective quadric NLO coefficient, $\theta = 59°$ is the angle between the optical axis and the type II PM direction in the KDP [16], L is the crystals thickness, $\alpha_{\omega,2\omega}$ are the absorption coefficients, ε_0 is the dielectric constant, c—the speed of light and τ and a are the incident pulse width (HW1/eM) and beam radius at the sample. The experimental data $\eta(\varepsilon_\omega)$ linear approximation slope contains the magnitude of the quadric NLO coefficient $|d_{36}|$ without taking into account the manifestation of other NLO effects [15]. The photoinduced variations of the total transmittance $\varepsilon_\omega^T/\varepsilon_\omega$ were measured simultaneously at the fundamental wavelength in order to separate properly the contribution of the parametric conversion and nonradiative losses in extinction of the pump beam.

The study of SHG process in Z-cut samples without PM conditions was held with the experimental setup presented in Fig. 24.2b, inset I. The focusing lens L^I ($f = 8$ cm) was used. The sample was positioned at beam waist of the laser beam. The monochromator MDR-12 with photomultiplier were used for the SH energy acquisition. The data treatment was similar to those described above for the case of phase match conditions [15].

In order to study the impact of cubic refractive nonlinear response on SHG process of KDP:TiO$_2$ crystals we performed the analysis of spatial laser beam profile transformation after the sample. With this purpose we used CCD-based beam profiler Ophir Spiricon SP-620U (1600 $\times$ 1200 px, 4.4 μm pixel spacing). The spatial profile of freely propagating and transformed beam was registered in 6 cm after the output face of the sample (Fig. 24.2c). We adjusted the polarization

of incident beam along the sample faces (polarization of o- or e-waves) in order to suppress oe-e parametric interaction. The high-frequency noise of the spatial profile was removed by Fourier low-pass filter. The averaging over concentric shells with 5 px width, centered on beam energy center, was held in order to obtain averaged radial intensity distribution across the beam.

24.3 Optical Properties and NLO Response Under CW Laser Beam Self-Action

High optical quality of KDP:TiO$_2$ SCs was shown experimentally by visible spectra, anomalous biaxiality and elastic scattering losses measurement [3, 17]. Optical absorption spectra of nominally pure KDP and KDP:TiO$_2$ crystals with 10^{-4} wt.% of TiO$_2$ NPs are presented at Fig. 24.3a. The measurements were performed for "thick" Z-cuts of SCs by Perkin-Elmer Lamda 1200 spectrometer at room temperature. All studied samples demonstrate high transparence in UV— near IR ranges. Nominally pure crystals cut from P sector are more transparent in comparison to Pr ones due to lower absorption of impurities from the mother liquor. Besides, the incorporation of 10^{-4} wt.% of TiO$_2$ NPs into Pr sector leads to small changes in transparency relatively to nominally pure KDP crystal. The phenomenon can be explained by the compensation effect of embedded anatase NPs. The concentration 10^{-4} wt.% is not high for efficient absorption of UV light by anatase NPs, but it is enough for adsorption of impurity atoms on their developed surface during the growth stage [17]. The effect of impurities compensation was also observed during EPR study of KDP:TiO$_2$ SCs [4].
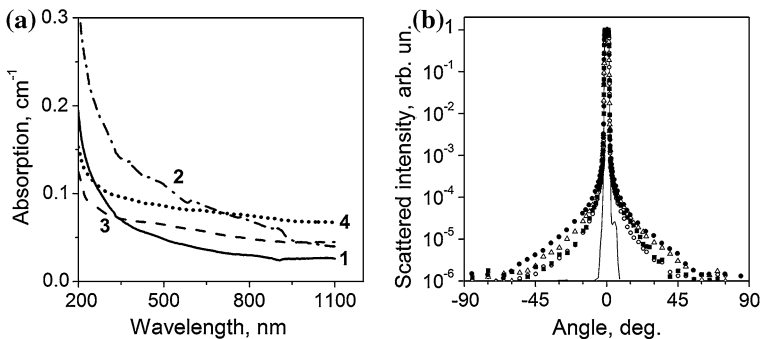
Fig. 24.3 **a** Optical absorption spectra of nominally pure KDP crystals ($L = 10$ mm) cut from pyramidal P (1) and prismatic Pr (3) sectors and corresponding KDP:TiO$_2$ crystals with 10^{-4} wt.% of TiO$_2$: P4 (2) and Pr4 (4); **b**–optical scattering indicatrices of Z-cut samples from prismatic growth sector of KDP:TiO$_2$ crystals at irradiation of 532 nm laser beam: *solid line* indicatrix of freely propagating laser beam, *circle* nominally pure KDP crystal (Pr), *filled triangle* Pr5, *filled square* Pr4, *filled circle* Pr3 samples

The transmittance of KDP:TiO$_2$ SCs in the optical range is also determined by the losses due to elastic scattering phenomena. Angular distribution of scattered light and scattering losses were measured under irradiation of 532 and 633 nm laser sources [17]. The wavelength 532 nm (quantum energy ~ 2.3 eV) is considered to be resonant due to interaction with intrinsic defect states of KDP matrix [18], and surface defect states of anatase NPs [12]. Scattering indicatrices of "thin" samples cut from Pr sector of KDP and KDP:TiO$_2$ crystals at 532 nm are presented on the Fig. 24.3b. Table 24.1 contains the comparison of scattering losses for resonant (532 nm) and nonresonant (633 nm) irradiation of KDP and KDP:TiO$_2$ Z-cuts from P and Pr growth sectors.

Scattering losses in nominally pure KDP crystals are almost independent on the wavelength of the laser beam and growth sector of the crystal (~ 1.0 %). Under nonresonant conditions (633 nm) the incorporation of anatase NPs leads to the rise of scattering losses in composite system (1.7 and 2.6 % for P and Pr growth sectors correspondingly), without dependence on the NPs concentration. However, under resonant conditions (532 nm) we have observed the monotonic rise of scattering losses in P sector with the increase of anatase NPs concentration (1.7 % for P5 and 2.5 % for P4 samples). Another peculiarity is that for Pr sector the scattering losses are reduced nonmonotonically in KDP:TiO$_2$ (Pr4) sample with concentration 10^{-4} wt.% of TiO$_2$.

The last effect is explained by wave-guiding phenomena in TiO$_2$ layers, which are situated along the propagation of the laser beam. The effect is caused by increasing of nonlinear refractive index around anatase layers under relatively high intensities of resonant laser beam. In case of P growth sector, where the layers are tilted to the propagation of laser beam, positive refractive index changes cause the rise of scattered intensity. This fact is also confirmed by the study of refractive index photoinduced variations under CW laser beam self-action [8].

We have studied the photoinduced variations of optical absorption and refractive index of KDP and KDP:TiO$_2$ SCs under self-action of CW laser beam with 532 and 1064 nm wavelengths (resonant and nonresonant conditions). Z-cut samples from both P and Pr parts demonstrate small changes in transmittance with the rise of intensity, with slight dependence of $\text{Im}\left(\chi^{(3)}\right)$ values on the concentration of TiO$_2$ NPs.

Much efficient response was obtained in NLO variations of refractive index (See Fig. 24.4a). The resonant excitation of both intrinsic defect states of KDP matrix [18] and surface defect states of TiO$_2$ nanocrystals [12] by quanta of light with energy ~ 2.3 eV causes low threshold refractive NLO response. The incorporation of anatase NPs leads to the nonlinear refractive index sign inversion: slight self-defocusing effect ($\Delta n < 0$) in nominally pure KDP crystal (Pr) turns to the efficient self-focusing ($\Delta n > 0$) in KDP:TiO$_2$ SCs (curves 1 (Pr) and 2 (Pr4) at initial intensity range at Fig. 24.4a). With the rise of intensity the effect saturates and turns into refractive NLO response that is similar to KDP matrix. The magnitudes of the real part of the cubic NLO susceptibilities $\text{Re}\left(\chi^{(3)}\right)$ at $I < 5$ W/cm^2 for KDP and KDP:TiO$_2$ crystals are presented in Table 24.1. For the P growth
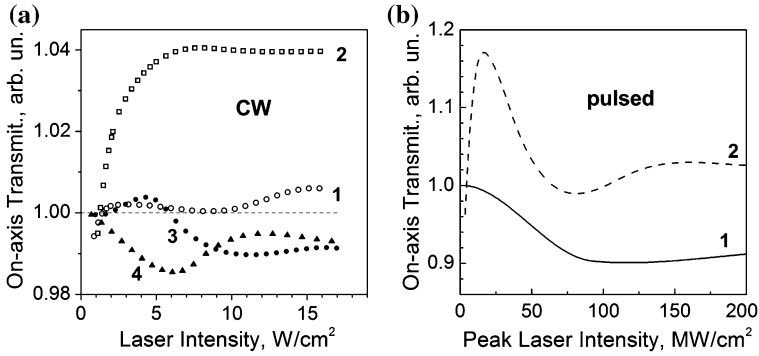
Fig. 24.4 a Normalized on-axis transmittance in the far field versus CW laser intensity of KDP:TiO$_2$ single crystals at 532 nm (1, 2) and 1064 nm (3, 4): *1, 3*—nominally pure KDP crystal (Pr), *2, 4*—Pr4 samples; **b** normalized on-axis transmittance in the far field versus peak laser intensity under self-action of picosecond pulses at 1064 nm: *1*—nominally pure KDP (P), *2*—KDP:TiO$_2$ (P4) Z-cut samples

sector the effect is opposite—self-focusing in KDP(P) turns into self-defocusing in KDP:TiO$_2$ (P5, P4). The significant variation of NLO response $\left(\Delta n \sim 10^{-5}\right)$ of the composite system due to TiO$_2$ NPs incorporation indicates resonant interaction of the subsystem of NPs with intrinsic defects of crystalline matrix.

The CW excitation at 1064 nm of the anatase NPs does not produce significant modification of the SC matrix NLO response. Nevertheless, the NPs induced variations of the NLO refractive index are also positive for Pr growth sector and negative for the P one (see Table 24.1).

Thus, the sign and the magnitude of the photoinduced refractive index variations in KDP:TiO$_2$ SCs under self-action of CW laser beam depend on the concentration of incorporated NPs, crystal growth sector, and irradiation wavelength. The effect can be utilized for characterization of KDP matrix intrinsic defects and incorporated subsystems of NPs [8].

24.4 Second Harmonic Generation

The results of the SHG efficiency study in KDP and KDP:TiO$_2$ SCs without PM conditions (a) and in PM conditions (b) are presented in Fig. 24.5. The realization of the PM approach allowed to obtain higher SH efficiency and to register absolute values of SH pulse energy and quadratic NLO coefficient d_{36}. The utilized "thin" (0.8 mm) samples have no significant effect of the high-order NLO responses on SHG efficiency and are appropriate for the use of given pump field approximation. In "thick" samples (10 mm) we have obtained higher SHG efficiency, but the response is complex due to the impact of the initial step of the pump field depletion and the laser beam self-action effects.
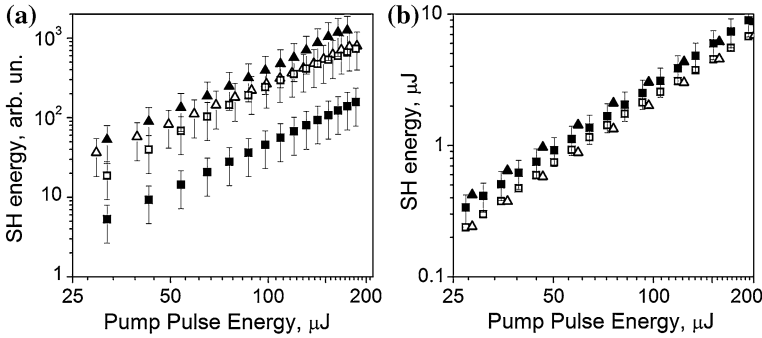
Fig. 24.5 Second harmonic pulse energy versus the pump pulse one at 1064 nm for "thin" Z-cut samples ($L = 0.8$ mm) without PM conditions (**a**), and for "thick" samples ($L = 10$ mm) with PM conditions (**b**): nominally pure KDP P (*triangle*), Pr (*square*) and KDP:TiO$_2$ P4 (*filled triangle*), Pr4 (*filled square*) crystals

The process of SHG without PM conditions of KDP and KDP:TiO$_2$ SCs was studied under ps pulse excitation for Z-cut samples. The obtained experimental dependencies of SH signal versus excitation pulse energy are presented in Fig. 24.5a. We estimated the effective order of NLO response of SH conversion $p:\varepsilon_{2\omega} \sim \varepsilon_\omega^p$ as a slope of linear dependence ranges of the experimental data $\varepsilon_{2\omega}(\varepsilon_\omega)$ in double logarithmic scale. The average slope magnitudes for KDP and KDP:TiO$_2$ are close to 2.0 (see Table 24.2), which indicates the quadratic nature of the process. SHG efficiency decreases about two times for KDP:TiO$_2$(Pr) crystals in comparison with nominally pure KDP(Pr) one in thin samples beyond the PM condition. The obtained reduction of SHG efficiency in KDP(Pr) crystals with incorporated NPs can be explained by resonant absorption of SH wavelength energy and TPA of the fundamental one by TiO$_2$ NPs. Similar experiments for KDP:TiO$_2$ crystals from P sector revealed slight increasing of SHG process efficiency in comparison with nominally pure KDP ones. The values of relative quadratic NLO coefficient d_{36}^{eff} of KDP:TiO$_2$ crystals normalized on corresponding d_{36} coefficient for nominally pure KDP crystals are presented in Table 24.2.

Table 24.2 The effective order of NLO response of SH conversion $p:\varepsilon_{2\omega} \sim \varepsilon_\omega^p$, quadratic NLO coefficient d_{36} at 1064 nm in Z-cut samples (beyond PM condition) and in samples within II type PM condition normalized at the corresponding magnitude of the KDP matrix (P/Pr)

Crystal	Sample	Z-cut		Type II PM	
		p	d_{36}, arb.un.	p	d_{36}, arb.un.
KDP	P	2.00 ± 0.07	1.00	2.00 ± 0.06	1.00
	Pr	1.98 ± 0.02	1.00	2.00 ± 0.03	1.00
KDP:TiO$_2$	P4	2.10 ± 0.04	1.10 ± 0.05	1.90 ± 0.02	0.73 ± 0.04
	Pr4	1.96 ± 0.02	0.50 ± 0.05	2.10 ± 0.04	0.88 ± 0.04

We studied the process of SHG under type II PM conditions in "thin" KDP:TiO$_2$ crystals from P and Pr sectors at energy range up to 200 μJ. The SHG efficiency values for "thin" (0.8 mm) KDP and KDP:TiO$_2$ crystals were calculated from the experimental dependences $\varepsilon_{2\omega}(\varepsilon_\omega)$. The incorporation of anatase NPs into KDP crystalline matrix with concentration 10^{-4} wt.% leads to reduction of the SHG process efficiency for "thin" KDP:TiO$_2$ slices from both P and Pr series.

The SHG efficiency for Pr4 crystal is higher than for the sample P4 with the same NPs concentration from P growth sector. The values of the quadratic NLO coefficient d_{36} for KDP and KDP:TiO$_2$ crystals were estimated. The obtained magnitudes of d_{36} for nominally pure crystals (0.40 pm/V) are in good agreement with reference data [16, 19]. Table 24.2 contains the values of relative quadratic NLO coefficient d_{36}^{eff} of "thin" KDP:TiO$_2$ samples normalized on corresponding d_{36} coefficient for nominally pure KDP crystals. Incorporation of TiO$_2$ NPs into the crystalline KDP matrix with concentration 10^{-5} wt.% leads to significant reduction of the magnitude of effective quadratic NLO coefficient. For the samples with anatase concentration 10^{-4} wt.% the magnitude of d_{36}^{eff} decreases by 25 and 15 % for P4 and Pr4, respectively, in comparison with nominally pure crystals. The values of NLO response order p estimated due to $\varepsilon_{2\omega} \sim \varepsilon_\omega^p$ for the SHG process in "thin" KDP and KDP:TiO$_2$ samples are presented in Table 24.2. In case $p > 2$, it means the deviation from quadric NLO process and impact of higher order NLO responses.

It is well-known that quadratic NLO processes in KDP crystal are mainly attributed to oscillations (vibrations) of $[PO_4]^{3-}$ tetrahedral units [20]. They contribute about 99 % to SHG coefficients, while the volume fraction of anatase NPs in KDP:TiO$_2$ SCs is low in comparison with them. Therefore, we suggest that the reason of observed SHG efficiency decreasing in "thin" KDP:TiO$_2$ crystals is energy absorption by anatase NPs at the excitation wavelength (resonant two-photon excitation of deep defect levels) and the wavelength of SH (resonant excitation).

The SHG efficiency in the "thick" crystals KDP, KDP:TiO$_2$ slices with thickness 10 mm was investigated. The crystals cut from P and Pr growth sectors within PM condition (II type, oe-e) were studied. Dependences of SH pulse energy on the pump energy for nominally pure crystals P, Pr, and crystals with incorporated anatase NPs P4, Pr4 are presented in Fig. 24.5b. The calculated SHG efficiencies η versus pump pulse energy for mentioned crystals are presented in Fig. 24.6a. KDP:TiO$_2$ crystals from both growth sectors demonstrate SHG efficiency enhancement in comparison with pure KDP matrix.

The rise of SHG efficiency in optically thick KDP:TiO$_2$ crystals (Fig. 24.6a) is caused by the developed internal self-focusing of pump irradiation. For the optically "thick" crystals, the spatial profiles of laser beam that passed through the sample were measured. It was shown that sample Pr4 demonstrates significant internal self-focusing of the laser beam (Fig. 24.7a) at intensity ~ 40 MW/cm^2.
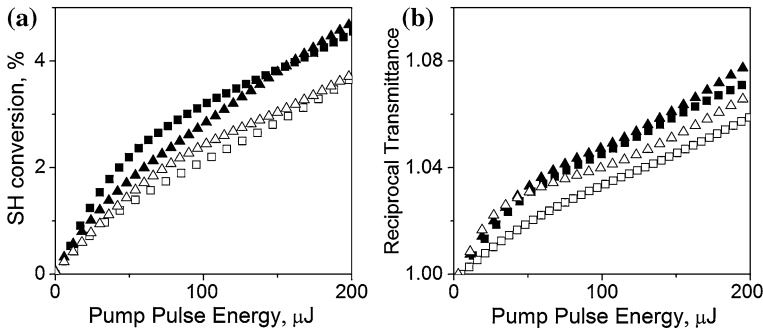
Fig. 24.6 a SHG efficiency versus the pump pulse energy; **b** reciprocal photoinduced pump transmittance variation normalized on spectral transmittance versus the pump pulse energy for the 10 mm plates of the KDP P (*triangle*), Pr (*square*) and KDP:TiO$_2$ P4 (*filled triangle*), Pr4 (*filled square*) crystals

Fig. 24.7 Spatial profiles of transmitted laser beam behind the output faces of 10 mm KDP Pr (*square*) and KDP:TiO$_2$ Pr4 (*filled square*) samples, solid line corresponds to freely propagating laser beam at different peak intensities: $I = 40$ MW/cm^2 (**a**); $I = 4.4$ GW/cm^2 (**b**)

Transmitted laser beam widths (FWHM) registered behind the samples output face are presented in Table 24.3. The data were normalized on FWHM of the freely propagated laser beam at the same registration plane. The efficient narrowing of the beam profile up to 0.6 in KDP:TiO$_2$ SC exceeds the slight focusing ~ 0.9 of the transmitted beam after the KDP crystal. These results correlate with the measurements of the photoinduced variations of the refractive index performed by the spatial profile distortion analysis in the far field due to the self-action effect (See Fig. 24.4b) [3].

Table 24.3 The comparison of relative width (FWHM) of laser beam registered behind the "thick" KDP (Pr) and KDP:TiO$_2$ (Pr4) output faces, normalized on the corresponding one of freely propagated laser beam at the same registration plane

Intensity	Laser	KDP	KDP:TiO$_2$
40 MW/cm^2	1	0.9	0.6
4.4 GW/cm^2	1	0.7	0.7

More than two orders of magnitude raise of the incident pump intensity (Fig. 24.7b) causes similar focusing of the transmitted beams ~ 0.7 for both Pr and Pr4 samples. We suppose that the mentioned self-focusing effect is determined by the matrix response contribution and it is studied for the nominally pure KDP [21] in the similar excitation range.

The temporal analog of the mentioned self-focusing effect is used for the optimization of the SHG of super powerful femtosecond laser pulses. The proper spectrum correction due to the NLO cubic polarizability provides shortening of the pulses and enhancement of the conversion process [22]. We suppose that the KDP:TiO$_2$ application can be useful for the proper self-modulation of ultrashort laser pulses even at moderate peak pump laser intensities.

24.5 Discussion

The photoinduced reduction of the transmitted beam energy with the rise of intensity of pump excitation is determined by two types of two-photon processes: non-dissipative process of SH generation and dissipative one of TPA in crystalline matrix with/without TiO$_2$ NPs. For the qualitative analysis of pump energy transformation via these two channels, we have used the well-known approach based on treating with the SH efficiency (Fig. 24.6a) and reciprocal pump transmittance (Fig. 24.6b) variations. It is possible to perform qualitative analysis of the pump field depletion in plane wave approximation within expression $T^{-1}(I_0) \sim 1 + \beta_{\text{eff}} L_{\text{eff}} I_0$. The slopes of the experimental data at Fig. 24.6b contain magnitude of the effective TPA coefficient β_{eff}. The approach is correct due to the wide aperture laser beams in SCs. A magnitude of the $\beta_{\text{eff}} = \beta^{SH} + \beta$ is determined by two different contributions from non-dissipative SH frequency conversion and the intrinsic TPA effect β.

Reciprocal transmittance plots (Fig. 24.6b) show total losses registered simultaneously with SHG measurements. The corresponding values of effective TPA coefficient β_{eff} in the initial pump energy range (<20 μJ) are higher for KDP:TiO$_2$ than for KDP SCs (42.3 and 21.0 cm/TW for KDP:TiO$_2$ and KDP, respectively). However, simultaneous registration of total transmittance variations of laser beam at fundamental wavelength allowed us to extract nonradiative losses (Fig. 24.8) and corresponding values of TPA coefficients β. At the initial energy range the

estimated values for Pr growth sector are $(4.9 \pm 0.1)/(4.7 \pm 0.1)$ cm/TW for KDP/KDP:TiO$_2$, while the further rise of pump pulse energy leads to significant difference in the β magnitudes: $(5.8 \pm 0.1)/(4.4 \pm 0.1)$ cm/TW. This fact indicates the reduction of the TPA effect in KDP matrix with incorporated TiO$_2$ NPs.

The comparison of TPA coefficients β for P and Pr growth sectors in the initial pump energy range reveals almost an order of magnitude higher value of β in nominally pure P crystal than in Pr one ($\beta_P \sim 8\beta_{Pr}$), and four times higher value for P4 samples than for Pr4 one ($\beta_{P4} \sim 4\beta_{Pr4}$). However, the incorporation of TiO$_2$ NPs into P sector leads to two times reduction of TPA coefficient relatively to pure P matrix: $\beta_{P4} \sim 0.5\beta_P$. Thus, the nonradiative losses reduction effect with the incorporation of anatase NPs is demonstrated in both P and Pr growth sectors, but it takes place in different energy ranges.

Relative gain of the SHG efficiency (a) and nonradiative losses (b) versus pump pulse energy for KDP:TiO$_2$ crystals from both P and Pr sectors, normalized on corresponding dependencies for nominally pure crystals are presented in Fig. 24.9. The significant enhancement (up to 70 %) of the second harmonic generation efficiency was shown in KDP:TiO$_2$ against the nominally pure KDP crystal under the mode-locked YAG:Nd laser pulses due to the observed internal self-focusing effect at moderate pump peak intensity (Fig. 24.9a). The effect is caused by the giant cubic NLO response [12] of the anatase NPs embedded into the matrix and its impact on the proton subsystem of the KDP crystal. Accumulation and long lifetimes of the photogenerated electrons at the NPs interface produces an efficient nanosized capacitor effect that causes SC hydrogen bonds network redistribution in the NPs vicinity.

For the first time, it was shown that the different growth sectors of the KDP and KDP:TiO$_2$ SCs have different SHG efficiencies and nonradiative photoinduced losses rates (Fig. 24.9b). Utilization of the KDP:TiO$_2$ SCs for the SHG gains at least 40 % enhancement in the peak intensity range <2.5 GW/cm^2 for the SC cut from P growth sector and in the $1 - 5$ GW/cm^2 range for the Pr one. Optimization of the SHG efficiency for the definite pump field operation level requires the selection of proper growth sector (P or Pr) of the NLO crystal.

To our mind the further step should be done in direction to obtain smart bulk heterogeneous structures based on KDP SC matrix within different metal oxides

Fig. 24.8 The nonradiative losses rate versus the pump pulse energy in the 10 mm KDP P (*triangle*), Pr (*square*) and KDP:TiO$_2$ P4 (*filled triangle*), Pr4 (*filled square*)
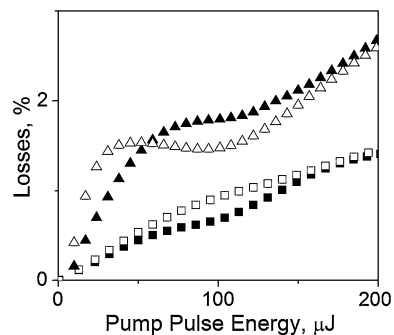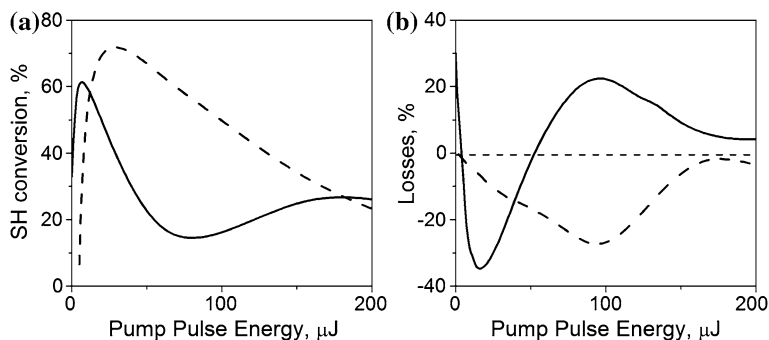
Fig. 24.9 a Normalized SHG efficiency versus the pump pulse energy; **b** relative nonradiative losses versus the pump pulse energy; in the 10 mm KDP:TiO$_2$ P4 (*solid line*) and Pr4 (*dashed line*); normalized on corresponding values for pure KDP crystal

NPs with controlled NLO response [23]. It can be realized by varying the crystallization conditions in order to achieve desymmetrization of the growth sectors and to control the crystal imperfections degree as well as distribution of the NPs in the matrix.

24.6 Conclusions

The possibility of cubic and quadratic NLO response control was presented for the composite functional material based on single crystalline KDP matrix with incorporated anatase NPs. It was shown that KDP:TiO$_2$ is a promising nano-composite NLO functional material for the efficient laser frequency conversion.

We have obtained the significant enhancement (up to 70 %) of the second harmonic generation efficiency in KDP:TiO$_2$ against the nominally pure KDP crystal under the mode-locked YAG:Nd laser pulses due to the observed internal self-focusing effect at moderate pump peak intensity. The effect is caused by the giant cubic NLO response of the anatase nanocrystals embedded into the matrix and its impact on the proton subsystem of the KDP crystal. Accumulation and long lifetimes of the photogenerated electrons at the NPs interface produces an efficient nanosized capacitor effect that causes SC hydrogen bonds network redistribution in the NPs vicinity.

It was shown that the different growth sectors of the KDP and KDP:TiO$_2$ SCs have different SHG efficiencies and nonradiative photoinduced losses rates. Utilization of the KDP:TiO$_2$ SCs for the SHG gains at least 40 % enhancement in the peak intensity range <2.5 GW/cm^2 for the SC cut from P growth sector and in the $1-5$ GW/cm^2 range for the Pr one. Optimization of the SHG efficiency for the definite pump field operation level requires the selection of proper growth sector (P or Pr) of the NLO crystal.

It was shown that the NLO refractive index variation is a very sensitive tool to perform the diagnostics of the KDP and KDP:TiO$_2$ SCs within CW (at 532 nm) and pulsed picosecond range (at 1064 nm) laser radiation due to the resonant excitation of the transient intrinsic defect states of the SC matrix and surface states at the anatase NPs interface. It can be also applied for the photoinduced PM conditions adjustment for the SHG and light parametric interaction processes.

References

1. Benedict JB, Wallace PM, Reid PJ et al (2003) Adv Mater 15:1068–1070
2. Rifani M, Yin Y-Y, Elliott DS et al (1995) J Am Chem Soc 117:7572–7573
3. Pritula I, Gayvoronsky V, Kolybaeva M et al (2011) Opt Mater 33:623–630
4. Pritula I, Gayvoronsky V, Kolybaeva M et al (2008) Funct Mater 15:420-428
5. Rudneva EB, Manomenova VL, Voloshin AE et al (2006) Crystallogr Rep 51:142–149
6. Bensouici A, Plaza JL, Halimi O et al (2008) J Optoelectron Adv Mater 10:3051–3053
7. Grachev V, Vrable I, Gayvoronsky V et al (2012) J Appl Phys 112:014315 (p 11)
8. Gayvoronsky V, Kopylovsky M, Yatsyna V et al (2012) Ukr J Phys 57:157–165
9. Pritula I, Bezkrovnaya O, Kolybayeva M et al (2011) Mater Chem Phys 129:777–782
10. Borshch A, Brodyn M, Gayvoronsky V et al (2004) Ukr J Phys 49:196–202
11. Lee Smith W, Weber MJ (eds) (1988) CRC handbook of laser science and technology, vol 3, Part 1, CRC Press Inc., Boca Raton, Florida, pp 229–258
12. Gayvoronsky V, Timoshenko V et al (2005) Appl Phys B 80:97–100
13. Sheik-Bahae M, Said AA, Wei T et al (1990) IEEE J Quant Elect 26:760–769
14. Gayvoronsky V, Yakunin S, Nazarenko V et al (2005) Mol Cryst Liq Cryst 426:231–241
15. Gayvoronsky V Ya, Kopylovsky MA, Brodyn MS et al (2013) Laser Phys Lett 10:035401 (p 5)
16. Nikogosyan DN (2005) Nonlinear optical crystals: a complete survey. Springer, New York
17. Gayvoronsky V, Starkov V, Kopylovsky M et al (2010) Ukr J Phys 55:875–884
18. Ogorodnikov I, Yakovlev V, Shul'gin B et al (2002) Phys Sol State 44:845–852
19. Nelson DF (2000) High frequency properties of dielectric crystals, Landolt-Bornstein New series, Group III, vol 30, Springer, Berlin
20. Lin Zh, Wang Zh, Chen Ch et al (2008) J Chem Phys 118:2349 (p 8)
21. Ganeev R, Kulagin I, Ryasnyansky A et al (2004) Opt Comm 229:403–412
22. Mironov Yu S, Lozhkarev VV, Ginzburg VN et al (2012) IEEE J Sel Top Quant Electron 18:7–13
23. Brodyn M, Gayvoronsky V (2012) International Conference on OMEE Lviv, Ukraine, p 197, 3–7 Sep 2012

Index